Localized Excitations in Superconducting Atomic Contacts: PROBING THE ANDREEV DOUBLET

Landry Bretheau

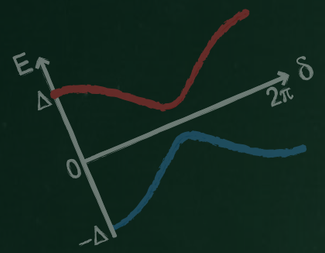

This thesis discusses two experiments highlighting the existence of a fermionic degree of freedom in the ***Josephson effect***: the ***Andreev doublet***. They are both performed on the most basic Josephson element, a ***one-atom contact*** between two superconducting electrodes.

In the first one, we observed the disappearance of the supercurrent, which reflects the ***spontaneous trapping of a quasiparticle*** in one of two Andreev bound states.

In the second experiment we achieved the ***photon-absorption spectroscopy*** of this two-level system, using a Josephson junction as an integrated on-chip microwave emitter and detector. The observed spectra are well accounted for by a spin-boson model including the Andreev doublet and an electromagnetic mode of the environment.

Cette thèse décrit deux expériences mettant en lumière l'existence d'un dégré de liberté fermionique dans l'***effet Josephson***: le ***doublet d'Andreev***. Elles sont toutes les deux réalisées sur l'élément Josephson le plus élémentaire qui soit, un ***contact atomique*** entre deux électrodes supraconductrices.

Dans la première, nous avons observé la disparition du supercourant, qui traduit le ***piégeage spontané d'une quasiparticule*** dans l'un des deux états liés d'Andreev.

Dans la seconde, nous avons réalisé la ***spectroscopie photonique*** de ce système à deux niveaux, en utilisant une jonction Josephson à la fois en tant qu'émetteur et détecteur microonde. On peut bien rendre compte des spectres observés avec un modèle spin-boson incluant le doublet d'Andreev et un mode électromagnétique de l'environnement.

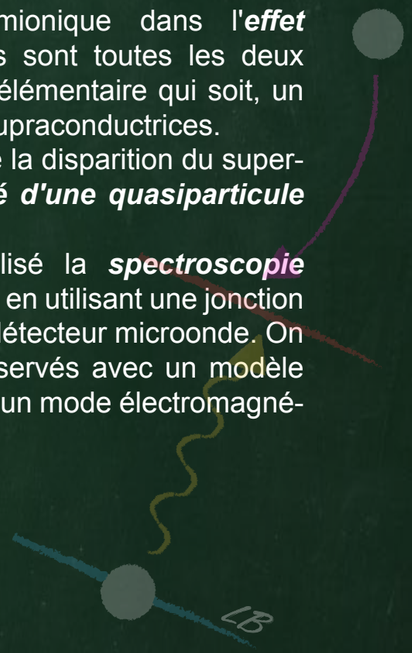

2013 | LOCALIZED EXCITATIONS IN SUPERCONDUCTING ATOMIC CONTACTS: PROBING THE ANDREEV DOUBLET

Landry BRETHEAU

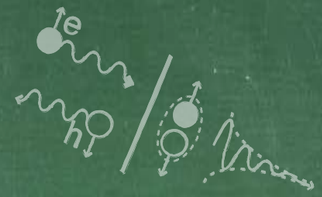

Localized Excitations in Superconducting Atomic Contacts: PROBING THE ANDREEV DOUBLET

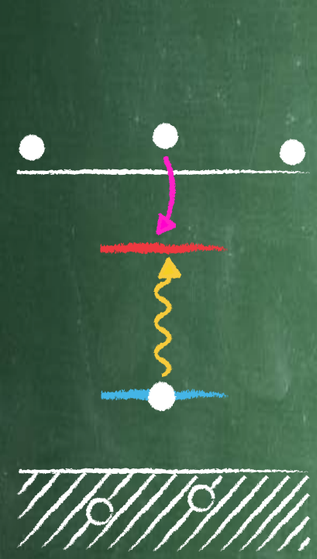

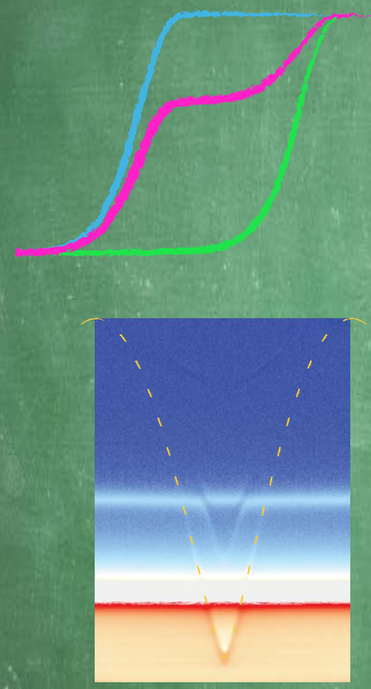

Landry BRETHEAU
Quantronics Group
SPEC - CEA Saclay

LOCALIZED EXCITATIONS IN SUPERCONDUCTING ATOMIC CONTACTS: PROBING THE ANDREEV DOUBLET

Ph.D. dissertation
by

Landry BRETHEAU

to obtain the degree of
DOCTEUR de l'ECOLE POLYTECHNIQUE

Ph.D. defense on February 1, 2013

Committee in charge:

Richard DEBLOCK
Antoine GEORGES
Leo KOUWENHOVEN
Alberto MORPURGO (Rapporteur)
Yuli NAZAROV (Rapporteur)
Cristián URBINA

Ph.D. Thesis directed by Hugues POTHIER and Cristián URBINA
realized in the Quantronics Group
Service de Physique de l'Etat Condensé, CEA-Saclay

Cover

Left picture: sketch of the energy spectrum of the Andreev bound states in the one-particle picture (see Part I, Fig. 2.8)

Upper right picture: anomalous switching probability due to quasiparticle trapping (see Part II, Fig. 4.12)

Lower right picture: measured excitation spectrum of the Andreev bound states (see Part III, Fig. 6.6)

Cover design by Landry Bretheau and Ioana Ocnarescu

An electronic version of this dissertation is available at
http://iramis.cea.fr/drecam/spec/Pres/Quantro/static/publications/phd-theses/
http://hal.archives-ouvertes.fr/

À mon Papa

C'est à force d'observations, de réflexion, que l'on trouve.
Ainsi, piochons, piochons continuellement.

— Claude Monnet

Il est idiot de monter une côte à bicyclette
quand il suffit de se retourner pour la descendre.

— Pierre Dac

L'imagination est la plus scientifique des qualités.

— Charles Baudelaire

Quantum physics makes me so happy.
It's like looking at the universe naked.

— Sheldon Cooper

J'reprendrais bien un peu de purée !

— Latex

REMERCIEMENTS

Bien qu'en général loquace, l'écriture de ces remerciements m'est fort difficile. C'est assurément parce qu'ils signifient beaucoup tant j'ai de la gratitude et même souvent de l'amitié pour les personnes qui apparaissent dans ces quelques lignes. Je pourrais simplement les résumer à un MERCI suivi d'une liste de noms, un peu comme à la fin d'un film, mais cela resterait assez insipide. En réalité, il s'agit d'être sincère, et d'agrémenter ces mercis d'anecdotes personnelles, drôles, si possible sans tomber dans la caricature et tout en restant concis. Devant la difficulté de l'exercice, j'ai un temps pensé proposer une page de remerciements vierge ou le lecteur et heureux possesseur de cette thèse pourrait écrire ses propres remerciements à mon égard. Pris par un excès de modestie et comme je sais qu'il s'agit du chapitre qui sera le plus lu, je me lance.

Les trois années (plus quelques mois) de thèse que j'ai passées au sein du groupe Quantronique ont été extrêmement intenses, d'un point de vue intellectuel, personnel et émotionnel.

En premier lieu, je tiens à remercier mes deux directeurs de thèse préférés Hugues Pothier et Cristián Urbina. Merci de m'avoir supporté pendant ces trois ans de thèse, merci pour votre générosité, votre disponibilité et votre motivation au quotidien (et merci pour le temps très conséquent que vous avez consacré à la correction de ce manuscrit). Quelle belle école de découvrir la recherche avec vous ! Chose assez extraordinaire, vous réussissez à allier rigueur, haut niveau, modestie, enthousiasme et autodérision. Cela se traduit par un travail d'équipe de qualité et dans la bonne humeur. On peut difficilement rêver mieux comme encadrants de thèse et comme collègues. Hugues, merci pour ton sens de l'humour sans pareil. J'adore ta vivacité d'esprit et ta faculté à conserver la moitié de ton cerveau à faire des blagues ou des vannes. Tu rends le quotidien plus léger. Cristián, merci pour ton humanité et ta sagesse. On a tellement discuté ensemble, et pas uniquement de physique. J'ai beaucoup appris et je te ressens un peu comme de ma famille.

Daniel Estève, merci pour ton affection, ton caractère franc du collier, et pour tous les moments que tu as passé à m'expliquer la physique au tableau. Si le groupe Quantronique est une famille, tu y es pour beaucoup et tu y assumes très bien le rôle de père. Face aux bébés, tu es parfois même en mode papy gâteau, et j'adore comme tu harcèles les gens avec ton tact légendaire d'un petit "alors, c'est pour quand le bébé ? Il faut s'y mettre là !". Je me souviens en particulier de ce formidable banquet chez toi, où on avait pu se délecter d'huitres format steak. Et le plaquage façon troisième ligne que tu avais mis à Andreas reste vraiment mémorable.

Merci Pief Orfila pour ta disponibilité, ta bienveillance et ton grand sourire : tu rends la vie au labo plus simple. Et merci aussi pour ton sens de la dérision à l'égard de tous les gens du groupe.

Marcelo Goffman, merci pour ton grand cœur et ta bonne humeur permanente. Même si c'était seulement pendant quelques mois, j'ai adoré travailler avec toi sur l'embryon de manip Majorana, et j'ai beaucoup appris. Et merci pour nous avoir donné accès à ta canne à 300 mK, et avoir gardé le sourire quand j'ai grillé les fils connectés aux batteries. Ton sourire justement et tes "che boludo" apportent le soleil dans le labo.

Merci Denis Vion pour ta disponibilité et ta générosité en toutes circonstances. Que ce soit pour le MEB, Mathematica, Sonnet, tu as toujours été présent pour m'aider ... et aider l'ensemble de la communauté. En plus d'être un super physicien, tu es un peu une sorte d'homme-outil qui pousse la maîtrise de l'outil jusqu'à la compréhension de la logique de conception de l'outil même. Logique, après générosité, c'est un autre mot qui te caractérise. Tu es même le Torquemada de la logique et de l'intégrité ; c'est fascinant.

Merci à Fabien Portier, mi-quantronicien, mi-nanoelectronicien et mi-molette (ex-travieille). Tu occupes une place bien à part pour moi. J'aime tellement parler physique, écouter de la zic, jouer à la coinche et manger des abats avec toi. Merci pour avoir participé à l'élaboration de ce pot dantesque. Et simplement, merci pour ta disponibilité, ta générosité et ton amitié.

Merci à Pascal Senat pour la conception de la mécanique basse température et de la boîte de camembert du frigo. Et merci pour les discussions de tous les jours, les vannes et le très bon esprit lors des pots. Par contre, quelle faute de goût d'aller à la machine à café !

Merci à Philippe Joyez pour le grand temps passé à parler notamment théorie $P(E)$ et états d'Andreev, et le petit temps à tenter de Majoraniser ensemble. Face à ton manque de loquacité, j'ai toujours aimé te rentrer dans le lard pour te forcer à répondre à mes questions. Merci également pour les bières chez toi quand tu me détournais de mon entraînement de volley.

Patrice Bertet, merci pour tout le temps que tu m'as donné à m'expliquer la physique. J'ai toujours adoré parler avec toi, car tu es d'une clarté rare. Merci aussi pour ton sens de l'humour quand je te charriais, notamment le fameux "Mais Patrice, tu ne connais pas le plaisir ..." de Cristián, que j'avais stoppé avant la fin de sa phrase (alors qu'on parlait de jouer au foot et marquer des buts).

Merci à Thomas David, mon mentor en mécanique, toujours prêt à donner un coup de main et à discuter Itech, jeux videos et autres... Mention spéciale à ta journée des nouveaux arrivants en mode *May the force be with you*.

Le groupe Quantronique, ce n'est pas que des vieux croutons, c'est aussi une armée de thésards et post-docs en pleine fleur de l'âge.

En premier lieu, merci à mes deux post-docs, Maciej "baguette" Zgirski et Çağlar Girit (freestylise it !). Maciej, it was great facing the poisoning experiment together. Thanks for teaching me nanofabrication techniques, for the long talks at night and for your honesty about your thoughts, even the most conservative ones. Çağlar, ça a été tout simplement extraordinaire de travailler avec toi. Tu m'as tellement appris. Merci pour ta générosité, ta passion, ta confiance et ton soutien dans les moments difficiles. Je me souviens en particulier que tu m'avais confié (très tôt) que Claire était enceinte du futur Jin et ça m'avait beaucoup touché.

Merci à Quentin Le Masne d'avoir eu la patience de me coacher lors de mes trois mois de stage précédant la thèse, et notamment de m'avoir fait découvrir les arcanes de la nano-fabrication. Merci à Andreas Dewes et Yuimaru Kubo, mes voisins de Bures-sur-Yvette, pour les soirées passés ensemble autour de bières allemandes et sakés japonais. Andreas, merci pour cette soirée magique après le pot de thèse de Simone ou tu as laissé JD conduire ta voiture. Yui, merci pour les supers cadeaux que tu m'as rapporté du Japon : gomu gomu no aligato ! Merci à Carles Altimiras, copain en devenir, pour ta passion contagieuse pour le foot, la physique, la bonne bière, et la bonne bouffe. Muchas gracias à Leandro Tosi pour m'avoir fait découvrir le maté : j'ai adoré le temps qu'on a passé ensemble, à maniper, discuter, jouer au foot et boire des bières ; c'était court mais intense.

Merci également à François Mallet que j'apprends à découvrir maintenant, Charis Quay qui rigole si fort, Florian Ong qui me faisait rêver en tongs en salle blanche (j'ai été soft, j'ai pas fait de blague sur ong et tong), Agustin Palacios-Laloy pour le coaching sur Lyx, Max Hofheinz pour les discussions physiques qu'on a eu et le super accueil à Grenoble, Romain Lauro blagueur chuchoteur en séries, Vivien Schmitt mention spéciale bon esprit lors des pots (et ton stock de gnole dans ton bureau en cas de coup dur), Cécile Grezes qui n'oubliait pas de me charrier régulièrement, Olivier Parlavecchio et son goût si prononcé pour le jaune, Michael Stern et son "ça va bien ?" quotidien où on sent qu'il se soucie vraiment de comment ça va, et Xin Zhou toujours fraiche et souriante.

Enfin, merci à Jean-Damien Pillet qui occupe une place bien à part ici étant donné qu'on est "super copains de la vie" depuis la primaire. C'était tout simplement génial de bosser dans le même groupe. Ça reste toujours un peu mystérieux pour moi qu'on se retrouve ensemble, après des chemins disjoints mais parallèles, et qui ne sont reliés qu'au moment de la thèse. La seule explication que je vois, c'est qu'on a tous deux excellent goût !

Mais le SPEC ne se réduit pas au groupe Quantronique. Merci à nos plus proches voisins du groupe nanoélectronique. Christian Glattli, c'est toujours passionnant de parler physique avec toi (et merci pour Moriond!). Patrice "Iznogoud" Roche, ça change d'air d'avoir un physicien comme toi ; merci en particulier pour l'ensemble de tes blagues, et tout particulièrement pour celle des prêtres sous la douche qui reste la meilleure que j'ai entendu ces cinq dernières années. Preden Roulleau, c'est marrant comme nos routes se sont recroisées après ces randos sur glacier dix ans plus tôt à Aussois. Merci aussi à Iouri Moukharski, l'ours venu du froid (et prends bien soin de ma petite AX !).

Merci aux nanomagnétiseurs, Olivier Klein, Michel Viret, Grégoire de Loubens, Claude Fermon, Myriam Pannetier-Lecœur et tous les jeunes pour nous avoir concurrencés sur la régularité des pots et des sessions gâteaux. Grâce à mon copain Benjamin Pigeau "marathonveganman" j'ai pu m'y incruster un bon nombre de fois ! Merci aussi à Olivier Rousseau pour tout le Kapton que tu nous as filé. Enfin merci aux membres des autres groupes qui participent à la vie du labo et que l'on peut croiser au détour de la salle café : entre autres Eric Varoquaux et Tito Williams, qui démontrent bien que la physique ça conserve, Alan Braslau, et mon fillot Ivan Dornic, docteur ès gravier. Merci à Jean-Marc Luck (dit Matthieu) de l'IPHT pour

son aide sur mes petites questions de physique quantique. Merci également aux thésards des autres groupes qui ont participé à la bonne ambiance du labo, entre autres Rémy Lassalle-Balier (Mr macaron), Phuong-Anh Huynh, Julie Dubois, Andrei Mostovoi, Aurélie Solignac et Joël Acevedo (respo foot).

Je tiens également à remercier les personnes qui font fonctionner le labo au quotidien. A la direction, Eric Vincent, François Daviaud et Patrice Roche. Au secrétariat, Nathalie Royer, Corinne Kopec-Coelho et Dijana Samson, les mamans du SPEC : Nathalie et Corinne, merci d'avoir eu la patience de m'expliquer une bonne dizaine de fois comment remplir un ordre de mission. A l'entretien, Nadine Le Bail avec qui j'ai pris plaisir à faire un petit brin de causette chaque jour. A l'atelier, Vincent Padilla, Dominique Duet, Jacques Prudowski, et Jean-Claude Tack : merci en particulier à Jean-Claude et Dominique pour la fabrication des pièces de la manip, et spéciale dédicace à Vincent pour ses conseils en harmonica et mobylette et pour sa folie grolandaise. J'y greffe Patrice Jacques qui m'a sauvé la mise en débouchant une bouteille d'hélium à coup de marteau. A la cryogénie, Philippe Forget, Mathieu de Combarieu et Patrick Pari : merci PP pour le rab d'hélium de ton doigt froid, pour la jolie manip de fontaine d'hélium superfluide avec le cryostat en verre, et pour si bien jouer ton personnage de PP ronchon. Au magasin, Pierre Janvier, toujours sympa et disponible et qui a toujours réussi à nous dégoter, même à la dernière minute, des bouteilles d'hélium. N'oublions pas le "maître de chantier" Jean-Michel Richomme et sa sonnerie Panthère Rose, la toujours souriante Nadine Genand-Riondet pour les subventions écoles, Claudine Chaleil responsable sécurité et salle blanche (avec Pief), et Roland Tourbot à la "bondeuse". J'ai également une pensée spéciale pour certains membres du CEA qui nous facilitent le travail au quotidien : les fans du PSG, de moto et de Darth Vador au service des badges, le super responsable sécurité et son goût pour les photos de bébés carbonisés, et les membres de la FLS pour les parties de cache-cache dans la forêt.

Pendant ma thèse, j'ai eu la chance de discuter avec de nombreux scientifiques qui m'ont permis d'améliorer ma compréhension de la physique. En premier lieu je remercie Manuel Houzet avec qui j'ai beaucoup échangé, ce qui s'est traduit par une collaboration sur la modélisation de notre manip (merci pour l'invitation à Grenoble !). Muchas gracias a los tres hispanohablantes Alfredo Levy Yeyati, Juan Carlos Cuevas y Sebastián Bergeret, por el recibimiento en Madrid y San Sebastián. Alfredo, te agradezco el haberme iniciado, junto a JD, al formalismo de Keldysh, y el haber sabido guardar silencio sobre nuestras correrías nocturnas por Madrid. Juan Carlos, gracias por habernos llevado de tapas por los mejores bares de Madrid. Sebastián, gracias por tu buen humor, tu pasión sin límites por la física y tu risa inimitable. Thanks to Hermann Grabert and Daniel Urban to show me the generalised Bogoliubov de Gennes formalism and to allow me to come to Capri. Special thanks to Vitaly Shumeiko and Yuli Nazarov for all you taught me about the Andreev bound states: thanks to you I understood the odd states ! And thanks Yuli for your "mauvaise foi" about $P(E)$ theory: "I call $\hbar$ banana and there is no longer anything quantum". Merci à Michel Devoret pour son grand optimisme à chacune de ses visites : "des états impairs avec 100 µs de temps de vie, ça vous fait un ex-

cellent qubit !". Thanks to Leonid Glazman for his questions about the odd states on the ski trails in the italian Alpes. Merci à Grégoire Ithier pour m'avoir fait visiter son labo pendant mon séjour à Windsor, à Eva Dupont-Ferrier pour son super accueil à Grenoble, and to Leo Kouwenhoven, Ronald Hanson and Leo Di Carlo for their warm welcome at Delft. Merci à Hélène Bouchiat pour les discussions dans les trains ou RER, à Silvano de Franceschi, sympa en toutes circonstances, au meethique Thierry Martin (j'ai un souvenir ému du plateau de fruits de mer "à la bonne franquette" en bord de mer) et au caustique Jérôme Cayssol (tu me dois toujours une bière). Merci aussi à Jean-Noël Fuchs, Hélène le Sueur, Tackis Kontos, Thibaut Jonckheere, Jacqueline Bloch, Julien Gabelli, Bertrand Reulet, Marco Aprili, Hervé Courtois et Francesco Giazotto.

Je souhaite aussi remercier mes anciens professeurs avec qui j'ai continué à échanger. Merci Michel Héritier pour votre bienveillance sur mon avancée dans la science. Un grand merci à Benoît Douçot qui a toujours répondu à mes questions par email et n'a jamais rechigné à venir faire un tour à Saclay quand je le lui demandais. Je ne cesserai jamais d'être impressionné par ta profondeur en physique. Par contre, tu ne connais pas Lapinot ! Merci à Marc Gabay pour m'avoir pris comme chargé de TD (et merci KV Pham) et avoir répondu à mes questions existentielles sur les supras. Merci aussi à Pascal Simon pour les discussions Majorana, pour Aussois et la Sardaigne et pour les vannes.

Une thèse c'est aussi l'opportunité au travers des conférences et des écoles de rencontrer d'autres jeunes apprenti-chercheurs de par le monde : Denis (*I like*), Alina, Mireia, Jörn and Pierre at Windsor, la team des grenoblois, Nico, Romain, Sergent, Whitehouse, Mathias à La Thuile, Anders and Alessandro at Capri, Natalia en Sardaigne, François et Mathias à Aussois. And Vincent, Daniel, Attila, Maja, Kun thanks for the warm welcome at Delft.

I would like to thank very much the members of my thesis committee. First, thanks to the "rapporteurs" Alberto Morpurgo and Yuli Nazarov for taking the time to read the whole manuscript, and for writing such enthusiastic reviews. Special thanks to Yuli who made me king for a day on his blog with his kind words "The discussion with the opponent could have been more smooth, yet Landry managed to stay within the restrictions of formal politeness". Richard Deblock, un grand merci pour ta lecture si attentive de mon manuscrit et l'ensemble des corrections que tu as fait l'effort de me transmettre. Leo Kouwenhoven, thanks for being part of my thesis committee, even if you could not be present the D-day. I'm glad that you are doing well now. Thanks for your interest and for your kind invitation to come to Delft. Enfin merci au président du jury, Antoine Georges, pour m'avoir fait découvrir "la physique des électrons dans les solides" et m'avoir conseillé, il y a de ça cinq ans, d'aller faire mon stage de M1 dans le groupe Quantronique. Je n'y étais pas allé, appelé par les sirènes parisiennes après deux ans passées sur le plateau de Palaiseau, mais j'avais bien gardé dans un coin de ma tête qu'il s'agissait d'une destination de choix.

Je veux aussi remercier ma nouvelle équipe au LPA, le groupe Qélec : Benjamin Huard, François Mallet, Philippe Campagne-Ibarcq et Manu Flurin. Merci pour ce

bel accueil et toutes les belles andouillettes à venir !

Merci à tous mes copains, qui ont vécu de près ou de loin mes trois années de thèse : Olivier, Jd, Cécile, Lolo, Romain, Cristian, Pouille, Marion, Michou, Hélène, Lorenzo, Emma, Cyril, Hédi, Koju, Stan, Fabien, Benjamin, Flo, Pc, Otilia, Mihai et Roxana. Merci d'être mes amis et d'être là dans les moments heureux et difficiles. Merci de me charier et me remettre régulièrement en place. Et merci d'être venus en masse à ma soutenance. On a quand même descendu une vingtaine de bouteilles !

Pour finir, je veux remercier ma famille pour leur amour et leur soutien sans borne. Merci à mon Papa, qui m'a fait tel que je suis et qui me manque tellement. Merci à ma Môman, qui m'a abreuvé et m'abreuve de son amour inconditionnel. Merci à ma meilleure grande soeur Lucile (virgule) que j'adore ; on sera toujours là l'un pour l'autre. Merci à mes grands-parents pour la merveilleuse usine à souvenir qu'ils m'ont offerte. Enfin, merci à ma Ioio, mon souffle, ma folie, mon picpalak pour la vie.

Le groupe quantronique fin 2010.
Devant, de gauche à droite : Çağlar Girit, Dijana Samson, Max Hofheinz, Patrice Bertet, Philippe Joyez, Denis Vion, Yuimaru Kubo, Landry Bretheau, Cristián Urbina, Thomas David. *Derrière, de gauche à droite :* Daniel Estève, Pief Orfila, Pascal Senat, Andreas Dewes, Hugues Pothier, Marcelo Goffman.

CONTENTS

ACRONYMS

ABS	Andreev bound states
JC	Josephson channel
JJ	Josephson junction
AC	Atomic contact
MAR	multiple Andreev reflections
JJS	Josephson junction spectrometer
DCB	dynamical Coulomb blockade

1 INTRODUCTION

A variety of circuits and devices have been developed based on the Josephson effect since its prediction and observation fifty years ago [1, 2, 3, 4, 5]. Currently, Josephson circuits that behave like artificial atoms [6] are revolutionizing the way we probe and exploit the laws of quantum physics. Experiments embedding these artificial atoms in microwave cavities can even surpass their atomic physics counterparts [7]. The crucial component in these circuits is the Josephson tunnel junction: two superconducting electrodes separated by a thin insulating barrier allowing weak tunneling of Cooper pairs. A Josephson junction (JJ) in a circuit acts as an anharmonic oscillator whose dynamics can be described in terms of a single bosonic degree of freedom: the superconducting phase difference across the junction. However, the Josephson effect is not only observed in tunnel junctions but also in other weak links such as point contacts, graphene, carbon nanotubes, semiconducting nanowires, and thin ferromagnetic layers [8]. The microscopic understanding of the Josephson effect applicable to all weak links is that discrete states called **Andreev bound states** [9, 10, 11], localized at the weak link, carry the supercurrent [12, 13, 14, 15]. Andreev states come in pairs in each conduction channel of the weak link, symmetric in energy about the Fermi level. A pair of states behaves like a spin-1/2 and introduces a fermionic degree of freedom to the Josephson effect. My thesis explores this additional fermionic degree of freedom, ignored in Josephson circuits developed up to now.

Is it possible to address and control "Andreev spins"? This thesis describes two experiments designed to answer this question using **atomic contacts between superconducting electrodes**. Superconducting atomic contacts are simple, ideal weak-links. They accommodate only a small number of channels, whose transmission can be varied and measured *in situ* [16, 17]. They allow quantitative comparison between theory and experiment, with no adjustable parameters. In our work, we have used nano-fabricated break junctions [18] to obtain atomic contacts. This allows for very stable contacts which can be integrated in on-chip circuits.

Part I of this manuscript presents the main concepts of the mesoscopic Josephson effect and of Andreev bound states (ABS) in a personal view developed as I worked through the vast literature on the subject. It also presents experimental evidence for the existence of ABS prior to my thesis. Although much had been achieved in atomic contacts and in carbon nanotubes, the transition between the two ABS in a channel had never been directly observed. **This was the main goal of my thesis work.**

While pursuing this goal we discovered that under some conditions **a single quasiparticle can be trapped in the Andreev bound states** of an atomic contact and stay there for remarkably long times. As we will see in Part II, this **"poisoning"** phenomenon illustrates the different types of microscopic excitations and the fermionic character of the ABS.

Using a JJ as an integrated on-chip microwave emitter and detector, we were able to perform **the first photon-absorption spectroscopy of Andreev bound states**. This experiment is described in Part III, which also contains the quantum theory I developed to explain the results. This result opens the way to coherent manipulation of this two level system, an Andreev qubit.

Part IV presents the experimental techniques that were used during this work.

Finally, several detailed calculations and additional experiments are presented in separate appendices (Part V).

1.1 Andreev bound states in a nutshell

Within the mesoscopic theory of the Josephson effect, the basic Josephson weak link is a single conduction channel of arbitrary transmission probability τ connecting two superconducting electrodes. For a channel shorter than the superconducting coherence length, the Josephson coupling between both sides is established by a single pair[1] of ABS [13, 14, 15]. As depicted in the left panel of Fig. 1.1, in the one-particle picture of the superconducting state [19] the ABS lie at energies $\pm E_A$ inside the superconducting gap $[-\Delta, \Delta]$:

$$E_A = \Delta\sqrt{1-\tau\sin^2\left(\frac{\delta}{2}\right)}. \tag{1.1}$$

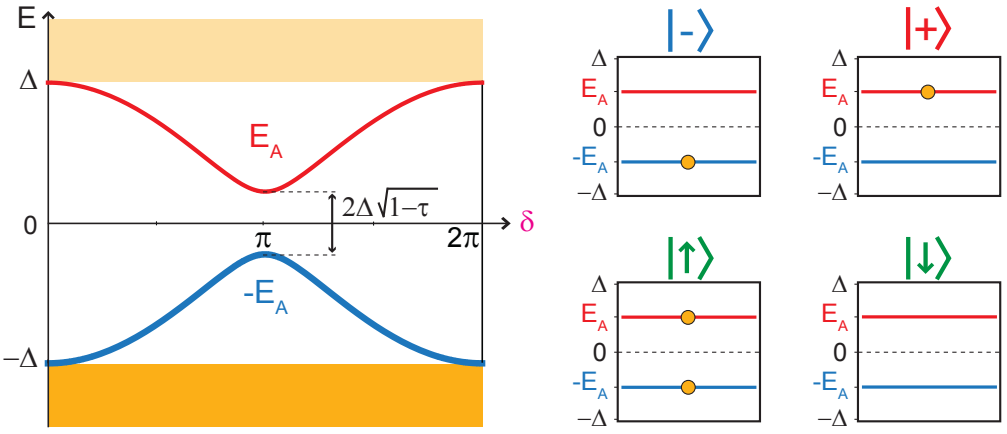

Figure 1.1: **Left**: Energy spectra in the one-particle picture of the ABS as a function of the phase difference δ between two superconducting electrodes through a single short channel $\tau = 0.95$. **Right**: The four states obtained with various occupation of the ABS.

These fermionic microscopic states are similar to Cooper pair states of the bulk superconductor (see Chapter 2). The crucial difference is that their condensation energy $-E_A$ can be smaller in absolute value than the energy gap Δ and depends on the phase difference δ. Contrary to states in the continuum, they are spatially localized inside the weak link when their energy is deep inside the gap. The right panel of Fig. 1.1 shows the four global states resulting from the possible fermionic

1 A new pair of ABS is likely to appear each time the length exceeds a multiple of the superconducting coherence length.

occupations of the ABS. There are two **even states**: the ground state $|-\rangle$ and the excited state $|+\rangle$ with energies $-E_A$ and $+E_A$, respectively. There are also two **odd excited states** [20] with zero energy, denoted by $|\uparrow\rangle$ and $|\downarrow\rangle$, obtained by adding or subtracting a single quasiparticle from the system in the ground state. The even and odd denomination comes from the number of electrons participating in these localized states. The two odd states are generally ignored in the literature because parity conservation is implicitly assumed.

Because phase is the quantum conjugate variable to the number of Cooper pairs that have gone through the channel, the phase dependence of the Josephson coupling energy leads to a supercurrent. In the ground state it is given by:

$$I_A = \frac{1}{\varphi_0}\frac{\partial(-E_A)}{\partial\delta} = \frac{\Delta}{4\varphi_0}\frac{\tau\sin(\delta)}{\sqrt{1-\tau\sin^2\left(\frac{\delta}{2}\right)}} \tag{1.2}$$

where $\varphi_0 = \hbar/2e$ is the reduced flux quantum. The energies and supercurrents of the four states $|-\rangle$, $|+\rangle$, $|\uparrow\rangle$ and $|\downarrow\rangle$ are represented in Fig. 1.2. The two even states

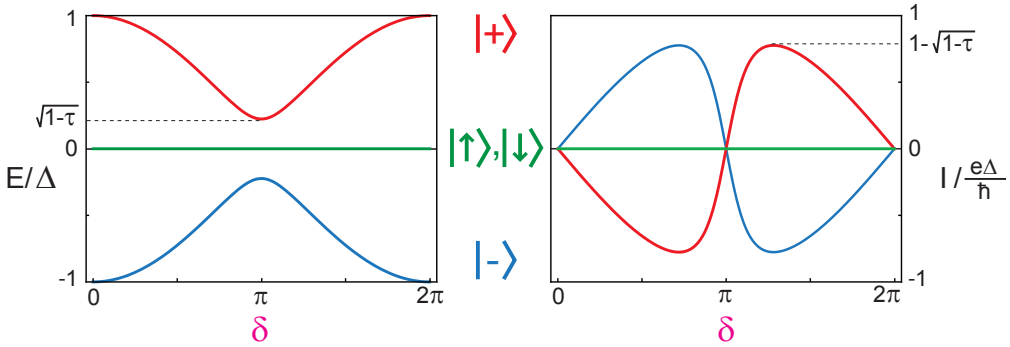

Figure 1.2: Energies (**left**) and supercurrents (**right**) of the four different configurations of the ABS versus the phase difference for a superconducting short single channel of transmission $\tau = 0.95$. Whereas the even states $|-\rangle$ and $|+\rangle$ carry opposite supercurrent, the odd ones $|\uparrow\rangle$ and $|\downarrow\rangle$ do not carry any.

$|-\rangle$ and $|+\rangle$ carry opposite supercurrents $+I_A$ and $-I_A$, and are those usually called the ABS. The two odd states $|\uparrow\rangle$ and $|\downarrow\rangle$ have zero energy, and therefore carry no supercurrent[2]. Hence, the phase dependence of the supercurrent reveals the occupation configuration of the Andreev system.

At zero temperature, only the negative-energy states are filled in the one-particle picture. The Josephson coupling energy is simply $-E_A$, and the supercurrent I_A is only[3] carried by the ABS of negative energy. It is remarkable that a single microscopic state determines the flow of a macroscopic current in a many-body system.

In prior work on ABS in the Quantronics group, the supercurrent-phase relation, *i.e.* the dc Josephson effect, has been measured and compared quantitatively with predictions [21]. At finite voltage, fractional Shapiro steps resulting from the non-harmonicity of the current-phase relation have been observed [22]. They fit well

2 This is valid in a spin degenerate system. However, in presence of spin-orbit interaction, the odd states can also carry supercurrent [20].

3 This is valid only in the short junction limit, where phase dependence of continuum states is negligible [14]. Then, the Josephson supercurrent is only transported by the Andreev States.

to the predictions of the mesoscopic theory for the ac Josephson effect. These two experiments probed successfully the ground state $|-\rangle$. On the other hand, measurements of the dissipative current at finite voltage [16], its associated shot noise [23], and photon assisted current [22] have been quantitatively explained in terms of Multiple Andreev Reflections (multiple Andreev reflections (MAR)). Although this MAR phenomenon relies on the Andreev internal degree of freedom, *i.e.* on the existence of the excited even state $|+\rangle$, the latter has never been directly observed.

Apart from atomic contacts, ABS physics has been explored in other systems, such as superconductor normal superconductor (SNS) junctions [24, 25, 26, 27]. But the direct observation of discrete ABS has been achieved only recently by tunneling spectroscopy of a carbon nanotube connected to two superconducting aluminum electrodes [28]. This experiment is a quasiparticle addition spectroscopy in which transitions between the ground state $|-\rangle$ and the odd states $|\uparrow\rangle$ and $|\downarrow\rangle$ are probed. It is complementary to the experiments presented here and does not address the even excited state $|+\rangle$.

1.2 Long-lived quasiparticles trapped in Andreev states

Both theory and experiment indicate that the number of **quasiparticles** in superconductors decreases exponentially as the temperature is lowered, while their recombination time increases [29, 30]. However at temperatures much lower than the transition temperature, it is difficult to reach an equilibrium Fermi-Dirac distribution. For example, Martinis *et al.* [31] measured that in a JJ Qubit, at temperatures below 70 mK, the number of quasiparticles saturates. These non-equilibrium quasiparticles are detrimental and set a limit to the proper functioning of superconducting devices such as microwave resonators [32] and Josephson qubits [33, 34].

More drastically, a single quasiparticle can determine the response of single Cooper pair devices [35, 36], which contain small superconducting islands in which the parity of the total number of electrons matters. The trapping of a single quasiparticle in such a superconducting island has been dubbed ***poisoning*** [37], as it inhibits the behavior expected of the ground state of the system. Remarkably, it has been argued [20] that quasiparticle trapping could also occur in ABS in a constriction between two superconductors, a system containing no island at all. This trapping should induce an excitation from the even ground state $|-\rangle$, to either one of the odd excited states $|\downarrow\rangle$ or $|\uparrow\rangle$, which in turn should manifest itself as a change of supercurrent. To reach these odd states one has to change the local parity of the system. This is exactly what happens in a tunneling spectroscopy experiment where electrons are injected from an auxiliary electrode [28]. This is also what happened spontaneously in our experiment [38].

The principle of the experiment is sketched in Fig. 1.3 (a). An Atomic contact (AC) in parallel with a JJ forms what we call an "**atomic-SQUID**". The current-voltage characteristic of a specific atomic-SQUID measured at 30 mK, with a distinct supercurrent branch, is shown in Fig. 1.3 (b). The Josephson supercurrent through the atomic-SQUID is modulated by the applied flux. Because of the large asymmetry between the AC and the JJ (critical current of the JJ $I_0 \simeq 550$nA much larger than the typical critical current of a one-atom aluminum contact ~ 50nA), the modula-

tion corresponds essentially to the current-phase relation of the atomic contact. In practice what is actually measured is the "switching current" of the SQUID, *i.e.* the current for which the system jumps from the zero-voltage state (or supercurrent branch) to the dissipative branch.

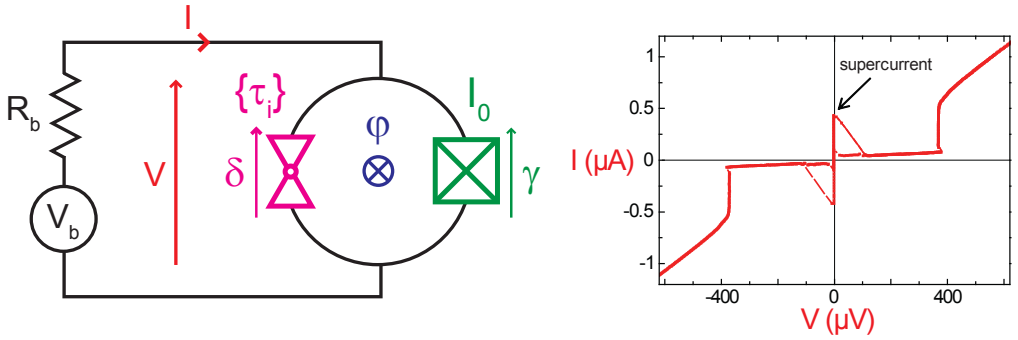

Figure 1.3: **Left**: Schematic setup: an atomic contact (magenta triangles) forms an atomic-SQUID with a Josephson junction (green checked box). Reduced flux threading the loop φ is imposed by a superconducting coil. Phases δ and γ across contact and junction are linked as $\delta - \gamma = \varphi$. The SQUID is connected through superconducting lines. It is biased by a voltage source V_b in series with a resistance R_b. The current I is measured from the voltage drop across R_b. **Right**: Current-voltage characteristics of an atomic-SQUID with contact transmissions $\{0.95, 0.45, 0.10\}$. The supercurrent of the SQUID, indicated with an arrow, is modulated by the applied flux. The finite subgap current is mainly due to MAR processes.

This technique has been used to measure accurately the supercurrent as a function of phase in the ground state $|-\rangle$ [21]. However, for a series of samples we observed discrepancies from the expected behavior [38]. For highly transmitting contacts the supercurrent is strongly reduced within a broad phase interval around π. This reduction corresponds exactly to the full suppression of the Andreev supercurrent of the most transmitted channel.

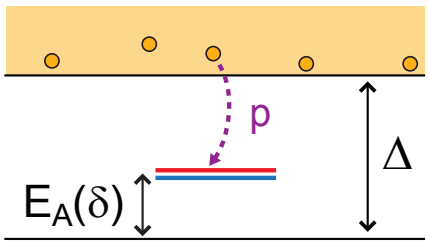

Figure 1.4: Excitation spectrum: besides the usual continuum of states above the energy gap which extends all across the structure there is a discrete Andreev spin degenerate doublet localized at the constriction. The doublet has energy $E_A(\delta)$ above the ground state and can trap quasiparticles with a probability p. The degeneracy has been lifted here for clarity.

We attribute this effect to the trapping of a spurious quasiparticle from the delocalized continuum states into the ABS of this channel. This is sketched in Fig. 1.4, drawn in the excitation picture where the two ABS are degenerate[4]. This trapping

4 The different representations are discussed in Chapter 2.

corresponds to an excitation from the even ground state $|-\rangle$, to either one of the odd excited states $|\downarrow\rangle$ or $|\uparrow\rangle$, which carry no supercurrent.

Quasiparticle trapping is stochastic and described by a probability p. We have measured the dynamics of this nonequilibrium phenomenon as a function of the phase for different atomic contacts. The corresponding relaxation time T_1 and asymptotic poisoning probability p_∞ are shown in Fig. 1.5 as a function of Andreev energy of the most transmitted channel. Trapping is more efficient when the ABS are deep inside the superconducting gap, *i.e.* for phase around π and for high transmission, in which case the lifetime of trapped quasiparticles is found to exceed 100 µs. Moreover, the trapping depends on Andreev energy in a non-trivial way: it occurs essentially when the Andreev energy is smaller than half the superconducting gap. The origin of this sharp energy threshold is not quite understood, but could be related to processes involving the emission of photons of the plasma mode of the SQUID.

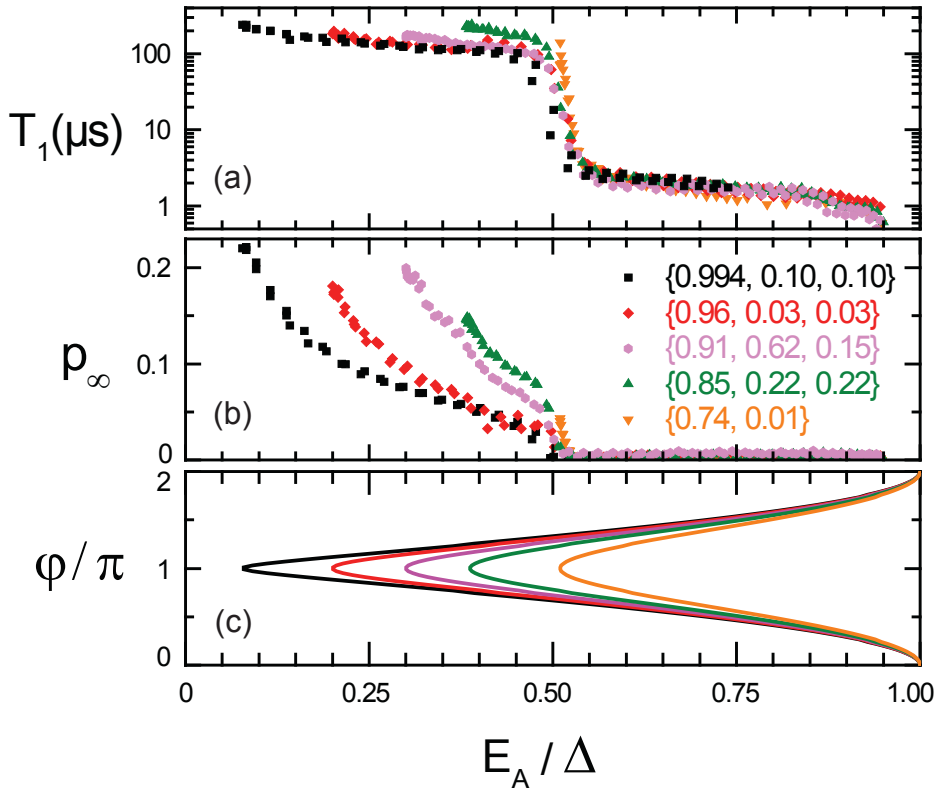

Figure 1.5: Relaxation data for five different atomic contacts [transmissions are given in panel (b)] as a function of Andreev energy of the most transmitted channel: (a) relaxation time T_1, (b) asymptotic poisoning probability p_∞. There is a sharp threshold at $E_A \simeq 0.5\,\Delta$ for all contacts. For each contact, the energy of the most transmitting channel varies between $\sqrt{1-\tau}\,\Delta$ and Δ, as shown in (c).

Let us mention that poisoning can be avoided altogether. If the large scale on-chip wires connecting the SQUID are made of either a normal metal or a superconductor with a lower gap than the device, they act as good quasiparticle traps and poisoning is not observed. In contrast, the samples described here had a fully superconducting environment. This was to optimize the lifetime of the even ex-

cited state $|+\rangle$ in order to allow for its detection in switching experiments.The idea was to shine microwaves through an on-chip coplanar antenna which couples to the flux threading the SQUID loop and to detect a change in supercurrent. We did not succeed in driving this transition, probably because the life-time of the excited state was still too short.

1.3 Andreev states spectroscopy with a Josephson junction

We then changed drastically the scheme to excite and detect transitions. Instead of measuring a change in the ABS current induced by an excitation, we measured the microwave power absorption by the ABS. This method has the advantage of not requiring a long-lived excited state. To perform this spectroscopy we used an on-chip voltage biased Josephson junction both as an emitter and a detector. Having an on-chip emitter allows a high-frequency, broadband coupling which greatly facilitates the experiments.

1.3.1 *The Josephson junction spectrometer*

When a JJ is voltage-biased below the superconducting gap $V_J < 2\Delta/e$, there is a vanishingly small dc quasiparticle current[5] and an ac Cooper pair current at the Josephson frequency

$$\nu_J = \frac{V_J}{2\pi\varphi_0}. \tag{1.3}$$

Therefore, from the electrical point of view, a voltage-biased JJ acts as an on-chip ac current generator. This current flows through the environment of the junction where it can excite electromagnetic modes. If this happens, a finite dc current I_J flows through the junction. From the microscopic point of view (see Fig. 1.6), it can be interpreted as arising from inelastic tunneling of Cooper pairs through the insulating barrier: the energy $2eV_J$ released by a Cooper pair is absorbed in the environment as a photon[6] of energy $h\nu_J$. Thus, each mode of the environment of the JJ should appear as a dc current peak in its sub-gap current-voltage $I_J(V_J)$ characteristic. The peak position gives the mode frequency, and its amplitude the rate at which the mode absorbs photons. Consequently, a voltage-biased JJ behaves as an on-chip broadband spectrometer[7]: we call it the Josephson junction spectrometer (JJS).

This physics, directly related to dynamical Coulomb blockade in superconducting systems [39, 40, 41], is an active research subject, with experiments involving superconducting resonators as perfectly controlled environments [42, 43]. Spectrometers based on Josephson junctions are also used to characterize microwave properties of materials [44, 45] or mesoscopic circuits [46, 47, 48, 49]. Here, we have chosen to use Josephson spectroscopy to explore the Andreev physics.

5 This is true for a tunnel junction where MAR processes are negligible.
6 This is valid for first order processes where one Cooper pair emits one photon.
7 The highest frequency is obtained when $V_J = 2\Delta/e$. For bulk aluminum, it is ~ 170 GHz.

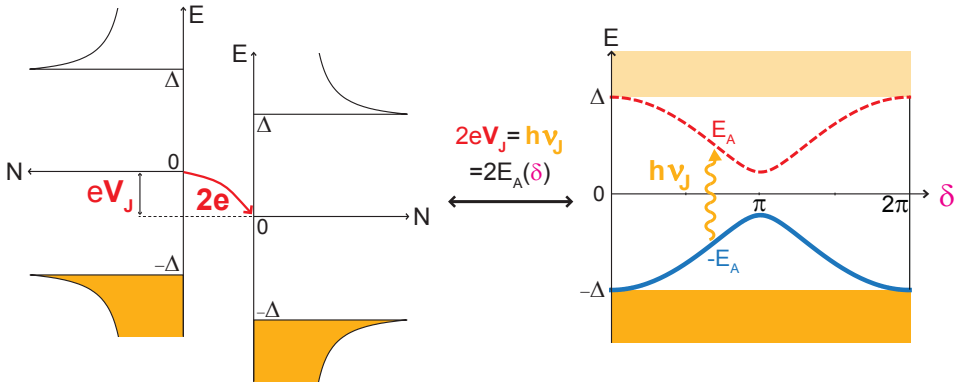

Figure 1.6: Principle of Andreev spectroscopy: **(left)** BCS density of states in the two electrodes of the JJS, shifted by the bias energy eV_J. A Cooper pair tunneling through the insulating barrier releases energy $2eV_J$ as a photon of frequency ν_J, which is absorbed in the atomic-contact by exciting the Andreev transition **(right)**.

1.3.2 *Detection of the excited Andreev state with the Josephson junction spectrometer*

As sketched in Fig. 1.6, the idea is to drive the Andreev transition by matching the Josephson frequency of the spectrometer to its energy: $h\nu_J = 2E_A(\delta, \tau)$. In practice (see Fig. 1.7 (a)), a JJS (critical current $I_{J0} \simeq 50\,nA$) is capacitively coupled through an on-chip capacitance Σ to an atomic-SQUID (critical current $I_{L0} \simeq 1\,\mu A$). Fig. 1.7 (b) shows an example of the spectrometer $I_J(V_J)$ characteristic for a particular atomic contact. In addition to a large peak near 45 μV, several smaller peaks are observed, which vary in position with the applied flux φ[8].

The two left-most panels of Fig. 1.8 display the current I_J through the spectrometer junction as a function of both the phase δ across the atomic contact and the bias voltage V_J, for two different atomic contacts. Some resonances depend strongly on flux and are very different from one contact to the other. We identify them as the Andreev resonances in the channels of the contacts. As shown by the dotted lines in the right-half of each panel, they are quite well accounted for by the Andreev transition energies $2E_A(\delta, \tau_i)$, calculated using Eq. 1.1 with the corresponding sets of transmissions $\{\tau_i\}$, independently measured from the $I(V)$ of each SQUID[9]. The Andreev lines become increasingly faint at high energy.

There are some additional lines in the spectra shown in Fig. 1.8 which do not correspond to Andreev transitions. Among them, two very large resonances, at $V_J \simeq 45\,\mu V$ and $90\,\mu V$, cross Andreev resonances and slightly vary with flux. They correspond to the plasma mode of the SQUID and its first harmonic, *i.e.* to transitions between the levels of the oscillator formed by the Josephson inductance of the SQUID and the total capacitance C in parallel with it. One can also see other lines, corresponding neither to an Andreev nor to a plasma resonance, which are explained below.

8 The peaks which depend neither on flux nor on the contact realization are related to resonances in the external environment and can be safely subtracted from all measured IVs.

9 In reality, the atomic-SQUID is also connected to a separate voltage source through additional lines not represented in Fig. 1.7 (a).

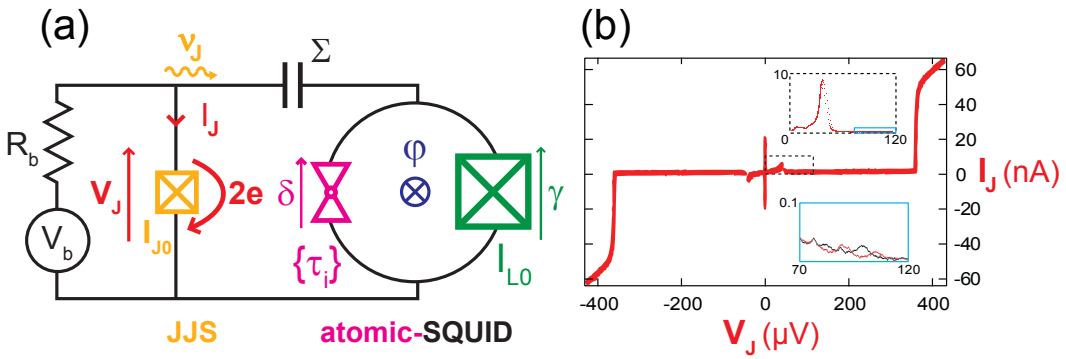

Figure 1.7: **(a)** Simplified schematic of the setup: a voltage-biased Josephson junction (yellow checked box) acts as a microwave source and detector. It is coupled through capacitor Σ to an atomic-SQUID. The ac Josephson current excites electromagnetic modes of the atomic-SQUID and Andreev transitions in the contact. The magnetic flux φ threading the loop imposes the phase δ across the contact and determines the Andreev transition frequency of each channel. These photonic excitations are detected as sub-gap current peaks in the current-voltage characteristics of the junction. **(b)** Example of a current-voltage $I_J(V_J)$ characteristic of the JJS . The large peak in the upper inset corresponds to the plasma mode of the atomic-SQUID. The $I_J(V_J)$ characteristic is shown for two different flux values at higher magnification (lower inset). The small flux-dependent peaks correspond to Andreev transitions.

1.3.3 *Quantum model*

To describe the full spectra we have developed a quantum model to treat the JJS coupled to its environment. In this model, tunneling of Cooper pairs through the JJS is treated as a perturbation. The current is obtained by a Fermi golden rule using eigenstates and eigenenergies of the environment alone[10].

The environment of the JJS is restricted to the atomic-SQUID. Its Hamiltonian

$$H_{SQUID} = H_A(\delta) + \hbar\omega_p(a^+a + \frac{1}{2}) \tag{1.4}$$

contains two terms. The first one describes the AC. In the two-level system approximation[11], the Andreev Hamiltonian [50] of a Josephson channel[12] is

$$H_A(\delta) = -E_A(\delta)\,\sigma_{z(\delta)} \tag{1.5}$$

where σ_z is the Pauli matrix. The physics of the ABS is analogous to that of a spin-1/2 in a magnetic field whose amplitude E_A and direction depend both on the phase δ. The second term describes the JJ of the SQUID, which is treated simply as a harmonic oscillator[13] of frequency $\omega_p/2\pi$, the plasma frequency. The destruction

10 This modeling is analogous to the well-known P(E) theory for Dynamical Coulomb Blockade [39, 40], except that the environment, which includes the Andreev doublet, is highly non-linear and cannot be described by an impedance.

11 This is valid only when neglecting the continuum and assuming that parity is conserved, thus restricting to the subspace $\{|-\rangle, |+\rangle\}$.

12 For multiple channels contacts, the Hamiltonian is just the sum $\sum_i H_{A,\tau_i}$ of the Hamiltonian of each channel.

13 It corresponds to a first order Taylor expansion of the Josephson Hamiltonian.

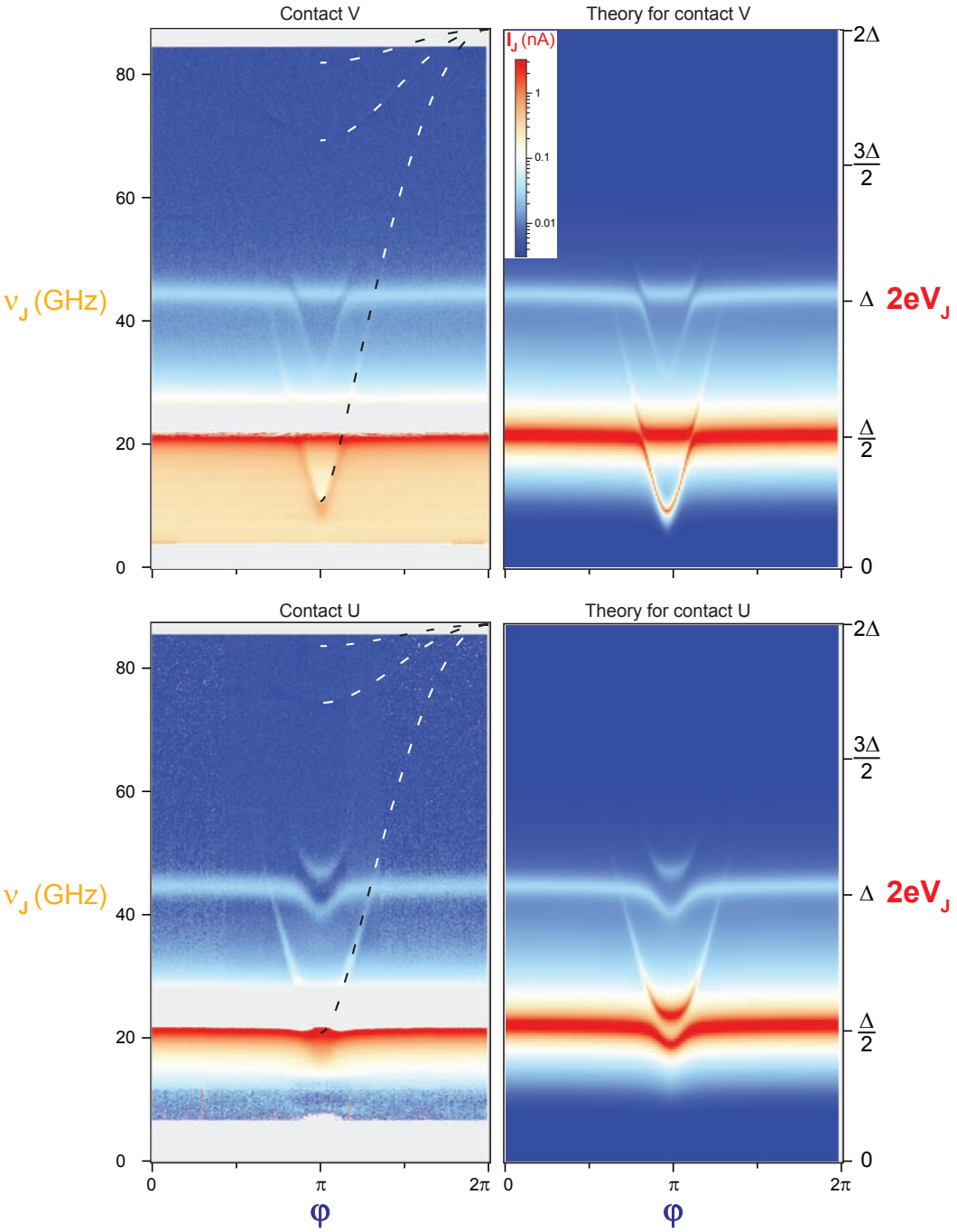

Figure 1.8: Experimental (**left**) and calculated (**right**) spectra $I_J(V_J, \varphi)$ for contact V ($\{0.987, 0.37, 0.12\}$ (**top**) and U $\{0.942, 0.26, 0.081\}$ (**bottom**). The blind regions (gray) are not accessible to measurement with this setup. The log current scale is the same for the two spectra. Dotted lines: theoretical Andreev resonances with the simple modeling $2E_A(\varphi, \tau_i)$. The theoretical spectra were obtained using the quantum model detailed in Chapter 7. The calculated currents have been multiplied by 0.56 to match the measured ones.

operator α is associated to the phase γ across the JJ. Since δ and γ are linked by the flux φ threading the superconducting loop, the two terms of the Hamiltonian are implicitly coupled.

This Hamiltonian (1.4), corresponding to the **spin-boson** problem [51, 52], can be solved either analytically by approximation (Jaynes-Cummings approximation, perturbation theory) or numerically (see Chapter 7).

This theory would predict infinitely sharp peaks in the $I_J(V_J)$ of the JJS at voltages corresponding to each excitation energy of the environment. To take into account dissipation[14], we introduced a single phenomenological damping parameter and replaced every peak by a Lorentzian peak with an empirical quality factor Q.

Fig. 1.8 compares the experimental spectra (left) with the calculated ones (right) for two different atomic contacts. To discuss the different transitions, it is useful to label the bare states by $|\sigma, n\rangle$, where $\sigma = \pm$ accounts for the Andreev spin and n is the plasmon number. The model describes both the Andreev resonances ($|-,0\rangle \rightarrow |+,0\rangle$, of energy $2E_A$) and the plasma resonance ($|-,0\rangle \rightarrow |-,1\rangle$, of energy $\hbar\omega_p$). It also describes the higher harmonic transitions: $|-,0\rangle \rightarrow |+,1\rangle$, of energy $2E_A + \hbar\omega_p$ and $|-,0\rangle \rightarrow |-,2\rangle$, of energy $2\hbar\omega_p$. These processes correspond to the tunneling of one Cooper pair emitting two photons. They are therefore less probable which results in fainter transitions as seen in both experiment and calculation. This theory also succeeds in predicting the anti-crossings arising from the coupling between the Andreev-spin and the plasma-boson. Finally, the weakening of the signal at high V_J is well captured by the model, but a rigorous calculation of the amplitude and width of the different peaks is needed.

1.4 Perspectives

The experiments performed during this thesis show that both odd and even excitations of ABS can be addressed. The results raise several questions and open new perspectives.

In the experiments on poisoning, what is the phenomenon behind the peculiar energy dependence of the lifetime of trapped quasiparticles? Could one takes advantage of the long life-times to implement the strategies proposed for individual spin manipulations and superconducting spin qubits [20]? In particular, there is a recent proposal to exploit the spin state of two trapped quasiparticles in a contact with two highly transmitting channels, based on the spin-blockade that inhibits quasiparticle recombination in triplet states [53]. Can the complete suppression of the macroscopic supercurrent when a single quasiparticle is trapped allow using a superconducting atomic contact as a quasiparticle detector? Quasiparticle trapping, which is likely to be a generic phenomenon in superconducting weak links, could be detrimental in some situations. It could be the case for experiments proposed to detect Majorana bound states in condensed matter systems [54]. Indeed, such

14 In practice, the actual environment of the junction contains besides the SQUID some additional electromagnetic impedance with a dissipative component. This results in a continuum of environmental modes and the peaks acquire some width. Although in principle it is possible to include in an Hamiltonian treatment this impedance, we have just introduced a single phenomenological damping parameter.

states are related to the physics of exotic ABS, with their topological protection relying on parity conservation [55]. Therefore, the different methods to prevent or get rid of poisoning discussed in Section 4.5 could be essential for such experiments.

In the photon-absorption spectroscopy experiment, what limits the lifetime of the excited even state $|+\rangle$? A long relaxation time is necessary to measure the supercurrent carried by $|+\rangle$ and to perform coherent manipulation of the ABS. A further step would be to couple the Andreev system to high quality resonators as is presently done in the field of cavity-QED. Can Josephson absorption spectroscopy be used to probe transitions in the GHz-THz range in other mesoscopic systems?

Part I

MESOSCOPIC JOSEPHSON EFFECT AND ANDREEV BOUND STATES

The first part is essentially theoretical and devoted to the presentation of the Andreev physics and its already existing experimental manifestations.

2

MESOSCOPIC SUPERCONDUCTIVITY AND ANDREEV BOUND STATES

Completely validating the mesoscopic theory of the Josephson effect requires detection of the excited Andreev state. The theoretical background necessary to understand the experiments achieving this goal are presented in this chapter.

First, we recall the standard description of a homogeneous superconductor in a mean-field approximation. This allows discussing the different representations of superconductors which are widely used in the literature but sometimes misleading: the one-particle picture, the excitation picture and the semiconductor picture. In particular it is useful to switch from one representation to another depending on the spectroscopy scheme being discussed.

Then, by introducing a superconducting phase gradient and a scattering potential, we build explicitly the Andreev Bound States and derive their corresponding two-level Hamiltonian and current operator. Although this calculation leads to well-known results, the Hamiltonian formulation is easier to grasp than the conventional path-integral based method.

At last, we discuss the case of the tunnel Josephson junction.

This chapter presents only the physical concepts and results, with the complete calculations found in Appendix A.

2.1 BCS Hamiltonian and Bogoliubov-de Gennes equation

The goal of this section is to introduce the notations of second quantization, which leads to the Bogoliubov-de Gennes equation.

One considers the case of an s-type superconductor. In a **BCS** mean-field approximation (see Ref. [56] and [57]), the effective Hamiltonian can be written as

$$\begin{aligned}\mathcal{H} = & \int dr \sum_{\sigma=\uparrow,\downarrow} \psi_\sigma^\dagger(r)\left[\frac{p^2}{2m} - \mu + U_\sigma(r)\right]\psi_\sigma(r) \\ & + \int dr \left[\Delta(r)\,\psi_\uparrow^\dagger(r)\psi_\downarrow^\dagger(r) + \Delta^*(r)\,\psi_\downarrow(r)\psi_\uparrow(r)\right]\end{aligned} \tag{2.1}$$

where $\psi_\sigma(r)$ (respectively $\psi_\sigma^\dagger(r)$) is the annihilation (creation) field operator of an electron of spin σ at position r, Δ is the self-consistent complex pairing field and U_σ the self-consistent potential. One notices that this approximate form, which is quadratic in fermion operators, does not conserve particle number. But spin and particle number parity are still good quantum numbers.

The pairing interaction introduces anomalous correlations $\left\langle \psi_\uparrow^\dagger(r)\psi_\downarrow^\dagger(r)\right\rangle$ and $\left\langle \psi_\downarrow(r)\psi_\uparrow(r)\right\rangle$. Following Bagwell and Datta [19], one aims at transforming $\mathcal{H}$ into a form that looks just like the second quantized Hamiltonian for a set of non-interacting particles. To do so, one introduces the **spinor** field

$$\Psi(r) = \begin{pmatrix} \psi_\uparrow(r) \\ \psi_\downarrow^\dagger(r) \end{pmatrix}. \tag{2.2}$$

One can understand this field operator as a global annihilation of a "**quasiparticle**" made of a spin-up electron annihilation field, and a spin-down hole annihilation field. It conserves the spin and the parity. Using the anti-commutation rules[1], the Hamiltonian reads

$$\mathcal{H} = \int dr \Psi^\dagger(r) H_{BdG} \Psi(r) \tag{2.3}$$

where H_{BdG} is a matrix Hamiltonian operator defined as

$$H_{BdG} = \begin{pmatrix} \frac{p^2}{2m} - \mu + U_\uparrow(r) & \Delta(r) \\ \Delta^*(r) & -\left[\frac{p^2}{2m} - \mu + U_\downarrow(r)\right] \end{pmatrix} \tag{2.4}$$

To diagonalize Eq. 2.3, one first needs to solve the one-particle stationary Schrödinger equation

$$H_{BdG} \begin{pmatrix} u_k(r) \\ v_k(r) \end{pmatrix} = E_k \begin{pmatrix} u_k(r) \\ v_k(r) \end{pmatrix}. \tag{2.5}$$

which is known as the **Bogoliubov-de Gennes equation**. Here, analogously to the Dirac equation, the wave function of this quasiparticle is a 2-dimensional vector. With the choice of spinor (2.2), the upper component of the vector represents the "spin-up electron" amplitude of the quasiparticle, and the lower component its "spin-down hole" amplitude.

One looks for an orthonormal basis of solutions $\{\overrightarrow{\varphi_k}\}_k$, with $\overrightarrow{\varphi_k}(r) = \begin{pmatrix} u_k(r) \\ v_k(r) \end{pmatrix}$, such that $\int dr\, {}^t\overrightarrow{\varphi_k}^*(r)\overrightarrow{\varphi_{k'}}(r) = \delta_{kk'}$. Then, one can decompose $\Psi(r)$ on this basis:

$$\Psi = \sum_k \gamma_k \overrightarrow{\varphi_k}, \tag{2.6}$$

where the γ_k are fermionic operators. Injecting in Eq. 2.3, one gets a diagonal Hamiltonian.

2.2 Homogeneous superconductor and representations

Let us first consider the space invariant case $U_\sigma(r) = U_\sigma$ and $\Delta(r) = \Delta e^{i\varphi}$. $\Delta > 0$ is the modulus of the superconducting order parameter and $\varphi \in \mathbb{R}$ its phase. $U_\sigma \in \mathbb{R}$ is spin-dependent, which allows to describe for instance the case of an external magnetic field[2]. We will first diagonalize the Hamiltonian and build all its eigenstates. Then, we will discuss the different representations of superconductors.

1 We are dropping the constant energy $\sum_{k\in\mathbb{R}} \xi_k + \sum_{k,k'\in\mathbb{R}} \int_F dr \left[\varphi_{k'}(r) U_\downarrow(r) \varphi_k^*(r)\right]$ resulting from the anti-commutation.

2 This lifts spin degeneracy, which is essential to discuss the different representations.

2.2.1 *Diagonalization of the Hamiltonian*

One can show (see Section A.2.2) that the purely propagating wave functions

$$\begin{cases} \overrightarrow{\varphi_{k-}} = & \begin{pmatrix} v_k \\ u_k \end{pmatrix} e^{ik.r} \\ \overrightarrow{\varphi_{k+}} = & \begin{pmatrix} u_k^* \\ -v_k^* \end{pmatrix} e^{ik.r} \end{cases} \tag{2.7}$$

are solutions of Eq. 2.5 of energies $E_{k\pm}$, with

$$\begin{cases} u_k = & e^{-i\frac{\varphi}{2}} \sqrt{\frac{1}{2}(1 + \frac{\tilde{\xi}_k}{\sqrt{\Delta^2+\tilde{\xi}_k^2}})} \\ v_k = & -e^{i\frac{\varphi}{2}} \sqrt{\frac{1}{2}(1 - \frac{\tilde{\xi}_k}{\sqrt{\Delta^2+\tilde{\xi}_k^2}})} \\ E_{k\pm} = \pm & \sqrt{\Delta^2 + \tilde{\xi}_k^2} + \beta \end{cases} . \tag{2.8}$$

$\tilde{\xi}_k = \frac{\hbar^2 k^2}{2m} - \mu + \frac{U_\uparrow + U_\downarrow}{2}$ is the renormalized kinetic energy, and $\beta = \frac{U_\uparrow - U_\downarrow}{2}$ can be seen as a Zeeman splitting energy. One considers that $|\beta| < \Delta$. Then, for each k, there is a negative energy E_{k-} and a positive energy E_{k+}.

$\{\overrightarrow{\varphi_{k-}}, \overrightarrow{\varphi_{k+}}\}_k$ forms an orthonormal basis of solutions, allowing to diagonalize the Hamiltonian:

$$\mathcal{H} = \sum_k E_{k-}\gamma_{k-}^\dagger \gamma_{k-} + E_{k+}\gamma_{k+}^\dagger \gamma_{k+}. \tag{2.9}$$

γ_{k-}, γ_{k+}, $\gamma_{k-}^\dagger$ and $\gamma_{k+}^\dagger$ are the fermionic annihilation and creation operator, nicknamed "Bogoliubons". They are related to the plane waves fermion operators by the Bogoliubov transformation

$$\begin{pmatrix} \gamma_{k-} \\ \gamma_{k+} \end{pmatrix} = R_k \Psi_k \tag{2.10}$$

where

$$R_k = \begin{pmatrix} v_k^* & u_k^* \\ u_k & -v_k \end{pmatrix} \tag{2.11}$$

is the unitary Bogoliubov matrix, and Ψ_k is the Fourier transform of the spinor (2.2)

$$\Psi_k = \begin{pmatrix} c_{k\uparrow} \\ c_{-k\downarrow}^\dagger \end{pmatrix}. \tag{2.12}$$

2.2.2 *Building the eigenstates: the one-particle picture*

This powerful description was first proposed by Bagwell and Datta [19]. We have found the Bogoliubons, the natural excitation operators of the problem, which diagonalize the Hamiltonian. We now build explicitly all the eigenstates of the system.

2.2.2.1 *Vacuum state*

To do so, one needs to know or guess one peculiar eigenstate[3]. Indeed, if $|V\rangle$ is an eigenstate of eigenenergy E_V, then any state $\gamma^\dagger_{k\pm}|V\rangle$ or $\gamma_{k\pm}|V\rangle$ is also an eigenstate (if not equal to zero) with eigenenergy respectively $E_V + E_{k\pm}$ and $E_V - E_{k\pm}$.

Guided by Eq. 2.9, we are looking for a "vacuum" state of Bogoliubons, *i.e.* a state such that $\begin{pmatrix} \gamma_{k-} \\ \gamma_{k+} \end{pmatrix}|V\rangle = \begin{pmatrix} 0 \\ 0 \end{pmatrix}$. Due to the unitary Bogoliubov transformation (2.10), it is equivalent to verify $\Psi_k|V\rangle = \begin{pmatrix} 0 \\ 0 \end{pmatrix}$. It is straightforward to see that the

"vacuum state"

$$|V\rangle = \prod_k c^\dagger_{-k\downarrow}|0\rangle \tag{2.13}$$

made of an empty band of up spins and a full band of down spins, fulfills this condition[4]. Therefore, it is an eigenstate[5] of the system with energy[6] $E_V = 0$.

2.2.2.2 *Ground state*

On the other hand $\gamma^\dagger_{k-}|V\rangle \neq 0$ and $\gamma^\dagger_{k+}|V\rangle \neq 0$ are eigenstates of respectively lower ($E_V + E_{k-} < E_V$) and higher energy ($E_V + E_{k+} > E_V$) than the vacuum. Therefore, one immediately sees that

$$|GS\rangle = \prod_k \gamma^\dagger_{k-}|V\rangle \tag{2.14}$$

is the lower energy eigenstate, *i.e.* the ground state[7], with eigenenergy $E_V + \sum_k E_{k-}$. It is obtained by populating the vacuum $|V\rangle$ with Bogoliubons of negative energies. Using Eq. 2.10 and Eq. 2.12, one finds that

$$|GS\rangle = \prod_k (u_k + v_k c^\dagger_{k\uparrow} c^\dagger_{-k\downarrow})|0\rangle \tag{2.15}$$

which is the usual BCS ground state, made of intricate states, the **Cooper pairs**. It has even parity, zero total spin and zero total momentum.

2.2.2.3 *Superconducting density of states*

Like in a free fermion gas, all the eigenstates can be built by applying products of $\gamma^\dagger_{k+}$ and $\gamma^\dagger_{k-}$ on $|V\rangle$. That is why this representation is called the "**one-particle picture**". Starting from the reference eigenstate $|V\rangle$, one can compute the one-particle states energy E, which can be positive or negative, and derive the corresponding

3 This is totally straightforward in the normal state, because $|0\rangle$, the vacuum of electrons, is an eigenstate. This is not the case here.

4 Note that this description is arbitrary in the choice of the spinor, and of the corresponding vacuum (see Section A.2.2).

5 Note that this "vacuum state" is not the ground state, but a very high energy excited state with maximally negative spin.

6 Had we not dropped out the constant energy resulting from the anti-commutation, this energy would be $E_V = \sum [\xi_k + U_\downarrow]$.

7 This is true for an even number number of electrons in the system.

superconducting density of states N_s by equating $N_s(E)dE = \frac{1}{2}N_n(\xi)d\xi$. The normal density of states N_n can be considered constant and equal to the one at the Fermi level $N_n(\xi) = N_n(0)$. This leads directly to

$$N_s(E) = \frac{1}{2}N_n(0)\begin{cases} \frac{|E-\beta|}{\sqrt{(E-\beta)^2-\Delta^2}} & \text{if } |E-\beta| > \Delta \\ 0 & \text{otherwise} \end{cases} . \tag{2.16}$$

As expressed by Eq. 2.16 and depicted in Fig. 2.1, the ground state is obtained by populating all the Bogoliubons of negative energies. One can create an excitation

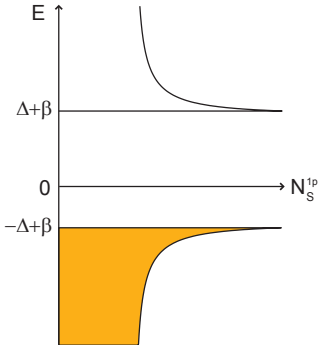

Figure 2.1: Superconducting density of states in the one-particle picture, in presence of a Zeeman splitting β. The filled region corresponds to states occupied in the ground state.

by adding a quasiparticle at positive energy by the action of $\gamma^\dagger_{k+}$ on the ground state. It costs an energy $E_{k+} > \Delta + \beta$. One can also remove a quasiparticle at negative energy by the action of γ_{k-} on the ground state, which costs an energy $-E_{k-} > \Delta - \beta$. Therefore, there is a gap in the excitation spectrum. When $\beta = 0$, this energy gap is exactly the modulus of the superconducting order parameter Δ.

This picture allows representing the ground state, which is obtained by populating energy states up to $-\Delta + \beta$, instead of up to $\xi = 0$ in the normal state. Therefore it has a lower energy, capturing well the idea of condensation. However, the vacuum state has disappeared in this representation, which can be misleading. Although useless for the excitation spectrum, the vacuum is essential to derive the exact energy, spin and momentum of all eigenstates.

2.2.3 *The excitation picture*

In the previous section, we have chosen the highly excited and spin polarized vacuum state $|V\rangle$ as our starting point to build the other excited states and the ground state. In the "**excitation picture**" (see Ref. [19]), one prefers to choose as a reference state the ground state, and to deal only with positive excitation energies.

To do so, one performs an electron-hole transformation on the Bogoliubons of negative energy:

$$\begin{cases} \gamma^\dagger_{k\uparrow} \equiv \gamma^\dagger_{k+} = & u^*_k c^\dagger_{k\uparrow} - v^*_k c_{-k\downarrow} \\ \gamma^\dagger_{-k\downarrow} \equiv \gamma_{k-} = & u^*_k c^\dagger_{-k\downarrow} + v^*_k c_{k\uparrow} \\ E_{k\uparrow} \equiv E_{k+} & > 0 \\ E_{-k\downarrow} \equiv -E_{k-} & > 0 \end{cases} \tag{2.17}$$

Then, the Hamiltonian writes[8]

$$\mathcal{H} = \sum_k \left(E_{k\uparrow} \gamma^\dagger_{k\uparrow} \gamma_{k\uparrow} + E_{k\downarrow} \gamma^\dagger_{k\downarrow} \gamma_{k\downarrow} \right) + \sum_k \left(\xi_k + U_\downarrow - E_{k\downarrow} \right). \tag{2.18}$$

Thus, a quasiparticle operator $\gamma^\dagger_{k\sigma}$ creates an excitation of momentum k and spin σ. The ground state is such as $\forall k, \sigma,\ \gamma_{k\sigma} |GS\rangle = 0$: it is the vacuum of excitations[9]. All the excited eigenstates are generated by repeated action of $\gamma^\dagger_{k\sigma}$ on $|GS\rangle$.

Then, the excitation superconducting density of states is given by

$$N_s(E_\sigma) = \frac{1}{2} N_n(0) \begin{cases} 0 & (E_\sigma < \Delta + \epsilon_\sigma \beta) \\ \frac{E_\sigma - \epsilon_\sigma \beta}{\sqrt{(E_\sigma - \epsilon_\sigma \beta)^2 - \Delta^2}} & (E_\sigma > \Delta + \epsilon_\sigma \beta) \end{cases} \tag{2.19}$$

where $\epsilon_{\uparrow\downarrow} = \pm 1$. It is represented in Fig. 2.2. One sees that the one-particle picture

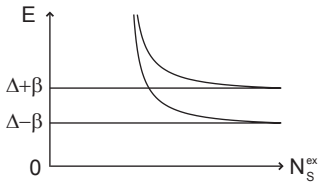

Figure 2.2: Spin-resolved superconducting density of states in the excitation picture, in presence of a Zeeman splitting β.

corresponds exactly to unfolding the density of states of the spin-down excitation to negative energy. Therefore, the degeneracy in the positive energy region is twice smaller in the one-particle picture. Contrary to the one-particle picture, this representation does not carry any information about the ground state. However, one keeps track here of the spin of the excitation.

2.2.4 *The semiconductor picture*

In the general Bogoliubov-de Gennes formalism (see Chap. 9 of [56]), which is needed for example in the presence of arbitrary spin-independent interactions,

8 Here was reincorporated the constant energy $E_V = \sum \left[\xi_k + U_\downarrow \right]$ resulting from the anti-commutation.

9 Note that, contrary to what we have done in 2.13, it is much more complicated, starting from the Hamiltonian 2.18 to "guess an eigenstate" such as $\forall k, \begin{pmatrix} \gamma_{k\uparrow} \\ \gamma_{k\downarrow} \end{pmatrix} |GS\rangle = 0$. One can however check that the ground state (2.15) satisfy this equation.

one has to double the degrees of freedom to bring the many-body Hamiltonian (2.1) to the non-interacting form (2.3). This is done by introducing a 4-dimensional spinor of the form

$$\widetilde{\Psi}_k = \begin{pmatrix} c_{k\uparrow} \\ c^\dagger_{-k\downarrow} \\ c^\dagger_{-k\uparrow} \\ c_{k\downarrow} \end{pmatrix}. \tag{2.20}$$

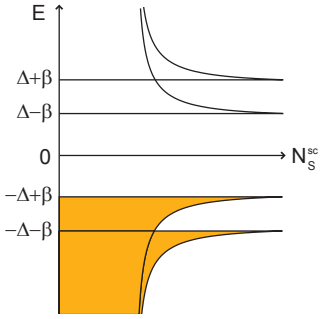

Figure 2.3: Superconducting density of states in the semiconductor picture, in presence of a Zeeman splitting β.

Thus the Hamiltonian becomes

$$\mathcal{H} = \frac{1}{2}\left(\sum_k \widetilde{\psi}^\dagger_k \widetilde{H}_k \widetilde{\psi}_k + \sum_\sigma \sum_k \xi_{-k\sigma}\right) \tag{2.21}$$

where $\widetilde{H}_k$ is a 4×4 matrix whose explicit form depends on the actual interactions at play. By diagonalizing it, one finds all the excitations of the system: two at negative energies, two at positive energies. The resulting density of states corresponds to the excitation DOS with a mirrored branch at negative energy, as shown in Fig. 2.3. Note that each band has a well-defined spin.

However, this description is redundant: creating a quasiparticle at positive energy is identical to annihilating a quasiparticle at negative energy, leading to the particle-hole symmetry relation $\gamma^\dagger_{E\uparrow} = \gamma_{-E\downarrow}$. The factor $\frac{1}{2}$ in Eq. 2.21 corrects the fact that we are counting the excitations twice (double counting). One could say that each energy state has a one-half occupancy.

In the simple case discussed before and which applies to the experiments discussed in this thesis, the matrix $\widetilde{H}_k$ is doubly degenerate and this description is not necessary. Nevertheless, it is needed for instance to discuss experiments on Majorana physics in superconducting circuits, where both spin-orbit interaction and an orthogonal Zeeman field are involved[10].

10 We have tried to perform such an experiment by coupling an indium arsenide (InAs) nanowire (a material with strong spin-orbit interaction) to superconducting aluminum electrodes. By applying a parallel magnetic field, one expects to observe, in a certain range of parameters, a topological transition where the ABS transform into Majorana fermions [58]. Our experiment was however unsuccessful because we were suppressing superconductivity before entering the topological phase. Very recently, similar experiments [59, 60] were performed in a different system, an indium antimonide

2.2.5 *Spectroscopy of superconductors*

Up to now, we have diagonalized the Hamiltonian and found all its eigenstates. We now discuss how one probes the excitation spectrum of a superconductor in an experiment. We will show that, depending on the process, it is more convenient to choose one representation or another.

2.2.5.1 *Quasiparticle-injection spectroscopy*

In a quasiparticle-injection spectroscopy, one typically connects the superconductor through a tunnel barrier to a normal metal, and shifts the electrochemical potential of the normal electrode by applying a voltage bias V. At positive voltage $V > 0$, an electron of spin σ and momentum k_0 can tunnel into the superconductor. The corresponding excitation operator is $c^\dagger_{k_0\sigma}$, which decomposes on the excitation Bogoliubons as $c^\dagger_{k_0\sigma} = u_{-k_0}\gamma^\dagger_{k_0\sigma} - v^*_{-k_0}\gamma_{-k_0-\sigma}$. Therefore, $c^\dagger_{k_0\sigma}|GS\rangle = u_{-k_0}\gamma^\dagger_{k_0\sigma}|GS\rangle$, and such an excitation is only possible when $eV>\Delta+\epsilon_\sigma\beta$. Similarly, at negative energy one can inject a hole $c_{-k_0-\sigma} = u^*_{k_0}\gamma_{-k_0-\sigma} - v_{k_0}\gamma^\dagger_{k_0\sigma}$ as soon as $eV<-\Delta-\epsilon_\sigma\beta$. In both cases the excited state is proportional to

$$\gamma^\dagger_{k_0\sigma}|GS\rangle = \prod_{k\neq k_0}(u_k + v_k c^\dagger_{k\uparrow}c^\dagger_{-k\downarrow})c^\dagger_{k_0\sigma}|0\rangle\,, \tag{2.22}$$

with $\sigma = \uparrow,\downarrow$, whose excitation energy is $E_{k_0\sigma} > \Delta + \epsilon_\sigma\beta$. This excited state has an odd parity and finite spin and momentum.The electron $c^\dagger_{k_0\sigma}|0\rangle$, which was part of one of the Cooper pairs is now present with certainty one. This state has a higher energy because this single electron does not benefit from the condensation energy.

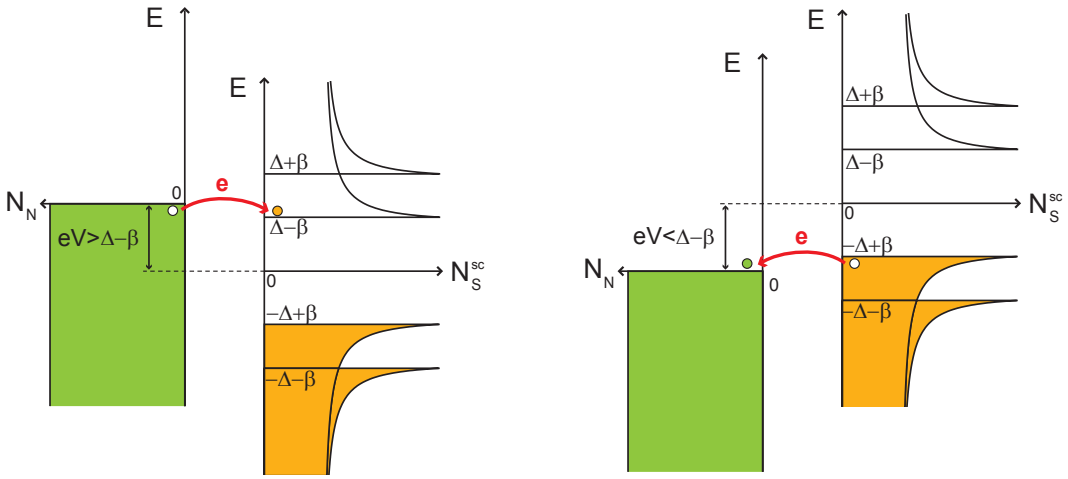

Figure 2.4: Sketch of the quasiparticle-injection spectroscopy, in the semiconductor picture for a positive (**left**) or negative (**right**) bias voltage.

The semiconductor picture is particularly well adapted to the representation of these excitations. In Fig. 2.4, the normal electrode DOS is on the left side. As

(InSb) nanowire, which has a stronger spin-orbit interaction, coupled to a superconducting electrode with a larger critical field (either niobium titanium nitride (NbTiN) or niobium). These observations (zero bias conductance peak or abnormal Shapiro steps) support
the existence of Majorana fermions in nanowires coupled to superconductors.

depicted one can inject either electrons at positive voltage bias or holes at negative voltage bias only if $|eV| > \Delta - |\beta|$.

2.2.5.2 *Photon-absorption spectroscopy*

In an unpolarised photon-absorption spectroscopy, one can neither change parity nor spin, and one can only transfer a small momentum compared to the Fermi wavevector $\|\delta k\| \ll k_F$. Therefore, the only possible excited states are

$$\gamma^\dagger_{-k_0-\sigma}\gamma^\dagger_{k_0\sigma}|GS\rangle = \prod_{k\neq k_0}(u_k + v_k c^\dagger_{k\uparrow}c^\dagger_{-k\downarrow}) * (v_{k_0} - u_{k_0}c^\dagger_{k_0\uparrow}c^\dagger_{-k_0\downarrow})|0\rangle\,. \tag{2.23}$$

Such states are made of all Cooper pair in their ground state except one. In the spin-analog description of superconductivity due to Anderson (see Chapter 8 of Ref. [61]), at fixed even parity a Cooper pair is like a spin in an effective magnetic field, representing the pairing energy. When aligned to the field, this spin has a negative energy: this is the ground state Cooper pair. When anti-aligned, it has the opposite positive energy: we interpret the k_0 component of Eq. 2.23 as such an excited Cooper pair. These excited states have, as the ground state, zero spin and zero momentum, and are thus accessible by photon-absorption spectroscopy. The excited state is reached by applying two excitation operators. Therefore, the corresponding energy gap is 2Δ, which as expected does not depend on the Zeeman energy.

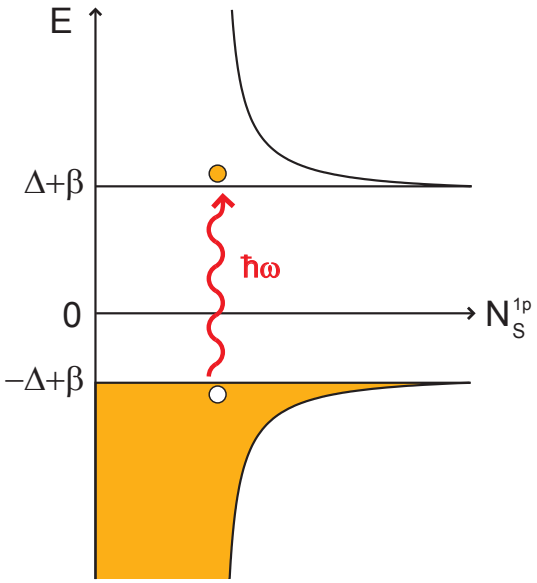

Figure 2.5: Sketch of the photon-absorption spectroscopy, in the one-particle picture.

The one-particle picture is well adapted to the representation of such excitation. The operation (2.23) was expressed in terms of the excitation Bogoliubons. In terms of the one-particle Bogoliubons, it amounts to applying $\gamma^\dagger_{-k_0+}\gamma_{-k_0-}$, which corresponds exactly to taking a quasiparticle of negative energy and promoting it to positive energy, as sketched in Fig. 2.5.

2.3 Normal-superconductor interface: the Andreev reflection

Andreev reflection is the key concept to understanding electronic transport in inhomogeneous superconducting structures. In this case, one can no longer label states by their momentum.

2.3.1 *Energy dependence of the one-particle states*

In one-dimension, as in the normal case, all the "one-particle" states $\gamma^\dagger_{k+}|V\rangle$ and $\gamma^\dagger_{k-}|V\rangle$ are four times degenerate in energy ($\pm k$ and $\pm\xi$). It is therefore more physical to index them by their excitation energy E in place of k. Instead of classifying the two types of solutions of Eq. 2.5 by their negative or positive energy E (labeled by $\pm$ in Eq. 2.8), it is more convenient to distinguish electron-like $\begin{pmatrix} u_e \\ v_e \end{pmatrix} \exp(\pm i k_e x)$ and hole-like solutions $\begin{pmatrix} u_h \\ v_h \end{pmatrix} \exp(\pm i k_h x)$, in the sense that this is what they describe when $\Delta \to 0$ or when $|E_k| \gg \Delta$. To do so, one defines (in a spin degenerate case $\beta = 0$)

$$\begin{cases} u_{e,h}(E,\varphi) = e^{i\frac{\varphi}{2}} & \left(\frac{1}{2}\left[1+\eta_{e,h}\sqrt{1-\left(\frac{\Delta}{E}\right)^2}\right]\right)^{1/2} \\ v_{e,h}(E,\varphi) = & e^{-i\frac{\varphi}{2}}\operatorname{sgn}(E)\left(\frac{1}{2}\left[1-\eta_{e,h}\sqrt{1-\left(\frac{\Delta}{E}\right)^2}\right]\right)^{1/2} \\ k_{e,h}(E) = & k_F\left(1+\eta_{e,h}\operatorname{sgn}(E)\frac{\sqrt{E^2-\Delta^2}}{\mu}\right)^{1/2} \end{cases} \tag{2.24}$$

where $\eta_{e,h} = \pm 1$ stands for the choice electron or hole ($\eta_{e,h} = \operatorname{sgn}(\xi)\operatorname{sgn}(E)$).

As long as $|E| > \Delta$, $k \in \mathbb{R}$ and one is dealing with purely propagating states. Such states are the only one possible in the spatially-invariant case.

When the potential or the pairing energy depend on space, new states will be possible with $|E| < \Delta$ and $k \notin \mathbb{R}$. By performing a Taylor expansion to first order, one gets

$$k_{e,h}(E) = k_F + i\eta_{e,h}\kappa(E) \tag{2.25}$$

with

$$\kappa(E) = k_F\frac{\sqrt{\Delta^2-E^2}}{2\mu} \ll k_F. \tag{2.26}$$

We have taken by convention:

$$\sqrt{E^2-\Delta^2} = i\operatorname{sgn}(E)\sqrt{\Delta^2-E^2} \quad \text{if } |E| < \Delta. \tag{2.27}$$

The Taylor expansion to first order is called the **Andreev approximation** and is valid when $\Delta \ll \mu$. These states are exponentially damped[11] on a length scale κ^{-1}.

11 Note that these states oscillate at the same time that they decay, in contrast to what one finds for bound states in the normal state.

2.3.2 *Andreev reflection*

Studying the elementary excitations in a normal metal layer backed by a semi-infinite superconductor, de Gennes and Saint-James found that electrons incoming from the normal side on the superconductor have a finite probability to be reflected as holes [9, 10]. Independently, Andreev performed similar calculations to explain the large change in thermal conductivity through a superconductor in an intermediate state, a regular arrangement of alternating normal and superconducting lamellas in an elongated plate, obtained by applying a magnetic field obliquely and close to the critical value [11]. In this lamellar S-N structure, he also found electron-hole reflections. The Bogoliubov-de Gennes formalism gives a simple way to calculate this "**Andreev reflection**".

The normal-superconductor interface corresponds to a discontinuity in the superconducting order parameter: $\Delta(r) = \Delta e^{i\varphi}\theta(x)$ (with θ the Heaviside function) and $U_\sigma(r) = 0$. This system is spatially invariant for $x < 0$ and for $x > 0$. From Section 2.2, one has a basis of solutions on each side. We just want here to produce one peculiar solution.

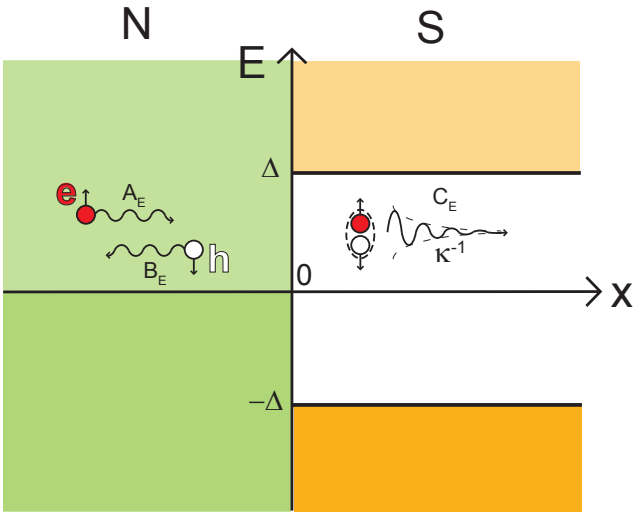

Figure 2.6: Sketch of the Andreev reflection. The discontinuity in the superconducting order parameter behaves as a barrier potential. In addition to the usual specular reflection (not represented), the pairing interaction in the superconductor induces a new type of reflection, the Andreev reflection, in which a spin-up electron (red) is reflected into a spin-down hole (white). When the energy of the incident propagating states in the normal region is smaller than Δ, they become evanescent in the superconducting region on a length scale κ^{-1}. Note that all waves should be at the same energy but are shifted for readability.

When a spin-up electron of energy E incident from the normal electrode ($k_e > 0$) impinges on the superconducting one at $x = 0$, it can be reflected as a spin-up electron in a usual specular reflection and not contribute to the current. But, due to the pairing interaction in the superconductor ($\Delta c^\dagger_{k\uparrow} c^\dagger_{-k\downarrow}$) that couples spin-up electrons and spin-down holes, it can also be reflected as a left-moving, spin-

down hole[12] with a probability $a(E,\varphi)$ in what is called an Andreev reflection process. This second situation is sketched in Fig. 2.6. The wavefunction describing this process is

$$\begin{aligned}\psi_E(x) = &\left[A_E\begin{pmatrix}1\\0\end{pmatrix}\exp\left(ik_e^N x\right) + B_E\begin{pmatrix}0\\1\end{pmatrix}\exp\left(ik_h^N x\right)\right]\theta(-x)\\ &+\left[C_E\begin{pmatrix}u_e\\v_e\end{pmatrix}\exp\left(ik_e x\right)\right]\theta(x)\end{aligned} \tag{2.28}$$

where $u_{e,h}$, $v_{e,h}$, $k_{e,h}$ and $k_{e,h}^N$ have been defined in Eq. 2.24 with the superscript N in the normal region denoting that we have let $\Delta \to 0$. Using the continuity equation at $x = 0$, one gets[13]:

$$\begin{cases} A_E = C_E u_e \\ B_E = C_E v_e \end{cases}. \tag{2.29}$$

By definition, the Andreev reflection probability is $a(E,\varphi) = \frac{B_E}{A_E} = \frac{v_e}{u_e}$. Using Eq. 2.24, one finds

$$a(E,\varphi) = \frac{e^{-i\varphi}}{\Delta}\begin{cases} E - \mathrm{sgn}(E)\sqrt{E^2-\Delta^2} & |E| > \Delta \\ E - i\sqrt{\Delta^2 - E^2} & |E| < \Delta \end{cases}. \tag{2.30}$$

Similarly, one can derive the Andreev reflection of a spin-down hole into a spin-up electron. It is simply given by $\frac{u_h}{v_h} = a(E,-\varphi)$. For an electron impinging with an energy inside the gap $|E| < \Delta$, the modulus of $a(E,\varphi)$ is unity, *i.e.* the Andreev reflection is complete (left panel of Fig. 2.7). But the complex phase acquired in this reflection depends on the energy E (right panel of Fig. 2.7).

In the Andreev approximation, the wavefunction (2.28) is a solution of Eq. 2.5 with eigenenergy E. If $|E| < \Delta$, the wave vector $k_e = k_F + i\kappa(E)$ is complex: the wavefunction is evanescent in the superconductor, on a length scale $\kappa^{-1} \gg k_F^{-1}$. When $E = 0$, this length is exactly the superconducting coherence length

$$\xi = \frac{2\mu}{\Delta}k_F^{-1} = \frac{\hbar v_F}{\Delta}. \tag{2.31}$$

12 This nomenclature makes sense in the one-particle picture described previously where all eigenstates are built upon the vacuum state.

13 The derivative has also to be continuous in $x = 0$. This is only achieved in the zero-order Andreev approximation $k_{e/h} \simeq k_{e/h}^N \simeq k_F$. Otherwise, one needs to introduce a bigger wave function of the form

$$\begin{aligned}\psi_E(x) = &\left[A_E\begin{pmatrix}1\\0\end{pmatrix}\exp\left(ik_e^N x\right) + B_E\begin{pmatrix}1\\0\end{pmatrix}\exp\left(-ik_e^N x\right) + C_E\begin{pmatrix}0\\1\end{pmatrix}\exp\left(ik_h^N x\right)\right]\theta(-x)\\ &+\left[D_E\begin{pmatrix}u_e\\v_e\end{pmatrix}\exp\left(ik_e x\right) + F_E\begin{pmatrix}u_h\\v_h\end{pmatrix}\exp\left(-ik_h x\right)\right]\theta(x)\end{aligned}$$

in order to take into account both Andreev and specular reflection.

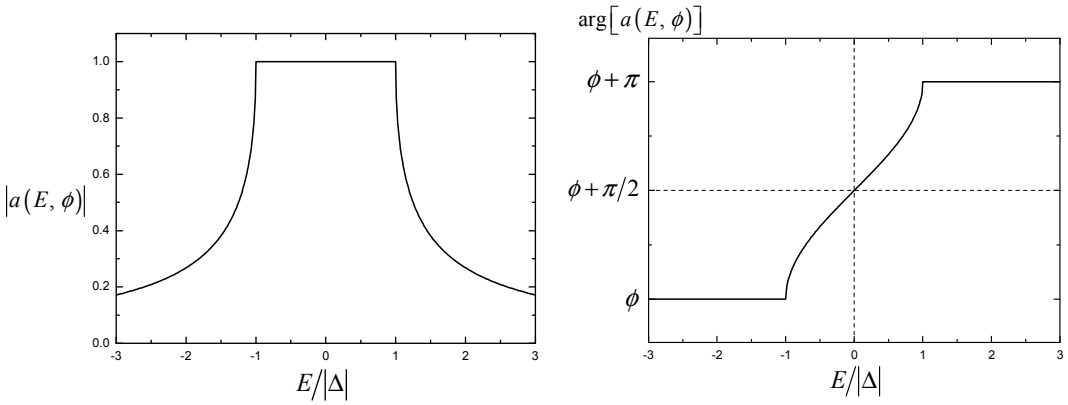

Figure 2.7: Andreev reflection probability (**left**) and phase of the probability amplitude (**right**) as a function of the one-particle energy E in units of Δ. ϕ is the phase of the superconducting order parameter.

2.4 Superconductor with both a phase gradient and a scattering potential

We now turn to the construction of the Andreev Bound States. The existence of these fermionic states, envisioned separately by Saint James [10] and Andreev [62] in normal-superconductor heterostructures[14], is the key concept which universally explains the mesoscopic Josephson effects [12, 13, 14, 15]. One considers two superconductors with a phase difference δ linked through a coherent conductor. In the Landauer formalism [64], the conductor is fully characterized by its set of transmission channels $\{\tau_i\}$. In this inhomogeneous geometry, new solutions are possible. If the conductor is very short[15], there is a pair of ABS of energy $\pm E_A(\delta, \tau_i)$ inside the superconducting gap for each conduction channel. Contrary to the Cooper pair states found in the homogeneous case (Section 2.2), these states are spatially localized at the weak link.

As Andreev reflection does not mix conduction channels, the problem can be treated as in the normal regime, in terms of independent conduction channels. We restrict ourselves to the one-channel case and the short-junction limit, where the length of the normal channel is zero. We model the scattering impurity as a repulsive delta function[16] at $x = 0$: $U(x) = V\delta(x)$, with $V > 0$. We force a phase difference δ across the scatterer: $\Delta(x) = \Delta e^{i\varphi(x)}$, with $\varphi(x) = \frac{\delta}{2}\mathrm{sgn}(x)$. One can show (see Section A.1.3) that the only parameter of interest is the transmission

$$\tau = \frac{1}{1 + \left(\frac{\eta}{k_F}\right)^2}, \tag{2.32}$$

14 The calculation of the electron-hole reflection and the formation of the bound states is described in great details in the paper authored by Saint-James [10]. It was unfortunately written in French and presumably largely ignored because of that. The paper of Andreev [11] was quoted much more frequently and the names "Andreev reflection" and "Andreev bound states" became the norm. Only recently, the name convention "Andreev-Saint-James" both for the reflections and for the bound states has been proposed to be used [63].

15 Meaning that its length l is smaller than the superconducting coherence length ξ, which provides a scale for the extension of Cooper pairs. For longer conductors, $n = \lfloor l/\xi \rfloor$ new pairs of ABS enter in the superconducting gap.

16 $\delta(x)$ is here the Dirac function, not to confuse with the phase difference δ.

where $\eta = \frac{mV}{\hbar^2}$ is the inverse of the scattering length. This model allows deriving explicitly both the energies and the wave functions of the ABS. Here we will present only the results. The full derivation can be found in Section A.2.4.

2.4.1 *Diagonalization of the Hamiltonian*

The two orthonormal wave functions ($\sigma = \pm$)

$$\begin{aligned}\overrightarrow{\phi^{B}_{\pm}}(x) = \; & \exp(\kappa x)\left(A_{\pm}\begin{pmatrix} b_{\pm}e^{-i\frac{\delta}{4}} \\ e^{i\frac{\delta}{4}}\end{pmatrix}\exp(ik_F x) + B_{\pm}\begin{pmatrix} e^{-i\frac{\delta}{4}} \\ b_{\pm}e^{i\frac{\delta}{4}}\end{pmatrix}\exp(-ik_F x)\right)\theta(-x) \\ & + \exp(-\kappa x)\left(C_{\pm}\begin{pmatrix} e^{i\frac{\delta}{4}} \\ b_{\pm}e^{-i\frac{\delta}{4}}\end{pmatrix}\exp(ik_F x) + D_{\pm}\begin{pmatrix} b_{\pm}e^{i\frac{\delta}{4}} \\ e^{-i\frac{\delta}{4}}\end{pmatrix}\exp(-ik_F x)\right)\theta(x)\end{aligned}, \tag{2.33}$$

with the coefficients $b_{\pm}$, $A_{\pm}$, $B_{\pm}$, $C_{\pm}$ and $D_{\pm}$ given in equations (A.69) and (A.70), are solutions of Eq. 2.5 of energies $\pm E_A$, where

$$\boxed{E_A = \Delta\sqrt{1 - \tau\sin^2\left(\frac{\delta}{2}\right)}} \tag{2.34}$$

is the Andreev energy. These wave functions are localized on a length scale

$$\boxed{\kappa_A^{-1} = \frac{\xi}{\sqrt{1 - \left(\frac{E_A}{\Delta}\right)^2}} = \frac{\xi}{\sqrt{\tau}\left|\sin\left(\frac{\delta}{2}\right)\right|}} \tag{2.35}$$

where ξ is the superconducting coherence length defined in Eq. 2.31.

The propagating solutions[17] form a continuum at energies $|E| > \Delta$. One can build an orthonormal set of propagating solutions of eigenenergy E $\left\{\overrightarrow{\phi_{1E}}, \overrightarrow{\phi_{2E}}, \overrightarrow{\phi_{3E}}, \overrightarrow{\phi_{4E}}\right\}$.

One can decompose the spinor field (2.2) Ψ on the bound and continuum states and the Hamiltonian becomes diagonal:

$$\boxed{\mathcal{H} = E_A\left(\gamma^{\dagger}_{A+}\gamma_{A+} - \gamma^{\dagger}_{A-}\gamma_{A-}\right) + \sum_{|E|>\Delta} E \sum_{i\in\{1,2,3,4\}} \gamma^{\dagger}_{iE}\gamma_{iE}}, \tag{2.36}$$

where $\gamma_{A\sigma}$ are the Andreev operators and γ_{iE} are the continuum operators.

2.4.2 *The Andreev Bound States*

In addition to the continuum states that already exists in the uniform case (Section 2.2), there are two new one-particle states[18] called the Andreev bound states (ABS) as shown in Fig. 2.8. In the one-particle picture (left panel of Fig. 2.8), they are non-degenerate, with energies $\pm E_A$. In the excitation picture (right panel of

17 We have not derived explicitly here the continuum states.

18 In the sense that one needs to apply only one Andreev creation operator $\gamma^{\dagger}_{A-}$ or $\gamma^{\dagger}_{A+}$ on the vacuum. These two states are the one usually called the "pair of ABS".

Fig. 2.8), they are degenerate[19], with energy E_A. Note that the density of states of the continuum is also modified[20]: the singularities at $\pm\Delta$ have transformed into the ABS.

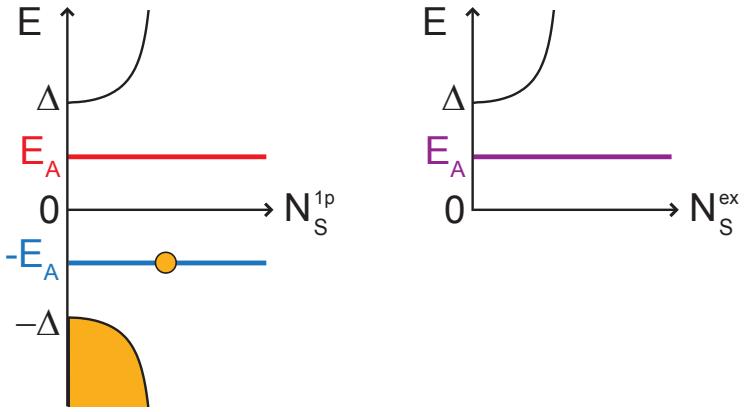

Figure 2.8: Density of states in the one-particle picture (**left**) and in the excitation picture (**right**), for a transmission $\tau = 0.9$ and a phase $\delta = 3\pi/4$.

As shown in Fig. 2.9, the energy $E_A(\delta, \tau)$ depends strongly on the phase difference. The ABS connect to the continuum states when $\delta = 0\ [2\pi]$. Indeed what

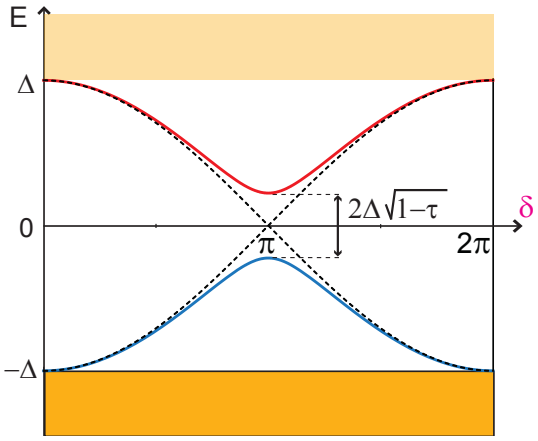

Figure 2.9: Energy spectrum of the ABS as a function of the phase δ in the one-particle picture. The continuous lines correspond to a transmission $\tau = 0.95$. The minimum gap between the ABS is obtained at $\delta = \pi$ and is given by $2\Delta\sqrt{1-\tau}$. The dashed lines correspond to the ballistic case $\tau = 1$.

creates the ABS is the twist of the phase around a region called the weak link[21].

19 In presence of a Zeeman field or a magnetic impurity, the degeneracy is lifted. These two cases are addressed in Section A.2.4.

20 This derivation is not done here since we have not exhibited the continuum states. The expression for the density of states of the continuum is calculated in Ref. [65] (Eq 53) and reads

$$N_s(E) = \frac{1}{2}N_n(0)\frac{|E|\sqrt{E^2-\Delta^2}}{E^2-\Delta^2\left(1-\tau\sin^2\left(\frac{\delta}{2}\right)\right)} \quad (|E| > \Delta)\,. \tag{2.37}$$

21 In a bulk superconductor, the phase is homogeneous. It is called weak in the sense that one can twist the phase in this region.

The impurity is not actually necessary to have the ABS: at transmission $\tau = 1$, the "ballistic ABS" are given by (dashed lines in Fig. 2.9)

$$E = \pm\Delta \cos\left(\frac{\delta}{2}\right). \tag{2.38}$$

A finite transmission allows specular reflexion in addition to Andreev reflexion: it couples these two reflectionless states, which opens a gap $2\Delta\sqrt{1-\tau}$ at $\delta = \pi$.

In contrast with the continuum states, which are delocalized and propagating, the ABS are bound to the weak link, and decay in the superconducting electrodes on a length scale κ_A^{-1}, which diverges at $\delta = 0$, where they melt in the continuum and become delocalized.

As in the uniform case, the ground state is obtained by populating the vacuum $|V\rangle$ with Bogoliubons of negative energies, which now includes the ABS of negative energy (see left panel of Fig. 2.8):

$$|GS\rangle = \left(\prod_{E<-\Delta}\prod_{i}\gamma_{iE}^{\dagger}\right)\gamma_{A-}^{\dagger}|V\rangle \tag{2.39}$$

Its energy is

$$E_{GS} = -E_A(\delta) + \sum_{E<-\Delta} E, \tag{2.40}$$

which depends on the phase and is minimum at $\delta = 0$[22]. This ground state is made of standard delocalized Cooper pairs, whose condensation energy E is bigger than Δ in absolute value, and one peculiar state localized at the channel, the "**Andreev Cooper pair**", whose condensation energy $-E_A$ is smaller in absolute value than the energy gap Δ and depends on the superconducting phase difference δ. It has an even parity and zero total spin.

Since $E_A < \Delta$, the excited states of lowest energy with one quasiparticle are $\gamma_{A-}|GS\rangle$ and $\gamma_{A+}^{\dagger}|GS\rangle$ of energy $E_{GS} + E_A$; the excited state of lowest energy with two quasiparticles is $\gamma_{A+}^{\dagger}\gamma_{A-}|GS\rangle$ of energy $E_{GS} + 2E_A$. Together with the ground state, these four states are represented in Fig. 2.10. The first and last one have an even parity and zero total spin and correspond to the ground and excited state of the Andreev Cooper pair. The two others have an odd parity, a finite spin and are here spin degenerate[23]. The one-particle picture (top panel of Fig. 2.10) is convenient to express that the ground state energy depend on the phase as $-E_A(\varphi)$. In the excitation picture (see Section 2.2.3), $\gamma_{A\uparrow}^{\dagger} \equiv \gamma_{A+}^{\dagger}$, $\gamma_{A\downarrow}^{\dagger} \equiv \gamma_{A-}$, and $E_{A\uparrow} = E_A = E_{A\downarrow} = -(-E_A)$. The four ABS are represented in the bottom panel of Fig. 2.10. This representation is better to keep track of the spin in the odd states.

Ignoring the continuum[24], one obtains four states, as shown in Fig. 2.11: two **even states**, $|-\rangle$ and $|+\rangle$, with energies $-E_A$ and $+E_A$, and two **odd states**, $|\uparrow\rangle$ and $|\downarrow\rangle$, with zero energy.

22 We have not derived the continuum states explicitly, but they should also depend on the phase difference δ. However, one can show (see Remark 14 of [14]) that in the short junction limit, the phase dependence of the continuum is negligible compared to the Andreev one.

23 This is not the case in presence of a Zeeman field or a magnetic impurity (see Section A.2.4).

24 This is relevant if one is interested in the supercurrent, since continuum do not depend on phase in the short junction limit [14].

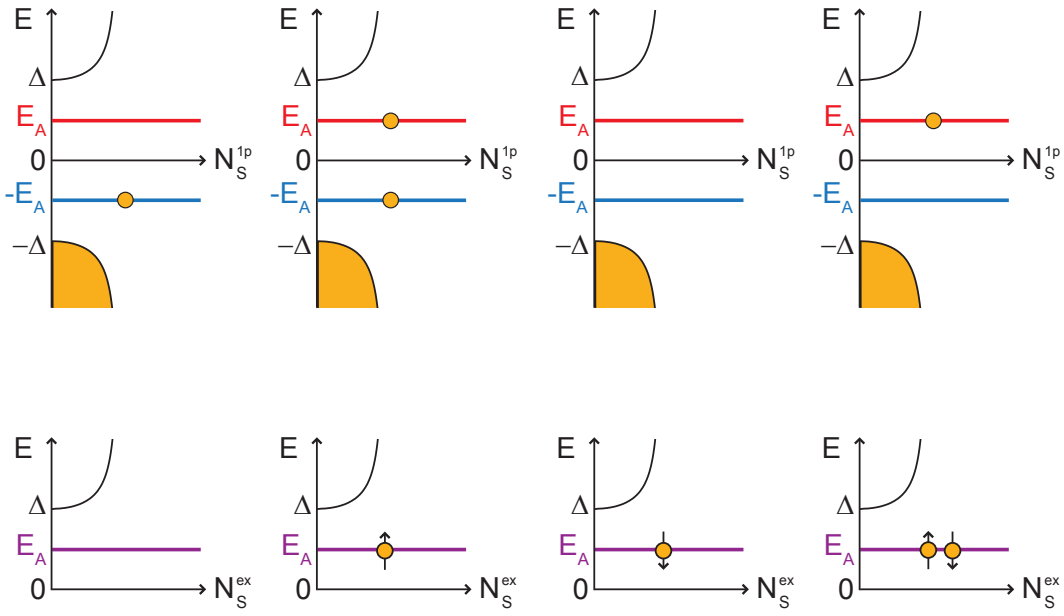

Figure 2.10: Ground state and lower excited states, in the one-particle picture (**top**) and in the excitation picture (**bottom**). From left to right: even ground state, spin degenerate excited odd states, excited even state.

2.5 The Andreev two-level system

When the ABS are deep inside the superconducting gap, *i.e.* when $E_A(\delta) \ll \Delta$ (at high transmission and for phase δ around π), the continuum states can be ignored and these four states can be considered an isolated, two-level system, with energies $-E_A$ and $+E_A$ (when spin-degenerate).

2.5.1 *The Andreev Hamiltonian*

In this limit, one can restrict to the first part of the Hamiltonian (2.36):

$$\mathcal{H}_A = -E_A \left(\gamma_{A-}^\dagger \gamma_{A-} - \gamma_{A+}^\dagger \gamma_{A+}\right) \tag{2.41}$$

One defines the Andreev spinor operator

$$\Psi_A = \begin{pmatrix} \gamma_{A-} \\ \gamma_{A+} \end{pmatrix} \tag{2.42}$$

and the usual Pauli matrices:

$$\begin{gathered} \mathbb{I} = \begin{bmatrix} 1 & 0 \\ 0 & 1 \end{bmatrix}, \ \sigma_x = \begin{bmatrix} 0 & 1 \\ 1 & 0 \end{bmatrix}, \ \sigma_y = \begin{bmatrix} 0 & -i \\ i & 0 \end{bmatrix}, \\ \sigma_z = \begin{bmatrix} 1 & 0 \\ 0 & -1 \end{bmatrix} \text{ and } \vec{\sigma} = \sigma_x \vec{e_x} + \sigma_y \vec{e_y} + \sigma_z \vec{e_z} \end{gathered} . \tag{2.43}$$

Then, the Andreev Hamiltonian reads

$$\boxed{\mathcal{H}_A = \Psi_A^\dagger \left(-E_A \sigma_z\right) \Psi_A}. \tag{2.44}$$

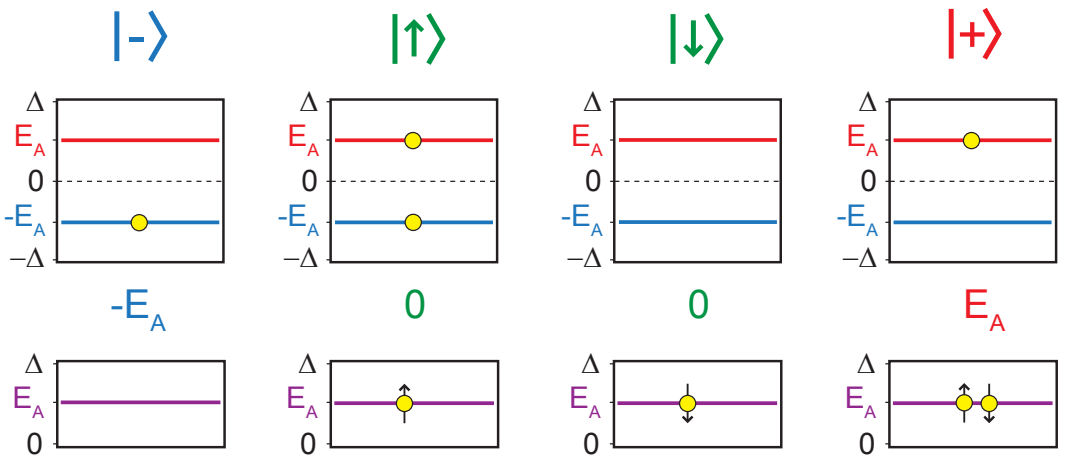

Figure 2.11: The four states obtained with various occupations of the ABS, represented in the one-particle picture (**top**) and in the excitation picture (**bottom**). From left to right: ground even state $|-\rangle$, spin-degenerate odd states $|\uparrow\rangle$ and $|\downarrow\rangle$, excited even state $|+\rangle$. In this representation, the continuum states are ignored.

2.5.2 *The Andreev current operator*

The current field operator is

$$\boxed{\mathcal{C}(x) = -i\frac{e\hbar}{2m}\sum_{\sigma=\downarrow\uparrow}\left(\psi_\sigma^\dagger(x)\nabla\psi_\sigma(x) - \nabla\psi_\sigma^\dagger(x)\psi_\sigma(x)\right)}. \tag{2.45}$$

One can restrict to the lower excitation energies by neglecting the continuum states:

$$\Psi(x) = \gamma_{A-}\overrightarrow{\phi_-^B}(x) + \gamma_{A+}\overrightarrow{\phi_+^B}(x). \tag{2.46}$$

Then one can derive the Andreev current operator, defined by[25]

$$\mathcal{C}_A = \lim_{x\to 0^-}\mathcal{C}(x) = \lim_{x\to 0^+}\mathcal{C}(x). \tag{2.47}$$

This calculation is done in Appendix A. One finds that

$$\boxed{\mathcal{C}_A = \Psi_A^\dagger I_A\left[\sigma_z + \sqrt{\tau}\tan\left(\frac{\delta}{2}\right)\sigma_x\right]\Psi_A} \tag{2.48}$$

where

$$\boxed{I_A(\delta,\tau) = -\frac{1}{\varphi_0}\frac{dE_A}{d\varphi} = \frac{\Delta}{4\varphi_0}\frac{\tau\sin(\delta)}{\sqrt{1-\tau\sin^2(\frac{\delta}{2})}}} \tag{2.49}$$

is the Andreev supercurrent with

$$\varphi_0 = \frac{\hbar}{2e} \tag{2.50}$$

25 Note that it is also equal to $\mathcal{C}_A = \frac{1}{\varphi_0}\frac{\partial\mathcal{H}_A}{\partial\delta}$, which is not straightforward. This point is partly discussed in Appendix A.

the reduced flux quantum and

$$r = 1 - \tau \tag{2.51}$$

the reflection coefficient.

Therefore, the current in the even states is given by $\langle \pm | \mathcal{C}_A | \pm \rangle = \mp I_A$: it exists in the absence of a voltage bias and is driven by the phase difference δ. This is the dc Josephson effect. On the contrary, the current in the odd states, which are annihilated by $\hat{\sigma_x}$ and $\hat{\sigma_z}$, is zero[26]. Note that the energy and current eigenstates are not the same ($[\mathcal{H}_A, \mathcal{C}_A] \neq 0$,).

The Andreev Hamiltonian (2.44) and the current operator (2.48) are written in the basis of energy states, called the Andreev basis[27]. They are in perfect agreement with the results of Zazunov and Shumeiko [66].

2.5.3 *The Andreev inverse inductance operator*

For convenience, we introduce here the inverse inductance operator

$$\mathcal{L}_A^{-1} = \frac{1}{\varphi_0^2} \frac{d^2 \mathcal{H}_A}{d\delta^2}. \tag{2.52}$$

One finds that

$$\boxed{\mathcal{L}_A^{-1} = \Psi_A^\dagger \frac{I_A}{\varphi_0} \left[\frac{\tau + (2-\tau)\cos(\delta)}{2\sin(\delta)} \sigma_z - \sqrt{r}\sigma_y \right] \Psi_A}. \tag{2.53}$$

2.5.4 *Andreev Bound States as a spin-1/2 in phase-dependent magnetic field*

If one assumes that the electron parity is even and conserved, there are only two states remaining, $|-\rangle$ and $|+\rangle$. Projecting $\mathcal{H}_A$ in the two-dimensional subspace $\{|-\rangle, |+\rangle\}$, the Andreev Hamiltonian reads[28]

$$\boxed{H_A = -E_A(\delta)\, \sigma_{z(\delta)}}. \tag{2.54}$$

The restriction to the even states allows dealing directly with Pauli matrices[29]. The physics of the Andreev states is analogous to that of a spin-1/2 in a magnetic field of amplitude $E_A(\delta)$. Both the amplitude and the direction of this effective magnetic field depend on the phase difference δ.

26 This is true for a spin degenerate system (see Section A.2.4).

27 One can also write them in other basis, like the current operator basis, or a phase independent basis (see Section A.2.4).

28 The states $|-\rangle$ and $|+\rangle$ are one-particle states, starting from the vacuum $|V\rangle$. We change the calligraphy from $\mathcal{H}$ to H to signal that one switches from second to first quantization.

29 $\sigma_{z(\delta)}$ is the z-Pauli matrix in the phase-dependent Andreev basis. It reads $\sigma_{z(\delta)} = \vec{n}(\delta).\vec{\sigma}$, where $\vec{n}(\delta) = \left(\mathrm{Im}(Z)\vec{e_y} + \mathrm{Re}(Z)\vec{e_z}\right)/|Z|$ is a phase-dependent unit vector, with $Z = \Delta\left[\cos(\frac{\delta}{2}) + i\sqrt{r}\sin(\frac{\delta}{2})\right]\exp(-i\sqrt{r}\frac{\delta}{2})$.

2.5.5 *Full quantization of the Andreev Hamiltonian*

Up to now, the superconducting phase difference δ has been treated classically as an external parameter that allows tuning the Andreev levels. We now promote to a quantum operator, anticipating the role of quantum phase fluctuations. We note byδ_0 its average value: $\delta \to \delta_0 + \hat{\delta}$ and[30] $\mathcal{H}_A(\delta) \to \mathcal{H}_A(\delta_0 + \hat{\delta})$.

There are two coupled degrees of freedom in this Hamiltonian: the electromagnetic degree of freedom and the spin-like Andreev degree of freedom. This corresponds to the **spin-boson** problem [51, 52]. In order to separate them, following Ref. [67], one performs a Taylor expansion of $\mathcal{H}_A$ around the average phase δ_0:

$$\boxed{\mathcal{H}_A(\delta_0 + \hat{\delta}) = \mathcal{H}_A(\delta_0) + \varphi_0\,\hat{\delta}\,\mathcal{C}_A(\delta_0) + \frac{1}{2}\varphi_0^2\,\hat{\delta}^2\,\mathcal{L}_A^{-1}(\delta_0)}. \tag{2.55}$$

This is correct as long as quantum fluctuations are small [31], *i.e.* $\sqrt{\langle\hat{\delta}^2\rangle} \ll 2\pi$.

Therefore, whereas diagonal terms of the current and inverse inductance operator only renormalize the mean Andreev energy, the non-diagonal ones allow transitions between the ABS. In particular, to zero order, the coupling term is $\langle +|\,\varphi_0\mathcal{C}_A\,|-\rangle = \langle -|\,\varphi_0\mathcal{C}_A\,|+\rangle = \varphi_0 I_A(\delta,\tau)\sqrt{\tau}\tan\left(\frac{\delta}{2}\right)$, which is maximum at $\delta = \pi$ and increases with the transmission.

2.5.6 *Extension to multiple channels*

Up to now, we have treated the case of a single conduction channel of finite transmission τ between two superconducting electrodes, referred further as Josephson channel (JC). Because Andreev reflection does not mix up conduction channels, any Josephson element can be seen as a collection of independent JCs[32]. Then, the Hamiltonian, current and inverse inductance operator are simply obtained by summing up the independent contribution of all conduction channels:

$$\begin{cases} \mathcal{H} = & \sum_i \mathcal{H}_A(\tau_i) \\ \mathcal{C} = & \sum_i \mathcal{C}_A(\tau_i) \\ \mathcal{L} = & \sum_i \mathcal{L}_A(\tau_i) \end{cases}, \tag{2.56}$$

where we neglect the continuum states.

30 We will not always keep the hat notation ˆ in the following.

31 This Taylor expansion is in general not trivial. This point is discussed in Section D.2.1.

32 Note that the problem is now analogous to the one of many spins and one bosons. Since each spin is coupled to the bosonic mode, there exists an indirect coupling between the different Andreev spins.

2.6 The tunnel Josephson junction

2.6.1 *The Josephson Hamiltonian*

The tunnel Josephson junction (JJ) is a large collection of JCs of small transmission channels $\tau_i \ll 1$ that share the same superconducting phase difference[33] γ. In this limit, $E_A(\gamma, \tau) \simeq \Delta\left(1 - \frac{\tau}{2}\sin^2\left(\frac{\gamma}{2}\right)\right)$ and the ABS are stuck at the gap edge. The corresponding excitation energy $2E_A$ is roughly 2Δ ($\sim$ 90 GHz for Aluminum) for all values of the phase . As long as one considers energies much lower than the superconducting gap, all the fermionic degrees of freedom (both Andreev and continuum) are frozen in the ground state[34]. Then, the Hamiltonian is written[35]

$$\mathcal{H}_J = -\sum_i E_A(\gamma, \tau_i) + \sum_{E<-\Delta} E. \tag{2.57}$$

One defines the Josephson energy

$$E_J = \frac{\Delta}{4}\sum_i \tau_i. \tag{2.58}$$

One neglect the continuum states which do not depend on the phase in the short junction limit. Then, up to constant energy, the Josephson Hamiltonian is

$$\boxed{\mathcal{H}_J = -E_J\cos(\gamma)}. \tag{2.59}$$

The corresponding current operator is simply

$$\mathcal{C}_J = I_0\sin(\gamma), \tag{2.60}$$

where

$$I_0 = E_J/\varphi_0 \tag{2.61}$$

is the critical current of the junction.

2.6.2 *Currents through a Josephson junction*

2.6.2.1 *Quasiparticle current*

Similarly to the normal-superconductor junction described in Section 2.2.5, dissipative current can flow through a voltage biased JJ only for large enough bias voltage $|eV| > 2\Delta$ (in a spin degenerate system $\beta = 0$). The energy gap is now twice larger because one needs to excite both left and right superconductors with $\gamma_L^\dagger\gamma_R^\dagger$, where the label denotes the electrode. It is well represented in the semiconductor picture, as shown in Fig. 2.12 (left).

33 We have on purpose changed the symbol of the phase difference, since it is what we will use in the following for a JJ.

34 On the contrary, for a superconducting atomic contact transmissions can be of order 1 and the dynamics of the Andreev spin-like degrees of freedom have to be considered.

35 The operators are averaged in the fermionic ground state in a mean-field approximation.

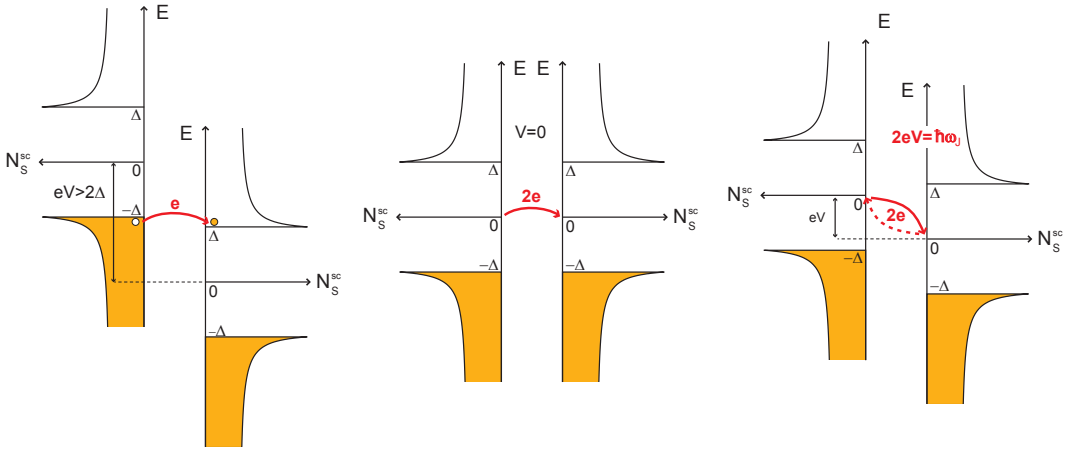

Figure 2.12: Sketch of the currents through a Josephson junction, in the semiconductor picture. **Left**: When voltage biased above twice the superconducting gap $|eV| > 2\Delta$, a dissipative quasiparticle current can flow. **Middle**: At zero voltage bias, a dc current can flow (dc Josephson effect). It is driven by the superconducting phase difference and corresponds to a coherent flow of Cooper pairs. To represent it, one can imagine that there is a condensate of Cooper pairs at the Fermi energy of each electrode. **Right**: At finite voltage V, due to the ac Josephson effect, Cooper pairs tunnel back and forth at the Josephson frequency $\nu_J = \frac{V}{2\pi\varphi_0}$. If the electromagnetic environment of the JJ can absorb at energy $h\nu_J = 2eV$, there is a net dc current of Cooper pairs at this voltage.

2.6.2.2 *Cooper pair current at zero voltage (dc Josephson effect)*

The supercurrent in the dc Josephson effect corresponds to a coherent flow of Cooper pairs and appears at zero bias voltage. To represent it in the semiconductor picture, one can imagine that there is a Cooper pair condensate at Fermi energy. As represented in the middle panel of Fig. 2.12, these Cooper pairs can flow between the two electrodes. The actual direction cannot be guessed in this representation since this current is driven by the phase difference.

2.6.2.3 *Cooper pair current at finite voltage (ac Josephson effect)*

In presence of a bias voltage V, the phase oscillates at the Josephson frequency $\nu_J = \frac{V}{2\pi\varphi_0}$. This is the ac Josephson effect. The oscillating phase causes the back and forth tunneling of Cooper pairs, as shown in the right panel of Fig. 2.12. In the absence of any electromagnetic environment, this tunneling at finite energy occurs through the emission and absorption of virtual photons of energy $h\nu_J = 2eV$, resulting in an ac current at frequency ν_J (see right panel of Fig. 2.12). In the presence of an external mode at frequency $\nu = \nu_J$, the emitted photon can be absorbed and lost to the environment, which results in a net dc current of Cooper pairs. This is called inelastic Cooper pair tunneling.

3

SIGNATURES OF ANDREEV BOUND STATES

This chapter discusses measurable signatures of Andreev Bound States and presents existing experimental results. Whereas properties of the ground state $|-\rangle$ have already been probed in different ways, the picture for excitation is far from comprehensive. In particular, the even excited state $|+\rangle$ had not been directly observed previously.

3.1 Current-phase relation

The supercurrent is a manifestation of the dc Josephson effect and is driven by the phase difference. From the microscopic point of view, it corresponds to a coherent flow of Cooper pairs. As shown in Fig. 3.1, the even Andreev Bound States $|-\rangle$ and $|+\rangle$ carry opposite supercurrents $I_\pm = \mp I_A$ (where I_A is defined in equation Eq. 2.49) whereas the odd states $|\uparrow\rangle$ and $|\downarrow\rangle$ do not carry any supercurrent[1]. Therefore, the supercurrent depends on the population of the ABS.

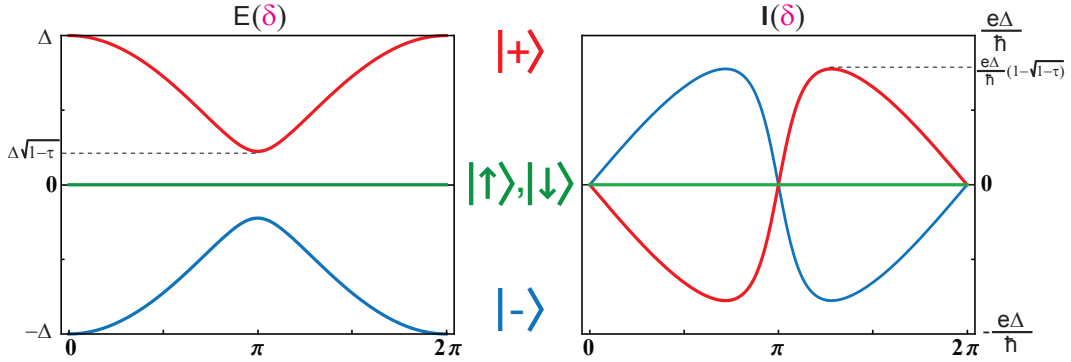

Figure 3.1: Energies (**left**) and supercurrents (**right**) of the four states corresponding to the possible occupations of the 2 ABS versus the phase difference for a JC of transmission $\tau = 0.95$. Whereas the even states $|-\rangle$ and $|+\rangle$ carry opposite supercurrent, the odd ones $|\uparrow\rangle$ and $|\downarrow\rangle$ do not carry any.

In thermal equilibrium, the supercurrent through a Josephson element of mesoscopic code $\{\tau_i\}$, at a given phase difference δ is given by [15]

$$\begin{aligned} I(\delta,\tau) &= \sum_i I_A[\delta,\tau_i]\left(f(-E_A[\delta,\tau_i]) - f(E_A[\delta,\tau_i])\right) \\ &= \boxed{\sum_i I_A[\delta,\tau_i]\tanh\left(\frac{E_A[\delta,\tau_i]}{2k_BT}\right)}. \end{aligned} \tag{3.1}$$

If the temperature is such that $k_BT \ll 2\Delta\sqrt{1-\tau}$, the system is essentially in the ground state and the supercurrent is simply

$$I(\delta) = \sum_i I_A[\delta,\tau_i]. \tag{3.2}$$

1 This is true for a spin degenerate system.

Fig. 3.2 depicts the current-phase relationship predicted for a typical atomic-size contact accommodating three conduction channels at zero temperature.

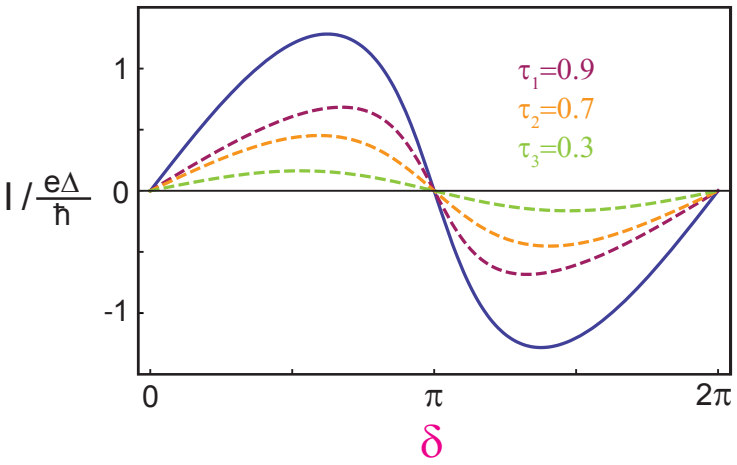

Figure 3.2: Theoretical current-phase relationship at zero temperature (equation 3.2), for a typical atomic-size contact accommodating three conduction channels $\{0.9, 0.7, 0.3\}$.

The maximum value of the supercurrent (with respect to the phase) at zero temperature is called the critical current. For a JC of transmission τ, it is given by

$$I_0(\tau) = \frac{\Delta}{2\varphi_0}\left(1 - \sqrt{1-\tau}\right). \tag{3.3}$$

In aluminum, where the superconducting gap is of the order of 200 µeV, the critical current is at most 50 nA[2] per channel.

TUNNEL JUNCTION In the case of a tunnel JJ, the ABS are stuck to the gap edges, and the system is in the ground state as long as $k_B T \ll 2\Delta$. The supercurrent at a given phase difference γ reads

$$I(\gamma) = I_0 \sin(\gamma) \tag{3.4}$$

where I_0 is the critical current defined in Eq. 2.61. In this case, it is proportional to the normal conductance $G_n = 2\frac{e^2}{h}\sum_i \tau_i$

$$I_0 = \frac{\pi}{2}\frac{\Delta}{e} G_n \tag{3.5}$$

which is the Ambegaokar-Baratoff relation at zero temperature [68].

EXPERIMENTAL EVIDENCE On the experimental side, the current-phase relation has been probed in superconducting atomic contacts, by switching measurements [21, 69], as shown in Fig. 3.3. This was achieved by placing a Josephson junction in parallel with an AC in a superconducting loop thus forming an "**atomic-SQUID**". This geometry permits either phase or voltage biasing an AC, allowing

2 Note that it is not proportional to τ^2: the supercurrent cannot be seen as independent tunneling events of Cooper pairs. It is a coherent process.

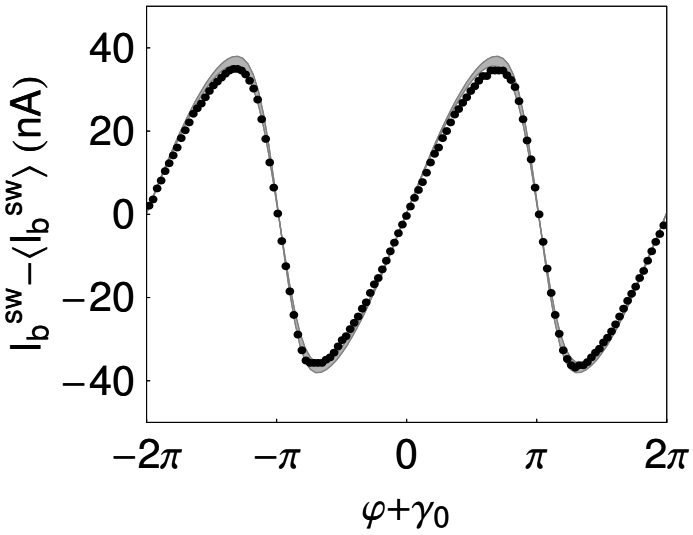

Figure 3.3: **Dots**: Measured switching current as a function of the reduced flux φ in the loop for an atomic-SQUID. **Grayed bands**: Theoretical prediction for the same current at finite temperature using equation 3.1, with the set of transmissions $\{0.95, 0.185\}$deduced from the$I(V)$ characteristic (figure taken from Ref. [70]).

measurement of both the current-phase relation and the $I(V)$ characteristic. Using the transmissions $\{\tau_i\}$ obtained from the $I(V)$[3], a quantitative agreement without any adjustable parameters was obtained between the measured and the theoretical current-phase relation[4]. The same technique is used here.

These experiments were performed at a temperature of 30 mK, such that $k_B T \ll 2\Delta\sqrt{1-\tau}$ for all values of τ explored. Only the negative energy ABS was therefore populated and comparison with the prediction (3.2) was quantitative. More recently, a similar experiment (see Ref. [72]) was performed at temperatures large enough to significantly populate the upper state, in which case a quantitative description was possible using Eq. 3.1.

Current-phase relation measurements were also performed in other systems. In superconductor normal superconductor (SNS) heterostructures, non-sinusoidal current-phase relations were also measured [26] as well as temperature dependence of the supercurrent [24]. An inversion of supercurrent could even be measured by inducing a non-equilibrium electronic distribution function in the normal weak link [25]. SNS junctions can be described as a large number of long channels resulting in a large number of ABS. Even though the physics is similar, the description of such systems in term of ABS is not the most appropriate[5]. Other experiments involve SQUIDs with junctions having nanotubes as weak links [74]. The presence of a barrier at the interface between the superconductors and the nanotubes leads to Coulomb interactions, and the description of such systems is more complex [75]. non-equilibrium electronic distribution function

3 This procedure relies on the MAR phenomenon and is explained in Section 3.4.1.

4 Koops *et al.* had already observed in 1996 a non-sinusoidal current-phase relation for Nb atomic contacts, but a quantitative comparison with theory could not be achieved at that time, since the transmissions of the channels were not measured simultaneously [71].

5 Eilenberger or Usadel equations are better adapted, see Ref. [73].

3.2 Phase-dependent inductance and flux modulation of the plasma frequency

3.2.1 *Classical inductance*

In experiments performed at finite frequency, a Josephson junction may behave as a non-linear inductor. The inductance can be found by taking the time-derivative of Eq. 3.2 and using $V = \varphi_0 \dot{\delta}$:

$$V = L_{class}(\delta) \frac{dI}{dt} \tag{3.6}$$

with

$$L^{-1}_{class}(\delta) = \varphi_0^{-1} \frac{\partial I}{\partial \delta}. \tag{3.7}$$

In the case of a JC of transmission τ (see blue curve in Fig. 3.4)

$$L^{-1}_{class}(\delta) = -\varphi_0^2 \left(\frac{\partial^2 E_A}{\partial \delta^2} \right)^{-1} = \frac{I_A}{\varphi_0 \sin(\delta)} \frac{\cos(\delta) + \tau \sin^4(\frac{\delta}{2})}{(1 - \tau \sin^2(\frac{\delta}{2}))} \tag{3.8}$$

Note that this expression is negative around π, and that $L^{-1}_{class}(\pi) \underset{\tau \to 1}{\to} -\infty$.

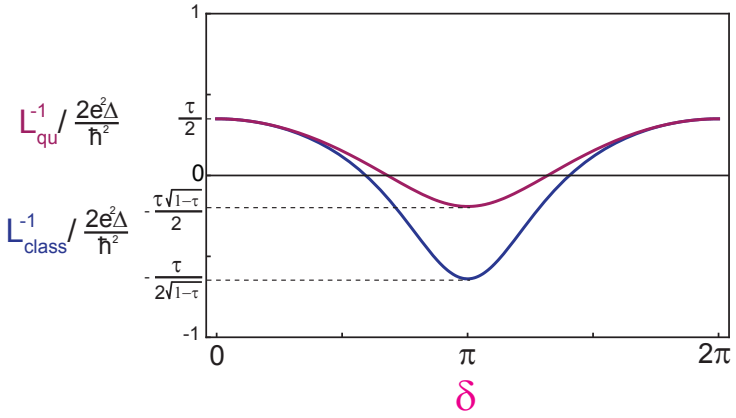

Figure 3.4: Theoretical inductance-phase relationship at zero temperature, for a JC of transmission $\tau = 0.7$. Whereas the blue line corresponds to the classical calculation (3.8), the purple one comes from the quantum derivation (3.10).

TUNNEL JUNCTION Similarly, a tunnel JJ can be seen as a non-linear inductor of inverse inductance at phase γ

$$L_J^{-1}(\gamma) = \frac{I_0}{\varphi_0} \cos(\gamma). \tag{3.9}$$

EXPERIMENTAL EVIDENCE Reflectometry experiments have been performed [70] to measure the inductance-phase relation. A microwave signal at frequency $\omega/2\pi$ is sent on a transmission line terminated by an atomic-SQUID. The parallel combination $L_{\|}$ of the two non-linear inductors associated with the AC and the JJ, combined with the junction capacitance C, form an oscillator with a resonant

frequency $\frac{1}{2\pi\sqrt{L_{\parallel}C}}$. This **plasma frequency** is modulated by the flux threading the loop. The reflected signal has a minimum at the plasma frequency. This modulation was detected in the experiment (see Fig. 3.5) but its shape could not be described quantitatively. This disagreement might lie in the use of the classical inductance (3.7) which does not take into account the Andreev degree of freedom.

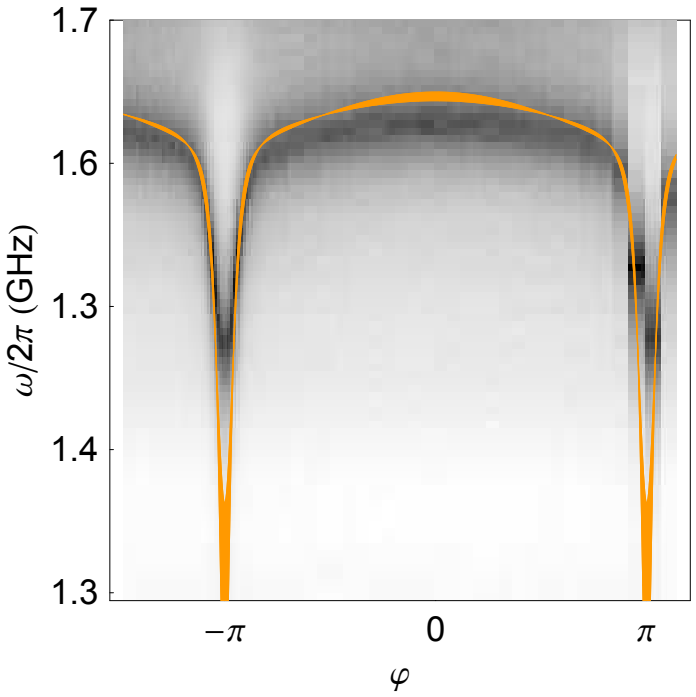

Figure 3.5: Measured reflection coefficient amplitude as a function of the excitation frequency $\omega/2\pi$ and reduced magnetic flux φ for a superconducting AC with transmissions $\{0.992, 0.089, 0.088\}$ in parallel with a JJ of critical current 720 nA. It is maximum at the plasma resonance of the atomic-SQUID. The lines correspond to the calculation with the classical definition of the Josephson inductance (figure taken from Ref. [70]).

Experiments on SNS systems have also probed a non-linear inductance by inductively coupling an NS ring to a multimode superconducting resonator [27]. A strong frequency dependence of the magnetic susceptibility is attributed to non-equilibrium occupation of the ABS.

3.2.2 *Quantum inductance*

From the quantum point of view, the inverse inductance operator is defined in Eq. 2.52. At zero temperature, the inductance in the ground state is (see purple curve in Fig. 3.4)

$$L_{qu}^{-1}(\delta) = \frac{I_A}{\varphi_0 \sin(\delta)} \frac{\tau + (2-\tau)\cos(\delta)}{2} \tag{3.10}$$

which differs from the classical expression[6]. In particular, $\frac{L_{qu}^{-1}}{L_{class}^{-1}}(\pi) = 1 - \tau$. This expression does not diverge at $\delta = \pi$ and $\tau \to 1$.

The quantity which is probed in a reflectometry experiment is the plasma frequency and one needs to derive the full Hamiltonian of the AC (using Eq. 2.41) and the Josephson junction (using Eq. 2.59). This treatment is done in Chapter 7 for a different experiment.

3.3 Fractional Shapiro steps

When a constant bias voltage V is applied to a Josephson element, its current oscillates at the Josephson frequency ν_J (Eq. 1.3). To probe the ac components of the current, one applies an external microwave signal of frequency $\omega_r/2\pi$. The beatings of this signal with the Josephson current give rise to resonances in the dc current-voltage $I(V)$ characteristic of the Josephson element, usually referred as "Shapiro steps".

This effect was first measured with a tunnel JJ by Shapiro [5]. Because the current phase relation of a Josephson junction (3.4) is sinusoidal, its current is purely harmonic at the frequency ν_J. Then, the beatings appear when the Josephson frequency is proportional to the external frequency and its harmonics ($\nu_J = p\omega_r/2\pi$, with $p \in \mathbb{Z}$). Therefore, the so-called Shapiro steps are replicas of the supercurrent peak at well defined values of the dc voltage, given by

$$V = p\varphi_0\omega_r. \tag{3.11}$$

In contrast, the current-phase relation of a JC of transmission τ close to 1 is non-sinusoidal (see Eq. 2.49 and Section 3.1). Therefore, the ac Josephson current oscillates not only at the Josephson frequency but also at higher harmonics $q\nu_J$. The bigger the transmission the higher the amplitude of the harmonics (see Fig. K.2 and Fig. K.3 in Appendix K). Thus, beatings are possible when the frequencies are commensurate ($\nu_J = \frac{p}{q}\nu_r$, with $p, q \in \mathbb{Z}$) and the Shapiro resonances appear at dc voltages given by:

$$V = \frac{p}{q}\varphi_0\omega_r.$$

Therefore new resonances with $q > 1$ are possible, called fractional Shapiro steps. The amplitudes of theses peaks have been calculated at zero temperature in Ref. [76], and with a more rigorous Fokker-Planck treatment in Ref. [77].

EXPERIMENTAL EVIDENCE As shown in Fig. 3.6, these fractional Shapiro resonances were observed in superconducting ACs [78, 22]. The fractional resonances appear only for highly transmitting channels and are small compared to the integer ones[7].

6 Note that for the current, the classical and quantum definitions give the same result. Moreover, in the tunnel case, the two definitions of the inductance are also the same.

7 This is due to the fact that thermal phase fluctuations have a stronger effect on the former than on the latter. Moreover, for highly transmitting channels, they are superimposed with a relatively big MAR current, which make them hard to measure.

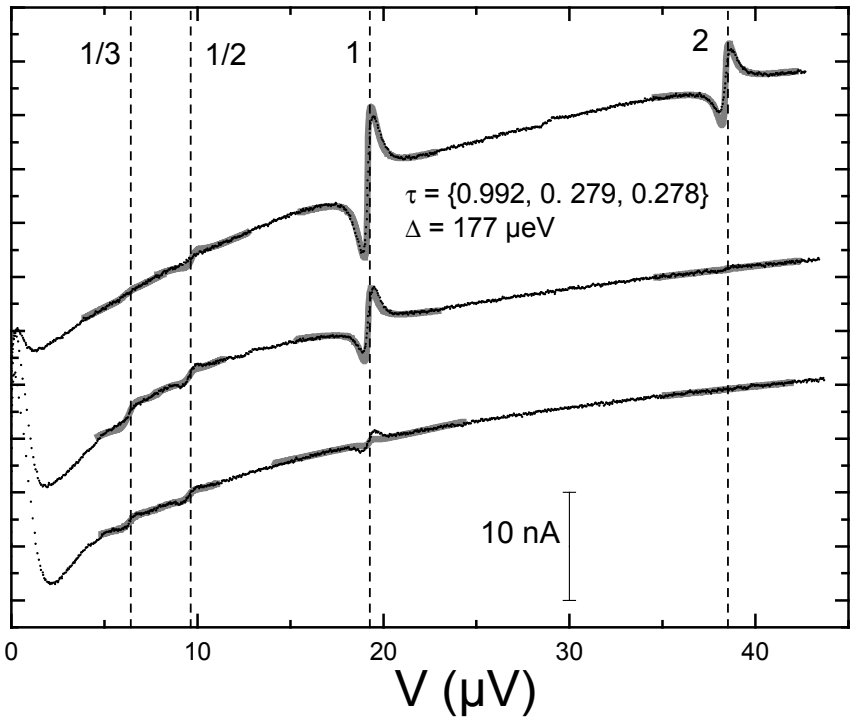

Figure 3.6: Shapiro resonances for an AC containing a high-transmission channel, under an external microwave frequency $\nu_r = 9.3156$ GHz , for three different values of the microwave power. Small fractional resonances are observed. Black dotted lines are experimental results. The full grayed lines are the predictions of the theory of replicas with no other adjustable parameter than the temperature (figure taken from Ref. [78]).

The three previous sections have presented experimental signatures of the properties of the ground state $|-\rangle$ of atomic contacts, in which only[8] the negative energy ABS is occupied.

3.4 Multiple Andreev reflections

3.4.1 *Dissipative MAR current*

In addition to the oscillating supercurrent discussed in the previous chapter, a dc-voltage biased Josephson element can also carry a dissipative dc current. As already explained in the case of a tunnel JJ (see Section 2.6.2), if the voltage V is big enough $|eV| > 2\Delta$, quasiparticles of charge e can tunnel through the barrier[9]. This results in a step in current in the $I(V)$ characteristic (see Fig. 3.7), for voltages $V = \pm\frac{2\Delta}{e}$. The exact shape of the step reflects the BCS density of states. When $|eV| \gg 2\Delta$, the DOS is essentially constant in energy and the current is linear and proportional to the normal state conductance. When $|eV| < 2\Delta$ the dc current is vanishingly small in an ideal JJ[10].

8 Except from thermal occupation or non-equilibrium distribution function of ABS in Refs. [24, 25, 72].
9 Note that in this case, these tunneling events are independent.
10 In absence of electromagnetic modes allowing inelastic tunneling of Cooper pairs.

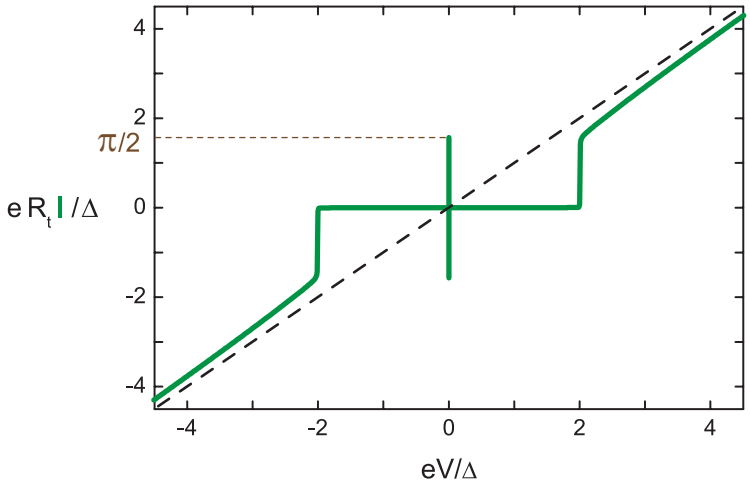

Figure 3.7: Current I of a Josephson junction, in units of Δ/eR_t, where R_t is the normal tunnel resistance, as a function of the voltage V, in units of Δ/e. At zero voltage, there is a supercurrent branch due to dc Josephson effect. At voltage larger than the superconducting gap $|eV| > 2\Delta$, quasiparticle current can flow.

3.4.1.1 *From ABS to MAR current*

Strikingly, due to the existence of ABS, a finite, dissipative current can flow below the superconducting gap in JCs. Indeed, in the presence of a constant bias voltage V, the phase difference δ evolves in time, according to

$$\dot{\delta}(t) = \frac{V}{\varphi_0}. \tag{3.12}$$

Consequently, the ABS energies, which depend on the phase, move inside the superconducting gap at the Josephson frequency ν_J:

$$\delta(t) = 2\pi\nu_J t. \tag{3.13}$$

In the adiabatic picture, the system is initially in its ground state. As the phase is swept across π, there is a finite probability to induce a non-adiabatic Landau-Zener transition [79] from the lower to the upper ABS as represented in the left panel of Fig. 3.8. If populated, the excited ABS empties in the continuum when the phase reaches 2π. At the same time, the ground ABS is filled by a quasiparticle, which can tunnel to the excited state through a Landau-Zener transition. Therefore, as sketched in the right panel of Fig. 3.8, the voltage-biased Andreev doublet behaves as a quasiparticle "elevator". This results in a finite quasiparticle flow in a direction determined by the bias voltage.

In the case of ABS, the Landau-Zener probability is (see Ref. [80] and Appendix D)

$$p_{LZ} = \exp\left(-\pi\frac{r\Delta}{e|V|}\right). \tag{3.14}$$

As the transmission of the channel increases, the Andreev gap at $\delta = \pi$ shrinks and the transition probability increases. When the voltage is increased the phase

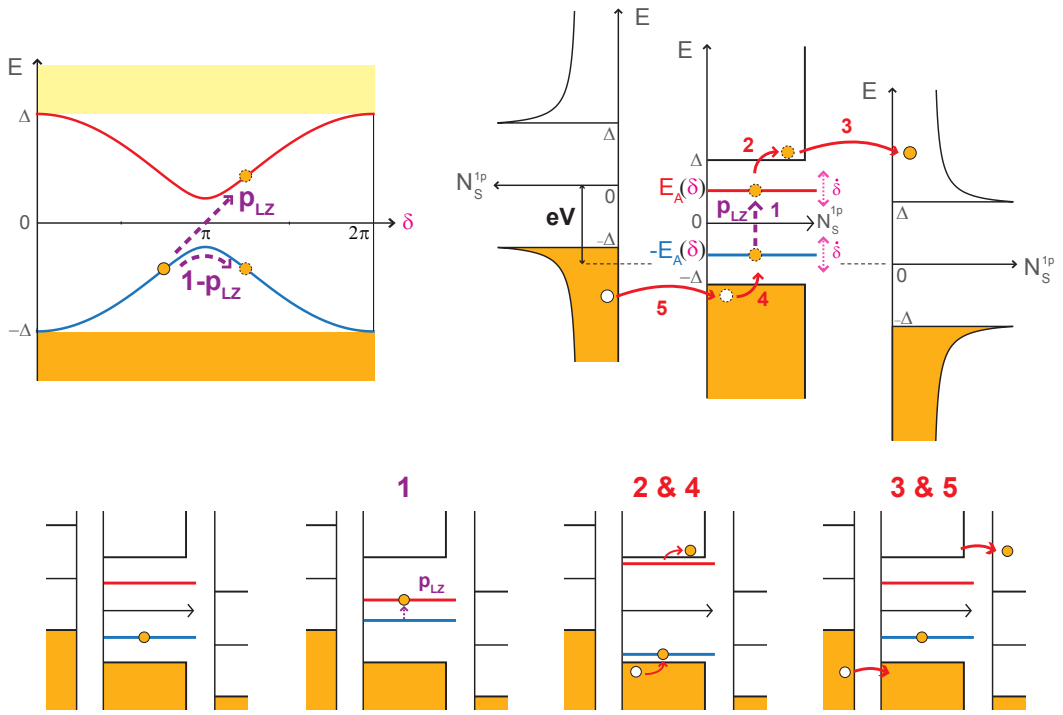

Figure 3.8: **Left:** Landau-Zener transition between the two ABS (in a channel of transmission 0.95): As the phase is swept at high speed across the Andreev gap ($2\Delta\sqrt{1-\tau}$) at $\delta = \pi$, a quasiparticle has a finite probability p_{LZ} to tunnel from the negative energy ABS to the positive energy ABS. **Right**: The Andreev elevator: Under a bias voltage V, the ABS oscillate in the superconducting gap. When a Landau-Zener transition occurs (**1**), a quasiparticle is promoted to the upper band of the continuum (**2**) and leaves to the right electrode (**3**). During the next cycle, a quasiparticle fills the lower ABS, thus emptying the lower band of the continuum (**4**). This hole is filled by a quasiparticle coming from the left electrode (**5**). This whole process leads to dc current from left to right.

is swept faster which also increases the probability. The associated dc current is simply [81]

$$I = Q\nu_J p_{LZ} \tag{3.15}$$

where Q is the charge transferred during one cycle[11]. By a simple argument of energy conservation,

$$Q = \frac{2\Delta}{V}. \tag{3.16}$$

Using equation Eq. 1.3, one gets

$$I(V) = \frac{\Delta}{\pi\varphi_0}\mathrm{sgn}(V)\exp\left(-\pi\frac{r\Delta}{e|V|}\right). \tag{3.17}$$

However, this description is only valid at small voltages $|eV| \ll r\Delta$, where the ABS can be defined as states slowly varying in time[12]. At higher voltage, this de-

11 We are using the fact that the different Landau-Zener events are independent. Note the similarity with a voltage biased channel of transmission τ, in the normal state $I = e\frac{eV}{h}\tau$.

12 This regime occurs at small voltages and connects quasistatic variations of the Josephson phase difference at $V \sim 0$ with MAR at larger voltages.

scription fails and one needs to develop a full theory for non-equilibrium ABS, which leads to the MAR phenomenon.

3.4.1.2 *The MAR phenomenon*

This mechanism was identified in 1982 within a semi-classical approach [82]. In the mid 1990s a complete quantum description was achieved by several groups [80, 83, 84]. Here, we sketch qualitatively this phenomenon in a scattering picture.

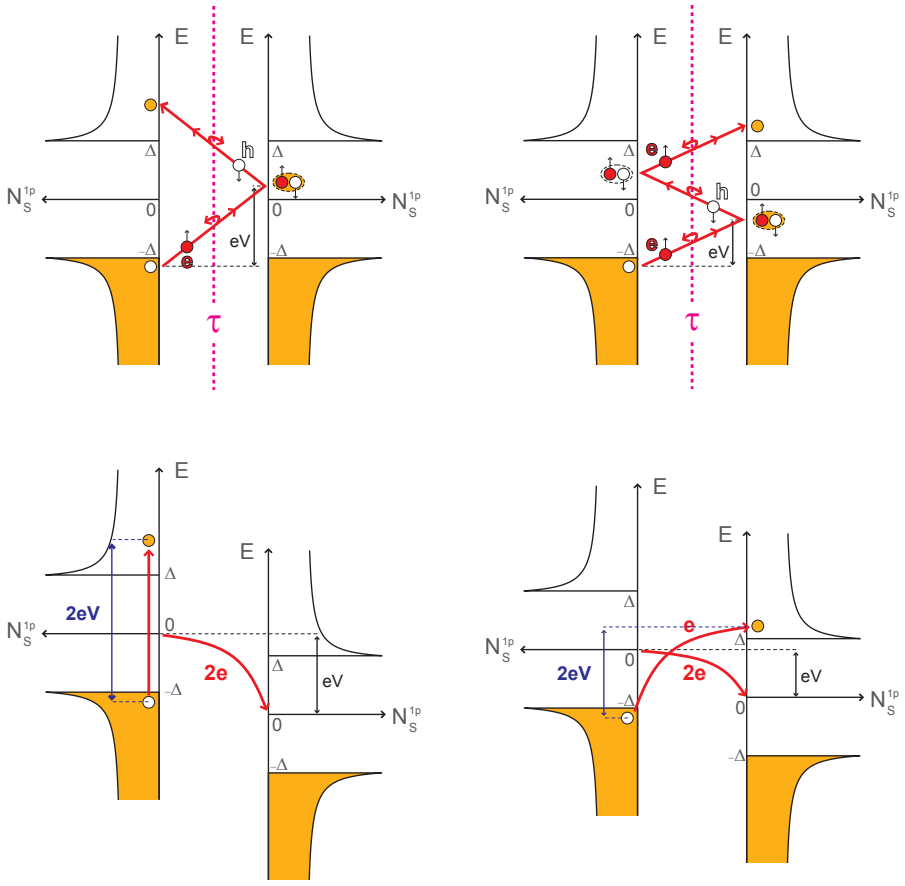

Figure 3.9: **Top**: MAR processes of order 2 (**left**) and 3 (**right**), in a JC of transmission τ. In this figure the chemical potential of both reservoirs are kept at the same level. The voltage is taken into account through the kinetic energy gained by the electrons and the holes from the electrical field across the channel. **Bottom**: Sketch of the same two MAR processes in term of inelastic tunneling events of Cooper pairs and one quasiparticle (the chemical potential are here shifted by the bias voltage eV).

Under a bias voltage V, electrons and holes gain or lose an energy eV when they propagate through the conduction channel. More precisely, a quasiparticle of energy E coming from the lower band of the left superconductor (see top of Fig. 3.9) is injected as an electron in the normal region[13]. After n[14] even (respectively odd)

13 With a probability amplitude $\sqrt{1-|a(E)|^2}$.

14 $n(E,V) = \left\lfloor \frac{\Delta - E}{eV} \right\rfloor$ is the minimum number of Andreev reflection for a quasiparticle of energy E in the lower band to reach the upper band, under a voltage bias V.

Andreev reflections, an electron (a hole) reaches the higher band of the right (left) superconductor where it recombines into a quasiparticle[15]. This process is called the multiple Andreev reflections (MAR) of order $n+1$[16]. After each Andreev reflection, a Cooper pair is created on the right or annihilated on the left. The n-th order process involves[17] the transfer of a charge ne. It results in a net current from left to right.

If one neglects the continuum and assumes that quasiparticles are essentially extracted at energy $E = -\Delta$ from the left electrode, the MAR process of the lowest possible order for a given voltage V is given by

$$n(V) = \left\lceil \frac{2\Delta}{eV} \right\rceil \tag{3.18}$$

and the corresponding transferred charge is

$$Q(V) = e \left\lceil \frac{2\Delta}{eV} \right\rceil . \tag{3.19}$$

which is the ceiling[18] of Eq. 3.16.

At each traversal of the conduction channel, an electron (a hole) has a probability τ to be transmitted. Therefore, the intensity of a MAR process of order n varies as the n-th power of the transmission τ^n. Because $\tau < 1$, the current at a given voltage V is mostly dominated by the MAR process of the lowest possible order $n(V)$[19]. When $\frac{2\Delta}{n} \leqslant |eV| < \frac{2\Delta}{n-1}$, the n-th order MAR process is dominant, and the current of a JC of transmission τ scales like τ^n. In the case of a multiple channel Josephson element, the MAR phenomenon happens in each channel independently. As the voltage bias is the same for all channels, the current scales like $\sum_i \tau_i^n$. It is essential to understand that the MAR phenomenon is a coherent process occurring independently in each conduction channel[20]. That is why this process is completely negligible in the tunnel case $\tau_i \ll 1$.

From the charge and energy point of view, a MAR process of order $2n$ can be understood as the inelastic tunneling of n Cooper pairs radiating an energy $n2eV$ (see bottom left panel of Fig. 3.9). This energy is absorbed by the superconducting electrodes, as a quasiparticle being promoted to the upper continuum, and must be bigger than 2Δ. Similarly, a MAR process of order $2n+1$ can be understood as a combined inelastic tunneling of n Cooper pairs and one quasiparticle (see bottom

15 With a probability amplitude $\sqrt{1-|a[E+n(E,V)eV]|^2}$.

16 Rigorously, this series is infinite and can continue on the continuum. Since the Andreev reflection probability becomes negligible for energies $|E| \gg \Delta$, to first order one can retain only those occurring in the superconducting gap. Note that the MAR process of order 1 is simply the transfer of one quasiparticle discussed in the tunnel case.

17 The $2n$-th order process involves the transfer of n Cooper pair. The $2n+1$-th order process involves the transfer of n Cooper pair and one quasiparticle. Therefore, it is a composite current of Cooper pairs and quasiparticles.

18 $\lceil x \rceil$ is the smallest integer greater than or equal to x

19 The more so as the transmission decreases. When τ approaches one, the MAR of all orders contribute coherently.

20 If it was incoherent, the current would scale as $\left(\sum_i \tau_i\right)^n$.

right of Fig. 3.9). The Cooper pairs emit an energy $n2eV$ which is absorbed by the tunneling quasiparticle and must be bigger than $2\Delta - eV$. We stress that these tunneling processes are coherent and must occur in the same conduction channel.

3.4.1.3 *Determination of the set of transmissions* $\{\tau_i\}$

Consequently, the $I(V)$ characteristic is highly non-linear below 2Δ and present current steps at voltages $2\Delta/ne$, which mark the onset of MAR of different orders (see Fig. 3.10). It depends on all powers of every transmission coefficient and carries

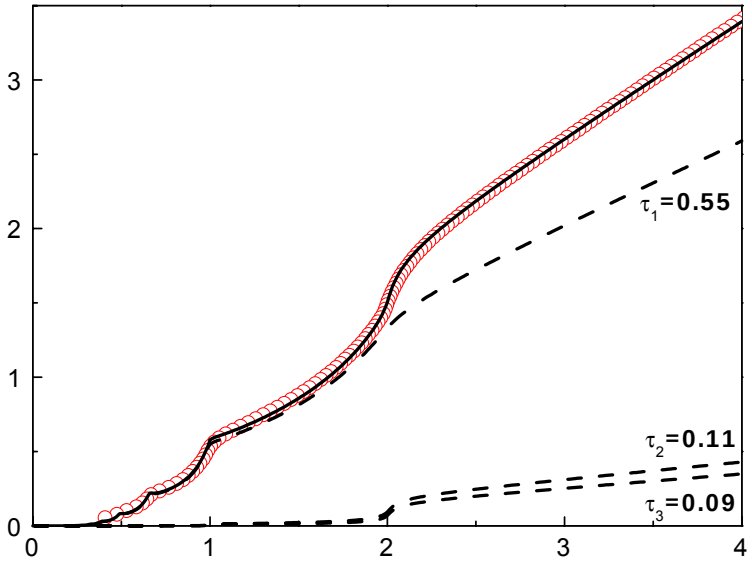

Figure 3.10: Determination of the set of transmissions of a one-atom aluminum contact. The experimental $I(V)$ characteristic (open dots) is decomposed into the sum of independent single channel characteristics (dashed curves). This particular contact contains three channels with transmission probabilities $\tau_1 = 0.55$, $\tau_1 = 0.11$ and $\tau_1 = 0.09$. These probabilities were adjusted to get the best fit (continuous curve) (figure taken from Ref. [85]).

sufficient information to reconstruct the set of transmissions. By decomposing the measured total current into a sum of such elementary characteristics, each of them corresponding to a given transmission probability, one can determine the set of transmissions of any atomic-size contact. The individual transmission probabilities of the channels are adjusted to get the best fit of the measured $I(V)$ characteristic [86]. This automatically yields the number of channels having a non-negligible transmission. This technique was first developed in Refs. [16, 85]. We have used this procedure throughout this thesis[21].

3.4.2 *MAR shot noise*

As shown in 1918 by Shottky, the discreteness of electric charge and the stochastic character of tunneling give rise to temporal fluctuations in the electrical current through vacuum diodes and tunnel junctions, called **shot noise**. When the current

21 See for instance Section 4.2.1. For a detailed discussion on this procedure, see Chapter 1 of Ref. [85].

I is made up from perfectly independent shots, the white noise power spectrum assumes the well-known Poissonian form

$$S_I = 2eI \tag{3.20}$$

where e is the electron charge transferred at each shot. In experiments with mesoscopic conductors in the normal state, the electrons in each transport channel are correlated due to the Pauli principle which leads to a noise reduction:

$$S_I = F \times 2eI \tag{3.21}$$

with F called the Fano factor[22]. The ratio

$$Q^* = \frac{S_I}{2I}, \tag{3.22}$$

is called the effective charge. In the tunnel limit, it is simply equal to the charge e.

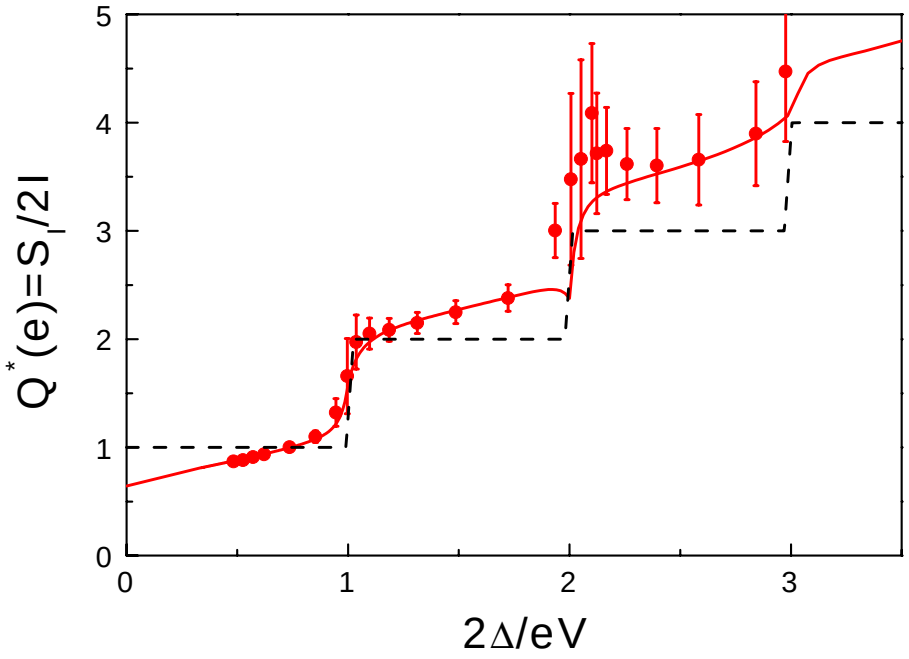

Figure 3.11: Effective charge, in units of e, as a function of the inverse reduced voltage for a contact in the superconducting state. Dashed line: MAR theory prediction in the tunnel limit. As the voltage increases, MAR processes of lower order set-in one by one leading to a perfect staircase pattern. Dots: Data for an aluminum atomic contact with transmissions $\{0.40, 0.27, 0.03\}$. Full line: MAR theory prediction for this set of transmissions (figure taken from Ref. [85]).

In the superconducting state, the current in the sub-gap region proceeds through MAR, which involves the transfer of multiple charge quanta. In the simple limit $|eV| \ll r\Delta$, the current spectral density at low frequency is given by

$$S_I = 2Q^2 \nu_J p_{LZ} (1 - p_{LZ}) \tag{3.23}$$

22 For a multichannel conductor $\{\tau_i\}$, $F = 1 - \sum_i \tau_i^2 / \sum_i \tau_i$.

where Q is the charge transferred during one cycle[23]. In the low voltage limit and for $\tau \ll 1$, $p_{LZ} \ll 1$ and, using Eq. 3.15, the effective charge is simply

$$Q^* = Q = \frac{2\Delta}{V} \tag{3.24}$$

which can be very large.

At higher voltage, this description fails and a full quantum MAR theory is necessary to compute the current spectral density [81, 87]. It predicts that in the tunnel limit, since $\tau^n \ll \tau^{n-1}$, only the MAR process of the lowest possible order $n\,(V)$ contributes significantly to the current at a given voltage. Consequently, the effective charge is a multiple of the electronic charge. On the contrary, for larger transmissions different order MAR processes contribute to the current at any given voltage. Furthermore, as in the normal state, a Fano reduction factor also contributes, leading to an effective charge which is not necessarily a multiple of e.

As shown in Fig. 3.11, this multiple-charge-quanta shot noise has been observed in superconducting ACs [23, 85]. For lower transmissions, the measured effective charge (red dots) resembles the ideal staircase pattern (dashed line) [24]. The exact shape is well taken into account by the MAR theory (solid red line).

In SNS junctions, due to the large number of channels with transmissions following Dorokhov's distribution, it is expected that[81]

$$Q^* = \left(1 - \frac{1}{\sqrt{2}}\right)\frac{2\Delta}{V}. \tag{3.25}$$

Experiments [88] do show an increased noise, but with a structure in voltage which goes beyond Eq. 3.25 and is not fully understood.

3.4.3 *Photon-assisted MAR current*

As mentioned before, when microwaves of frequency $\omega_r/2\pi$ are applied to a contact, Shapiro resonances appear on the dc $I\,(V)$ characteristic superimposed on the background MAR current. The background itself is also modified by the microwaves due to absorption or stimulated emission of one or several photons during the inelastic transfer of electronic charges through MAR processes. The voltage threshold for the onset of an m-photon assisted MAR process of order n is given by:

$$eV = \frac{2\Delta}{n} \pm \frac{m\hbar\omega_r}{n}. \tag{3.26}$$

This photon assisted MAR current is described by the microscopic MAR quantum theory [76]. As shown in Fig. 3.12, it has been measured in superconducting ACs [22, 78].

The experimental evidence presented above were obtained in superconducting ACs and are reviewed in Refs. [89, 90]. The first three experiments are direct probes

23 Note the similarity with the result for a voltage biased channel of transmission τ in the normal state for which $I = 2e^2\frac{eV}{h}\tau(1-\tau)$.

24 Which is valid in the tunnel limit. The low value of the current when the transmission is small makes it difficult to measure the noise in a regime closer to tunnel.

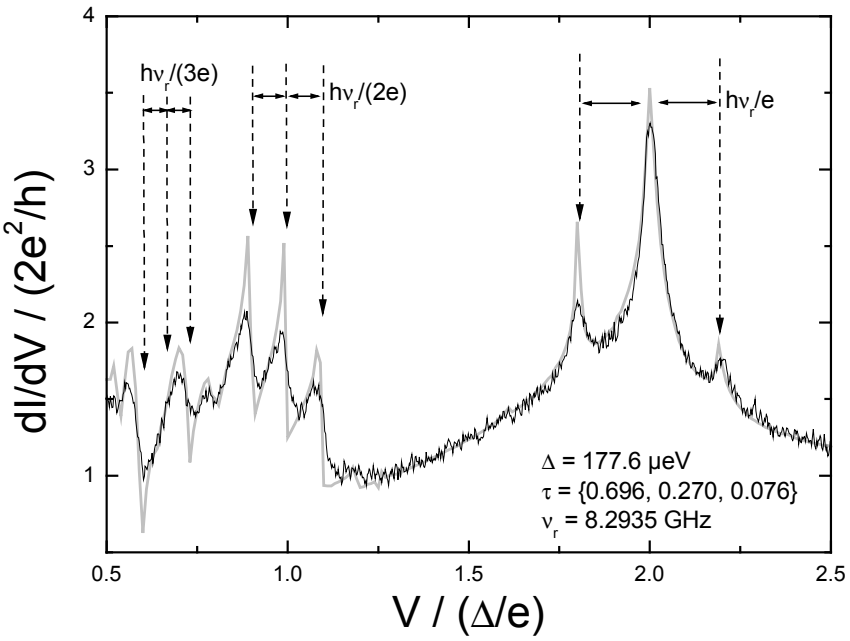

Figure 3.12: Measured (black line) differential conductance of an AC in presence of microwave irradiation at $\nu_r = 8.2935$ GHz. The sidebands around $2\Delta/e$ correspond to photon assisted tunneling of single electrons from one superconducting electrode to the other. The sidebands around $2\Delta/2e$ and $2\Delta/3e$ correspond to photon assisted MAR of order two and three, respectively. The grayed line is the prediction of the theory of photon assisted MAR (for a perfectly voltage biased contact), in which the independently measured transmissions of the contact have been plugged (figure taken from Ref. [78]).

of the ground state $|-\rangle$. On the contrary, the MAR phenomenon relies fundamentally on the Andreev internal degree of freedom. However, this non-equilibrium phenomenon is not a direct probe of the excited states.

3.5 Quasiparticle-injection spectroscopy

Direct measurement of ABS has been performed recently by Pillet *et al.* [28]. By tunneling spectroscopy, they measured the phase dependence of the density of states in a carbon nanotube connected to two superconducting electrodes, which reveals directly the ABS (see Fig. 3.13). As discussed in Section 2.2.5, such a spectroscopy induces transitions between the ground even state $|-\rangle$ and the excited odd states $|\downarrow\rangle$ and $|\uparrow\rangle$, by addition of a quasiparticle. Therefore, the excitation energy is $E_A(\varphi)$. This measurement is a direct probe of the odd states [25]. However, the only quantity measured is the excitation absorption energy $E_A(\varphi)$.

25 Similar tunneling spectroscopy experiments were performed in other systems [91, 92]. In these experiments, a quantum dot, either a self-assembled InAs quantum dot or a graphene quantum dot, was connected to a single superconducting terminal, which prevents form measuring the phase dependence of the ABS.

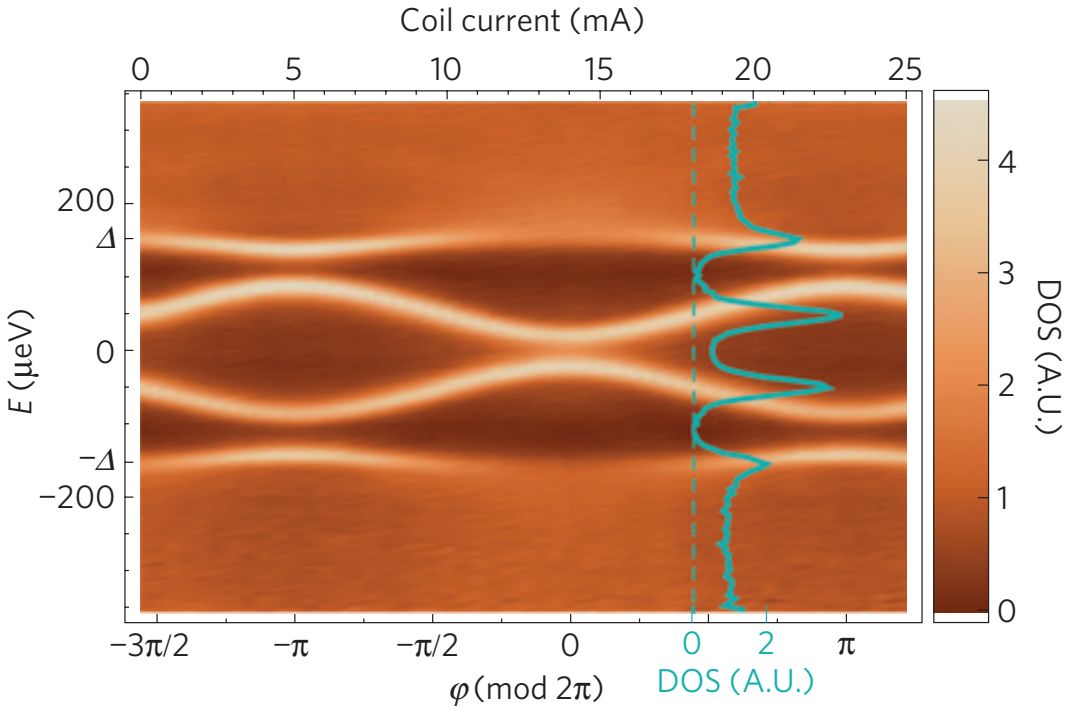

Figure 3.13: Differential conductance of the tunnel probe as a function of the bias voltage V of the probe junction (vertical axis) and of the current in a coil (top axis) that controls the flux through the loop. The ABS appear as sharp resonances periodic in phase (figure taken from Ref. [28]).

We conclude this chapter by stressing that although there is a full body of experiments probing ABS in different systems, the properties of the odd states $|\downarrow\rangle$, $|\uparrow\rangle$ and the excited even state $|+\rangle$ have not been directly measured.

The two experiments presented in this thesis work are:

1. In Part II, measurement of the properties of the odd states $|\downarrow\rangle$ and $|\uparrow\rangle$ (supercurrent and relaxation time)

2. In Part III, photon-absorption spectroscopy of transitions from the ground state $|-\rangle$ to the excited even state $|+\rangle$.

Part II

LONG-LIVED QUASIPARTICLES TRAPPED IN ANDREEV BOUND STATES

The second part is dedicated to the presentation of the first experiment, where we have observed the spontaneous trapping of quasiparticles in ABS, and to its modeling.

4

POISONING MEASUREMENTS

In this chapter we present an experiment in which we observed the odd states $|\uparrow\rangle$ and $|\downarrow\rangle$ in a superconducting atomic contact. The excitation toward these states is uncontrolled and due to spontaneous trapping of spurious quasiparticles in one of the discrete subgap ABS *formed at the contact. We call this phenomenon poisoning. We have measured the lifetime of the odd states: it is maximum at phase difference around π, when the* ABS *are deep inside the superconducting gap, and is found to exceed* 100 *µs. This work completes and extends the thesis of Quentin Le Masne, my predecessor in the Quantronics group, started in 2009* [69].

4.1 Experimental setup

4.1.1 *Superconducting atomic contacts*

We use the mechanically controllable break junction technique [93, 94] in its micro-fabricated version [18] to create atomic contacts. At cryogenic temperature, we break a suspended metallic thin-film micro-bridge (shown in Fig. 4.1 (d)) by bending a flexible substrate (Fig. 4.1 (e)) (see Chapter 10). The resulting electrodes are then brought back into contact and gently pulled apart while monitoring the $I(V)$ characteristic. The advantages of this well-established technique are the following:

- The channel transmissions are accessible from the $I(V)$ characteristics (see Section 3.4.1).
- They can be modified *in situ* by changing the stress on the constriction.
- The contacts are stable up to several months at low temperatures.
- The contacts can be integrated in on-chip circuits.

4.1.2 *The atomic-SQUID*

Measuring both the current-phase relation of an atomic contact and its $I(V)$ characteristics requires apparently contradictory conditions:

- For the former, one needs to phase-bias the atomic contact. To do so, the atomic contact must be placed in a small superconducting loop. The flux threading the loop fixes the phase φ.
- For the latter, one needs to voltage-bias the same atomic contact, which cannot be achieved if it is shunted by a superconducting loop.

To fulfill both conditions, one must be able to open and close this loop *in situ* with a reversible superconducting switch. This is achieved by placing a Josephson

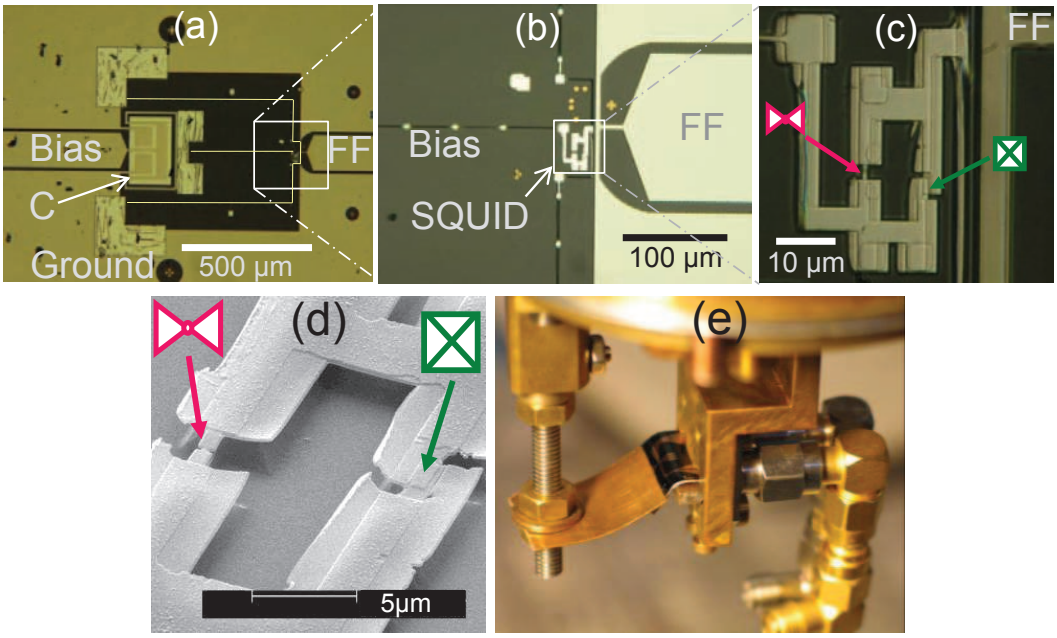

Figure 4.1: **(a)** Large scale micrograph of the sample PAL7, showing the end of the current bias coplanar and fast flux (FF) lines. The bias line and the ground plane form planar capacitors with a common, floating, superconducting rectangular electrode placed below (capacitor C). From there the connections to the atomic-SQUID are made with 0.9 µm-wide aluminum wires which are not visible at this scale, and have been redrawn for clarity. They appear on the photograph **(b)** as three dark lines with regularly spaced bright spots, one connected to the bias line, the two others to the ground plane. The bright spots are wider pillars that hold on the substrate since they are large enough not to be completely freed during the etching step. The fast flux coplanar line ends with a short close to the atomic-SQUID, the current in the upper half of the short creating a magnetic flux in the loop. Photograph **(c)** shows the SQUID loop, with the Josephson junction on the right and the suspended bridge where the atomic contacts are formed on the left. Five small square gold electrodes, intended as quasiparticle traps [95], are barely visible through the Aluminum layers. **(d)** SEM micrograph of the SQUID, seen under an angle: two angle evaporation of aluminum define the superconducting loop with a tunnel junction on the right arm, and a suspended micro-bridge on the left arm, which is broken at low temperature to form atomic contacts. **(e)** View of the sample holder, with a bent sample. The sample is clamped between the launchers of two SMA connectors, which are visible on the right-hand side, and a small metallic plate held with two screws at the bottom. The sample is bent with a brass blade held by a rod moving vertically (on the left). For this photograph, the bending was exaggerated, and the superconducting coil placed immediately above the sample was removed.

junction on the loop in parallel to the atomic contact, forming a device named the "**atomic-SQUID**" (see Fig. 4.1 (c,d)). In the sample used for the experiments described in this chapter, the critical current $I_0 \sim 500$ nA of the JJ is chosen to be much larger than the one of a typical aluminum one-atom contact (~ 50 nA), so that, as far as the supercurrent is concerned, the atomic-SQUID essentially behaves like a slightly perturbed Josephson junction. A shielded superconducting coil (which had been withdrawn before taking the picture in Fig. 4.1 (e)) is placed 1 mm above the SQUID, for dc flux biasing.

4.1.3 *A new design*

The experiment was originally intended to detect the even excited state $|+\rangle$. The idea was to shine microwaves at the Andreev transition frequency $2E_A/h$, and to detect a change in the supercurrent[1]. Compared to samples previously fabricated to measure the current-phase relation [78, 70, 21, 72], we have completely redesigned the circuit around the atomic-SQUID:

- The atomic-SQUID is connected to thin aluminum lines (Fig. 4.1 (a,b)) instead of large gold (normal) electrodes [78, 70, 21]. The thin lines provide inductance, and are combined to a planar capacitor (Fig. 4.1 (a)). This LC filter setup allows dc-biasing the atomic-SQUID while isolating it at microwave frequencies from the rest of the circuit. The purpose of this design was to optimize the relaxation time of the excited Andreev state[2].
- We use an on-chip, shorted $50\,\Omega$ coplanar wave-guide (fast flux (FF) on Fig. 4.1 (a,b,c)) as an antenna. The current through the short couples to the flux threading the atomic-SQUID loop located nearby.
- The substrate is made out of Kapton® (Fig. 4.1 (e)), an insulating polymer, instead of bronze, a metal, used in previous experiments. This allows having a coplanar waveguide and reduces dissipation which could be detrimental for the lifetime of $|+\rangle$.

The bending mechanism was also changed (see Chapter 10) to improve the coupling to microwaves[3]. The sample is clamped on one side with two SMA launchers, and bending is forced by a pusher acting on the opposite side, as shown in Fig. 4.1 (e).

1 The two even states $|-\rangle$ and $|+\rangle$ carry opposite supercurrent (see Section 3.1).

2 The details on the impedance seen from the contact and the corresponding expected relaxation time of the ABS are discussed in Section 5.2.

3 In the previous setup, the sample was connected using spring-loaded pins that could follow the bending of the sample, but have very poor microwaves properties.

Fabrication details are given in Section 9.1. The equivalent schematic of the setup is shown in Fig. 4.2.

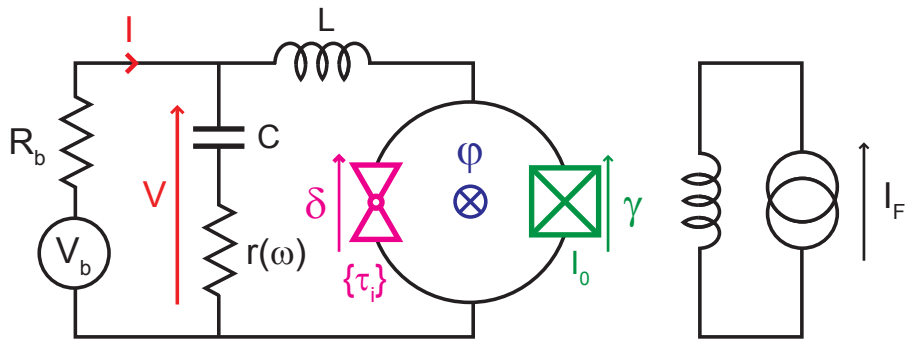

Figure 4.2: Full schematic of the sample. An atomic contact (magenta triangles), of channel transmissions $\{\tau_i\}$, forms a SQUID with a Josephson junction (green checked box). Reduced flux threading the loop φ is imposed by a superconducting coil. Phases δ and γ across contact and junction are linked as $\gamma - \delta = \varphi$. The atomic-SQUID is biased through an on-chip LC circuit ($L \simeq 0.75\,\mathrm{nH}$, $C \simeq 60\,\mathrm{pF}$). The losses in the capacitor are modeled by frequency-dependent series resistance $r(\omega)$. The voltage V measured across the full on-chip circuit corresponds, at low frequency, to the voltage drop across the SQUID. The current I is determined from the voltage across the bias resistor $R_b \simeq 200\,\Omega$.

The results presented in this chapter were obtained on a sample, referred to further as sample PAL7, whose parameters are listed in Table 4.1 (see Section E.1).

PARAMETER	SAMPLE PAL7
Capacitor C	60 pF
Inductor L	750 pH
JJ critical current I_0	554 nA
JJ capacitance C_0	0.22 pF
JJ equivalent inductance $L_0 = \frac{\varphi_0}{I_0}$	594 pH
Bias resistor	$R_b \simeq 200\,\Omega$
Environment frequency $\nu_e \simeq \frac{1}{2\pi}\sqrt{\frac{1}{(L+L_0)C}}$ (contact open)	560 MHz
Bare plasma frequency $\nu_{p0} = \frac{1}{2\pi}\sqrt{\frac{1}{L_0 C_0}}$ (contact open)	14 GHz
Dressed plasma frequency $\nu_p \simeq \frac{1}{2\pi}\sqrt{\left(\frac{1}{L}+\frac{1}{L_0}\right)\frac{1}{C_0}}$ (contact open)	19 GHz

Table 4.1: Parameters of Sample PAL7 presented in this chapter.

While characterizing samples of this new geometry, we found that the current-phase relation measurements presented strong anomalies, which became the focus of the experiment. We do not discuss here the unsuccessful attempts to induce transitions to $|+\rangle$ (this point is addressed in Section 5.2). Several atomic contacts were measured with this sample.

4.2 Principle of the measurements

4.2.1 *Characterization of the atomic contact:* I(V) *measurement*

The current-voltage characteristic of the JJ alone, taken after opening completely the atomic contact, is shown with black open symbols in Fig. 4.3. As observed in other experiments with similar junctions [21, 72, 96], some current is found at sub-gap voltages[4], here for $|V| \lesssim 200$ μeV.

The same figure presents with red solid symbols the I(V) characteristic of a SQUID with an atomic contact (called AC0): as compared to the previous curve, the large scale conductance is slightly increased, and a significant sub-gap current is visible. The difference between the two characteristics, which represents the contribution of the atomic contact to the dissipative current, is shown in the bottom of Fig. 4.3 with green open symbols. It is fitted (solid line) with the MAR theory (see Section 3.4.1) in order to obtain the transmission of its conduction channels, here $\{0.95, 0.45, 0.10\}$. The region $|V| \lesssim 200$ μeV, where significant sub-gap current was already found in the I(V) characteristic of the JJ by itself, was excluded from the fit. As a consequence, the accuracy on the determination of the transmissions of the channels is not as good as in experiments with atomic contacts alone [89]. It is here of the order of 1% for the largest transmission, and 3% for the second largest.

4.2.2 *Switching current measurements*

4.2.2.1 *From the switching current of the SQUID to the current-phase relation of the AC*

The superconducting loop allows to phase-bias the atomic contact by applying an external magnetic flux ϕ_{ext}. If the loop is sufficiently small so that the screening flux can be neglected[5], the phase differences γ (across the tunnel junction) and δ (across the atomic-size contact) are linked through the reduced flux threading the loop $\varphi = \phi_{ext}/\varphi_0$:

$$\delta = \varphi + \gamma. \tag{4.1}$$

The total current through the atomic-SQUID is simply given by the sum of the current in the JJ and the current in the atomic contact.

$$I = I_0 \sin(\gamma) + I_{AC}(\varphi + \gamma). \tag{4.2}$$

4 This is probably due to inelastic tunneling of Cooper pairs emitting energy in parasitic modes of the electromagnetic environment.

5 The geometric inductance of a 10 μm×10 μm loop is typically of the order of 10 pH, which is negligible as compared to the inductance of both the JJ ($L_J \sim 1$ nH) and the atomic contact ($L_{AC} \sim 10$ nH). In this way, the phase drops essentially across these two last elements.

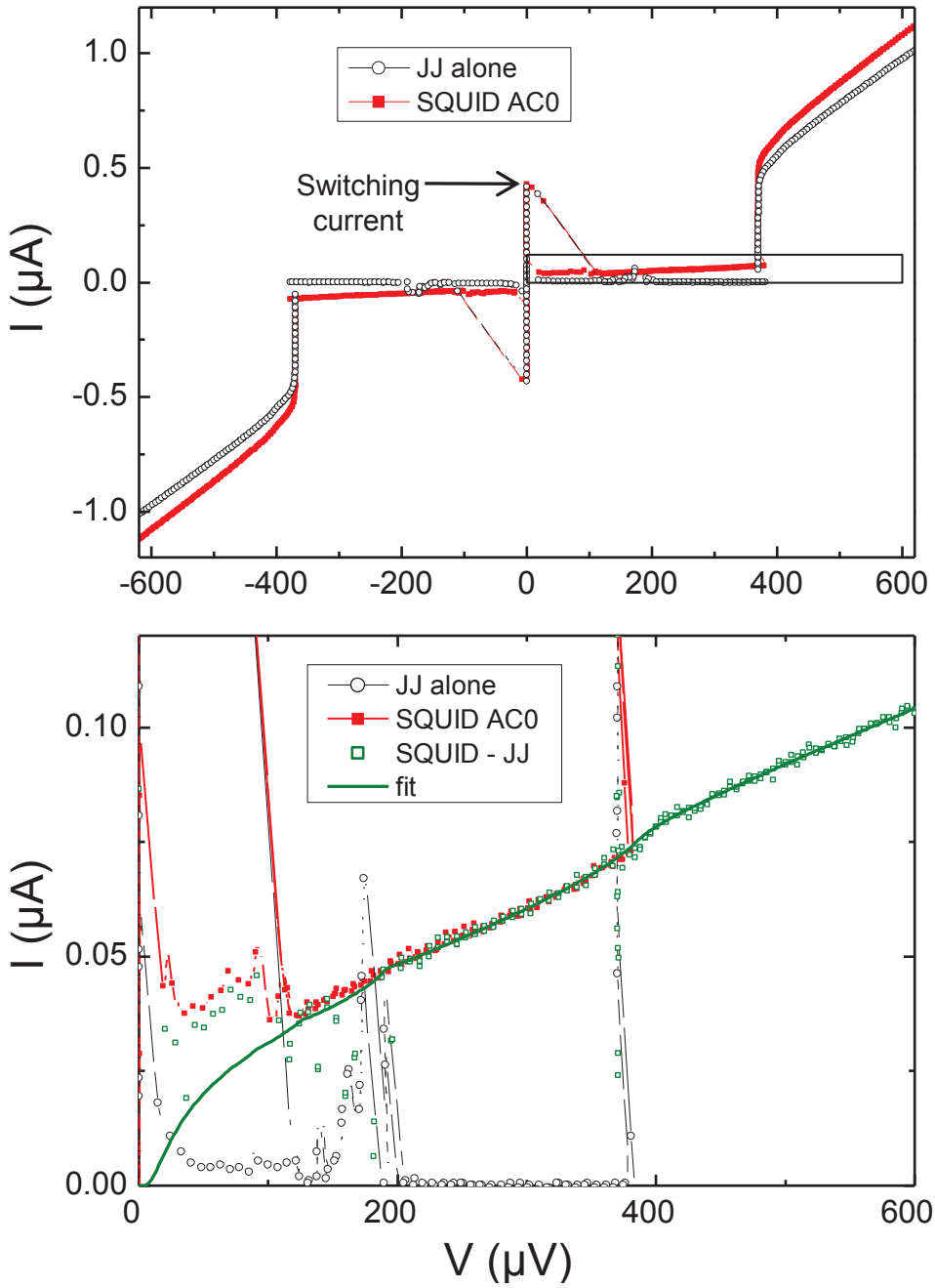

Figure 4.3: **Top**: $I(V)$ characteristics of the JJ alone (black open symbols) and of a SQUID with an atomic contact labeled AC0 (red filled symbols). The switching current of the SQUID, indicated with an arrow, is modulated by the applied flux. **Bottom**: same data, and (green open symbols) $I(V)$ characteristic of the atomic contact alone obtained by subtraction of the one of the junction from that of the SQUID. The transmissions $\{0.95, 0.45, 0.10\}$ are found by fitting this $I(V)$ characteristic with the MAR theory (green solid curve), excluding the region $|V| < 200$ μeV where the $I(V)$ characteristics of the JJ alone presents resonances.

The critical current $I^0_{aSQUID}(\varphi)$ of the atomic-SQUID is the maximum of this function for one value of φ. Because the critical current of the JJ I_0 is much bigger

than the one of the atomic contact, the critical current of the atomic-SQUID is reached for $\gamma \simeq \frac{\pi}{2}$ and is given by

$$I^0_{aSQUID}(\varphi) = I_0 + I_{AC}\left(\varphi + \frac{\pi}{2}\right). \tag{4.3}$$

The flux dependence of the critical current of the atomic-SQUID provides the current-phase relation of the atomic contact.

4.2.2.2 *Switching as a stochastic phenomenon*

To measure the critical current, a bias current I_b is applied to the atomic-SQUID. The phase γ across the JJ is a dynamical variable governed by a Langevin equation, equivalent to the one obeyed by the position of a massive particle evolving in a tilted washboard potential [97, 98, 99]:

$$U(\gamma) = -E_J \cos(\gamma) - E_J s\gamma + E_{AC}(\gamma + \varphi). \tag{4.4}$$

The first term is the Josephson energy of the JJ, with $E_J = \varphi_0 I_0$. The second one is the energy arising from the coupling to the bias source, with $s = \frac{I_b}{I_0}$ the normalized current amplitude called the "tilt", and the last term is the total Andreev energy of the atomic contact, which depends on the population of the different ABS of the contact (see Section E.2 for a detailed discussion of the potential). This potential, which is modulated by the flux, is sketched in Fig. 4.4.

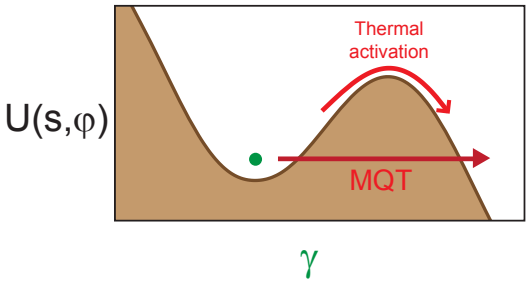

Figure 4.4: Tilted washboard potential. Due to thermal or quantum fluctuations, the particle can escape from the well. This corresponds to the switching from a zero voltage state to a finite voltage state.

In the absence of thermal or quantum fluctuations, two states are possible for the particle:

- When $I_b < I^0_{aSQUID}(\varphi)$, the potential U presents local minima, and the equivalent particle is trapped in one of them. Its position is fixed and the velocity $\dot{\gamma} = V/\varphi_0$ is zero. This corresponds to the supercurrent branch on the $I(V)$ characteristic, resulting from the dc Josephson effect.
- When $I_b \geqslant I^0_{aSQUID}(\varphi)$, the local minima disappear and the particle runs down the potential. This corresponds to a running state with a finite voltage.

Switching between these two states should arise exactly at $I_b = I^0_{aSQUID}(\varphi)$. In an experiment, thermal and quantum fluctuations cause the particle to oscillate in the well and to have a finite probability to escape out of the well. Consequently the switching is stochastic, occurs for $I_b < I^0_{aSQUID}(\varphi)$, and described by a switching probability P_{sw}.

4.2.2.3 *Probing the switching current statistics: experimental protocol*

A standard method to measure the switching probability consists in applying N current pulses and monitoring the number n of voltage pulses appearing across the atomic-SQUID that signal the switching. In practice, we use pulses with shape shown in Fig. 4.5.

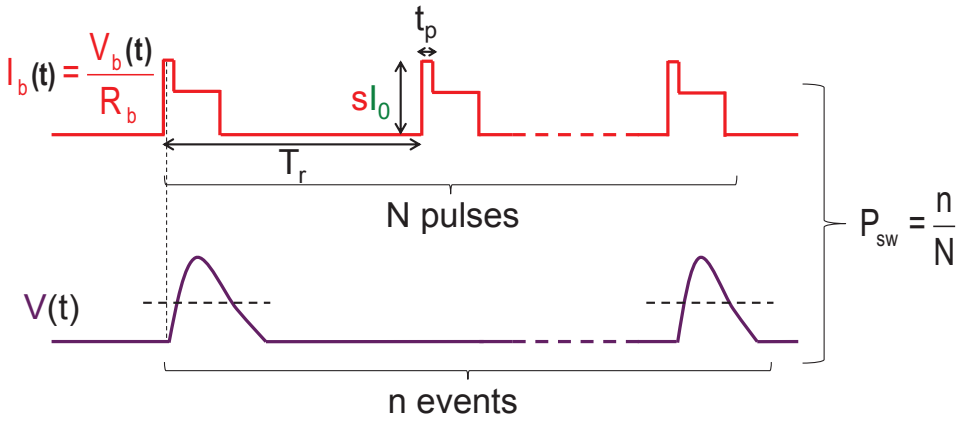

Figure 4.5: Standard switching probability measurement scheme: a train of N pulses with normalized height $I_b = sI_0$ and duration t_p is applied on the bias of the atomic-SQUID. The repetition period is T_r. Typically, we use $N = 10^4$, $t_p = 1$ µs and $T_r = 20$ µs. The 40 % lower plateau following each pulse holds the voltage at a finite value if switching has occurred, during a sustain time of 5 µs, hence facilitating detection. The number n of voltage pulses resulting from switching events is recorded by a counter detecting crossings through a threshold value (dotted line). The switching probability is $P_{sw} = \frac{n}{N}$.

During a pulse, the phase γ has a finite probability P_{sw} to go over the barrier and escape. If escape occurs, the phase runs down the potential and a finite voltage $\langle V \rangle = \varphi_0 \langle \dot{\gamma} \rangle$ develops across the junction. In order to lengthen this voltage pulse and facilitate its measurement, the bias current is reduced to a value $I_{sus} < I_b$ during a sustain time 5 µs. The probability that switching occurs during this "sustain" is negligible. The voltage pulse is amplified and detected at room temperature by a counter. The system is then "reset" by lowering the current to zero. If the junction had switched, it gets retrapped on the supercurrent branch.

The switching probability P_{sw} is obtained as the ratio of number of voltage pulses across the JJ over N. It is measured as a function of the normalized current amplitude $s = \frac{I_b}{I_0}$, in the range of current where P_{sw} goes from 0 to 1. An example of such an "s-curve" is shown in Fig. 4.6. It was obtained for the Josephson junction alone, after breaking the AC. The switching probability varies fast from 0 to 1 around a normalized current s_0. The exact shape of such an s-curve is well understood (see Section E.2).

4.2.2.4 *Previous measurements*

Switching measurements were already performed in similar samples. As an example, we plot in Fig. 4.7 the switching probability as a function of the normalized bias current and the reduced flux $P_{sw}(\varphi, s)$, measured on a sample made of an atomic-SQUID connected to gold normal electrodes [72].

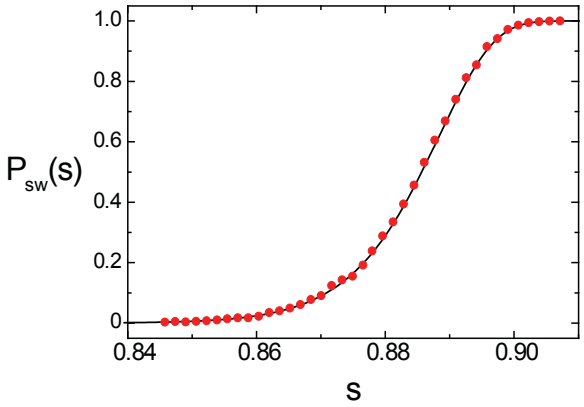

Figure 4.6: Switching probability $P_{sw}(s)$ as a function of the normalized current amplitude $s = \frac{I_b}{I_0}$, for the Josephson junction of the SQUID. Data (red dots) obtained using $N = 10^4$ pulses of duration $t_p = 1$ µs and repetition period $T_r = 20$ µs. Fit (black line) using the thermal escape theory (see Section E.2) with $I_0 = 554$ nA and $T_{sw} = 100$ mK.

Clearly, the switching probability evolves very rapidly from 0 to 1 in a narrow range of bias current which depends on the applied flux. Due to the large asymmetry between the JJ and the atomic contact, the reduced bias current $s^*(\varphi)$ leading to a switching probability $P_{sw} = 0.5$ is given to first order by

$$s^*(\varphi) = s_0 + \frac{I_{AC}(\varphi + \arcsin(s_0))}{I_0}. \tag{4.5}$$

Therefore, it corresponds essentially to the current-phase relation of the atomic contact, modulated around the switching current of the JJ alone and shifted in flux by $\arcsin(s_0) \simeq 0.3\pi$. To predict the exact dependence, one needs to consider the full dynamics of the phase in the potential (4.4) (see Section E.2).

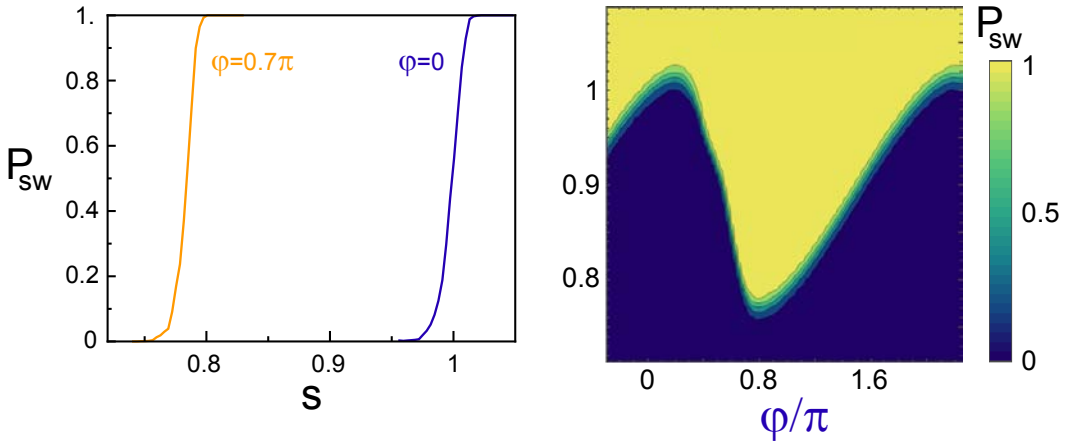

Figure 4.7: **Left:** Switching probability as a function of the reduced bias current, for two values of the external flux. **Right:** Switching probability $P_{sw}(\varphi, s)$ as a function of both the bias current and the flux. These measurements were obtained in a previous experiment (figure adapted from Ref. [72]), with a sample made of an atomic-SQUID connected to gold normal electrodes, for an atomic contact of transmissions $\{0.969, 0.137\}$.

4.3 Evidence for poisoning

We now present measurements of the switching probability $P_{sw}(\varphi, s)$ for different atomic contacts on sample PAL7.

4.3.1 *Correlation between switching events*

The right panel of Fig. 4.8 shows the switching probability P_{sw} as a function of both the flux and the normalized pulse height s for the contact AC0. As compared to the sample of Fig. 4.7, the switching probability does not vary sharply from $P_{sw} \simeq 0$ (purple) to $P_{sw} \simeq 1$ (red) for all values of the flux. Indeed, an anomalous region with an almost constant intermediate step at $P_{sw} \simeq 0.1$ (blue) is observed for $0.7\pi < \varphi < 1.1\pi$.

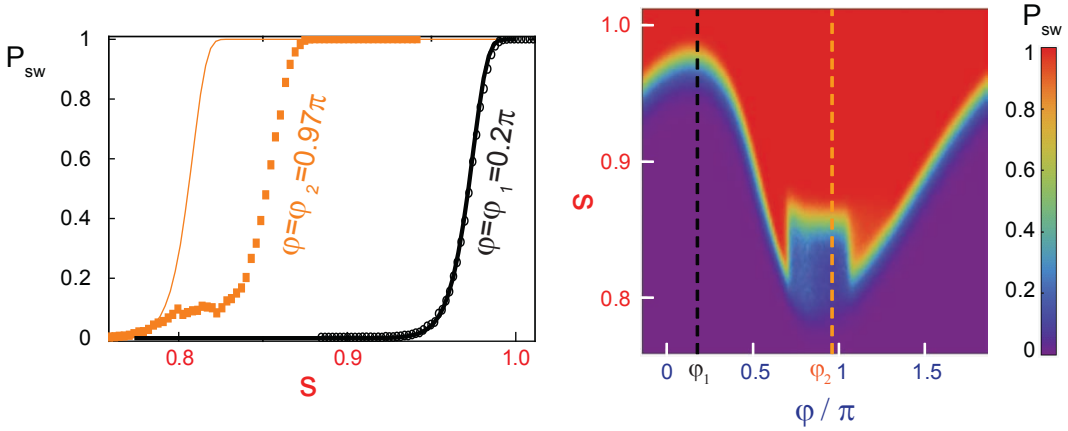

Figure 4.8: **Left:** Switching probability $P_{sw}(s)$ measured as a function of the normalized pulse height s for fluxes $\varphi_1 = 0.20\pi$ (black, open symbols) and $\varphi_2 = 0.97\pi$ (orange, full symbols). Solid curves correspond to theoretical predictions. **Right:** Switching probability $P_{sw}(\varphi, s)$ as a function of both the flux φ and the normalized pulse height s. These data are obtained for the SQUID with contact AC0 ($\{0.95, 0.45, 0.10\}$), using the standard method described in Fig. 4.5.

The left panel of Fig. 4.8 presents two cuts for two values of the flux phase corresponding to switching currents close to its maximum and minimum values: $\varphi_1 = 0.20\pi$ (black symbols) and $\varphi_2 = 0.97\pi$ (orange symbols). These data are compared with the expected theoretical curves (solid lines) obtained using the escape theory described in Section E.2, with all the ABS taken in the ground state. Whereas the curve taken at φ_1 is well fitted by theory, the one taken at φ_2 has in common with theory only the value of s where the switching probability starts to rise.

The inset of Fig. 4.9 shows a time-trace of switching events at a flux $\varphi = 0.85\pi$ in the anomalous region. One observes long "blind" periods without any switching followed by bunched switching events. This intermittent behavior is reminiscent of the "blinking" observed in the fluorescence of molecules or quantum dots [100, 101]. The histogram of time delays between switching events in the main panel

of Fig. 4.9 displays a huge peak at short times and a long foot extending to large times. This proves that the associated switching events are correlated.

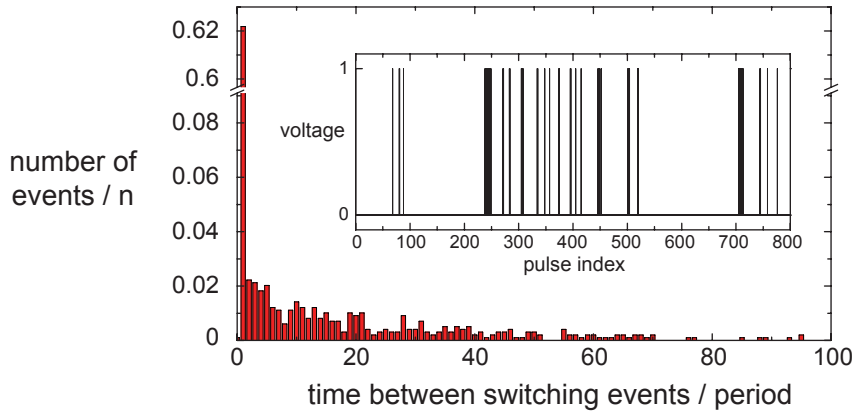

Figure 4.9: $n = 989$ successive switching events are recorded, during a sequence of bias current pulses as in Fig. 4.5 with a pulse height such as $P_{sw} \simeq 0.1$. **Inset**: Digitized voltage (0 if voltage below threshold, 1 if voltage above threshold) across the atomic-SQUID as a function of time (we only show the trace corresponding to the first 800 bias current pulses). **Main panel**: Histogram of time delays between switching events. Mind the gap in the vertical axis, introduced because the number of events following one another is very large. These data were obtained for the SQUID with contact AC0 ($\{0.95, 0.45, 0.10\}$), at a flux $\varphi = 0.85\pi$ in the anomalous region of Fig. 4.8.

To ensure that the measurements are statistically independent, additional short prepulses are applied before each measurement pulse (see Fig. 4.10). The prepulse height is 30% higher than the measurement pulse so as to force switching with certainty. Of course, the corresponding forced switching events are ignored in the counting. During the prepulses, a voltage develops across the atomic contact, and

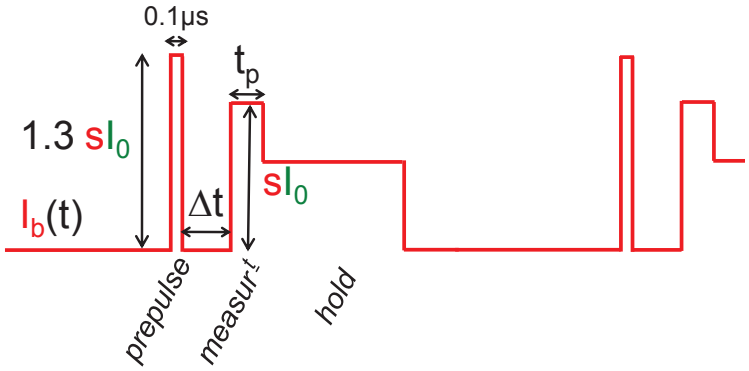

Figure 4.10: Measurement scheme used in the following. Short prepulses 30% higher than the actual measurement pulses cause the system to always switch. With such pulses, successive switching events are uncorrelated.

both the energy and the occupation of the Andreev levels evolve at the Josephson frequency. When the current is reset to zero, the Andreev levels are back to their energies $\pm E_A(\delta, \tau_i)$. The system is left in a stochastic out-of-equilibrium situation which does not depend on the result of the previous measurement. In other words,

the prepulse induces a **reinitialization** of the system[6]. The measurement pulse is applied a time Δt after this reset. Using such "switching prepulses", the switching events do correspond to independent processes. Unfortunately, we kept no record of the corresponding switching time distribution.

Another way to get rid of correlations is to use dc flux pulses (see Section 4.5.0.3). We do not explain this technique here, but we show in Fig. 4.11 a time-trace of switching events and the corresponding histogram of time delays between switching events, obtained for the same atomic contact and at the same flux value. Then, the switching events do correspond to independent processes.

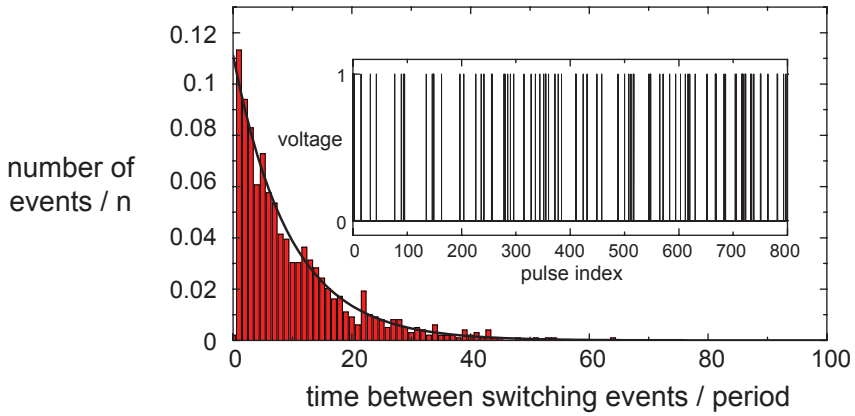

Figure 4.11: Same measurements (for the same contact AC0 ($\{0.95, 0.45, 0.10\}$) and flux $\varphi = 0.85\pi$) as in Fig. 4.9, while using flux pulses. The pulse height was reduced compared to Fig. 4.9 to keep the switching probability at $P_{sw} \simeq 0.1$. The solid line corresponds to the statistical distribution for independent events $P_{sw}\,(1 - P_{sw})^{x-1}$, where x corresponds to the horizontal axis.

4.3.2 *Stochastic suppression of the Andreev supercurrent*

Measurements of the switching probability with prepulses are presented in Fig. 4.12, for contact AC0. Although the correlations have disappeared, there is still an anomalous region in the curves $P_{sw}(s, \varphi)$ (see right panel of Fig. 4.12) in the same flux range. However, the shape of $P_{sw}\,(s)$ in this region has changed. It now rises in two steps and displays a flat intermediate plateau, as seen for flux φ_2 in the left panel of Fig. 4.12 (black symbols).

This curve can be very precisely accounted for by the weighted sum of two different theoretical $P_{sw}(s)$ curves:

$$P_{sw}(s) = (1-p)P^{-}_{sw}(s) + pP^{\uparrow,\downarrow}_{sw}(s)\,, \tag{4.6}$$

with $p = 0.36$. The first one (blue, solid curve), $P^{-}_{sw}(s)$, is the one predicted for the "pristine contact", *i.e.* with all channels in the ground state. The second one (green, solid curve), $P^{\uparrow,\downarrow}_{sw}(s)$, is that of the "poisoned contact". It corresponds ex-

6 When two prepulses are applied (instead of a single one) with more than 1 µs delay between them, the first one has no effect, which indicates that a single prepulse does erase the memory of the system.

actly to the one predicted **without taking into account the contribution of the most transmitting channel**.

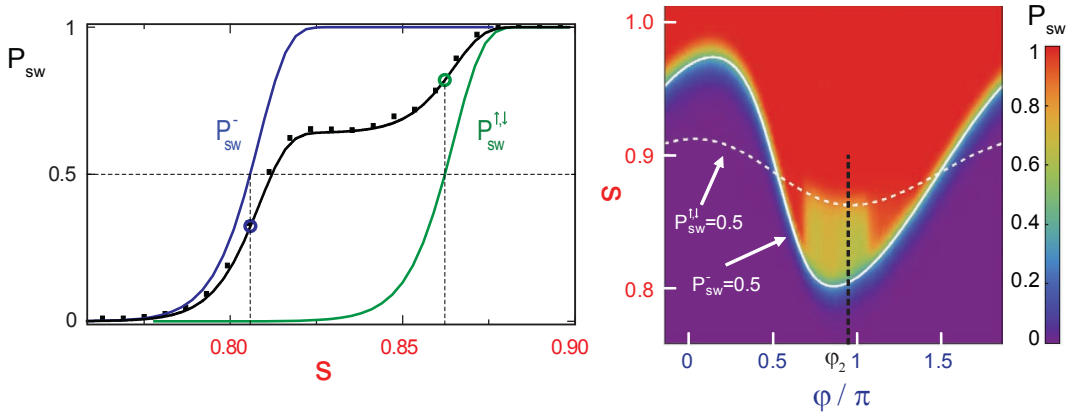

Figure 4.12: Switching probability $P_{sw}(s,\varphi)$ using switching prepulses (see Fig. 4.10, $\Delta t = 0.5$ µs) for the SQUID with contact AC0 with transmissions $\{0.95, 0.45, 0.10\}$. **Left**: at $\varphi_2 = 0.97\pi$ (corresponds to the dashed line in the right panel). Black symbols: $P_{sw}(s)$ as measured. Solid curves: theoretical curves, $P^{-}_{sw}(s)$ (blue) for the pristine contact ($\{0.95, 0.45, 0.10\}$) and $P^{\uparrow,\downarrow}_{sw}(s)$ (green) for the poisoned contact, *i.e.* without the contribution of the most transmitting channel; intermediate line (black): fit of the data with the linear combination given by Eq. 4.6 with $p = 0.36$. **Right**: Color plot of $P_{sw}(s,\varphi)$. The white curves show the lines corresponding theoretically to $P_{sw} = 0.5$ for the pristine contact ($\{0.95, 0.45, 0.10\}$, solid line) and for the contact with the first channel poisoned (dashed line). Inset:

This interpretation holds in the whole flux region where the switching curves have an intermediate plateau. This is illustrated in the right panel of Fig. 4.12, where the two lines corresponding to the equations $P^{-,\uparrow,\downarrow}_{sw}(s,\varphi) = 0.5$ are superimposed with the data. In the regions where $P_{sw}(s)$ has a standard shape, $P_{sw}(s)$=0.5 occurs at the position predicted for the pristine contact ($P^{-}_{sw}(s,\varphi) = 0.5$, solid line). In the region $0.7\pi < \varphi < 1.1\pi$, $P_{sw}(s)$ has two steps (which appear in the figure as color gradients): one occurs at the position where $P^{-}_{sw}(s,\varphi) = 0.5$ (solid line), the other one at the position where $P^{\uparrow,\downarrow}_{sw}(s,\varphi) = 0.5$ (dashed line), showing that

$$P_{sw}(s,\varphi) = (1 - p(\varphi))P^{-}_{sw}(s,\varphi) + p(\varphi)\,P^{\uparrow,\downarrow}_{sw}(s,\varphi)\,. \tag{4.7}$$

The function $1 - p(\varphi)$ describes the height of the intermediate plateau in $P_{sw}(s)$.

In Fig. 4.13, similar comparisons are presented for three other ACs on the same sample. They all have one almost perfectly transmitting channel, the other ones with transmissions lower than 0.65. There again, in all cases, in a broad phase range around π, $P_{sw}(s)$ shows a plateau delimited by the predictions for the pristine (solid line) and for the poisoned configurations, *i.e.* with the more transmitting contact in an odd configuration (dashed line).

Therefore, the interpretation in term of a suppression of the supercurrent of the most transmitting channel seems correct. This suppression is stochastic with a probability[7] $p(\varphi)$, since the data is precisely accounted for by the linear combination (4.7).

7 One can observe vertical stripes in the anomalous regions. This reflects the flux dependence of $p(\varphi)$, which is non-trivial and will be analyzed in Section 4.4.6.

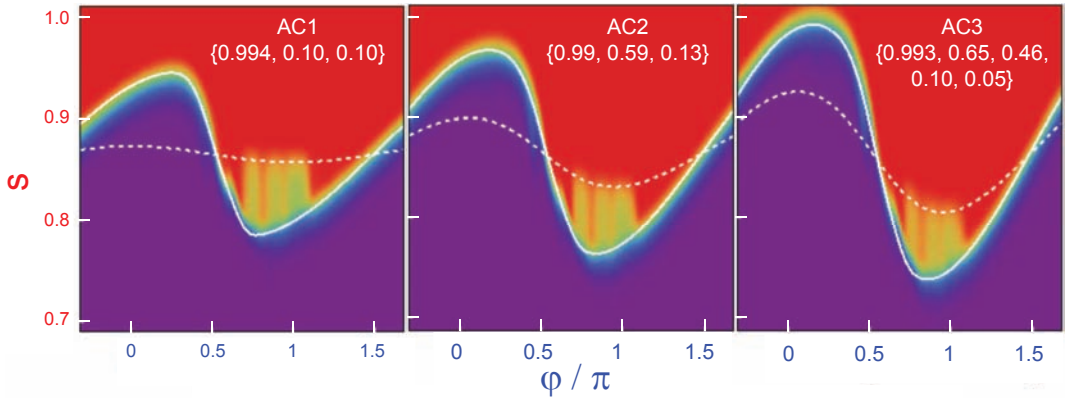

Figure 4.13: Color plot of the switching probability $P_{sw}(s, \varphi)$ using switching prepulses (see Fig. 4.10, with $\Delta t = 2\,\mu s$) for SQUIDs made with three different ACs, each having one channel with a transmission close to 1: AC1: $\{0.994, 0.10, 0.10\}$; AC2: $\{0.998, 0.59, 0.13\}$ and AC3: $\{0.993, 0.65, 0.46, 0.10, 0.05\}$. The color scale is the same as the one used in Fig. 4.12.The white curves correspond theoretically to $P_{sw} = 0.5$ for the pristine contact (solid line) and for the poisoned contact (dashed line).

4.3.3 *Poisoning and odd states*

The suppression of the supercurrent of the most transmitting channel reflects the fact that the system must be, in this channel, in one of the two odd states $|\uparrow\rangle$ and $|\downarrow\rangle$[8]. We think that the excitation from the ground Andreev state towards one of the two odd states $|\uparrow\rangle$ and $|\downarrow\rangle$ is induced by the trapping of a spurious quasiparticle from the delocalized continuum to one of the discrete subgap ABS localized at the contact (as sketched in Fig. 4.14). This trapping is stochastic with a probability p.

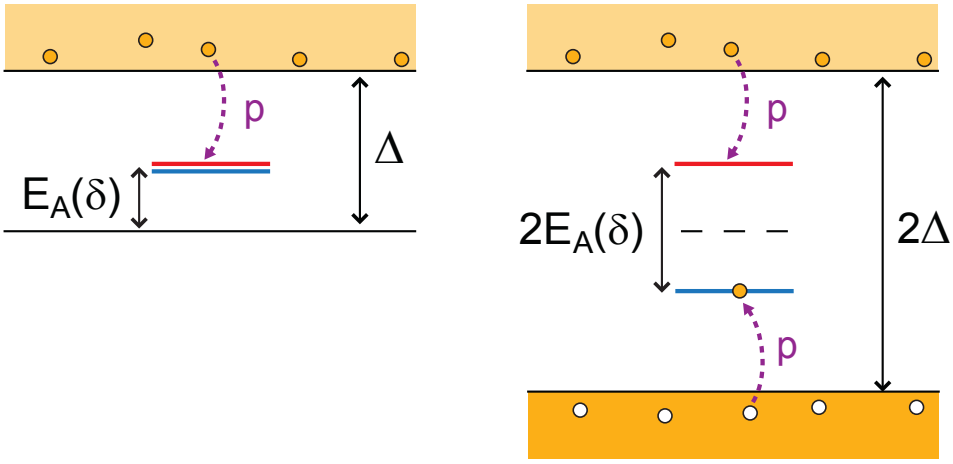

Figure 4.14: Sketch of the poisoning phenomenon. Non-equilibrium quasiparticles in the continuum can get trapped with a probability p into the ABS localized at the constriction. **Left**: in the excitation picture. The trapping occurs in one of the two ABS (the spin degeneracy has been lifted for clarity). **Right**: in the one-particle picture. Either a quasiparticle falls from the upper continuum into the positive energy ABS or a quasihole jumps from the bottom continuum into the negative energy ABS.

8 In a spin degenerate system, they do not carry any supercurrent (see Section 3.1).

A similar phenomenon has first been observed in single Cooper pair devices [35, 36] containing small superconducting islands in which the parity of the total number of electrons matters. It has been dubbed *"poisoning"* [37], as it inhibits the behavior expected in the ground state of the system. Thus, we call p the **poisoning probability**, *i.e.* the probability for the AC to have a quasiparticle trapped in its most transmitting channel.

4.3.4 *Multiple poisoning*

In a contact with more than one highly transmitting channel, poisoning can affect several channels at once, as shown in Fig. 4.15 where the switching probability presents two intermediate plateaus. The first one near 0.5 corresponds to either one of the two first channels being poisoned: indeed, since they have very similar transmissions, one cannot distinguish two plateaus. The second one at 0.95 corresponds to the situation in which both channels are poisoned.

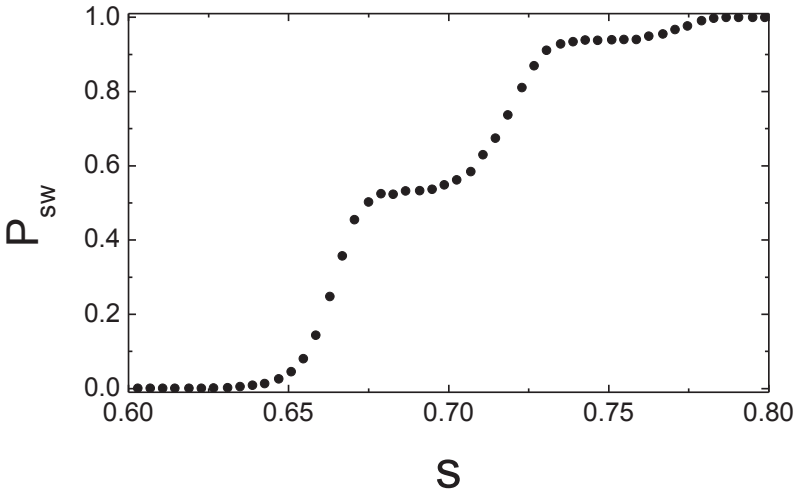

Figure 4.15: Measured switching probability as a function of s for a contact with two well transmitting channels: {0.96, 0.95, 0.60, 0.34, 0.30, 0.29, 0.27, 0.26, 0.24, 0.2}, taken at a flux within the poisoned region. The first plateau ($P_{sw} \simeq 0.55$) can be attributed to situations where one of the two channels with highest transmission is poisoned, while the second one corresponds to situations where both are poisoned.

4.4 Measurements of poisoning dynamics

The previous experiments demonstrate that, in a certain parameter region, the system has a finite probability p to trap a quasiparticle, thus ending in an odd configuration after the prepulse. The poisoning seems to be more efficient for phases around π and for high transmissions, *i.e.* when ABS are deep inside the superconducting gap. In the following, we describe experiments exploring the dynamics of trapping and untrapping, by varying the delay Δt between the prepulse and the measurement pulse (see Fig. 4.10).

4.4.1 *Exponential relaxation*

Data illustrating the method, taken on a contact with transmissions {0.91, 0.62, 0.15}, in a flux region exhibiting poisoning, are shown in Fig. 4.16. The left panel shows $P_{sw}(s)$ for both a short (1 µs) and long (500 µs) delay Δt. The right panel presents the complete dependence of P_{sw} on Δt at a bias value $s = 0.826$, for which $P_{sw}^{-} \approx 1$ and $P_{sw}^{\uparrow,\downarrow} \approx 0$. The data are well fitted with an exponential dependence

$$P_{sw}(\Delta t) = P_\infty + (P_0 - P_\infty)\exp(-\Delta t/T_1). \tag{4.8}$$

One can then extract the initial poisoning probability just after the prepulse $p_0 = 1 - P_0$, the asymptotic value at long times $p_\infty = 1 - P_\infty$, and the relaxation time T_1.

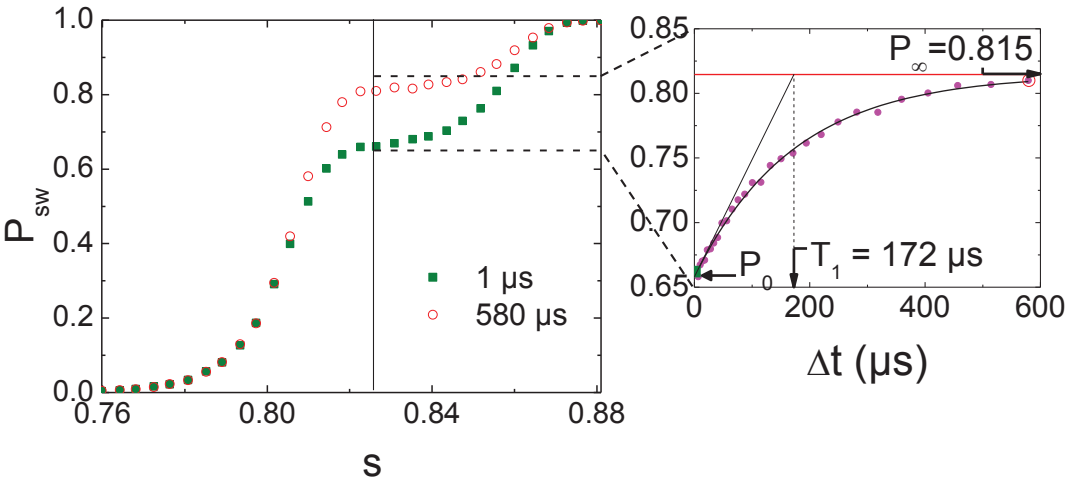

Figure 4.16: **Left panel**: Switching probability of contact {0.91, 0.62, 0.15} as a function of bias pulse height at fixed φ, for short ($\Delta t = 1\,\mu s$, green solid squares) and long ($\Delta t = 580\,\mu s$, red open circles) delay between the prepulse and the measurement pulse. **Right panel**: Dots: Evolution with Δt of the plateau height, measured at $s = 0.826$ (vertical line on the left panel). Solid line: exponential fit with $P_{sw}(\Delta t) = P_\infty + (P_0 - P_\infty)\exp(-\Delta t/T_1)$.

Note that the asymptotic probability is not zero. Therefore, switching during the prepulse is not the only mechanism producing quasiparticles in the continuum.

4.4.2 *Relaxation time and asymptotic probability as a function of the phase*

The dynamics of quasiparticle poisoning is strongly phase dependent. Measuring this phase dependence is however not trivial, because during the pulse sequence shown in Fig. 4.10, δ is not constant: it takes a value close to the imposed flux φ during Δt, but is significantly shifted during the measurement pulse. This leads to situations in which relaxation is dominated by the one occurring at measurement.

To circumvent this complication, we have designed a procedure that takes advantage of the fast flux line. It allows probing the relaxation from a fixed initial poisoning probability p_0, with measurement occurring always at the same flux, the only variable being the phase δ during the waiting time.

4.4.2.1 *Method*

The protocol is shown in Fig. 4.17. We set the flux imposed by the external coil to a value φ_i such that p_0 is large, and that the relaxation time during the measurement pulse (at phase $\varphi_i + \arcsin(s)$) is much longer than the duration of the measurement pulse (1 µs), so that relaxation during the measurement can be neglected. We first take a switching curve $P_{sw}(s)$ and fit it with a weighted sum of two shifted curves as in the left panel of Fig. 4.12. We then fix a working point s_0 corresponding to the intermediate plateau, and determine the switching probabilities corresponding to the pristine contact $P^{-}_{sw}(s_0)$ and to the poisoned contact $P^{\uparrow,\downarrow}_{sw}(s_0)$. For all the data presented in the following, the working point was chosen such that[9] $P^{-}_{sw}(s_0) > 0.99$ and $P^{\uparrow,\downarrow}_{sw}(s_0) \leqslant 0.12$. The probability p to be in an odd configuration is then inferred from

$$P_{sw}(s_0) = (1-p)P^{-}_{sw}(s_0) + pP^{\uparrow,\downarrow}_{sw}(s_0), \tag{4.9}$$

which is slightly more precise than the identification of p with $1 - P_{sw}(s_0)$. A measurement similar to that presented in Fig. 4.16 is then used to characterize the system at flux φ_i :

$$p(\varphi_i, \Delta t) = \mathcal{E}^{p_\infty(\varphi_i)}_{T_1(\varphi_i)}\left(p_0(\varphi_i), \Delta t\right) \tag{4.10}$$

where we have introduced the function $\mathcal{E}^{p_\infty}_{T_1}(p_0, t)$ accounting for an exponential variation during time t starting from p_0, with characteristic time T_1 and asymptotic value p_∞ :

$$\mathcal{E}^{p_\infty}_{T_1}(p_0, t) \equiv p_\infty + (p_0 - p_\infty)\exp(-t/T_1). \tag{4.11}$$

Using a dc flux pulse applied through the fast flux line between the prepulse and the measurement pulse, the flux phase is changed to a value φ_w for a time t_w (in practice, we leave a 1 µs delay between the prepulse and the flux pulse to let the system stabilize; we also leave a delay of t^0_w =15 µs between the flux pulse and the measurement pulse to get rid of ringing effects after the fast flux pulse). During this dc flux pulse, the phase across the AC is then simply[10] $\delta = \varphi_w$.

From the switching probability $P_{sw}\left(t_w + t^0_w\right)$ we calculate using Eq. 4.9 the probability $p\left(t_w + t^0_w\right)$ to be in an odd configuration after the complete sequence. We observe that $p\left(t_w + t^0_w\right)$ is not an exponential function of t_w. The reason is that this probability results from two exponential relaxations with different parameters, as illustrated at the bottom of Fig. 4.17. The initial value $p(0) = p_0(\varphi_i)$ results from the prepulse applied at phase flux φ_i (the function $p_0(\varphi_i)$ is discussed farther). Follows an exponential evolution at phase flux φ_w during t_w, leading to

$$p(t_w) = \mathcal{E}^{p_\infty(\varphi_w)}_{T_1(\varphi_w)}\left(p(0), t_w\right). \tag{4.12}$$

During the last $t^0_w = 15\,\mu s$, the phase flux is φ_i, so that

$$p\left(t_w + t^0_w\right) = \mathcal{E}^{p_\infty(\varphi_i)}_{T_1(\varphi_i)}\left(p(t_w), t^0_w\right). \tag{4.13}$$

9 Except for the data taken at higher temperatures, where the rounding of the curves becomes comparable to their width, and $P^{\uparrow,\downarrow}_{sw}(s_0)$ can be as high as 0.32.

10 The phase drop $\arcsin(I(\delta/I_0))$ across the JJ, at most of the order of 0.03π, is neglected.

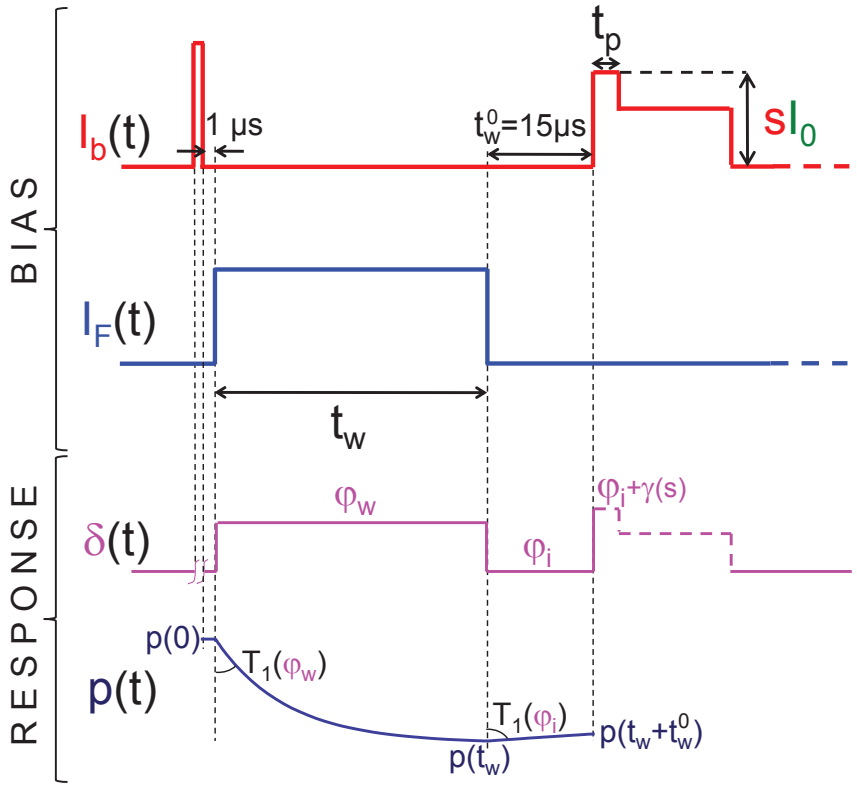

Figure 4.17: Pulse sequence used to measure the phase dependence of the relaxation process. The first line corresponds to the signal applied to the current bias, the second one to the fast flux line. The two last lines sketch the corresponding evolution of the phase δ across the AC and of the poisoning probability $p(t)$ respectively. The prepulse causes systematic switching, and the "running away" of the phase is not represented. The dotted line in $\delta(t)$ during the measurement pulse indicates that either the SQUID switches and the phase runs away, or it does not switch and δ simply follows the bias current. The prepulse and the measurement pulse are always applied at the same flux phase φ_i. The probability $p(t)$ starts from $p(0)$ after the prepulse, a value that depends on the flux φ_i; a flux phase φ_w is then applied during a time t_w, and $p(t)$ relaxes exponentially with a time constant $T_1(\varphi_w)$ towards $p_\infty(\varphi_w)$, reaching $p(t_w)$. In the last step, the phase flux is restored to φ_i during $t_w^0 = 15\,\mu s$ and $p(t)$ evolves with the time constant $T_1(\varphi_i)$ towards $p_\infty(\varphi_i)$, reaching finally $p(t_w + t_w^0)$, the actual value accessed by the measurement (the schematic corresponds to a situation where $p(t_w) < p_\infty(\varphi_i)$, hence $p(t)$ increases in the last step). In the time interval between the prepulse and the measurement pulse, the bias current I_b is zero, and the phase δ across the AC is equal to the flux phase: $\delta = \varphi_w$ during t_w, then $\delta = \varphi_i$ during t_w^0.

Since the parameters $p(0)$, $T_1(\varphi_i)$ and $p_\infty(\varphi_i)$ have been determined in the first measurement without the flux pulse, Eq. 4.13 can be used to deduce $p(t_w)$ from $p\left(t_w + t_w^0\right)$. The function $p(t_w)$ is then an exponential, as expected, and its fit with Eq. 4.12 yields the asymptotic poisoning $p_\infty(\delta)$ and the relaxation time $T_1(\delta)$.

4.4.2.2 *Results*

Both $p_\infty(\delta)$ and $T_1(\delta)$, measured at 30 mK, are shown in Fig. 4.18 for the SQUID with contact AC1. For this measurement, φ_i was $0.9\,\pi$, $p_0(\varphi_i) = 0.29$, and the

relaxation time at the measurement phase $\simeq \varphi_i + 1$ rad exceeded 100 µs. The phase

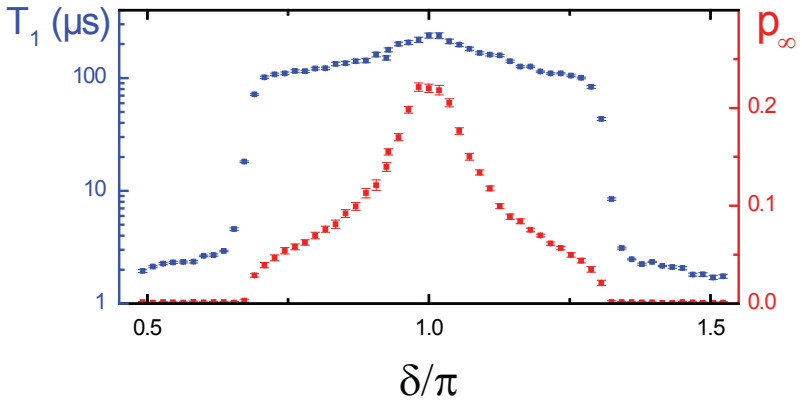

Figure 4.18: Relaxation time T_1 (blue points) and asymptotic poisoning probability p_∞(red points) as a function of the phase δ imposed for a time Δt between prepulse and measurement pulse. Data taken on SQUID with AC1 $\{0.994, 0.10, 0.10\}$ at 30 mK. Measurements at $|\delta - \pi| > 0.5\pi$ show very fast relaxation that could not be resolved reliably in our setup.

dependence of p_∞ and T_1 is symmetric and peaked at $\delta = \pi$, where the relaxation is the slowest and p_∞ the largest. A rapid decay of T_1 by almost two orders of magnitude and a drop of p_∞ to 0 are observed at $|\delta - \pi| \simeq 0.3\pi$.

Similar data taken on a variety of ACs are shown in Fig. 4.19. The phase interval in which poisoning occurs reduces when the transmission of the most transmitting channel diminishes. For contacts having all channels with transmissions smaller than 0.7, the poisoning probability p was too small to be measured.

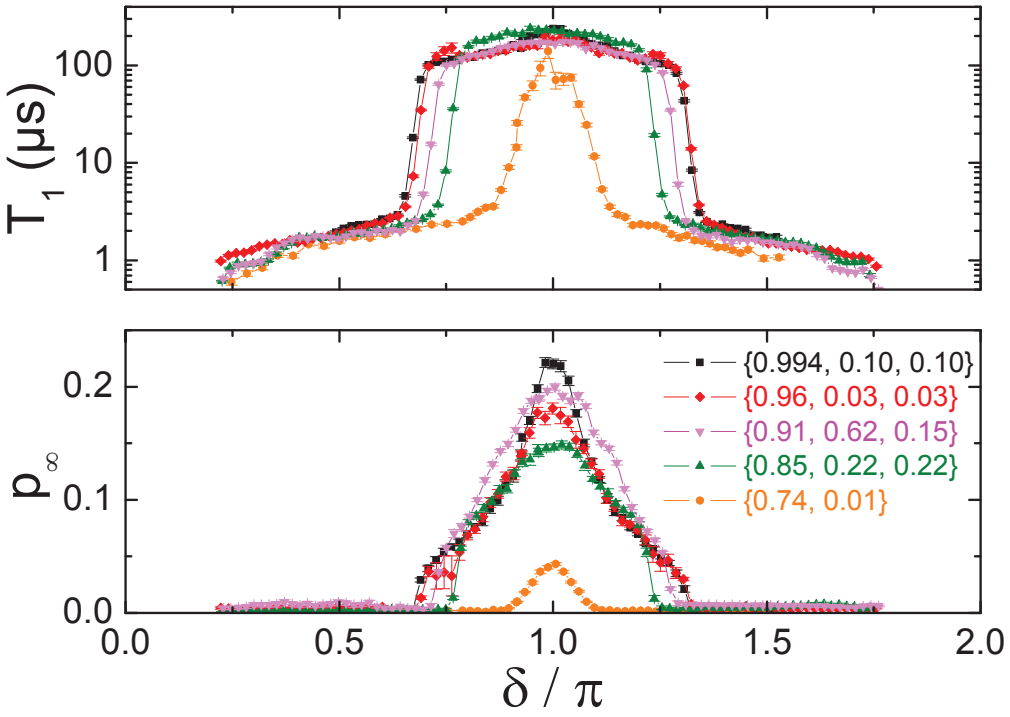

Figure 4.19: Relaxation time T_1 (upper panel) and asymptotic poisoning probability p_∞ (lower panel), measured at $T = 20$ mK, for five different ACs with the shown transmissions.

The overall shape of both $p_\infty(\delta)$ and $T_1(\delta)$ remains very similar when temperature is varied. The functions $p_\infty(\delta)$ and $T_1(\delta)$ measured at various temperatures, are shown in Fig. 4.20 for contact AC1. Whereas the asymptotic poisoning probability $p_\infty(\delta)$ hardly changes, the relaxation time $T_1(\delta)$ falls rapidly with temperature, and relaxation becomes too short to be measured above 250 mK.

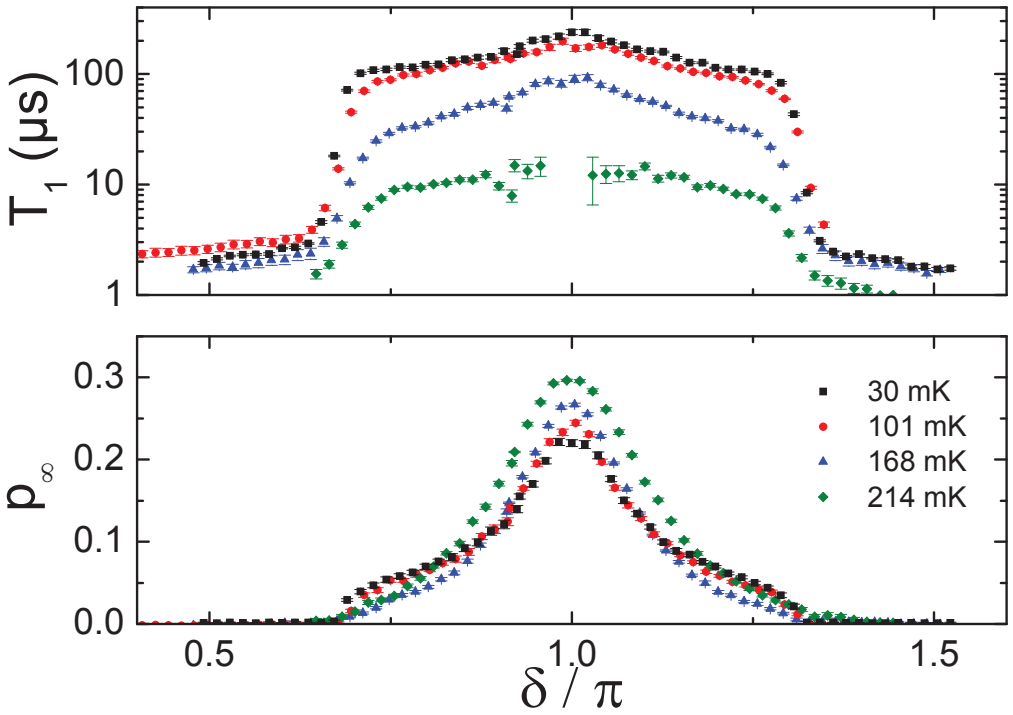

Figure 4.20: Relaxation time T_1 and asymptotic poisoning probability p_∞, as a function of the phase $\delta = \varphi_w$ applied during the dc flux pulse imposed for a time t_w between the prepulse and the measurement pulse. The data are taken on the atomic contact AC1 ($\{0.994, 0.10, 0.10\}$), and at four different temperatures T indicated in the figures.

4.4.3 *Relaxation time and asymptotic probability as a function of the Andreev energy*

Instead of plotting the relaxation time T_1 and the asymptotic poisoning probability p_∞ as a function of the applied flux δ as in Fig. 4.19, we choose in Fig. 4.21 for the x-axis the Andreev energy $E_A(\delta)$ of the most transmitting channel. Although the Andreev energy is clearly not the only relevant parameter, the relaxation times for all contacts roughly coincide. The most apparent differences are in the asymptotic poisoning probability p_∞ which, for a given E_A, diminishes when the transmission of the most transmitting channel increases. Two distinct regimes are evidenced in Fig. 4.21: when $E_A/\Delta > 0.5$, the relaxation time is very short and the asymptotic poisoning is negligible. In contrast, when the Andreev energy lies deep in the gap ($E_A/\Delta < 0.5$), relaxation is much slower and the asymptotic poisoning probability becomes sizable.

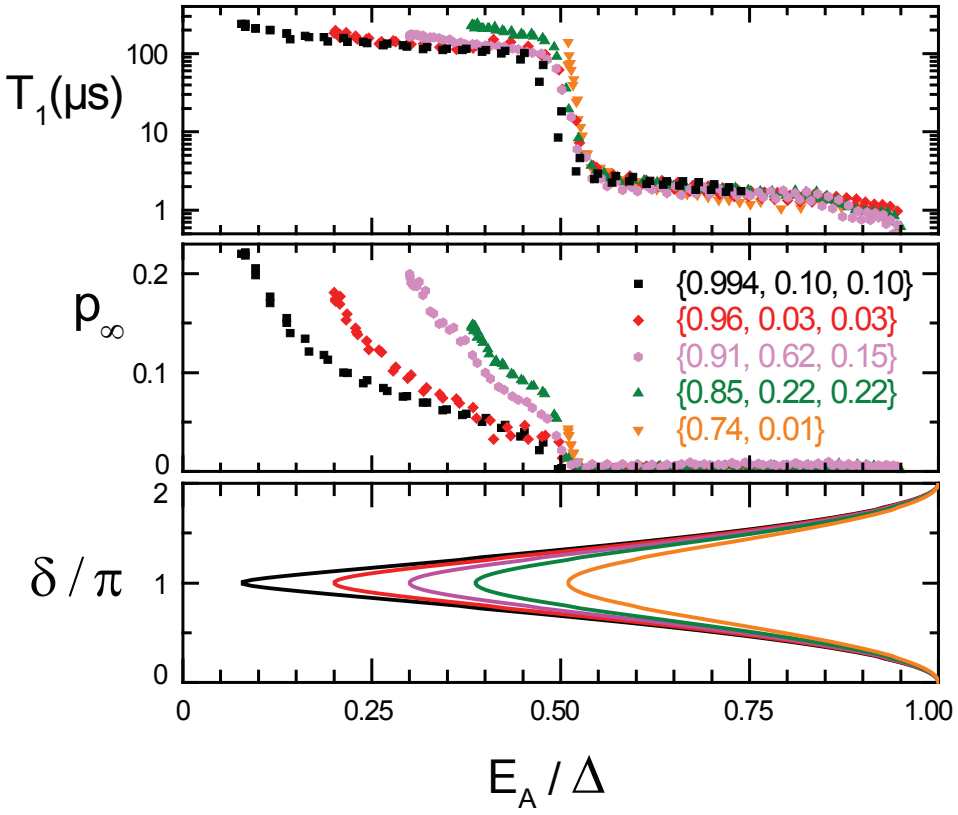

Figure 4.21: Same relaxation data as Fig. 4.19 as a function of normalized Andreev state energy E_A/Δ of most transmitting channel. Minimal value of E_A/Δ is $\sqrt{1-\tau}$ (0.08 for the black points, 0.5 for the orange points) and is reached when $\delta = \pi$, as shown in the lower panel. The relaxation time falls dramatically by two orders of magnitude above $E_A/\Delta \approx 0.5$ for all contacts.

4.4.4 *Origin of the boundaries of the anomalous phase region in* $P_{sw}(\varphi, s)$ *data*

Coming back to the results presented in Fig. 4.13 and Fig. 4.12, the boundaries of the phase range in which poisoning occurs can be understood in the light of Fig. 4.21: the left boundary corresponds to the phase φ_L at which $T_1(\varphi_L)$ becomes comparable with $\Delta t = 2\,\mu s$, leading to significant relaxation in the time interval between the prepulse and the measurement pulse. The nature of the right boundary is different: it corresponds to the phase φ_R at which $T_1(\varphi_R + \gamma(s))$ becomes comparable with $t_p = 1\,\mu s$ (we recall that $\gamma(s)$ is the phase across the Josephson junction during the measurement pulse), leading to significant relaxation during the measurement pulse. In contrast with the left boundary, the position of the right one depends slightly on s through $\gamma(s)$, which explains why it is slightly tilted. Hence, in the simplest procedure where the flux is the same during the whole sequence, the effect of relaxation during the measurement pulse becomes predominant for $\varphi > \pi$, explaining why the intervals where poisoning is observed is not centered at π.

4.4.5 *Origin of correlations in data without prepulses*

The anomalous statistics of the time intervals between switching events observed in the absence of prepulses (Fig. 4.8) can also be explained. If poisoning occurs after a measurement pulse, the system remains poisoned during a time T_1 in average. Switching is then suppressed, giving rise to long "blind" periods. When the system unpoisons switching occurs again. The probability to get poisoned again being of the order of $0.1 - 0.4$, several switching events can occur in a row.

4.4.6 *Initial poisoning*

4.4.6.1 *Observations*

We have measured the initial poisoning p_0 as a function of the phase δ across the atomic contact AC1 ($\{0.994, 0.10, 0.10\}$). The measurement protocol is shown in Fig. 4.22. The flux phase φ_{pp} is applied till 100 ns after the end of the prepulse; then the flux is reset to φ_i. Here again, the effect of relaxation at φ_i during the 15 µs between the end of the flux pulse and the measurement pulse has to be corrected.

The result of the measurement is displayed in Fig. 4.23. The chosen value of $\varphi_i \simeq 0.9\,\pi$ is indicated with a dashed line. At this flux, the relaxation before measurement is characterized by $T_1 = 167\,\mu s$ and $p_\infty = 0.12$.

The initial poisoning phase dependence is roughly symmetric and maximum at $\varphi_{pp} = \pi$, which tells that the Andreev energy when the flux pulse is applied is the important parameter. However, the exact behavior is non trivial with clear oscillations in $p_0(\varphi_{pp})$. This irregular pattern is responsible for the vertical stripes in the data shown in Fig. 4.13. Similar patterns were found on the other contacts.

To understand the influence of the different parameters, we have increased the duration of the current prepulse from 0.1 µs to 1 µs and decreased the one of the flux pulse[11] to 0.5 µs. We have seen that the flux pulse has an effect only when applied at the end of the prepulse. We have then increased the fall time of the bias current prepulse from 100 ns to 1 µs and seen that the effect appears when the flux pulse is applied during the last 500 ns of the prepulse. We conclude that **what matters is the energy of the ABS when the phase stops evolving and the voltage goes to zero**.

4.4.6.2 *Qualitative description of the mechanism leading to the initial poisoning*

During the prepulse, the system always switches and a voltage V develops across the AC. The phase δ then varies rapidly, at the rate V/φ_0, and a finite dissipative current flows through the AC via MAR phenomena (see Section 3.4.1). This creates quasiparticles in the continuum on both sides of the contact, typically 10^4 per prepulse[12]. When the bias current is reset to zero, the phase eventually stops in a

11 The flux pulse used was identical to the one in Fig. 4.24.

12 The voltage across the SQUID after switching is of the order of $V = 0.1\,mV$. For a contact of unit transmission, two quasiparticles are being created for each turn of the phase. For a 0.1 µs-long prepulse, the resulting number of quasiparticles is therefore $2 \times 0.1\,\mu s \times 0.1\,mV \times 2e/h \simeq 10^4$.

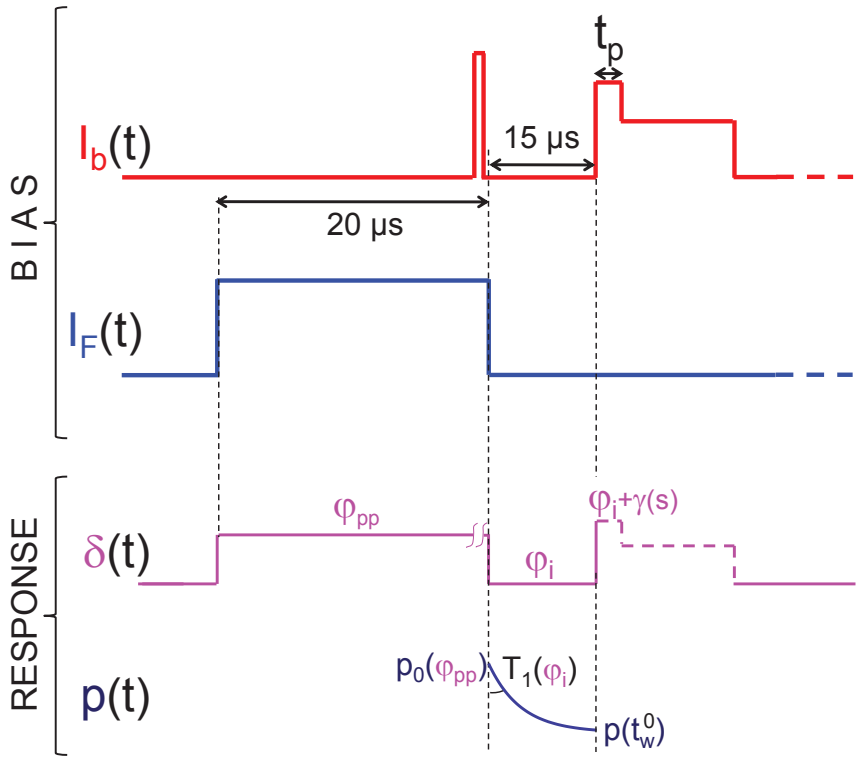

Figure 4.22: Pulse sequence used to measure the phase dependence of the initial poisoning probability p_0. The first line corresponds to the bias current, and the second one to the fast flux line. The third line sketches the evolution of the phase δ across the AC, and the last one that of the poisoning probability. The quantity that is studied is the poisoning probability $p_0(\varphi_{pp})$ just after the prepulse, which depends on the phase flux φ_{pp} applied to the contact during the prepulse. Note that the measuring pulse gives access to $p\left(t_w^0\right)$, which includes relaxation at flux φ_i during the last $t_w^0 = 15\,\mu s$. This relaxation is taken into account to obtain $p_0(\varphi_{pp})$.

local minimum of the global potential (this is retrapping), and the configuration of the Andreev levels freezes. The experiment indicates that after this step, the population of the Andreev states generally does not correspond to the equilibrium situation: there is a poisoning probability p_0 from which relaxation is subsequently observed.

The exact process of poisoning after switching is not understood. One can however qualitatively grasp the mechanisms that can be relevant using the picture of the Andreev elevator that describes transport in the finite voltage state (see Section 3.4.1). This description is valid for small voltages, and should correctly describe the last oscillations preceding the retrapping. In this picture, the Andreev levels oscillate and coincide periodically with the gap edges of the continuum (when $\delta = 2n\pi$), loading the lower level with a quasiparticle at the lower continuum, and unloading it in the upper one. The quasiparticle is sometimes transferred from the lower level to the upper one by Landau-Zener tunneling. In this scenario, the system is always in an even configuration. However, many quasiparticles are created in the continuum, and the "loading" (or "unloading") process can fail, leading to a situation where, after going through [102] $\delta = 2n\pi$, the lowest state

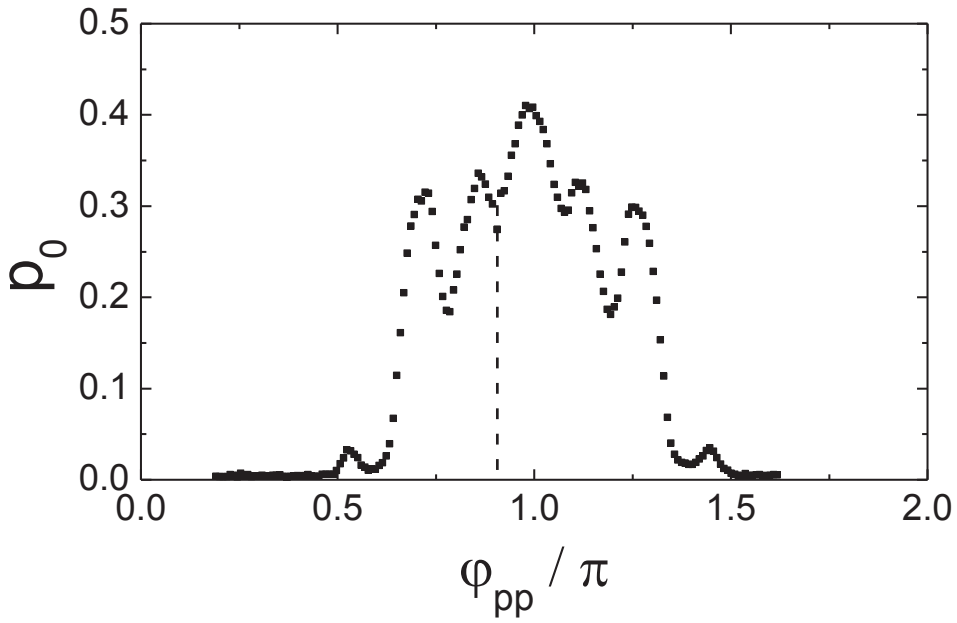

Figure 4.23: Initial poisoning p_0 as a function of the phase $\delta = \varphi_{pp}$ across the atomic contact AC1 at the end of the prepulse. The pulse sequence used to gather this data-set is shown in Fig. 4.22. The dashed line indicates the value of the phase δ across the AC when only the dc flux φ_i is applied.

is unoccupied while the upper one has emptied (or *vice versa*), leading to an odd configuration. If the system returns to the zero voltage state at this stage, the system stays trapped in the odd configuration. The oscillating structure for $p_0(\varphi_{pp})$ in Fig. 4.23 suggests that interferences during the phase dynamics may also play a role. Could this be linked with coherent Landau-Zener transitions (like in [103]) in the last oscillations of the phase? To test this idea we varied the rate of decay of the current at the end of the prepulse, which should change the Landau-Zener rates exponentially. The very weak dependence of $p_0(\varphi_{pp})$ on this parameter is not compatible with this scenario. No clear effect of the shape of the prepulses could be identified, and we did not find any explanation for the phase dependence of p_0.

4.5 Eliminating poisoning

It is desirable to eliminate quasiparticle poisoning because it can be detrimental to measuring the even excited state $|+\rangle$.

4.5.0.3 *Quasiparticle poisoning antidote*

The experimental data indicate that when the phase δ across the AC is driven far from π, the system quickly relaxes to the ground state. Based on this result, we have developed a procedure to remove trapped quasiparticles. The principle, illustrated in Fig. 4.24, is to sweep the flux phase over 2π, with a pair of symmetric[13]

13 The symmetric shape also prevents from "ringing" effects.

"antidote" pulses with amplitude π each, hence insuring that whatever the starting phase, δ crosses 0 or 2π.

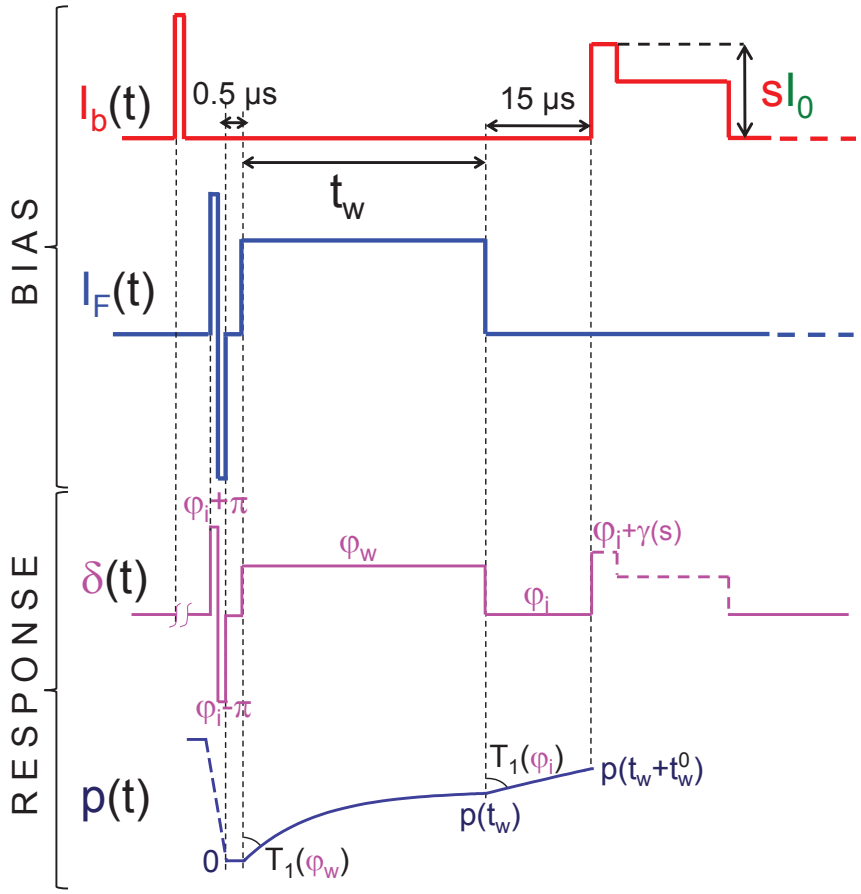

Figure 4.24: Pulse sequence used to measure the phase dependence of the relaxation process after the application of "antidote pulses". The first line corresponds to the current bias, and the second one to the fast flux line. The third line sketches the evolution of the phase δ across the AC, and the last one that of the poisoning probability $p(t)$. The antidote pulses are pairs of dc flux pulses applied in both directions, with an amplitude corresponding to a phase excursion of π on the phase δ. Their total duration was 0.5 µs; they are applied 1.5 µs after the prepulse. During the pair of antidote pulses, the phase visits regions where a trapped quasiparticle escapes rapidly, and the poisoning probability decays to 0.

Antidote pulses were employed to record $P_{sw}(\varphi, s)$ on the SQUID with contact AC0, as shown in Fig. 4.25. We used the simplest current bias pulses, shown in Fig. 4.24, with antidote pulses applied on the flux line 1 µs before the measurement pulse. The region displaying poisoning in Fig. 4.12 has completely disappeared, and switching is regular for all values of the flux phase φ. Therefore, the antidote pulses allow curing poisoning by bringing the ABS to the gap edge where the trapped quasiparticle can diffuse away into the continuum at the electrodes.

We have probed the poisoning dynamics starting from a "cured" situation (*i.e.* the ground Andreev state). Even starting from a cured configuration, the system relaxed to a poisoned one. In Fig. 4.26, we compare relaxation curves with and without the antidote pulses for contact AC1 ($\{0.994, 0.10, 0.10\}$) at $\varphi_w = \pi$, where

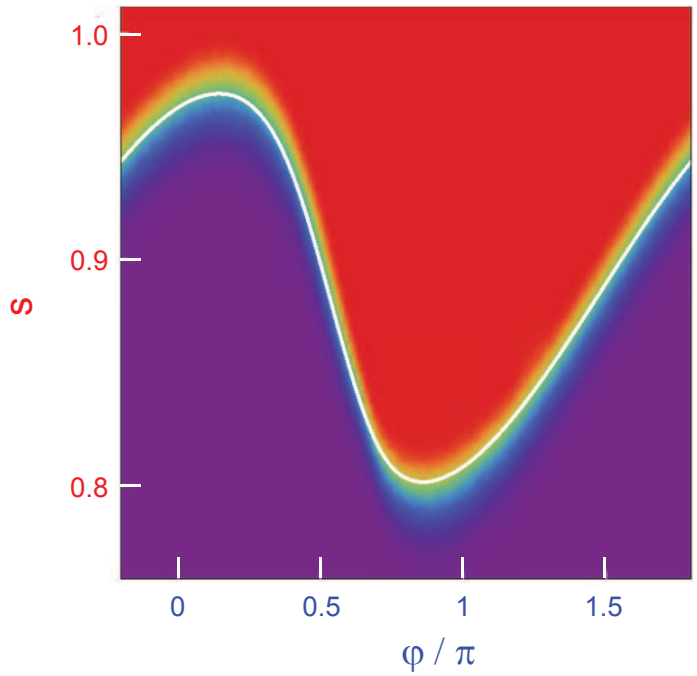

Figure 4.25: Color plot of the switching probability $P_{sw}(\varphi, s)$ using an antidote flux pulse 1 µs before the measurement pulse, and without prepulse, for the SQUID with contact AC0 with transmissions $\{0.95, 0.45, 0.10\}$. The color scale is the same as the one used in Fig. 4.12. The white curve show the lines corresponding theoretically to $P_{sw} = 0.5$ for the full contact. This plot is to be compared with Fig. 4.12.

the poisoning probability was the highest. Whereas data taken as in Fig. 4.16 show initial poisoning with a probability $p_0 = 0.37$, the poisoning probability extrapolates to 0 at $t_w = 0$ when antidote pulses are applied (Fig. 4.26, top curve), indicating that poisoning is absent just after the pulses. The subsequent evolution is identical in both situations, tending exponentially to $p = 0.23$ with a time constant $T_1 = 220\,\mu s$. This fact was checked for different flux values and on many ACs. This data proves that **the exponential behavior is robust**, and that poisoning associated with residual quasiparticles has the same effect whatever the initial configuration.

The procedure presented here allows obtaining unpoisoned configurations (as shown in Fig. 4.25) after the antidote pulses.

4.5.0.4 *Quasiparticle traps*

In previous experiments with ACs in SQUIDs [21, 78, 70, 72], poisoning was not observed. It is therefore possible to avoid poisoning altogether. In those experiments, the superconducting loop was directly connected to large normal metal electrodes, which acted as quasiparticle traps[14].

In contrast, our SQUID is contacted through very narrow and thin superconducting lines. Although we have placed small pieces of gold in direct contact with the present SQUID body (see Fig. 4.1 (b,c)), they did not act as efficient quasiparticle

14 In the normal state, the density of states is not gapped. Therefore, excited quasiparticles from the superconductors which reach the normal metal rapidly relax to the Fermi energy.

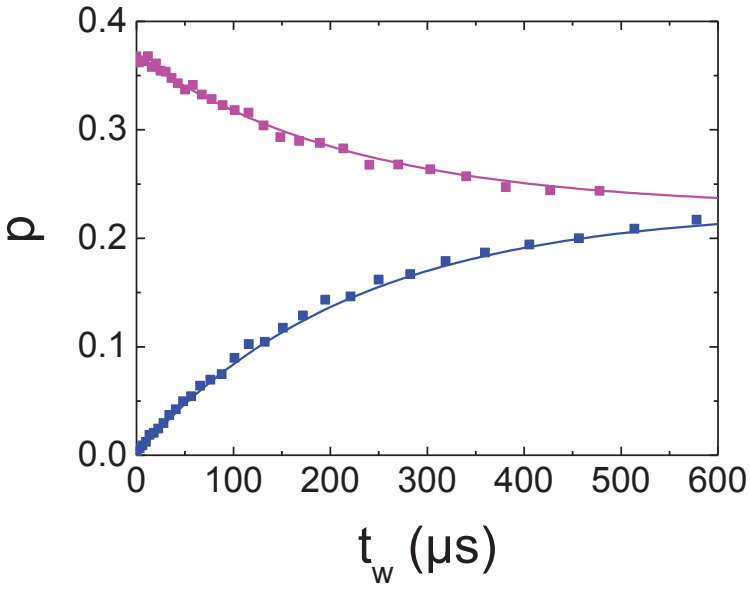

Figure 4.26: Symbols: Poisoning probability as a function of time t_w spent at phase π, for contact AC1 ($\{1, 0.07, 0.07\}$). Top curve is taken with the pulse sequence shown in Fig. 4.17, and shows frequent poisoning ($p(0) = 0.37$). Bottom curve has "antidote" flux pulses after the current prepulse (see Fig. 4.24), which suppress initial poisoning ($p(0) = 0$). Solid lines are exponential curves with identical time constants $T_1 = 220\,\mu s$ and asymptotic value $p = 0.23$.

traps. In fact, a normal metal electrode can only act as a trap if it is so large that the diffusion time of a quasiparticle through it exceeds the relaxation time of its energy, which was only marginally the case here.

On the other hand, decoupling from dissipative parts of the circuit is an important requirement (see Ref. [67] and Section 5.2) in order to explore the physics of the Andreev qubit [104, 50, 66], and the use of normal metal traps is probably not advisable. As a consequence, there would always be quasiparticles ready to get trapped in the Andreev bound states. One method to get rid of them is to apply the "antidote pulses" described in the previous sub-section. Another method is to use connecting wires and a capacitor with a lower gap than the SQUID. We have fabricated such a sample using bilayers of aluminum and copper (45 nm of Al and 3 nm of Cu). The superconducting gap in this region is reduced by $\sim 30\%$ (see[15] Ref. [105]). Fig. 4.27 shows $P_{sw}(\varphi, s)$ for the sample RAC4, with a highly-

15 According to BCS theory, the critical temperature is given by

$$T_c = 1.14\, T_D \exp\left(-\frac{1}{N(0)\,V}\right)$$

where T_D is the Debye temperature, $N(0)$ the electronic density of states at the Fermi level in the normal state and V the pairing energy. For Al, $T_c = 1.2$ K and $T_D = 426$ K. For a Superconductor-Normal bilayer of widths d_S and d_N, the effective pairing energy V_{eff} is reduced by the amount of time the electrons are in the normal region:

$$V_{eff} = V \frac{d_S}{d_S + d_N}.$$

transmitting channel (~ 0.993). Even with such a high transmission, no poisoning is observed[16].

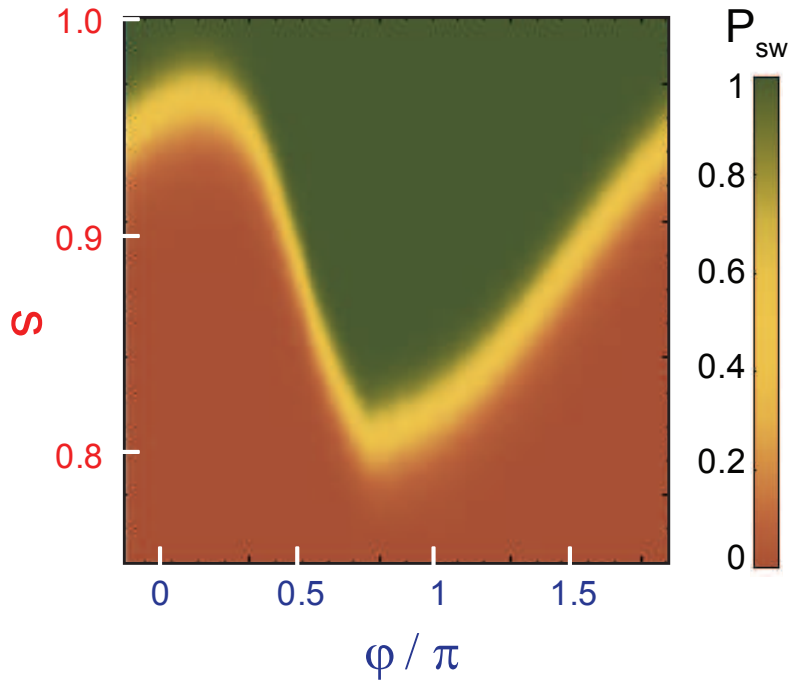

Figure 4.27: Color plot of the switching probability $P_{sw}(\varphi, s)$, using standard pulses (see Fig. 4.5). These measurements were obtained in an experiment on sample RAC4, with aluminum-copper electrodes, for an atomic contact of transmissions $\{0.993, 0.387, 0.17, 0.16\}$.

This rough estimation is a lower bound since it does not take into account the reflection of electrons at the S-N interface. Then, the bilayer critical temperature is

$$T_{Al/Cu} = T_{Al}\left(\frac{T_{Al}}{1.14\,T_D}\right)^{d_N/d_S} \simeq 0.67\,T_{Al}.$$

Since the gap is proportional to the critical temperature, it is reduced by a factor 0.67.

16 Sample RAC4 was fabricated for another experiment (reflectometry measurements of an atomic-SQUID in a superconducting cavity), not presented in this manuscript. As samples RAC4 and PAL7 have different geometries and because quasiparticle diffusion depends on the actual geometry, this is not firm proof that poisoning was suppressed by the gap engineering.

5

MODELING OF THE POISONING EXPERIMENT

In this chapter, we present modeling of the observed poisoning dynamics. Then, we discuss why our attempts to address the excited state $|+\rangle$ have been unsuccessful.

5.1 Model for poisoning dynamics

We have modeled our results with a master equation approach, taking into account all the relaxation processes which allow transitions from one Andreev configuration to another. Although this model captures some of the observed features (exponential relaxation), it does not describe the energy dependence observed in Fig. 4.21, and fails to explain the striking threshold behavior. Clearly, an ingredient is missing in the model. Only recently, a new idea emerged involving the plasma frequency of the SQUID, which could at least qualitatively explain this behavior.

5.1.1 *Master equation approach*

5.1.1.1 *Poisoning and unpoisoning rates*

The left panel of Fig. 5.1 depicts the different relaxation and excitation processes conserving parity and spin, and involving the Andreev doublet. We define the rates Γ_{in} (solid blue arrows) and Γ_{out} (dashed orange arrows) corresponding to an increase or a decrease of the number of quasiparticles[1] in the Andreev doublet. Note that the single arrow processes conserve the number of quasiparticles: the excitation in red is of the form $\gamma^\dagger_{k\sigma}\gamma_{A\sigma}$ (where these operators have been defined in Chapter 2) with the energy $\Delta - E_A$; the relaxation in blue is of the form $\gamma^\dagger_{A\sigma}\gamma_{k\sigma}$ with the energy $-(\Delta - E_A)$. On the contrary, the double arrow processes do not conserve the number of quasiparticles (but conserve the electron parity): the relaxation in red is of the form $\gamma_{k-\sigma}\gamma_{A\sigma}$ with the energy $-(\Delta + E_A)$; the excitation in blue is of the form $\gamma^\dagger_{A\sigma}\gamma^\dagger_{k-\sigma}$ with the energy $\Delta + E_A$. The big black arrow (Γ_{+-}) does not involve continuum states. It corresponds to a relaxation from the excited even state $|+\rangle$ to the the ground state $|-\rangle$; it is of the form $\gamma_{A\sigma}\gamma_{A-\sigma}$ with the energy $-2E_A$. Since we do not inject microwaves in the system, we have not included excitations from $|-\rangle$ to $|+\rangle$. The right panel of Fig. 5.1 shows all the processes that induce transitions among the four configurations accessible to the Andreev doublet.

All the microscopic processes involved are in principle rather slow because they either require energy absorption or the presence of quasiparticles in the continuum [20]. However, since the data show no trace of the even excited state $|+\rangle$ (which should carry an opposite supercurrent with respect to the ground state), we as-

1 The word "quasiparticles" has to be understood here in its meaning within the excitation picture.

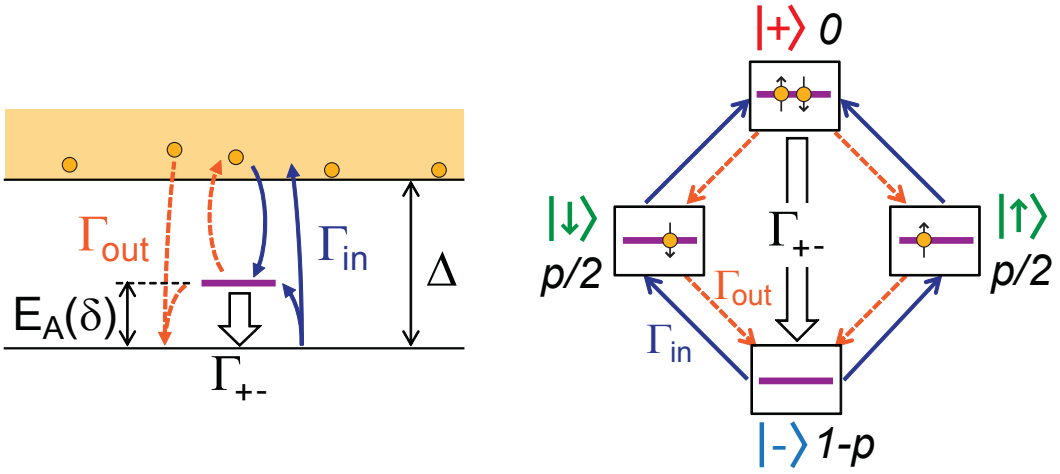

Figure 5.1: Model for the dynamics of the population of the Andreev configurations in the excitation representation (**left**), and in the configurations space (**right**). Quasiparticles can jump in and out the Andreev levels at rates Γ_{in} and Γ_{out}. If both levels of the Andreev doublet are occupied, the system can decay directly to the ground state (rate Γ_{+-} assumed to be much faster than all other rates). The occupations of all four configurations are $1-p$ (ground state), $p/2$ (odd configurations), and 0 (excited state).

sume that the relaxation rate Γ_{+-} is much larger than Γ_{in} and Γ_{out}. This hypothesis is discussed in Section 5.2.

The master equation for the population $1-p$ of the ground state $|0\rangle$, and $p/2$ of each of the odd configurations[2] $|\uparrow\rangle$ and $|\downarrow\rangle$ (see right hand side of Fig. 5.1), is:

$$\frac{d(1-p)}{dt} = -2(1-p)\,\Gamma_{in} + p\,(\Gamma_{out}+\Gamma_{in}), \tag{5.1}$$

the term $+p\Gamma_{in}$ corresponding to transitions from the odd configurations through the excited state $|+\rangle$ which relaxes very fast to the ground state. Since we observe an exponential dependence of $p(t)$ (see Fig. 4.26), Γ_{in} and Γ_{out} must be time-independent.

Under this assumption, one gets for the relaxation time and the asymptotic poisoning probability:

$$\boxed{T_1 = \frac{1}{\Gamma_{out}+3\Gamma_{in}}, \qquad p_\infty = \frac{2\Gamma_{in}}{\Gamma_{out}+3\Gamma_{in}}}. \tag{5.2}$$

The energy dependence of Γ_{in} and Γ_{out} can then be extracted from the data (see Fig. 5.2) using these expressions.

Although the Andreev energy is clearly not the only relevant parameter, the rates for all contacts roughly coincide. When $E_A/\Delta > 0.5$, Γ_{in} is smaller than Γ_{out} by 2 to 3 orders of magnitude. In contrast, the regime when the Andreev energy lies deep in the gap ($E_A/\Delta < 0.5$) corresponds to a smaller ratio Γ_{out}/Γ_{in}. At $E_A/\Delta \simeq 0.5$, Γ_{out} drops by two orders of magnitude. Therefore the peculiar energy dependence of both the relaxation time and the asymptotic probability, with a sharp threshold, is essentially ruled by the unpoisoning mechanism of rate Γ_{out}.

2 We assume a perfect spin degeneracy. Then, the two odd configurations are perfectly equivalent.

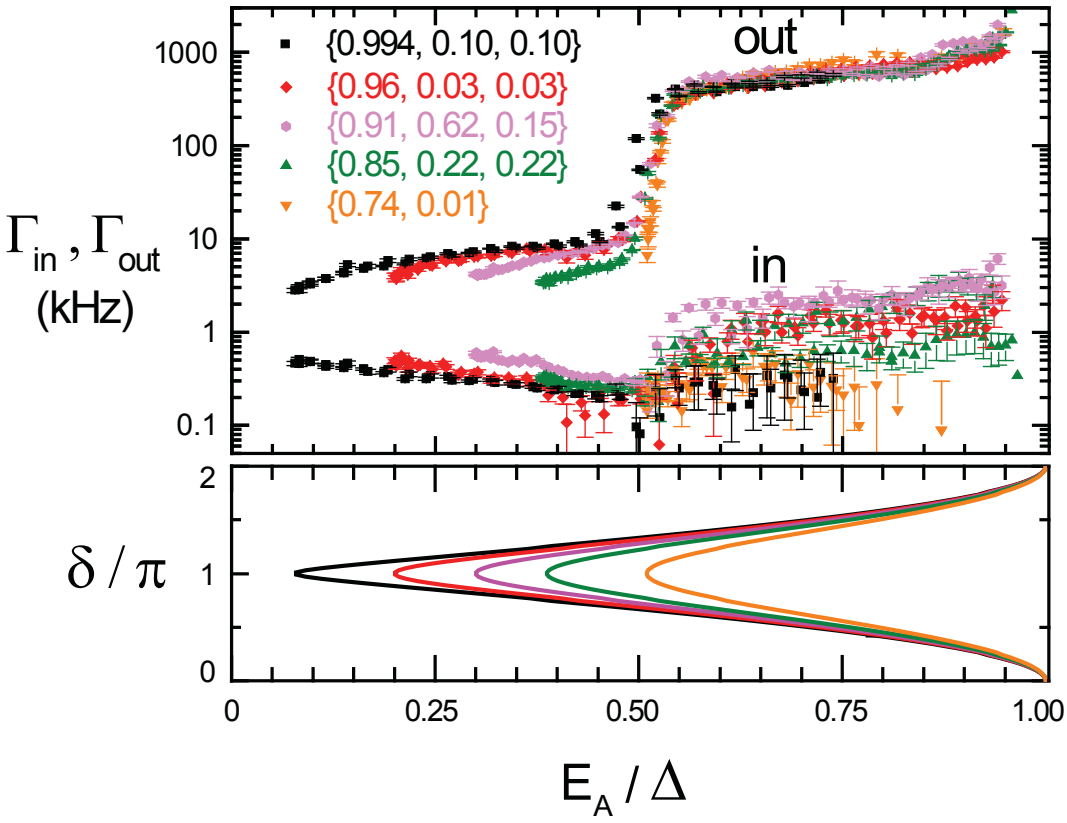

Figure 5.2: Relaxation rates Γ_{in} and Γ_{out} extracted from the data of Fig. 4.21, as a function of the Andreev energy E_A/Δ of the most transmitting channel, for five different ACs. There is a sharp threshold at $E_A/\Delta \approx 0.5$ for all contacts. Minimal value of E_A/Δ is $\sqrt{1-\tau}$ (0.08 for the black points, 0.5 for the orange points) and is reached when $\delta = \pi$, as shown in (d). Inset of panel (c): Rates Γ_{in} (resp. Γ_{out}) are for processes increasing (resp. decreasing) the number of quasiparticles in contact.

5.1.1.2 *Discussion of time-independence of rates: decay of the extra quasiparticles created during the prepulse*

All the relaxation processes involving the continuum are proportional to the quasiparticle density. An important observation is that when two switching prepulses are applied separated by more than 1 µs, the first one has no effect. This indicates that quasiparticles created by switching matter only during 1 µs. Therefore the quasiparticle density is constant at the time scales probed by relaxation experiments, which is compatible with the fact that Γ_{in} and Γ_{out} are time-independent. One possibility for quasiparticles to disappear is through recombination. However, we think that they most probably diffuse away very quickly, as shown by the following evaluation.

To evaluate the decay of the density n_{qp} of quasiparticles due to diffusion, we start from the number of quasiparticles created during the prepulse, 10^4, as we evaluated at the beginning of Section 4.4.6.2. Within the duration of the prepulse, they spread over $\sim \sqrt{D_{qp} \times 0.1\,\mu s} > \sqrt{D_N \times 0.1\,\mu s} \simeq 50\,\mu m$ (with $D_{qp} = D_N / \left(1 - (\Delta/E)^2\right)$ the diffusion constant for quasiparticles of energy E in the su-

perconducting state[3], D_N being the value in the normal state), *i.e.* over the whole area of SQUID (see Fig. 4.1 (c)). The density at the end of the prepulse is therefore $n^0_{qp} \approx 100\,\mu m^3$. Diffusion is then one-dimensional because it is limited by the three thin and narrow inductive lines, and a rough estimate (using again the diffusion constant D_N instead of D_{qp}) indicates that the density decays within a few microseconds below $10\,\mu m^3$, which is the typical background value found for Al films at low temperatures in Refs. [33, 31]. The quasiparticles created by the prepulse can therefore be neglected when describing the dynamics of poisoning relaxation.

5.1.1.3 *Non-equilibrium quasiparticles in stationary state*

Our experiment indicates that in the steady state quasiparticles are present in the continuum. Given the low temperatures, these cannot be equilibrium quasiparticles: from the gap $\Delta \sim k_B \times 2\,K$, the normal density of states at Fermi energy $N_n(0) \sim 2.15 \times 10^{47}\,J^{-1}m^{-3}$, one estimates at $T = 100\,mK$ a density of $\sim 10^{-2}$ qp.μm^{-3}, i.e. less than a single quasiparticle in the SQUID area ($\sim 10\,\mu m \times 10\,\mu m \times 0.1\,\mu m$).

In fact, several experiments [33, 32, 34] find that the number of quasiparticles saturate below 100 mK. For example, Shaw *et al.* measured an out-of-equilibrium quasiparticle density of 10 qp.μm^{-3} at a base temperature of 18 mK. These nonequilibrium quasiparticles are attributed to spurious noise. Blackbody radiation, cosmic rays and background radioactivity are listed as plausible sources [31].

5.1.1.4 *Temperature dependence*

The temperature dependence of the relaxation time and asymptotic probability shown in Fig. 4.20 demonstrate that the rates Γ_{in} and Γ_{out} increase with temperature in the same manner. However, the narrow temperature range in which they could be measured does not allow to extract a clear activation energy.

5.1.1.5 *Quasiparticle dynamics in superconductors*

To go further one needs to plug microscopic ingredients to model the rates Γ_{in} and Γ_{out}. The mechanisms commonly used to describe quasiparticle dynamics in superconductors are the emission and absorption of photons or phonons. However, it is difficult to imagine how any of these processes could lead to such a sharp threshold at energy $0.5\,\Delta$, so that by the time we wrote the paper [38] we did not have an explanation for this observation.

5.1.2 *Towards an interpretation of the energy threshold ?*

Only recently, a new idea emerged involving the plasma frequency of the SQUID that could qualitatively explain this behavior. The threshold energy at $0.5\,\Delta$ could be a mere coincidence and actually be related to the plasma frequency instead of

3 In contrast with what is often stated, Usadel theory indicates that quasiparticles in superconductors diffuse much faster than in the normal state (see for example Ref. [106]).

the gap, since $\nu_p \sim 19$ GHz and $0.5\,\Delta \sim h * 21.5$ GHz. In the following we propose a scenario in which the plasma mode is involved.

5.1.2.1 *Unpoisoning mechanisms*

The threshold in the relaxation is essentially due to the unpoisoning rate Γ_{out} (see Fig. 5.2). As shown in Fig. 5.3, one can distinguish four different mechanisms[4] which induce a transition from a poisoned odd state $|\uparrow\rangle$ or $|\downarrow\rangle$ to the ground state $|-\rangle$. The second and third ones are relaxation mechanisms and involve the presence of a quasiparticle in the continuum. One can reasonably consider that the extra quasiparticles are at the gap edge, therefore these processes involve a well-defined energy difference: a threshold is not expected.

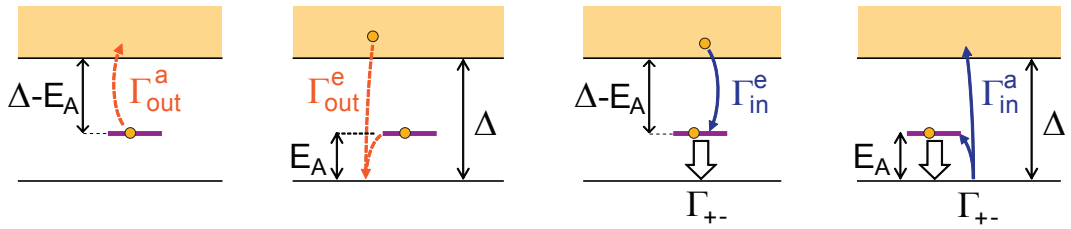

Figure 5.3: Unpoisoning mechanisms. The exponent a (resp. e) labels processes in which absorption (resp. emission) of energy is involved.

The first and last mechanisms are possible only in presence of an external source of energy. The quasiparticle can be promoted at any energy larger than the gap: there is a threshold. Since the threshold energy is much smaller for the first process ($\Delta - E_A$ vs. $\Delta + E_A$), it can be considered as the dominant unpoisoning mechanism.

5.1.2.2 *Emission of photons by the plasma mode*

The energy threshold could be understood if the energy $\Delta - 0.5\Delta = 0.5\Delta$ was available in the environment. It happens that 0.5Δ is also very close to our estimation of the plasma energy $h \times 19\,\text{GHz}$. Could it be that the plasma oscillator is not in its ground state, but is instead cooled by the Andreev state by untrapping of quasiparticles when $h\nu_p > \Delta - E_A$? If the plasma mode is well coupled to the Andreev doublet, one would also expect a resonance in the inverse process Γ_{in} by emission instead of absorption? Further theoretical work is in progress to quantify these effects [107].

5.2 Why have we failed to detect the even excited state $|+\rangle$? Relaxation between $|+\rangle$ and $|-\rangle$

Whether by trapping of quasiparticles or as a result of a microwave excitation, one expects the system to reach the even excited state $|+\rangle$. However, $|+\rangle$ is never observed in this experiment. We attribute this fact to a large value of the relaxation rate Γ_{+-} to the ground state. Two contributions to this rate can be evaluated.

4 The two last processes involve in addition the instantaneous relaxation from $|+\rangle$ to $|-\rangle$.

5.2.1 *Relaxation due to photon emission*

The first one is the rate Γ_{+-}^{em} of the process in which a photon is emitted into the electromagnetic environment of the AC. It reads (see Section D.2.2 and Ref. [67])

$$\boxed{\Gamma_{+-}^{em} = \frac{\pi\Delta}{2\hbar}\frac{\mathrm{Re}\left[Z(\frac{2E_A}{\hbar})\right]}{R_Q}\frac{(1-\tau)\left(1-\frac{E_A}{\Delta}\right)^2}{\left(\frac{E_A}{\Delta}\right)^3}} \tag{5.3}$$

where Z is the environment impedance seen from the atomic contact and

$$R_Q = \frac{h}{4e^2} \simeq 6\,\mathrm{k}\Omega \tag{5.4}$$

is the superconducting resistance quantum. The scale of this rate is given by $\pi\Delta/\left(2\hbar R_Q\right) \simeq 660\,\mathrm{MHz}/\Omega$.

MICROWAVE ENVIRONMENT SEEN BY THE ATOMIC CONTACT For the actual circuit design (Fig. 4.2), the environment impedance Z as seen from the atomic contact is:

$$Z^{-1}(\omega) = jC_0\omega + \frac{1}{jL_0\omega} + \frac{1}{jL\omega + \frac{1}{\left(r(\omega)+\frac{1}{jC\omega}\right)^{-1}+R_b^{-1}}}, \tag{5.5}$$

where $L_0 = \varphi_0/I_0$, C_0 are the Josephson junction equivalent inductance and capacitance, respectively. The dissipation is modeled through a frequency-dependent resistance $r(\omega)$ in series with the capacitor. Unfortunately, we could only characterize it at low-frequency $\sim [400\,\mathrm{MHz}, 800\,\mathrm{MHz}]$ (see Section E.1). In that range, the average value was $r \simeq 0.33 \pm 0.04\,\Omega$. As we do not have more information, we simply use the same value for all frequencies.

Fig. 5.4 shows $\mathrm{Re}[Z]$ between 0 and 100 GHz. It presents two widely separated modes:

- A low-frequency mode corresponding to the LC-oscillator, slightly modified by the inductance of the Josephson junction:

$$\nu_e \simeq \frac{1}{2\pi}\sqrt{\frac{1}{(L+L_0)\,C}} \simeq 560\,\mathrm{MHz}.$$

- A high-frequency mode which is essentially the bare plasma frequency of the junction, slightly modified by the inductance of the environment:

$$\nu_p \simeq \frac{1}{2\pi}\sqrt{\frac{1}{C_0}\left(\frac{1}{L}+\frac{1}{L_0}\right)} \simeq 19\,\mathrm{GHz}.$$

Between 0.65 GHz and 16 GHz and above 20.7 GHz, $\mathrm{Re}[Z]$ is smaller than $1\,\Omega$. This tank circuit was designed to give a small $\mathrm{Re}[Z]$ in a broad frequency range so as to ensure a small relaxation rate for the ABS in the atomic contact.

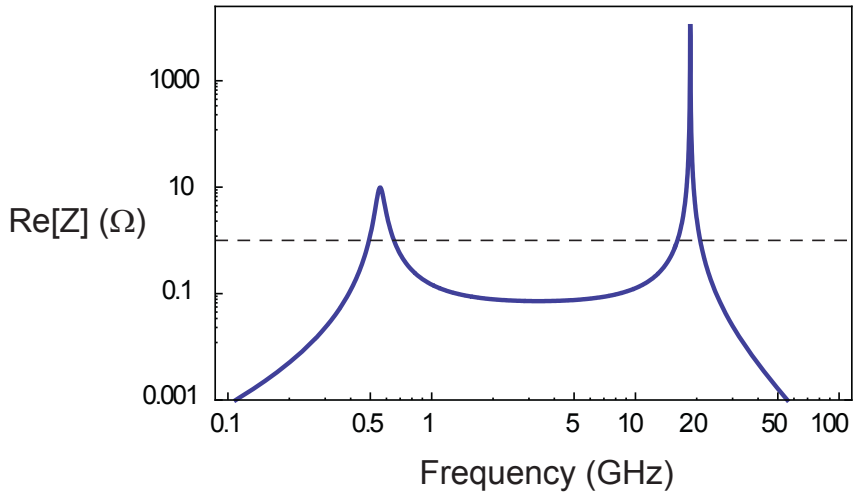

Figure 5.4: Real part of the impedance of the environment seen from the atomic contact, for a constant series resistance $r = 0.33\,\Omega$.

ESTIMATED RELAXATION RATE The resulting rate Γ^{em}_{+-} is shown as solid lines in Fig. 5.5 for different transmissions. It decreases rapidly as the Andreev energy increases. For $\tau = 0.995$, a peak is visible in Γ^{em}_{+-}, corresponding to the Andreev frequency $2E_A/h$ coinciding with the high frequency mode at 19 GHz.

5.2.2 *Relaxation due to phonon emission*

The second contribution to Γ_{+-} is the rate Γ^{ph}_{+-} of the process in which a phonon is emitted. An upper bound to this rate[5] has been calculated in Refs. [66, 108] in the limit $E_A \ll \Delta$:

$$\boxed{\Gamma^{ph}_{+-} \simeq (1-\tau)\,\frac{\Delta}{E_A}\tau^{-1}_{ph}(E_A)}, \tag{5.6}$$

with $\tau^{-1}_{ph}(E) = \kappa_{ph} E^3$ the bulk electron-phonon relaxation rate at energy E. Experiments[6] [109, 111] on similar Al films give $\kappa_{ph} \simeq 3\,\mathrm{MHz.(k_B.K)^{-3}}$. The corresponding predictions are shown with dashed lines in Fig. 5.5 for transmissions 0.80, 0.95 and 0.995. Contrary to the photon emission rate, the phonon emission rate increases with Andreev energy.

5 The rate is reduced due to the confinement of the bridge where the atomic contact is formed (see Ref. [66]). Recently Y. Nazarov pointed out that there is an additional reduction factor of 10^{-5} [53].

6 The definition of the electron-phonon scattering rate $\tau^{-1}_{ph}(E)$ in Ref. [66] is related to the characteristic rate τ_0^{-1} introduced in Ref. [29] by $\tau_0^{-1} = \tau^{-1}_{ph}(k_B T_c)$. It differs by a factor $6\xi(3) \approx 7$ from the inelastic rate $\tau^{-1}_{ep}(T)$ due to electron-phonon processes in Ref. [109], which is an average on the scattering rates of electrons with energies in the width of the Fermi distribution [110]. Assuming that the matrix element for emission of phonons with energy ε is $\kappa_{ph}\varepsilon^2$, one has $\tau^{-1}_{ph} = \kappa_{ph}E^3$ and $\tau^{-1}_{ep} = 6\xi(3)\,\tau^{-1}_{ph}$.

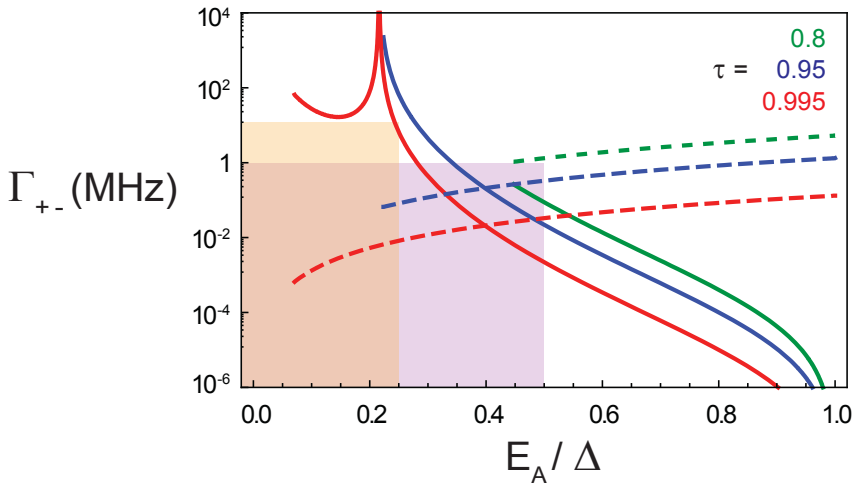

Figure 5.5: Calculated relaxation rate Γ_{+-} from the excited singlet to the ground state, as a function of the Andreev energy E_A/Δ, for transmissions $\tau = 0.8$, 0.95 and 0.995. Two contributions are plotted: rate for photon emission into the electromagnetic environment Γ^{em}_{+-} (solid lines) and upper bound for the phonon emission rate Γ^{ph}_{+-} (dashed lines). The two colored areas indicate the experimental windows for the two different detection strategies of state $|+\rangle$. Purple area: for spontaneous quasiparticle trapping after a prepulse, which is only observed for $E_A/\Delta < 0.5$ and after a delay of 1 µs. Orange area: for microwave excitation, which can be sent up to 20 GHz ~ $0.25\,\Delta$, and with a detection bandwidth estimated roughly around 10 MHz.

5.2.3 *Discussion*

In the phase interval where poisoning is observed (below $0.5\,\Delta$, purple area), the large value of Γ_{+-} (at the MHz scale, which is the upper bound to the measured values of $\Gamma_{in,out}$, see Fig. 5.2) can be attributed to losses in the electromagnetic environment of the AC and, to a lesser amount, to phonon emission. Only for high transmission $\tau > 0.95$ and Andreev energy $E_A \sim 0.4\,\Delta$ do these estimates suggest than$|+\rangle$ could have been detected.

In order to detect $|+\rangle$ when microwaves are applied, its lifetime must be significant at the scale of the measurement pulse, which is not evident from the results of our estimation of relaxation by photon emission (see orange area).

Note however that the estimation of Γ_{+-} depends crucially on the value of losses in the capacitor, which has only been characterized at low frequency. In Fig. 5.5, the series resistance is taken constant and equal to $r = 0.33\,\Omega$. At the Andreev frequency $2E_A/h$, the losses could easily be different, and the conclusions that we draw irrelevant.

5.3 Conclusion

We have observed and characterized the excited odd states $|\uparrow\rangle$ and $|\downarrow\rangle$. As expected for a spin-degenerate system, they do not carry supercurrent. In this experiment the excitation is uncontrolled and results from trapping of spurious quasiparticles but we have implemented strategies to eliminate poisoning. The phenomenon be-

hind the peculiar energy dependence of the dynamics of trapped quasiparticles remains to be understood. Is it intrinsic or related to the plasma mode?

5.4 Towards measuring the excited even state $|+\rangle$

Attempts to induce transitions from $|-\rangle$ to $|+\rangle$ with microwaves applied on the fast flux line were unsuccessful in this experiment. This is probably due to the short life-time of $|+\rangle$, as explained in Section 5.2.

To measure this transition, we decided to change drastically the scheme to excite and detect transitions. Instead of measuring a change in the ABS current induced by an excitation, we measured the microwave power absorption by the ABS, in which case a short life-time is favorable.

Part III

SPECTROSCOPY OF ANDREEV BOUND STATES WITH A JOSEPHSON JUNCTION

The third part describes the second experiment, where we have performed the first photon-absorption spectroscopy of ABS using a voltage-biased Josephson junction as an on-chip spectrometer, together with the quantum theory we developed to explain the results. At last, a new type of spectroscopy is presented involving both excitation by a Josephson junction spectrometer and switching measurement.

6

PHOTON-ABSORPTION SPECTROSCOPY OF THE ANDREEV BOUND STATES USING A JOSEPHSON JUNCTION SPECTROMETER

In this chapter, we present an experiment accessing the transition between the ground state $|-\rangle$ and the excited even state $|+\rangle$ by photon-absorption spectroscopy. It was performed by coupling a superconducting atomic contact to a voltage-biased Josephson junction, used as an on-chip, broadband spectrometer.

6.1 Experimental setup

A simplified equivalent circuit is shown in Fig. 6.1. A schematic closer to the actual geometry is shown in Fig. G.1.

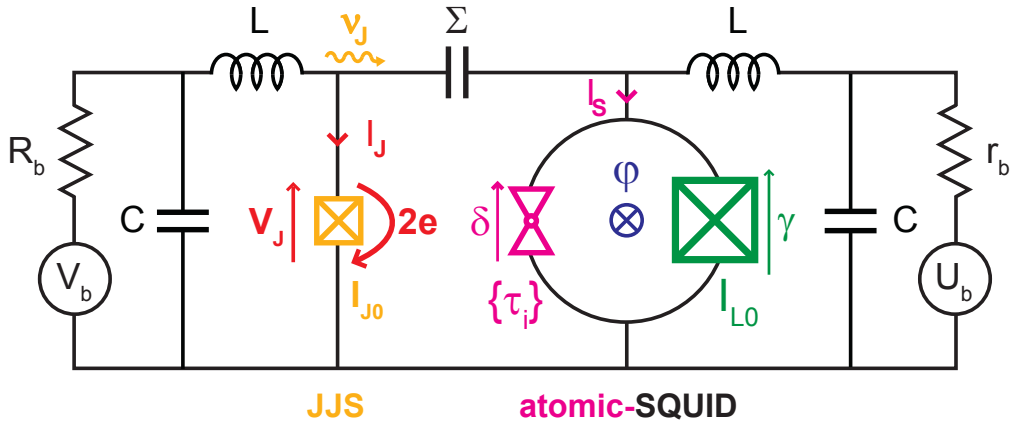

Figure 6.1: Simplified equivalent circuit of sample JT6. Left part: a voltage-biased Josephson junction (yellow checked box) behaves as a microwave current source, emitting photons at Josephson frequency ν_J. Right part: an atomic contact (magenta triangles), of channel transmissions $\{\tau_i\}$, forms a SQUID with a Josephson junction (green checked box). Reduced flux threading the loop φ is imposed by a superconducting coil and allows to tune the ABS energy. Phases δ and γ across contact and junction are linked as $\delta - \gamma = \varphi$. The JJS [respectively the SQUID] is biased by a voltage source V_b [U_b] through an on-chip LC filter ($L \simeq 0.89$ nH, $C \simeq 20$ pF) and a series resistance $R_b = 2k\Omega$ [$r_b = 200\Omega$] placed at the same temperature as the sample. The current I_J (red) [I_S (magenta)] is measured from the voltage drop across R_b [r_b]. These two parts, which are independent from the dc point of view, are coupled through an on-chip capacitor $\Sigma \simeq 30$ pF.

- On the right-hand, an aluminum AC is placed in parallel with a tunnel JJ (critical current $I_{L0} \sim 1\,\mu$A about 20 times larger than the critical current of atomic contacts) to form an atomic-SQUID (see Fig. 6.2 (e,c,d)). An external superconducting coil is used to apply a dc flux φ through the SQUID loop.

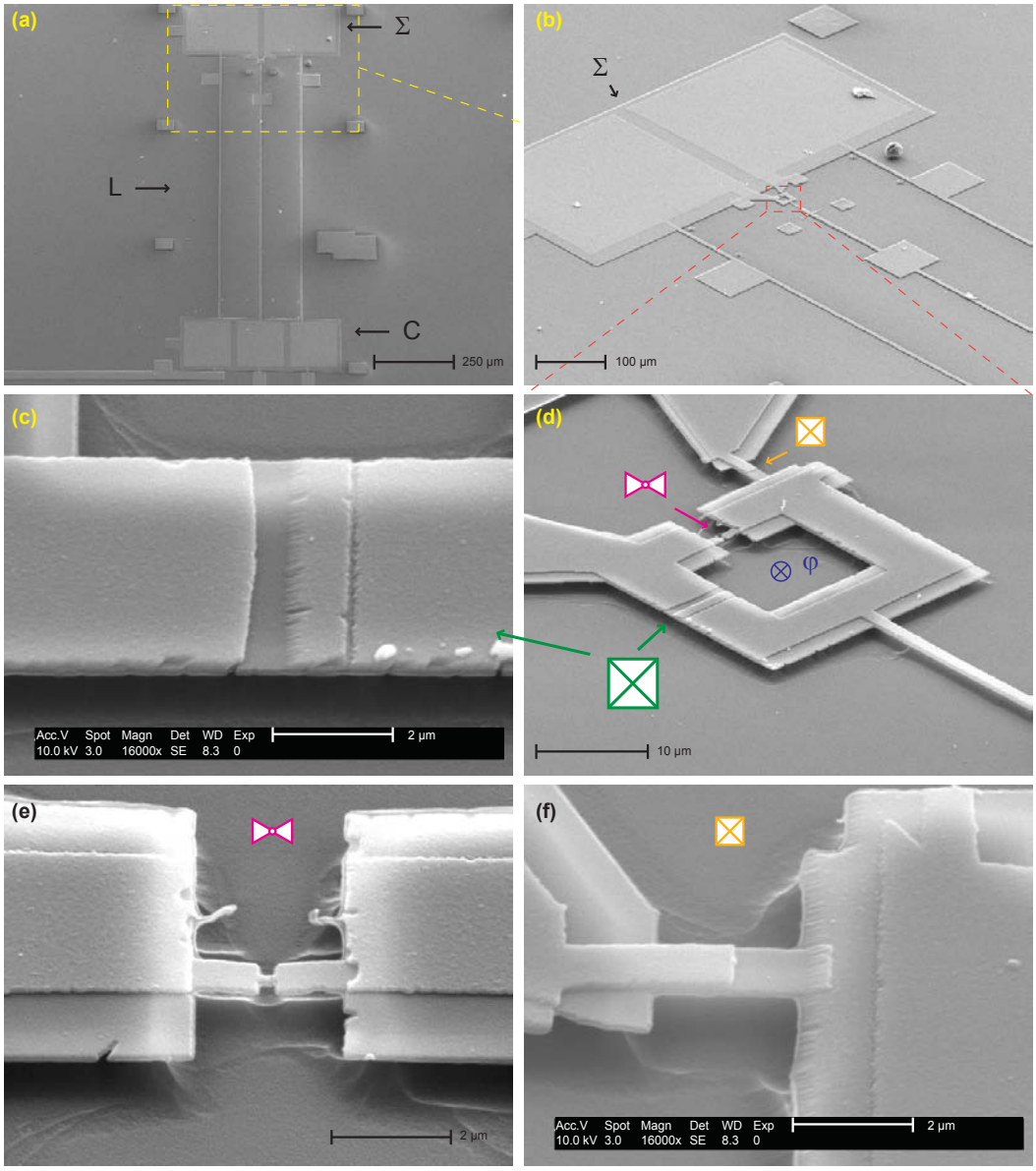

Figure 6.2: SEM micrograph of the sample JT6 at different magnifications. **(a)** The end of the current bias lines contact three rectangular electrodes which form planar capacitors with a common, floating and superconducting rectangular electrode placed below, implementing the filtering capacitors C. From there the connections to the atomic-SQUID and the JJS are made with three 5 µm-wide aluminum wires, which serve as the inductors L. **(b)** The SQUID and the JJS are connected to two rectangular electrodes which form the coupling capacitor Σ with the superconducting rectangular electrode underneath. **(d)** Tilted SEM micrograph shows the Josephson junction of the SQUID (enlarged in **(c)**), the suspended micro-bridge (enlarged in **(e)**) and the JJS (enlarged in **(f)**).

- On the left-hand, a second JJ (critical current $I_{J0} \sim 50\,\mathrm{nA}$, much smaller than the critical current of the SQUID) is used as an on-chip broad-band microwave source and detector [44, 45, 48], the Josephson junction spectrometer (JJS) (see Fig. 6.2 (f,d)).

- The two parts are independent at dc but coupled at high frequencies through an on-chip capacitor $\Sigma \simeq 30$ pF (see Fig. 6.2 (b)).
- Each part of the circuit is connected to low frequency biasing and measurement circuits through on-chip LC filters. The inductors L are realized with long aluminum wires, while the capacitors C are planar capacitors (see Fig. 6.2 (a)). At the high frequencies relevant for spectroscopy measurements, the LC filters present high impedance compared to the coupling capacitor Σ. The currents I_J and I_S in the JJS and the atomic-SQUID are measured from the voltage drop across the bias resistors R_b and r_b with low-noise voltage amplifiers. A third twisted-pair is used to measure the voltage V_S across the atomic-SQUID. The voltage V_J across the JJS is determined from the bias voltage V_b with an accurate calibration of the bias line (see Section G.2).

Fabrication details are given in Section 9.2.

As already explained (see Section 4.1), the atomic-SQUID geometry allows for each atomic contact either to measure the current-voltage characteristic, from which one determines the transmissions of its conduction channels (see Section 3.4.1 and Section 4.2.1), or to tune with the external flux φ the ABS energies $\pm E_A(\delta, \tau)$: at zero bias voltage ($U_b = 0$), $\gamma \simeq 0$ and $\delta \simeq \varphi$ due to the large asymmetry of the SQUID[1].

The idea behind this setup is to use the JJS to drive and detect the Andreev transition. When the JJS is biased at voltage V_J, it emits microwaves at the Josephson frequency

$$\nu_J = \frac{V_J}{2\pi\varphi_0} \tag{6.2}$$

which can be absorbed by its electromagnetic environment. When photons are absorbed at a rate Γ, a finite dc current

$$\langle I_J \rangle = 2e\Gamma \tag{6.3}$$

must flow through the junction so that the dc power $\langle I_J \rangle V_J$ delivered by the voltage source compensates for the microwave power $h\nu_J\Gamma$ dissipated in the environment. As depicted in Fig. 6.3, at the microscopic level, this dc current arises from inelastic tunneling of Cooper pairs through the insulating barrier: the energy $2eV_J$ released by a Cooper pair is absorbed in the environment as a photon[2] of energy $h\nu_J$.

Thus, each mode of the environment of the JJS should appear as a dc current peak in its sub-gap current-voltage $I_J(V_J)$ characteristic. The peak position gives the mode frequency, and its amplitude the rate at which the mode absorbs photons. Consequently, the spectroscopy consists simply in measuring the dc current I_J though the JJS, as a function of both the voltage V_J across the JJS and the phase

1 The error of this approximation is of the order of $I_{ac}(\varphi)/I_{L0}$ (where I_{ac} is the current through the atomic contact), since the loop current is $\simeq I_{ac}(\varphi)$ and the phase across the JJ

$$\gamma \simeq \arcsin\left(\frac{I_{ac}(\varphi)}{I_{L0}}\right) \ll 1. \tag{6.1}$$

2 This is valid for first order processes where one Cooper pair emits one photon. The higher order terms are discussed in Chapter 7 and Appendix J.

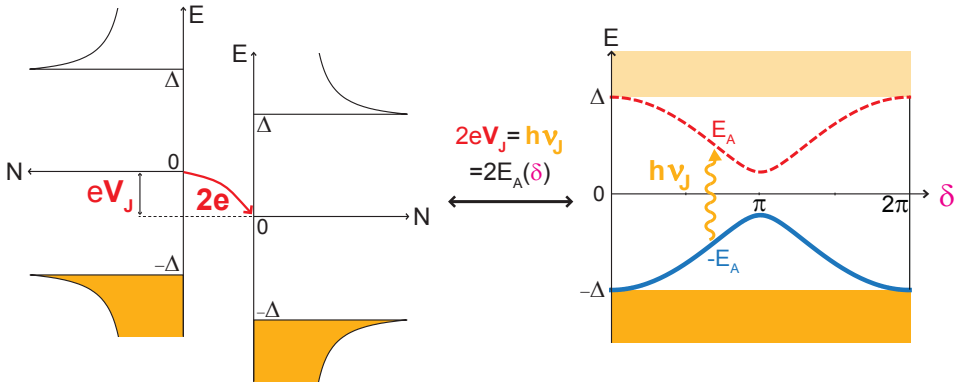

Figure 6.3: Principle of Andreev spectroscopy: **(left)** BCS density of states in the two electrodes of the JJS, shifted by the bias energy eV_J. A Cooper pair tunneling through the insulating barrier releases energy $2eV_J$ as a photon of frequency ν_J, which is absorbed in the atomic-contact by exciting the Andreev transition **(right)**.

$\delta \simeq \varphi$ across the atomic contact. Note that this method is particularly well adapted to the spectroscopy of the Andreev doublet $h\nu_J = 2E_A(\delta, \tau)$, since the excitation frequency ν_J is widely tunable (up to $\frac{4\Delta}{h} \sim$ 170 GHz for aluminum, compared to the maximum energy of the Andreev transition $2\Delta \sim h \times 85$ GHz) and does not require a long-lived excited state.

The results presented in this chapter were obtained on a sample, JT6 (see Fig. 6.2), whose parameters are listed in Table 4.1.

PARAMETER	SAMPLE JT6
Filtering capacitor C	20 pF
Inductor L	0.89 nH *
Coupling capacitor Σ	30 pF
JJS critical current I_{J0}	48 nA
SQUID JJ critical current I_{L0}	1.06 µA
Junctions total capacitance C_t	280 fF *
SQUID JJ equivalent inductance $L_0 = \frac{\varphi_0}{I_{L0}}$	311 pH
Loop inductance L_l	20 pH
JJS bias resistor R_b	200 Ω
Atomic-SQUID bias resistor r_b	2 kΩ
Plasma frequency $\nu_p \simeq \frac{1}{2\pi}\sqrt{\left(\frac{2}{L} + \frac{1}{L_0}\right)\frac{1}{C_t}}$ (contact open)	22.1 GHz

Table 6.1: Parameters of Sample JT6 presented in this chapter. Stars (*) indicate values inferred from fits of the spectra (see Section 7.2.2).

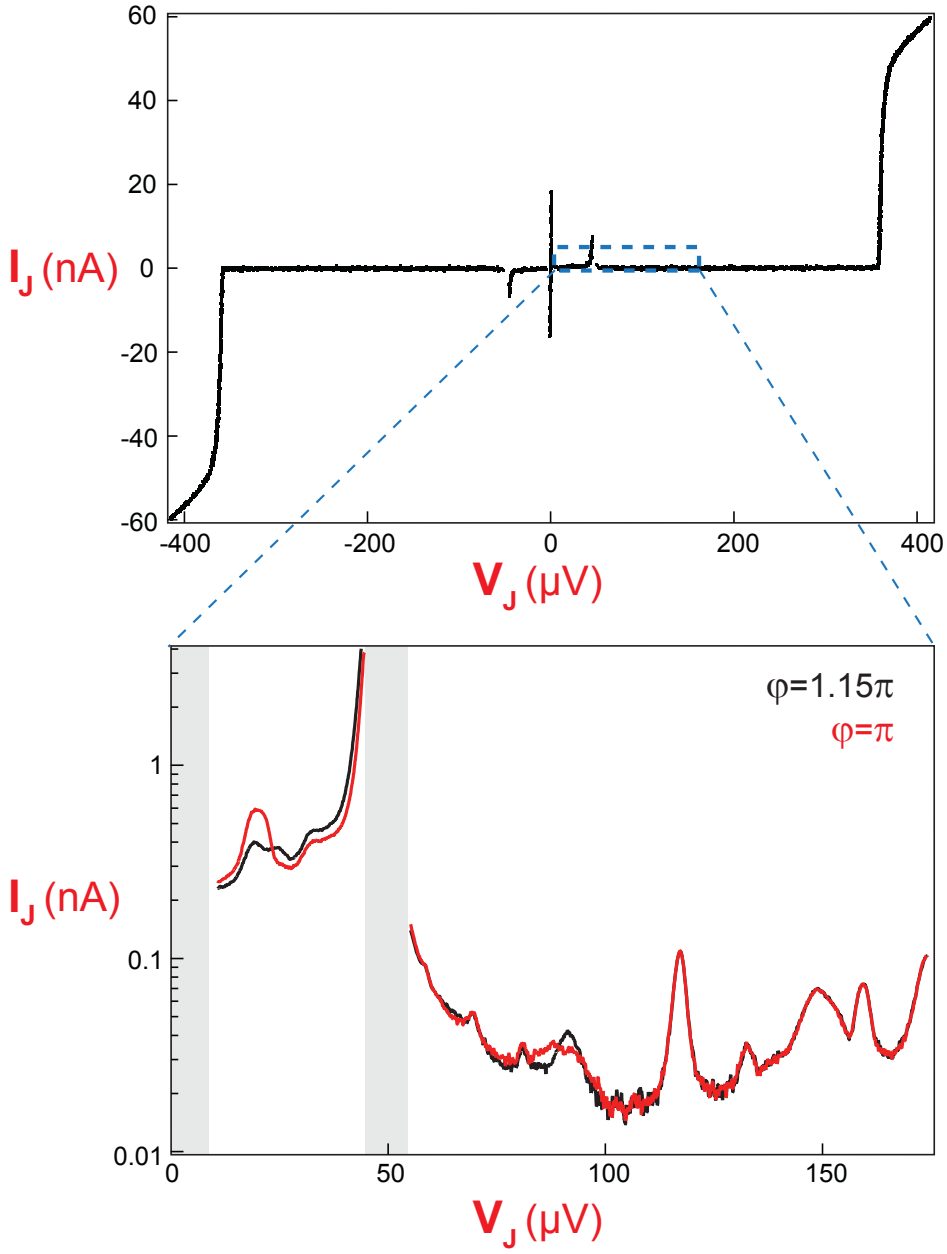

Figure 6.4: Current-voltage $I_J(V_J)$ characteristic of the JJS, for contact V $\{0.985, 0.37, ..\}$, at different magnifications. **Top**: at large scale and at flux $\varphi = 0$. In the subgap region, a large peak is visible near 45 μV. **Bottom**: at higher magnification (log current scale) and for two different flux values $\varphi = 1.15\,\pi$ (black line) and $\varphi = \pi$ (red line). The gray regions are unstable and thus not accessible to measurement. In addition to the large peak, several smaller peaks are observed.

6.2 Experimental results

We now present spectroscopy measurements $I_J(\varphi, V_J)$, for different atomic contacts.

6.2.1 *Current-voltage characteristic of the Josephson junction spectrometer*

Fig. 6.4 shows the current-voltage $I_J(V_J)$ characteristic of the JJS at two values of the flux, for a particular contact, measured at 30 mK. The fit of the IV curve at $eV > 2\Delta$ and the Ambegaokar-Baratoff formula [68] yield the critical current of the JJS: $I_{J0} \simeq 48$ nA. At large scale (see top panel of Fig. 6.4), one essentially sees a single sub-gap peak near 45 µV. Several smaller peaks are observed in the blow-up shown in the bottom panel of Fig. 6.4. The position of some of the peaks changes with flux φ indicating that they correspond to modes associated with the SQUID.

Two sections of the IV curve are not accessible to measurement (gray regions in the bottom panel of Fig. 6.4):

- around 50 µV, the local differential conductance exceeds the slope $-R_b^{-1}$ of the load-line [112];
- near zero voltage, the junction retraps onto the supercurrent branch.

These instability regions are responsible for the hysteretic behavior of the IV curve of the junction. In practice, the junction is set to final voltage by applying a bias larger than the critical current; then the $I_J(V_J)$ characteristic is recorded while decreasing V_J.

6.2.2 *Spectrum construction*

The top panel of Fig. 6.5 shows the $I_J(V_J)$ characteristic for two different flux values, with flux-independent background subtracted (see Section G.4. The bottom panel of Fig. 6.5 shows the current I_J through the JJS as a function of both the flux φ and the voltage V_J across the JJS.

6.2.3 *Comparison of contacts*

Fig. 6.6 displays the spectra $I_J(\varphi, V_J)$ for two different atomic contacts, U and V. The most remarkable features are the V-shaped resonances which fan out from $\varphi = \pi$ toward higher energies. These resonances, which depend strongly on flux and are very different on U and V, are the Andreev resonances. To confirm this, we superpose on each spectrum plots (dashed lines in the right-half of each panel) of the expected Andreev transition energies $2eV_J = 2E_A(\varphi, \tau_i)$, calculated using Eq. 1.1 with the known sets of transmissions $\{\tau_i\}$. The transmissions were independently measured from the IVs of the SQUID: contact U $\{0.942, 0.26, ...\}$ and contact V $\{0.985, 0.37, ...\}$[3]. Andreev resonances corresponding to the most-transmitting

3 In addition to the two most-transmitted channels, both contact U and V are made of 4 other channels of mean transmission 0.08 for U and 0.12 for V (see Section G.2 for the determination of the transmissions).

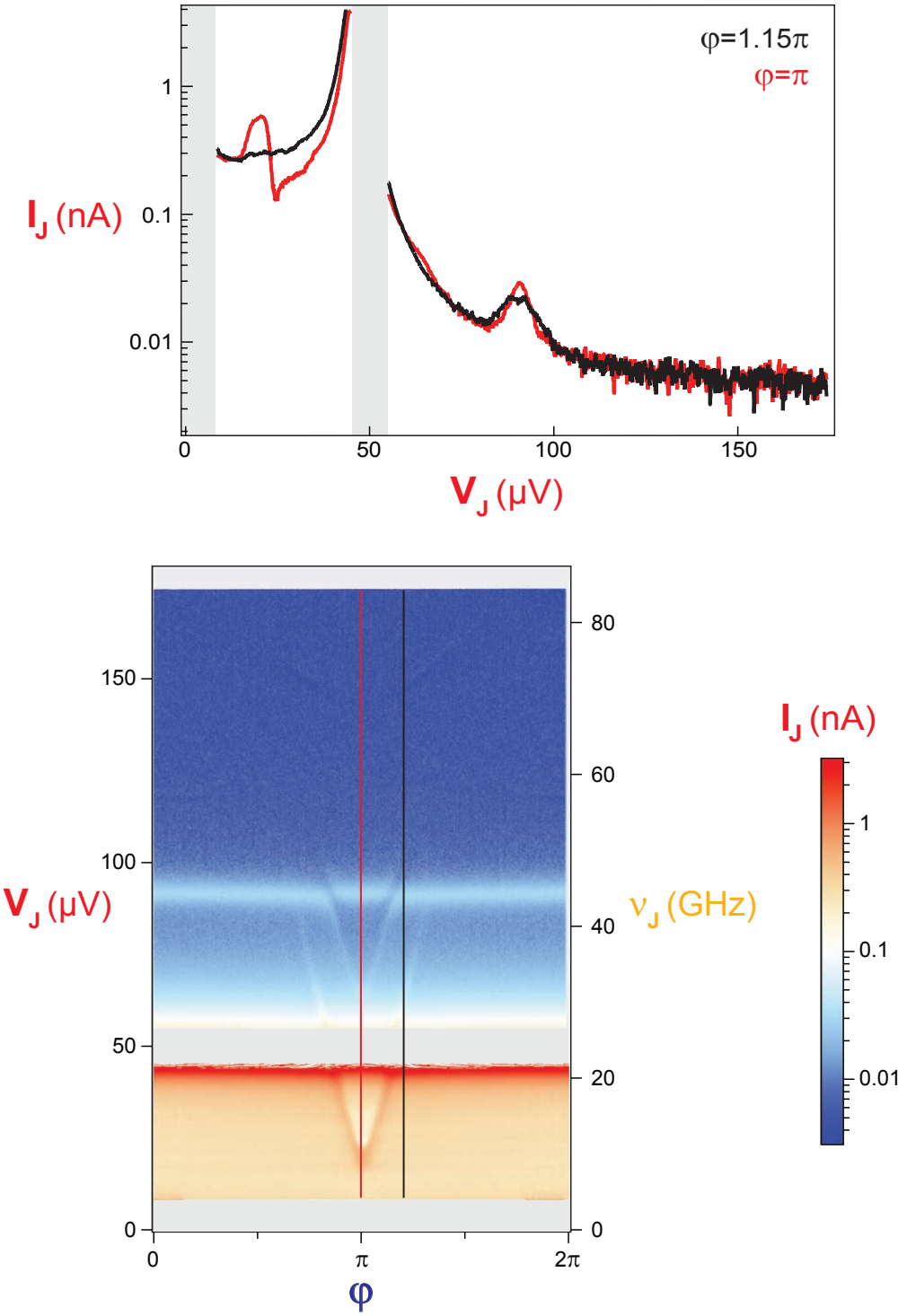

Figure 6.5: **Top**: Current-voltage $I_J(V_J)$ characteristic of the JJS for contact V, for fluxes $\varphi = 1.15\,\pi$ (black line) and $\varphi = \pi$ (red line). A flux-independent background has been subtracted (see Section G.4). **Bottom**: Current I_J as a function of both the flux φ and the voltage V_J. The right axis gives the corresponding Josephson frequencies ν_J. The gray regions near 0 and 50 μV are not accessible to measurement, as discussed in Section 6.2.1.

channel are visible and well reproduced by theory, but they become increasingly faint at high energy and when φ is far from π. The resonances corresponding to the second channels are barely visible.

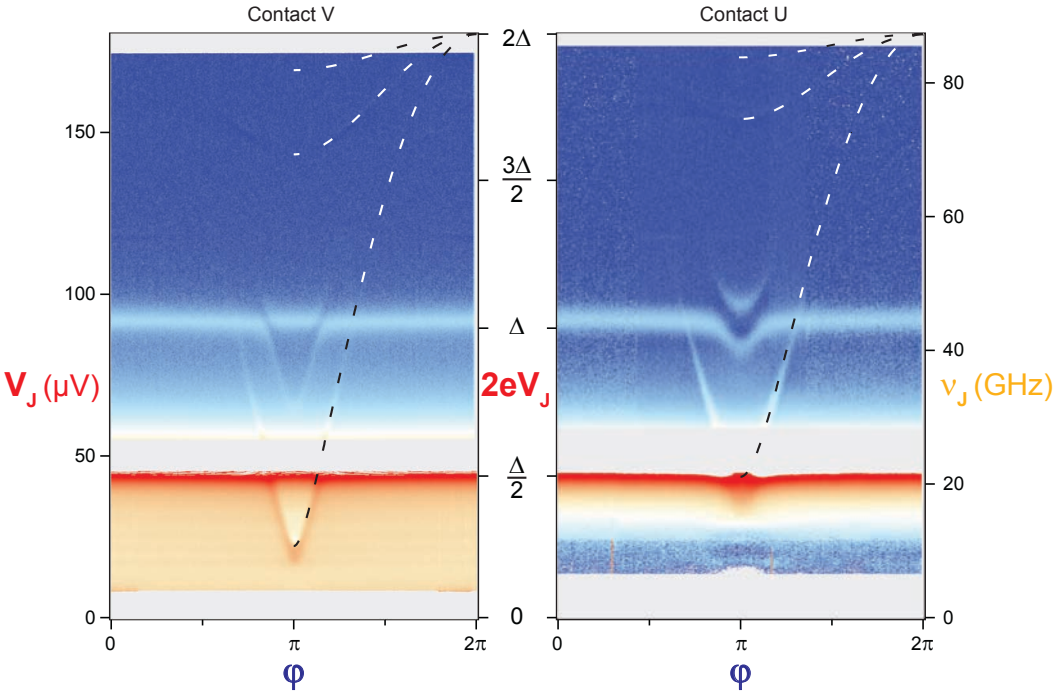

Figure 6.6: Spectra $I_J(\varphi, V_J)$ for contact V $\{0.985, 0.37, ...\}$ (**left**) and contact U $\{0.942, 0.26, ...\}$ (**right**). The color scale is the same as for Fig. 6.5. The dashed lines are the theoretical positions of the Andreev resonances according to the simple modeling $2eV_J = 2E_A(\varphi, \tau_i)$.

In addition to the Andreev transitions, there is a much brighter spectroscopic line ($\sim$ 4 nA, color scale red) common to the two contacts which is located at $2eV_J \simeq 0.5\Delta$ (22 GHz) and hardly varies with flux. This line corresponds to the large peak at $V_J \simeq 45\,\mu V$ in Fig. 6.4 and Fig. 6.5. Only the low energy half of this resonance is accessed because of the too-large negative differential conductance on the high-energy side, as discussed in Section 6.2.1. We identify this resonance as excitation of the plasma mode of the SQUID, at frequency ν_p, the plasma frequency. The bare plasma frequency is the resonant frequency of the oscillator formed by the Josephson inductance of the SQUID L_{SQ} and the parallel capacitance $C_t \simeq$ 280 fF (sum of the SQUID and spectrometer capacitances). It is renormalized by the environment inductance L and is given by

$$\nu_p(\varphi) = \frac{1}{2\pi}\sqrt{\left(\frac{2}{L} + \frac{1}{L_{SQ}(\varphi)}\right)\frac{1}{C_t}}. \tag{6.4}$$

Its flux dependence is inherited from $L_{SQ}(\varphi)$, the inductance of the parallel combination of the atomic contact and the Josephson junction. Since the atomic-SQUID is in general very asymmetric, the inductance is dominated by the JJ inductance

$L_0 = \frac{\varphi_0}{I_0} \simeq 0.3$ nH, and ν_p only slightly modulates in flux. In first approximation, the plasma frequency is given by

$$\nu_p^0 \simeq \frac{1}{2\pi\sqrt{L_{eff}C_t}} \tag{6.5}$$

with

$$L_{eff}^{-1} = 2L^{-1} + L_0^{-1}. \tag{6.6}$$

The energy $2eV_J = h\nu_p^0$ associated with the plasma frequency is plotted as a blue dashed-line in Fig. 6.7 and concurs with the experimental data. The Andreev lines cross the plasma resonance and become fainter at higher energies. This abrupt decrease in spectrometer signal can be understood as the shunting of emitted microwaves by the capacitance C_t.

In the spectra shown in Fig. 6.6, there are some additional lines above the plasma resonance and of smaller amplitude ($\sim$ 100 pA). These lines appear to be replicas of Andreev and plasma transitions shifted up in frequency by ν_p^0, at energies $2eV_J = \nu_p + 2E_A(\varphi, \tau_1)$ and $2eV_J = 2\nu_p^0$ (purple and cyan dotted lines in Fig. 6.7). One also observes anti-crossings between some of the spectroscopy lines. These observations and the resonance amplitudes are accounted for by the following model.

6.3 Comparison with quantum model

6.3.1 *Andreev spin and plasma boson*

We sketch here a quantum model to calculate the spectra, and compare experiment and theory; details are given in Chapter 7.

In this model, tunneling of Cooper pairs through the JJS is treated as a perturbation. The current is obtained by a Fermi golden rule using eigenstates and eigenenergies of the JJS environment alone. The environment of the JJS, which is restricted to the atomic-SQUID, has two types of degrees of freedom:

- the Andreev modes (one per channel), which are fermionic spin-like degrees of freedom, with energies $2E_A(\varphi, \tau_i)$;
- the plasma mode, which is a bosonic degree of freedom, with energy $h\nu_p$.

They share the phase γ and are coupled through a spin-boson Hamiltonian, derived in Chapter 7. One labels the bare states by $|\{\sigma_i\}, n\rangle$, where $\sigma_i = \pm$ accounts for the Andreev spin[4] of the channel i and $n \in \mathbb{N}$ is the plasmon number. In the left side of Fig. 6.7, we show the uncoupled energy spectrum for the combined system, in the case of a single channel. Associated to each Andreev state there is a ladder of plasmon excitations.

The JJS shines microwaves on its environment and may induce transitions from the ground state $|-, 0\rangle$ to any excited state. The one-photon processes drive either the plasma mode $2eV_J = h\nu_p$ (blue dashed arrow in Fig. 6.7) or the Andreev one

4 We assume parity conservation and neglect quasiparticle poisoning. Thus, one only considers the even states $|-\rangle$ and $|+\rangle$.

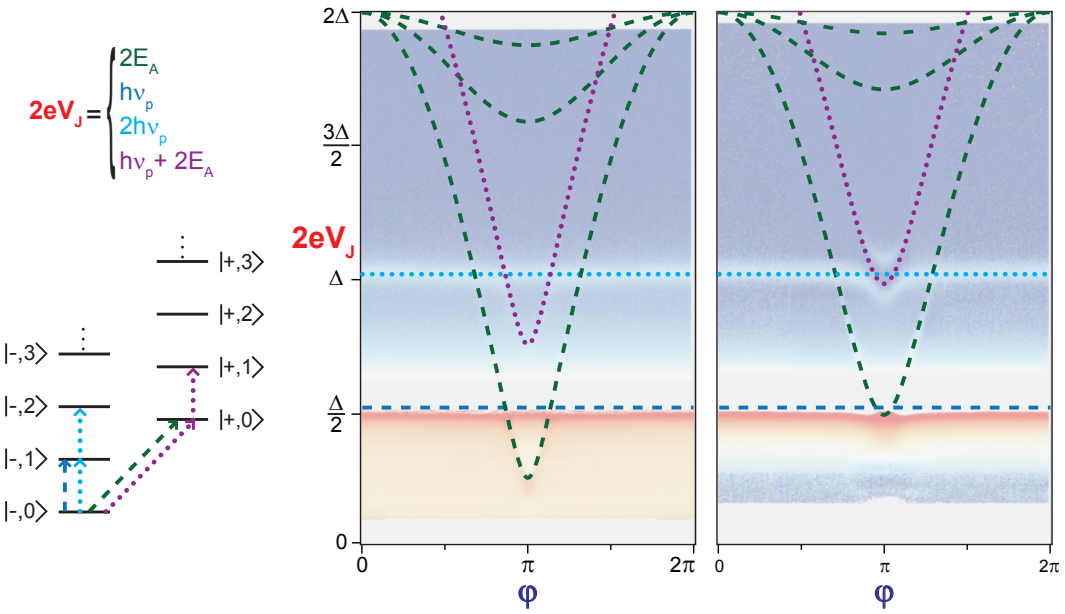

Figure 6.7: **Left**: Uncoupled energy spectrum schematics: each state is labeled $|-,n\rangle$ or $|+,n\rangle$ for Andreev spin in the ground ($|-\rangle$) or excited ($|+\rangle$) state and n photons in the plasma mode. Starting from the ground state $|-,0\rangle$, single photon processes can excite the plasma mode $|-,1\rangle$ (blue dashed arrow) or the Andreev transition $|+,0\rangle$ (green dashed arrow), or two-photon processes can doubly excite the plasma mode $|-,2\rangle$ (cyan dotted arrow) or excite both the Andreev transition and the plasma mode $|+,1\rangle$ (purple dotted arrow). **Right**: Theoretical bare transition energies as a function of the flux φ for contact V (central panel) and U (right panel). The green dashed lines are the Andreev resonances $2E_A$. The blue dashed lines are the plasma resonance of the JJ alone $h\nu_p$. The dotted lines are the two-photon processes $2h\nu_p$ (cyan) and $2E_A + h\nu_p$ (purple). The measured spectra of Fig. 6.6 are used as semi-transparent backgrounds.

$2eV_J = 2E_A$ (green dashed arrow); they correspond to the simultaneous tunneling of one Cooper pair and absorption of one photon. There can also be two-photon transitions $2eV_J = 2h\nu_p$ (cyan dotted arrow) and $2eV_J = 2E_A + h\nu_p$ (purple dotted arrow), which correspond to the tunneling of one Cooper pair and absorption of two photons. As will be discussed in Chapter 7, these harmonic processes arise from the non-linearity of the JJS. The corresponding bare transition energies are plotted as a function of the flux φ in Fig. 6.7 for contact V and U. They are overlaid on the spectra and agree with the data everywhere except where the two-types of two-photon transitions intersect, near $\varphi = \pi$ and $2eV_J = \Delta$.

Here, at degeneracy $2E_A = h\nu_p$, the plasmon and Andreev states hybridize and there is an avoided crossing (left side of Fig. 6.8). The hybridization is especially strong for contact U, where at flux π the expected undressed excitations $2eV_J = 2E_A + h\nu_p$ and $2eV_J = 2h\nu_p$ almost intersect (right panel of Fig. 6.7, crossing of dotted cyan and purple lines), but the data shows a level repulsion of 0.14Δ[5]. One computes the eigenstates and eigenenergies analytically by approximation (Jaynes-

5 This corresponds to a large effective coupling constant $\Omega_{x,1} = 0.14\Delta/\sqrt{2} \simeq 0.1\Delta$ (4.3 GHz), which is a significant fraction of the transition frequency: $\Omega_{x,1}/2h\nu_p \simeq 10\,\%$. This is close to enter the "ultrastrong-coupling regime" [113, 114, 115] but no significant deviations from the Jaynes–Cummings physics was observed.

Cummings approximation, perturbation theory) or numerically (see Chapter 7). The calculated transition frequencies are shown in Fig. 6.8, for contact V and U and one predicts anti-crossings.

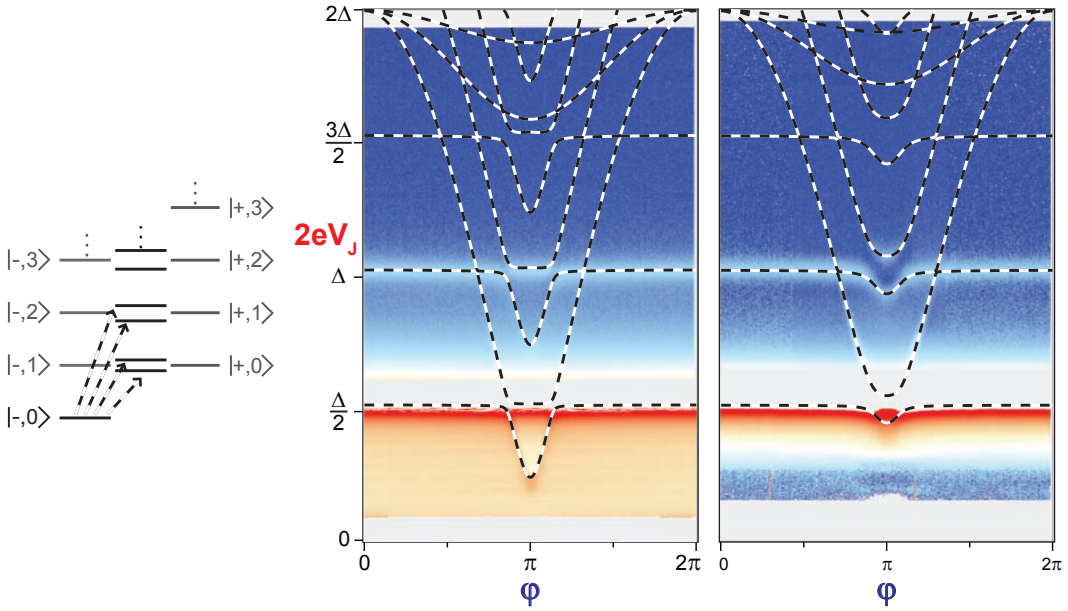

Figure 6.8: **Left**: Energy spectrum schematics: at degeneracy $2E_A(\varphi, \tau_i) = h\nu_p$, the plasma and Andreev transitions hybridize. **Right:** The black and white solid lines are the transition energies as a function of the flux φ for contact V (central panel) and U (right panel), when the coupling of the plasma mode and the Andreev spin are taken into account. They are obtained by numerical diagonalization of a 56×56 matrix Hamiltonian. The measured spectra Fig. 6.6 are used as backgrounds.

6.3.2 *Calculation of the spectra* $I_J(\varphi, V_J)$

Once the eigenstates and eigenenergies are known, the Cooper pair current current through the JJS is obtained using Fermi's golden rule (see Eq. 7.21). This model, which ignores the dissipative part of the environment of the SQUID, predicts infinitely sharp transitions. We have arbitrarily given them a Lorentzian shape with a quality factor of 13, which corresponds to that of the plasma peak.

The calculated $I_J(V_J, \delta)$ spectra are shown as color plots in the right-most panels of Fig. 6.9, for contacts V and U. The model describes both the Andreev resonances ($|-,0\rangle \to |+,0\rangle$, of energy $2E_A$) and the plasma resonance ($|-,0\rangle \to |-,1\rangle$, of energy $h\nu_p$). It also describes the higher harmonic transitions: $|-,0\rangle \to |+,1\rangle$, of energy $2E_A + h\nu_p$ and $|-,0\rangle \to |-,2\rangle$, of energy $2h\nu_p$. These harmonics processes are less probable which results in fainter transitions as seen in both experiment and calculation. The theory also predicts the anti-crossings arising from the coupling between the Andreev-spin and the plasma-boson.

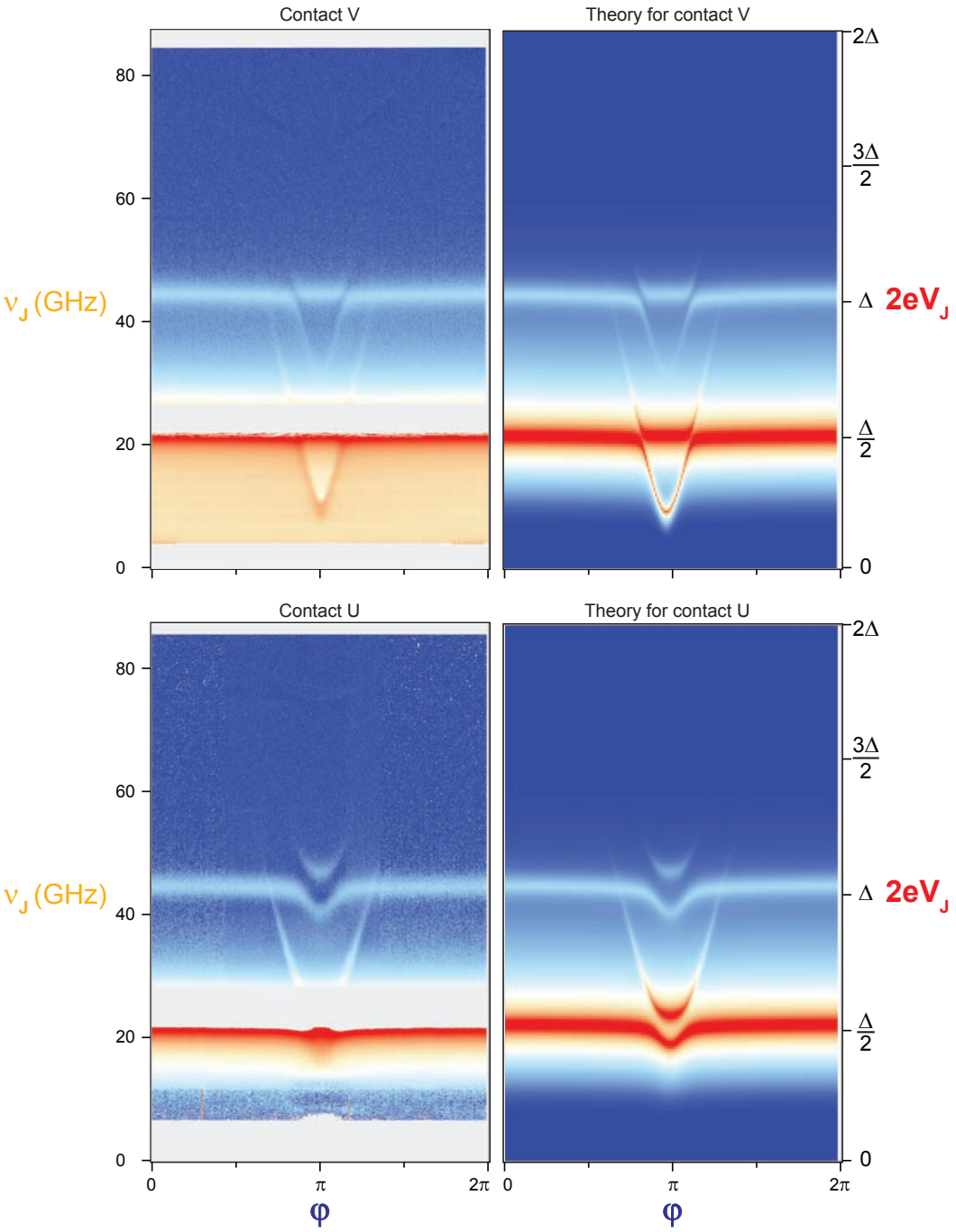

Figure 6.9: Comparison between experimental (**left**) and calculated (**right**) spectra $I_J(\varphi, V_J)$ for contact V (**top**) and U (**bottom**). The color scale is the same as for Fig. 6.5. The calculated spectra were obtained using the quantum model detailed in Chapter 7. The calculated currents have been multiplied by 0.56 to match the measured ones.

6.3.3 *Amplitude of the resonances*

The global weakening of the signal at high V_J is well captured by the model. However, the agreement for the amplitude and width of the different peaks is not quantitative, as shown in Fig. 6.10. There is a factor ~ 0.56 in amplitude between theory and experiment which is not understood. This may be related to the fact that we have neglected in our quantum model the external impedance made of the on-chip inductors and capacitors, and the circuit outside the chip. A rigorous treatment of dissipation is needed.

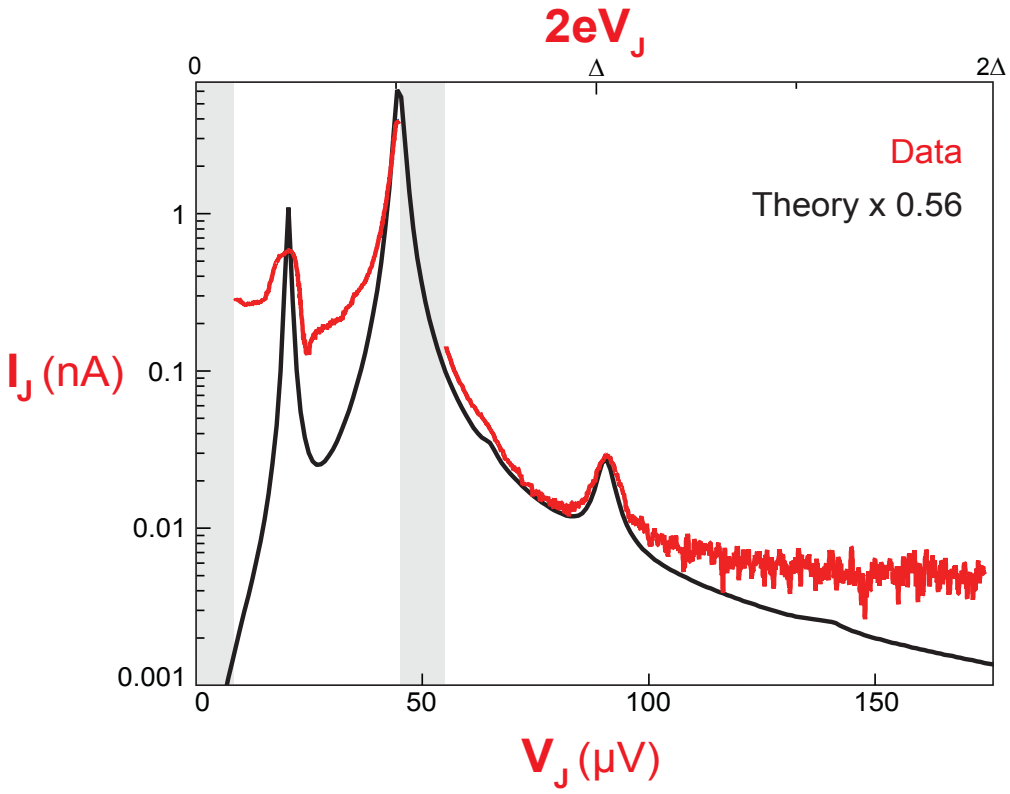

Figure 6.10: Comparison between measured (red) and calculated (black) $I_J(V_J)$ at $\varphi = \pi$, for contact V. The theoretical curve is multiplied by 0.56 to match the measured one.

6.3.4 *Absorption and relaxation rates*

From the amplitude I_J of a resonance, one extracts a lower bound to the absorption rate

$$\Gamma_{min} = \frac{I_J}{2e}. \tag{6.7}$$

From the width δV_J, one extracts an upper bound to the relaxation rate

$$\gamma_{max} = \frac{2e\delta V_J}{h}. \tag{6.8}$$

For the Andreev resonance around 25 μV in Fig. 6.10, one obtains $\Gamma_{min} \simeq 1$ GHz and $\gamma_{max} \simeq 2$ GHz to give orders of magnitude. The fine analysis of the spectra remains to be done to extract the phase dependence of the rates.

6.4 Additional measurements

6.4.1 *Big contact*

Fig. 6.11 shows the spectrum $I_J(\varphi, V_J)$ for contact Y, which is made of a large number of channels. Its transmissions could not be accurately extracted from the IV characteristic of the SQUID, but one can estimate from the MAR current about ~ 25 channels. In Fig. 6.11, the plasma frequency modulates with flux on a wider range ($0.1\Delta = h \times 4$ GHz) than for contacts U and V and one can resolve a large number of Andreev transitions for φ close to π[6]. Such a spectrum is however too complicated to be quantitatively described by our model.

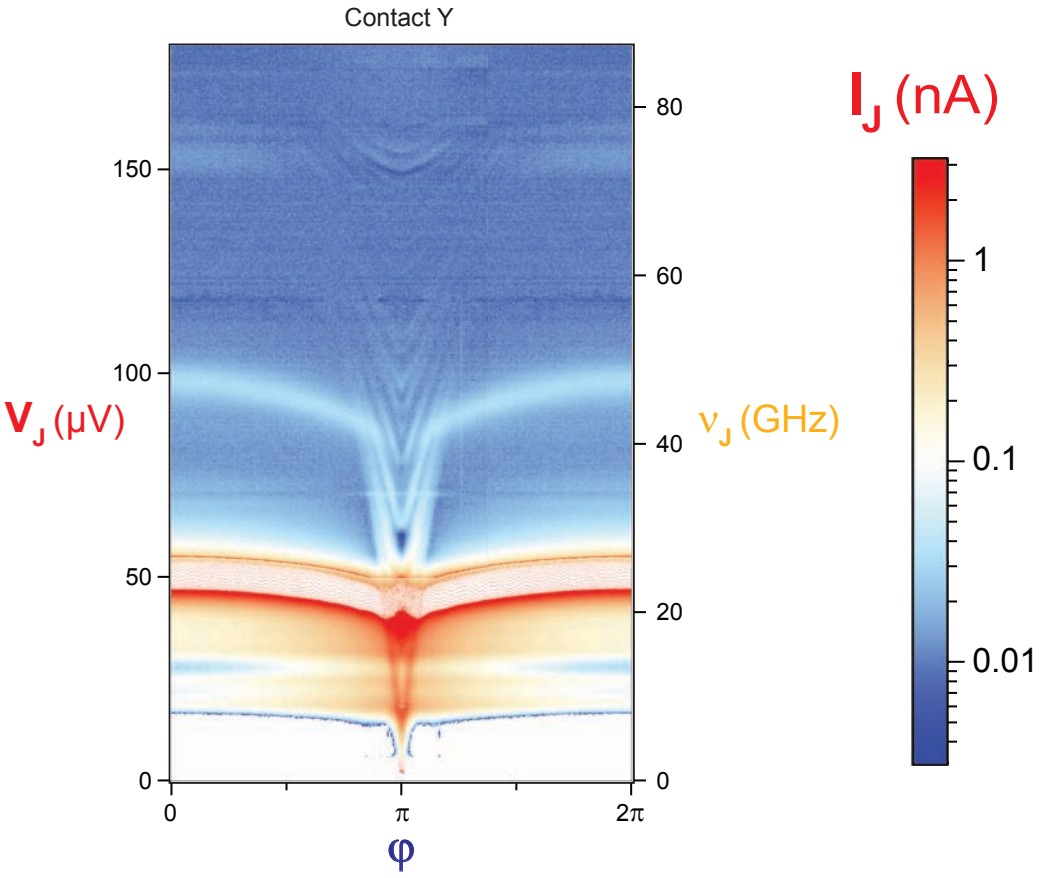

Figure 6.11: Spectrum $I_J(\varphi, V_J)$ for contact Y, made of a large number of channels. The region $[1.38\,\pi, 2\pi] \times [52\,\mu V, 180\,\mu V]$ has not been measured and is just obtained by symmetrization around π of the left region.

6 The atomic contact being no longer small compared to the JJ of the SQUID, the phase drop across the JJ γ can no longer be neglected in the relation $\delta - \gamma = \varphi$. Therefore, the reduced flux φ and the phase δ across the atomic contact are no longer equal. As a consequence, δ varies rapidly with φ when $\varphi \simeq \pi$.

6.4.2 *Library of spectra*

The spectra of a several other contacts have been measured with a slightly different protocol. Instead of measuring $I_J(V_J)$ curves for each value of φ, we have measured $I_J(\varphi)$ curves for each value of V_J. Moreover each curve was measured with coupling so that $\langle \delta I_J \rangle = 0$ over a period. With this technique, phase-independent resonances are not seen, but the absolute value of the dc current through the JJS is lost.

Fig. 6.12 and Fig. 6.13 show the corresponding $\delta I_J(\varphi, V_J)$ spectra for different atomic contacts[7].

Data taken for small contacts are well reproduced by theory, as shown in Fig. 6.14 and Fig. 6.15 for contacts K, L N and D[8]. The theory for the other contacts are shown in Section G.5. Most of the features have already been discussed for contacts V and U.

7 The ac coupling yields a zero time-averaged current at each value of V_J. In the spectra, we have furthermore subtracted the flux-averaged current on one period.

8 In the theoretical spectrum for contact D, only the three most-transmitted channels have been taken into account.

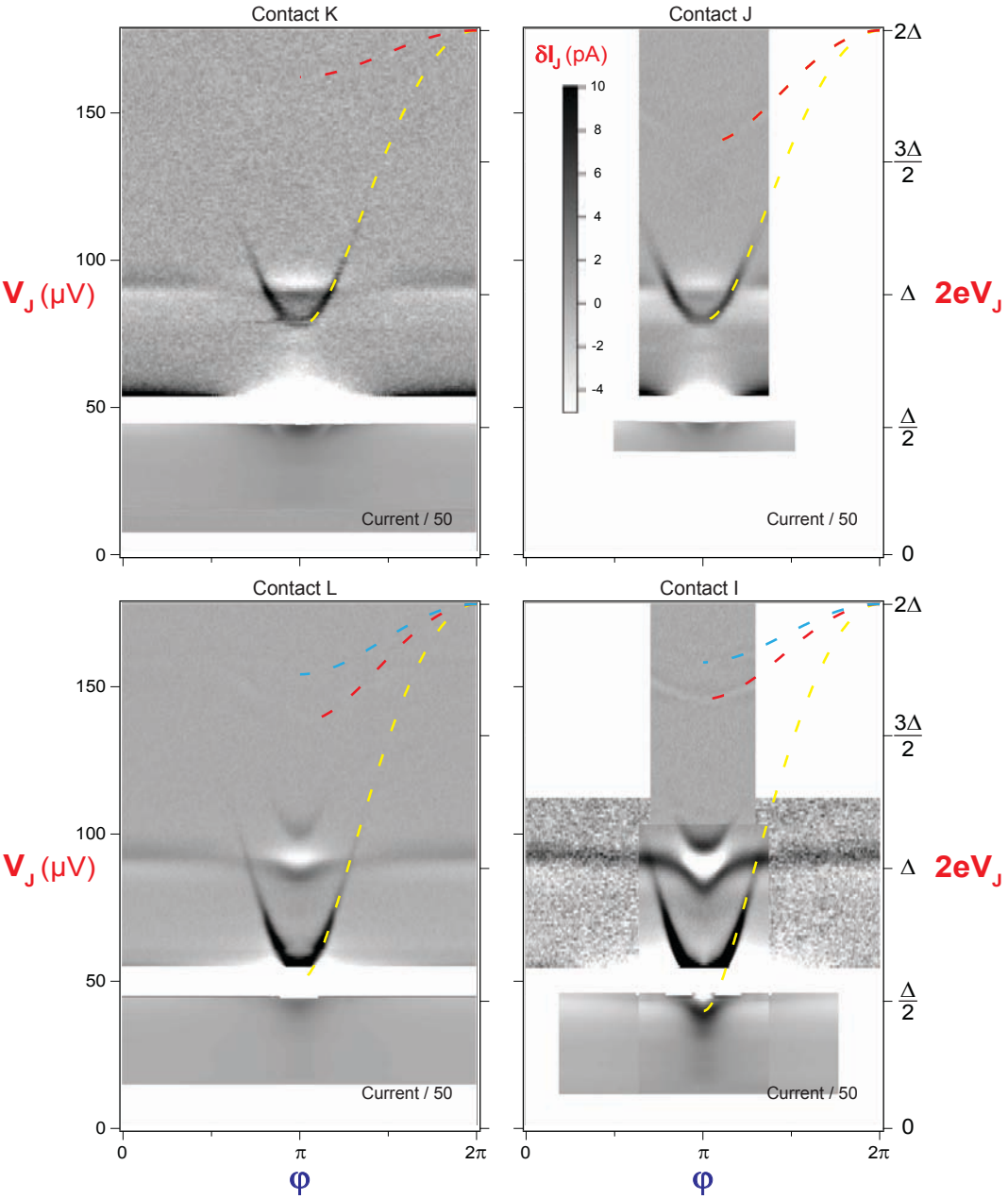

Figure 6.12: Spectra $\delta I_J(\varphi, V_J)$ for different atomic contacts: contact K ($\{0.81, 0.17\}$), J ($\{0.8, 0.385, 0.385\}$), L ($\{0.92, 0.4, 0.25\}$) and I ($\{0.95, 0.33, 0.21\}$). The currents below the plasma resonance have been divided by 50. The (linear) current gray scale is the same for the four spectra. The dashed lines are the theoretical Andreev resonances according to the simple modeling $2eV_J = 2E_A(\varphi, \tau_i)$.

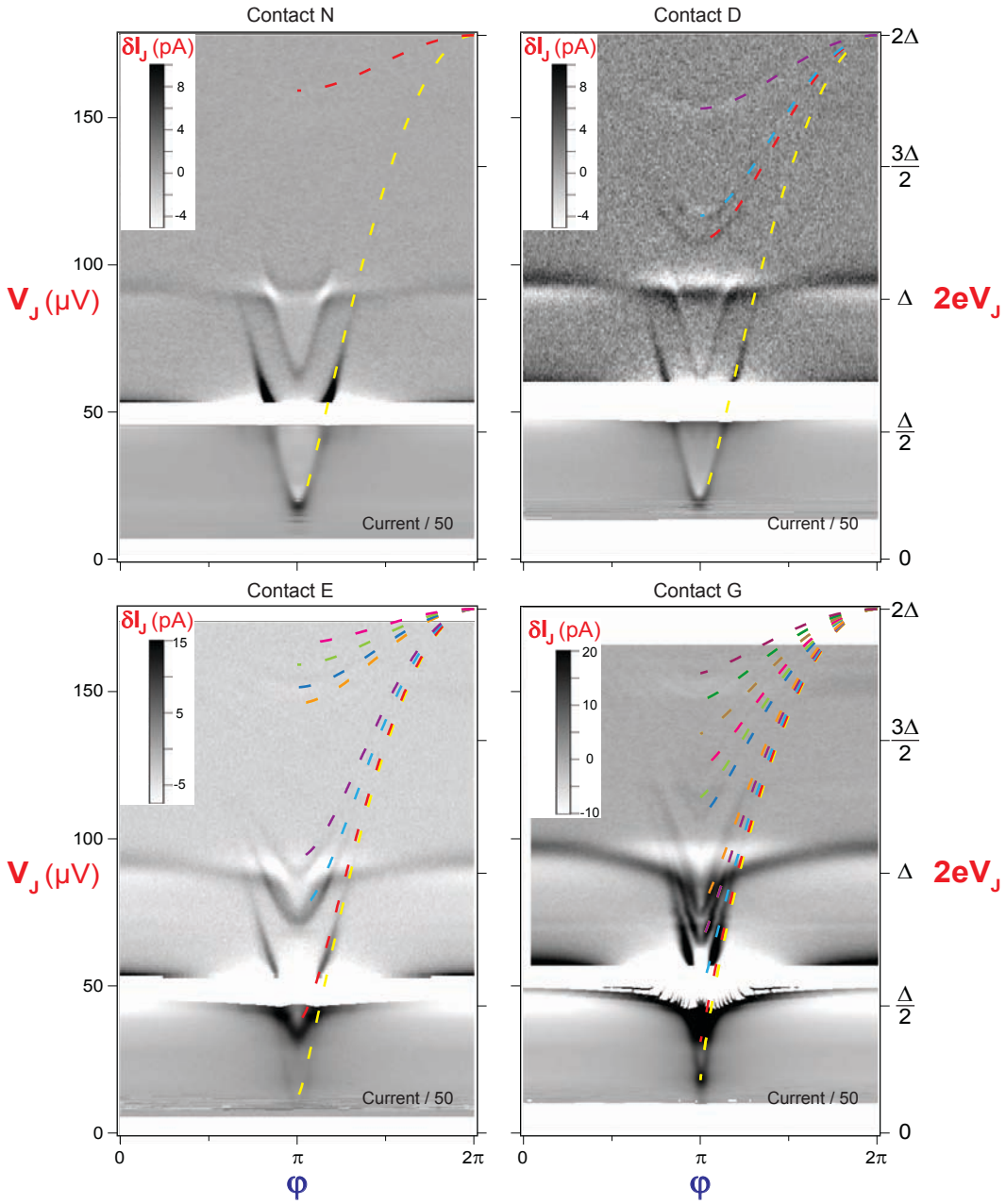

Figure 6.13: Spectra $\delta I_J(\varphi, V_J)$ for different atomic contacts: contact N ($\{0.99, 0.2\}$), D ($\{0.987, 0.63, 0.57, 0.26\}$), E (big) and G (big). The currents below the plasma resonance have been divided by 50. The dashed lines are the theoretical Andreev resonances according to the simple modeling $2eV_J = 2E_A(\varphi, \tau_i)$. For contact E and G, we also show a tentative fit of the positions of the Andreev transitions with transmissions $\{0.995, 0.955, 0.82, 0.725, 0.328, 0.328, 0.276, 0.201, 0.127\}$ for E and $\{0.99, 0.99, 0.97, 0.93, 0.87, 0.87, 0.82, 0.64, 0.59, 0.52, 0.52, 0.42, 0.42, 0.32, 0.32, 0.23\}$ for G, which are compatible with the MAR currents.

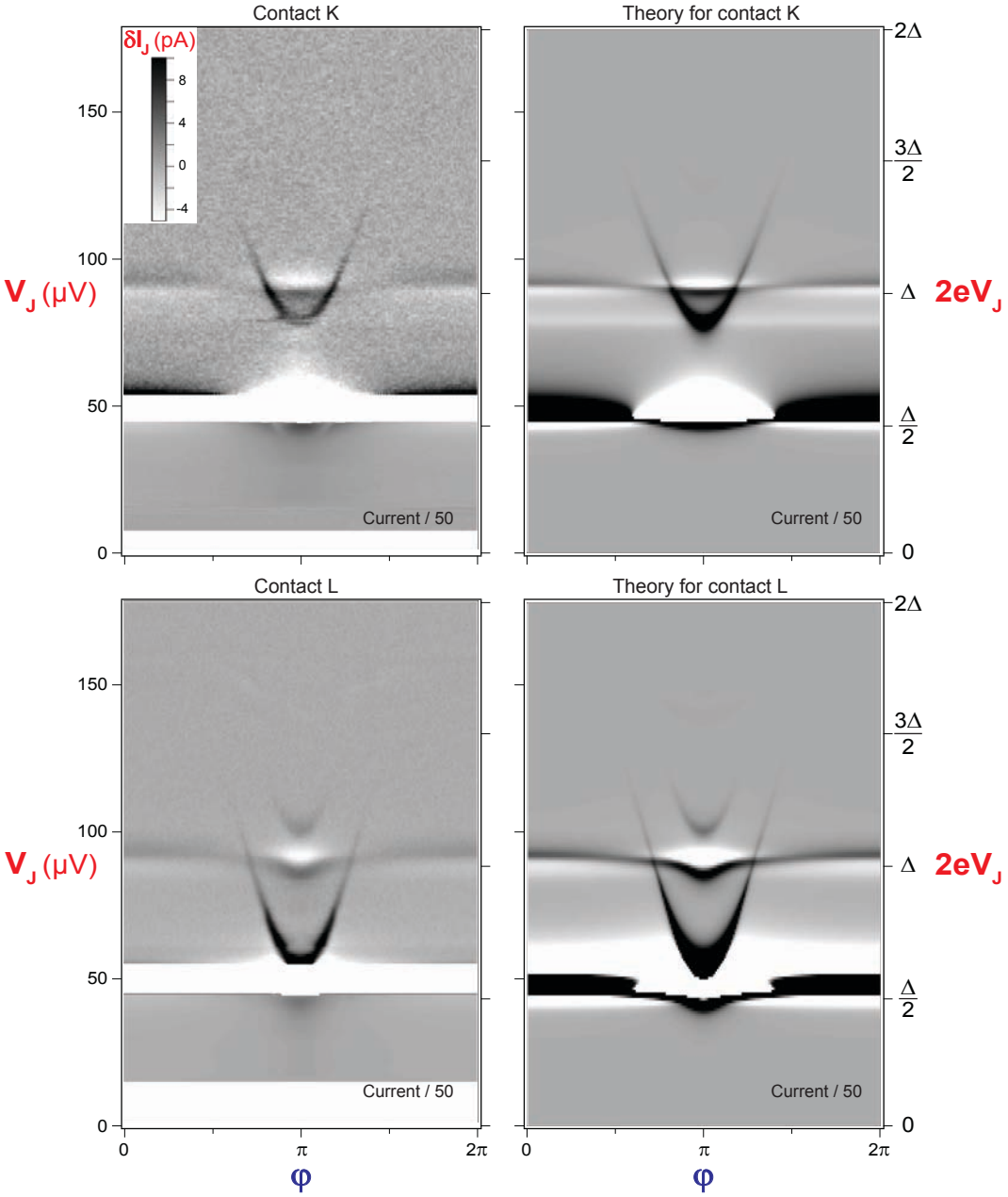

Figure 6.14: Comparison between experimental (**left**) and calculated (**right**) spectra $\delta I_J(\varphi, V_J)$ for contact K (**top**) and L (**bottom**). The currents below the plasma resonance have been divided by 50 (in theory plots, currents for $2eV_J < \Delta/2$). The calculated spectra were obtained using the quantum model detailed in Chapter 7. The current gray scale is the same for the four spectra. The calculated currents have been multiplied by 0.56 to match the measured ones.

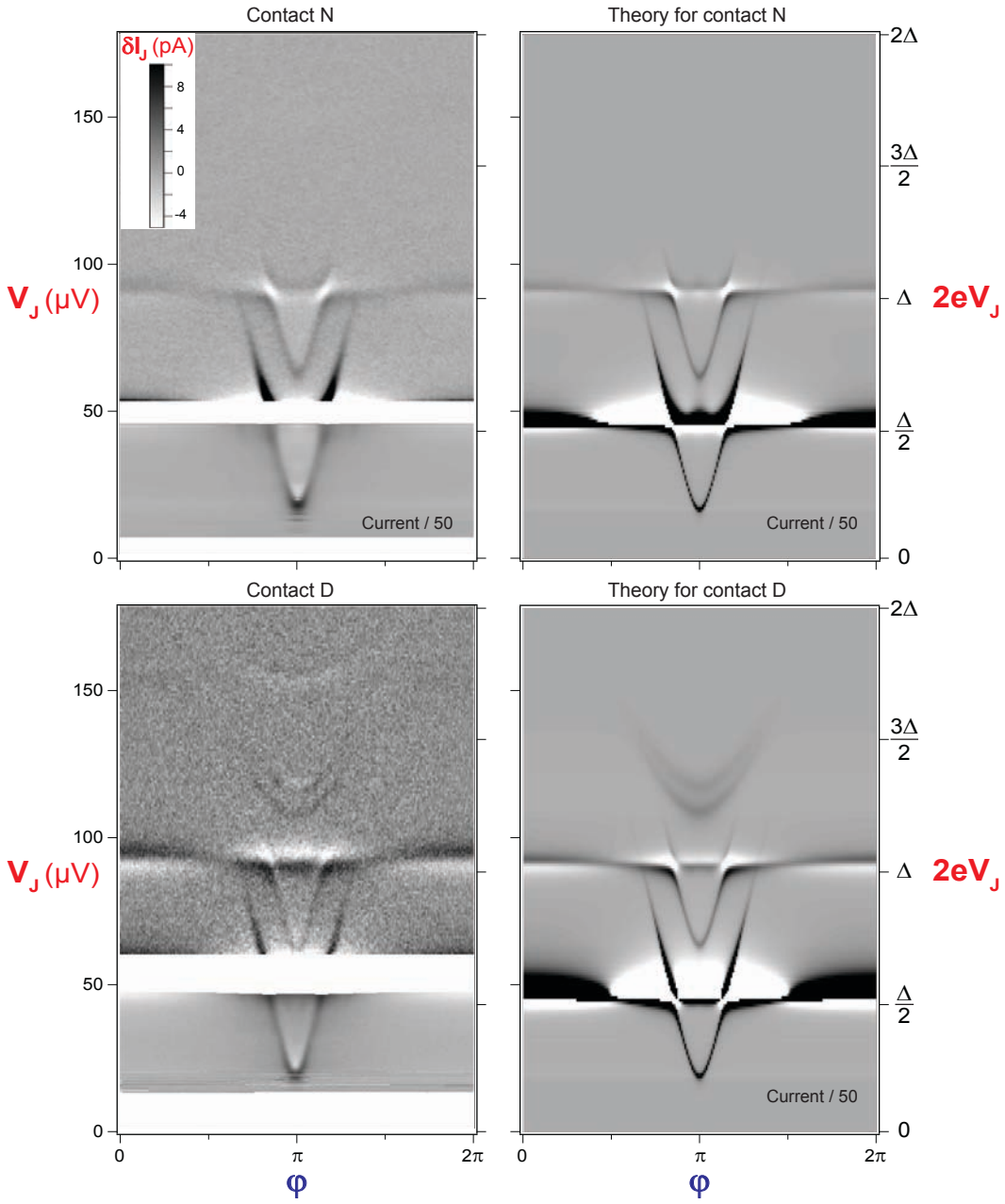

Figure 6.15: Comparison between experimental (**left**) and calculated (**right**) spectra $\delta I_J(\varphi, V_J)$ for contact N (**top**) and D (**bottom**). (following of Fig. 6.14)

6.4.3 *Out-of-equilibrium processes*

In the spectra of contacts K and J, there is an anti-resonance just below the plasma frequency which is not described by the modeling[9]. It might correspond to a transition from $|-,1\rangle$ to $|+,1\rangle$, at frequency $2E_A - h\nu_p$ (see Fig. 6.16). This process requires that the initial state is not the ground state but the excited state $|-,1\rangle$, which is populated by the simultaneous drive of the plasma transition $|-,0\rangle \rightarrow |-,1\rangle$. This would explain why this transition is observed when its frequency is close to the plasma frequency: $2E_A - h\nu_p \sim h\nu_p$.

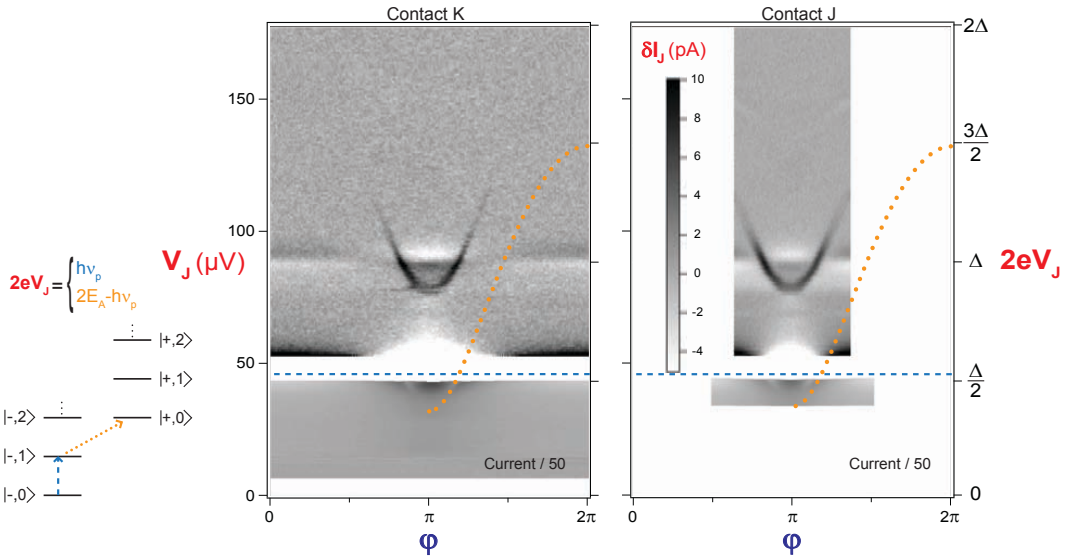

Figure 6.16: **Left**: Uncoupled energy spectrum schematics. When $2eV_J = h\nu_p$, single photon process can excite the plasma transition$|-,0\rangle \rightarrow |-,1\rangle$ (blue dashed arrow). If $|-,1\rangle$ has not yet relaxed, the transition $|-,1\rangle \rightarrow |+,1\rangle$ can subsequently happen (orange dashed arrow). It is possible only when the resonant frequencies of these two transitions are close, $2E_A - h\nu_p \sim h\nu_p$. **Right**: Transition energies $2E_A - h\nu_p$ as a function of the flux φ for contact K (central panel) and J (right panel). The measured spectra of Fig. 6.12 are used as backgrounds.

6.5 Experiment on sample JS6

This spectroscopy experiment was also performed on a similar but different sample, named JS6 (see fabrication details in Section 9.2.5). The main difference was that the critical current of the JJS was larger $I_{J0} \simeq 180\,\text{nA}$, and that of the JJ of the SQUID was smaller $I_{L0} \simeq 400\,\text{nA}$.

Fig. 6.17 displays the spectrum $\frac{dI_J}{d\varphi}(V_J, \varphi)$ for two different atomic contacts. In a voltage window between 65 μV and 130 μV, one can clearly see few transitions that depend strongly on flux and are very different between spectra. These are the Andreev resonances in the different channels of the contacts, whose transition energies $h\nu_J = 2E_A(\varphi, \tau_i)$ are plotted in the right-half of each panel as dashed-lines, using the known sets of transmissions $\{\tau_i\}$ independently measured from

9 It is also barely visible in the spectrum of contact N.

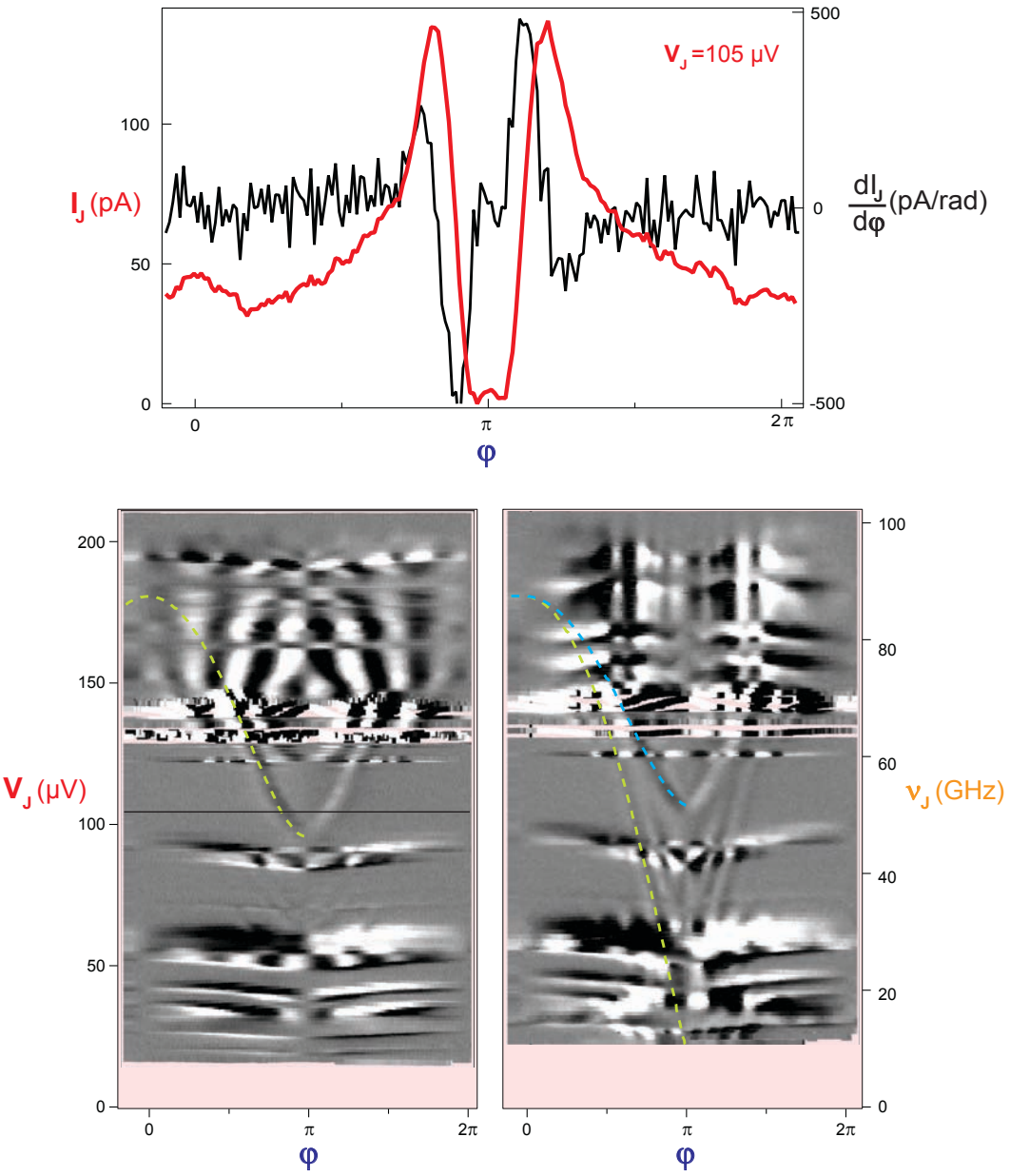

Figure 6.17: **Top**: Flux derivative of the current through the JJS $\frac{dI_J}{d\varphi}(\varphi)$ (black) and integrated current I_J (red) as a function of the flux φ. These data were obtained on sample JS6, for contact with transmissions $\{0.72\}$ and for voltage $V_J = 105$ μV. **Bottom**: Spectra $\frac{dI_J}{d\varphi}(V_J, \varphi)$ on sample JS6 for two different atomic contacts with transmissions $\{0.72\}$ (left) and $\{0.99, 0.66\}$ (right). The dashed lines are the theoretical Andreev resonances with the simple modeling $2E_A(\varphi, \tau_i)$.

the $I(V)$ of the SQUID. Note that, compared to the spectra (see Fig. 6.6) measured on sample JT6, one can detect the Andreev transitions to higher frequency (till 60 GHz).

In addition to the Andreev resonances, there are many other flux dependent resonances, which make the spectra much more complex. We think that because the excitation by the JJS was much stronger it could drive higher order harmonics. This is compatible with the fact that the aspect ratio between the JJS and the JJ of the SQUID was much bigger than in the experiment on sample JT6[10]: $I_{J0}/I_{L0} \sim 0.45$ compared to 0.045. In this strong-drive regime, both multi-Cooper pair and multi-photon processes are possible (see Chapter 7 and Appendix J). In particular, in the low frequency region [10 µV, 95 µV], one can see both harmonics and sub-harmonics of the plasma resonance. Above 130 µV, there are many parasitic resonances that could be related to higher order processes involving both the plasma resonance and the superconductor continuum. This forest of peaks prevent from seeing Andreev resonances above this threshold. This experiment is much more complicated to model since one needs to take into account those higher order processes (see Chapter 7).

6.6 Conclusions and perspectives

Our experiment demonstrates photon-absorption spectroscopy of the ABS spectrum, *i.e.* transitions between the ground state $|-\rangle$ to the excited even state $|+\rangle$. At the microscopic level, these transitions are excitations of a single Cooper pair in a one-atom contact. Not only do we clearly resolve the transitions between the ABS, but we also identify spectroscopic lines arising from hybridization with electromagnetic modes of the circuit in which the contact is embedded, as well as multi-photon processes.

The photon spectrometry of ABS was achieved using a voltage-biased Josephson junction as a spectrometer. This excitation scheme which has already been used in a wide range of situations [44, 45] has many advantages. The source is directly on-chip, its frequency is widely tunable (up to 170 GHz for aluminum) and is controlled by an external dc voltage. One measures a dc response. In contrast, it would not be an easy task to use an external microwave source and fabricate a cryogenic wiring working in this broad frequency range.

In our experiments, the spectroscopy sensitivity at frequencies larger than the plasma frequency is much weaker than below because of the shunting of the ac current by the SQUID JJ capacitor. Improved performances and simpler spectra should be achieved by replacing the JJ of the SQUID by an inductor l. The plasma mode will be determined by l and the JJS capacitor. By choosing $l \sim 10$ pH, and increasing the critical current of the JJS to ~ 1 µA in order to keep a similar coupling, the plasma mode will be repelled above the superconducting gap 2Δ. Since the spectrum suffices to characterize the contacts, we are also planning to remove the connecting wires to the atomic-SQUID. The lifetime of the ABS should then get larger. An experiment along these lines is in preparation.

10 Experiment on sample JS6 was performed first. Sample JT6 was designed with a JJS with much smaller critical current in order to get rid of high order resonances.

7

QUANTUM THEORY FOR THE SPECTROSCOPY OF AN ATOMIC-SQUID BY A JOSEPHSON JUNCTION

In this chapter, we develop a quantum model to describe the experiment presented in Chapter 6. The basic idea is to divide the circuit in two parts: the Josephson junction spectrometer and its environment. The Hamiltonian of the Josephson junction spectrometer is treated as a perturbation. Using Fermi's golden rule, one can derive the Cooper pair current through this junction as a function of the eigenstates and eigenenergies of the environment. Because the Hamiltonian describing the environment is not analytically diagonalizable, one finds its eigenstates and eigenenergies either analytically by approximation (Jaynes-Cummings approximation, perturbation theory) or numerically. This derivation was performed in collaboration with Manuel Houzet.

7.1 Quantum description of electrical dipoles

This section is mainly intended to fix the notations.

7.1.1 *Josephson junction*

The physics of an ideal JJ is ruled by the two Josephson relations:

$$I = I_0 \sin(\gamma) \text{ and } V = \varphi_0 \dot{\gamma} \tag{7.1}$$

withγ the phase difference across the junction and $\varphi_0 = \frac{\hbar}{2e}$ the reduced flux quantum. The junction can be seen as a non-linear inductor of inductance

$$L_J(\varphi) = \frac{\varphi_0}{I_0 \cos(\gamma)}. \tag{7.2}$$

The Hamiltonian (2.59) of an ideal JJ is derived in Section 2.6. A real Josephson junction corresponds to an ideal one in parallel with a capacitor of capacitance C. It is thus an anharmonic oscillator whose quantum dynamics is described by the Hamiltonian

$$H = Q^2/2C - E_L \cos(\gamma), \tag{7.3}$$

with the Josephson energy

$$E_L = \varphi_0 I_0. \tag{7.4}$$

One defines $N = -Q/2e$, the dimensionless charge operator, such as $[N, \gamma] = -i$. Thus

$$H = E_C N^2 - E_L \cos(\gamma) \tag{7.5}$$

with

$$E_C = \frac{2e^2}{C} \tag{7.6}$$

the charging energy for pairs.

When $\gamma \ll 1$, one can perform the Taylor expansion $\cos(\gamma) = 1 - \frac{1}{2}\gamma^2 + O(\gamma^4)$. Retaining only the second order term one can view the junction as a harmonic oscillator (see Section C.1.2),

$$H = \hbar\nu_p(a^\dagger a + \frac{1}{2}). \tag{7.7}$$

This oscillation mode is called the plasma mode and its frequency

$$\boxed{\nu_p = \frac{\sqrt{2E_C E_L}}{\hbar} = \frac{1}{2\pi}\sqrt{\frac{I_0}{\varphi_0 C}}} \tag{7.8}$$

the **plasma frequency**. The eigenstates of this Hamiltonian are "the **plasmon** states" $(a^\dagger)^n |0\rangle$ of eigenenergies $(n + \frac{1}{2})\hbar\nu_p$. The phase and charge operators can be written as a function of the annihilation and creation operators as

$$\boxed{\gamma = \sqrt{z}\left(a + a^\dagger\right) \text{ and } N = i\sqrt{z}(a - a^\dagger)}. \tag{7.9}$$

We have here introduced a dimensionless parameter z as

$$\boxed{z = \frac{\pi Z_p}{R_Q} = \sqrt{\frac{E_C}{2E_L}}} \tag{7.10}$$

where $Z_p = \sqrt{\frac{\varphi_0}{I_0 C}}$ is the junction characteristic impedance and $R_Q = \frac{\hbar}{4e^2} \simeq 6\,k\Omega$ the superconducting resistance quantum. z determines the size of phase and charge fluctuations:

$$\sqrt{\langle 0|\gamma^2|0\rangle} = 2\sqrt{z} \text{ and } \sqrt{\langle 0|N^2|0\rangle} = 1/\sqrt{z}. \tag{7.11}$$

The Taylor expansion used above is therefore justified to describe the states with few excitations[1] as long as $z \ll 1$.

Despite the ideal JJ being the best known Josephson element, there is a more fundamental Josephson element, described hereafter.

7.1.2 *Josephson channel*

The most basic Josephson element is a single conduction channel of arbitrary transmission τ, connecting two superconducting reservoirs, nicknamed JC. The two Josephson relations are in this case $I = I_A(\delta, \tau)$ and $V = \varphi_0\dot{\delta}$, where δ is the superconducting phase difference across the JC and I_A is defined in Eq. 2.49. In addition to the plasma mode describing the dynamics of the phase, there is an **additional spin-like degree of freedom** governed by the Andreev states physics. As described in **Section 2.5**, the Hamiltonian describing this system is $H_A(\delta)$ (Eq. 2.54), the two-level Hamiltonian, with the phase δ considered as a quantum operator. Therefore, it accounts both for the inductive energy of the Josephson element and for the internal energy of the Andreev states.

1 Corrections to harmonicity can be dealt with by considering quartic terms in a, $a^\dagger$.

7.2 Quantum description of the electrical circuit used for spectroscopy

Under a voltage bias V, a Josephson junction spectrometer (JJS) of energy $E_J = \varphi_0 I_{J0}$ radiates microwaves into its electromagnetic environment. The goal is to predict the dc current flowing through the JJS as a function of V, as a result of processes in which a Cooper pair tunnels through the barrier's junction while emitting photons that are absorbed in its environment. This physics is directly related to dynamical Coulomb blockade (dynamical Coulomb blockade (DCB)), in which tunneling of charge through a small tunnel junction is modified by its electromagnetic environment [39, 116, 117, 40]. It was first observed in small normal tunnel junctions [118, 119, 120], for which the presence of an environment reduces the conductance at low bias voltage, hence the name blockade [2]. Oppositely, for a superconducting Josephson junction the presence of an environment allows a dc current of Cooper pairs [41, 46, 47, 48, 49, 42, 43]. In these experiments, the electromagnetic environment is something well defined, like a superconducting resonator or a diffusive resistor, and described as a collection of bosonic modes. In our experiment, this excitation scheme drives a fermionic mode, the Andreev doublet.

7.2.1 *Hamiltonian derivation*

The equivalent electrical circuit was shown in Fig. 6.1. Assuming that the capacitors are essentially shorts at the relevant frequencies and using Thevenin's theorem, the circuit as seen from the spectrometer Josephson junction is represented in Fig. 7.1.

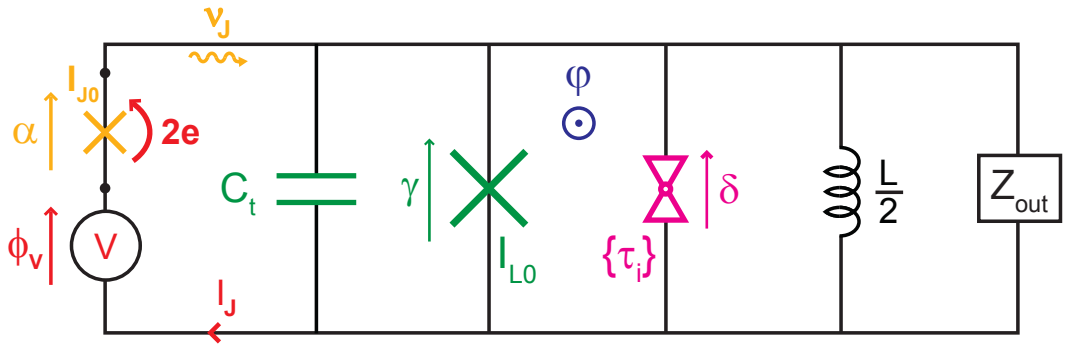

Figure 7.1: Electrical circuit as seen from the Josephson junction spectrometer.

Z_{out} is an electromagnetic impedance accounting for the circuit outside the chip. The total Hamiltonian of the circuit is

$$H = H_J + H_{source} + H_{env}. \tag{7.12}$$

2 This blockade phenomenon also occurs in quantum point contacts with arbitrary transmissions. The physics of strong blockade has been recently explored by embedding a single quantum channel of tunable transmission in an adjustable on-chip circuit of impedance comparable to the resistance quantum [121].

We model the source as a large capacitor $C_V \to \infty$, with an initial charge number $N_{V_i} = \frac{C_V V}{2e}$. Thus, this capacitor is described through the quantum conjugated variables N_V and ϕ_V, with $[N_V, \phi_V] = -i$, and

$$H_{source} = E_{C_V} N_V^2 \tag{7.13}$$

with $E_{C_V} = \frac{2e^2}{C_V}$ the charging energy[3]. Its eigenstates are the number states $|N_V\rangle$ ($N_V \in \mathbb{R}$), with eigenenergy $E_{C_V} N_V^2$.

The environment is made of an atomic contact, in parallel with an ideal JJ of critical current I_{L0}, a capacitance $C_t = C_{L0} + C_{J0}$ (combination of the SQUID JJ and JJS capacitors), an inductor $L/2$ and an impedance Z_{out}. In the linear approximation for the SQUID JJ, the inductor only renormalizes the Josephson energy: $E_L = \varphi_0 \left(I_{L0} + \frac{2\varphi_0}{L}\right)$. The environment Hamiltonian is

$$H_{env} = E_C N^2 - E_L \cos(\gamma) + H_{ac}(\delta) + H_{out}, \tag{7.14}$$

where $H_{ac} = \sum_i H_A(\tau_i)$ is the Hamiltonian of the atomic contact and H_{out} the one of the external impedance Z_{out}. The phase across the SQUID JJ γ and the phase across the atomic contact δ are linked[4] by the external flux applied through the loop: $\delta = \gamma + \varphi$, with $\varphi = \frac{B_{ext} S}{\varphi_0}$. The environment Hamiltonian can therefore be written just in terms of the SQUID Josephson junction phase γ:

$$H_{env} = E_C N^2 - E_L \cos(\gamma) + H_{ac}(\varphi + \gamma) + H_{out}, \tag{7.15}$$

with $[N, \gamma] = -i$.

The JJS Hamiltonian is $H_J = -E_J \cos(\alpha)$, where α is the phase across it. In this geometry, the phases are linked by $\alpha = \gamma - \phi_V$. Thus,

$$H_J = -\frac{E_J}{2}\left(e^{i\gamma} e^{-i\phi_V} + e^{-i\gamma} e^{i\phi_V}\right). \tag{7.16}$$

7.2.2 *Order of magnitudes of the parameters in our experiment*

In our experiments, at 30 mK, the superconducting gap Δ was of the order of $180\,\mu eV = h * 43.5\,GHz$. The parameters of sample JT6 are displayed in Table 7.2. Both the plasma frequency and the critical currents of the junctions were measured. Ignoring the parallel inductance $L/2$, the bare parameter z is $z_0 \simeq 0.021$. We found $z = 0.012$ by fitting the anti-crossing in the spectrum of contact U, which corresponds[5] to a parallel inductor $L/2 \simeq 0.44$ nH and a total capacitance for the junctions $C_t \simeq 280$ fF. This value of z was used to calculate all the spectra.

3 Classically, $\varphi_V = \frac{V}{\varphi_0} t$. The quantum treatment of the voltage source V as a capacitor allows to introduce $\hat{\varphi}_V$, which is a quantum operator. One has to take the limit $C_V \to \infty$ only at the end.

4 We neglect the geometrical inductance of the loop, which is of the order of 20 pH.

5 The inductor value is compatible with the estimation 0.3 pH/µm obtained by *Sonnet*. This estimation takes into account the ground plane, the measured 2 µm polyimide thickness and its dielectric constant 2.7 [122]. The relevant inductor length is ~ 1.35 mm and corresponds to the length of the central inductive wire L′ (see Section G.1). The capacitance is in agreement with the value expected from the size of both Josephson junctions (4.9 μm^2), assuming the conversion factor 57 fF/μm^2. It is reduced by 30% compared to the factor 75 fF/μm^2 given in Section E.1 for sample PAL7. That is explained by the fact that the oxidation was performed at higher pressure (300 mbar), which gives a thicker oxide layer.

	$\frac{E_J}{\Delta}$	$\frac{h\nu_p}{\Delta}$	z	$\frac{E_L}{\Delta}$	$\frac{E_C}{\Delta}$	Z_p
JT6	0.55	0.51	0.012	20.5	0.012	25.4 Ω

Table 7.2: Parameters of sample JT6.

7.3 Formal calculation of the Cooper pair current

The total Hamiltonian H cannot be diagonalized analytically. Along the lines of the $P(E)$ theory for DCB [39, 40], the tunneling rate of Cooper pairs through the JJS is obtained with Fermi's golden rule using H_J as a perturbation, and assuming that the environment is initially in thermal equilibrium.

7.3.1 *Fermi's golden rule*

Let us suppose that the eigenstates $|k\rangle$ and eigenenergies E_k of H_{env} are known (ground state $|0\rangle$, E_0). The eigenstates of $H_{source} + H_{env}$ are then the $|N_V, k\rangle$, with eigenenergy $E_{C_V} N_V^2 + E_k$ (ground state $|N_{V_i}, 0\rangle$, $E_{C_V} N_{V_i}^2 + E_0$).

At zero temperature[6] and finite voltage V, the forward tunneling rate for Cooper pairs corresponds to the transition rate from the ground state to all excited states, as given by Fermi's golden rule:

$$\Gamma(V) = \frac{2\pi}{\hbar} \sum_{N_V,k} |\langle N_V, k| H_J |N_{V_i}, 0\rangle|^2 \, \delta\left(E_k - E_0 + E_{C_V}\left(N_V^2 - N_{V_i}^2\right)\right). \tag{7.17}$$

Since $e^{-i\phi_V}$ is a translation operator of charge that verifies $e^{-i\phi_V}|N_V\rangle = |N_V - 1\rangle$, one gets

$$\left|\langle N_{Vf}| e^{-i\phi_V} |N_{Vi}\rangle\right|^2 = \begin{cases} 1 & \text{if } |N_{Vf}\rangle = |N_{Vi} - 1\rangle \\ 0 & \text{otherwise} \end{cases}. \tag{7.18}$$

From the energy point of view

$$E_f - E_i = E_{C_V}\left(N_{V_f}^2 - N_{V_i}^2\right) = E_{C_V}\left(-2N_{V_i} + 1\right) \underset{C_V \to \infty}{\to} -2eV, \tag{7.19}$$

which corresponds to the work done by the voltage source when a Cooper pair goes across the JJS. Therefore, the tunneling rate is

$$\Gamma(V) = \frac{\pi}{2\hbar} E_J^2 \sum_k \left|\langle k| e^{i\gamma} |0\rangle\right|^2 \delta\left[2eV - (E_k - E_0)\right]. \tag{7.20}$$

By symmetry, the backward tunneling rate is $\Gamma(-V)$ and the dc current through the JJS is $I_J(V) = 2e\left(\Gamma(V) - \Gamma(-V)\right)$, *i.e.*[7]

$$\boxed{\frac{I_J(V)}{I_{J0}} = \frac{\pi}{2} E_J \sum_k \left|\langle k| e^{i\gamma} |0\rangle\right|^2 \left(\delta\left[2eV - (E_k - E_0)\right] - \delta\left[2eV + (E_k - E_0)\right]\right)}. \tag{7.21}$$

6 At finite temperature, the initial state is no longer the ground state but a thermal distribution.

7 Note that the current through the JJS I_J is derived here as a function of the bias voltage V and not as a function of the dc voltage V_J across the JJS. They are however equal within the framework of this theory, which is a perturbative expansion to first order in E_J (see Appendix J for a classical derivation of higher order terms, which induce a correction in V_J).

From the microscopic point of view, it corresponds to the inelastic tunneling of a Cooper pair through the JJS's barrier while emitting the energy[8] $2eV_J = h\nu_J$ in the JJS's environment (see Fig. 6.3).

To derive the current, one needs to calculate the excitation energies $E_k^{ex} = E_k - E_0$ and the transition probabilities $P_k = \left|\langle k| e^{i\gamma} |0\rangle\right|^2$.

7.3.2 *Comparison with the usual* P(E) *theory*

In the usual P(E) theory [39, 40], the environment is purely electromagnetic and describable by an impedance $Z(\omega)$. Then, following Caldeira and Leggett [123], one can decompose it as a continuous sum of harmonic oscillators to derive an exact expression for the current:

$$\frac{I_J(V)}{I_{J0}} = \frac{\pi}{2} E_J \left[P(2eV) - P(-2eV)\right]. \tag{7.22}$$

$P(E)$ is the probability to emit the energy E in the environment and is

$$P(E) = \frac{1}{2\pi\hbar}\int_{-\infty}^{\infty} dt \exp\left[J(t) + i\frac{E}{\hbar}t\right] \tag{7.23}$$

where $J(t)$ is the phase-phase correlation function, at zero temperature[9]:

$$J(t) = 2\int_0^{\infty} \frac{d\omega}{\omega}\frac{ReZ(\omega)}{R_Q}\left[\exp\left(-i\omega t\right) - 1\right] \tag{7.25}$$

that only depends on the impedance.

In our experiment, due to the strong non-linearity of the Andreev degree of freedom the environment cannot be reduced to a simple impedance. Therefore, one cannot use this result and has to extend this theory for our peculiar environment. To do so, one must find the eigenenergies and eigenstates of this environment as will be shown in Section 7.5.

7.4 Dealing with dissipation

According to Eq. 7.21, the Cooper pair current is given by a sum of Dirac peaks, whose position correspond to an excitation energy of the environment, and whose weight is proportional to the corresponding transition probability. In this theory, the current is finite only if the environment is made of a continuum of states. In our model, this is provided by the parallel electromagnetic impedance Z_{out}. To deal

8 To first order, this energy is emitted in the form of one photon of frequency $2eV_J/h$. To higher order, multi-photon processes are possible: one Cooper pair tunnels while emitting n photons, each of frequency $2eV_J/nh$.

9 At finite temperature T,

$$J(t) = 2\int_0^{\infty} \frac{d\omega}{\omega}\frac{ReZ(\omega)}{R_Q}\left[\coth\left(\frac{\hbar\omega}{2k_BT}\right)\left(\cos\left(\omega t\right) - 1\right) - i\sin\left(\omega t\right)\right], \tag{7.24}$$

where k_B is the Boltzmann constant.

with this impedance, one can perform a Caldeira-Leggett decomposition [123] into an infinite sum of harmonic oscillators (see Section C.2):

$$H_{out} = \sum_{n=1}^{\infty} \hbar\omega_n (a_n^+ a_n + \frac{1}{2}) \tag{7.26}$$

$$\text{with } \gamma_n = \sqrt{\frac{\pi Z_n}{R_Q}}(a_n + a_n^+), \quad Z_n = \frac{1}{n}\mathrm{Re}[Z_{out}(\omega_n)] \text{ and } \sum_{n=1}^{\infty} \gamma_n = \gamma. \tag{7.27}$$

This is a hard problem because it corresponds to a spin coupled to a continuum of bosonic modes. To simplify it, we are just going to consider that the environment consists only of the Andreev mode and the plasma mode of the SQUID and introduce a phenomenological damping parameter that represents the effect of all the other modes. Concretely, we drop out H_{out} and replace any Dirac peak $\frac{\pi}{2}E_J\delta[E - E_0]$ by a quasi-Lorentzian distribution[10]

$$Q\frac{E_J}{E_0}\frac{1}{1 + \left(Q\frac{1-(E/E_0)^2}{E/E_0}\right)^2} \tag{7.28}$$

where Q is an empirical quality factor.

7.5 Diagonalizing the environment Hamiltonian H_{env}

To compute the excitation energies and their corresponding transition probabilities, one needs to find the eigenstates and eigenenergies of the environment. The main issue is that H_{env} is not analytically solvable. It reduces to a **spin-boson** problem [51, 52], which is ubiquitous in physics. It appears in the physics of a two-level atom coupled to a single mode of the quantized radiation field (Complement A_{VI} of Ref. [124]), or to its own center-of-mass motion in an atomic trap [125, 126]. To solve this problem, one proceeds through successive approximations.

7.5.1 *First approximation*

The Hamiltonian is

$$H_{env}(\varphi) = E_C N^2 - E_L \cos(\gamma) + H_{ac}(\varphi + \gamma). \tag{7.29}$$

First, we restrict to the case of a single channel of transmission τ: $H_{ac} = H_A$. Second, we treat the Josephson junction as a simple harmonic oscillator. This is valid at small plasmon number $n \ll \frac{E_L}{2E_C} \sim 10^3$ and thus legitimate here. Then, up to a constant energy the Hamiltonian becomes

$$\boxed{H_{env}(\varphi) = \hbar\nu_p(a^\dagger a + \frac{1}{2}) + H_A(\varphi + \gamma)}. \tag{7.30}$$

10 Actually, this function is the real part of the impedance of a harmonic oscillator of resonant energy E_0 and quality factor Q (see Section C.2).

There are two types of degrees of freedom in this Hamiltonian: the bosonic degree of freedom, whose characteristic energy is the plasma frequency of the atomic-SQUID, and the spin-like Andreev degree of freedom, whose characteristic energy is the Andreev energy. They are coupled through $H_A(\varphi+\gamma)$. In order to separate them, one performs a Taylor expansion of H_A around the average phase $\gamma_0 = \langle\hat{\gamma}\rangle$:

$$\begin{aligned} H_A(\varphi+\hat{\gamma}) = \; & H_A(\varphi+\gamma_0) + \varphi_0\,\delta\hat{\gamma}\,C_A(\varphi+\gamma_0) \\ & + \tfrac{1}{2}\varphi_0^2\,\delta\hat{\gamma}^2\,L_A^{-1}(\varphi+\gamma_0) \end{aligned} \tag{7.31}$$

where $\delta\hat{\gamma} = \hat{\gamma} - \gamma_0$. This is correct as long as quantum fluctuations are small, *i.e.* $\sqrt{\left\langle\delta\hat{\gamma}^2\right\rangle} \ll 2\pi$. In our system, due to the large asymmetry between $E_L \simeq h * 900$ GHz and $E_A \leqslant \Delta \simeq h * 43$ GHz, the phase dynamics is essentially ruled by the big Josephson junction of the SQUID. Thus, to a good approximation $\sqrt{\left\langle\delta\hat{\gamma}^2\right\rangle} = 2\sqrt{z} \simeq 0.22 \ll 2\pi$ and γ_0 is given[11] by the minimum of $-E_L\cos(\gamma)$, *i.e.* $\gamma_0 = 0$. Therefore, the Hamiltonian becomes

$$\begin{aligned} H_{env}(\varphi) = \; & h\nu_p(a^\dagger a + \tfrac{1}{2}) + H_A(\varphi) \\ & + \varphi_0\sqrt{z}(a+a^\dagger)C_A(\varphi) + \tfrac{1}{2}\varphi_0^2 z(a+a^\dagger)^2 L_A^{-1}(\varphi). \end{aligned} \tag{7.33}$$

7.5.2 *The spin-boson model*

Thus, in the Andreev basis (see Section B.2.3), the Hamiltonian is

$$\boxed{H_{env}(\varphi) = H_0 + H_c} \tag{7.34}$$

with

$$\boxed{H_0 = h\nu_p(a^\dagger a + \frac{1}{2}) - E_A\sigma_z + \Omega_{z2}\left(a^\dagger a + \frac{1}{2}\right)\sigma_z} \tag{7.35}$$

and

$$\boxed{\begin{aligned} H_c = \; & \Omega_{z1}(\varphi)(a+a^\dagger)\sigma_z(\varphi) + \Omega_{x1}(\varphi)(a+a^\dagger)\sigma_x(\varphi) \\ & + \tfrac{1}{2}\Omega_{z2}(\varphi)\left[a^2 + a^{\dagger 2}\right]\sigma_z(\varphi) \\ & + \Omega_{y2}(\varphi)\left[a^\dagger a + \tfrac{1}{2}\left(1 + a^2 + a^{\dagger 2}\right)\right]\sigma_y(\varphi) \end{aligned}}. \tag{7.36}$$

We have here introduced the coupling energies

$$\boxed{\begin{aligned} \Omega_{x1} &= \Omega_A\sqrt{z}\sqrt{1-\tau}\tan(\tfrac{\varphi}{2}) \\ \Omega_{z1} &= \Omega_A\sqrt{z} \\ \Omega_{y2} &= -\Omega_A z\sqrt{1-\tau} \\ \Omega_{z2} &= \tfrac{1}{2}\Omega_A z\frac{\tau+(2-\tau)\cos(\varphi)}{\sin(\varphi)} \end{aligned}} \tag{7.37}$$

11 If the SQUID is current biased below its critical current $I_B < I_{S0}(\varphi)$, one would have

$$\gamma_0 \simeq \arcsin\left(\frac{I_B}{I_{S0}(\varphi)}\right), \tag{7.32}$$

where $I_{S0}(\varphi)$ is the total critical current of the SQUID. This Taylor expansion should totally fail down as the "tilt" $\frac{I_B}{I_{S0}(\varphi)}$ approaches 1.

with a natural prefactor

$$\boxed{\Omega_A(\varphi) = \varphi_0 I_A(\varphi) = \Delta \frac{\tau \sin(\varphi)}{4\sqrt{1-\tau\sin^2(\frac{\varphi}{2})}}}. \tag{7.38}$$

Their phase-dependence is represented in Fig. 7.2. A similar derivation can be found in Ref. [127].

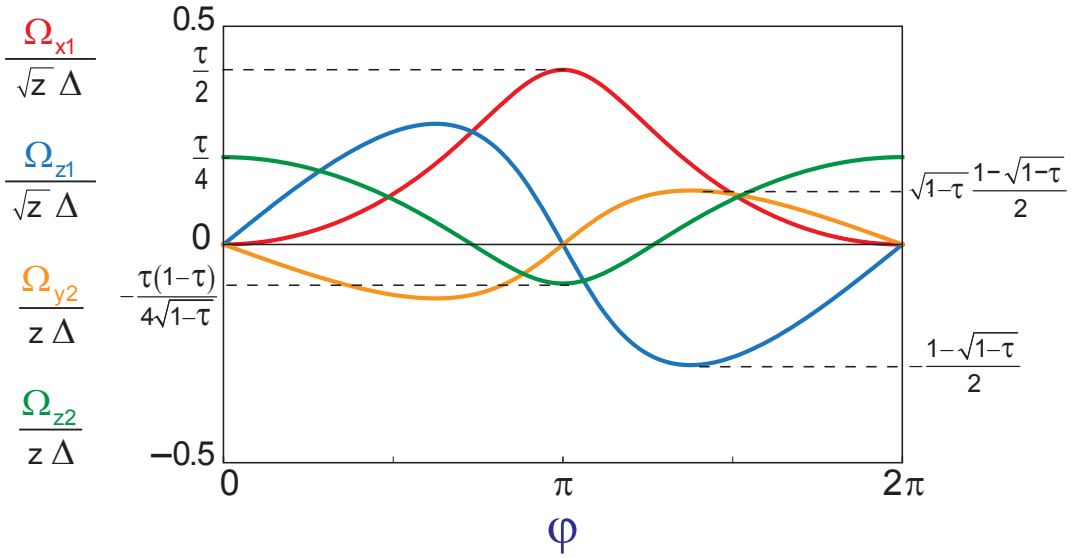

Figure 7.2: Phase dependence of the coupling energies Ω_{x1} (red) and Ω_{z1} (blue) in unit of $\sqrt{z}\Delta$, and Ω_{y2} (orange) and Ω_{z2} (green) in unit of $z\Delta$. In the figure, $\tau = 0.8$.

In H_0, the terms commute and therefore share the same eigenstates $|\sigma, n\rangle$, where $\sigma = \pm$ accounts for the Andreev spin and $n \in \mathbb{N}$ is the plasmon number. This set of eigenstates $\{|\sigma, n\rangle \mid \sigma = \pm \text{ and } n \in \mathbb{N}\}$ is a basis for the Andreev⊗plasmon Hilbert space. Their eigenenergies are

$$\boxed{E_{\sigma n} = \sigma E_A + (n + \frac{1}{2})\,(\hbar\nu_p - \sigma\Omega_{z2})}. \tag{7.39}$$

The first two terms account respectively for the dynamics of the plasmon and the Andreev spin. The third term can be seen as a dc-Stark shift. Although small (of order z), its flux dependence, with a maximum at $\varphi = 0$ and minimum at $\varphi = \pi$ (see Fig. 7.2), is essential to account for the flux modulation of the SQUID plasma frequency.

The spin and boson degrees of freedom are coupled through H_c. The most important term is $\Omega_{x,1}$, which is of order $\sqrt{z}$ and allows transition between Andreev states. As seen in Fig. 7.2, it is minimum at $\varphi = 0$ and maximum at $\varphi = \pi$.

Due to the coupling terms, this spin-boson Hamiltonian cannot be analytically diagonalized. We will first present analytical results obtained using perturbation theory, by assuming that the coupling coefficients are much smaller than the plasma and Andreev energies $|\Omega_{i,k}| \ll \hbar\nu_p\ ,\ 2E_A$. This is always true except for highly transmitted channels ($\tau \geqslant 1 - \sqrt{z}/4 \simeq 0.97$) around $\varphi \simeq \pi$. We will use $\sqrt{z}$ as a small dimensionless parameter ($\sqrt{z} \simeq 0.11$). In a second step, we compare with numerical solutions.

7.5.3 *Standard perturbation theory far from degeneracies*

The eigenstates and eigenvalues of $H_{en\nu}$ are derived using a standard perturbation theory, in the eigenbasis$|\sigma, n\rangle$ of H_0, with H_c the perturbation. This is valid as long as the $|\sigma, n\rangle$ are non-degenerate.

To lighten the formula, we introduce the notation

$$\begin{cases} E_p & = h\nu_p \\ E_{p\sigma A} & = h\nu_p + \sigma E_A \\ E_{p\sigma 2A} & = h\nu_p + \sigma 2E_A \end{cases} . \tag{7.40}$$

7.5.3.1 *Ground state*

To second order in $\sqrt{z}$, the ground state $|GS\rangle$ is

$$\begin{aligned} |GS\rangle = & \left(1 - \frac{\Omega_{x1}^2}{2E_{p+2A}^2} - \frac{\Omega_{z1}^2}{2E_p^2}\right)|-,0\rangle - \frac{\Omega_{z1}}{E_p}|-,1\rangle \\ & - \frac{\Omega_{x1}}{E_{p2A}}|+,1\rangle + \left(\frac{\Omega_{x1}\Omega_{z1}}{E_p E_{p+2A}} - i\frac{\Omega_{y2}}{4E_A}\right)|+,0\rangle \\ & + \frac{1}{\sqrt{2}E_p}\left(\frac{\Omega_{x1}^2}{E_{p+2A}} + \frac{\Omega_{z1}^2}{E_p} - \frac{\Omega_{z,2}}{2}\right)|-,2\rangle \\ & + \left(\frac{\sqrt{2}\Omega_{x1}\Omega_{z1}E_A}{E_p E_{p+A} E_{p+2A}} - i\frac{\Omega_{y2}}{2\sqrt{2}E_{p+A}}\right)|+,2\rangle . \end{aligned} \tag{7.41}$$

Its eigenenergy is, to second order:

$$E_{GS} = E_{-0} - \frac{\Omega_{z1}^2}{E_p} - \frac{\Omega_{x1}^2}{E_{p+2A}}. \tag{7.42}$$

To derive the transition probabilities, one has to compute $e^{i\gamma}|GS\rangle$:

$$\begin{aligned} e^{i\gamma}|GS\rangle &= \exp\left[i\sqrt{z}(a + a^\dagger)\right]|GS\rangle \\ &= e^{-\frac{z}{2}}\exp\left[i\sqrt{z}a^\dagger\right]\exp\left[i\sqrt{z}a\right]|GS\rangle . \end{aligned} \tag{7.43}$$

Up to second order in $\sqrt{z}$,

$$\begin{aligned} e^{i\gamma}|GS\rangle = & e^{-\frac{z}{2}}\left\{\left(1 - \frac{\Omega_{x1}^2}{2E_{p+2A}^2} - \frac{\Omega_{z1}^2}{2E_p^2} - i\sqrt{z}\frac{\Omega_{z1}}{E_p}\right)|-,0\rangle \right. \\ & + \left(i\sqrt{z} - \frac{\Omega_{z1}}{E_p}\right)|-,1\rangle - \frac{\Omega_{x1}}{E_{p+2A}}|+,1\rangle \\ & + \left(\frac{\Omega_{x1}\Omega_{z1}}{E_p E_{p+2A}} - i\sqrt{z}\frac{\Omega_{x1}}{E_{p+2A}} - i\frac{\Omega_{y2}}{4E_A}\right)|+,0\rangle \\ & + \left(\frac{1}{\sqrt{2}E_p}\left[\frac{\Omega_{x1}^2}{E_{p+2A}} + \frac{\Omega_{z1}^2}{E_p} - \frac{\Omega_{z2}}{2} - 2i\sqrt{z}\Omega_{z1}\right] - \frac{z}{\sqrt{2}}\right)|-,2\rangle \\ & \left. + \left(\frac{\sqrt{2}\Omega_{x1}\Omega_{z1}E_A}{E_p E_{p+A} E_{p+2A}} - i\frac{\sqrt{2}\Omega_{y2}}{4E_{p+A}} - i\sqrt{z}\frac{\sqrt{2}\Omega_{x1}}{E_{p+2A}}\right)|+,2\rangle\right\} . \end{aligned} \tag{7.44}$$

It has a zero order component on $|-,0\rangle$, an order one component on $|-,1\rangle$ and $|+,1\rangle$, and an order two component on $|+,0\rangle$, $|-,2\rangle$ and $|+,2\rangle$.

7.5.3.2 *Excited eigenstates*

Because of the form of the ground state, in order to calculate the transition probabilities to fourth order in $\sqrt{z}$, one only needs to find the excited eigenstates up to order 2 on $|-,0\rangle$, order 1 on $|-,1\rangle$ and $|+,1\rangle$, and order 0 on $|+,0\rangle$, $|-,2\rangle$ and $|+,2\rangle$. Thus

$$\left\{\begin{array}{rcl}
|\lambda_{+0}\rangle = & |+,0\rangle - \frac{\Omega_{x1}}{E_{p-2A}}|-,1\rangle + \frac{\Omega_{z1}}{E_p}|+,1\rangle \\
& - \left(\frac{\Omega_{x1}\Omega_{z1}}{E_p(E_{p-2A})} + i\frac{\Omega_{y2}}{4E_A}\right)|-,0\rangle \\
|\lambda_{+1}\rangle = & |+,1\rangle + \frac{\Omega_{x1}}{E_{p+2A}}|-,0\rangle \\
|\lambda_{+2}\rangle = & |+,2\rangle + \frac{\sqrt{2}\Omega_{x1}}{E_{p+2A}}|-,1\rangle - \frac{\sqrt{2}\Omega_{z1}}{E_p}|+,1\rangle \\
& - \frac{1}{E_{pA}}\left(\frac{\sqrt{2}\Omega_{x1}\Omega_{z1}E_A}{E_pE_{p+2A}} + i\frac{\Omega_{y2}}{2\sqrt{2}}\right)|-,0\rangle \\
|\lambda_{-1}\rangle = & |-,1\rangle + \frac{\Omega_{z1}}{E_p}|-,0\rangle \\
|\lambda_{-2}\rangle = & |-,2\rangle + \frac{\sqrt{2}\Omega_{z1}}{E_p}|-,1\rangle + \frac{\sqrt{2}\Omega_{x1}}{E_{p-2A}}|+,1\rangle \\
& + \frac{1}{\sqrt{2}E_p}\left(\frac{\Omega_{z1}^2}{E_p} + \frac{\Omega_{x1}^2}{E_{p-2A}} + \frac{1}{2}\Omega_{z2}\right)|-,0\rangle
\end{array}\right. . \tag{7.45}$$

The corresponding energies are:

$$\left\{\begin{array}{l}
\tilde{E}_{+n} = E_{+n} - \frac{\Omega_{z1}^2}{E_p} + \Omega_{x1}^2\frac{(2n+1)2E_A+E_p}{4E_A^2-E_p^2} \\
\tilde{E}_{-n} = E_{-n} - \frac{\Omega_{z1}^2}{E_p} - \Omega_{x1}^2\frac{(2n+1)2E_A-E_p}{4E_A^2-E_p^2}
\end{array}\right. \tag{7.46}$$

7.5.3.3 *Transition probabilities, excitation energies and current*

To fourth order in $\sqrt{z}$, only three transition probabilities from the ground state are non-zero:

$$\boxed{\left\{\begin{array}{rcl}
\left|\langle\lambda_{-1}|\, e^{i\gamma}\,|GS\rangle\right|^2 & = & ze^{-z} \\
\left|\langle\lambda_{-2}|\, e^{i\gamma}\,|GS\rangle\right|^2 & = & \frac{1}{2}z^2e^{-z} \\
\left|\langle\lambda_{+0}|\, e^{i\gamma}\,|GS\rangle\right|^2 & = & ze^{-z}\left(\frac{2\Omega_{x1}E_p}{4E_A^2-E_p^2}\right)^2
\end{array}\right.} . \tag{7.47}$$

They are shown in the top panel of Fig. 7.3.

Therefore, at lowest order, the current (7.21) displays three peaks at the bias voltage matching the three excitation energies:

$$\boxed{2eV = \pm\left\{\begin{array}{l}
\tilde{E}_{-1} - E_{GS} = E_p + \Omega_{z2} - \Omega_{x1}^2\frac{4E_A}{4E_A^2-E_p^2} \\
\tilde{E}_{-2} - E_{GS} = 2(E_p+\Omega_{z2}) - \Omega_{x1}^2\frac{8E_A}{4E_A^2-E_p^2} \\
\tilde{E}_{+0} - E_{GS} = 2E_A - \Omega_{z2} + \Omega_{x1}^2\frac{4E_A}{4E_A^2-E_p^2}
\end{array}\right.} . \tag{7.48}$$

The excitation spectrum is represented in the bottom panel of Fig. 7.3.

The amplitudes of these peaks are proportional to the matrix elements (7.47). The first and second one modulate with flux and correspond, respectively, to the plasma resonance of the atomic-SQUID and its second harmonic. The first peak is

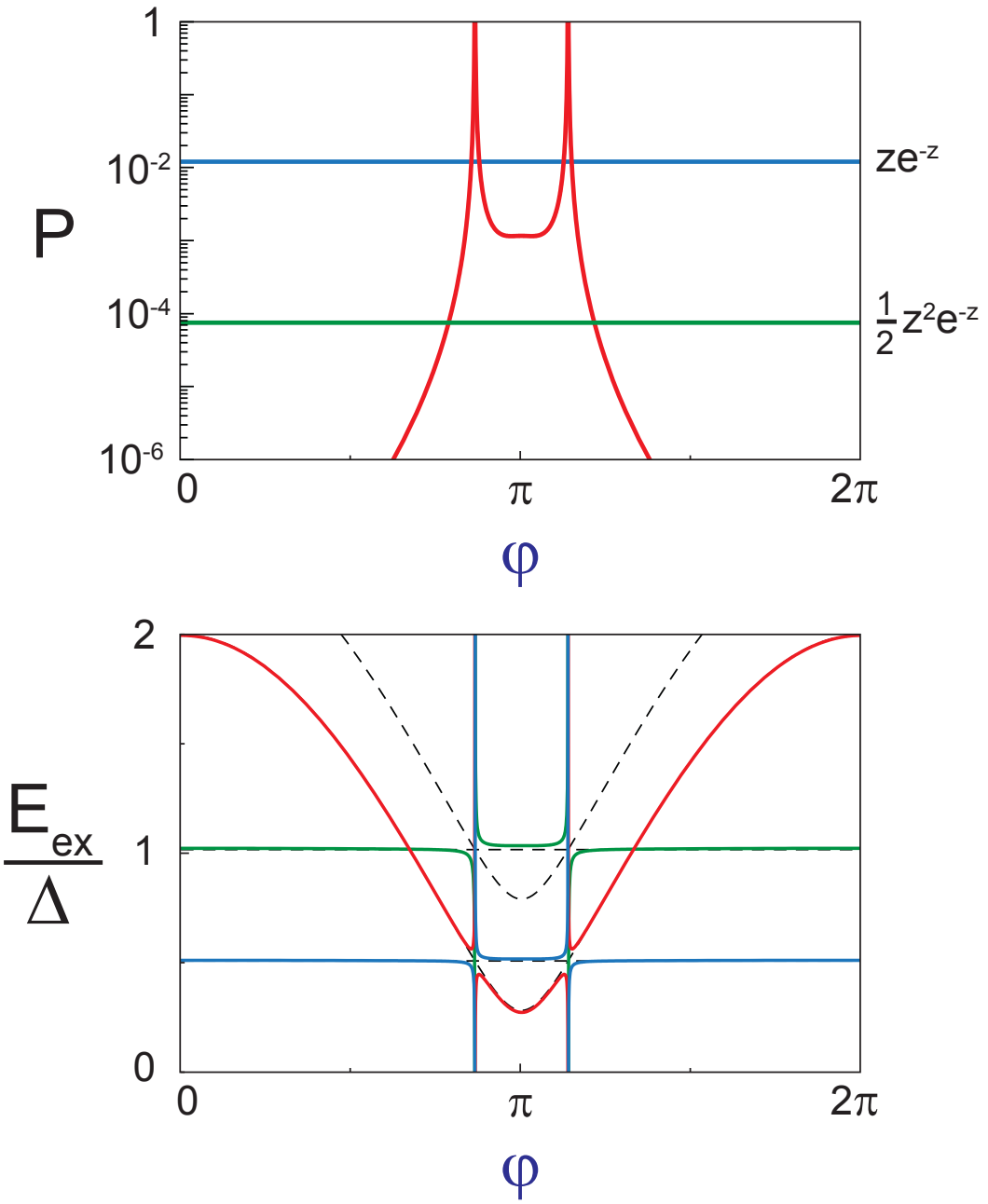

Figure 7.3: Results of the theory at the lowest order in perturbations, for a channel of transmission $\tau = 0.98$. Transition probabilities P (**top**) and excitation energies E_{ex} in units of Δ (**bottom**) of the first resonances, as a function of the reduced flux φ. Blue corresponds to one plasmon excitation, green to two plasmons and red to Andreev excitation. This perturbation theory is not valid close to the degeneracy point $\hbar\nu_p = 2E_A(\varphi)$, where a divergence is found. The black dashed lines represent the bare plasma frequency, its second harmonic, the Andreev energy and the sum of the plasma and Andreev energy.

of order z and the largest. The second one is of order z^2. This first two peak weights are exactly the same as those of a standard $P(E)$ derivation, with just a bosonic mode. The third resonance corresponds essentially to the Andreev transition. It modulates with flux through $2E_A(\varphi)$ in a much wider range. It is also of order z^2. The existence of this resonance is the goal of our calculation.

However, these calculations are only valid far from degeneracy[12] $\hbar\nu_p = 2E_A(\varphi)$. At degeneracy, one cannot considered the coupling parameters as a perturbation and this treatment leads to non-physical divergences. Another model is necessary.

7.5.4 *Jaynes-Cummings model close to degeneracy* $\hbar\nu_p = 2E_A(\varphi)$

In the region close to degeneracy $\hbar\nu_p = 2E_A$, the problem can be reduced to a Jaynes-Cummings model [128].

7.5.4.1 *Resolution*

One introduces the Pauli matrices $\sigma_+ = \frac{1}{2}(\sigma_x - i\sigma_y)$ and $\sigma_- = \frac{1}{2}(\sigma_x + i\sigma_y)$. Moving from the Schrödinger picture to the interaction picture (rotating frame), we obtain

$$\begin{aligned} H_c = \quad & \Omega_{z1}\, a\sigma_z \exp(-i\omega_p t) \\ & + \Omega_{x1}\, a\left[\sigma_- \exp\left(-i\tfrac{E_{p+2A}}{\hbar}t\right) + \sigma_+ \exp\left(-i\tfrac{E_{p-2A}}{\hbar}t\right)\right] \\ & + \tfrac{\Omega_{z2}}{2} a^2 \exp(-i2\omega_p t)\, \sigma_z \\ & - i\Omega_{y2}\left[\left(a^\dagger a + \tfrac{1}{2}\right)\left(\sigma_- \exp\left[-i\tfrac{2E_A}{\hbar}t\right]\right)\right] \\ & - i\tfrac{1}{2}\Omega_{y2} a^2\left[\sigma_- \exp\left(-i\tfrac{2E_{p+A}}{\hbar}t\right) + \sigma_+ \exp\left(-i\tfrac{2E_{p-A}}{\hbar}t\right)\right] \\ & + \text{h.c.} \end{aligned} \tag{7.49}$$

where $\omega_p = 2\pi\nu_p$ is the angular plasma frequency. This Hamiltonian contains both fast and slow oscillating components. To get a solvable model, one does the rotating wave approximation and keeps only the slowest oscillating terms, at frequency $\frac{E_{p-2A}}{\hbar}$. This is valid when $|\hbar\nu_p - 2E_A(\varphi)| \ll \hbar\nu_p$, *i.e.* in the vicinity of the degeneracy.

Transforming back into the Schrödinger picture we get

$$\boxed{H^{JC}_{env} = H_0 + \Omega_{x1}\left(a\sigma_+ + a^\dagger\sigma_-\right)}. \tag{7.50}$$

The ground state of this Hamiltonian is

$$|GS\rangle = |-,0\rangle\,, \text{ of eigenenergy } E_{GS} = -E_A + \frac{1}{2}(\hbar\nu_p + \Omega_{z2})\,. \tag{7.51}$$

We find the excited eigenstates by block-diagonalization of the Hamiltonian in the subspace $\{|+,n\rangle\,, |-,n+1\rangle\}$:

$$\begin{pmatrix} E_A + (n+\frac{1}{2})(\hbar\nu_p - \Omega_{z2}) & \Omega_{x1}\sqrt{n+1} \\ \Omega_{x1}\sqrt{n+1} & -E_A + (n+\frac{3}{2})(\hbar\nu_p + \Omega_{z2}) \end{pmatrix} \tag{7.52}$$

12 Actually, this standard perturbation theory should fail and diverge at any degeneracy. Here, it does not happen at $2\hbar\nu_p = 2E_A(\varphi)$ because we have kept all the terms up to order 4 in $\sqrt{z}$.

One introduces the detuning

$$\boxed{\delta_{n1} = E_A - \frac{1}{2}h\nu_p - (n+1)\,\Omega_{z2}}. \tag{7.53}$$

Then the eigenstates are

$$\begin{cases} |\nu_n^-\rangle = -\sin\left(\frac{\theta_{n1}}{2}\right)|+,n\rangle + \cos\left(\frac{\theta_{n1}}{2}\right)|-,n+1\rangle \\ \text{of eigenenergy } E_{\nu_n^-} = h\nu_p(n+1) + \frac{1}{2}\Omega_{z2} - W_{n1} \\ |\nu_n^+\rangle = \cos\left(\frac{\theta_{n1}}{2}\right)|+,n\rangle + \sin\left(\frac{\theta_{n1}}{2}\right)|-,n+1\rangle \\ \text{of eigenenergy } E_{\nu_n^+} = h\nu_p(n+1) + \frac{1}{2}\Omega_{z2} + W_{n1} \end{cases} \tag{7.54}$$

with

$$\boxed{W_{n1} = \sqrt{\delta_{n1}^2 + \Omega_{x1}^2\,(n+1)} \text{ and } \theta_{n1} = \arctan\left(\frac{\Omega_{x1}\sqrt{n+1}}{\delta_{n1}}\right)}. \tag{7.55}$$

Let us mention that

$$\begin{cases} \cos^2\left(\frac{\theta_{n1}}{2}\right) = \frac{1}{2}\left(1 + \text{sgn}\left[\delta_{n1}\right]\left(1 + \left[\frac{\Omega_{x1}\sqrt{n+1}}{\delta_{n1}}\right]^2\right)^{-\frac{1}{2}}\right) \\ \sin^2\left(\frac{\theta_{n1}}{2}\right) = \frac{1}{2}\left(1 - \text{sgn}\left[\delta_{n1}\right]\left(1 + \left[\frac{\Omega_{x1}\sqrt{n+1}}{\delta_{n1}}\right]^2\right)^{-\frac{1}{2}}\right) \end{cases} \tag{7.56}$$

Therefore, at zero detuning ($\delta_{n1} = 0$), $\cos\left(\frac{\alpha_{n1}}{2}\right) = \sin\left(\frac{\alpha_{n1}}{2}\right) = \frac{1}{\sqrt{2}}$; then, $|\nu_n^-\rangle$ and $|\nu_n^+\rangle$ are equal weight superpositions of $|+,n\rangle$ and $|-,n+1\rangle$.

7.5.4.2 *Transition probabilities, excitation energies and current*

To second order

$$e^{i\gamma}|GS\rangle = |-,0\rangle + i\sqrt{z}|-,1\rangle - \frac{z}{\sqrt{2}}|-,2\rangle\,. \tag{7.57}$$

To fourth order in $\sqrt{z}$, only four matrix elements are non-zero:

$$\boxed{\begin{cases} \left|\langle\nu_0^-|\,e^{i\gamma}\,|GS\rangle\right|^2 &= ze^{-z}\cos^2\left(\frac{\theta_{01}}{2}\right) \\ \left|\langle\nu_0^+|\,e^{i\gamma}\,|GS\rangle\right|^2 &= ze^{-z}\sin^2\left(\frac{\theta_{01}}{2}\right) \\ \left|\langle\nu_1^-|\,e^{i\gamma}\,|GS\rangle\right|^2 &= \frac{1}{2}z^2e^{-z}\cos^2\left(\frac{\theta_{11}}{2}\right) \\ \left|\langle\nu_1^+|\,e^{i\gamma}\,|GS\rangle\right|^2 &= \frac{1}{2}z^2e^{-z}\sin^2\left(\frac{\theta_{11}}{2}\right) \end{cases}}. \tag{7.58}$$

They are shown in the top panel of Fig. 7.4.

The current (7.21) through the JJS displays four peaks at the bias voltages matching the excitation energies:

$$\boxed{2eV = \pm\begin{cases} E_{\nu_0^-} - E_{GS} = E_A + \frac{1}{2}h\nu_p - W_{01} \\ E_{\nu_0^+} - E_{GS} = E_A + \frac{1}{2}h\nu_p + W_{01} \\ E_{\nu_1^-} - E_{GS} = E_A + \frac{3}{2}h\nu_p - W_{11} \\ E_{\nu_1^+} - E_{GS} = E_A + \frac{3}{2}h\nu_p + W_{11} \end{cases}} \tag{7.59}$$

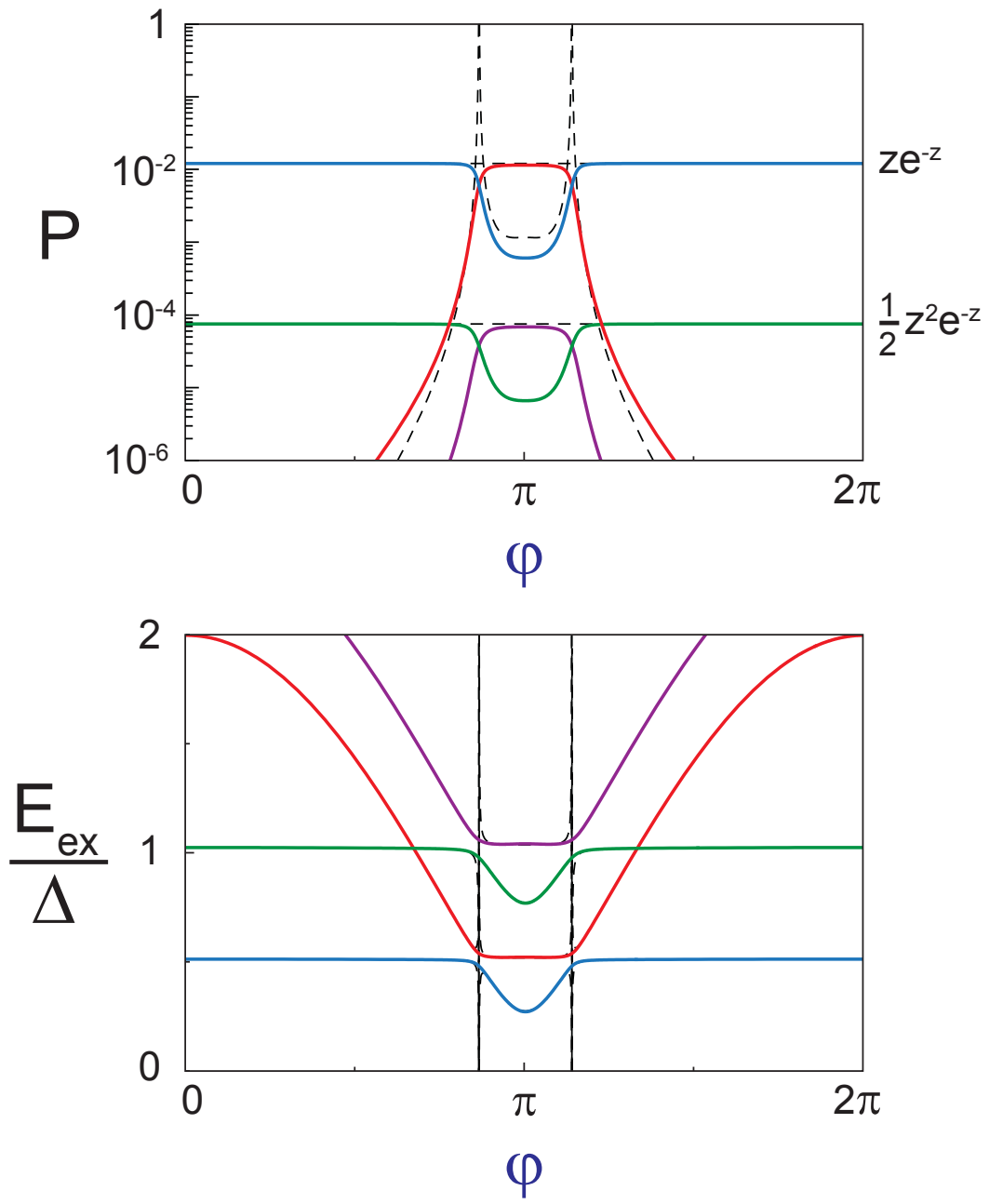

Figure 7.4: Results of the theory with the Jaynes-Cummings approximation (solid lines), for a channel of transmission $\tau = 0.98$. They are compared with the results obtained using the standard perturbation theory (black dashed lines). Transition probabilities P (**top**) and excitation energies E_{ex} (in units of Δ) (**bottom**) of the first resonances, as a function of the reduced flux φ. Blue corresponds to transition towards $|\nu_0^-\rangle$, red towards $|\nu_0^+\rangle$, green towards $|\nu_1^-\rangle$ and purple towards $|\nu_1^+\rangle$.

with W_{n1} and θ_{n1} defined in Eq. 7.55. The excitation spectrum is shown in the bottom panel of Fig. 7.4. Contrary to the standard perturbation theory, the Jaynes-Cummings approximation does not predict any divergence. It is only valid close to degeneracy[13] $|h\nu_p - 2E_A| \ll h\nu_p$ and one should expect corrections far from degeneracy.

The amplitudes of the current peaks are proportional to the matrix elements (7.58). They correspond to excitations towards composite states. The first two resonances describe the anti-crossing between the plasma ($h\nu_p$) and the Andreev resonance ($2E_A$). The last two resonances describe the anti-crossing between higher harmonic resonances at $2h\nu_p$ and $h\nu_p + 2E_A$. Far from degeneracy, this last resonance is of higher order in $\sqrt{z}$ and thus invisible. One can see it here only through the coupling to the second harmonic of the plasma frequency.

7.5.4.3 *Limitations of the Jaynes-Cummings model far from degeneracy*

The Jaynes-Cummings model is valid when $|\delta_{01}| \ll h\nu_p$. In the following, we analyze it far from degeneracy $|\delta_{01}| \gg h\nu_p$.

If $\delta_{01} > 0$, the first resonance at lower energy corresponds essentially to the plasma transition, the second one at higher energy corresponds essentially to the Andreev transition. Using Eq. 7.55 and Eq. 7.56, one finds:

$$\begin{cases} \left|\langle \nu_0^- | e^{i\gamma} | GS\rangle\right|^2 = ze^{-z} \\ \left|\langle \nu_0^+ | e^{i\gamma} | GS\rangle\right|^2 = ze^{-z}\left(\frac{\Omega_{x1}}{E_{p-2A}}\right)^2 \end{cases}, \begin{cases} E_{\nu_0^-} - E_{GS} = h\nu_p + \Omega_{z2} + \frac{\Omega_{x1}^2}{E_{p-2A}} \\ E_{\nu_0^+} - E_{GS} = 2E_A - \Omega_{z2} - \frac{\Omega_{x1}^2}{E_{p-2A}} \end{cases}.$$

The opposite case, when $\delta_{01} < 0$ (when the Andreev energy is much smaller than the plasma frequency, which happens for highly transmitting channel and φ around π), gives

$$\begin{cases} \left|\langle \nu_0^- | e^{i\gamma} | GS\rangle\right|^2 = ze^{-z}\left(\frac{\Omega_{x1}}{E_{p-2A}}\right)^2 \\ \left|\langle \nu_0^+ | e^{i\gamma} | GS\rangle\right|^2 = ze^{-z} \end{cases}, \begin{cases} E_{\nu_0^-} - E_{GS} = 2E_A - \Omega_{z2} - \frac{\Omega_{x1}^2}{E_{p-2A}} \\ E_{\nu_0^+} - E_{GS} = h\nu_p + \Omega_{z2} + \frac{\Omega_{x1}^2}{E_{p-2A}} \end{cases}.$$

These results are very similar to the ones obtained earlier using the standard perturbation theory (Eq. 7.46 and Eq. 7.47). The only error made by using Jaynes-Cummings approximation far from degeneracy is in $\frac{\Omega_{x1}^2}{2E_A + h\nu_p}$, which is small but not negligible. For instance, for φ around π, and Andreev frequency small compared to plasma frequency, it leads to an underestimation of the Andreev weight by a factor 4. But in most cases, the error is completely negligible and the Jaynes-Cummings model gives an excellent description. An improvement is obtained by a perturbation theory in the basis of the states found by the Jaynes-Cummings model.

13 One can also solve this Hamiltonian at a second degeneracy point $2h\nu_p = 2E_A(\varphi)$ introducing an other Jaynes-Cummings Hamiltonian

$$H_{env}^{JC2} = H_0 + \frac{\Omega_{y,2}}{2i}\left[a^2\sigma_+ - a^{\dagger 2}\sigma_-\right]. \tag{7.60}$$

This would allow to predict the anti-crossing between the second harmonic of the plasma resonance and the Andreev resonance. However, this correction is one order of magnitude smaller than the one at degeneracy $h\nu_p = 2E_A(\varphi)$ ($z \ll \sqrt{z}$) and we will not derive it here.

7.5.5 *Beyond Jaynes-Cummings model: general perturbation theory*

The Jaynes-Cummings model gives the exact eigenstates of H^{JC}_{env}. They correspond to the eigenstates of H_{env} as long as $|\delta_{01}| \ll \hbar\nu_p$. Results valid in a broader parameter range are found by a perturbative treatment of the terms of H_{env} not included in H^{JC}_{env}, using as an unperturbed basis the eigenstates of H^{JC}_{env}, which are no longer degenerate.

7.5.5.1 *Eigenstates and eigenenergies*

One introduces $H^{fast}_{env} = H_{env} - H^{JC1}_{env}$. To second order in $\sqrt{z}$, one needs to compute

$$\begin{cases} |\tilde{\nu}^{\sigma}_n\rangle = |\nu^{\sigma}_n\rangle + \sum\limits_{\{k_1,\sigma_1\}\neq\{n,\sigma\}} \dfrac{\left|\nu^{\sigma_1}_{k_1}\right\rangle}{E_{\nu^{\sigma}_n} - E_{\nu^{\sigma_1}_{k_1}}} \left(\left\langle \nu^{\sigma_1}_{k_1} \right| H^{fast}_{env} |\nu^{\sigma}_n\rangle \right. \\ \qquad\qquad \left. + \sum\limits_{\{k_2,\sigma_2\}\neq\{n,\sigma\}} \dfrac{\left\langle \nu^{\sigma_1}_{k_1} \right| H^{fast}_{env} \left| \nu^{\sigma_2}_{k_2} \right\rangle \left\langle \nu^{\sigma_2}_{k_2} \right| H^{fast}_{env} |\nu^{\sigma}_n\rangle}{E_{\nu^{\sigma}_n} - E_{\nu^{\sigma_2}_{k_2}}} \right) \\ E_{\tilde{\nu}^{\sigma}_n} = E_{\nu^{\sigma}_n} + \sum\limits_{\{k_1,\sigma_1\}\neq\{n,\sigma\}} \dfrac{\left| \left\langle \nu^{\sigma_1}_{k_1} \right| H^{fast}_{env} |\nu^{\sigma}_n\rangle \right|^2}{E_{\nu^{\sigma}_n} - E_{\nu^{\sigma_1}_{k_1}}} \end{cases} . \tag{7.61}$$

I have done this analytically in *Mathematica*. However, the corresponding expressions are quite cumbersome so I do not write them explicitly here.

7.5.5.2 *Transition probabilities and excitation energies*

Using the expressions of the first eigenstates and eigenenergies, the probabilities for the first transitions read:

$$\begin{cases} \left| \left\langle \tilde{\nu}^{-}_0 \right| e^{i\gamma} |GS\rangle \right|^2 = z e^{-z} \left(\cos\left(\frac{\theta_{01}}{2}\right) \right. \\ \left. + \Omega_{x1} \frac{(2E_A + 3E_p)\sin\left(\frac{\theta_{01}}{2}\right) + |E_{p-2A}| \left(\sqrt{2}\cos\left(\frac{\theta_{01}}{2}\right)\sin(\theta_{11}) - \sin\left(\frac{\theta_{01}}{2}\right)\cos(\theta_{11}) \right)}{4E_p E_{p+2A}} \right)^2 \\ \left| \left\langle \tilde{\nu}^{+}_0 \right| e^{i\gamma} |GS\rangle \right|^2 = z e^{-z} \left(\sin\left(\frac{\theta_{01}}{2}\right) \right. \\ \left. - \Omega_{x1} \frac{(2E_A + 3E_p)\cos\left(\frac{\theta_{01}}{2}\right) - |E_{p-2A}| \left(\sqrt{2}\sin\left(\frac{\theta_{01}}{2}\right)\sin(\theta_{11}) + \cos\left(\frac{\theta_{01}}{2}\right)\cos(\theta_{11}) \right)}{4E_p E_{p+2A}} \right)^2 \end{cases} \tag{7.62}$$

and their corresponding excitation energies

$$\begin{cases} E_{\tilde{\nu}^{-}_0} - E_{GS} = E_A + \frac{1}{2}\hbar\nu_p - W_{01} + E^{-}_{p0} \\ E_{\tilde{\nu}^{+}_0} - E_{GS} = E_A + \frac{1}{2}\hbar\nu_p + W_{01} + E^{+}_{p0} \end{cases} . \tag{7.63}$$

The expressions of E^{-}_{p0} and E^{+}_{p0}, both of second order in $\sqrt{z}$, are not given here for simplicity.

This result is more general and compatible with the two limits computed above. Indeed, close from degeneracy, $\sqrt{z} \ll \left|\cos\left(\frac{\alpha_{01}}{2}\right)\right| \simeq \left|\sin\left(\frac{\alpha_{01}}{2}\right)\right| \simeq \frac{1}{\sqrt{2}}$, and one recovers the result (7.58) of the Jaynes-Cummings model. Far from degeneracy, $|\delta_1| \gg \Omega_{x,1}$ with $\delta_1 < 0$ for instance, $\sin\left(\frac{\alpha_{01}}{2}\right) = \sin\left(\frac{\alpha_{11}}{2}\right) = 1$, $\cos\left(\frac{\alpha_{01}}{2}\right) = -\frac{\Omega_{x1}}{\delta_1}$, $\cos\left(\frac{\alpha_{11}}{2}\right) = -\sqrt{2}\frac{\Omega_{x1}}{\delta_1}$ and $\Omega_{11} = -\frac{\delta_1}{2}$. Thus $\sin\left(\frac{\alpha_{01}}{2} - \alpha_{11}\right) = -1$, $\left|\left\langle \tilde{\nu}^{+}_0 \right| e^{i\gamma} |GS\rangle\right|^2 =$

ze^{-z} and $\left|\left\langle\tilde{\nu}_0^-\right| e^{i\gamma}\left|GS\right\rangle\right|^2 = ze^{-z}\Omega_{x1}^2\left(-\frac{1}{2E_A-h\nu_p}+\frac{1}{2E_A+h\nu_p}\right)^2$, which corresponds exactly to the results (7.47) obtained far from degeneracy. It also works fine for the energies: in this limit $E_{p0}^- \simeq \frac{\Omega_{x1}^2}{2E_A+h\nu_p}$ and $E_{p0}^+ \simeq -\frac{\Omega_{x1}^2}{2E_A+h\nu_p}$.

Using the same technique, the next two transition probabilities $\left|\left\langle\tilde{\nu}_1^-\right| e^{i\gamma}\left|GS\right\rangle\right|^2$ and $\left|\left\langle\tilde{\nu}_1^+\right| e^{i\gamma}\left|GS\right\rangle\right|^2$ and their corresponding energies were derived. These probabilities are an order smaller than the previous ones. Up to second order, they essentially correspond to the second harmonic of the plasma frequency.

Fig. 7.5 shows the transition probabilities (top panel) and the excitation spectrum (bottom panel). One sees that the Jaynes-Cummings approximation is excellent for the spectrum and one can safely extend its range of validity. With respect to the transition probabilities, the error made by using the Jaynes-Cummings approximation is not negligible and one needs the perturbation model. Indeed, the corrections can be of the same order of magnitude and are thus essential.

This derivation is laborious but useful to understand the physics. These solutions are valid both at degeneracy $|h\nu_p - 2E_A| \ll h\nu_p$ and far from it. However, they are not strictly valid at $|2h\nu_p - 2E_A| \ll h\nu_p$, and we are neglecting here this anti-crossing. To have something valid everywhere, one needs to diagonalize the Hamiltonian numerically.

7.5.6 *Numerical resolution*

7.5.6.1 *Eigenstates and eigenenergies*

The former results are analytical but cumbersome. It is easier to diagonalize the environment Hamiltonian numerically. To do so, it has to be written as a matrix in the basis of the $\{|\sigma,n\rangle\}$. This matrix being infinite, it needs to be truncated. In the subspace $\{|-,0\rangle,|+,0\rangle,|-,1\rangle,|+,1\rangle,|-,2\rangle,|+,2\rangle,|-,3\rangle,|+,3\rangle\}$, the matrix Hamiltonian is

$$\begin{pmatrix}
E_{-0} & -i\frac{1}{2}\Omega_{y2} & \Omega_{z1} & \Omega_{x1} & \frac{1}{\sqrt{2}}\Omega_{z2} & -i\frac{1}{\sqrt{2}}\Omega_{y2} & 0 & 0 \\
i\frac{1}{2}\Omega_{y2} & E_{+0} & \Omega_{x1} & -\Omega_{z1} & i\frac{1}{\sqrt{2}}\Omega_{y2} & -\frac{1}{\sqrt{2}}\Omega_{z2} & 0 & 0 \\
\Omega_{z1} & \Omega_{x1} & E_{-1} & -i\frac{3}{2}\Omega_{y2} & \sqrt{2}\Omega_{z1} & \sqrt{2}\Omega_{x1} & \sqrt{\frac{3}{2}}\Omega_{z,2} & -i\sqrt{\frac{3}{2}}\Omega_{y,2} \\
\Omega_{x1} & -\Omega_{z1} & i\frac{3}{2}\Omega_{y2} & E_{+1} & \sqrt{2}\Omega_{x1} & -\sqrt{2}\Omega_{z1} & i\sqrt{\frac{3}{2}}\Omega_{y,2} & -\sqrt{\frac{3}{2}}\Omega_{z,2} \\
\frac{1}{\sqrt{2}}\Omega_{z2} & -i\frac{1}{\sqrt{2}}\Omega_{y2} & \sqrt{2}\Omega_{z1} & \sqrt{2}\Omega_{x1} & E_{-2} & -i\frac{5}{2}\Omega_{y2} & \sqrt{3}\Omega_{z,1} & \sqrt{3}\Omega_{x,1} \\
i\frac{1}{\sqrt{2}}\Omega_{y2} & -\frac{1}{\sqrt{2}}\Omega_{z2} & \sqrt{2}\Omega_{x1} & -\sqrt{2}\Omega_{z1} & i\frac{5}{2}\Omega_{y2} & E_{+2} & \sqrt{3}\Omega_{x,1} & -\sqrt{3}\Omega_{z,1} \\
0 & 0 & \sqrt{\frac{3}{2}}\Omega_{z,2} & -i\sqrt{\frac{3}{2}}\Omega_{y,2} & \sqrt{3}\Omega_{z,1} & \sqrt{3}\Omega_{x,1} & E_{-3} & -i\frac{7}{2}\Omega_{y,2} \\
0 & 0 & i\sqrt{\frac{3}{2}}\Omega_{y,2} & -\sqrt{\frac{3}{2}}\Omega_{z,2} & \sqrt{3}\Omega_{x,1} & -\sqrt{3}\Omega_{z,1} & i\frac{7}{2}\Omega_{y,2} & E_{+3}
\end{pmatrix} \tag{7.64}$$

where $E_{\sigma n}$ was introduced in Eq. 7.39. Then, one finds numerically its eigenvectors and eigenvalues. Such a truncation is a low energy approximation that only allows finding the low energy states. Of course, the bigger the subspace, the more accurate the results. The zeros in the matrix arise from the fact that we are using a Taylor expansion limited to second order (Eq. 7.33) of the Hamiltonian that allows coupling between states separated at maximum by two photons. This is an approximation and a limitation of our modeling.

7.5.6.2 *Transition probabilities and excitation energies*

To obtain accurate enough results, I have used a 14×14 matrix. Fig. 7.6 shows the transition probabilities (top panel) and the excitation spectrum (bottom panel)

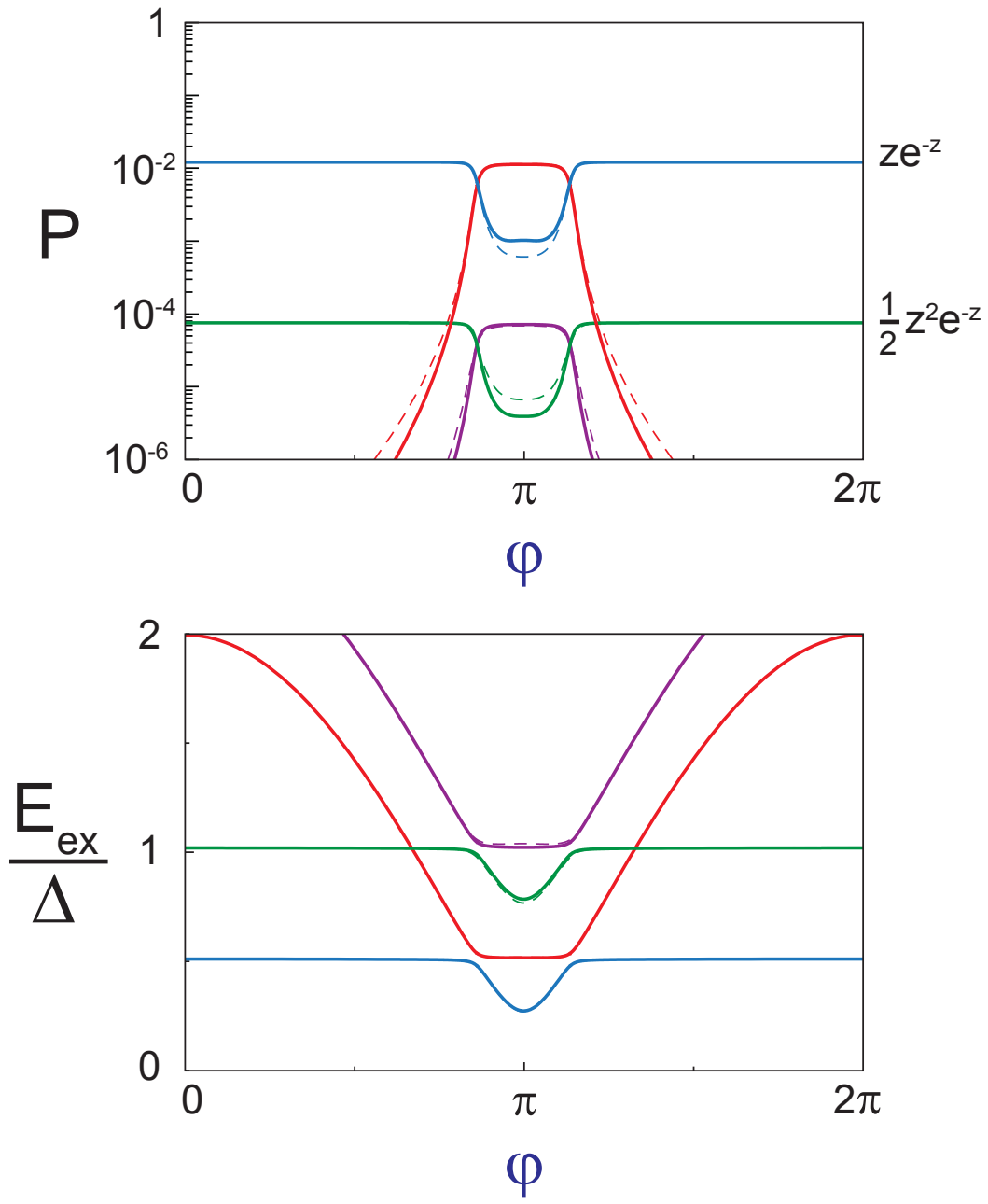

Figure 7.5: Results of the general perturbation theory (solid lines) for a channel of transmission $\tau = 0.98$. They are compared with the results obtained using the Jaynes-Cummings approximation (thin dashed lines). Transition probabilities P (**top**) and excitation energies E_{ex} (in units of Δ) (**bottom**) of the first resonances, as a function of the reduced flux φ. Blue corresponds to transition towards $|\nu_0^-\rangle$, red towards $|\nu_0^+\rangle$, green towards $|\nu_1^-\rangle$ and purple towards $|\nu_1^+\rangle$.

for a channel of transmission $\tau = 0.98$. With this method, one has a direct access to the full spectrum. Here, we have computed all the resonances whose energy is smaller than 2Δ. These results are in excellent agreement with the analytical perturbation theory. However, one can notice some unexpected asymmetry of the transition probabilities around π. This is probably due to the finite Taylor expansion performed at the beginning. But as it only concerns the very small transition probabilities, one can safely neglect this error in practice. We present in Appendix H an alternative numerical method which consists in writing the Hamiltonian in another basis and which does not require such approximations. The transition probabilities are then symmetrical around π.

7.6 Extension to multiple channels

Up to now, we have considered the case of a single channel contact. In the experiment, the contacts have several channels (usually 3 for Aluminum one-atom contacts), and the theory has to be extended. To do so, one adds the Hamiltonians of all channels: $\sum_i H_{A,\tau_i}$. We restrict here to 3 channels.

We are now dealing with the physics of 3 spins and a boson. These spins are coupled to the same bosonic mode but not directly coupled one with another. All the approximations made before are still valid as long as the whole atomic contact critical current remains small as compared to the critical current of the SQUID junction, that is to say as long as the atomic-SQUID remains very asymmetrical. Typically, a 3 channels contact has a critical current below 100 nA, which is 10 times smaller than the critical current of the SQUID junction.

7.6.1 *Analytical resolutions*

It is straightforward to extend the standard perturbation theory since it is just at the lowest order a sum of the results of the previous theory. Thus, one predicts one plasma resonance and three Andreev resonances. This is only valid far from degeneracies, and therefore not very interesting.

The extension of the Jaynes-Cummings model and the perturbation theory in Jaynes-Cummings basis to multiple channels is much more involved. If only one Andreev resonance crosses the plasma resonance, one can treat it in a 2×2 Jaynes-Cummings model as done previously, in each subspace $\{|+,\sigma_2,\sigma_3,n\rangle,|-,\sigma_2,\sigma_3,n+1\rangle\}$. Then, one has to perform a general perturbation theory in the Jaynes-Cummings basis. This is not just a sum of results of the previous calculation and requires an extension, which I have not done.

At last, if n Andreev resonances cross the plasma resonance, one has to solve this in a $2n \times 2n$ Jaynes-Cummings model, which is even more complicated. At this point numerical calculations are needed.

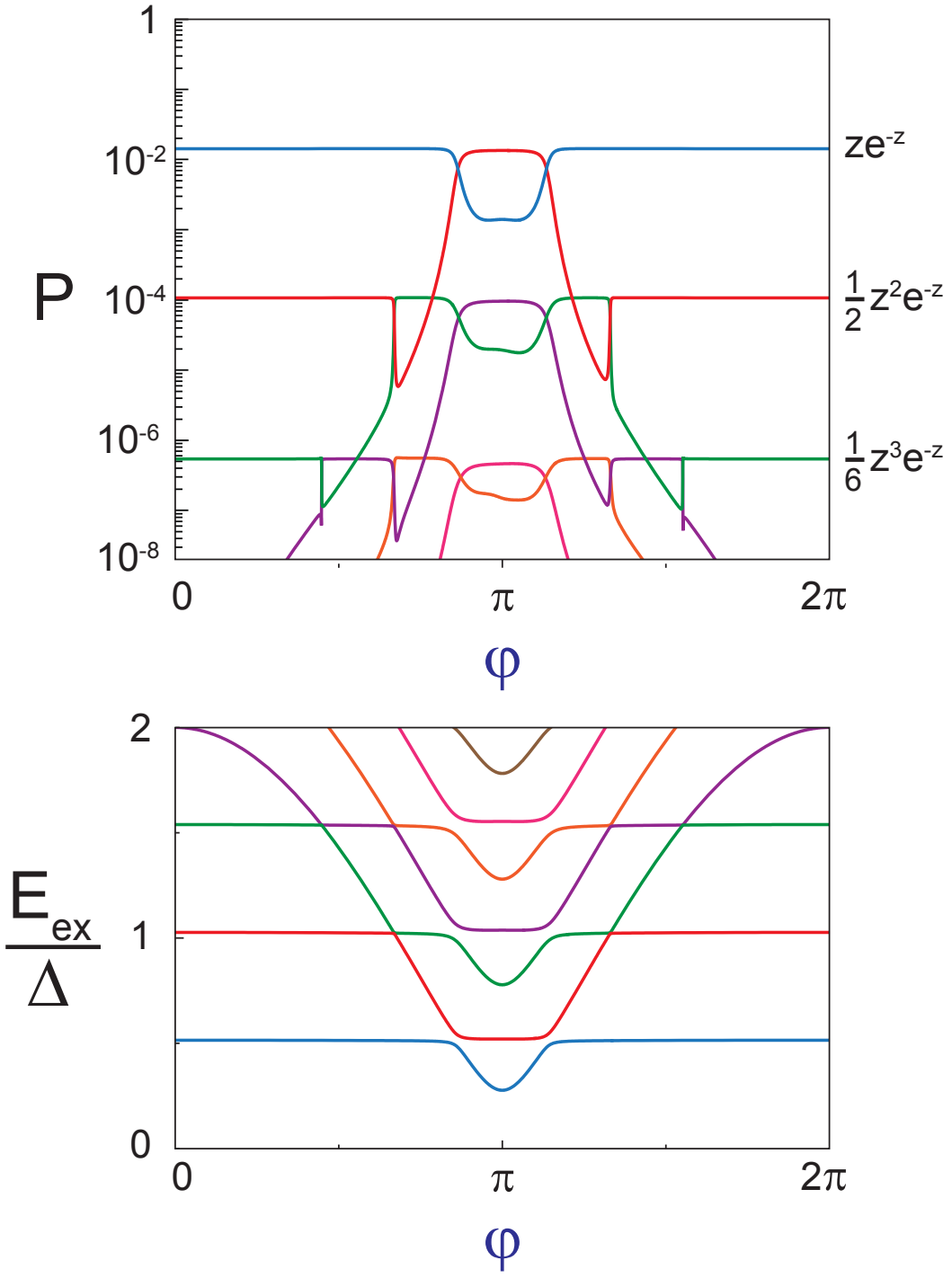

Figure 7.6: Transition probabilities P (**top**) and excitation energies E_{ex} (in units of Δ) (**bottom**) of the first resonances, as a function of the reduced flux φ, for a channel of transmission $\tau = 0.98$. The solid lines are obtained by numerical diagonalization of a 14×14 matrix Hamiltonian.

7.6.2 *Numerical solution*

As before, the Hamiltonian is written as a truncated matrix in the basis of the $\{|\sigma_1, \sigma_2, ..., \sigma_N, n\rangle\}$, where $\sigma_i = \pm$labels the Andreev spin of the i^{th} channel, N is the number of channels and n the photon number. Larger matrices are necessary to obtain accurate results.

The corresponding calculation was done for a one-atom contact with three channels $\tau_1 = 0.99$, $\tau_2 = 0.8$ and $\tau_3 = 0.6$, and a 56×56 matrix. The transition probabilities and excitation energies are shown in Fig. 7.7.

7.7 $I_J(\varphi, V_J)$ spectra

The theoretical spectra shown in Fig. 6.9, Fig. 6.14, Fig. 6.15, Fig. G.4 and Fig. G.5 were obtained with the numerical method sketched in 7.6.2, using 6 photon levels.

7.8 Possible extensions

7.8.1 *Modeling dissipation*

We have modeled the dissipation by introducing a phenomenological damping parameter. In doing so, one does not model microscopically the width of the resonances. In particular, one looses the information on the natural width of the ABS, *i.e.* on their relaxation time. To do better, one needs to deal with the actual external impedance $Z_{out}(\omega)$. Such a derivation is not straightforward: it is the problem of one (or a few) spin coupled to a continuum of bosons. An additional difficulty is that in practice, it is difficult to determine the electromagnetic impedance seen by the atomic-SQUID at the frequencies corresponding to the Andreev transitions.

7.8.2 *Beyond first order perturbation*

Through Fermi's golden rule, this theory is a perturbative expansion to first order in E_J. It can only predict current peaks corresponding to inelastic tunneling of 1 Cooper pair emitting n photons. In $P(E)$ theory [40], it is legitimate[14] as long as $E_J P(2eV) \ll 1$. From the experimental point of view, a convenient criterion is $I_{DC} \ll I_0$.

The higher order terms have been formally[15] derived in Ref. [129]. They correspond to higher harmonics in the Josephson ac current which can be seen micro-

14 $P(E)$ theory describes the phenomenon of DCB, which is usually observed in junctions in "charge regime" $E_J/E_C \ll 1$. In our experiment, this condition is not fulfilled, but we can still use this perturbative expansion to first order as the actual validity condition $E_J P(2eV) \ll 1$ can be achieved with a weakly absorbing environment.

It is also interesting to notice that this dimensionless term $E_J P(E) \underset{E\to\infty}{\to} 2\frac{E_J}{E}\frac{ReZ(\frac{E}{\hbar})}{R_Q} = \frac{1}{\pi}\frac{ReZ(\frac{2eV}{\hbar})I_0}{V}$ which is (within a factor of π) the same dimensionless term as the one used in the perturbative resolution of the classical treatment of this problem derived in Appendix J.

15 It is an exact expansion (*i.e.* not perturbative) of the form $\Gamma(V) = \frac{i}{2\hbar}E_{J_0}\sum_{n=0}^{+\infty}\left[i\frac{E_{J_0}}{2eV}\right]^{2n+1}a_n(V)$.

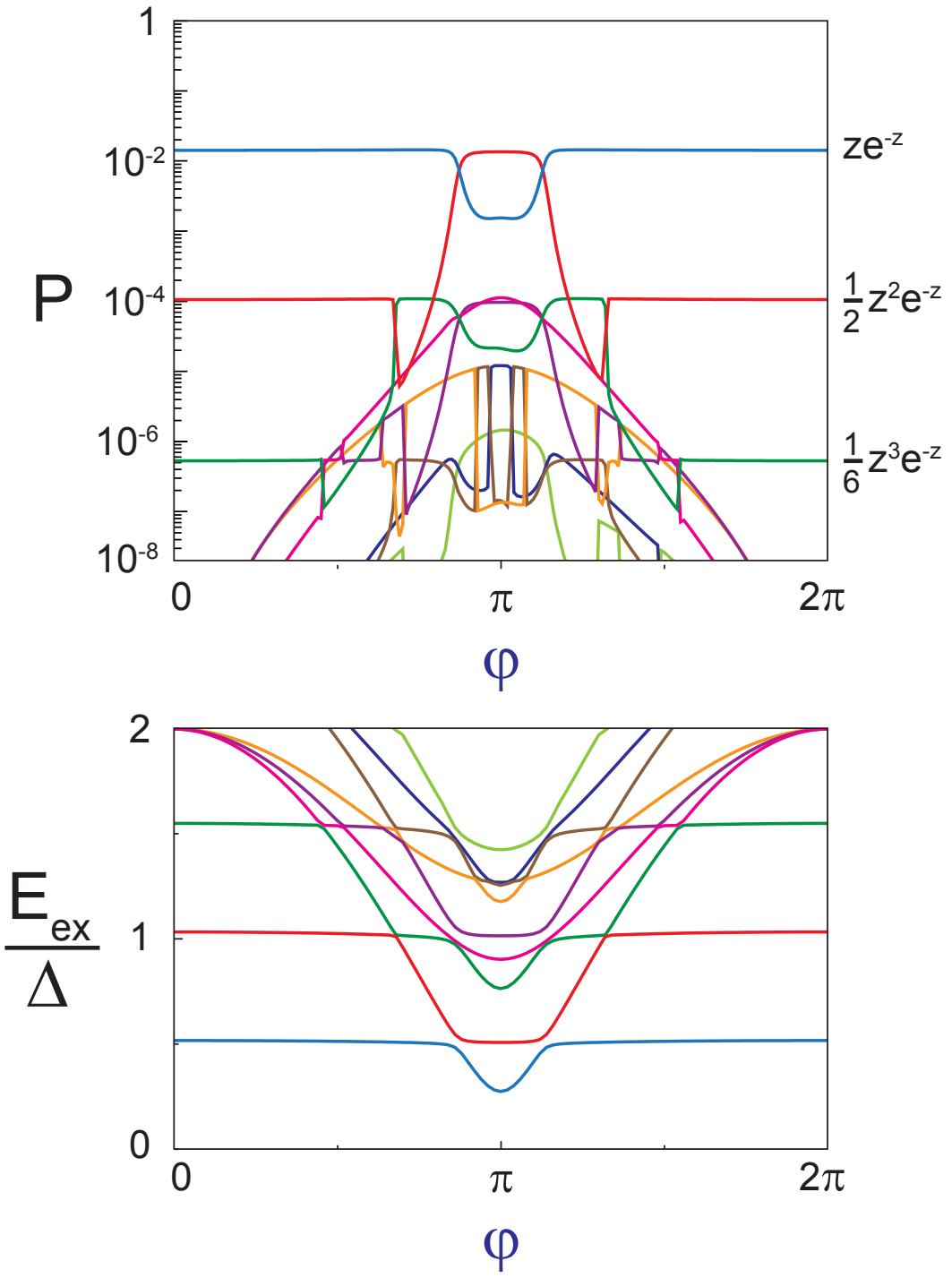

Figure 7.7: Transition probabilities P (**top**) and excitation energies E_{ex} (in units of Δ) (**bottom**) of the first resonances, as a function of the reduced flux φ, for a one-atom contact with three channels $\tau_1 = 0.98$, $\tau_2 = 0.8$ and $\tau_3 = 0.6$. The solid lines are obtained by numerical diagonalization of a 56×56 matrix Hamiltonian.

scopically as the inelastic tunneling of p Cooper pairs emitting q photons. The first one is of the order of $(E_J P(2eV))^3$. In experiment on sample JT6, $\frac{I_{DC}}{I_0} < 0.15$ and we have not seen such higher processes[16]. This is why this first order expansion is legitimate. However, in the experiment on sample JS6, the spectrometer Josephson junction had a larger critical current, and it is necessary to consider higher order terms. They could lead to sub-harmonics arising from multi-Cooper pair tunneling (see Appendix J for a discussion on harmonics and sub-harmonics).

7.8.3 *Out-of-equilibrium environment*

It was assumed that the environment is in its ground state each time a Cooper pair tunnels. This requires for the relaxation time of the excited environment states to be shorter than the inverse tunnel rate. If this is not the case, there is a feedback from the environment on the tunneling rate and it can change significantly the physics. For a bosonic mode, it can lead to stimulated emission and lasing. For a fermionic mode, such as the Andreev one, it is even more drastic because it can totally saturate the absorption and thus block Cooper pair tunneling. In a coherent regime, it could lead to Rabi oscillations of the Andreev two level system that could be directly detected as a Cooper pair current at the Rabi frequency. To account for these effects, one needs another theoretical framework. This is what A. C. Doherty has recently developed in a master equation approach [130] for a bosonic environment.

In our experiment, we might have observed out-of-equilibrium effects, as shown in Section 6.4.3, with transitions at energy $2E_A - h\nu_p$. They become possible when the bosonic mode is simultaneously driven out-of-equilibrium.

On the other hand, up to now, we have not seen evidence of a fermionic saturation. But such a regime seems accessible since we can reach situations where the relaxation rate and absorption rates become comparable (see Section 6.3.4). Therefore, we would benefit from an extension of Doherty's model [130] to our system containing a fermionic mode.

16 Except in switching experiments.

8

SWITCHING SPECTROSCOPY OF ANDREEV BOUND STATES

In this chapter, we present a complementary experiment to the one presented in Chapter 6, performed on the same sample JT6 and with the same experimental setup. It is also a spectroscopy of Andreev bound states, relying on excitation by a Josephson junction spectrometer and on the poisoning phenomenon discussed in Part II. With this alternative technique, we measured the Andreev transition in a broader energy range, up to 2Δ. We also accessed more complex transitions, involving both the Andreev bound states and the continuum.

8.1 Current-phase relation measurement at equilibrium

The experimental setup presented in Section 6.1 also allows us to probe the supercurrent-phase relation of the atomic contact, which is a direct signature of the configuration of the Andreev two level system of each channel (see Section 3.1). As in the poisoning experiment in Chapter 4, the supercurrent-phase relation is obtained through switching measurements, by applying trains of pulses with the voltage source U_b (see Fig. 6.1) and monitoring the number of voltage pulses appearing across the atomic-SQUID that signal switching (see Section 4.2.2). With this setup however, this measurement can be done either at equilibrium (*i.e.* in absence of microwaves) or under irradiation from the JJS.

Fig. 8.1 shows the switching probability P_{sw} as a function of both the flux φ and the normalized pulse height s for contact V ($\{0.985, 0.37, ...\}$). This measurement is obtained in absence of microwaves, *i.e.* when the JJS is at zero voltage bias. The

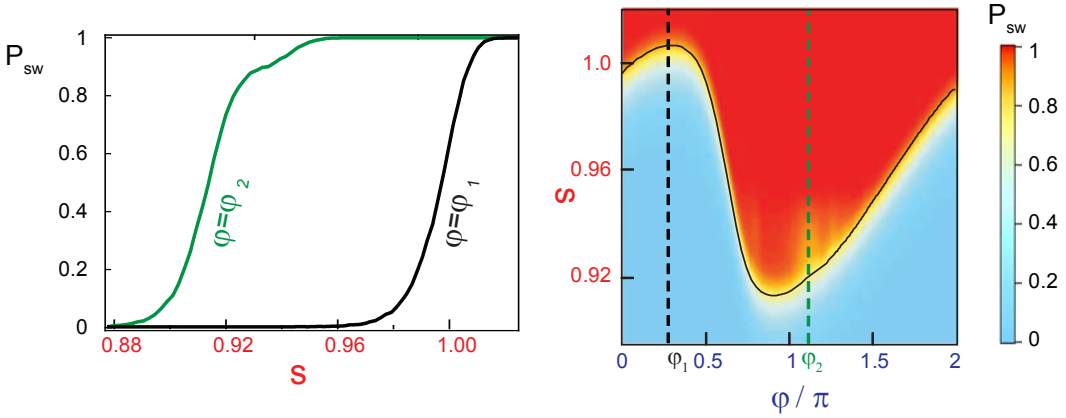

Figure 8.1: **Right**: Switching probability $P_{sw}(\varphi, s)$ as a function of both the reduced bias current s and the flux φ, at equilibrium. These data are obtained for the SQUID with contact V ($\{0.985, 0.37, ...\}$) using the method described in Fig. 4.10 with switching pre-pulses. The solid line is the theoretical reduced current-phase relation $s^*(\varphi)$ predicted from escape theory (see Section E.2). **Left:** Cuts $P_{sw}(s)$ at the positions of the dashed lines.

switching probability does not vary sharply from $P_{sw} \simeq 0$ (light blue) to $P_{sw} \simeq 1$ (red) for all values of the flux: there is an anomalous region in a flux range around π with an intermediate step at $P_{sw} \simeq 0.9$ (vertical yellow stripes). As already discussed in Chapter 4, this is due to spontaneous poisoning of ABS by quasiparticles from the continuum. With this sample however the poisoning probability is much weaker than what has been measured for sample PAL7. This may be related to the different geometries[1] of samples JT6 and PAL7.

8.2 Switching spectroscopy

The experiment presented in *Chapter 6* clearly demonstrates that transitions from the ground state $|-\rangle$ to the excited even state $|+\rangle$ are induced by the JJS. The present experiment probes the change in supercurrent associated with this transition.

8.2.1 *Experimental protocol*

In the power absorption spectroscopy presented in *Chapter 6*, we measured the dc current through the JJS $I_J(\varphi, V_J)$ as a function of its voltage V_J (which is proportional to the emitted Josephson frequency ν_J) and the flux φ in the SQUID loop (which tunes the ABS energies $\pm E_A(\delta, \tau)$). Here we perform the same experiment except that we measure the switching probability $P_{sw}(\varphi, V_J)$ of the SQUID instead of the dc current of the JJS.

The protocol is the following:

- In absence of microwaves ($V_J = 0$), for each flux value φ, one fixes a working point s^* such as $P_{sw}(s^*, \varphi) = 0.5$.
- Then, one "switches on the microwaves": at each flux φ, one measures the switching probability $P_{sw}(s^*, \varphi, V_J)$ as a function of the voltage V_J across the JJS.

One thus detects a change in the switching probability of the atomic-SQUID associated to the excitation by the JJS. Fig. 8.2 shows a gray scale plot of the corresponding $P_{sw}(\varphi, V_J)$ curves for contact V ($\{0.985, 0.37, ...\}$). This spectrum differs in several respects from the ones presented in *Chapter 6*. (the two spectra are replotted side by side in Fig. 8.6). A similar spectrum for contact U is shown and discussed in Section G.6.

1 In sample PAL7, the atomic-SQUID is at the end of long and narrow superconducting lines. In sample JT6, the atomic-SQUID is directly connected to large superconducting electrodes. This could play a role since quasiparticle diffusion and thus poisoning depend on the actual geometry.

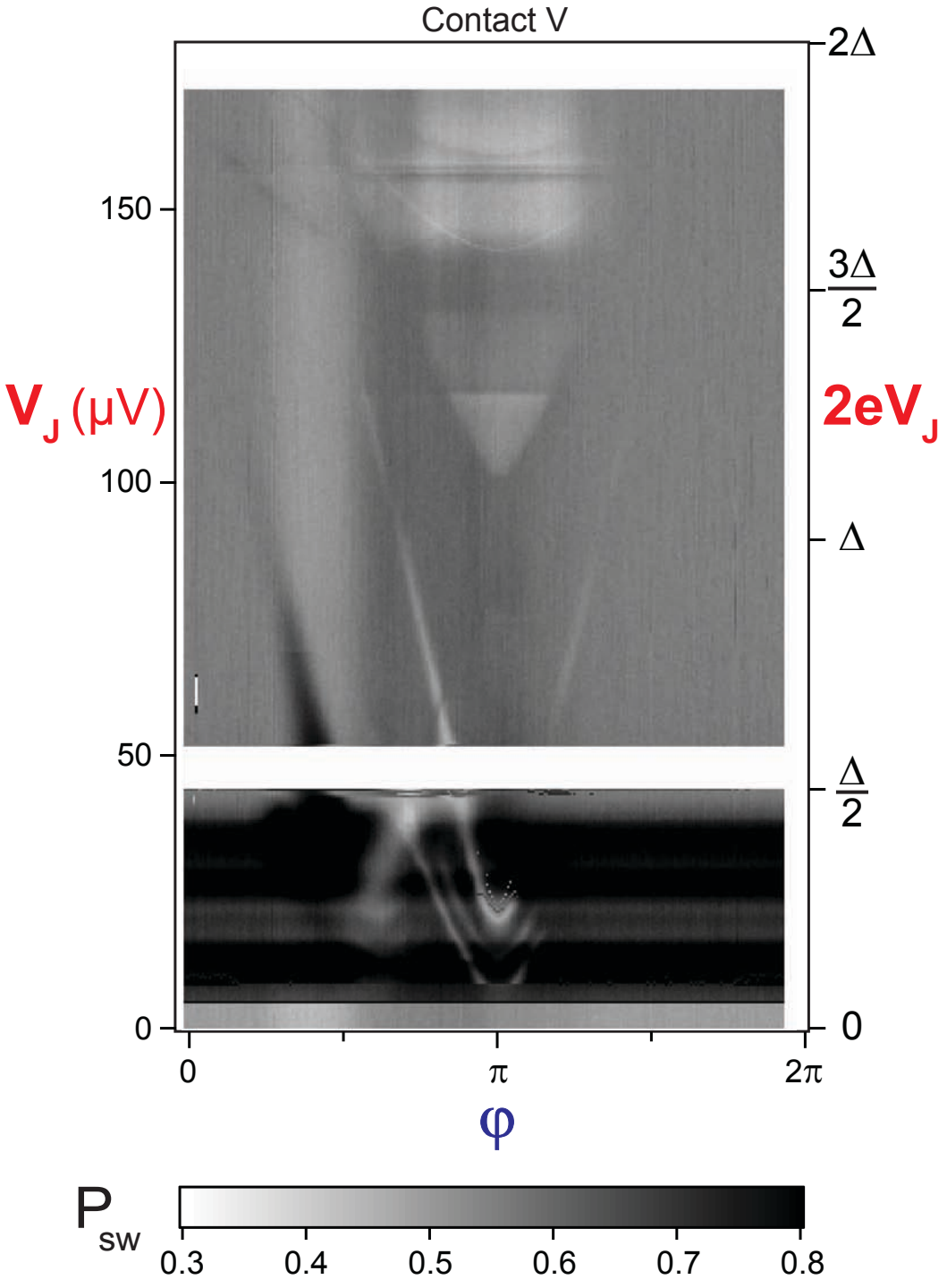

Figure 8.2: Switching probability $P_{sw}(\varphi, V_J)$ as a function of both the voltage V_J across the JJS and the flux φ threading the SQUID loop. The reduced bias current s^* is chosen to satisfy $P_{sw}(s^*, \varphi) = 0.5$ at $V_J = 0$. These data were obtained on contact V.

8.2.2 *Andreev transitions up to* 2Δ

Among all resonances, we clearly identify the Andreev lines of the two most-transmitting channels. The dashed-lines in the right panel of Fig. 8.3 show the Andreev transition energies $2eV_J = 2E_A(\varphi, \tau_i)$ calculated using Eq. 1.1 with the known sets of transmissions $\{\tau_i\}$ for contact V. Note that the Andreev transitions are detected in a broader energy range (almost[2] up to 2Δ) compared to the power absorption spectrum presented in *Chapter 6*. The transition corresponding to the second channel with transmission 0.37 is very well resolved, as a very narrow line. The resonances corresponding to the low-transmission channels ~ 0.12 are however still not visible.

8.2.3 *Transitions from the lower ABS to the continuum*

Some additional structures in the spectrum do not correspond to simple Andreev transitions. In particular, there is a broad pocket centered at $\varphi = \pi$, with a minimum at $V_J \simeq 110\,\mu V$, whose lower border resembles an Andreev line. Its position is well accounted for by the energy $\Delta + E_A(\varphi, \tau_1)$ (solid blue line in the right panel of Fig. 8.3), where $\tau_1 = 0.985$. We interpret this feature as transitions from the lower ABS to the continuum (see Fig. 8.3), which explains the threshold behavior[3]. We could not detect such transitions in the power absorption spectroscopy. The pocket intensity presents horizontal stripes: the intensity changes seem related to crossing of external modes of the electromagnetic environment (see for instance a decrease of the intensity around $120\,\mu V$).

8.2.4 *Higher order processes*

In the low energy part of the spectrum, one can see sharp resonances that modulate strongly in flux. They correspond to transition energies $E_A(\varphi, \tau_1) + 3\,\mu eV$ and $E_A(\varphi, \tau_1) - 11\,\mu eV$ (yellow dotted lines in the right panel of Fig. 8.3). They could be related to higher order processes in which two Cooper pairs tunnel through the barrier of the JJS while emitting one photon at energy $2E_A$ and emitting (respectively absorbing) another photon at energy $7\,\mu eV$ (respectively $22\,\mu eV$): $4eV_J = 2E_A + 7\,\mu eV$ and $4eV_J = 2E_A - 22\,\mu eV$. These extra modes are not understood.

2 Unfortunately, the spectrum for contact V was measured only until $V_J \simeq 170\,\mu V$, i.e. $2eV_J \simeq 0.95 \times 2\Delta$. The spectrum for contact U in Fig. G.6 was however taken on a broader voltage range and one clearly detects the Andreev lines up to the continuum.

3 A line is also found at $\Delta + E_A(\varphi, \tau_2)$ (solid red line above $V_J \simeq 110\,\mu V$ in the right panel of Fig. 8.3), with $\tau_2 = 0.37$, but it does not appear as a boundary, strangely enough.

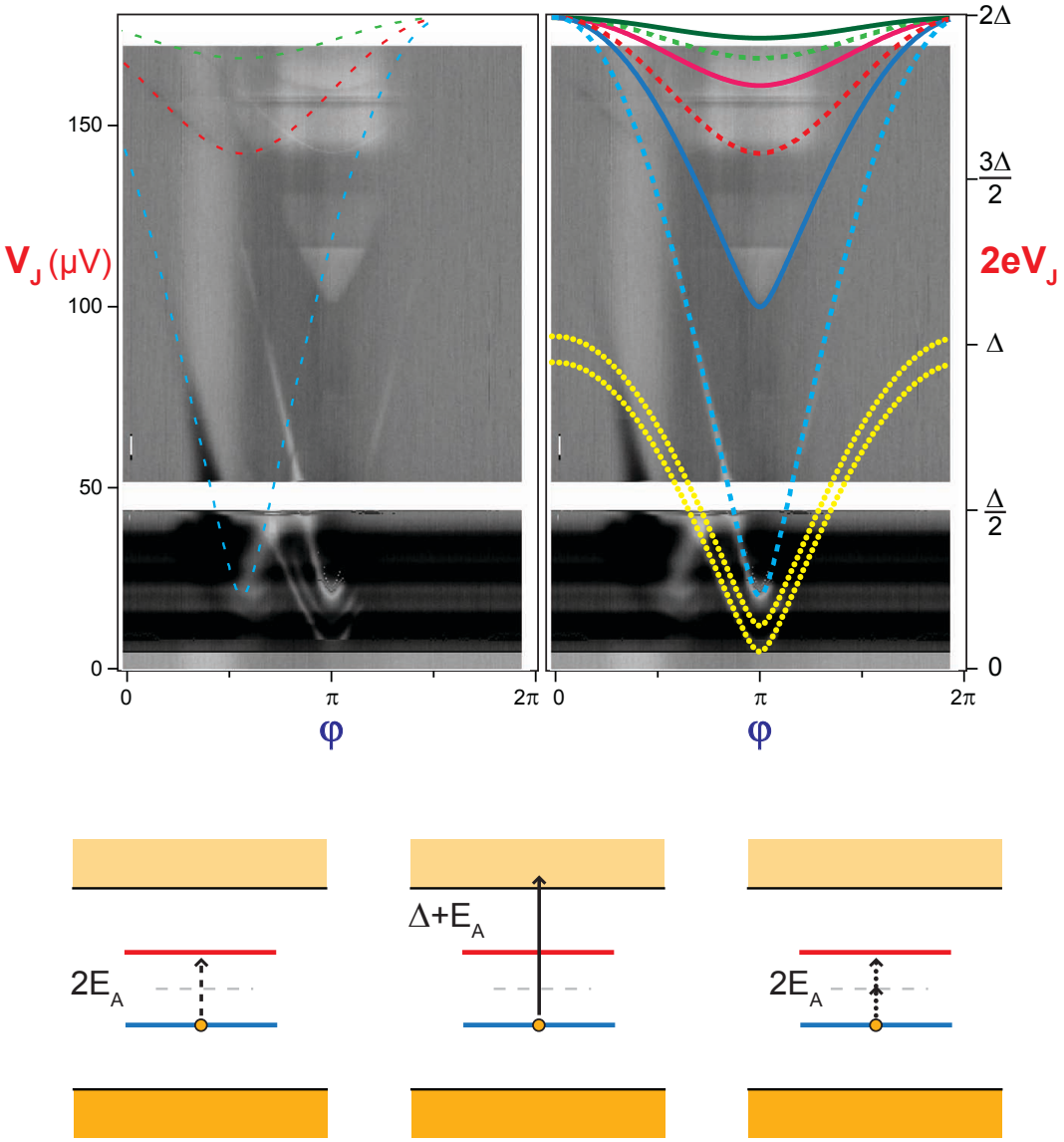

Figure 8.3: Switching spectrum $P_{sw}(\varphi, V_J)$ for contact V (same scale as Fig. 8.2). **Right**: The dashed lines are the Andreev resonances $2eV_J = 2E_A(\varphi, \tau_i)$. The solid lines correspond to the energy thresholds of transitions from the lower ABS to the continuum $2eV_J = \Delta + E_A(\varphi, \tau_i)$. The dotted lines correspond to higher order transitions of energies $2eV_J = E_A(\varphi, \tau_1) + 3\,\mu eV$ and $2eV_J = E_A(\varphi, \tau_1) - 11\,\mu eV$. **Left**: The thin dashed lines are the Andreev resonances $2eV_J = 2E_A(\varphi + 0.3\pi, \tau_i)$ shifted in flux by $\arcsin(s_0) \simeq 0.3\pi$. These transitions occur during the measurement pulse. **Bottom**: Sketch of the different transitions.

8.2.5 *Driving excitation during the bias measurement pulse*

At last, there are two images of the same spectrum. This is especially visible for the Andreev lines (see left panel of Fig. 8.3). The flux shift between the two images exactly corresponds to $\arcsin(s_0) \simeq 0.3\pi$, where s_0 is the reduced bias current through the JJ of the SQUID during the measurement pulse. Therefore, the leftmost image corresponds to transitions induced during the measurement pulse, when $\delta = \varphi + \arcsin(s_0)$. These transitions are more blurred, probably because the top of the pulse is not flat enough.

8.2.6 *Long-lived excited states ?*

More importantly, the transitions that we discussed above (shown in the right panel of Fig. 8.3) are induced during the time interval between two measurement pulses, when no current flows through the SQUID and $\delta = \varphi$. Therefore, the states which are detected must live long enough to be subsequently detected during the measurement pulse, through a resonant change of the switching probability. By resetting V_J to 0 a time Δt before the measurement pulse, we have measured the lifetime of the detected states. At $V_J = 140\,\mu V$ and $\varphi = \pi$ (the red dashed line in the right panel of Fig. 8.3), we found a time $\simeq 10\,\mu s$. This time is much larger than the typical relaxation (500 ps) and absorption (1 ns) times of the excited state $|+\rangle$ extracted from the width and amplitude of the Andreev resonance in the power absorption spectroscopy (see Section 6.3.4). The interpretation, developed below, is that the state detected is not the excited state $|+\rangle$.

8.3 **Sample and hold detector based on poisoning**

Until now, we have only shown the place in the (V_J, φ) plan where the switching probability changes under the action of the JJS. However, we have not analyzed the nature of the change in term of P_{sw}.

8.3.1 *Reduction of the atomic contact critical current*

Apart from the black stripes in the bottom of the spectrum, all the resonances appear as white lines (or area) in the central region, vanish at flux $\sim \pi/2$ and $\sim 3\pi/2$ and become black beyond these values. This change of sign is related to the one of the equilibrium current-phase relation $s^*(\varphi)$ displayed as a solid line in the right panel of Fig. 8.1. This indicates that the changes in switching probability associated to these resonances all correspond to a **decrease in absolute value** of the critical current of the atomic contact.

8.3.2 *Current-phase relation measurement in presence of microwaves*

Measurements of the switching probability $P_{sw}(\varphi, s)$ as a function of both the reduced bias current s and the flux φ were performed while emitting microwaves. In Fig. 8.4, the JJS was biased at a voltage $V_J = 150\ \mu V$.

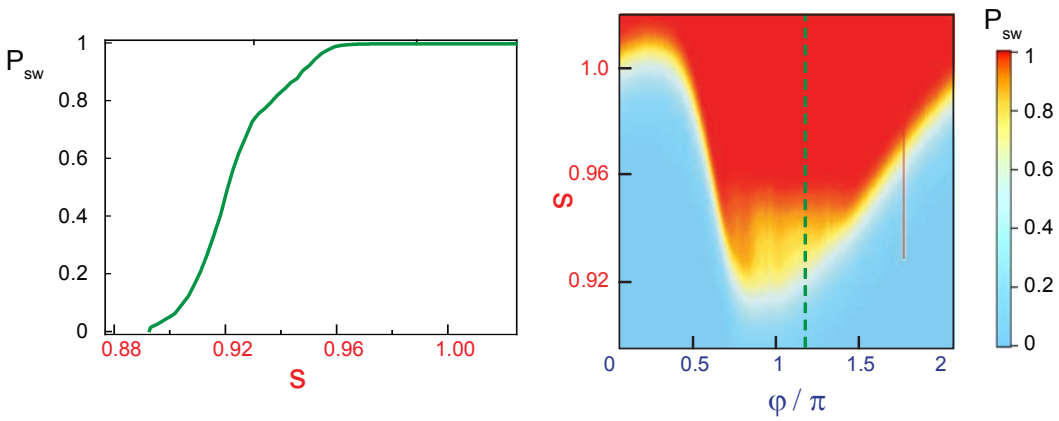

Figure 8.4: **Right**: Switching probability $P_{sw}(\varphi, s)$ as a function of both the reduced bias current s and the flux φ, for contact V, while the JJS is biased at a voltage $V_J = 150\ \mu V$. **Left:** Cut $P_{sw}(s)$ at the position of the dashed line.

Fig. 8.4 is different from Fig. 8.1, with a much bigger anomalous region. In this flux region, the JJS induces transitions from the lower Andreev state of the most transmitting channel to the continuum (see Section 8.2.3), leaving the ABS in an odd configuration. Since the odd states $|\uparrow, \downarrow\rangle$ do not carry supercurrent, it reduces the switching probability.

Similar measurements were performed at different voltages V_J. One could as well observe anomalous regions arising from the reduction of the critical current of the atomic contact. In all cases, this reduction corresponds to a cancellation of the Andreev supercurrent of one (or more) of the channels. An inversion of the supercurrent was however never observed.

8.3.3 *Odd states*

Therefore, the changes in switching probability displayed in Fig. 8.2 (apart from the black stripes) reflect the fact that the system is found (for one of the channels) in one of the two odd states $|\uparrow\rangle$ and $|\downarrow\rangle$. This explains the long measured relaxation times.

With respect to the transitions from the lower Andreev states to the continuum, this is expected since the Andreev doublet ends after the excitation in an odd configuration. Moreover, the long life time of the odd states explains why this transition was not observed in the absorption spectroscopy.

Regarding the transitions from the lower Andreev states $|-\rangle$ to the upper Andreev states $|+\rangle$, one would however expect to measure an inversion of the supercurrent. This detection was unsuccessful in this experiment, probably due to a too short life-time of $|+\rangle$ compared to the absorption time[4].

However, the Andreev transition could be detected in the switching spectrum due to another phenomenon. As sketched in Fig. 8.5, while being in the excited state $|+\rangle$, a spurious quasiparticle from the delocalized continuum can get trapped in the lower ABS localized at the contact (in the one-particle picture). The system then stays blocked in one of the two odd states, which live long enough to be subsequently detected by switching[5].

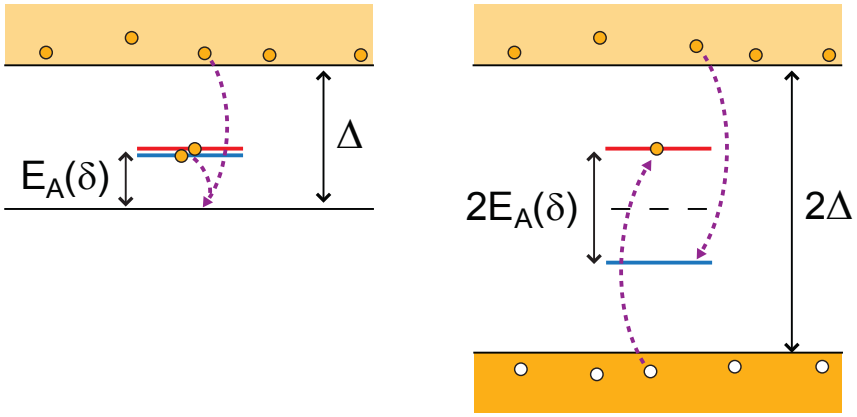

Figure 8.5: Sketch of the poisoning phenomenon. Starting from the excited even state $|+\rangle$, non-equilibrium quasiparticles in the continuum can get trapped into the ABS localized at the constriction. **Left**: in the excitation picture. A quasiparticle from the continuum can recombine with one of the two quasiparticles excited in the ABS (the spin degeneracy has been lifted for clarity). **Right**: in the one-particle picture. Either a quasiparticle decays from the upper continuum into the negative energy ABS, or a quasihole jumps from the bottom continuum into the positive energy ABS.

4 These two times seem yet comparable at low Andreev energy (see Section 6.3.4)...

5 To make this scenario work, the trapping probability in the upper ABS must be larger than the one in the lower ABS. This is reasonable since the energy lost by trapping is bigger in the first case.

8.4 Comparison between spectra by absorption and by switching

Fig. 8.6 shows a comparison between spectra by absorption and by switching for contact V. Strikingly, and thanks to poisoning[6], the switching spectroscopy allows an even more accurate detection of the Andreev transition than the power absorption spectroscopy. It also allows to access more complex transitions that could not be detected in absorption spectroscopy, such as transitions from ABS to the continuum.

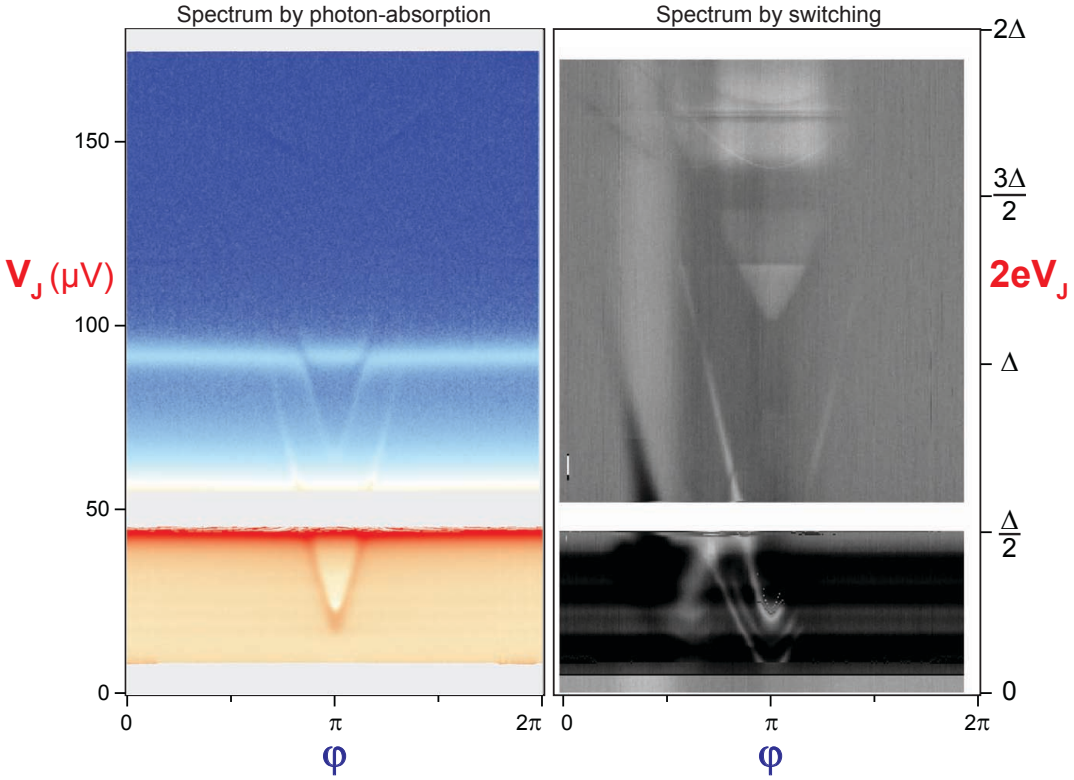

Figure 8.6: Comparison between spectra by photon-absorption $I_J(\varphi, V_J)$ (**left**) and by switching (**right**) for contact V $\{0.985, 0.37, ...\}$.

At low frequency, one can see large black stripes in the switching spectrum, indicating an increase of the switching probability. They might correspond to resonant activation of the current-biased atomic-SQUID [131]. This phenomenon happens when the excitation frequency ν_J matches the plasma frequency in the tilted washboard potential $\nu_p \left(1 - s^2\right)^{1/4} \sim 15$ GHz, which is largely reduced compared to the one at zero bias (see Section E.2).

On the other hand, the plasma resonance at zero bias $h\nu_p$ and its harmonics $2h\nu_p$ are not detecting by switching. Since the plasma mode has a low quality factor $Q \sim 13$, the excitation achieved during the time interval before the measurement pulse relaxes very fast (in ~ 0.6 ns) and has no effect on the switching probability. However, the hybrid resonance at energy $h\nu_p + 2E_A$ is not detected either by switching, which is not explained by this argument.

6 Note however, that the poisoning phenomenon limits in principle the microwave absorption by the Andreev doublet.

Part IV

EXPERIMENTAL TECHNIQUES

9

SAMPLE FABRICATION

Most of the techniques used to fabricate the samples measured in this thesis are standard, based on microlithography and thin-film deposition. However, the design of capacitors deserves some description, as well as sample fabrication on flexible substrates. This chapter gives detailed recipes for the fabrication of samples in the poisoning experiment (PAL7) and the spectroscopy experiment (JT6).

9.1 Sample PAL7 for switching experiment

The development phase of the manufacturing of sample PAL7 was essentially done during the thesis of Quentin Le Masne, my predecessor in the Quantronics group [69].

9.1.1 *Kapton wafer preparation*

Atomic contacts are obtained by bending a substrate with a microlithographed suspended bridge. The samples are fabricated on a flexible substrate; silicon wafers cannot be used. For sample PAL7, to achieve good microwave transmission through the flux line, an insulating wafer was required to allow the design of a coplanar waveguide. We have used Kapton (Kapton® HN from DuPont™), a plastic material with dielectric constant $\epsilon_r = 3.2$.

Kapton plates (500 µm-thick) are first cut into 2-inch wafers. The wafer is polished using a polisher (P320 MECAPOL, PRESI):

1. The wafer is glued with wax on a large metallic block:
2. Rough polishing is performed using Nylon disks and diamond paste with 9 µm-large grains, for 30 min at 150 rpm. This removes the largest scratches and diminishes the thickness of the wafer by typically 50 µm.
3. Three fine polishes (6 µm, 3 µm and 1 µm) are performed with soft disks at 150 rpm. The local residual roughness is eventually of the order of 50 nm, with a few deeper scratches.

Planarization is improved using a polyimide layer. We used a solution of pure PI2610 (HD MicroSystems™). This solution is spun at 2000 rpm during 1 min (initial slow ramp of 10 s), terminated by 3 s at 6000 rpm to avoid edge effects. The wafer is then baked 1 h in an oven at 180 °C (or on a hot plate 3 min at 120 °C and 3 min at 180 °C depending on the wafers), and cured for one hour at 350 °C in a vacuum chamber under a residual pressure of 10^{-6} mbar (~ 1 h 20 to reach 350 °C at 4 °C/min, then 1 h at 350 °C). The final thickness of the layer is typically 2.5 µm. This process reduces the local roughness to less than 5 nm, and fills most of the scratches.

9.1.2 *Optical lithography*

Three consecutive steps of optical lithography (the actual recipes are detailed in Section 9.3.1) are then used to fabricate the capacitors, the on-chip antenna, the large contact pads, the connecting wires, and the quasiparticle traps, using the three masks shown in Fig. 9.1. A wafer contains seven 14 mm × 14 mm chips.

CAPACITOR FABRICATION Each capacitor is obtained by two electrodes overlapping a common bottom electrode buried under a thin dielectric layer. As a result, one obtains two capacitors in series. We have used 5 to 10 nm-thick aluminum oxide (AlOx) as a dielectric, obtained by depositing a stack of several ~ 1.5 nm-thick layers, oxidized one-by-one. A difficulty with this method is that the edges of the bottom electrode are not completely covered with the thin AlOx layer, creating possibly short circuits with the top electrode. To circumvent this difficulty[1], both bottom electrode and dielectric layer are deposited under angles in the first step (red pattern in Fig. 9.1). The top electrodes are then deposited under an angle in the second step (blue pattern in Fig. 9.1). The key point is that connecting wires to the top electrodes all climb from the soft edge (top edge of red rectangle in Fig. 9.1), thus preventing from short at the edges. This is the reason for the cumbersome design of the capacitor. These steps are illustrated in Fig. 9.2.

MASK 1: BOTTOM CAPACITOR ELECTRODES Mask 1 defines the bottom capacitor electrodes. 29.5-nm of aluminum[2] are deposited at 0.1 nm/s under an angle of 50°. To diminish the grain size, the films are deposited on the wafer held at low temperature (≃ 160 K) using a liquid nitrogen flow cooling. It is then oxidized during 5 min at 500 mbar in Ar-O_2 (85% − 15%). Five ~ 1.5 nm aluminum layers are subsequently deposited, at a rate of 0.1 nm/s, under different angles (47°, 45°, 42°, 39° and 36°), each oxidized at 500 mbar during 5 min in Ar-O_2 (85% − 15%).

MASK 2: TOP CAPACITOR ELECTRODES, CONTACT PADS, ANTENNA Mask 2 defines the top electrodes of the capacitors (overlap over 0.01 mm^2), the large scale contact pads and the antenna. 30-nm of aluminum are deposited at 0.1 nm/s under an angle of 50°, at ≃ 160 K. To avoid the oxidation of this layer and facilitate the connection to it, 2 nm-thick copper layer and then 2 nm-thick gold layer are deposited at 0.5 nm/s on top of it. The copper buffer layer prevents from the formation of a gold-aluminum intermetallic with poor conductivity.

With this technique, the capacitor $C = 60 \pm 5$ pF (corresponding to 6 ± 0.5 nF/mm^2) was obtained with a good reproducibility. At dc, the measured capacitors leakage was a few MΩ. In sample PAL7, we have measured at room temperature a capacitor $C = 58$ pF.

MASK 3: QUASIPARTICLE TRAPS AND ALIGNMENT CROSSES The last mask defines the quasiparticle traps and alignment crosses. 2 nm of titanium are first

1 This technique allows to save one lithography step, compared to what was done in [72], where an additional polyimide protecting layer was involved.

2 The thicknesses given in this chapter for layers evaporated under an angle θ take into account the angle correction cos (θ): here $46 * \cos(50°) \simeq 29.5$ nm.

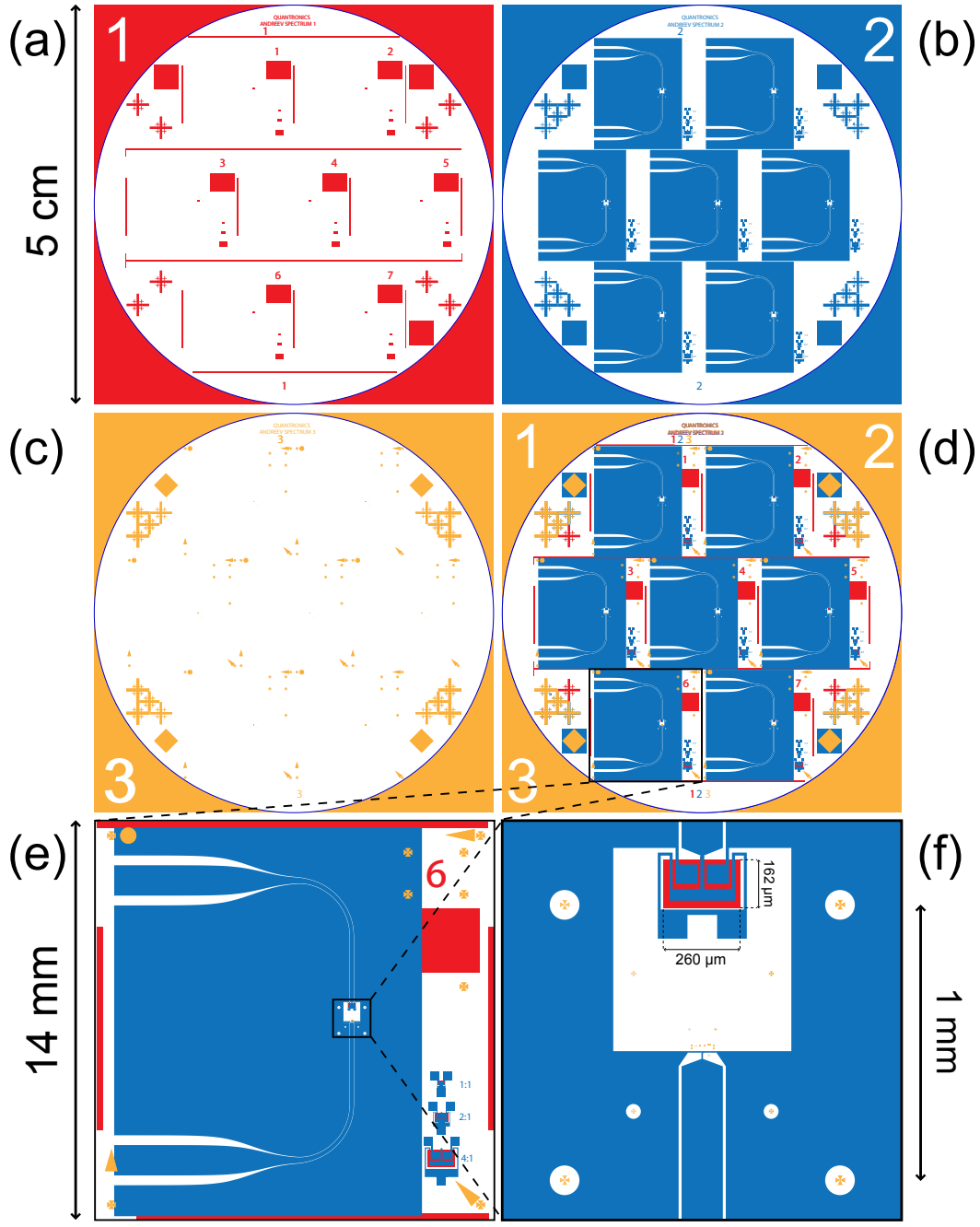

Figure 9.1: **(a,b,c)** Masks 1, 2 and 3 used for sample PAL7. Colored region are transparent in the masks, white areas are opaque. **(d)** Result of the overlap of the three patterns; **(e)** single chip: the blue area defines the coplanar waveguides; the red square defines a buried aluminum pad to monitor by laser interferometry the RIE (see Section 9.3.4); test capacitors are designed in the bottom right corner. **(f)** The antenna (blue) is terminated by a short; the current bias line ends with the top electrode (blue) of the capacitor, which superimpose the bottom electrode (red). In the central region, which only contains gold quasiparticle traps and alignment marks (gold), the SQUID and the long inductive lines will be pattern in the next step, by e-beam lithography.

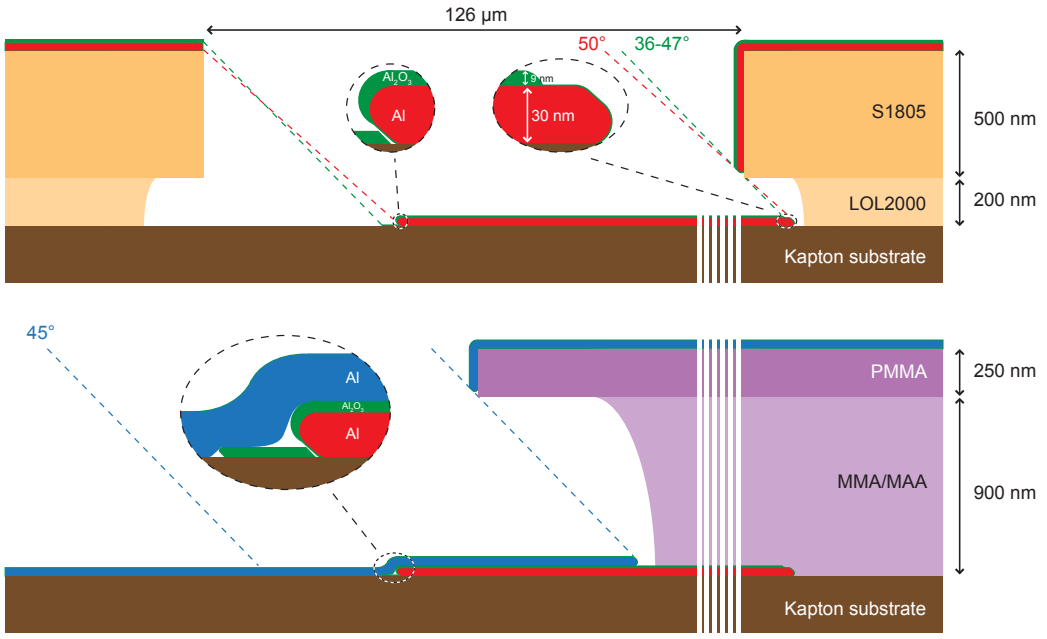

Figure 9.2: Scheme for the fabrication of capacitor C for sample PAL7. **Top**: Deposition of the Al bottom electrode (red) and the AlOx dielectric layer (green) through the mask in optical resist (orange) on the Kapton substrate (brown). **Bottom**: Deposition of the Al top electrode (red) through the mask in e-beam resist (purple).

deposited at 0.5 nm/s and $\simeq$ 160 K, as an adhesion layer. Then, 30 nm of gold are deposited at 0.5 nm/s and $\simeq$ 190 K.

9.1.3 *Electron beam lithography*

The wafer is then prepared for e-beam lithography (see recipes in Section 9.3.2) and cut into samples using a guillotine or scissors. The pattern shown in Fig. 9.3 is drawn in the resist to obtain the atomic-SQUID loop and the inductive lines connecting to the capacitor:

- The loop containing the bridge and the junction (purple) is aligned on the alignment crosses (yellow). Semi-transparent areas are "undercut boxes", where the dose is reduced (typically down to 90 µC/cm^2). In these regions, the dose is sufficient to expose the MMA, more electrosensitive than the PMMA, which remains overhanging. This allows subsequent evaporation of metals under large angles.

- The loop is connected with three narrow (0.9 µm) and long (0.4 and 0.8 mm) lines which form inductors (green), which then contact the capacitor formed in the previous step. At regular spacings, the lines are made wider. The reason is that in the last fabrication step the substrate is etched to suspend the bridge. Since the lines forming the inductors are very narrow, they also get suspended: wider areas allow to anchor them on the substrate.

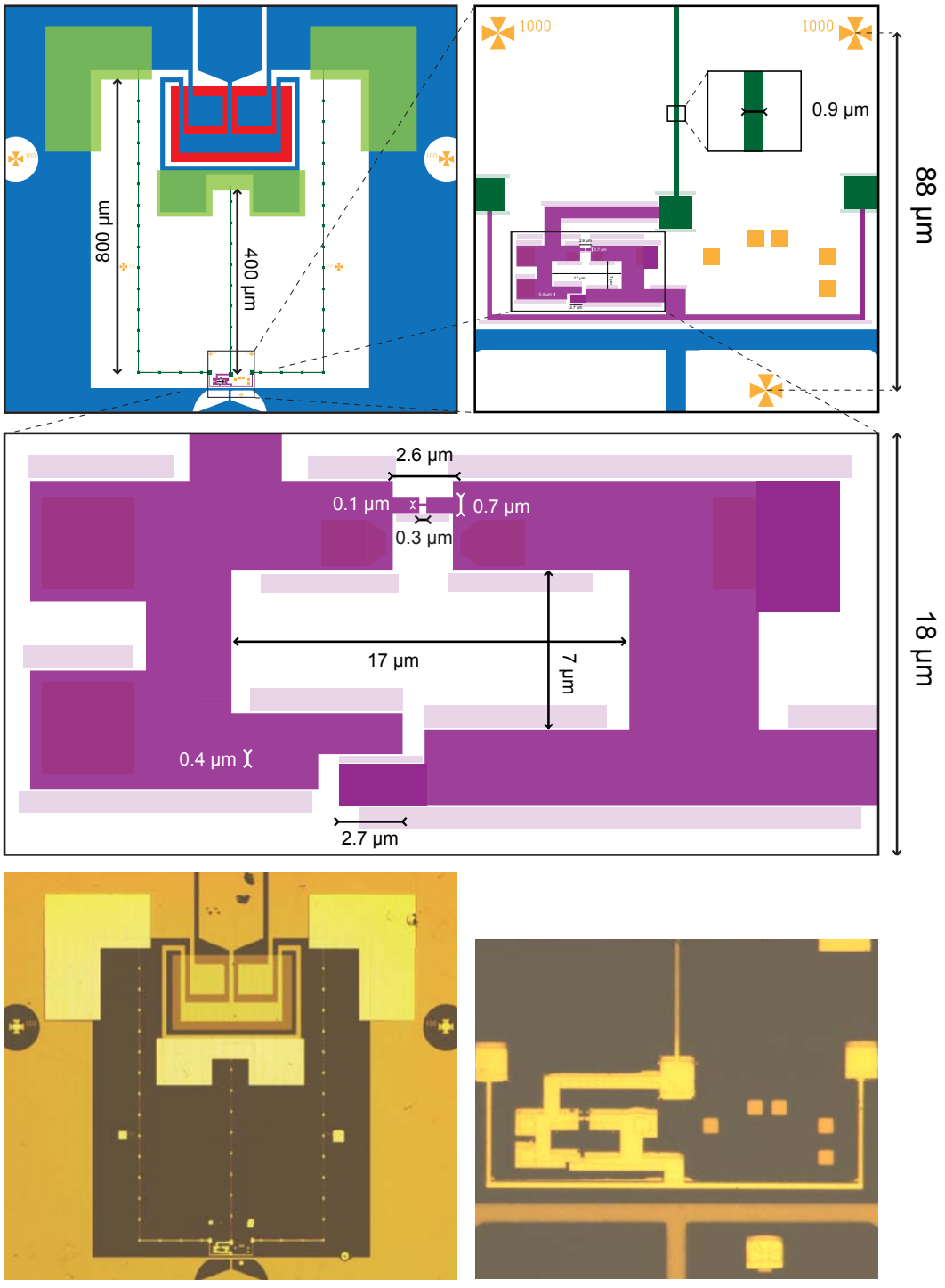

Figure 9.3: **Top**: e-beam lithography design of sample PAL7 at three different magnifications. One first draws the atomic-SQUID (**purple**) and then the inductive lines and large contact pads (**green**). Semi-transparent areas are undercut boxes. The **red**, **blue** and **yellow** patterns were done in a former step by optical lithography (see Fig. 9.1). **Bottom**: optical micrograph of sample PAL7 at two magnifications corresponding to the drawings on the top.

Then, the exposed chip is developed. The PMMA bridge formed with e-beam lithography is used to form a tunnel junction, using the shadow mask evaporation technique:

- 70 nm of aluminum are deposited at 1 nm/s under zero angle;
- oxidation follows at 18.2 mbar for 5 min in Ar-O_2 (85% – 15%);
- finally, 54 nm of aluminum is deposited at 1 nm/s under an angle of 53°.

The resulting overlaps are visible in the bottom left picture of Fig. 9.4.

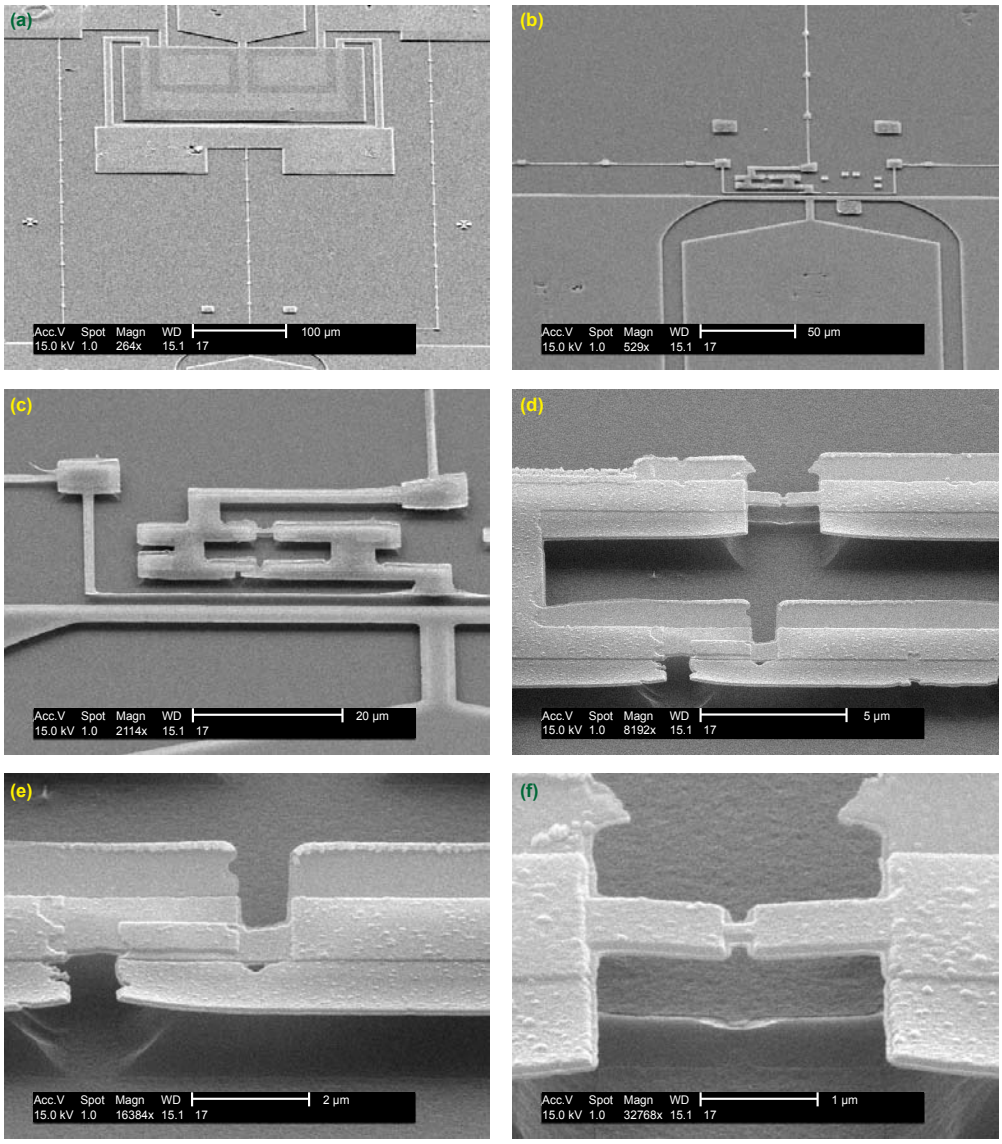

Figure 9.4: SEM micrograph of sample PAL7 at different magnifications and under a tilt angle. **(a)** Capacitor; **(b)** the SQUID loop and the fast flux line, large scale and **(c)** small scale; **(d)** SQUID loop with JJ (enlarged in **(e)**) and bridge for atomic contacts (enlarged in **(f)**).

At last, the sample is etched by a reactive ion etching (see Section 9.3.4) to suspend the bridge, as shown in the bottom right picture of Fig. 9.4.

In sample PAL7 (see Fig. 9.4), the Josephson junction has an area of 2.8 μm^2 and a critical current $I_0 = 554\,nA$ (resistance $R_J = 550\,\Omega$). The aluminum wires correspond to an inductance per unit length of 1.2 nH/mm.

9.2 Sample JT6 for spectroscopy experiment

The fabrication of sample JT6 was simpler since it required only two e-beam lithography steps and no optical lithography. For this sample, we have developed a new technique to form capacitors consisting in directly depositing an aluminum oxide dielectric layer by e-beam evaporation.

9.2.1 *Bronze wafer preparation*

In the spectroscopy experiments, since both bias and measurements are made at low-frequency, on-chip coplanar waveguides are not needed and it is not compulsory to fabricate on an insulating substrate. We have used for simplicity commercial 300 µm-thick bronze plates ($CuSn_3Zn_9$, chrysocal in french), which present three advantages:

- They are already polished.
- It is easier to perform e-beam lithography on a metallic substrate (no charging effects).
- When bending the sample, the heat is evacuated much faster.

A polyimide layer is spun on the whole wafer. The conditions are the same as in Section 9.1.1. The measured thickness of the layer is 2 µm.

9.2.2 *First electron beam lithography lithography*

A 10 cm × 5 cm wafer is prepared for e-beam lithography. A wafer contains 10 12.5 mm × 12.5 mm chips. The pattern shown in red in Fig. 9.5 is drawn into the resist to obtain the bottom capacitor electrodes (500 × 250 µm) and the alignment crosses. Then, the exposed wafer is developed.

9.2.3 *Capacitor fabrication*

The geometry of the capacitors is similar to the one presented in Fig. 9.1.2. However, for these samples, we have developed a new technique to form the dielectric. The aim of this first fabrication step is twofold: define alignment crosses and obtain bottom electrodes for the capacitors. Capacitor electrodes need to be superconducting and therefore one uses aluminum. But aluminum does not have enough contrast for subsequent alignment and it is better to have gold. The solution is to deposit both, and to separate them by an insulator to avoid inverse proximity effect in the aluminum. As a consequence, the following sandwich is deposited:

- 1.9 nm of titanium at 0.2 nm/s under an angle of 20° (adhesion layer);

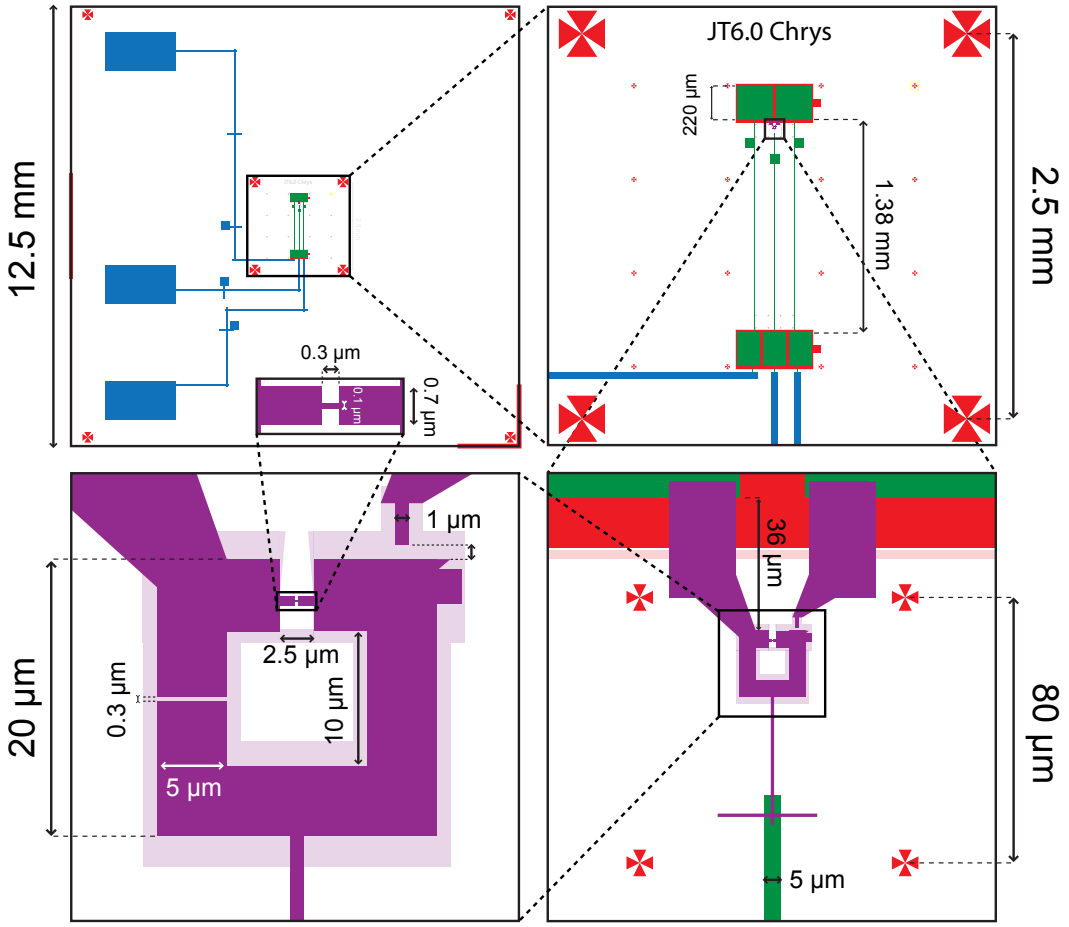

Figure 9.5: e-beam lithography design of sample JT6 at four different magnifications. During the first step, one patterns the bottom capacitor electrodes and alignment crosses (**red**). During the second one, one draws the atomic-SQUID and the JJS (**purple**), the inductive lines and top capacitors (**green**) and the large scale connecting wires (**blue**). Semi-transparent areas are undercut boxes.

- 14 nm of gold at 0.1 nm/s under an angle of 20° (contrast layer);
- 2.8 nm of aluminum oxide at 0.1 nm/s under an angle of 20° (buffer layer);
- 23.5 nm of aluminum at 0.1 nm/s under an angle of 20° (bottom capacitor electrode);
- oxidation follows at 300 mbar for 3 min in Ar-O_2 (85% – 15%) to insure a layer of insulator on all side of the bottom capacitor electrode;
- 54 nm of aluminum oxide at 0.1 nm/s under an angle of 40° (dielectric layer);
- before venting, the sample is placed at 800 mbar for 3 min in Ar-O_2 (85% – 15%).

To ensure that the whole bottom metallic electrode is covered by dielectric, all these angle-evaporations are performed under a constant planetary rotation at 19°/s (maximum speed available in our machine) and at the lowest possible rates.

With this technique (after deposition of the top electrode, see next step), a capacitor of $0.57 \pm 0.01\,\mathrm{nF/mm^2}$ was obtained with a good reproducibility. This is ~ 10 times smaller than with the previous technique, which is compatible with the oxide thickness which is ~ 6 times larger. At dc, the capacitor leakage was measured above $6\,\mathrm{M\Omega}$. For sample JT6, this gives a coupling capacitor $\Sigma \simeq 28.8$ pF and a filtering capacitor $C \simeq 18.3$ pF.

9.2.4 *Second electron beam lithography lithography*

The wafer is again prepared for e-beam lithography and cut into samples using a guillotine or scissors. The pattern shown in Fig. 9.5 (in purple, green and blue) is drawn in the resist to obtain the top capacitor electrodes, the inductive lines and the atomic-SQUID loop for sample JT6:

- The $20 \times 20\,\mu\mathrm{m}$ loop containing the bridge and the junction, as well as the spectroscopy Josephson junction (purple pattern in the bottom panels of Fig. 9.5) are aligned on the alignment crosses. Because the JJS is small, it gets suspended during the RIE (see Fig. 9.7 (e,f)). To prevent it from breaking during the bending, it is placed perpendicular to the bending direction.
- The SQUID and the JJS are connected to two $230 \times 220\,\mu\mathrm{m}$ rectangular electrodes which form the top electrodes of the coupling capacitor, to three narrow (5 µm) and long (1.38 mm) lines which form the inductor and to three $146 \times 220\,\mu\mathrm{m}$ rectangular electrodes which forms the top electrodes of the environment capacitors, represented in green in the top right panel of Fig. 9.5.
- The large scale connecting wires (40 µm-width) and contact pads ($2\,\mathrm{mm} \times 1.1$ mm) are patterned (blue drawings in the top left panel of Fig. 9.5).

Then, the exposed chip is developed and a two-angle evaporation is performed:

- 50 nm of aluminum are deposited at 1 nm/s under zero angle;
- oxidation follows at 300 mbar for 3 min in Ar-O_2 ($85\% - 15\%$);
- finally, 78 nm of aluminum is deposited at 1 nm/s under an angle of 53°.

At last, the sample is etched by reactive ion etching to suspend the bridge (see Section 9.3.4).

In sample JT6 (see Fig. 9.6 and Fig. 9.7), the JJ of the SQUID had an area of $\sim 4.7\,\mu\mathrm{m}^2$ and a critical current $I_{L0} = 1.06\,\mu\mathrm{A}$ (resistance $R_L = 285\,\Omega$). The JJS of the SQUID had an area of $\sim 0.23\,\mu\mathrm{m}^2$ and a critical current $I_{J0} = 48\,\mathrm{nA}$ (resistance $R_J = 6.3\,\mathrm{k\Omega}$). The total capacitance of the junctions $C_t = C_{L0} + C_{J0}$ was found by fitting the anti-crossing between the Andreev and plasma mode in contact U (see Section 7.2.2): $C_t \simeq 280$ fF. This gives a conversion factor 57 $\mathrm{fF/\mu m^2}$, which 30% smaller than the factor 75 $\mathrm{fF/\mu m^2}$ given in Section E.1 for sample PAL7. This is explained by the fact that the oxidation was performed at higher pressure, which gives a thicker oxide layer[3]. The aluminum wires corresponded to an inductance

3 Characterization of oxide layer thicknesses was performed using the quartz crystal monitor in the evaporator. It was found that when oxidizing at 800 mbar the thickness is 30% larger than at 100 mbar.

per unit length 345 pH/mm ($L/2 \simeq 716$ pH, also found from fit). This is compatible with an estimation obtained with Sonnet calculation, which gives ~ 0.3 pH/µm for a 2 µm-thick polyimide layer with dielectric constant 2.7 [122].

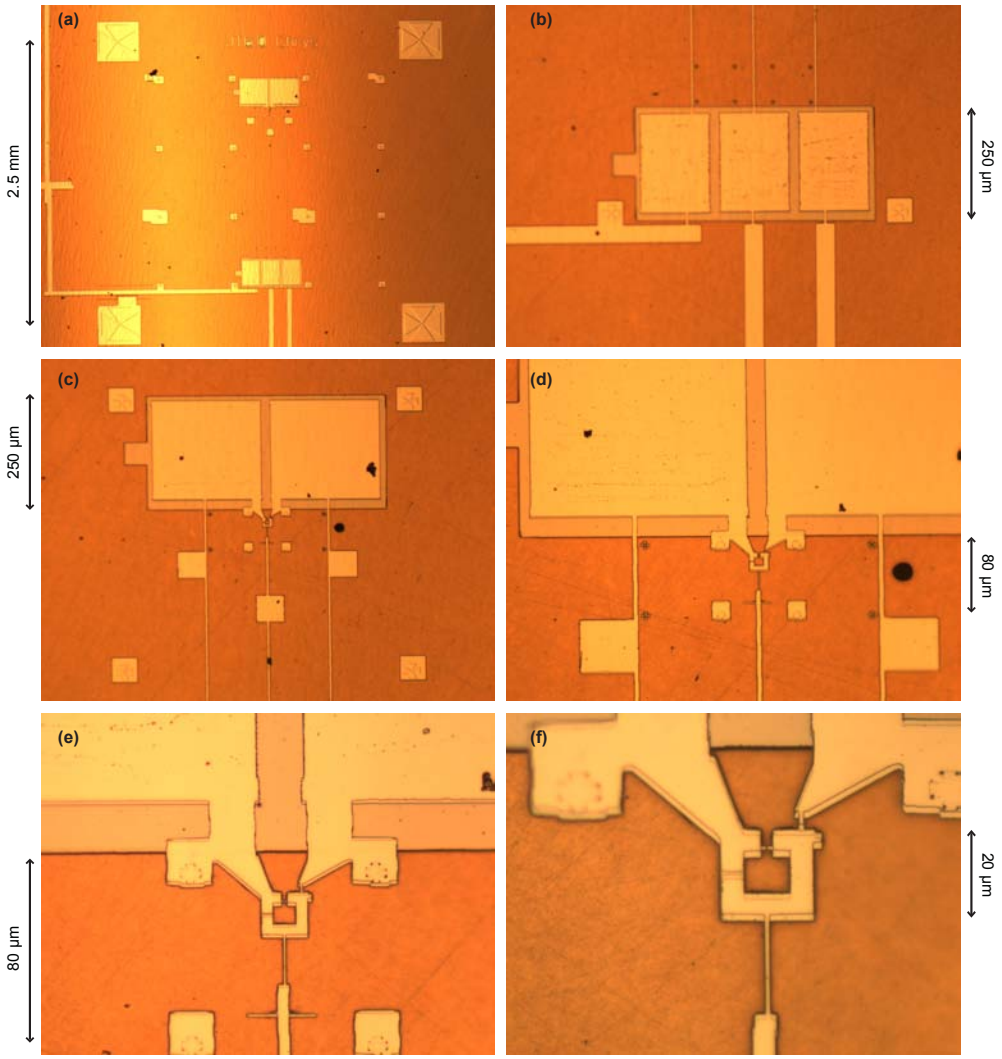

Figure 9.6: **O**ptical micrograph of sample JT6 at different magnifications: **(a)** large scale connecting wires, capacitors and inductive lines; **(b)** filtering capacitors; **(c)** coupling capacitors; **(d,e,f)** SQUID loop and JJs.

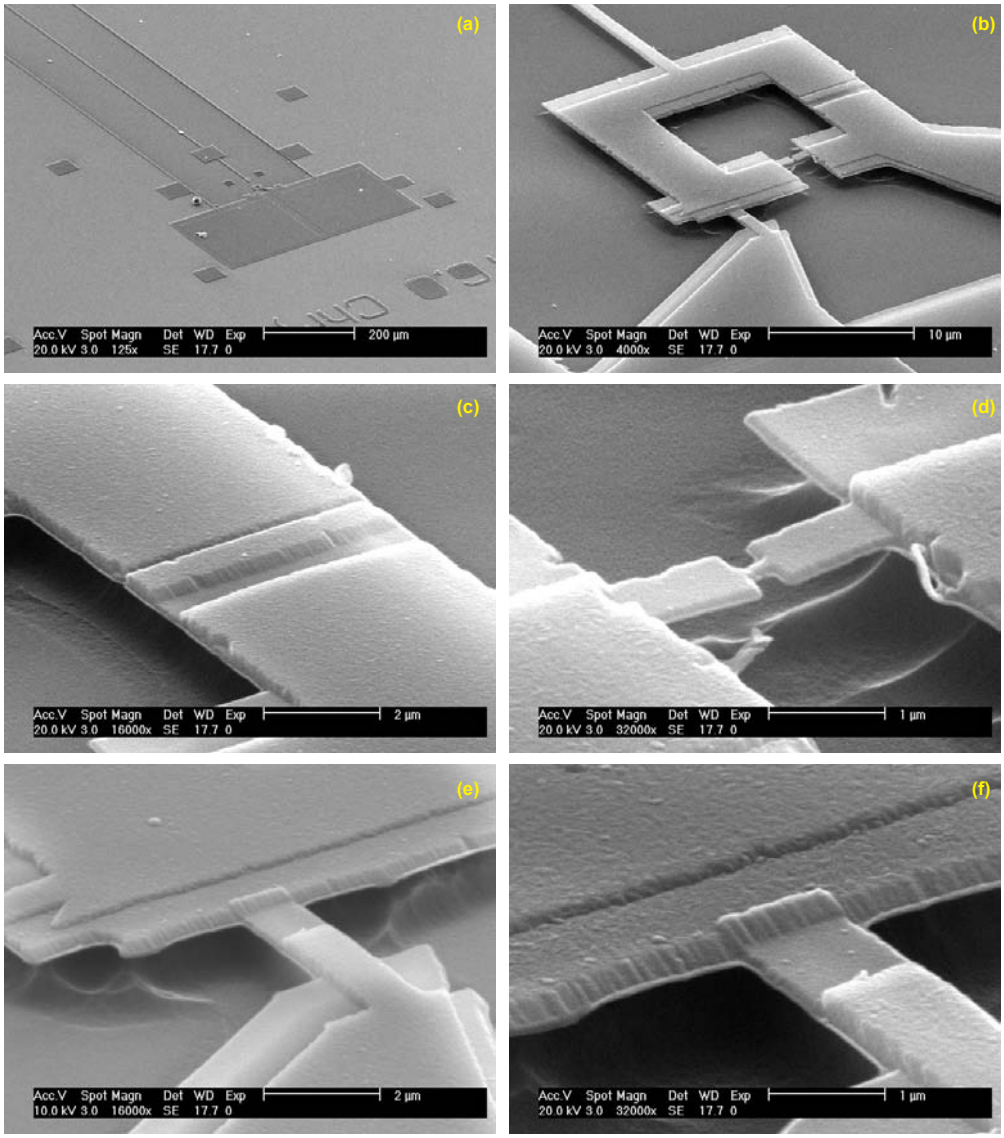

Figure 9.7: SEM micrograph of sample JT6 at different magnifications: **(a)** capacitors and inductive lines; **(b)** SQUID loop and JJS at large scale; **(c)** JJ of the SQUID; **(d)** bridge for atomic contacts; **(e,f)** JJS. The six pictures are taken under both tilt and planetary angle.

9.2.5 *Sample JS6*

Sample JS6 was fabricated before sample JT6 and is very similar, with essentially two differences:

- It was fabricated on a Kapton substrate[4] (see recipes in Section 9.1.1).
- As shown in Fig. 9.8, the SQUID and JJS (purple) were designed in a different way (similar to the one of sample PAL7). However, the large scale patterns (red, blue, green) are identical for sample JS6 and JT6 (top panels of Fig. 9.5).

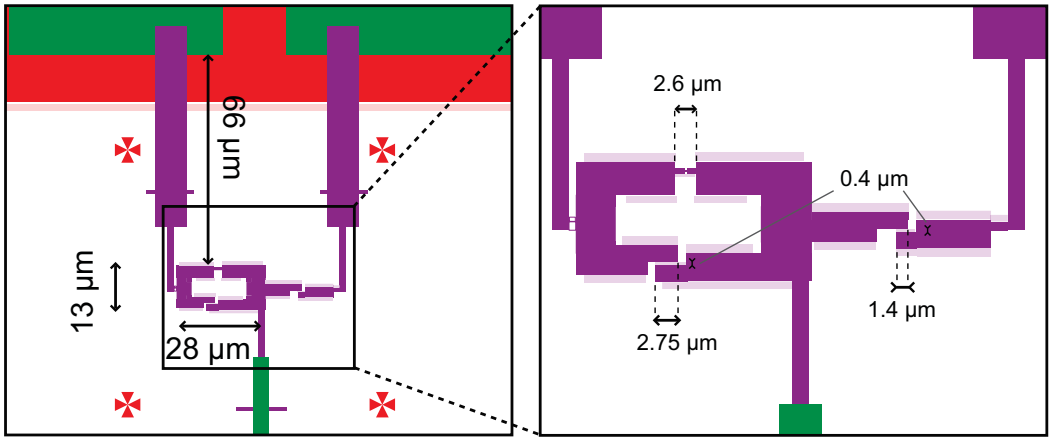

Figure 9.8: e-beam lithography patterns of sample JS6 at high magnifications. The low magnification patterns (**red**, **blue**, **green**) are identical to the one of sample JT6 (top panels of Fig. 9.5). However, the atomic-SQUID and the JJS (**purple**) have a different design and are further from the coupling capacitors. Semi-transparent areas are undercut boxes.

In sample JS6 (see Fig. 9.9), the JJ of the SQUID had an area of $\sim 2.23\ \mu m^2$ and a critical current $I_{L0} \simeq 320\,nA$ (resistance $R_L \simeq 945\,\Omega$). The JJS of the SQUID had an area of $\sim 1.05\ \mu m^2$ and a critical current $I_{J0} \simeq 150\,nA$ (resistance $R_J \simeq 2\,k\Omega$).

4 For JT6, we switched to chrysocal because we were short of polished Kapton wafers and because it is easier to perform e-beam lithography on metallic substrates.

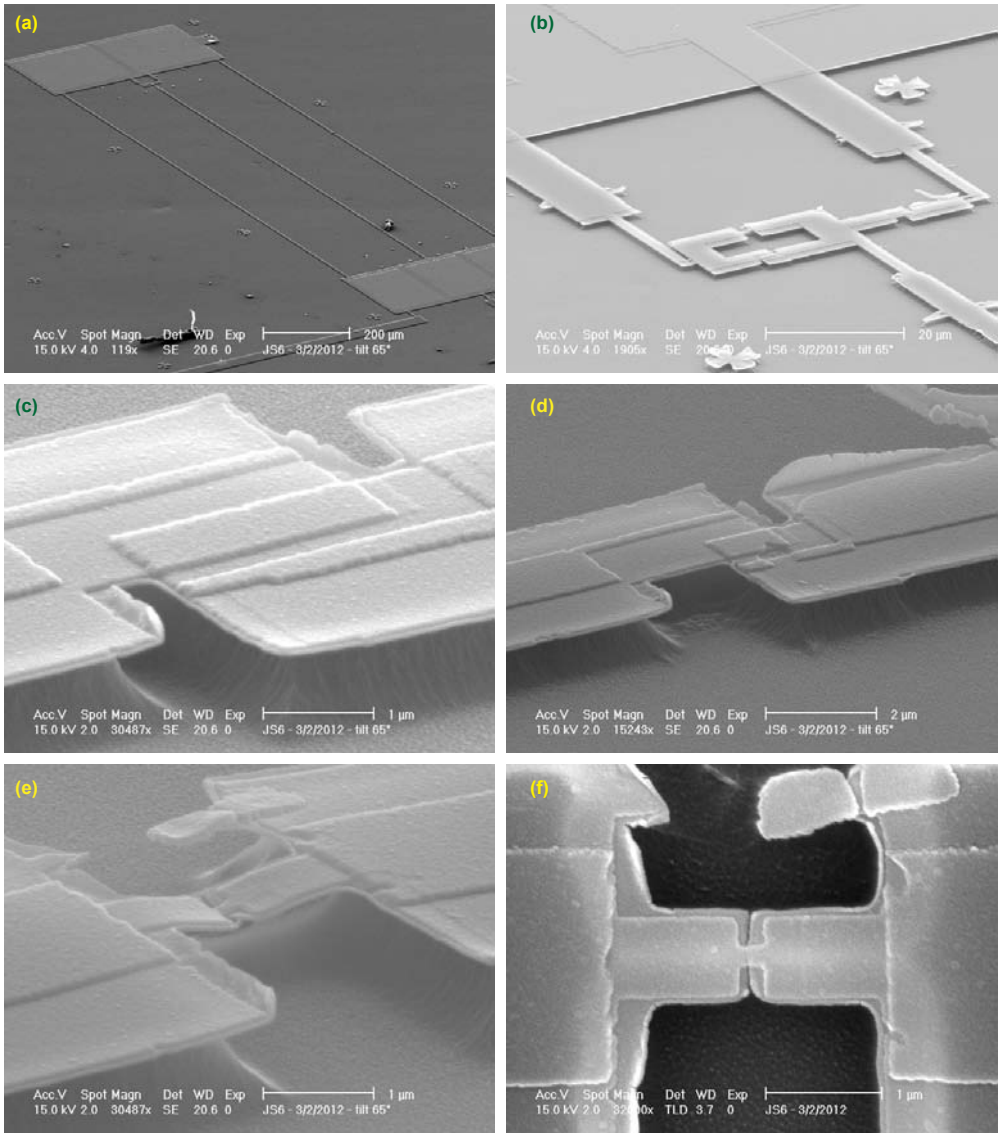

Figure 9.9: SEM micrograph of sample JS6 at different magnifications: **(a)** capacitors and inductive lines; **(b)** SQUID loop and JJS at large scale; **(c)** JJ of the SQUID; **(d)** JJS; **(e,f)** bridge for atomic contacts. The first five pictures are taken under both tilt and planetary angle.

9.3 Nano-fabrication recipes

The fabrication of the samples required both photo-lithography and e-beam lithography. The principle of lithography relies on the use of resist coatings, sensitive either to UV light or to an electron beam. In both cases, multilayers were used to allow for angled evaporation. The exposed regions are dissolved in a development step, leaving cavities where metal is deposited by evaporation. The resist is then removed (lift-off process), and the metallic design is revealed. We give in this section the parameters of the various recipes that we used.

9.3.1 *Optical lithography*

Optical-lithography is in general used for designing patterns at a resolution above 1 µm. Several samples are patterned simultaneously on a single wafer. The masks were drawn using AutoCad. They were fabricated in chromium on quartz glass by Toppan Photomasks.

9.3.1.1 *Resist-spinning: LOL2000 + S1805*

Prior to resist deposition, a primer (Shipley Microposit) is deposited on the wafer, and after 30 s waiting time, spun 60 s at 3000 rpm (speed reached in 2 s). Filtered Shipley resist LOL2000 is poured and spun at 3000 rpm during 60 s, then baked at 155 °C on a hot plate for 5 min, resulting in a thickness of typically 200 nm. Shipley resist S1805 is then poured and spun at 2000 rpm during 60 s, then baked at 120 °C on a hot plate during 60 s. The layer thickness is 500 nm.

9.3.1.2 *Exposure and development*

The wafer is then exposed through a chromium mask using a mask aligner. Two different mask aligners were used:

- A MJB3-SUSS Aligner: lamp with power density 5 mW/cm^2, 15 s exposure time.
- A MJB4-SUSS Aligner: lamp with power density 25 mW/cm^2, 3 s exposure time.

The wafer is developed during 37 s in MF-319 (Shipley) and then dipped in water to stop development.

9.3.2 *Electron-beam lithography*

9.3.2.1 *Resist-spinning: MMA/PMMA bilayer*

A bottom layer of meta-acrylate/meta-acrylate acid (MMA/MAA (8.5) EL 10 from MicroChem) is spun at 2000 rpm during 60 s, then baked at 170 °C on a hot plate for 90 s. This step is performed twice to obtain a thickness of 900 nm.

A top layer of polymethyl-meta-acrylate (PMMA A6 950 from MicroChem) is deposited and spun at 5200 rpm during 60 s, then baked at 170 °C during 15 min, yielding a typical thickness of 250 nm.

9.3.2.2 *Additional conducting layer*

When using an insulating Kapton wafer (samples PAL7 and JS6), the resist is finally covered with 7 to 10 nm of aluminum, deposited at 0.1 nm/s, to avoid charging effects. After exposure and before development, this layer is removed in a bath of potassium hydroxide (KOH) during ~ 1 min, then cleaned with isopropanol.

9.3.2.3 *Exposure and development*

The sample is exposed in a Philips XL30 SFEG scanning electron microscope using Elphy Quantum from Raith. The electron beam is steered on the areas of the resist that are to be removed. The time spent on each zone depends on the current, and is fixed to yield a typical charge density of 250 $\mu C/cm^2$ (fine details are exposed with a density increased by a factor up to 1.6). The exposure is performed with a beam current in the range of 15 pA for the smaller details, and up to 70 nA for coarse patterns (such a current results in a loss of resolution which is then unimportant).

For sample JS6 on Kapton wafer, the patterning of the top capacitor electrodes was performed in several passes, to reduce charging effects and avoid cracking of the dielectric.

The sample is then developed in methyl-iso-butyl keton (MIBK) diluted 1:3 in volume with isopropanol for 35 s to 55 s depending on the design (a longer development time allows larger undercut). This development removes both the exposed PMMA and the MMA/MAA. After this development step, the sample is dipped for 25 s in isopropanol.

9.3.3 *Material deposition and lift-off*

Metals used in our experiments (aluminum, gold, titanium, copper) as well as aluminum oxide were evaporated in the same electron gun evaporator (fabricated by PLASSYS), which is free of magnetic materials, thus avoiding contamination. In the load-lock chamber, where the sample sits, the pressure is in the $10^{-7} - 10^{-6}$ mbar range. The material sources are located in the lower chamber about 40 cm below the sample and at a pressure of 10^{-8} mbar.

A high voltage (~ 10 kV) electron gun sublimates the target material. The evaporated atoms enter the load-lock chamber and deposit on the sample. The rate of deposition is measured in real time with a quartz crystal monitor and is tuned typically between 0.1 nm/s and 1 nm/s depending on the material. At the low pressures considered, deposition is anisotropic. The sample holder can be tilted and rotated in a planetary way, thus allowing for angled evaporations in all directions.

When needed, oxidation is performed in the load-lock isolated from the main chamber. A mixture of 85 % argon, 15 % oxygen is leaked in the load-lock for ~ 5 min.

To get good contacts between layers obtained in different lithography steps, ion milling with an argon plasma (about 10^{-4} mbar of argon, $V = 500\,V$ and $I = 5\,mA$ during $\sim$ 3 s) is performed in the evaporator chamber prior to the deposition. Resists are not altered significantly by this treatment.

Lift-Off

OPTICAL RESIST After deposition, the resist is removed in acetone and ultrasonic bath during $\sim$ 5 min. It is then dipped between 5 and 10 min in R1165 remover (Shipley) to get rid of resist residues.

E-BEAM RESIST After deposition, the resist is removed in a hot acetone bath (65 °C) during $\sim$ 20 min.

9.3.4 *Reactive ion etching*

To suspend the bridge, the polyimide underneath is etched by reactive ion etching (RIE). The sample is placed in the chamber of the RIE machine (fabricated by PLASSYS), on a hot, large metallic block (previously heated on a hot plate at 175°C) which maintains the sample at $\sim$ 170°C during the etching. This increases the etching rate and makes it more isotropic. The chamber is pumped down to a few 10^{-5} mbar.

Under 45 V, a flow of 50 sccm of O_2 and 2 sccm of SF_6 (at a total pressure of 0.25 mbar) is ionized thus forming a plasma which etches the polyimide. The vertical etch depth is monitored by laser interferometry ($\sim$ 3.5 fringes). Typically, the etching time is $\sim$ 1 min. Etching 1 µm in the vertical direction is sufficient to free the metallic bridge from the surface, and suspend it over 2 µm.

10 LOW TEMPERATURE MEASUREMENTS

10.1 Sample Holder

To form atomic contacts, we have used the mechanically controllable break junction technique presented in detail in Refs. [85, 78].

The sample holder and bending mechanism used for Samples PAL7, JT6, and JS6 have been developed during the thesis of Quentin Le Masne (see p. 218-219 of Ref. [72]). Photographs of the setup are shown in Fig. 10.2. Samples were clamped on one side by two screws pressing the sample between a small copper plate placed underneath and the half-cylindrical central pins of two SMA launchers, which connect to the bias and fast flux lines. Connections of the ground plane to the sample holder were achieved in the same manner. Small indium pads placed on the contact pads and on the ground plane allowed for more reliable contacts. On the opposite side, a pusher displaced with a micro-metric screw could bend the sample (see Fig. 4.1 (e). This setup was intended to achieve efficient and flat coupling of the microwaves.

In the case of samples PAL7 and JS6 , the substrate was made of Kapton, an elastic insulating material. In the case of sample JT6, the substrate was made of a bronze alloy (chrysocal), a flexible metal. Compared to Kapton, its bending radius is smaller. To obtain a more distributed bending, we have designed a new shim, made out of bronze, with a circular profile (see Fig. 10.1).

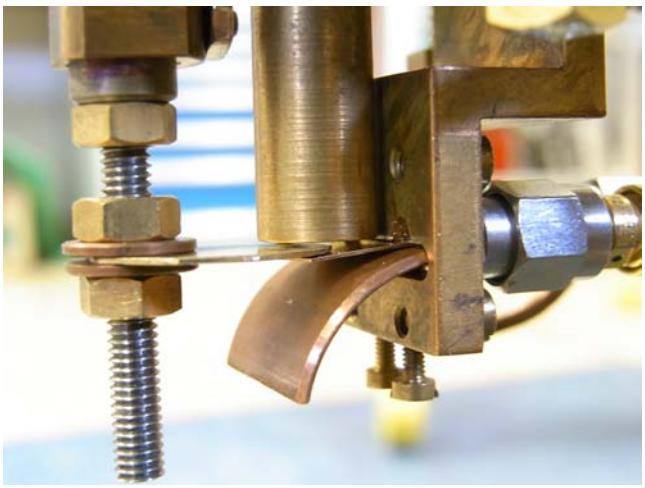

Figure 10.1: Bending setup for sample JT6 fabricated on a bronze substrate. We have used a curved shim made out of copper, to obtain a more distributed bending.

Note that in all experiments involving an atomic-SQUID, a superconducting coil was placed 1 mm above the superconducting loop, for dc flux biasing. It is visible in Fig. 10.2 (a) and has been withdrawn before taking the picture in Fig. 10.2 (b). The

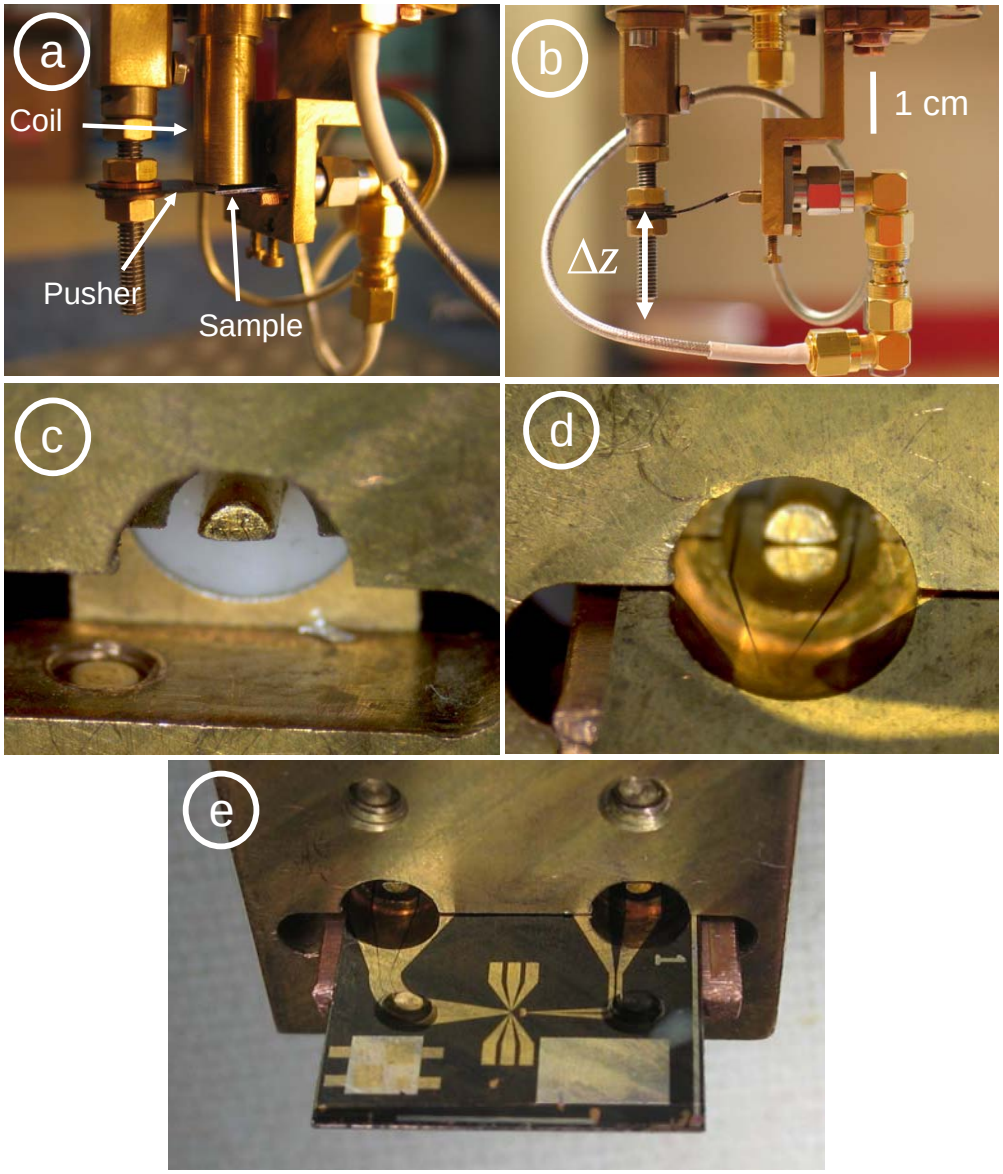

Figure 10.2: Sample holder used for the measurements on samples PAL7, JS6 and JT6. **(a,b)** The sample (on a 14 mm × 14 mm, 500 µm thick Kapton substrate) is held tightly against two SMA launchers, by pushing with two screws a small piece of copper, also visible in **(d)** and **(e)**, on the back of the substrate. A small superconducting coil is placed in a copper electrostatic shield placed immediately above the sample (the coil is absent in **(b)**). In **(a)**, the sample is not yet bent, in **(b)** the bending is exaggerated. **(c)** SMA Launcher, without sample; one of the pushing screws shows out on the bottom left; **(d)** SMA launcher with sample: the pin contacts the central line of the coplanar waveguide on the sample; **(e)** sample in position (coil and pusher removed) The right launcher connects to the current bias line. The left to the microwave antenna.

whole setup shown in Fig. 10.2 was enclosed in an (superconducting) aluminum box to shield from electromagnetic noise.

10.2 Cryostat wiring

All experiments were performed in an Oxford Kelvinox 300 dilution refrigerator with a base temperature of 20 mK.

Bias lines connected to the SQUID and to the antenna (in experiment PAL7) were large bandwidth coaxial lines, equipped with discrete XMA attenuators (Omni Spectra®). A large attenuation is necessary to reduce the amplitude of the Johnson-Nyquist noise associated with the room temperature impedances [132]. The total attenuation was between 50 and 60 dB for the bias lines and 30 dB for the antenna[1]. In addition to the attenuators, two different types of filters were used on the bias lines to further reduce the noise: MiniCircuit® low-pass filters [133] (cutoff frequency between 15 MHz and 1.3 GHz) and Marki® low-pass filters (1.55 GHz cutoff frequency). This set of attenuators and filters allows to reduce the noise temperature of the experiment below 100 mK.

The coil responsible for the dc flux was biased through a heavily attenuated twisted pair.

To measure currents and voltages at low frequency, we performed differential voltage measurements using lossy twisted pairs, which act as RC distributed filters above a few MHz. Each of theses lines was equipped, at the lowest temperature stage, with a micro-engineered RC distributed low pass filter (below a few MHz) [132, 134].

In the reflectometry experiment on sample PAL7, a bias tee (Anritsu K250) and a directional hybrid coupler (Pasternack) were also used to allow for both dc biasing of the atomic-SQUID and rf coupling. In the reflectometry experiment on samples RAC, the wiring was quite different to access high frequency (up to 14 GHz). In particular, cryogenic circulators (Pamtech) and a cryogenic microwave amplifier (Caltech) were used.

The wiring used for each experiment is presented schematically in Fig. 10.3, Fig. 10.4, Fig. 10.5 and Fig. 10.6.

1 Since the attenuators, made of resistive films, themselves cause Johnson-Nyquist noise, they are thermally anchored to the cryostat. The positioning of the attenuators is determined as follows:

- One first determines the total attenuation needed to obtain the amount of noise on the sample tolerated in the experiment.
- This attenuation is then distributed at different temperature stages of the cryostat. Considering the maximum amplitude of the signals used in the experiment, the power dissipated by each attenuator is not allowed to exceed the cooling power of the refrigerator at the stage where it is attached. Due to this constraint, all attenuators cannot be placed at the base temperature.
- At last, one checks that the total noise due to the chain of attenuators placed at various temperatures is acceptable.

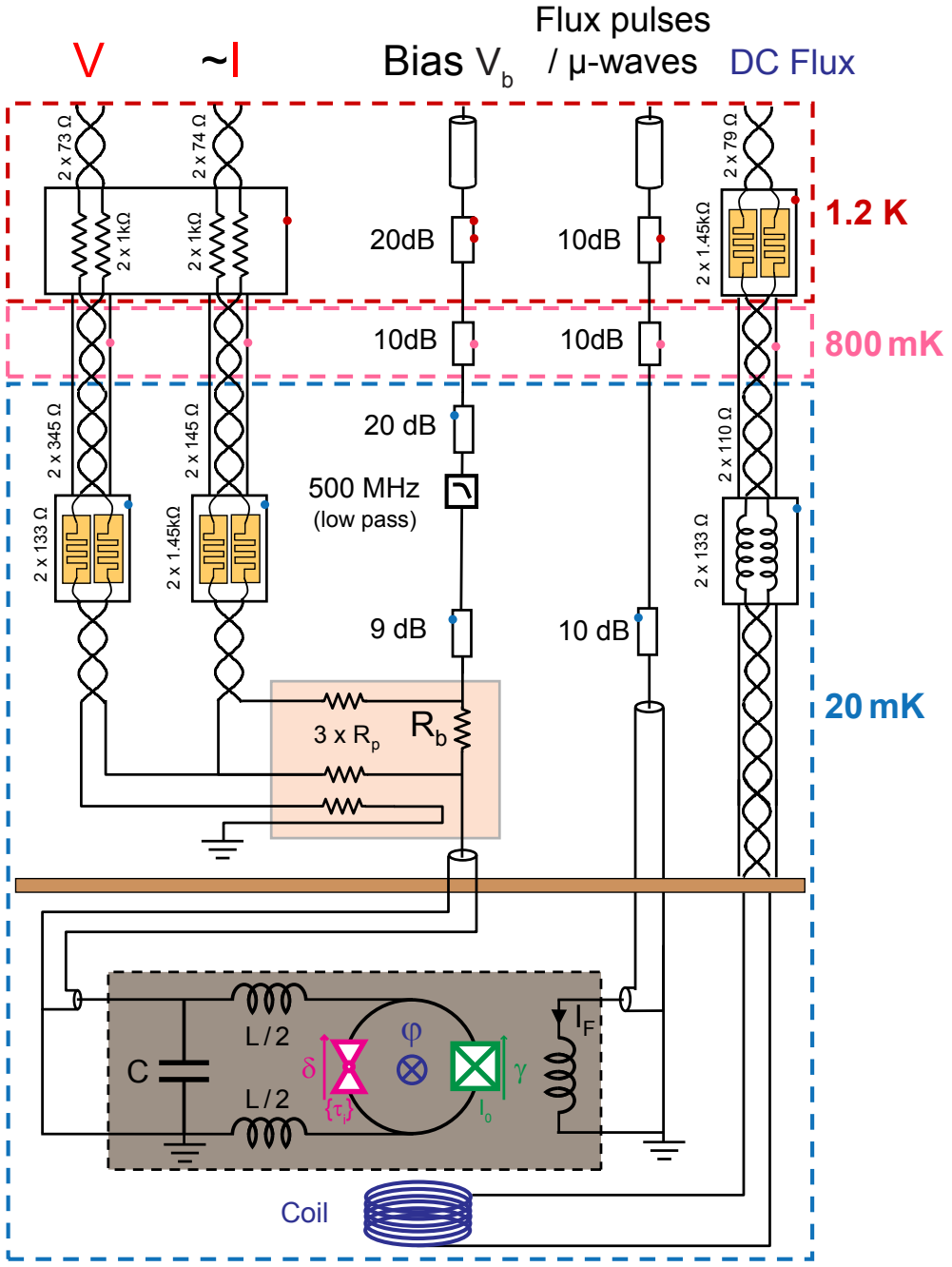

Figure 10.3: Cryostat wiring used for the switching experiment with sample PAL7. The measurement pulses are sent through the bias line, which is heavily attenuated (XMA attenuators) and filtered (MiniCircuit filter) with commercially available components. Two twisted pairs terminated by series resistors $R_p = 1\,\mathrm{k}\Omega$ allow to measure the dc voltage and current of the SQUID. The boxes with meander lines symbolize home-made microfabricated filters. The current is determined accurately from the voltage across a bias resistor R_b ($= 198\,\Omega$ at 4 K) placed at 20 mK. The microwave line feeding the on-chip flux antenna is only equipped with attenuators. The dc flux biasing line feeding the coil is also heavily attenuated.

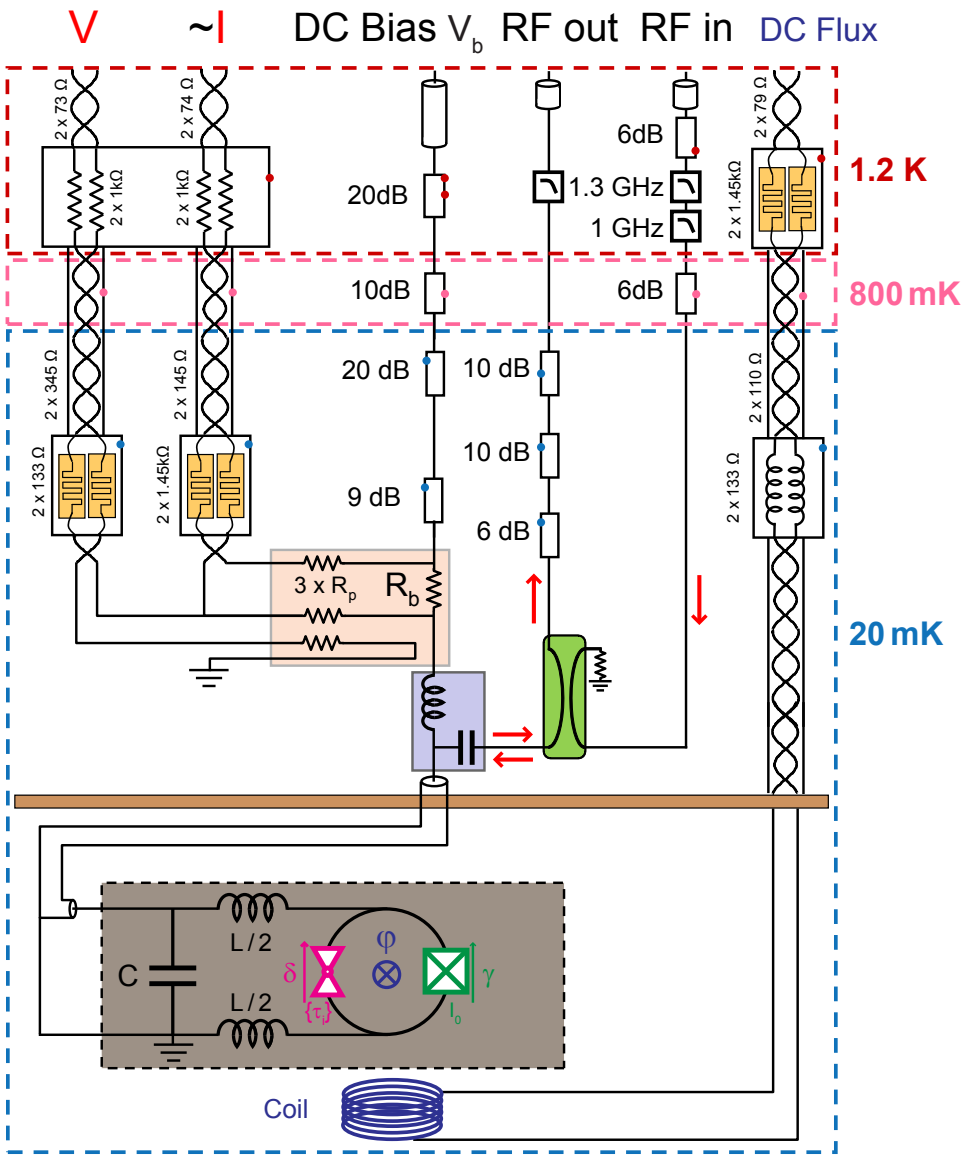

Figure 10.4: Cryostat wiring used for the reflectometry experiment with sample PAL7. A bias tee (Anritsu K250) (blue, $c = 1$ nF and $l = 0.9$ µH) allows both dc bias of the atomic-SQUID and rf coupling. A microwave signal is sent to the sample through the input line (RF in) and one measures the reflected signal channeled by a separate output line (RF out). These two lines are both heavily attenuated (XMA attenuators) and filtered (MiniCircuit filters) coaxial lines. A directional hybrid coupler (Pasternack) (green) allows for the isolation ($r' = 50\,\Omega$, coupling 20 dB, leak 40 dB) between the input and output line.

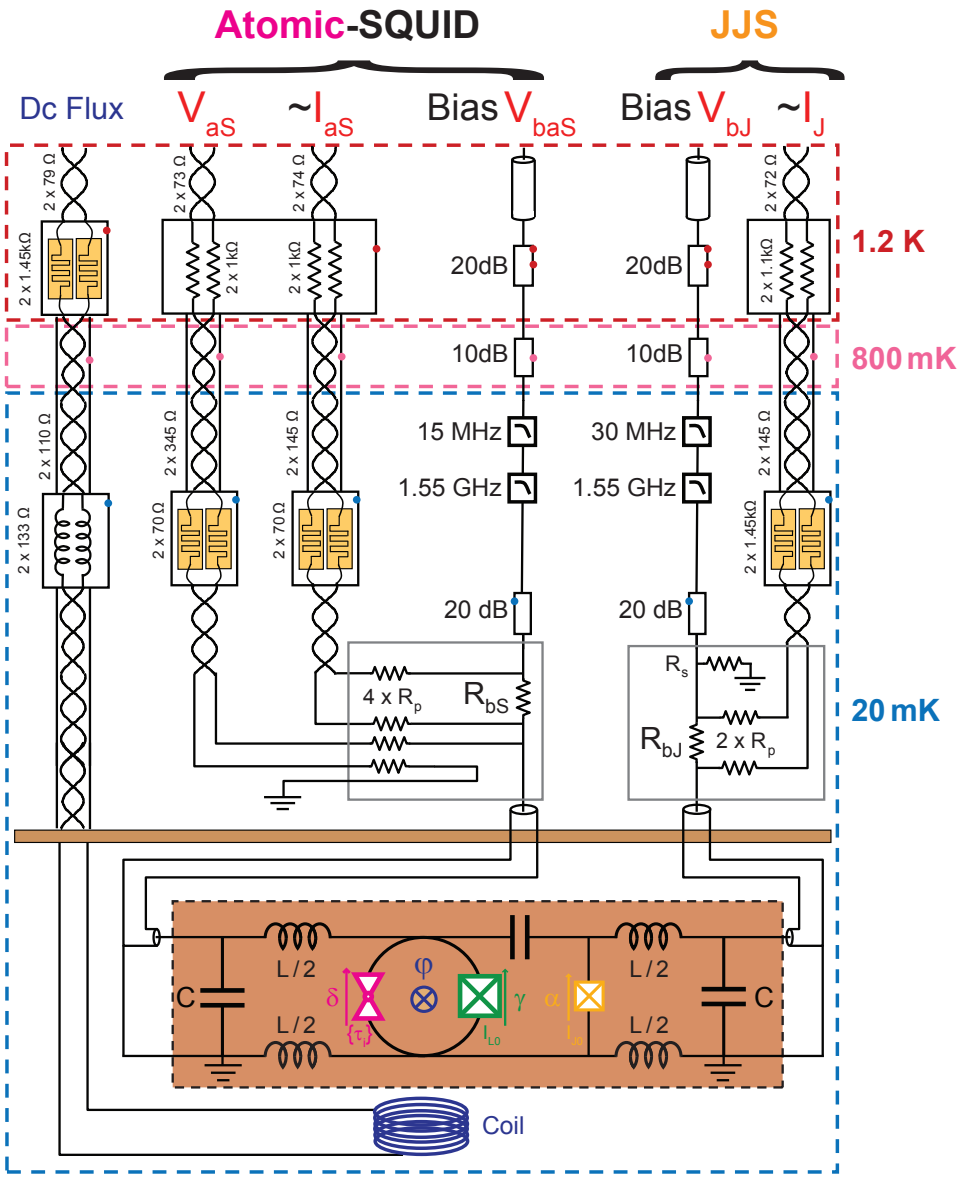

Figure 10.5: Cryostat wiring used for samples JS6 and JT6. In addition to the dc flux biasing line feeding the coil and to the bias and measurement lines of the atomic-SQUID (which are similar to experiment on sample PAL7), a heavily attenuated (XMA attenuators) and filtered (MiniCircuit + Marki filters) coaxial line feeds the JJS. Only the current through the JJS is measured. The resistors values are $R_p = 1.2\,k\Omega$, $R_s = 51\,\Omega$, $R_{bS} = 198\,\Omega$ and $R_{bJ} = 2\,k\Omega$.

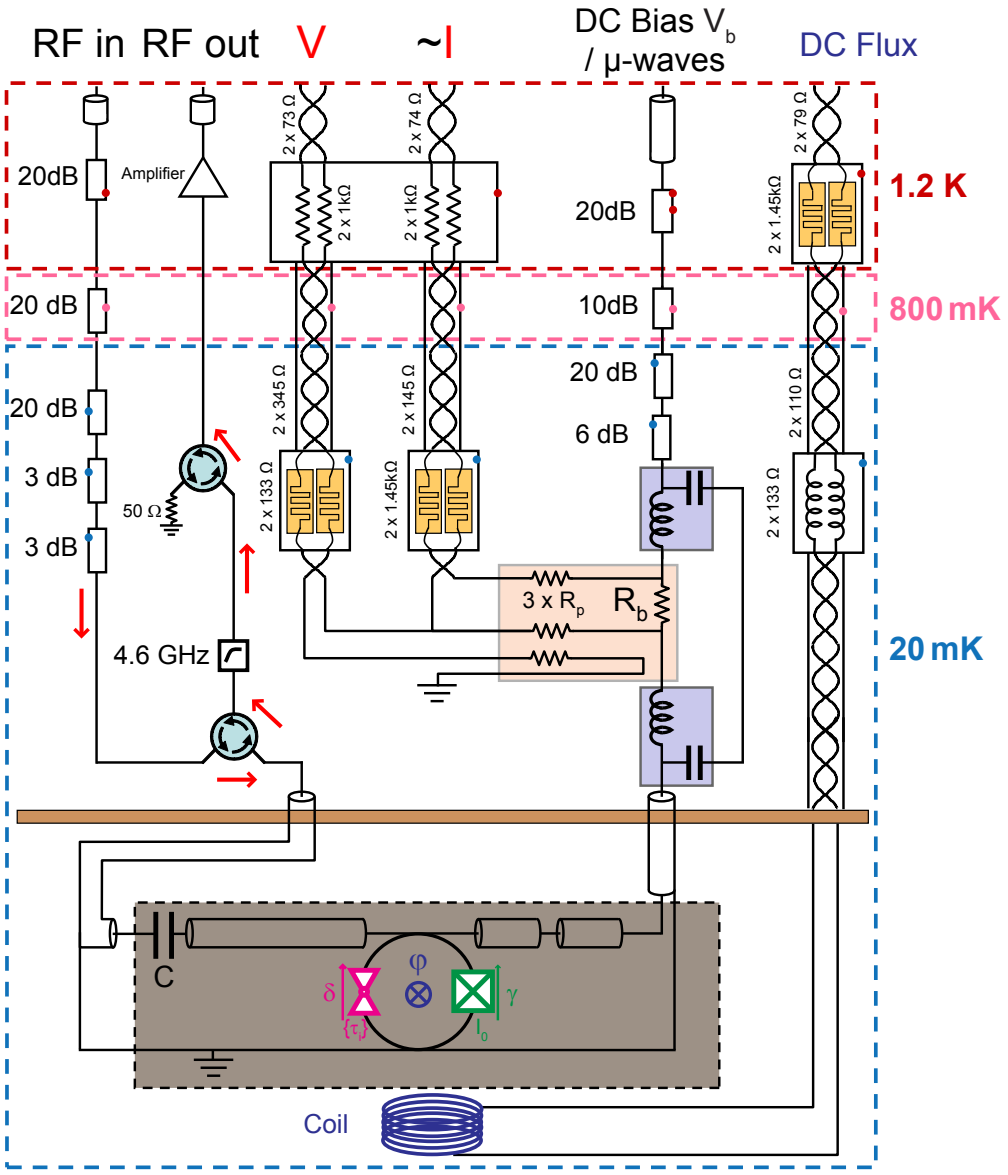

Figure 10.6: Cryostat wiring used for samples RAC. **Left**: A microwave signal is sent to the sample through an heavily attenuated (XMA attenuators) input line (RF in) and one measures the reflected signal channeled by a separate filtered (MiniCircuit high pass filter, cut-off frequency 4.6 GHz) output line (RF out), which is amplified by a cryogenic microwave amplifier (CITCRYO 1-12 from Caltech, gain 38 dB). Two circulators (Pamtech, $8-12$ GHz) (blue) allow for isolation. **Right**: The measurement pulses are sent through the bias line, which is heavily attenuated (XMA attenuators). Two twisted pairs terminated by series resistors $R_p = 1\,\mathbf{k}\Omega$ allow to measure the dc voltage and current of the SQUID. Two consecutive bias tees allow for both dc bias and ac excitation of the atomic-SQUID.

10.3 Room temperature connections and instruments

10.3.1 *Biasing*

In the experiments on samples PAL7, JS6 and JT6, the dc flux coil was connected to a floating dc stabilized voltage source Yokogawa 7651 through a series resistance, either 1 kΩ or 5.12 kΩ, depending on the desired current range which depends on the loop size.

In the switching experiments on samples PAL7 and RAC4, both current pulses (through bias line) and flux pulses (through antenna line) were synthesized with an arbitrary waveform generator Agilent 33250A. Microwave signals (sent through the antenna line, intended to drive the Andreev transition) were generated using an Anritsu MG3694B.

In the spectroscopy experiments on samples JS6 and JT6, current pulses were synthesized with an Agilent 33250A. Decoupling of the ground was achieved with a gain-1 buffer.

In the reflectometry experiment on samples RAC2 and RAC3, biasing was performed with an Anritsu 3734D Vector Network Analyzer (40 MHz – 20 GHz).

10.3.2 *Amplification*

In the low-frequency experiments on samples PAL7, JS6 and JT6, the small voltages measured with the lossy twisted pairs were amplified at room temperature by low noise voltage preamplifiers NF LI75A (1.2nV/$\sqrt{\text{Hz}}$, 1 MHz bandwidth, $\times$100 gain), followed by Stanford amplifiers SR560 with selectable gain and bandwidth.

In the reflectometry experiment on sample PAL7, RAC2 and RAC3, additional room-temperature attenuators and amplifiers (MiniCircuits / Miteq AM-1634-3000) were also used. For sample PAL7, a total amplification of 100 dB has been used. For sample RAC2, a total amplification of 45 dB has been used.

10.3.3 *Measurements*

In the low-frequency experiments on samples PAL7, JS6 and JT6, $I(V)$ characteristics were registered with a Yokogawa DL750 oscilloscope.

In the switching experiments on samples PAL7, the switching voltage pulses were counted using two PM6680 counters (Fluke or Philips). A Tektronix TDS7104 digital oscilloscope was used to visualize the pulses.

In spectroscopy experiments on samples JS6 and JT6, the $\frac{dI}{dV}(V)$ measurements were performed with a Stanford SR830 Lock-in amplifier.

In the reflectometry experiment on samples RAC2 and RAC3, measurement was performed with an Anritsu 3734D VNA.

The monitoring of all the instruments was controlled by Testpoint programs.

Part V

APPENDICES

A

MICROSCOPIC CONSTRUCTION OF THE ANDREEV BOUND STATES

This chapter presents an extensive derivation of the calculations sketched in Chapter 2.

The goal of this chapter is three fold. First, in the normal state, we will set up the notations of second quantization, derive the scattering matrix and define the notion of conductance channels. Then, we will solve the standard problem of an homogeneous superconductor, in a mean-field approximation. We will not discuss the different representations since it has been already done extensively in Chapter 2. Finally, by adding a superconducting phase gradient and a scattering potential, we will build explicitly the Andreev Bound States and derive their corresponding two-level Hamiltonian, as well as their current operator. Our derivation (performed in collaboration with Manuel Houzet), which is purely Hamiltonian, recovers with a more basic method the results of Ref. [66] obtained using a path integral approach.

A.1 Normal state

In this section, we consider the normal state. The goal is first to set up the notations of second quantization, then to derive the scattering matrix and finally to define the notion of conduction channels.

Let us consider a three-dimensional space $\mathcal{F} = \left[-\frac{l_x}{2}, \frac{l_x}{2}\right] \times \left[-\frac{l_y}{2}, \frac{l_y}{2}\right] \times \left[-\frac{l_z}{2}, \frac{l_z}{2}\right]$, with periodic boundary conditions along y and z. $\nu = l_x l_y l_z$ is the volume of this space. $r = (x, y, z)$ labels the position of a particle. x is the longitudinal direction and y and z are the transverse directions, with $l_x \gg l_y, l_z$. We will typically consider that $l_x = \infty$ in the following.

A.1.1 *Second quantization formalism*

Let us first derive the Hamiltonian description of the scattering problem in the normal state. We are studying the problem of N non-interacting electrons in the space F, in a spin-dependent potential $U_\sigma(r)$. In second quantization, the Hamiltonian reads

$$\mathcal{H} = \sum_{\sigma=\uparrow,\downarrow} \int_F dr \psi_\sigma^\dagger(r) H_\sigma \psi_\sigma(r) \tag{A.1}$$

where $\psi_\sigma(r)$ (respectively $\psi_\sigma^\dagger(r)$) is the annihilation (creation) field operator of an electron of spin σ at position r. They verify the anti-commutation relations $\{\psi_\sigma(r), \psi_{\sigma'}(r')\} = \left\{\psi_\sigma^\dagger(r), \psi_{\sigma'}^\dagger(r')\right\} = 0$, $\left\{\psi_\sigma(r), \psi_{\sigma'}^\dagger(r')\right\} = \delta(r - r')\,\delta_{\sigma\sigma'}$. $\psi_\sigma(r)$ can be decomposed over any orthonormal basis of the Hilbert space of the periodical square-integrable functions $\mathcal{L}^2(F)$.

H_σ is the one-particle stationary Hamiltonian in first quantization, for an electron of spin σ:

$$H_\sigma = \frac{p^2}{2m} - \mu + U_\sigma(r) \tag{A.2}$$

where $\frac{p^2}{2m} = -\frac{\hbar^2}{2m}\triangle$ is the kinetic energy operator, m the electron mass and μ the chemical potential. One first needs to solve the one-particle stationary Schrödinger equation

$$H_\sigma \varphi_{k\sigma}(r) = \xi_{k\sigma}\varphi_{k\sigma}(r). \tag{A.3}$$

Then, one can decompose $\psi_\sigma(r)$ on the orthonormal basis of solutions $\{\varphi_{k\sigma}\}_k$ and inject it in Eq. A.1 to get a diagonal Hamiltonian.

A.1.2 *Free electrons*

Let us first consider the elementary problem with $U = 0$. The plane waves

$$\varphi_k(r) = \frac{1}{\sqrt{\nu}}\exp(ik.r). \tag{A.4}$$

are solutions of the Schrödinger equation (A.3) with an energy

$$\xi_k = \frac{\hbar^2\|k\|^2}{2m} - \mu. \tag{A.5}$$

The periodic boundary conditions along y and z impose that $k \in E = \mathbb{R}\times E_t$, with $E_t = \left\{2\pi\left(\frac{m}{L_y}, \frac{p}{L_z}\right)/(m,p)\in\mathbb{Z}^2\right\}$. It leads to a continuum of states of positive energy $\xi_k \geqslant 0$.

Due to Fourier transform properties, the set of $\{\varphi_k/k\in E\}$ is an orthonormal basis of $\mathcal{L}^2(F)$[1]. Therefore, one can decompose ψ_σ on this basis as

$$\psi_\sigma(r) = \sum_{k\in E} c_{k\sigma}\varphi_k(r). \tag{A.6}$$

$c_{k\sigma}$ and $c^\dagger_{k\sigma}$ are the annihilation and creation operator of an electron of spin σ and momentum k, in a plane wave state. They also verify the anti-commutation relations $\{c_{k\sigma}, c_{k'\sigma'}\} = \left\{c^\dagger_{k\sigma}, c^\dagger_{k'\sigma'}\right\} = 0$, $\left\{c_{k\sigma}, c^\dagger_{k'\sigma'}\right\} = \delta_{kk'}\delta_{\sigma\sigma'}$. The relation (A.6) can be inverted to give

$$c_{k\sigma} = \int dr\,\varphi^*_k(r)\,\psi_\sigma(r) \tag{A.7}$$

Then, one injects Eq. A.6 in Eq. A.1 and the second quantized Hamiltonian becomes

$$\mathcal{H} = \sum_{\sigma=\uparrow,\downarrow}\sum_{k\in E}\xi_k c^\dagger_{k\sigma}c_{k\sigma} \tag{A.8}$$

1 When $l_x = \infty$, the plane waves φ_k cannot be normalized, and do not belong to $\mathcal{L}^2(F)$. Nevertheless, $\int_{-\infty}^{\infty} dx \exp\left(i(k_x - k'_x)x\right) = \delta\left(k_x - k'_x\right)$ and due to Fourier transform properties, any function of $\mathcal{L}^2(F)$ can be decomposed in an infinite continuous sum of φ_k. That is why the set of $\{\varphi_k/k\in E\}$ can be seen as an orthonormal "Hilbert basis" of $\mathcal{L}^2(F)$. Then, instead of a discrete sum, one should perform a continuous sum on the k_x in Eq. A.6 . Out of habit, we will conserve the discrete sum and keep the infinite normalization factor ν in Eq. A.4. In the following, we will always consider the limit $l_x = \infty$.

Thus, all the multi-particles eigenstates are of the form $\prod_{k\sigma} c^\dagger_{k\sigma} |0\rangle$ of energy $\sum_{k\sigma} \xi_k$, where $|0\rangle$ is the vacuum of electrons of energy 0. For instance $c^\dagger_{k\sigma} |0\rangle$ is a one-particle eigenstate of energy ξ_k and wave function $\langle r, \sigma | c^\dagger_{k\sigma} |0\rangle = \varphi_k(r)$, where $|r, \sigma\rangle = \psi^\dagger_\sigma(r) |0\rangle$.

A.1.3 *Repulsive scattering potential*

A.1.3.1 *First quantization*

Now, let us add a delta function[2] as a scattering potential at $x = 0$: $U(r) = V\delta(x)$, with $V > 0$. One defines the scattering states

$$\begin{cases} \phi_{lp}(r) = & \frac{1}{\sqrt{v}} \exp(i(p_y y + p_z z)) \left[t_{p_x} \exp(ip_x x)\, \theta(x) \right. \\ & \left. + (\exp(ip_x x) + r_{p_x} \exp(-ip_x x))\, \theta(-x) \right] \\ \phi_{rp}(r) = & \frac{1}{\sqrt{v}} \exp(i(p_y y + p_z z)) \left[t_{p_x} \exp(-ip_x x)\, \theta(-x) \right. \\ & \left. + (\exp(-ip_x x) + r_{p_x} \exp(ip_x x))\, \theta(x) \right] \end{cases} \tag{A.9}$$

To satisfy the Schrödinger equation (A.3), these wave functions must satisfy the continuity equations[3] in $x = 0$:

$$\forall j \in \{l, r\}, \quad \begin{cases} \phi_{jp}(0^+) = \phi_{jp}(0^-) \\ \frac{\partial \phi_{jp}}{\partial x}(0^+) - \frac{\partial \phi_{jp}}{\partial x}(0^-) = 2\frac{\eta}{p_x} \phi_{jp}(0) \end{cases} \tag{A.10}$$

where

$$\boxed{\eta = \frac{mV}{\hbar^2}} \tag{A.11}$$

is the inverse of the scattering length. Therefore the reflexion and transmission amplitudes are

$$\begin{cases} r_{p_x} = -\frac{i\eta}{p_x + i\eta} \\ t_{p_x} = \frac{p_x}{p_x + i\eta} \end{cases} \tag{A.12}$$

Thus, the scattering states ϕ_{lp} and ϕ_{rp} are solutions of the Schrödinger equation (A.3) with an energy $\xi_p = \frac{\hbar^2 \|p\|^2}{2m}$. If $p \in \mathbb{R}^3$, the periodic boundary conditions on y and z impose that $p = (p_x, p_y, p_z) \in F = \mathbb{R}^{+*} \times E_t$[4]. Those states form a continuum of positive energy $\xi_p > 0$.

2 We are mainly interested in the scattering states, far from the scatterer. Therefore, any localized potential can be approximated by a delta function.

3 The second equation is obtained by integrating the Schrödinger equation (A.3) along x over an infinitely small interval around $x = 0$.

4 One takes $p_x \in \mathbb{R}^{+*}$ instead of $p_x \in \mathbb{R}$ because the solution $p_x = 0$ is uniform in x, which is not compatible with a discontinuous derivative, and because the solutions $p_x < 0$ are redundant.

A.1.3.2 *Second quantization*

When the potential is repulsive $V > 0$, there is no bound state and the set of $\{\phi_{lp}, \phi_{rp}/p \in F\}$ is an orthonormal basis of $\mathcal{L}^2(F)$[5]. Therefore, one can decompose ψ_σ on this basis as

$$\psi_\sigma(r) = \sum_{i\in\{l,r\}} \sum_{p\in F} d_{ip\sigma}\phi_{ip}(r) \tag{A.14}$$

$d_{ip\sigma}$ and $d^\dagger_{ip\sigma}$ are annihilation and creation operator of an electron of spin σ, in a scattering wave state, which also verify the anti-commutation relations and can be expressed as a function of ψ_σ:

$$\forall j \in \{l, r\}, \quad d_{ip\sigma} = \int dr \phi^*_{jp}(r)\,\psi_\sigma(r) \tag{A.15}$$

Then, one injects Eq. A.14 in Eq. A.1 and the second quantized Hamiltonian becomes[6]

$$\mathcal{H} = \sum_{\sigma=\uparrow,\downarrow} \sum_{j\in\{l,r\}} \sum_{p\in F} \xi_p d^\dagger_{jp\sigma} d_{jp\sigma} \tag{A.16}$$

Using Eq. A.15 and Eq. A.6, one gets

$$d_{jp\sigma} = \sum_{k\in E} c_{k\sigma} \left\langle \phi_{jp} \middle| \varphi_k \right\rangle. \tag{A.17}$$

A.1.3.3 *Scattering representation*

In general, a diffusion state of positive energy can be written as

$$\phi_p(r) = \frac{1}{\sqrt{\nu}} \exp(i(p_y y + p_z z)) \begin{cases} A\exp(ip_x x) + B\exp(-ip_x x) & x < 0 \\ C\exp(ip_x x) + D\exp(-ip_x x) & x > 0 \end{cases} \tag{A.18}$$

Using the continuity equations (A.10), one finds that

$$\begin{bmatrix} B \\ C \end{bmatrix} = S_{p_x} \begin{bmatrix} A \\ D \end{bmatrix} \tag{A.19}$$

---

5 When $V < 0$, there is an extra class of solutions, whose energy $\xi_p = \frac{\hbar^2}{2m}\left(-p_0^2 + p_y^2 + p_z^2\right)$ can be negative, the bound states:

$$\phi_{0p_t\sigma}(r) = \sqrt{\frac{p_{0\sigma}}{L_y L_z}} \exp(i(p_y y + p_z z)) \exp(-p_{0\sigma}|x|) \tag{A.13}$$

with $p_t = (p_y, p_z) \in E_t$. The longitudinal wave vector is here purely imaginary $p_x = ip_0$, with $p_{0\sigma} = -\eta_\sigma > 0$. Note that it corresponds to the only pole of the reflexion and transmission amplitudes. As expected, these states are orthogonal to the scattering states. Then, one has to add the bound states to the scattering states to form a complete basis. As previously, one can switch to second quantization. Because we are only interested in the following in the repulsive case, we won't make this derivation.

6 By decomposing ψ_σ on the φ_k, one can also express $\mathcal{H}$ as a function of the $c_{k\sigma}$ of the free electrons: $\mathcal{H} = \sum_{\sigma=\uparrow,\downarrow} \left(\sum_{k\in E} \xi_k c^\dagger_{k\sigma} c_{k\sigma} + \frac{1}{L_x} U_\sigma \sum_{k,k'\in E} c^\dagger_{k'\sigma} c_{k\sigma} \delta_{k_y k'_y} \delta_{k_z k'_z} \right)$. It is not diagonal and obviously not adapted.

where $S_{p_x\sigma}$ is the scattering matrix, which relates the incoming waves to the outgoing waves[7]:

$$\boxed{S_{p_x} = \begin{bmatrix} r_{p_x} & t_{p_x} \\ t_{p_x} & r_{p_x} \end{bmatrix}} \tag{A.20}$$

This matrix is unitary $S^\dagger S = 1$ and thus conserves the norm: $|B|^2 + |C|^2 = |A|^2 + |D|^2$. This matrix is fully defined by one quantity, the transmission coefficient

$$\boxed{\tau_{p_x} = |t_{p_x}|^2 = \frac{1}{1 + \left(\frac{n}{p_x}\right)^2}} \tag{A.21}$$

Indeed, if one defines the angle θ_{p_x} as

$$\boxed{e^{i\theta_{p_x}} = \sqrt{\tau_{p_x}} - i\sqrt{1-\tau_{p_x}}}, \tag{A.22}$$

one gets

$$\boxed{\begin{cases} t_{p_x} = \sqrt{\tau_{p_x}} e^{i\theta_{p_x}} \\ r_{p_x} = -i\sqrt{1-\tau_{p_x}} e^{i\theta_{p_x}} \end{cases}}. \tag{A.23}$$

A.1.3.4 *The conduction channels*

In a transport experiment in the normal state, one applies a bias voltage V across the scatterer. This voltage bias is in general very small compared to the Fermi energy $eV \ll E_F$ and the response of the system is essentially determined by the low excitation energies. Then, one can reasonably assume that the one-particle eigenstates to consider are such as $\|p\|^2 = p_x^2 + p_y^2 + p_z^2 \simeq k_F^2$, where k_F is the Fermi wave-vector. Therefore, the number of conductance channels is given by the number of pair integer $\{m, n\}$ that satisfy the inequality $\left(\frac{m}{l_y}\right)^2 + \left(\frac{n}{l_z}\right)^2 \leqslant \left(\frac{k_F}{\pi}\right)^2$. When the system is strongly confined in the transverse directions, there are only few conductance channels. Instead of labeling the eigenstates by (p_y, p_z), one can label them by an integer n, the channel index. Because the transmission τ_{p_x} depends on $p_x^2 = k_F^2 - p_y^2 - p_z^2$ (see Eq. A.21), it depends on the channel, and we will write it τ_n. Note that in full generality, this transmission can depend on the electron spin. This is easily modeled by taking a spin dependent barrier $V_\sigma \delta(x)$.

Of course, the previous derivation is strictly valid for the peculiar geometry $\mathcal{F}$. It should describe well the physics of a two-dimension electron gas. However, in our experiment we are dealing with atomic-size contacts, which have a completely different geometry. To describe properly such systems, one needs to perform an on-site tight-binding model [135]. In particular, it has been demonstrated that the number of channels is not related to the transverse width but given by the chemical valence of the atoms [17]. Although this toy-model is not able to predict the set

7 In general, a scattering matrix reads $S = \begin{bmatrix} r & t' \\ t & r' \end{bmatrix}$, with $S^\dagger S = Id$ due to flux conservation. In a system time reversal symmetry (no magnetic field), one gets $t' = t$. If in addition it is symmetric around $x = 0$ (which is the case for a delta function), one also gets $r' = r$.

of $\{\tau_n\}$ of an atomic contact, it is enough to describe correctly this physics. Indeed, most of the properties measurable in the normal state, like the conductance and the current spectral density, are characterized by the set of the transmissions of the conductance channels $\{\tau_n\}$. Surprisingly, in the superconducting regime, the supercurrent driven by the phase difference is also characterized by the transmissions $\{\tau_n\}$.

A.2 Superconducting regime

In this section, we will consider the case of a type-s superconductor. The goal is first to set up the notations of second quantization, which leads to the general Bogoliubov-de Gennes equation. Then, we will solve this problem in the case of an homogeneous superconductor. At last, by adding a superconducting phase gradient and a scattering potential, we will build the microscopic Andreev Bound States, and derive their corresponding two-level Hamiltonian, as well as their current operator.

A.2.1 *BCS Hamiltonian and Bogoliubov-de Gennes equation*

In a **BCS** mean-field approximation (see Refs. [56, 57]), the effective Hamiltonian can be written as

$$\begin{aligned}\mathcal{H} = \quad & \int_F dr \sum_{\sigma=\uparrow,\downarrow} \psi_\sigma^\dagger(r) \left[\frac{p^2}{2m} - \mu + U_\sigma(r)\right] \psi_\sigma(r) \\ & + \int_F dr \left[\Delta(r)\, \psi_\uparrow^\dagger(r)\psi_\downarrow^\dagger(r) + \Delta^*(r)\, \psi_\downarrow(r)\psi_\uparrow(r)\right]\end{aligned} \tag{A.24}$$

where Δ is the self-consistent complex pairing field and U_σ the self-consistent potential[8]. Note that in gaining the simplicity of eliminating quartic terms from the Hamiltonian, this approximate form, which is now quadratic in fermion operator, does not conserve particle number. But spin and particle number's parity are still good quantum numbers.

The pairing interaction introduces anomalous correlations $\psi_\uparrow^\dagger(r)\psi_\downarrow^\dagger(r)$ and $\psi_\downarrow(r)\psi_\uparrow(r)$. Following [19], one aims at transforming $\mathcal{H}$ into a form that looks just like the sec-

8 This is obtained within a mean-field approximation, starting from the BCS Hamiltonian

$$\mathcal{H} = \int_F dr \sum_{\sigma=\uparrow,\downarrow} \psi_\sigma^\dagger(r) \left[\frac{p^2}{2m} - \mu\right] \psi_\sigma(r) - \int_F dr\, g(r)\, \psi_\uparrow^\dagger(r)\psi_\downarrow^\dagger(r)\psi_\downarrow(r)\psi_\uparrow(r) \tag{A.25}$$

where $g(r)$ is a four-body interaction field. The self-consistent fields U_σ and Δ are defined as

$$U_{-\sigma}(r) = -g(r) \left\langle \psi_\sigma^\dagger(r)\psi_\sigma(r) \right\rangle = U_{-\sigma}^*(r) \text{ and } \Delta(r) = -g(r) \left\langle \psi_\downarrow(r)\psi_\uparrow(r) \right\rangle. \tag{A.26}$$

U_σ can also contains external potential. In A.24, we have dropped out the constant energy

$$\int_F dr \left[U_\uparrow(r)U_\downarrow(r)/g(r)\right] + \int_F dr \left[|\Delta(r)|^2/g(r)\right], \tag{A.27}$$

which only renormalizes the eigenergies. Note however that it is essential if one wants to derive the condensation energy of the ground state and compare it with the results of the variational approach.

ond quantized Hamiltonian for a set of non-interacting particles. To do so, one introduces the **spinor** field

$$\boxed{\Psi(r) = \begin{pmatrix} \psi_\uparrow(r) \\ \psi_\downarrow^\dagger(r) \end{pmatrix}}. \tag{A.28}$$

One can understand this field operator as a global annihilation of a "**quasiparticle**" made of a spin-up electron annihilation field, and a spin-down hole annihilation field. It conserves the spin and the parity. Using the anti-commutation rules[9], the Hamiltonian reads

$$\mathcal{H} = \int_F dr \Psi^\dagger(r) H_{BdG} \Psi(r) \tag{A.29}$$

where H_{BdG} is a matrix Hamiltonian operator defined as

$$H_{BdG} = \begin{pmatrix} \frac{p^2}{2m} - \mu + U_\uparrow(r) & \Delta(r) \\ \Delta^*(r) & -\left[\frac{p^2}{2m} - \mu + U_\downarrow(r)\right] \end{pmatrix} \tag{A.30}$$

To diagonalize the Hamiltonian (A.29), one first needs to solve the one-particle stationary Schrödinger equation

$$H_{BdG} \begin{pmatrix} u_k(r) \\ v_k(r) \end{pmatrix} = E_k \begin{pmatrix} u_k(r) \\ v_k(r) \end{pmatrix}. \tag{A.31}$$

which is known as the **Bogoliubov-de Gennes equation**. Here, analogously to the Dirac equation, the wave function of this quasiparticle is a 2-dimensional vector. With this choice of spinor (A.28), the upper component of the vector represents the "spin-up electron" amplitude of the quasiparticle, and the lower component its "spin-down hole" amplitude.

One looks for an orthonormal basis of solutions $\{\overrightarrow{\varphi_k}\}_k$, with $\overrightarrow{\varphi_k}(r) = \begin{pmatrix} u_k(r) \\ v_k(r) \end{pmatrix}$, such as $\int_F dr\, {}^t\overrightarrow{\varphi_k}^*(r)\overrightarrow{\varphi_{k'}}(r) = \delta_{kk'}$. Then, one can decompose $\Psi(r)$ on this basis and inject it in Eq. A.29 to get a diagonal Hamiltonian.

A.2.2 *Homogeneous superconductor*

Let us first consider the uniform case where the potentials are independent of the position $U_\sigma(r) = U_\sigma$ and $\Delta(r) = \Delta e^{i\varphi}$. $\Delta > 0$ is the modulus of the superconducting order parameter and $\varphi \in \mathbb{R}$ its phase. $U_\sigma \in \mathbb{R}$ is spin-dependent, which allows to describe for instance the Zeeman effect due to an external magnetic field. *We will diagonalize the Hamiltonian but we will not build here the eigenstates and discuss the different representations since it is already done extensively in* Chapter 2.

9 We are dropping the constant energy $\sum_{k\in\mathbb{R}} \xi_k + \sum_{k,k'\in\mathbb{R}} \int_F dr \left[\varphi_{k'}(r) U_\downarrow(r) \varphi_k^*(r)\right]$ resulting from the anti-commutation.

A.2.2.1 *Diagonalization of the Hamiltonian*

One looks for a solution of the form

$$\overrightarrow{\varphi_k}(r) = \begin{pmatrix} a_k \\ b_k \end{pmatrix} \varphi_k(r) \tag{A.32}$$

where φ_k is the plane wave defined in Eq. A.4. Using Eq. A.31, one gets

$$H_k \begin{pmatrix} a_k \\ b_k \end{pmatrix} = E_k \begin{pmatrix} a_k \\ b_k \end{pmatrix} \tag{A.33}$$

with

$$H_k = \begin{pmatrix} \xi_k + U_\uparrow & \Delta e^{i\varphi} \\ \Delta e^{-i\varphi} & -\left[\xi_k + U_\downarrow\right] \end{pmatrix}. \tag{A.34}$$

Therefore, one needs for each k to diagonalize the scalar 2×2 matrix H_k. At a fixed k, H_k has two orthonormal eigenvectors $\begin{pmatrix} v_k \\ u_k \end{pmatrix}$ and $\begin{pmatrix} u_k^* \\ -v_k^* \end{pmatrix}$, with eigenenergies E_{k-} and E_{k+}:

$$\boxed{\begin{cases} u_k = & e^{-i\frac{\varphi}{2}} \sqrt{\frac{1}{2}\left(1 + \frac{\tilde{\xi}_k}{\sqrt{\Delta^2 + \tilde{\xi}_k^2}}\right)} \\ v_k = & -e^{i\frac{\varphi}{2}} \sqrt{\frac{1}{2}\left(1 - \frac{\tilde{\xi}_k}{\sqrt{\Delta^2 + \tilde{\xi}_k^2}}\right)} \\ E_{k\pm} = \pm & \sqrt{\Delta^2 + \tilde{\xi}_k^2} + \beta \end{cases}} \tag{A.35}$$

where $\tilde{\xi}_k = \xi_k + \frac{U_\uparrow + U_\downarrow}{2}$ is the averaged kinetic energy, and $\beta = \frac{U_\uparrow - U_\downarrow}{2}$ can be seen as a Zeeman splitting energy. One considers that $|\beta| \ll \Delta$. Then, for each k, there is a negative energy E_{k-} and a positive energy E_{k+}, which explains the label. Note that in the case of spin degeneracy $\beta = 0$, $E_{k-} = -E_{k+}$, which can be interpreted as a particle-hole symmetry of the system[10].

One defines

$$\begin{cases} \overrightarrow{\varphi_{k-}} = & \begin{pmatrix} v_k \\ u_k \end{pmatrix} \varphi_k \\ \overrightarrow{\varphi_{k+}} = & \begin{pmatrix} u_k^* \\ -v_k^* \end{pmatrix} \varphi_k \end{cases}. \tag{A.36}$$

10 For each eigenstate $\overrightarrow{\varphi_E} = \begin{pmatrix} u \\ v \end{pmatrix}$ of Eq. A.31 with energy E, there is another eigenstate $\overrightarrow{\varphi_{-E}} = \begin{pmatrix} v^* \\ -u^* \end{pmatrix}$ of opposite energy.

The set of $\{\overrightarrow{\varphi_{k-}}, \overrightarrow{\varphi_{k+}}/k \in E\}$ forms a complete orthonormal basis[11]. Therefore, one can decompose Ψ on this basis as

$$\Psi = \sum_{k\in E} \left(\gamma_{k-}\overrightarrow{\varphi_{k-}} + \gamma_{k+}\overrightarrow{\varphi_{k+}}\right). \tag{A.37}$$

γ_{k-}, γ_{k+}, $\gamma^\dagger_{k-}$ and $\gamma^\dagger_{k+}$ are the fermionic annihilation and creation operator, nicknamed "Bogoliubons"[12]. By inverting Eq. A.37, one gets

$$\begin{pmatrix} \gamma_{k-} \\ \gamma_{k+} \end{pmatrix} = \int dr \begin{pmatrix} {}^t\overrightarrow{\varphi_{k-}}^*(r) \\ {}^t\overrightarrow{\varphi_{k+}}^*(r) \end{pmatrix} \Psi(r) \tag{A.38}$$

where ${}^t\overrightarrow{\varphi}$ is the transpose of $\overrightarrow{\varphi}$. Using Eq. A.36, it reads

$$\boxed{\begin{pmatrix} \gamma_{k-} \\ \gamma_{k+} \end{pmatrix} = R_k \int dr \varphi^*_k(r)\Psi(r)} \tag{A.39}$$

where

$$R_k = \begin{pmatrix} v^*_k & u^*_k \\ u_k & -v_k \end{pmatrix} \tag{A.40}$$

is the unitary Bogoliubov matrix. The unitarity ensures that the Bogoliubons are fermionic operators verifying the anti-commutation relations. Using Eq. A.7, it simplifies in

$$\begin{pmatrix} \gamma_{k-} \\ \gamma_{k+} \end{pmatrix} = R_k \Psi_k \tag{A.41}$$

where we have introduced the Fourier transform of the spinor

$$\Psi_k = \begin{pmatrix} c_{k\uparrow} \\ c^\dagger_{-k\downarrow} \end{pmatrix}. \tag{A.42}$$

The formulas (A.37), (A.38) and (A.41) are the well-known Bogoliubov transformations[13].

Then, one injects (A.37) in Eq. A.29 and the Hamiltonian becomes

$$\boxed{\mathcal{H} = \sum_{k\in E} E_{k-}\gamma^\dagger_{k-}\gamma_{k-} + E_{k+}\gamma^\dagger_{k+}\gamma_{k+}}. \tag{A.43}$$

11 One can check that

$$\forall k, k' \in E,\ n, m \in \{-,+\} \quad \int_F dr\, {}^t\overrightarrow{\varphi_{kn}}^*(r)\overrightarrow{\varphi_{k'm}}(r) = \delta_{kk'}\delta_{nm}.$$

12 This choice of Bogoliubons is usually called the "one-particle" picture.

13 They are also often written explicitly as

$$\begin{cases} \gamma_{k-} = & \int dr \varphi^*_k(r)\left[v^*_k\psi_\uparrow(r) + u^*_k\psi^\dagger_\downarrow(r)\right] \\ \gamma_{k+} = & \int dr \varphi^*_k(r)\left[u_k\psi_\uparrow(r) - v_k\psi^\dagger_\downarrow(r)\right] \end{cases}$$

and

$$\begin{cases} \gamma_{k-} = & v^*_k c_{k\uparrow} + u^*_k c^\dagger_{-k\downarrow} \\ \gamma_{k+} = & u_k c_{k\uparrow} - v_k c^\dagger_{-k\downarrow} \end{cases}.$$

REMARK: When one considers a spatial invariant problem, one usually express the Hamiltonian (A.24) directly in k space. To do so, one just has to decompose the ψ_σ on the plane waves φ_k. Then, the Hamiltonian reads

$$\mathcal{H} = \sum_{k\in E} \left[\xi_k + U_\uparrow\right] c^\dagger_{k\uparrow} c_{k\uparrow} + \left[\xi_k + U_\downarrow\right] c^\dagger_{k\downarrow} c_{k\downarrow} + \Delta c^\dagger_{k\uparrow} c^\dagger_{-k\downarrow} + \Delta^* c_{-k\downarrow} c_{k\uparrow}. \quad \text{(A.44)}$$

Using the spinor (A.42), it becomes

$$\mathcal{H} = \sum_{k\in E} \Psi^\dagger_k H_k \Psi_k + \sum_{k\in E} \left[\xi_k + U_\downarrow\right], \quad \text{(A.45)}$$

where H_k has been defined in Eq. A.34. We have here chosen to keep the constant energy $\sum_{k\in E} \left[\xi_k + U_\downarrow\right]$ resulting from the anti-commutation. By diagonalizing H_k as previously one finds again the expression (A.43).

A.2.2.2 *Arbitrariness of the choice of the spinor and of the vacuum*

It is important to notice that this description is arbitrary in the choice of the spinor. The key point is that the two species of electrons that build the spinor must not be coupled in the Hamiltonian. For instance

$$\Psi'_k = \begin{pmatrix} c_{k\downarrow} \\ c^\dagger_{-k\uparrow} \end{pmatrix}, \quad \text{(A.46)}$$

which has only inverted spin component with respect to the spinor (A.42), also allows to diagonalize the Hamiltonian. Thus, one is naturally incline to choose as a vacuum

$$|V'\rangle = \prod_{k\in E} c^\dagger_{k\uparrow} |0\rangle \quad \text{(A.47)}$$

an empty band of spin down and a full band of spin up. Then, the ground state is find as

$$|GS\rangle = \prod_k \gamma_{k\uparrow} |V'\rangle, \quad \text{(A.48)}$$

with energy

$$E_{GS} = \sum_k \left(\xi_{k\uparrow} - E_{k\uparrow}\right). \quad \text{(A.49)}$$

Of course, this is exactly the same state as (2.14).

The spinor used to diagonalize $\mathcal{H}$ can be adapted to the symmetry of the system. For instance, if one adds spin-orbit interaction in the system, it is more convenient to use the spinor

$$\tilde{\Psi}_{k\sigma} = \begin{pmatrix} c_{k\sigma} \\ c^\dagger_{-k-\sigma} \end{pmatrix} \quad \text{(A.50)}$$

with $k > 0$. The associated vacuum

$$|\widetilde{V}\rangle = \prod_\sigma \prod_{k>0} c^\dagger_{-k-\sigma} |0\rangle \quad \text{(A.51)}$$

corresponds to an empty band of $k > 0$ and a full band of $k < 0$ and Bogoliubons are described in terms of electron with positive momentum and holes with negative momentum.

A.2.3 *Normal-superconductor interface: the Andreev reflection*

The discussion on the Andreev reflection is done in Section 2.3. We only give here the expressions in presence of a finite Zeeman splitting $\beta \neq 0$.

A.2.3.1 *Energy dependence of the one-particle states*

One gets

$$\begin{cases} u_{e,h}(E,\varphi) = e^{i\frac{\varphi}{2}} & \left(\frac{1}{2}\left[1+\eta_{e,h}\sqrt{1-\left(\frac{\Delta}{E-\beta}\right)^2}\right]\right)^{1/2} \\ v_{e,h}(E,\varphi) = & e^{-i\frac{\varphi}{2}}\,\mathrm{sgn}(E-\beta)\left(\frac{1}{2}\left[1-\eta_{e,h}\sqrt{1-\left(\frac{\Delta}{E-\beta}\right)^2}\right]\right)^{1/2} \\ k_{e,h}(E) = & k_F\left(1+\eta_{e,h}\,\mathrm{sgn}(E-\beta)\,\frac{\sqrt{(E-\beta)^2-\Delta^2}}{\mu}\right)^{1/2} \end{cases} \tag{A.52}$$

where $\eta_{e,h} = \pm 1$ stands for the choice electron or hole ($\eta_{e,h} = \mathrm{sgn}(\xi)\,\mathrm{sgn}(E-\beta)$).

As long as $|E-\beta| > \Delta$, one deals with purely propagating states. Such states are the only one possible in the spatially invariant case.

When the potential or the pairing energy depend on space, new states will be possible with $|E-\beta| < \Delta$ and $k \in \mathbb{C}$. In the Andreev approximation,

$$k_{e,h}(E) = k_F + i\sigma_{e/h}\kappa(E) \tag{A.53}$$

with

$$\kappa(E) = k_F\frac{\sqrt{\Delta^2-(E-\beta)^2}}{2\mu} \ll k_F. \tag{A.54}$$

We have taken by convention:

$$\sqrt{(E-\beta)^2-\Delta^2} = i\,\mathrm{sgn}(E-\beta)\sqrt{\Delta^2-(E-\beta)^2} \text{ if } |E-\beta| < \Delta. \tag{A.55}$$

These states are exponentially damped on a length scale κ^{-1}. Note that they oscillate at the same time that they decay, in contrast to what one finds for bound states in the normal state.

A.2.3.2 *The Andreev reflection*

In presence of a finite Zeeman splitting $\beta \neq 0$, the Andreev reflection probability is

$$\boxed{a(E,\varphi) = \frac{e^{-i\varphi}}{\Delta}\begin{cases} E-\beta-\mathrm{sgn}(E-\beta)\sqrt{(E-\beta)^2-\Delta^2} & |E-\beta|>\Delta \\ E-\beta-i\sqrt{\Delta^2-(E-\beta)^2} & |E-\beta|<\Delta \end{cases}}. \tag{A.56}$$

A.2.4 *Construction of the Andreev Bound States*

We now turn into the construction of the Andreev Bound States. These fermionic states, envisioned separately by Andreev [11] and Saint James [10], are the key concept which universally explain the mesoscopic Josephson effects. One considers two superconducting conductors with a phase difference δ linked through a coherent conductor. In the Landauer formalism [64], the conductor is fully characterized by the set of its transmission channels $\{\tau_i\}$. In this non-homogeneous geometry, new types of solutions are possible. If the conductor is very short[14], there is a pair of ABS, of energy $\pm E_A(\delta, \tau_i)$ inside the superconducting gap, for each conduction channel. Oppositely to the Cooper pair states found in the homogeneous case, these states are spatially localized in the weak link.

As Andreev reflection does not mix up conduction channels, the problem can be treated, as in the normal regime, in terms of independent conduction channels. We restrict here to the one channel case, *i.e.* to a 1-dimensionnal problem. Focusing on the short junction limit, we consider that the length of the normal channel is zero. We model the scattering impurity as a repulsive delta function at $x = 0$: $U(r) = V\delta(x)$, with $V > 0$. We force a phase difference δ across the scatterer: $\Delta(x) = \Delta e^{i\varphi(x)}$, with $\varphi(x) = \frac{\delta}{2}\mathrm{sgn}(x)$. One looks for a basis of solutions of Eq. A.31.

A.2.4.1 *Bound states*

This system is spatially invariant for $x < 0$ and for $x > 0$. From Section A.2.2, one knows a basis of solutions on each side. Because the spectrum is four fold degenerate (see Section A.2.3.1), one needs in full generality to express any solution on each side as a sum over four vectors: $\begin{pmatrix} u_e \\ v_e \end{pmatrix} \exp(\pm ik_e x)$ and $\begin{pmatrix} u_h \\ v_h \end{pmatrix} \exp(\pm ik_h x)$. We will first look for bound state solutions, at energy $|E| \leqslant \Delta$. According to Eq. A.53, the wave vectors k_e and k_h have both a real and an imaginary component. Normalization forbids from using diverging solutions. It reduces the degeneracy, and one looks for a solution of the form

$$\begin{aligned}\overrightarrow{\phi_E^B}(x) = \quad & \exp(\kappa x)\left(A_E \begin{pmatrix} u_h\left(-\frac{\delta}{2}\right) \\ v_h\left(-\frac{\delta}{2}\right) \end{pmatrix} \exp(ik_F x) + B_E \begin{pmatrix} u_e\left(-\frac{\delta}{2}\right) \\ v_e\left(-\frac{\delta}{2}\right) \end{pmatrix} \exp(-ik_F x)\right)\theta(-x) \\ & + \exp(-\kappa x)\left(C_E \begin{pmatrix} u_e\left(\frac{\delta}{2}\right) \\ v_e\left(\frac{\delta}{2}\right) \end{pmatrix} \exp(ik_F x) + D_E \begin{pmatrix} u_h\left(\frac{\delta}{2}\right) \\ v_h\left(\frac{\delta}{2}\right) \end{pmatrix} \exp(-ik_F x)\right)\theta(x).\end{aligned} \tag{A.57}$$

It is convenient to introduce the function

$$b(E) = \frac{E}{\Delta} - i\sqrt{1 - \left(\frac{E}{\Delta}\right)^2} \tag{A.58}$$

such that $a(E, \varphi) = e^{-i\varphi} b(E)$. Thus, one can write the wavefunction as

14 Meaning that its length l is smaller than the superconducting coherence length ξ, which provides a scale for the extension of Cooper pairs. For longer conductors, $n = \lfloor l/\xi \rfloor$ new pairs of ABS enter in the superconducting gap.

$$\boxed{\begin{aligned}\overrightarrow{\phi_E^B}(x) = \quad & \exp(\kappa x)\left(A_E\begin{pmatrix} be^{-i\frac{\delta}{4}} \\ e^{i\frac{\delta}{4}}\end{pmatrix}\exp(ik_F x) + B_E\begin{pmatrix} e^{-i\frac{\delta}{4}} \\ be^{i\frac{\delta}{4}}\end{pmatrix}\exp(-ik_F x)\right)\theta(-x) \\ & + \exp(-\kappa x)\left(C_E\begin{pmatrix} e^{i\frac{\delta}{4}} \\ be^{-i\frac{\delta}{4}}\end{pmatrix}\exp(ik_F x) + D_E\begin{pmatrix} be^{i\frac{\delta}{4}} \\ e^{-i\frac{\delta}{4}}\end{pmatrix}\exp(-ik_F x)\right)\theta(x)\end{aligned}} \tag{A.59}$$

where $u_e\left(-\frac{\delta}{2}\right)e^{i\frac{\delta}{4}} = v_h\left(-\frac{\delta}{2}\right)e^{i\frac{\delta}{4}} = u_e\left(\frac{\delta}{2}\right)e^{-i\frac{\delta}{4}} = v_h\left(\frac{\delta}{2}\right)e^{-i\frac{\delta}{4}}$ has been absorbed in the coefficients A_E, B_E, C_E and D_E.

As in the normal case, one needs to use the continuity equations at $x = 0$ to match the left and right solutions:

$$\begin{cases} \overrightarrow{\phi_k}(0^+) = \overrightarrow{\phi_k}(0^-) \\ \frac{\partial\overrightarrow{\phi_k}}{\partial x}(0^+) - \frac{\partial\overrightarrow{\phi_k}}{\partial x}(0^-) = 2\frac{\eta}{k}\overrightarrow{\phi_k}(0)\end{cases}. \tag{A.60}$$

In the zero order Andreev approximation[15], these two equations can be rewritten in term of the normal scattering matrix:

$$\begin{cases} \begin{bmatrix} B_E \\ C_E\end{bmatrix} = b(E)\,S\begin{bmatrix} A_E \\ D_E\end{bmatrix} \\ \begin{bmatrix} A_E \\ D_E\end{bmatrix} = b(E)\,S^*\begin{bmatrix} B_E \\ C_E\end{bmatrix}\end{cases} \tag{A.61}$$

where

$$S = \begin{bmatrix} r & te^{i\frac{\delta}{2}} \\ te^{-i\frac{\delta}{2}} & r\end{bmatrix}. \tag{A.62}$$

r and t are the normal reflexion and transmission coefficients defined in Eq. A.23, with

$$\boxed{\tau = \frac{1}{1+\left(\frac{\eta}{k_F}\right)^2}}. \tag{A.63}$$

Note that S, $S^*$are unitary matrix and $|b|^2 = 1$. Therefore $|A_E|^2 + |D_E|^2 = |B_E|^2 + |C_E|^2$.

In the Andreev approximation, the normalization condition $\int_{-\infty}^{\infty} dx\, {}^t\overrightarrow{\phi_E^B}^*(x)\,\overrightarrow{\phi_E^B}(x) = 1$ implies that $|A_E|^2 + |D_E|^2 + |B_E|^2 + |C_E|^2 = \kappa$. Therefore,

$$|A_E|^2 + |D_E|^2 = |B_E|^2 + |C_E|^2 = \frac{\kappa}{2}. \tag{A.64}$$

Combining the equations (A.61), one gets

$$\begin{bmatrix} A_E \\ D_E\end{bmatrix} = b^2(E)\,S^*S\begin{bmatrix} A_E \\ D_E\end{bmatrix} \tag{A.65}$$

15 One needs to neglect κ compared to k_F which is legitimate as long as $\Delta \ll \mu$.

and

$$S^*S = \begin{bmatrix} 1+\tau\left(e^{-i\delta}-1\right) & -2\sqrt{\tau}\sqrt{1-\tau}\sin\left(\frac{\delta}{2}\right) \\ 2\sqrt{\tau}\sqrt{1-\tau}\sin\left(\frac{\delta}{2}\right) & 1+\tau\left(e^{i\delta}-1\right) \end{bmatrix}.$$

This unitary matrix has two eigenvalues

$$\lambda_\pm = 1-2\tau\sin^2\left(\frac{\delta}{2}\right) \pm 2i\sqrt{\tau}\left|\sin\left(\frac{\delta}{2}\right)\right|\sqrt{1-\tau\sin^2\left(\frac{\delta}{2}\right)}. \tag{A.66}$$

Note that $|\lambda_\pm|^2 = 1, \lambda_+^* = \lambda_- = \lambda_+^{-1} = \lambda_-^{-1*}$ and $\lambda_\pm = \left(\sqrt{1-\tau\sin^2\left(\frac{\delta}{2}\right)} \pm i\sqrt{\tau}\left|\sin\left(\frac{\delta}{2}\right)\right|\right)^2$. Thus, the equation (A.65) is valid for $b_\pm^2(E)\lambda_\pm = 1$. Using Eq. A.58, one gets

$$\boxed{E = \pm E_A(\delta,\tau)} \tag{A.67}$$

with

$$\boxed{E_A(\delta,\tau) = \Delta\sqrt{1-\tau\sin^2\left(\frac{\delta}{2}\right)}}. \tag{A.68}$$

We have found the two possible eigenenergies of the bound states. The corresponding eigenvectors $(A_\pm, D_\pm)$ of $\pm E_A$ verify

$$S^*S\begin{bmatrix} A_\pm \\ D_\pm \end{bmatrix} = \lambda_\pm \begin{bmatrix} A_\pm \\ D_\pm \end{bmatrix}.$$

Then, one finds the associated $(B_\pm, C_\pm)$[16] using Eq. A.61. With Eq. A.64, one gets

$$\boxed{\begin{cases} A_\pm(\delta,\tau) = \frac{1}{2} & \sqrt{\kappa(\delta,\tau)\left(1 \mp s(\delta)\, g(\delta,\tau)\right)} \\ B_\pm(\delta,\tau) = & \mp i e^{i\theta}\frac{1}{2}\sqrt{\kappa(\delta,\tau)\left(1 \pm s(\delta)\, g(\delta,\tau)\right)} \\ C_\pm(\delta,\tau) = & -s(\delta)\, e^{i\theta}\frac{1}{2}\sqrt{\kappa(\delta,\tau)\left(1 \mp s(\delta)\, g(\delta,\tau)\right)} \\ D_\pm(\delta,\tau) = & \mp i s(\delta)\,\frac{1}{2}\sqrt{\kappa(\delta,\tau)\left(1 \pm s(\varphi)\, g(\delta,\tau)\right)} \end{cases}} \tag{A.69}$$

with

$$\boxed{\begin{cases} \kappa(\delta,\tau) = & \frac{\sqrt{\tau}\left|\sin\left(\frac{\delta}{2}\right)\right|}{\xi} \\ s(\delta) = & \operatorname{sgn}\left[\sin\left(\frac{\delta}{2}\right)\right] \\ g(\delta,\tau) = & \frac{\sqrt{\tau}\cos\left(\frac{\delta}{2}\right)}{\sqrt{1-\tau\sin^2\left(\frac{\delta}{2}\right)}} \end{cases}}. \tag{A.70}$$

Because $A_-^*A_+ + B_-^*B_+ = C_-^*C_+ + D_-^*D_+ = 0$, the two wave functions $\overrightarrow{\phi_\pm^B} \equiv \overrightarrow{\phi_{\pm E_A}^B}$ are orthogonal, as expected.

16 We have implicitly define $(A_\pm, B_\pm, C_\pm, D_\pm) \equiv (A_{\pm E_A}, B_{\pm E_A}, C_{\pm E_A}, D_{\pm E_A})$.

A.2.4.2 *Continuum states*

Similarly, one can build the propagating solutions of eigenenergies $|E| > \Delta$ as

$$\begin{aligned}\overrightarrow{\phi_E}(x) = &\left(F_E \begin{pmatrix} e^{-i\frac{\delta}{4}} \\ be^{i\frac{\delta}{4}} \end{pmatrix} \exp(ik_e x) + G_E \begin{pmatrix} e^{-i\frac{\delta}{4}} \\ be^{i\frac{\delta}{4}} \end{pmatrix} \exp(-ik_e x)\right.\\ &+I_E \begin{pmatrix} be^{-i\frac{\delta}{4}} \\ e^{i\frac{\delta}{4}} \end{pmatrix} \exp(ik_h x) + J_E \begin{pmatrix} be^{-i\frac{\delta}{4}} \\ e^{i\frac{\delta}{4}} \end{pmatrix} \exp(-ik_h x)\Big)\,\theta(-x)\\ &\left(K_E \begin{pmatrix} e^{i\frac{\delta}{4}} \\ be^{-i\frac{\delta}{4}} \end{pmatrix} \exp(ik_e x) + L_E \begin{pmatrix} e^{i\frac{\delta}{4}} \\ be^{-i\frac{\delta}{4}} \end{pmatrix} \exp(-ik_e x)\right.\\ &+M_E \begin{pmatrix} be^{i\frac{\delta}{4}} \\ e^{-i\frac{\delta}{4}} \end{pmatrix} \exp(ik_h x) + N_E \begin{pmatrix} be^{i\frac{\delta}{4}} \\ e^{-i\frac{\delta}{4}} \end{pmatrix} \exp(-ik_h x)\Big)\,\theta(x).\end{aligned} \tag{A.71}$$

These continuum states are solutions of Eq. A.31 for any eigenenergy $|E| > \Delta$. They must satisfy the continuity equations in $x = 0$:

$$\begin{pmatrix} G_E + \gamma J_E \\ K_E + \gamma M_E \end{pmatrix} = S \begin{pmatrix} F_E + \gamma I_E \\ L_E + \gamma N_E \end{pmatrix} \text{ and } \begin{pmatrix} \gamma F_E + I_E \\ \gamma L_E + N_E \end{pmatrix} = S^* \begin{pmatrix} \gamma G_E + J_E \\ \gamma K_E + M_E \end{pmatrix}. \tag{A.72}$$

There are four equations and eight unknown parameters: one can build 4 orthogonal solutions of same energy E, noted $\left\{\overrightarrow{\phi_{1E}}, \overrightarrow{\phi_{2E}}, \overrightarrow{\phi_{3E}}, \overrightarrow{\phi_{4E}}\right\}$[17].

A.2.4.3 *Diagonalized Hamiltonian*

The set $\left\{\overrightarrow{\phi_{jE}} / |E| > \Delta, j \in \{1,2,3,4\}\right\} \cup \left\{\overrightarrow{\phi^B_{-E_A}}, \overrightarrow{\phi^B_{E_A}}\right\}$ forms an orthonormal basis of solutions. One can decompose Ψ on this basis as

$$\Psi = \gamma_{A-}\overrightarrow{\phi^B_-} + \gamma_{A+}\overrightarrow{\phi^B_+} + \sum_{|E|>\Delta}\sum_{j\in\{1,2,3,4\}} \gamma_{jE}\overrightarrow{\phi_{jE}}. \tag{A.73}$$

Then, the Hamiltonian reads

$$\boxed{\mathcal{H} = E_A\left(\gamma^\dagger_{A+}\gamma_{A+} - \gamma^\dagger_{A-}\gamma_{A-}\right) + \sum_{|E|>\Delta} E \sum_{j\in\{1,2,3,4\}} \gamma^\dagger_{jE}\gamma_{jE}}. \tag{A.74}$$

A.2.4.4 *The Andreev Bound States*

For the discussion on the ABS*, see* Section 2.4.2.

A.2.4.5 *Decomposing the ABS on the plane waves*

Using Eq. A.38 and Eq. A.6, one can derive the Andreev fermionic operators as

$$\begin{pmatrix} \gamma_{A-} \\ \gamma_{A+} \end{pmatrix} = \sum_{k\in E}\int dr \begin{pmatrix} {}^t\overrightarrow{\phi^B_-}^*(r) \\ {}^t\overrightarrow{\phi^B_+}^*(r) \end{pmatrix} \begin{pmatrix} c_{k\uparrow}\varphi_k(r) \\ c^\dagger_{k\downarrow}\varphi^*_k(r) \end{pmatrix}. \tag{A.75}$$

17 Here, we do not specify explicitly these wavefunctions.

Although complicated, this equation gives insight on their fermionic nature. Like the Bogoliubons, the "**Andreevons**" are a superposition of electrons of spin-up and holes of spin-down. However, the plane waves are not a good basis to decompose them since they correspond to localized solutions.

This decomposition can be understood with the cartoon in **Fig. A.1**.A right-moving spin-up electron is Andreev reflected at the right interface (with a probability amplitude $a(E, \phi_R)$) into a left-moving spin-down hole at the same energy and a Cooper pair is transferred to the electrode. In turn, this left-moving spin-down hole is Andreev reflected (with a probability amplitude $a(E, \phi_L)$) as a right-moving spin-up electron at the left electrode, leading to the annihilation of a Cooper pair. These successive reflections interfere constructively, like in a Fabry-Pérot interferometer. A similar process occurs for left-moving electrons reflected as right-moving holes. From theses two processes, two resonant quasiparticle states appear, the ABS. If the channel is not perfectly transmitted ($\tau < 1$), these two reflectionless resonances are coupled.

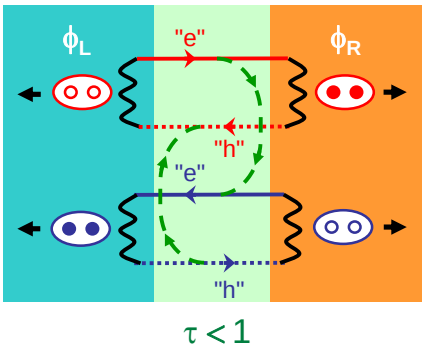

Figure A.1: Schematic representation of the two one-particle ABS in a short reflectionless channel connecting two superconducting electrodes with different phases ϕ_L and ϕ_R, such as $\phi_R - \phi_L = \delta$. The wiggly lines represent an Andreev reflection in which a right-moving spin-up electron (right-moving spin-down hole) is reflected as a left moving spin-down hole (left-moving spin-up electron) acquiring the local superconducting phase. The upper (lower) loop corresponds to the transfer of Cooper pairs to the right (left). In presence of a scattering impurity, a normal reflection process (green dashed lines) connects electron (hole) states traveling in different directions, thus mixing the two reflectionless states.

A.2.4.6 *Effect of a spin-dependent potential over the Andreev Bound States*

In presence of a Zeeman field or a magnetic impurity, they are two different Andreev excitation energies $E_{A\uparrow} \neq E_{A\downarrow}$. Then, up to a constant energy, the four Andreev states have the following energy:

$$\left\{\begin{array}{c} |GS\rangle \ : \ -\frac{1}{2}\left(E_{A\uparrow}+E_{A\downarrow}\right) \\ \gamma^{\dagger}_{A\downarrow}|GS\rangle \ : \ \frac{1}{2}\left(E_{A\downarrow}-E_{A\uparrow}\right) \\ \gamma^{\dagger}_{A\uparrow}|GS\rangle \ : \ \frac{1}{2}\left(E_{A\uparrow}-E_{A\downarrow}\right) \\ \gamma^{\dagger}_{A\uparrow}\gamma^{\dagger}_{A\downarrow}|GS\rangle \ : \ \frac{1}{2}\left(E_{A\uparrow}+E_{A\downarrow}\right) \end{array}\right. . \tag{A.76}$$

The case of a Zeeman field is simple. One describes it by a spin-dependent uniform potential U_σ. It essentially shifts all the energies by β:

$$\boxed{E_{A\sigma} = E_A + \sigma\beta}. \tag{A.77}$$

This lifts the degeneracy of the two odd states $|\downarrow\rangle$ and $|\uparrow\rangle$ but has no influence on the even states $|-\rangle$ and $|+\rangle$.

The case of a magnetic impurity is more complicated. One can describe it by a spin-dependent repulsive delta function $U_\sigma(r) = V_\sigma\delta(x)$, which results in a spin-dependent transmission τ_σ. Then, the scattering equations read

$$\begin{cases} \begin{bmatrix} B_E \\ C_E \end{bmatrix} = \gamma(E)\, S_\uparrow \begin{bmatrix} A_E \\ D_E \end{bmatrix} \\ \begin{bmatrix} A_E \\ D_E \end{bmatrix} = \gamma(E)\, S_\downarrow^* \begin{bmatrix} B_E \\ C_E \end{bmatrix} \end{cases}. \tag{A.78}$$

To lighten the formula, we introduce

$$r_\sigma = 1 - \tau_\sigma. \tag{A.79}$$

Because

$$S_\downarrow^* S_\uparrow = e^{i(\theta_\uparrow - \theta_\downarrow)} \begin{bmatrix} \left(\sqrt{r_\uparrow r_\downarrow} + e^{-i\delta}\sqrt{\tau_\uparrow\tau_\downarrow}\right) & i\left(e^{i\frac{\delta}{2}}\sqrt{\tau_\uparrow r_\downarrow} - e^{-i\frac{\delta}{2}}\sqrt{\tau_\downarrow r_\uparrow}\right) \\ -i\left(e^{i\frac{\delta}{2}}\sqrt{\tau_\uparrow r_\downarrow} - e^{-i\frac{\delta}{2}}\sqrt{\tau_\downarrow r_\uparrow}\right) & \left(\sqrt{r_\uparrow r_\downarrow} + e^{i\delta}\sqrt{\tau_\uparrow\tau_\downarrow}\right) \end{bmatrix}, \tag{A.80}$$

one finds

$$\begin{aligned} \lambda_\pm = \; & e^{i(\theta_\uparrow - \theta_\downarrow)}\left(\sqrt{r_\uparrow r_\downarrow} + \sqrt{\tau_\uparrow\tau_\downarrow}\cos(\delta)\right. \\ & \left. \pm i\sqrt{1 - \left(\sqrt{r_\uparrow r_\downarrow} + \sqrt{\tau_\uparrow\tau_\downarrow}\cos(\delta)\right)^2}\right) \end{aligned} \tag{A.81}$$

which leads to

$$\boxed{\begin{cases} E_{A\sigma} = & \frac{1}{\sqrt{2}}\left[1 + \left(\sqrt{\tau_\uparrow\tau_\downarrow} + \sqrt{r_\uparrow r_\downarrow}\right)\left(\sqrt{\tau_\uparrow\tau_\downarrow}\cos(\delta) + \sqrt{r_\uparrow r_\downarrow}\right)\right. \\ & \left. -\sigma\left(\sqrt{\tau_\uparrow r_\downarrow} - \sqrt{\tau_\downarrow r_\uparrow}\right)\sqrt{1 - \left(\sqrt{\tau_\uparrow\tau_\downarrow}\cos(\delta) + \sqrt{r_\uparrow r_\downarrow}\right)^2}\right]^{1/2} \end{cases}}. \tag{A.82}$$

The energy of the four Andreev states as a function of the phase difference is represented in Fig. A.2. Note that the odd states energies now depend on the phase, which is also found in Ref. [20, 136]. They should therefore carry supercurrent.

A.2.5 *The Andreev two-level system*

When the ABS are deep inside the superconducting gap, *i.e.* when $E_A(\delta) \ll \Delta$ (true for high transmissions channels and for phase δ around π), one can forget about the continuum states and look at these four states as an isolated system. One can see them as a two-level system, of energy $-E_A$ and $+E_A$ (when spin-degenerate).

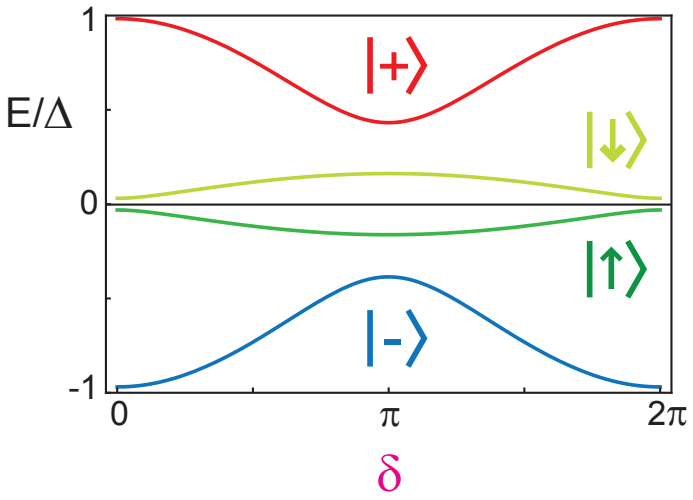

Figure A.2: Energy of the four states corresponding to the different occupation of the ABS as a function of the phase difference δ, in the case of a magnetic impurity of spin-dependent transmissions $\tau_\uparrow$ and $\tau_\downarrow$. This particular curve corresponds to $\tau_\uparrow = 0.95$ and $\tau_\downarrow = 0.7$.

A.2.5.1 *The Andreev Hamiltonian*

One can restrict to the first part of the Hamiltonian A.74:

$$\mathcal{H}_A = -E_A \left(\gamma_{A-}^\dagger \gamma_{A-} - \gamma_{A+}^\dagger \gamma_{A+}\right) \tag{A.83}$$

One defines the Andreev spinor operator

$$\Psi_A = \begin{pmatrix} \gamma_{A-} \\ \gamma_{A+} \end{pmatrix} \tag{A.84}$$

and the usual Pauli matrices:

$$\begin{aligned} \mathbb{I} = \begin{bmatrix} 1 & 0 \\ 0 & 1 \end{bmatrix},\ \sigma_x = \begin{bmatrix} 0 & 1 \\ 1 & 0 \end{bmatrix},\ \sigma_y = \begin{bmatrix} 0 & -i \\ i & 0 \end{bmatrix},\ \\ \sigma_z = \begin{bmatrix} 1 & 0 \\ 0 & -1 \end{bmatrix} \text{ and } \vec{\sigma} = \sigma_x \vec{e_x} + \sigma_y \vec{e_y} + \sigma_z \vec{e_z} \end{aligned}. \tag{A.85}$$

One also defines the operators

$$\begin{cases} \hat{\mathbb{I}} = & \Psi_A^\dagger \, Id \Psi_A \\ \hat{\sigma}_x = & \Psi_A^\dagger \sigma_x \Psi_A \\ \hat{\sigma}_y = & \Psi_A^\dagger \sigma_y \Psi_A \\ \hat{\sigma}_z = & \Psi_A^\dagger \sigma_z \Psi_A \end{cases}. \tag{A.86}$$

Then, the Andreev Hamiltonian reads

$$\boxed{\mathcal{H}_A = \Psi_A^\dagger \left(-E_A \sigma_z\right) \Psi_A = -E_A \hat{\sigma}_z}. \tag{A.87}$$

A.2.5.2 *Calculation of the Andreev current operator*

The current field operator is

$$\boxed{\mathcal{C}(x) = -i\frac{e\hbar}{2m}\sum_{\sigma=\downarrow\uparrow}\left(\psi_\sigma^\dagger(x)\nabla\psi_\sigma(x) - \nabla\psi_\sigma^\dagger(x)\psi_\sigma(x)\right)}. \tag{A.88}$$

One can restrict to the lower excitation energies by neglecting the continuum states:

$$\Psi(x) = \gamma_{A-}\overrightarrow{\phi_-^B}(x) + \gamma_{A+}\overrightarrow{\phi_+^B}(x). \tag{A.89}$$

The Andreev current operator, defined as[18]

$$\mathcal{C}_A = \lim_{x\to 0^-}\mathcal{C}(x) = \lim_{x\to 0^+}\mathcal{C}(x). \tag{A.90}$$

reads, using Eq. A.59

$$\begin{aligned}\mathcal{C}_A = ev_F \Big[&\sum_{\sigma=\pm}\left(\gamma_{A\sigma}^\dagger\gamma_{A\sigma}\left(|b_\sigma|^2|A_\sigma|^2 - |B_\sigma|^2\right)\right) + \gamma_{A-}^\dagger\gamma_{A+}\left(b_-^* b_+ A_-^* A_+ - B_-^* B_+\right)\\ &+\gamma_{A+}^\dagger\gamma_{A-}\left(b_+^* b_- A_+^* A_- - B_+^* B_-\right) + \sum_{\sigma=\pm}\left(\gamma_{A\sigma}\gamma_{A\sigma}^\dagger\left(-|A_\sigma|^2 + |b_\sigma|^2|B_\sigma|^2\right)\right)\\ &+\gamma_{A-}\gamma_{A+}^\dagger\left(-A_-A_+^* + b_- b_+^* B_- B_+^*\right) + \gamma_{A+}\gamma_{A-}^\dagger\left(-A_+A_-^* + b_+ b_-^* B_+ B_-^*\right)\Big].\end{aligned} \tag{A.91}$$

Using Eq. A.69, one finds that $|b_\sigma|^2 = 1$, $b_-^* b_+ = -b_+^2$, $|A_\sigma|^2 - |B_\sigma|^2 = -\frac{1}{2}\sigma\kappa s g$ and $A_-^* A_+ = A_+^* A_- = -B_-^* B_+ = -B_+^* B_- = \frac{\kappa}{4}\sqrt{1-g^2}$. Therefore, one gets[19]

$$\begin{aligned}\mathcal{C}_A &= ev_F\kappa\Big[sg\left(\gamma_{A-}^\dagger\gamma_{A-} - \gamma_{A+}^\dagger\gamma_{A+}\right)\\ &+\tfrac{1}{2}\sqrt{1-g^2}\left(\left(1-b_+^2\right)\gamma_{A-}^\dagger\gamma_{A+} + \left(1-b_+^{*2}\right)\gamma_{A+}^\dagger\gamma_{A-}\right)\Big].\end{aligned} \tag{A.92}$$

Note that $1 - b_+^2 = ib_+ 2\sqrt{\tau}\left|\sin\left(\frac{\delta}{2}\right)\right|$ and $1 - b_+^{*2} = -ib_+^* 2\sqrt{\tau}\left|\sin\left(\frac{\delta}{2}\right)\right|$. The eigenvectors (A.69) are defined up to a global phase shift. Thus, one can absorb ib_+: $(A_+, B_+, C_+, D_+) \to -ib_+^*(A_+, B_+, C_+, D_+)$. Then, using Eq. A.86, it simplifies in

$$\mathcal{C}_A = ev_F\kappa\left[sg\hat{\sigma_z} + \sqrt{\tau}\left|\sin\left(\frac{\delta}{2}\right)\right|\sqrt{1-g^2}\hat{\sigma_x}\right]. \tag{A.93}$$

One defines the Andreev supercurrent as

$$\boxed{I_A(\varphi,\tau) = -\frac{1}{\varphi_0}\frac{dE_A}{d\varphi} = \frac{\Delta}{4\varphi_0}\frac{\tau\sin(\delta)}{\sqrt{1-\tau\sin^2(\frac{\delta}{2})}}}. \tag{A.94}$$

Using Eq. A.70, one finally finds

$$\boxed{\mathcal{C}_A = I_A(\delta,\tau)\left[\hat{\sigma}_z + \sqrt{r}\tan\left(\frac{\delta}{2}\right)\hat{\sigma}_x\right]} \tag{A.95}$$

18 Before taking the limit $x \to 0^-$ or $x \to 0^+$, one neglect the fast oscillating terms at $\pm 2k_F$ (this is discussed in Ref. [137], passing from Eq. (2.21) to Eq. (2.22)).

19 One uses the fermionic nature of the $\gamma_{A\sigma}$. The constant resulting from the anti-commutation is exactly equal to zero $\sum_{\sigma=\pm}\left(|B_\sigma|^2 - |A_\sigma|^2\right) = 0$, which is essential because one cannot have a superconducting current in the vacuum of bogoliubons $|V\rangle$.

with $r = 1 - \tau$.

Therefore, the current in the even states is given by $\langle \pm | \mathcal{C}_A | \pm \rangle = \mp I_A$: it exists in absence of voltage bias and is driven by the phase difference δ. This is the dc Josephson effect. On the contrary, the current in the odd states, which are annihilated by $\hat{\sigma_x}$ and $\hat{\sigma_z}$, is zero. Note that $[\mathcal{H}_A, \mathcal{C}_A] \neq 0$, they don't have the same eigenstates. By consequence, when the system is in an eigenstate of $\mathcal{H}_A$, *i.e.* in an even state, current undergoes quantum fluctuations with spectral function [138, 50]

$$S(\omega, \delta) = I_A^2(\delta, \tau) r \tan^2(\frac{\delta}{2}) \delta(\omega - 2E_A). \tag{A.96}$$

where $\delta(\omega)$ is here the Dirac function, not to confuse with the phase difference δ. The off-diagonal terms of $\mathcal{C}_A$ in $\hat{\sigma}_x$ couples the ground and excited even states as $\langle + | \mathcal{C}_A | - \rangle = \langle - | \mathcal{C}_A | + \rangle = I_A(\delta, \tau)\sqrt{r} \tan\left(\frac{\delta}{2}\right)$, which allows transitions between them.

The Andreev Hamiltonian (A.87) and the current operator (A.95) are written in the basis of the energy states, called the Andreev basis. They are in perfect agreement with the results of Zazunov and Shumeiko [66].

A.2.5.3 *Current operator basis*

One can diagonalize $\mathcal{C}_A$, which is quadratic. To do so, one defines the angle α such as

$$\tan(\alpha) = \sqrt{r} \tan\left(\frac{\delta}{2}\right). \tag{A.97}$$

Thus, $\mathcal{C}_A$ reads

$$\mathcal{C}_A = J_A \Psi_A^\dagger \left(\cos(\alpha)\, \sigma_z + \sin(\alpha)\, \sigma_x\right) \Psi_A \tag{A.98}$$

where

$$J_A = \frac{\Delta}{2\varphi_0} \tau \sin(\frac{\delta}{2}). \tag{A.99}$$

One writes the unitary rotation matrix of angle α, along the unitary vector $\vec{n}$

$$R_{\vec{n}}(\alpha) = \exp\left(-i\frac{\alpha}{2}\vec{\sigma}.\vec{n}\right) = \cos\left(\frac{\alpha}{2}\right) \mathrm{Id} - i \sin\left(\frac{\alpha}{2}\right) \vec{\sigma}.\vec{n}. \tag{A.100}$$

Hence $\cos(\alpha)\, \sigma_z + \sin(\alpha)\, \sigma_x = R_y(\alpha)\, \sigma_z R_y(-\alpha)$. One defines the Andreev current spinor

$$\Psi_I = \begin{pmatrix} \gamma_{I-} \\ \gamma_{I+} \end{pmatrix} = \sigma_x R_y(-\alpha) \Psi_A. \tag{A.101}$$

Then, using the fact that $\sigma_x \sigma_z \sigma_x = -\sigma_z$, $\mathcal{C}_A$ reads

$$\boxed{\mathcal{C}_A = \Psi_I^\dagger \left(-J_A \sigma_z\right) \Psi_I}. \tag{A.102}$$

The Andreev current operator has two eigenvalues $\pm J_A$ and is diagonalized over the fermionic operators $\gamma_{I\pm}$.

In this basis, the Andreev Hamiltonian reads

$$\boxed{\mathcal{H}_A = \Psi_I^\dagger \Delta \left(\cos\left(\frac{\delta}{2}\right) \sigma_z + \sqrt{r} \sin(\frac{\delta}{2}) \sigma_x\right) \Psi_I}. \tag{A.103}$$

This Hamiltonian is analogous to the one derived by Ivanov and Feigelman [108], except that it is written in a phase-dependent basis, *i.e.* $\Psi_I(\delta)$.

A.2.5.4 *Phase independent basis*

Up to now, we have considered the phase as an external time-independent classical parameter. But in quantum mechanics, the phase difference δ and the number of Cooper pair N are quantum conjugated $[N, \delta] = -i$. Therefore, the current should be given by[20]

$$\mathcal{C}_A = \frac{1}{\varphi_0}\frac{\partial \mathcal{H}_A}{\partial \delta}. \tag{A.104}$$

One looks for a phase independent basis such as

$$\begin{cases} \Psi_0 = & \exp(-i\chi)\,\Psi_A \\ \mathcal{H}_A = & \Psi_0^\dagger H_A \Psi_0 \\ \mathcal{C}_A = & \Psi_0^\dagger \frac{1}{\varphi_0}\frac{\partial H_A}{\partial \delta}\Psi_0 \end{cases}. \tag{A.105}$$

Using Eq. A.87 and Eq. A.95, one finds

$$\begin{cases} H_A = & \exp(-i\chi)\,(-E_A\,\sigma_z)\exp(i\chi) \\ \frac{\partial H_A}{\partial \delta} = \varphi_0 & \exp(-i\chi)\,I_A\left[\sigma_z + \sqrt{r}\tan\left(\frac{\delta}{2}\right)\sigma_x\right]\exp(i\chi) \end{cases}. \tag{A.106}$$

One derives the first equation and equates it with the second one:

$$\left[\frac{\partial \chi}{\partial \delta}, \sigma_z\right] = -i\varphi_0\frac{I_A}{E_A}\sqrt{r}\tan\left(\frac{\delta}{2}\right)\sigma_x. \tag{A.107}$$

It implies that

$$\chi = \frac{1}{4}\left(\sqrt{r}\delta - 2\alpha\right)\sigma_y, \tag{A.108}$$

where α is an angle depending on δ, defined in Eq. A.97. Therefore, the rotation matrix is

$$\begin{cases} \exp(-i\chi) & = \exp\left(-i\frac{\sqrt{r}}{4}\delta\sigma_y\right)\left(\cos\left(\frac{\alpha}{2}\right)\mathrm{Id} + i\sin\left(\frac{\alpha}{2}\right)\sigma_y\right) \\ & = \cos\left(\frac{1}{4}\left(\sqrt{r}\delta - 2\alpha\right)\right)\mathbb{I} - i\sin\left(\frac{1}{4}\left(\sqrt{r}\delta - 2\alpha\right)\right)\sigma_y \end{cases} \tag{A.109}$$

Using Eq. A.97 and the fact that $H_A = -E_A\exp(-i\chi)\,\sigma_z\exp(i\chi)$, one gets

$$\boxed{H_A = -\mathrm{Re}(Z)\,\sigma_z + \mathrm{Im}(Z)\,\sigma_x} \tag{A.110}$$

with

$$\boxed{\begin{cases} z = & \Delta\left[\cos(\frac{\delta}{2}) + i\sqrt{r}\sin(\frac{\delta}{2})\right] \\ Z = & z\exp(-i\sqrt{r}\frac{\delta}{2}) \end{cases}}. \tag{A.111}$$

This expression is exactly the same as the one derived in Ref. [66].

20 This is actually not trivial. One can summon Ehrenfest theorem, but it only connects the mean values as $2e\frac{d\langle N\rangle}{dt} = \frac{1}{\varphi_0}\left\langle\frac{\partial H}{\partial \delta}\right\rangle$. At finite temperature, this relation reads $I = \frac{1}{\varphi_0}\frac{\partial F}{\partial \delta}$ (see Ref. [139]). In any case, this only concern mean values and I do not know how to prove this directly in term of operators by invoking arguments of symmetry.

There is another phase independent basis which is frequently used:

$$\Psi_{0'} = \frac{1}{\sqrt{2}} \begin{pmatrix} 1 & 1 \\ 1 & -1 \end{pmatrix} \Psi_0. \tag{A.112}$$

Then, the Andreev Hamiltonian simply reads

$$\begin{cases} \mathcal{H}_A &= -\Psi_{0'}^\dagger \left(\mathrm{Re}\left(Z\right) \sigma_x + \mathrm{Im}\left(Z\right) \sigma_y \right) \Psi_{0'} \\ &= -\Psi_{0'}^\dagger \begin{pmatrix} 0 & Z \\ Z^* & 0 \end{pmatrix} \Psi_{0'} \end{cases} \tag{A.113}$$

and the Andreev current operator is

$$\mathcal{C}_A = -\Psi_{0'}^\dagger J_A \begin{pmatrix} 0 & \exp(-i\sqrt{\tau}\frac{\delta}{2}) \\ \exp(i\sqrt{\tau}\frac{\delta}{2}) & 0 \end{pmatrix} \Psi_{0'}. \tag{A.114}$$

The new spinor operators $\Psi_0 = \begin{pmatrix} \gamma_{0-} \\ \gamma_{0+} \end{pmatrix}$ and $\Psi_{0'} = \begin{pmatrix} \gamma_{0'-} \\ \gamma_{0'+} \end{pmatrix}$ do not depend on the phase δ[21]. However, it is hard to give a physical sense to these operators.

A.2.5.5 *Andreev Bound States as a spin-1/2 in phase-dependent magnetic field*

When the electron parity is even and conserved, one can project $\mathcal{H}_A$ in the two-dimensional subspace $\{|-\rangle, |+\rangle\}$. Using Eq. A.110, the Andreev Hamiltonian reads in a phase-independent basis

$$\boxed{H_A(\delta) = -\vec{\sigma}.\overrightarrow{h_A}(\delta)}. \tag{A.115}$$

The physics of the ABS is then analogous to the one of a spin-1/2 in a phase dependent magnetic field

$$\boxed{\overrightarrow{h_A}(\delta) = (\mathrm{Re}(Z)\sigma_z - \mathrm{Im}(Z)\sigma_y)} \tag{A.116}$$

whose both amplitude and orientation depend on the phase difference φ and on the transmission τ. The amplitude of this field is

$$\left|\overrightarrow{h_A}(\delta,\tau)\right| = |Z(\delta)| = E_A(\delta,\tau), \tag{A.117}$$

and the two eigenvalues of this spin are the Andreev energies $\pm E_A(\delta,\tau)$. Note that this Hamiltonian is in general not periodic with phase because $\exp(-i\sqrt{\tau}\frac{\delta}{2})$ is $\frac{4\pi}{\sqrt{\tau}}$ periodic. This seems pathological but most of the measurable quantities like the Andreev energies, are 2π-periodic[22].

21 To be consistent, one should check using equations (A.105), (A.108), (A.97) and (A.112) that $\frac{\partial \Psi_0}{\partial \delta} = \frac{\partial \Psi_{0'}}{\partial \delta} = 0$. This is very cumbersome and I have not done it. Moreover, the fact that we neglect the continuum could be problematic to satisfy these equalities.

22 This is problematic concerning the Berry-phase of the ABS (see Appendix D).

B

NOTES ON THE ANDREEV TWO-LEVEL SYSTEM

In Chapter 2 and Appendix A, we have derived the Andreev two-level Hamiltonian in a purely Hamiltonian method. The first calculation was made in 1999 by Ivanov and Feigelman [108]. In 2003, Zazunov and Shumeiko performed another derivation using a path integral approach [50], which gives a slightly different result, now considered to be the correct one. This appendix briefly sums up the different ways of writing the Andreev operators in different basis.

B.1 First derivation (Ivanov and Feigelman, Ref. [108])

The first derivation of the Andreev two-level Hamiltonian was made in Ref. [108]. It reads:

$$H_A = \mathrm{Re}(z)\sigma_z + \mathrm{Im}(z)\sigma_x \tag{B.1}$$

where $z = \Delta\left[\cos(\frac{\delta}{2}) + i\sqrt{r}\sin(\frac{\delta}{2})\right]$. This Hamiltonian is written in what the authors call the "ballistic states basis" (in the sense that it is diagonal for a transmission $\tau = 1$)[1]. Its eigenvalues are $\pm E_A(\delta)$. In a later work [50], it was argued that this Hamiltonian is not correct because charge neutrality was not correctly taken into account.

B.2 Second derivation (Zazunov *et al.*, Ref. [50, 66])

B.2.1 *Phase-independent basis*

In Ref. [50], the Hamiltonian is written in a phase-independent basis, which we note $\{|X\rangle, |Y\rangle\}$[2]:

$$H_A = -\begin{bmatrix} 0 & Z \\ Z^* & 0 \end{bmatrix} \tag{B.2}$$

where $Z = z\exp(-i\sqrt{r}\frac{\delta}{2})$. In Ref. [66], it written in a different basis$\{|x\rangle, |y\rangle\}$, also independent on phase:

$$\begin{aligned} H_A &= \exp\left(-i\sigma_x\sqrt{r}\tfrac{\delta}{2}\right)\left(\mathrm{Re}(z)\sigma_z + \mathrm{Im}(z)\sigma_y\right) \\ &= -\left(\mathrm{Re}(Z)\sigma_z + \mathrm{Im}(Z)\sigma_y\right). \end{aligned} \tag{B.3}$$

1 The authors claim that this basis is phase-independent, which is incorrect as shown in the next section.

2 I do not see any physical meaning of this basis.

One goes from one basis to the other by the rotation matrix $P = \frac{1}{\sqrt{2}}\begin{bmatrix} 1 & 1 \\ 1 & -1 \end{bmatrix}$, $\begin{pmatrix} |X\rangle \\ |Y\rangle \end{pmatrix} = P \begin{pmatrix} |x\rangle \\ |y\rangle \end{pmatrix}$. The first line of Eq. B.3 differs from the Hamiltonian derived in Ref. [108] (Eq. B.1) only by the additional exponential prefactor. The second line of Eq. B.3 is the same as the Hamiltonian (A.110) derived in *Appendix A*.

The current operator is defined as $C_A = \frac{1}{\varphi_0}\frac{dH_A}{d\delta}$. In $\{|X\rangle, |Y\rangle\}$basis, it writes

$$C_A = \frac{\tau\Delta}{2\varphi_0}\sin(\frac{\delta}{2})\begin{bmatrix} 0 & \exp(-i\sqrt{r}\frac{\delta}{2}) \\ \exp(i\sqrt{r}\frac{\delta}{2}) & 0 \end{bmatrix}. \tag{B.4}$$

The inverse inductance operator is defined as $L_A^{-1} = \frac{1}{\varphi_0^2}\frac{dH_A}{d\delta}$. In $\{|X\rangle, |Y\rangle\}$basis, it writes

$$L_A^{-1} = \frac{\tau}{4\varphi_0^2}\begin{bmatrix} 0 & z^* \exp(-i\sqrt{r}\frac{\delta}{2}) \\ z\exp(i\sqrt{r}\frac{\delta}{2}) & 0 \end{bmatrix}. \tag{B.5}$$

B.2.2 *Current operator basis*

By diagonalizing the current operator, one finds the phase-dependent current operator eigenbasis $\{|\rightarrow\rangle, |\leftarrow\rangle\}$:

$$\begin{pmatrix} |\rightarrow\rangle \\ |\leftarrow\rangle \end{pmatrix} = Q\begin{pmatrix} |X\rangle \\ |Y\rangle \end{pmatrix} \quad \text{with} \quad Q = \frac{1}{\sqrt{2}}\begin{bmatrix} \exp(-i\frac{\sqrt{r}\delta}{4}) & \exp(i\frac{\sqrt{r}\delta}{4}) \\ \exp(-i\frac{\sqrt{r}\delta}{4}) & -\exp(i\frac{\sqrt{r}\delta}{4}) \end{bmatrix}. \tag{B.6}$$

In this basis, using phase-dependent Pauli matrices[3]

$$\begin{cases} C_A = & \frac{e\Delta}{\hbar}\tau\sin(\frac{\delta}{2})\sigma_{z(\delta)} \\ H_A = & \Delta(\mathrm{Re}(z)\sigma_{z(\delta)} + \mathrm{Im}(z)\sigma_{y(\delta)}) \end{cases}. \tag{B.7}$$

This way of writing is exactly the same as the Hamiltonian derived in Ref. [108], except that it is written in a phase-dependent basis.

B.2.3 *Andreev states basis*

By diagonalizing the Hamiltonian, one finds the phase-dependent Andreev states basis $\{|-\rangle, |+\rangle\}$:

$$\begin{pmatrix} |-\rangle \\ |+\rangle \end{pmatrix} = R\begin{pmatrix} |X\rangle \\ |Y\rangle \end{pmatrix} \quad \text{with} \quad R = \frac{1}{\sqrt{2}}\begin{bmatrix} \exp(-i\frac{\sqrt{r}\delta-\theta}{4}) & \exp(i\frac{\sqrt{r}\delta-\theta}{4}) \\ \exp(-i\frac{\sqrt{r}\delta-\theta}{4}) & -\exp(i\frac{\sqrt{r}\delta-\theta}{4}) \end{bmatrix}. \tag{B.8}$$

In this basis, using phase-dependent Pauli matrices

$$\begin{cases} H_A = & -E_A(\delta)\sigma_{z(\delta)} \\ C_A = & I_A(\delta)[\sigma_{z(\delta)} + \sqrt{r}\tan(\frac{\delta}{2})\sigma_{x(\delta)}] \end{cases}. \tag{B.9}$$

3 In the sense that the axes $\{x, y, z\}$ depend on the phase.

The diagonal part of the current operator corresponds to what is expected[4]: supercurrent carried in state $|\pm\rangle$ is $\langle\pm| C_A |\pm\rangle = \mp I_A$. The off-diagonal part

$$\langle +| C_A |-\rangle = \langle -| C_A |+\rangle = \frac{e\Delta}{\hbar}\frac{\sqrt{1-\tau}}{\sqrt{1-\tau\sin^2(\frac{\delta}{2})}}\tau\sin^2(\frac{\delta}{2}), \tag{B.10}$$

is different from what is found in Ref. [108]. There is an additional $\tau\sin^2(\frac{\delta}{2})$ factor. This non diagonal term is important because it allows transition between $|-\rangle$ and $|+\rangle$ states.

Note that $[H_A\ ,\ C_A] \neq 0$, they do not have the same eigenstates. By consequence, when the system is in an eigenstate of H_A, *i.e.* in an Andreev state, current undergoes quantum fluctuations with spectral function[5]

$$S(\omega,\delta) = I_A^2(\delta)(1-\tau)\tan^2(\frac{\delta}{2})\delta(\omega - 2E_A) \tag{B.11}$$

where I_A is defined in equation Eq. 2.49. This result was first found in Ref. [138] with Green functions (formula 11) and is not restricted to high transmissions channels and phase δ around π. The spectral density of the current fluctuations was later calculated in Ref. [50] by using the two-level Hamiltonian (B.2) with the same result. Note however that the Hamiltonian (B.1) would give a different result.

One can also derive the inverse inductance operator: $L_A^{-1} = \frac{\tau}{4\varphi_0^2}|z|\left[\cos(\theta)\,\sigma_{z(\delta)} - \sin(\theta)\,\sigma_{y(\delta)}\right]$. Therefore

$$L_A^{-1} = \frac{\Delta\tau}{4\varphi_0^2}\frac{1}{\sqrt{1-\tau\sin^2(\frac{\delta}{2})}}\left[\frac{\tau+(2-\tau)\cos(\delta)}{2}\sigma_{z(\delta)} - \sqrt{1-\tau}\sin(\delta)\sigma_{y(\delta)}\right]. \tag{B.12}$$

Thus, $\left[H_A\ ,\ L_A^{-1}\right] \neq 0$, and the two operators do not have the same eigenstates.

4 Actually, it is not straightforward. The reason why this is true is that $\langle +|\frac{\partial|-\rangle}{\partial\delta} = \langle -|\frac{\partial|+\rangle}{\partial\delta} = 0$ due to equation D.5.

5 $\delta(\omega)$ is here the Dirac function, not to confuse with the phase difference.

C

HAMILTONIAN DESCRIPTION OF AN ELECTROMAGNETIC ENVIRONMENT OF IMPEDANCE $Z(\omega)$

This chapter briefly presents frequently used formulas: the classical impedance of an harmonic oscillator and the Hamiltonian of an arbitrary electromagnetic environment described by a linear impedance $Z(\omega)$.

C.1 Single-mode environment: the LC harmonic oscillator

In linear response theory, an electromagnetic environment can be described by its impedance $Z(\omega)$. The energy absorption of the environment is related to $\mathrm{Re}[Z(\omega)]$. We will first derive the one of the most basic element, the LC harmonic oscillator.

C.1.1 *Impedance calculation*

We consider an inductor of inductance L in parallel with a capacitor of capacitance C. One defines

$$\boxed{\begin{cases} \omega_0 = \frac{1}{\sqrt{LC}} \\ Z_0 = \sqrt{\frac{L}{C}} \end{cases}} \tag{C.1}$$

the resonance angular frequency and characteristic impedance. The reduced impedance $z = \frac{Z}{Z_0}$ of the LC circuit reads

$$z(\omega_r) = i\frac{\omega_r}{1-\omega_r^2} \tag{C.2}$$

where $\omega_r = \frac{\omega}{\omega_0}$ is the reduced pulsation.

A pedestrian way[1] to derive the real part of the impedance is to add a small conductance g in parallel with the inductor and capacitor (see Fig. C.1). Then

$$z(\omega_r) = \frac{i\omega_r}{1-\omega_r^2+i\frac{\omega_r}{Q}} \tag{C.3}$$

with

$$Q = (gL\omega_0)^{-1}. \tag{C.4}$$

Therefore

$$\boxed{\mathrm{Re}[z(\omega_r)] = \frac{Q}{1+\left(Q\frac{1-\omega_r^2}{\omega_r}\right)^2}} \tag{C.5}$$

1 More directly, one uses the relation

$$\frac{1}{1-\omega_r^2} = \frac{1}{2}\left[\frac{1}{1-\omega_r}+\frac{1}{1+\omega_r}\right] = \frac{1}{2}\left[\mathcal{P}\left(\frac{1}{1-\omega_r^2}\right)+i\pi(\delta(1-\omega_r)+\delta(1+\omega_r))\right]$$

where $\mathcal{P}$ is the Cauchy principal value.

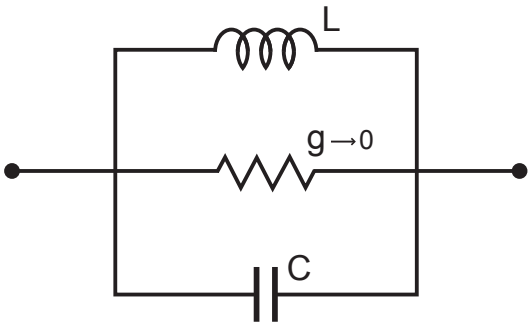

Figure C.1: Schematic circuit of an LC harmonic oscillator, with a small conductance g in parallel.

and

$$\mathrm{Im}\left[z(\omega_r)\right] = \frac{\omega_r\left(1-\omega_r^2\right)}{\left(1-\omega_r^2\right)^2 + \left(\frac{\omega_r}{Q}\right)^2}. \tag{C.6}$$

They are both represented in Fig. C.2. The real part of the impedance is a Lorentzian-

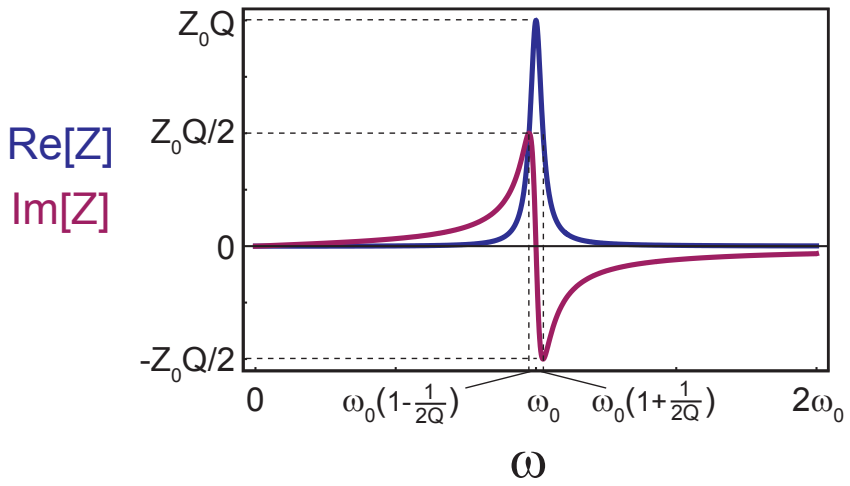

Figure C.2: Real part (blue) and imaginary part (purple) of the impedance of an LC harmonic oscillator. This plot is done for a quality factor $Q = 20$.

like function, centered at ω_0, of height $1/g$, full width half maximum $gL\omega_0^2$ and quality factor Q. The imaginary part of the impedance is also regularized by the presence of the parallel conductance g. In particular, it is now zero at resonance ($\mathrm{Im}\left[z(1)\right] = 0$) and is maximum close to ω_0 with values $Z_0Q/2$.

When $g \to 0$, $\mathrm{Re}\left[Z\right]$ tends to a double Dirac distribution[2]:

$$\boxed{\mathrm{Re}\left[Z_{\omega_0}(\omega)\right] = \frac{\pi}{2} Z_0\omega_0\left[\delta\left(\omega-\omega_0\right) + \delta\left(\omega+\omega_0\right)\right]}. \tag{C.7}$$

2 One gets the proportionality coefficient by integrating over ω_r.

C.1.2 *Hamiltonian derivation in second quantization formalism*

The quantum dynamics of an LC harmonic oscillator is fully described by the Hamiltonian

$$H = \frac{Q^2}{2C} + \frac{\Phi^2}{2L} \tag{C.8}$$

where Q, the charge imbalance on the capacitor, and Φ, the flux associated to the inductance, are quantum conjugated variables $[Q, \Phi] = i\hbar$. It is solved in the formalism of second quantization. One defines the annihilation and creation operators

$$a = \frac{\Phi}{\Phi_0} + i\frac{Q}{Q_0}, \quad a^\dagger = \frac{\Phi}{\Phi_0} - i\frac{Q}{Q_0} \tag{C.9}$$

with $\Phi_0 = \sqrt{2\hbar Z_0}$, $Q_0 = \sqrt{2\hbar/Z_0}$, such as $\left[a, a^\dagger\right] = 1$. Then H becomes

$$\boxed{H = \hbar\omega_0(a^\dagger a + \frac{1}{2})}. \tag{C.10}$$

Its eigenstates are the photon states $\forall n \in \mathbb{N}$, $|n\rangle = (a^\dagger)^n |0\rangle$ of eigenenergies $(n + \frac{1}{2})\hbar\omega_0$, obtained from vacuum $|0\rangle$ by successive application of the creation operator $a^\dagger$. The quantum fluctuations of the ground state are $\sqrt{\langle 0| \Phi^2 |0\rangle} = \Phi_0$ and $\sqrt{\langle 0| Q^2 |0\rangle} = Q_0$.

C.2 Arbitrary electromagnetic environment of impedance $Z(\omega)$

C.2.1 *Impedance calculation: Caldeira-Leggett decomposition*

Every linear electromagnetic environment can be seen as an infinite continuous sum of harmonic oscillators [123]. Indeed

$$\forall \omega, \quad \mathrm{Re}\left[Z(\omega)\right] = \int_0^\infty \mathrm{Re}\left[Z(\omega')\right] \delta(\omega - \omega') d\omega'. \tag{C.11}$$

By discretizing this sum in step of $\Delta\omega$, one gets

$$\boxed{\mathrm{Re}\left[Z(\omega)\right] = \lim_{\Delta\omega \to 0} \sum_{n=-\infty}^{\infty} \frac{\pi}{2} \omega_n Z_n \delta\left(\omega - \omega_n\right)} \tag{C.12}$$

with

$$\boxed{\begin{cases} \omega_n = & n\Delta\omega \\ Z_n = & \frac{1}{n}\mathrm{Re}[Z(\omega_n)] \end{cases}}. \tag{C.13}$$

Due to Kramers-Kronig causality relation

$$Z^*(-\omega) = Z(\omega). \tag{C.14}$$

Therefore, $Z_{-n} = Z_n$ and

$$\mathrm{Re}\left[Z(\omega)\right] = \lim_{\Delta\omega \to 0} \sum_{n=1}^{\infty} \mathrm{Re}\left[Z_{\omega_n}(\omega)\right]. \tag{C.15}$$

Consequently, every electromagnetic environment can be decomposed in a discrete sum of harmonic oscillators, of resonant pulsation ω_n and characteristic impedance Z_n. One can define their inductance and capacitance as $L_n = \frac{Z_n}{\omega_n}$ and $C_n = \frac{1}{Z_n \omega_n}$.

In order to work out the effect of such an impedance in a network, one can explicitly perform the decomposition and work out the dynamics of each elementary oscillator. In the end, when evaluating a quantity of interest, one usually finds a result of the form $\sum Z_n f(\omega_n)$, which in the continuum limit becomes an integral on ReZ:

$$\sum_{n=1}^{\infty} Z_n f(\omega_n) \underset{\Delta\omega \to 0}{\longrightarrow} \frac{2}{\pi} \int_0^{\infty} \frac{1}{\omega} \mathrm{Re}\left[Z(\omega)\right] f(\omega) d\omega. \tag{C.16}$$

C.2.2 *Hamiltonian derivation in second quantization formalism*

Now, one naturally defines

$$\forall n \epsilon \mathbb{N}^{\star}, \quad \begin{cases} \Phi_{0n} = \sqrt{2\hbar Z_n} \\ Q_{0n} = \sqrt{\frac{2\hbar}{Z_n}} \end{cases} \quad \text{and} \quad \begin{cases} a_n = \frac{\Phi_n}{\Phi_{0n}} + i\frac{Q_n}{Q_{0n}} \\ a_n^{\dagger} = \frac{\Phi_n}{\Phi_{0n}} - i\frac{Q_n}{Q_{0n}} \end{cases} \tag{C.17}$$

and the Hamiltonian writes

$$\boxed{H = \sum_{n=1}^{\infty} \hbar\omega_n (a_n^{\dagger} a_n + \frac{1}{2})}. \tag{C.18}$$

Note that the total phase γ over the impedance is given by

$$\boxed{\gamma = \frac{1}{\varphi_0} \sum_{n=1}^{\infty} \Phi_n = \sum_{n=1}^{\infty} \sqrt{\frac{\pi Z_n}{R_Q}} (a_n + a_n^{\dagger})} \tag{C.19}$$

with $R_Q = \frac{h}{4e^2}$ being the superconducting resistance quantum. This a quantity of interest when one deals with Coulomb blockade theory (Chapter 7) or calculating transition rates of a Qubit in parallel with an environment (Appendix D).

D

ANDREEV BOUND STATES DYNAMICS

In this chapter, we restrict to the one-particle Andreev two-level Hamiltonian

$$H_A(\delta) = -E_A(\delta)\,\sigma_z(\delta) \tag{D.1}$$

derived in Appendix A, valid when the ABS are deep inside the superconducting gap, and when their parity is even and conserved. The goal of this chapter is to derive different approaches, both semi-classical and quantum, to deal with the dynamics of phase and hence the dynamics of the ABS.

D.1 Semi-classical treatment

D.1.1 *Instantaneous two-level Hamiltonian*

When the phase depends on time, the Hamiltonian (D.1) also depends on time and the Andreev eigenstates are no longer stationary states. A general way of taking this time dependence into account is to derive an instantaneous Hamiltonian. Let us consider an arbitrary superposition of states $|-\rangle$ and $|+\rangle$ written in the Andreev states instantaneous eigenbasis

$$|\psi(t)\rangle = a(t)\,|-(t)\rangle + b(t)\,|+(t)\rangle\,. \tag{D.2}$$

It verifies Schrödinger equation

$$i\hbar\frac{\partial\,|\psi\rangle}{\partial t} = H_A\,|\psi\rangle\,. \tag{D.3}$$

Since

$$\begin{cases} H_A\,|\psi\rangle = & E_A\,[-a(t)\,|-\rangle + b(t)\,|+\rangle] \\ \frac{\partial|\psi\rangle}{\partial t} = & \dot{a}\,|-\rangle + \dot{b}\,|+\rangle + \dot{\delta}[a(t)\frac{\partial|-\rangle}{\partial\delta} + b(t)\frac{\partial|+\rangle}{\partial\delta}] \end{cases} \tag{D.4}$$

and (using equation Eq. B.8)

$$\begin{cases} \frac{\partial|-\rangle}{\partial\delta} = \theta'\,|+\rangle \\ \frac{\partial|+\rangle}{\partial\delta} = -\theta'\,|-\rangle \end{cases}, \tag{D.5}$$

with

$$\theta' = \frac{1}{4}(r - \frac{\partial\theta}{\partial\delta}) = -\frac{\sqrt{r}\tau\sin^2(\frac{\delta}{2})}{4\left(1-\tau\sin^2(\frac{\delta}{2})\right)}, \tag{D.6}$$

one gets, by projecting on $|-\rangle$ and $|+\rangle$:

$$\begin{cases} i\hbar\left[\dot{a} - \dot{\delta}\theta' b(t)\right] = -E_A\,a(t) \\ i\hbar\left[\dot{b} + \dot{\delta}\theta' a(t)\right] = E_A\,b(t) \end{cases}. \tag{D.7}$$

Then, one can derive an effective Hamiltonian

$$\boxed{\bar{H}_A = -E_A(\delta)\sigma_{z(\delta)} - \hbar\dot{\delta}(t)\theta'\sigma_{y(\delta)}}. \tag{D.8}$$

such that

$$i\hbar\frac{\partial}{\partial t}\begin{pmatrix} a \\ b \end{pmatrix} = \bar{H}_A \begin{pmatrix} a \\ b \end{pmatrix}. \tag{D.9}$$

A similar result can be found in Ref. [140].

This effective Hamiltonian is written in the instantaneous Andreev eigenbasis and describe the dynamics of population in each level for any time dependence of the phase. The ABS are no longer stationary states and are coupled through its non-diagonal part, whose absolute value is $\left|\hbar\dot{\delta}(t)\theta'\right|$, which is maximum in $\delta = \pi$. Such a derivation is useful in numerical calculations [140] where the time is discretized. However, it is not very convenient to derive approximate analytical results, as it will be done in the next two sections.

D.1.2 *Landau-Zener transition*

Let us first consider a situation where the phase varies linearly with time, which is what happens in presence of a constant voltage bias V,:

$$\dot{\delta}(t) = \frac{V}{\varphi_0}. \tag{D.10}$$

Then, starting from the ground state $|-\rangle$, one can reach the state $|+\rangle$ by a Landau-Zener transition [141, 79], if phase is swept sufficiently fast, i.e. if voltage is big enough (see Fig. D.1). As explained in Section 3.4.1, such a process is responsible for the dc current at low voltage in ACs which is better described at larger voltages with the MAR processes.

Provided that the system satisfies certain "reasonable restrictions"[1], the Landau-Zener probability reads:

$$p_{LZ} = \exp\left(-\pi\frac{|2\epsilon_{12}|^2}{2\hbar\left|\frac{d}{dt}(\epsilon_1 - \epsilon_2)\right|}\right), \tag{D.11}$$

where $2\epsilon_{12}$ (respectively $\epsilon_1 - \epsilon_2$) is the transition energy between the adiabatic (ballistic) levels, estimated at the level crossing.

In the case of the ABS,

$$2\epsilon_{12} = 2E_A(\pi,\tau) = 2\Delta\sqrt{r} \text{ and } \epsilon_1 - \epsilon_2 = 2\left(E_A(\pi,1) + \delta\lim_{\delta\to\pi^-}\varphi_0 I_A(\delta,1)\right) = \Delta\delta, \tag{D.12}$$

where we have performed a Taylor expansion to first order. Using Eq. D.10, the probability reads

$$\boxed{p_{LZ} = \exp\left(-\pi\frac{r\Delta}{eV}\right)}. \tag{D.13}$$

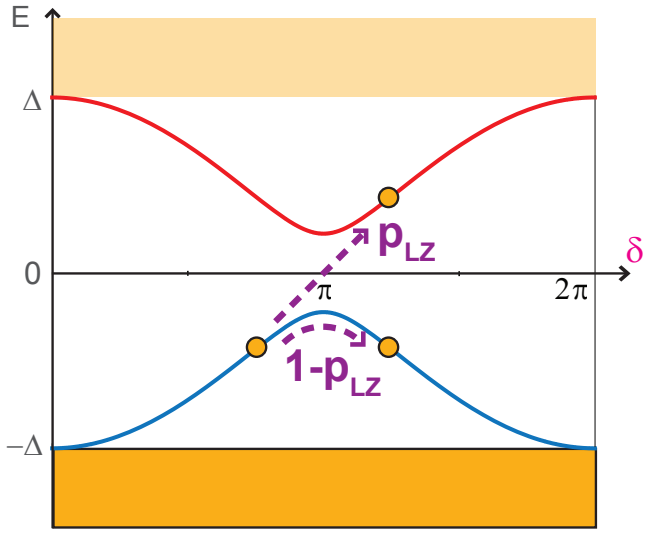

Figure D.1: Landau-Zener transition between the two ABS (in a channel of transmission 0.95): As the phase is swept at high speed across the Andreev gap ($2\Delta\sqrt{1-\tau}$) at $\delta = \pi$, a quasiparticle has a finite probability p_{LZ} to tunnel from the ground to the excited even state.

Note that the probability (D.11) is asymptotic and computed after an infinite time when the two levels are far apart. In the case of the ABS, it is quite different since their energies are periodical function of the phase and thus of the time. Therefore, the original calculation is not strictly valid. However, it makes sense under the reasonable assumption that each time the ABS connect to the continuum the two-level system is no longer in a quantum superposition and the system is reinitialized with a quasiparticle in the lower ABS (the upper quasiparticle empties in the upper continuum and another quasiparticle fills the lower ABS). In this sense, (D.13) is the probability to jump from the ground to the excited ABS per cycle of period $2\pi\frac{\varphi_0}{V}$.

D.1.3 *Rabi oscillations in presence of a classical microwave excitation*

Let us now consider the case of an ac voltage bias at pulsation ω. Then, the phase oscillates around a dc phase δ_0 as

$$\delta(t) = \delta_0 + \delta_1 \cos(\omega t). \tag{D.14}$$

Such an excitation is commonly used in superconducting qubits to manipulate the quantum state of two-level systems.

We consider that the amplitude of the microwave excitation is very small $\delta_1 \ll 2\pi$. Therefore, one performs a Taylor expansion of H_A around the average phase δ_0:

$$H_A(\delta_0, t) = H_A(\delta_0) + \varphi_0\delta_1 \cos(\omega t)\, C_A(\delta_0). \tag{D.15}$$

1 The transition region is so small that one may treat $\epsilon_1 - \epsilon_2$ as a linear function of time, and $2\epsilon_{12}$ as independent of time.

One looks for a state (in the rotating basis)

$$|\psi(t)\rangle = \alpha(t)\exp\left(\frac{i}{2}\omega t\right)|-\rangle + \beta(t)\exp\left(-\frac{i}{2}\omega t\right)|+\rangle\,, \tag{D.16}$$

solution of the Schrödinger equation (D.3):

$$\begin{cases} 2i\dot{\alpha} = \left[\omega - \omega_A + \omega_R\left(e^{i\omega t} + e^{-i\omega t}\right)\right]\alpha + \omega_C\left(1 + e^{-i2\omega t}\right)\beta \\ 2i\dot{\beta} = -\left[\omega - \omega_A + \omega_R\left(e^{i\omega t} + e^{-i\omega t}\right)\right]\beta + \omega_C\left(1 + e^{i2\omega t}\right)\alpha \end{cases}, \tag{D.17}$$

with

$$\begin{cases} \hbar\omega_A(\delta_0) = & 2E_A(\delta_0) \\ \hbar\omega_R(\delta_0) = & \varphi_0\delta_1 I_A(\delta_0) \\ \hbar\omega_C(\delta_0) = & \varphi_0\delta_1 I_A(\delta_0)\sqrt{\tau}\tan\left(\frac{\delta}{2}\right) \end{cases}. \tag{D.18}$$

The probability to be in the excited ABS (starting from a pure ground state at the time zero $\alpha(0) = 1$ and $\beta(0) = 0$) is $P_{-\to+}(t) = |\beta(t)|^2$. It is hard to solve analytically this system of differential equations. One neglects the fast oscillating terms, which is valid in the vicinity of the resonance $\omega = \omega_A$. Then, one gets

$$P_{-\to+}(t) = \left(\frac{\omega_C}{\Omega}\right)^2 \sin^2\left(\frac{\Omega t}{2}\right) \tag{D.19}$$

with

$$\Omega^2 = (\omega - \omega_A)^2 + \omega_C^2. \tag{D.20}$$

Therefore, the system oscillates between the two ABS in a Rabi cycle [142] at the pulsation $\frac{\Omega}{2}$. The probability to be in the excited state $|+\rangle$ is maximum at times $(2n+1)\frac{\pi}{2}$. The closer the excitation frequency from the Andreev transition frequency, the higher this probability is. Note that this derivation is valid only when the excitation δ_1 is small $\delta_1 \ll 2\pi$. Then, the ABS do not connect to the continuum and remain a true two-level system (contrary to the Landau-Zener tunneling under a dc voltage bias) .

D.1.4 *Berry phase of the Andreev bound states*

As explained in Section 2.5.4 and Section A.2.5.5, the Andreev two-level system is like a spin$-\frac{1}{2}$ in an effective magnetic field

$$\overrightarrow{h_A}(\delta,\tau) = \mathrm{Im}(Z)\overrightarrow{e_y} + \mathrm{Re}(Z)\overrightarrow{e_z} \tag{D.21}$$

whose amplitude and orientation depend on the phase δ and on the transmission τ. By slowly varying δ, one can adiabatically rotate $\overrightarrow{h_A}$ in the Oyz plane around a loop C, so that the system remains always in its local ground state. Then, whereas the Hamiltonian is back to its initial point, the ground state can be different from the starting one by a phase $\gamma(C)$, called the Berry phase [143, 144], whose magnitude is given by the enclosed solid angle $\Omega(C)$ multiplied by $-\frac{1}{2}$:

$$\gamma(C) = -\frac{1}{2}\Omega(C)\,. \tag{D.22}$$

However, for this specific Hamiltonian, the field $\overrightarrow{h_A}$ is in general not periodic in phase ! Indeed, whereas the amplitude E_A of the field is 2π-periodic, its direction, which is related to the angle between $\overrightarrow{e_y}$ and $\overrightarrow{h_A}$

$$\alpha_A(\delta,\tau) = \arctan\left(\frac{\mathrm{Re}(Z)}{\mathrm{Im}(Z)}\right) = \arctan\left(\frac{\cos(\frac{\delta}{2})\cos(r\frac{\delta}{2})}{r\sin(\frac{\delta}{2})\sin(r\frac{\delta}{2})}\right), \tag{D.23}$$

is $4\pi/r$ periodic. For specific values of the transmission, 2π and $4\pi/r$ can be commensurate, and then the field is periodic. For instance, for $\tau = 0.75 \Leftrightarrow r = 0.5$, by sweeping slowly the phase δ of 8π , the ground state picks a Berry phase $\gamma = \pi$. But in general, the Hamiltonian is not periodic and the Berry phase is not defined.

This seems quite pathological[2]. One can give two elements of answer:

1. The two-level Hamiltonian has been derived for a stationary phase. When it is time-dependent, one needs to specify the gauge, which we have not done and can be a source of problem.

2. The two-level Hamiltonian is valid for ABS deep inside the superconducting gap, *i.e.* for phase δ around π. The thought experiment to measure a Berry phase consists in sweeping the phase δ over 4π. Doing so, one connects to the continuum and probably looses the quantum coherence of the ground state necessary for measuring the Berry phase of the ABS. Therefore, being pragmatic, one does not care about the non-periodicity of the two-level Hamiltonian since all the measurable quantities are 2π periodic.

Consequently, despite the fact that the ABS resemble a spin$-\frac{1}{2}$ in a magnetic field, considerations on the Berry phase do not seem very relevant.

D.2 Quantum fluctuations of the phase

D.2.1 *Full quantization of the Andreev Hamiltonian*

As done in Section 2.5.5, one can simply consider in the Andreev Hamiltonian (D.1) δ as a quantum operator. To separate the Andreev degree of freedom from the phase degree of freedom, following Ref. [67], one performs a Taylor expansion of H_A around the average phase δ_0:

$$\boxed{H_A(\delta_0+\hat{\delta}) = H_A(\delta_0) + \varphi_0\,\hat{\delta}\,C_A(\delta_0) + \frac{1}{2}\varphi_0^2\,\hat{\delta}^2\,L_A^{-1}(\delta_0)}. \tag{D.25}$$

2 Note that there is not such a problem with the incorrect Hamiltonian (B.1) derived in Ref. [108]. Indeed $\overrightarrow{h_A}(\delta,\tau) = -\mathrm{Im}(z)\overrightarrow{e_x} - \mathrm{Re}(z)\overrightarrow{e_z}$ and

$$\alpha_A(\delta,\tau) = \arctan\left(\frac{\mathrm{Re}(z)}{\mathrm{Im}(z)}\right) = \arctan\left(\frac{1}{r\tan(\frac{\delta}{2})}\right) = \frac{\pi-\theta(\delta)}{2}, \tag{D.24}$$

which is 4π periodic in δ. Thus, by sweeping slowly the phase δ over 4π, the equivalent field $\overrightarrow{h_A}$ rotates around a loop in the Oxz plane and the Andreev ground state picks a Berry phase $\gamma = \pi$.

This is correct as long as quantum fluctuations are small[3], *i.e.* $\sqrt{\langle\delta^2\rangle} \ll 2\pi$.

Therefore, whereas the diagonal terms of the current and inverse inductance operator only renormalize the mean Andreev energy, the off-diagonal ones allow transitions between the ABS. In particular, to zero order, the coupling term is

$$\Omega_{x1} = \langle +|\, \varphi_0 C_A\, |-\rangle = \langle -|\, \varphi_0 C_A\, |+\rangle = \varphi_0 I_A(\varphi,\tau)\sqrt{\tau}\tan\left(\frac{\delta_0}{2}\right). \tag{D.26}$$

Its maximum $\Delta\tau/2$ is reached at $\delta_0 = \pi$, as shown in Fig. D.2.

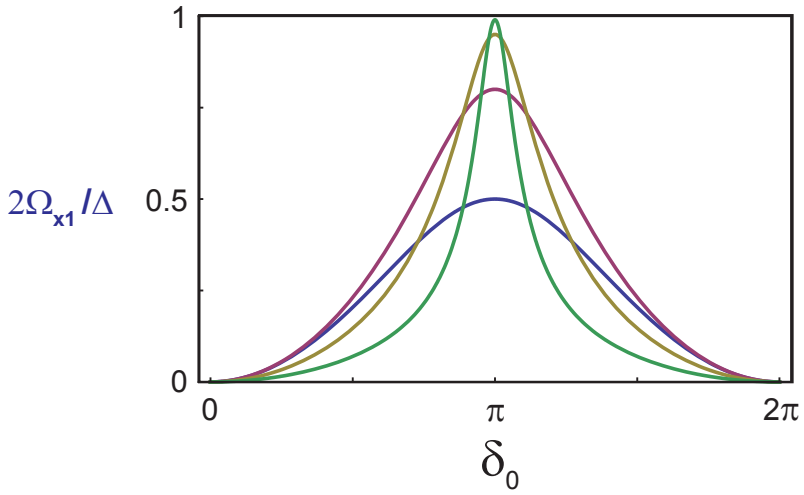

Figure D.2: Coupling energy Ω_{x1} as a function of the phase difference δ_0, for four different transmissions: $\tau = 0.5$ (blue), 0.8 (purple), 0.95 (yellow) and 0.99 (green).

D.2.2 *Transition rates of an Andreev two-level system coupled to its electromagnetic environment*

When coupled to an electromagnetic environment, the excited state $|+\rangle$ have a finite life-time. We perform here the calculations of the rates between $|-\rangle$ and $|+\rangle$. This derivation is close from the one performed in Chapter 7. Note that a similar result was already found in 2001 by Desposito and Levy Yeyati [67]. However at this time, their calculation was done by using the two-level Hamiltonian derived in Ref. [108].

D.2.2.1 *The system*

We consider a JC of transmission τ inserted in a superconducting ring threaded by a reduce magnetic flux φ. Its electromagnetic environment is a bosonic bath characterized by a parallel impedance $Z(\omega)$ (see Fig. D.3). The Hamiltonian describing

3 Actually, it's not that easy to define and derive $\sqrt{\langle\hat{\delta}^2\rangle}$ and δ_0. Indeed, these mean values depend on the actual quantum states of the system, which are unknown since we do not know how to diagonalize the exact Hamiltonian. One can solve it in perturbation, using this Taylor expansion, and solve a self-consistent equation $\delta_0 = \langle GS(\delta_0)|\,\hat{\delta}\,|GS(\delta_0)\rangle$. In this thesis work, we are always considering a big JJ in parallel with the AC. Then this approximation is valid.

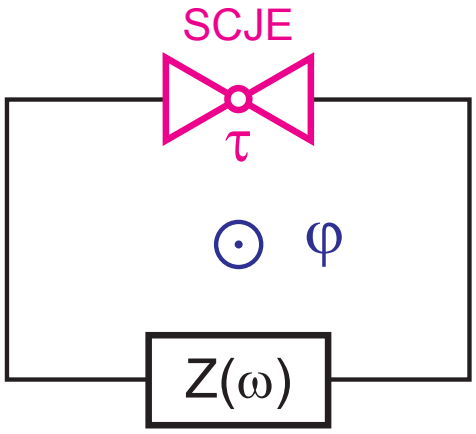

Figure D.3: Schematic circuit: a JC of transmission τ is inserted in a superconducting ring threaded by a reduce magnetic flux φ. $Z(\omega)$ denotes the effective impedance seen by the contact.

this system is

$$H = H_A(\delta) + H_{env} \tag{D.27}$$

where H_A is the Andreev two-level Hamiltonian D.1 and H_{env} is the Hamiltonian of the environment. One decomposes the latter in a discrete sum of harmonic oscillators (see Section C.2):

$$H_{env} = \sum_{n=1}^{\infty} \hbar\omega_n (a_n^+ a_n + \frac{1}{2}) \tag{D.28}$$

with $\delta = \sum_{n=1}^{\infty} \sqrt{\frac{\pi Z_n}{R_Q}}(a_n + a_n^+)$ and $Z_n = \frac{1}{n}\mathrm{Re}[Z(\omega_n)]$. Then, using Eq. D.25, the total Hamiltonian writes:

$$\begin{aligned} H(\varphi) = & \sum_{n=1}^{\infty} \hbar\omega_n (a_n^+ a_n + \tfrac{1}{2}) + [-E_A(\varphi) + \varphi_0 I_A(\varphi) \sum_{n=1}^{\infty} \sqrt{\tfrac{\pi Z_n}{R_Q}}(a_n + a_n^+)]\sigma_z(\varphi) \\ & + \varphi_0 I_A(\varphi) r \tan(\tfrac{\delta_0}{2}) \sum_{n=1}^{\infty} \sqrt{\tfrac{\pi Z_n}{R_Q}}(a_n + a_n^+)\sigma_x(\varphi). \end{aligned} \tag{D.29}$$

We have here neglected the terms coming from the inductance operator, which are an order of magnitude smaller. We have also assumed that $\langle\delta\rangle = \varphi$, which is valid in the limit of a JC "small" compared to the environment. This Hamiltonian cannot be diagonalize: it is a spin-boson problem [51, 52]. But one can calculate its approximate eigenvalues in perturbation.

D.2.2.2 *Explicit zero temperature calculation*

Here we are only interested in calculating the downward transition rate at zero temperature. The states can be labeled

$$|\pm\rangle \otimes |n_1, n_2, ..., n_k, ...\rangle\,, \tag{D.30}$$

where $|\pm\rangle$ accounts for the Andreev degree of freedom and $|n_1, n_2, ..., n_k, ...\rangle$ for the electromagnetic degrees of freedom, with n_k photons in the k^{th} oscillator

mode. We only consider one-photon transitions, thus neglecting higher harmonic orders. Therefore, at zero temperature, the system starts from the initial state $|i\rangle = |+\rangle \otimes |0, ..., 0, ...\rangle$ and reaches any final state $|f_k\rangle = |-\rangle \otimes |0, ..., 0, 1, 0, ...\rangle$, 1 being in k^{th} position. Using Fermi Golden rule, one gets:

$$\Gamma_0 = \frac{2\pi}{\hbar} \sum_{k=1}^{\infty} |\langle f_k | H | i \rangle|^2 \, \delta(E_{f_k} - E_i) \tag{D.31}$$

where δ is here the Dirac function. In the Hamiltonian (D.29), only the third term in σ_x couples $|+\rangle$ and $|-\rangle$. Hence

$$\Gamma_0 = \frac{2\pi}{\hbar} \left[\varphi_0 I_A(\varphi) r \tan(\frac{\varphi}{2})\right]^2 \sum_{k=1}^{\infty} \left| \sum_{n=1}^{\infty} \sqrt{\frac{\pi Z_n}{R_Q}} \langle f_k | (a_n + a_n^+)\sigma_x(\varphi) | i \rangle \right|^2 \delta(E_{f_k} - E_i). \tag{D.32}$$

Because $\sigma_x(\varphi)|+\rangle = |-\rangle$ and $\langle 1_k | (a_n + a_n^+) | 0 \rangle = \delta_{k,n}$, one finds

$$\Gamma_0 = \frac{2\pi}{\hbar} [\varphi_0 I_A(\varphi) r \tan(\frac{\varphi}{2})]^2 \sum_{n=1}^{\infty} \frac{\pi Z_n}{R_Q} \delta[\hbar\omega_n - 2E_A(\varphi)]. \tag{D.33}$$

One passes from a discrete to a continuous sum using Eq. C.16. Then[4]:

$$\boxed{\Gamma_0 = \frac{\pi\Delta}{2\hbar} \frac{\mathrm{Re}\left[Z(2E_A(\varphi)/\hbar)\right]}{R_Q} \frac{(1-\tau)\,\tau^2 \sin^4(\frac{\varphi}{2})}{\left[1 - \tau \sin^2(\frac{\varphi}{2})\right]^{3/2}}}. \tag{D.34}$$

At zero temperature, the coupling to any bosonic bath induces quantum fluctuations of the ABS, which provokes spontaneous emission. This gives a finite lifetime to the excited Andreev state $T_1 = \Gamma_0^{-1}$, which depends only on the real part of the impedance of the environment.

D.2.2.3 *Extension to finite temperature*

At finite temperature, the energy stored in the bosonic bath can be absorbed by the ABS and allows transition from the ground to the excited state. It also increases relaxation from excited to ground state by stimulated emission. Following Ref. [67], we make two approximations to simplify the rate expressions: large cutoff frequency for the environment (compared to $\Delta/\hbar$) and Markov approximation in the evolution equations (short memory approximation).Then, the emission and absorption rates simple read as a function of the zero temperature relaxation rate:

$$\boxed{\begin{cases} \Gamma_{20}^{em} = \Gamma_0 * [N(2E_A) + 1] \\ \Gamma_{02}^{abs} = \Gamma_0 * N(2E_A) \end{cases}} \tag{D.35}$$

where

$$N(2E_A) = \frac{1}{\exp\left(\frac{2E_A}{k_B T}\right) - 1} \tag{D.36}$$

is the Bose-Einstein mean occupation number of photons at temperature T.

4 This result is analogous to the one derived in Ref. [67], except that they have used the Hamiltonian derived in Ref. [108]. However, apart from the additional $\left(\tau \sin^2(\frac{\varphi}{2})\right)^2$ factor, I also find a factor 2 difference.

E

SUPPLEMENTARY MATERIALS ON THE SWITCHING EXPERIMENT

E.1 Characterization of PAL7

The equivalent schematic of the setup is shown in Fig. E.1.

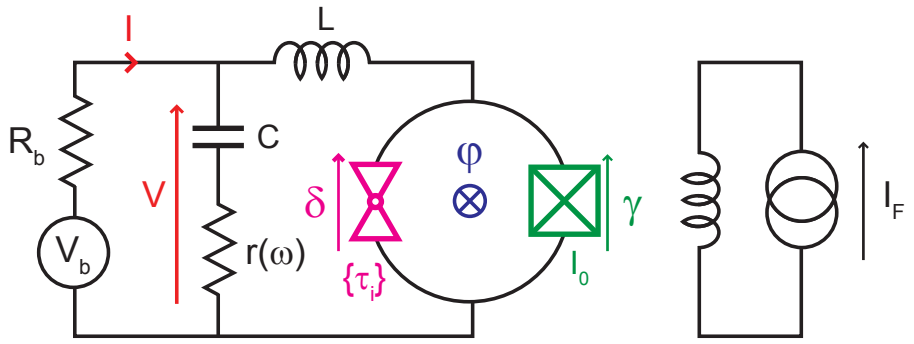

Figure E.1: Full schematic of the sample. The SQUID is biased through an on-chip LC circuit ($L \simeq 0.75\,nH$, $C \simeq 60\,pF$). The losses in the capacitor are modeled by frequency-dependent series resistance $r(\omega)$. The voltage V measured across the full on-chip circuit corresponds, at low frequency, to the voltage drop across the SQUID. The current I is determined from the voltage across the bias resistor $R_b \simeq 200\,\Omega$.

The critical current of the JJ of the SQUID was measured in the switching experiment. Its capacitance is deduced from its area (2.8 μm^2), using the conversion factor 75 $fF/\mu m^2$. The value of the loop inductance was inferred from an experiment with a similar loop geometry (see Fig 6.18 in Ref. [72]).

The low-frequency environment of the atomic-SQUID was probed in a separate experiment by microwave reflectometry. Essentially, we have used a nominally $50\,\Omega$ line to inject microwaves into the circuit and measured the reflected signal (see wiring in Chapter 10). Fig. E.2 shows the magnitude of the reflected signal as a function of the microwave frequency for two different configurations of the contact.

The resonance near 0.6 GHz, which strongly depends on the contact, is interpreted as the mode of the LC-oscillator slightly modified by the inductance of the SQUID (see Eq. 5.2.1). The left-most peak at frequency

$$\nu_e \simeq \frac{1}{2\pi}\frac{1}{\sqrt{(L+L_0)\,C}} \simeq 560\,MHz$$

corresponds to the open contact and includes the JJ equivalent inductance $L_0 = \frac{\varphi_0}{I_0}$. From the capacitance $C \simeq 60pF$, which was measured at room temperature, one gets the inductance[1] $L \simeq 750\,pH$.

1 These values are different from those we reported in Ref. [38] where we had neglected the contribution of the junction.

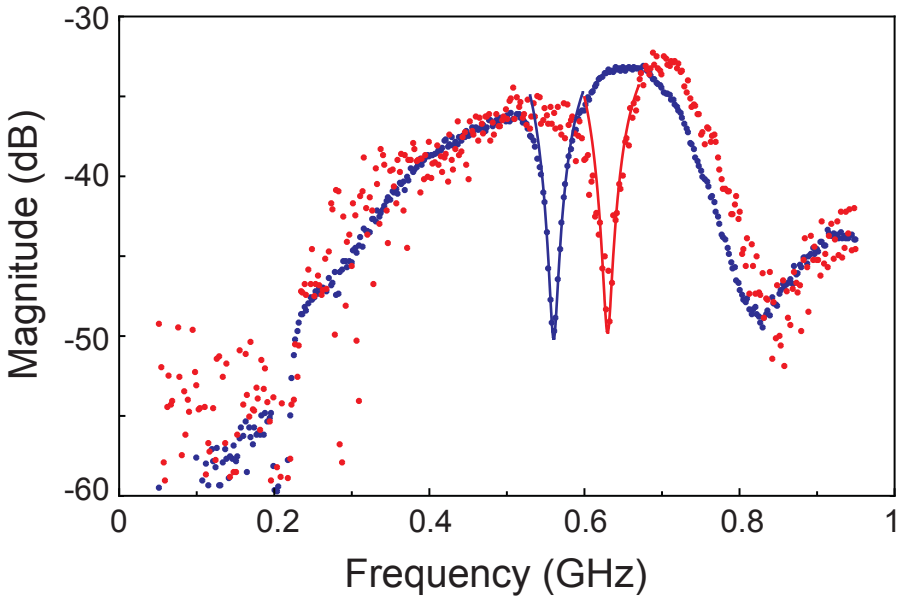

Figure E.2: Measured (dots) magnitude of the reflected signal as a function of the microwave frequency for two different configurations of the contact (open contact in blue and big contact in red). These data were obtained on sample PAL7 in a separate microwave reflectometry experiment (see wiring in Chapter 10). The continuous lines are fits which give the resonant frequencies and the values of the resistance r that models the dissipation at microwaves.

The resonances are fitted with the expression for the reflection coefficient $20 \log \left| \frac{Z(\nu)-50}{Z(\nu)+50} \right|$ (continuous lines), where Z is the impedance presented by the chip to the $50\,\Omega$ transmission line. To model the losses, we have introduced a resistance r in series with the capacitor. Each fit gives a different value for the resistance: $r\,(560\,\mathrm{MHz}) \simeq 0.37\,\Omega$ and $r\,(632\,\mathrm{MHz}) \simeq 0.29\,\Omega$. This measurement only gives an estimation of the frequency-dependent dissipation at low frequency.

PAL7 parameters are listed in Table E.1.

E.2 Calculation of the switching probability

In Chapter 4, we presented measurements of the switching probability of various atomic-SQUIDs. This section briefly describes the theoretical model used to determine the exact shape of an s-curve $P_{sw}(s, \varphi)$ as a function of both the reduced current s and the flux φ.

E.2.1 *Escape theory for a single Josephson junction*

Let us first consider the case when the atomic contact is open, *i.e.* when the JJ is by itself.

The phase γ across the JJ is a dynamical variable governed by a Langevin equation, equivalent to the one obeyed by the position of a massive particle evolving

PARAMETER	SAMPLE PAL7
Capacitor C	60 pF
Inductor L	750 pH
Environment bare frequency $\nu_{e0} = \frac{1}{2\pi}\sqrt{\frac{1}{LC}}$	750 MHz
Loop inductance L_l	20 pH
Critical current I_0	554 nA
JJ capacitance C_0	0.22 pF
JJ equivalent inductance $L_0 = \frac{\varphi_0}{I_0}$	594 pH
Environment frequency $\nu_e \simeq \frac{1}{2\pi}\sqrt{\frac{1}{(L+L_0)C}}$ (contact open)	560 MHz
Bare plasma frequency $\nu_{p0} = \frac{1}{2\pi}\sqrt{\frac{1}{L_0 C_0}}$ (contact open)	14 GHz
Dressed plasma frequency $\nu_p \simeq \frac{1}{2\pi}\sqrt{\frac{1}{C_0}\left(\frac{1}{L}+\frac{1}{L_0}\right)}$ (contact open)	19 GHz

Table E.1: Parameters of Sample PAL7 presented in Part II.

in a "tilted washboard potential" [97, 98, 99]. In presence of a bias current I_b, the potential of the JJ is given by:

$$U(\gamma) = -E_J \cos(\gamma) - E_J s\gamma. \tag{E.1}$$

The first term is the Josephson energy of the JJ, with $E_J = \varphi_0 I_0$, and the second one is the energy arising from the coupling to the bias source, with $s = \frac{I_b}{I_0}$ the normalized current amplitude called the "tilt". This potential is sketched in Fig. E.3. Due to thermal or quantum fluctuations, the particle oscillates in the well and has a finite probability P_{sw} to escape out of it.

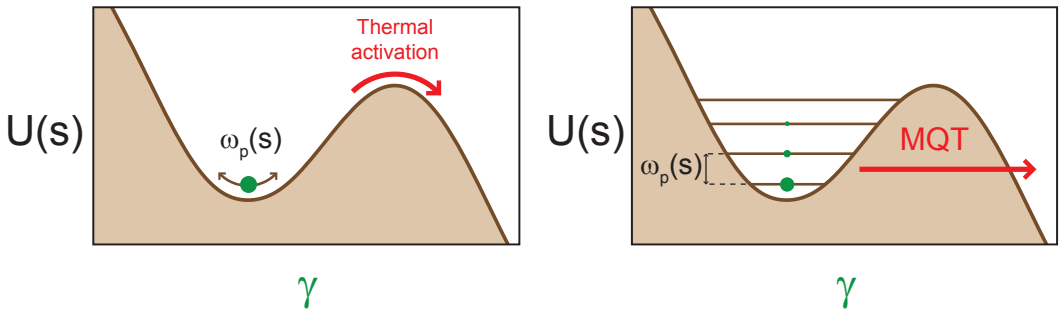

Figure E.3: Tilted washboard potential. Due to fluctuations in the environment, the particle can escape from the well. Depending on the amplitude of the thermal fluctuations, this escape can be thermally activated (**left**), or occur through quantum tunneling of the phase (**right**). The plasma frequency ω_p is the frequency of the small oscillations in the tilted well.

This switching probability P_{sw} is related to the switching rate Γ and to the bias current pulse duration t_p (defined in Fig. 4.5) by

$$P_{sw} = 1 - e^{-\Gamma t_p}. \tag{E.2}$$

When the thermal fluctuations of the phase dominate, the rate Γ is given by an Arhenius law

$$\Gamma = \frac{\omega_p}{2\pi} \exp\left[-\beta \Delta U\right] \tag{E.3}$$

where

$$\omega_p = \omega_p^0 \left(1 - s^2\right)^{1/4} \tag{E.4}$$

and

$$\Delta U = \frac{4\sqrt{2}}{3} E_J \left(1 - s\right)^{3/2} \tag{E.5}$$

are respectively the plasma pulsation and the barrier height in the tilted potential. This regime is called the "thermal activation" regime [145], and is valid when $k_B T \geqslant \frac{\hbar \omega_p}{2\pi}$ (see left panel of Fig. 4.4). In the opposite limit, coined "macroscopic quantum tunneling" (MQT) regime [146], the switching is dominated by quantum fluctuations and leading to tunneling through the barrier (see right panel of Fig. 4.4). Then, the rate Γ is given by ([123])

$$\Gamma = 6^{3/2} \pi^{-1/2} \omega_p \sqrt{\frac{\Delta U}{\hbar \omega_p}} \exp\left[-\frac{36}{5} \frac{\Delta U}{\hbar \omega_p}\right]. \tag{E.6}$$

The crossover temperature between these two regimes occurs at

$$T_{co} = \hbar \omega_p / \left(2\pi k_B\right). \tag{E.7}$$

In practice, the s-curves produced by the MQT theory resemble very much those predicted by the thermal escape theory in which temperature is replaced by $\hbar\omega_p$. For simplicity, we have always used here the thermal escape theory, although the experiment presented in Chapter 4 are in intermediate regime ($T_{co} = 95$ mK).

E.2.2 *Escape theory for an atomic-SQUID*

When an atomic contact is formed, there is one additional spin-like Andreev degree of freedom per channel. Therefore, the phase γ is no longer the only degree of freedom and the problem is more complicated. Since in the experiment the transitions between the configurations are slow[2] (at most ($\sim$ 1 MHz) compared to the plasma frequency ($\sim$ 12.5 GHz in the tilted well), which is the characteristic timescale for the dynamics in $U(\gamma)$, the escape rate is determined by the potential corresponding to the instantaneous configuration[3]. The potentials are given by

$$U\left(\gamma\right) = -E_J \cos\left(\gamma\right) - E_J s\gamma + E_{AC}\left(\gamma + \varphi\right), \tag{E.8}$$

where $E_{AC} = \sum_i c_i E_A\left(\tau_i\right)$ is the total Josephson coupling introduced by the atomic contact, which depends on the configuration c_i of the different ABS ($c_i = -1$ if channel i is in its ground state $|-\rangle$, $c_i = 0$ in an odd excited state $|\uparrow\rangle$ or $|\downarrow\rangle$, and $c_i = 1$ in even excited state $|+\rangle$).

2 This is true for the transitions between the odd states and the ground state. It is not correct for the relaxation of the excited state $|+\rangle$.

3 In the opposite limit, the effective potential is build from the average current (see Refs. [72, 147]). In intermediate regime, one needs to derive a full quantum theory, as the one in Chapter 7.

As an example, we plot in Fig. E.4 the three potentials for a contact with a single channel of transmission 0.99, at $\varphi/\pi = 0.9$, and for $s = 0.87$. The energies $E_J = 1.14\,\text{meV}$ and $\Delta = 0.193\,\text{meV}$ correspond to the parameters of the Josephson junction of the experiment. The distance in energy between the potentials is the smallest when $\delta = \pi$, *i.e.* $\gamma = \pi - \varphi = 0.1\,\pi$. We also indicate the ground state energy in each potential, as obtained from semi-classical calculations. The quantum fluctuations of γ (and hence of δ) are of the order of 0.1π. Fig. E.4 illustrates why the switching rates are very different in the ground state $|-\rangle$ of the channel and in the odd configurations $|\uparrow\rangle$ or $|\downarrow\rangle$.

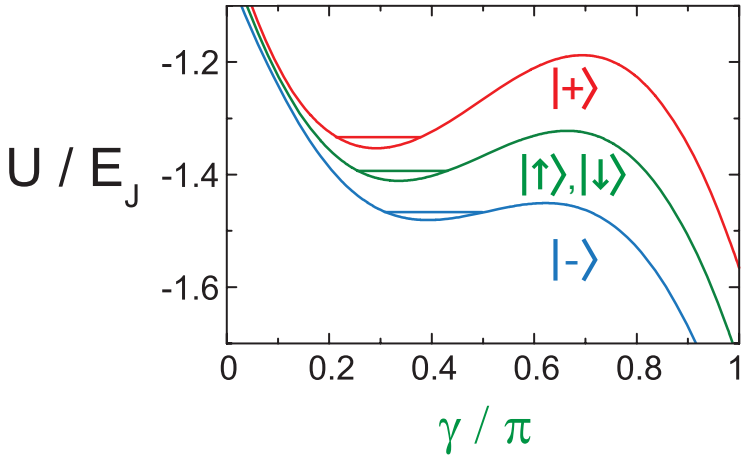

Figure E.4: SQUID potentials for a JC with transmission $\tau = 0.99$, at $\varphi/\pi = 0.9$ and $s = 0.87$. The three curves correspond, from bottom to top, to the atomic contact in the ground state $|-\rangle$ (blue), in one of the odd states $|\uparrow\rangle$ or $|\downarrow\rangle$, and in the excited state $|+\rangle$ (red). Horizontal lines indicate the energy of the first level $\frac{1}{2}\hbar\omega_p$ in each potential, with the plasma frequency $\omega_p/2\pi$ calculated semi-classically: $\omega_p^{|0\rangle}/2\pi = 7.9\,\text{GHz}$; $\omega_p^{|1\rangle}/2\pi = 9.7\,\text{GHz}$; $\omega_p^{|2\rangle}/2\pi = 10.9\,\text{GHz}$. The energy scale is $E_J = 1.14\,\text{meV} \approx 13\,k_B\text{K}$.

In this example, and in general for a one-atom contact in this experiment, the two first terms in Eq. 4.4 dominate because $E_J/\Delta \simeq 5.7 \gg 1$. Therefore, the shape of the tilted potential resembles that of a single JJ, with just a slightly modified barrier height $\Delta U(s,\varphi)$ and plasma pulsation $\omega_p(s,\varphi)$. To calculate the exact switching probability $P_{sw}(s,\varphi)$, we use the thermal escape theory and perform a **numerical determination** of the barrier height $\Delta U(s,\varphi)$, and of the plasma frequency $\omega_p(s,\varphi)$ from the semi-classical calculation of the energy levels[4] in the actual potential U.

4 By imposing the quantization of the action on one oscillation period.

F

CLASSICAL CALCULATION OF THE CRITICAL CURRENT AND PLASMA FREQUENCY OF ASYMMETRICAL SQUIDS

F.1 Two tunnel Josephson junctions in parallel

F.1.1 *Critical current*

Let us first consider a SQUID, made of two tunnel JJ of phases δ and γ and critical currents I_0 and I_1 (see Fig. F.1). One defines

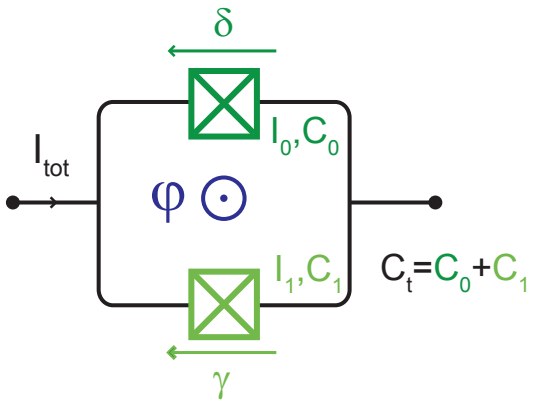

Figure F.1: Schematic of the SQUID made of two tunnel JJ of phases δ and γ, critical currents I_0 and I_1 and capacitors C_0 and C_1.

$$\alpha = \frac{I_0 - I_1}{I_0 + I_1} \tag{F.1}$$

the critical current asymmetry. The two phases are linked through the reduce flux φ threading the loop by

$$\delta - \gamma = \varphi. \tag{F.2}$$

One defines the average phase

$$x = \frac{\gamma + \delta}{2}. \tag{F.3}$$

Then, the total current through the SQUID reads

$$\begin{aligned} I_{tot}(x, \varphi) &= I_0 \sin(\delta) + I_1 \sin(\gamma) \\ &= I_0 \sin(x + \tfrac{\varphi}{2}) + I_1 \sin(x - \tfrac{\varphi}{2}) \\ &= (I_0 + I_1)\left(\sin(x)\cos(\tfrac{\varphi}{2}) + \alpha\cos(x)\sin(\tfrac{\varphi}{2})\right). \end{aligned} \tag{F.4}$$

Therefore, one finds

$$\boxed{I_{tot}(x, \varphi) = I_c(\varphi)\sin\left(x + x_0(\varphi)\right)} \tag{F.5}$$

with

$$\boxed{I_c(\varphi) = (I_0 + I_1)\sqrt{(1-\alpha^2)\cos^2(\frac{\varphi}{2}) + \alpha^2}} \tag{F.6}$$

and $x_0(\varphi)$ is such as

$$\begin{aligned} \sin(x_0(\varphi)) &= \frac{\alpha \sin(\frac{\varphi}{2})}{\sqrt{(1-\alpha^2)\cos^2(\frac{\varphi}{2})+\alpha^2}} \\ \cos(x_0(\varphi)) &= \frac{\cos(\frac{\varphi}{2})}{\sqrt{(1-\alpha^2)\cos^2(\frac{\varphi}{2})+\alpha^2}} \end{aligned} . \tag{F.7}$$

Consequently, a SQUID can be seen as a JJ, whose critical current $I_c(\varphi)$ is tunable with the flux. As shown in Fig. F.2, its maximum $I_0 + I_1$ is reached at $\varphi = 0\ [2\pi]$ and its minimum $|I_0 - I_1|$ at π. When the SQUID is perfectly symmetrical ($\alpha = 0$), the interferences are fully destructive when $\varphi = \pi$ and $I_c(\pi) = 0$.

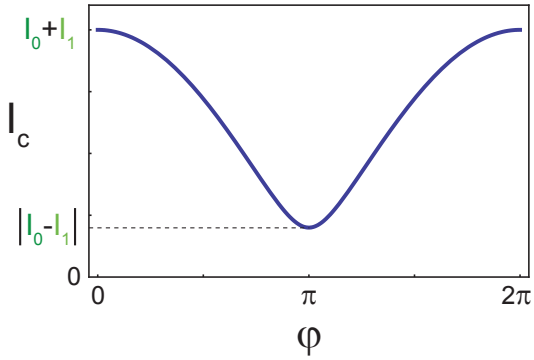

Figure F.2: Critical current of a SQUID made of two different JJ as a function of the phase, for a critical current asymmetry $\alpha = 0.2$. Note that the minimum of the critical current is always found at $\varphi = \pi$, independently on the critical current asymmetry α.

F.1.2 *Plasma frequency*

According to Josephson effects, the voltage V across the SQUID is

$$V = \varphi_0 \dot{x} = \frac{\varphi_0}{I_c \cos(x + x_0(\varphi))} \dot{I}_{tot}. \tag{F.8}$$

Thus a SQUID can be seen as a tunable non-linear inductor of inductance

$$L_{SQUID}(x, \varphi) = \frac{\varphi_0}{I_c(\varphi)\cos(x + x_0(\varphi))}. \tag{F.9}$$

In presence of a bias current I_b smaller than I_c, one gets

$$I_b = I_{tot}(x, \varphi) \Rightarrow \cos(x + x_0(\varphi)) = \sqrt{1 - \left(\frac{I_b}{I_c(\varphi)}\right)^2}. \tag{F.10}$$

Then, the SQUID inductance reads

$$L_{SQUID}(\varphi, I_b) = \frac{\varphi_0}{I_c(\varphi)\sqrt{1 - \left(\frac{I_b}{I_c(\varphi)}\right)^2}}. \tag{F.11}$$

With its parallel capacitance $C_t = C_0 + C_1$, the SQUID forms an anharmonic oscillator of plasma pulsation

$$\omega_p(\varphi, I_b) = \sqrt{\frac{I_c(\varphi)}{\varphi_0 C_t}} \left(1 - \left(\frac{I_b}{I_c(\varphi)}\right)^2\right)^{1/4} \tag{F.12}$$

which depends on the flux φ and on the bias current I_b. It is represented in Fig. F.3. Note that it is maximum at $\varphi = 0\ [2\pi]$ and minimum at $\varphi = \pi$ for all values of the bias current I_b.

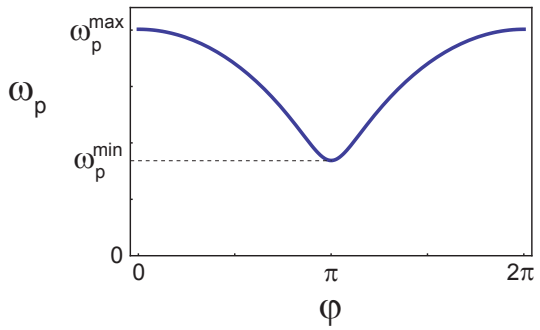

Figure F.3: Plasma pulsation of a SQUID made of two different JJ as a function of the phase, for a critical current asymmetry $\alpha = 0.2$ and a bias current $I_b = 0.1$. Note that independently on the bias current I_b or the critical current asymmetry α, the minimum of the plasma pulsation is always in $\varphi = \pi$, and is $\omega_p^{min} = \omega_{p0}\left[\alpha^2 - \left(\frac{I_b}{I_0+I_1}\right)^2\right]$, and the maximum is in $\varphi = 0$ and is $\omega_p^{max} = \omega_{p0}\left[1 - \left(\frac{I_b}{I_0+I_1}\right)^2\right]$, with $\omega_{p0} = \sqrt{\frac{I_0+I_1}{\varphi_0 C_t}}$.

F.2 Tunnel JJ in parallel with a JC of transmission τ

F.2.1 *Critical current*

Let us now consider a SQUID (see Fig. F.4) made of a JC of transmission τ (critical current $I_0(\tau)$, capacitance C_0, phase δ) and a tunnel JJ (critical current I_1, capacitance C_1, phase γ).

The total current through the SQUID reads

$$I_{tot}(x, \varphi) = I_0(\tau) \frac{\tau}{2\left(1 - \sqrt{1-\tau}\right)} \frac{\sin(x + \frac{\varphi}{2})}{\sqrt{1 - \tau \sin^2(x + \frac{\varphi}{2})}} + I_1 \sin(x - \frac{\varphi}{2}) \tag{F.13}$$

where $I_0(\tau) = \frac{\Delta}{2\varphi_0}\left(1 - \sqrt{1-\tau}\right)$ is the critical current of the JC. Contrary to the previous case, this expression cannot be factorized, and one can only compute the critical current numerically. In Fig. F.5 is plotted the critical current as a function of the phase, for $\tau = 0.95$ and an asymmetry of $\alpha = 0.2$. Remarkably, the minimum is no longer at $\varphi = \pi$. Actually, the critical current is now different for positive or negative values. Moreover, the minimum value is larger than the one that one

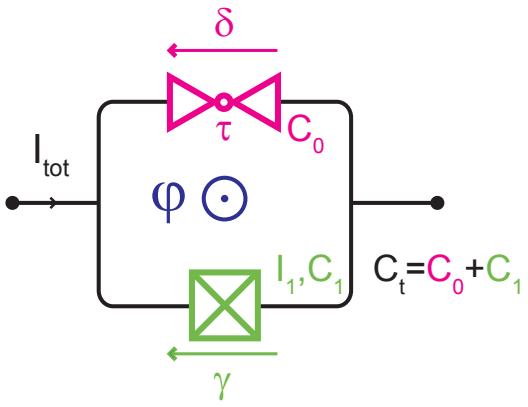

Figure F.4: Schematic of the SQUID made of a JC of transmission τ and a tunnel JJ of critical current I_0.

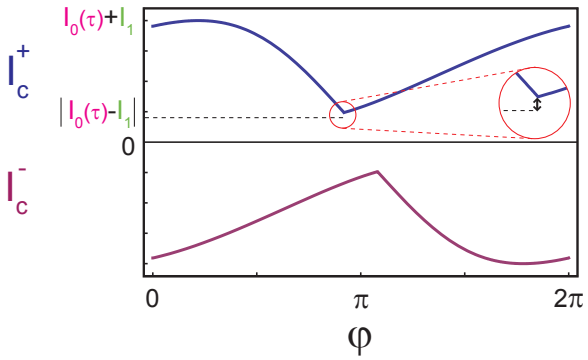

Figure F.5: Positive (blue) and negative (purple) critical current as a function of the phase φ , for $\tau = 0.95$ and an asymmetry $\alpha = 0.2$.

could expect ($|I_1 - I_0(\tau)|$) from the tunnel case (zoom). Since the system is invariant under a change of sign of both the magnetic field and the current, one gets $I_c^-(\pi - \theta) = -I_c^+(\pi + \theta)$.

Typically, we are using very asymmetrical atomic-SQUIDs ($I_1 \sim 10 * I_0(\tau)$). In Fig. F.6 is represented the positive critical current as a function of the phase, for two different transmissions $\tau = 0.1$ and $\tau = 0.95$ and the same asymmetry $\alpha = 0.8$. At very small transmission, one recovers the tunnel case, symmetrical around $\varphi = \pi$.

F.2.2 *Plasma frequency*

The SQUID inductance is defined as

$$L_{SQUID}(x, \varphi) = \frac{\varphi_0}{\frac{dI_{tot}}{dx}(x, \varphi)} \tag{F.14}$$

and

$$\begin{aligned}\frac{dI_{tot}}{dx}(x, \varphi) = \; & \frac{\Delta\tau}{4\varphi_0}\left(\frac{\cos\left(x+\frac{\varphi}{2}\right)}{\sqrt{1-\tau\sin^2\left(\frac{1}{2}\left(x+\frac{\varphi}{2}\right)\right)}}\right. \\ & \left.+\frac{\tau\sin\left(\frac{1}{2}\left(x+\frac{\varphi}{2}\right)\right)\sin\left(x+\frac{\varphi}{2}\right)\cos\left(\frac{1}{2}\left(x+\frac{\varphi}{2}\right)\right)}{2\left(1-\tau\sin^2\left(\frac{1}{2}\left(x+\frac{\varphi}{2}\right)\right)\right)^{3/2}}\right) \\ & +I_1\cos\left(x-\frac{\varphi}{2}\right).\end{aligned} \tag{F.15}$$

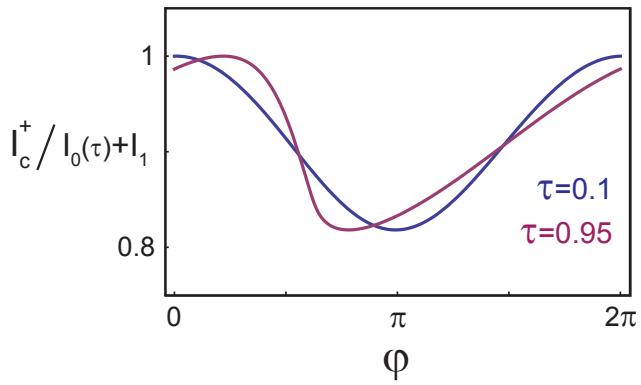

Figure F.6: Positive critical current as a function of the phase φ , for two different transmissions $\tau = 0.1$ and $\tau = 0.95$ and the same asymmetry $\alpha = 0.8$.

When current biased, the phase $x_0(\varphi, I_b)$ satisfies $I_b = I_{tot}(x_0(\varphi, I_b), \varphi)$. However, this equation cannot be inverted analytically. One can only compute this phase numerically, as well as the inductance $L_{SQUID}(\varphi, I_b) = L_{SQUID}(x_0(\varphi, I_b), \varphi)$ and the plasma frequency $\omega_p(\varphi, I_b) = \sqrt{\frac{1}{L_{SQUID}(\varphi, I_b) C_t}}$. The latter is represented in Fig. F.7 (left) as a function of the phase, for a transmission $\tau = 0.95$ and an asymmetry $\alpha = 0.8$, for different bias currents. At zero bias current (blue curve), the plasma frequency is minimum and symmetrical around $\varphi = \pi$. Under a finite bias current, the critical current globally diminishes and the position in phase of its minimum moves to smaller phases (blue dots in Fig. F.7 (right)), in contrast with the tunnel case (see Fig. F.3). We find that, for large transmissions,

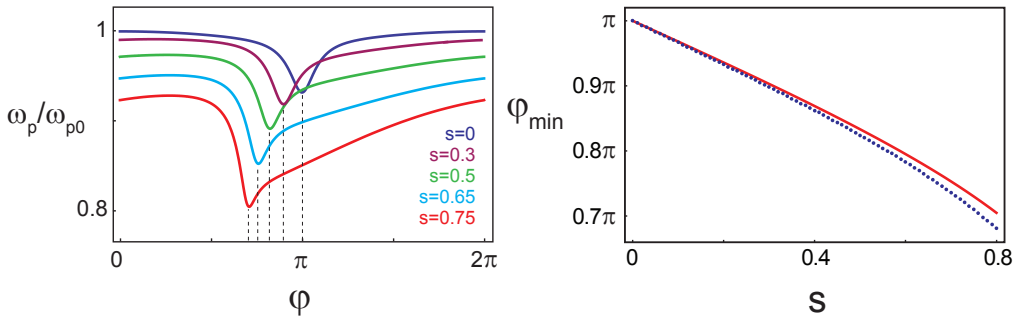

Figure F.7: **Left**: Plasma pulsation of a SQUID made of a JC and a tunnel JJ as a function of the phase, for a transmission $\tau = 0.95$, a critical current asymmetry $\alpha = 0.8$. Each curve corresponds to a different reduced bias current $s = \frac{I_b}{I_0(\tau)+I_1}$. **Right**: The minimum of the plasma pulsation φ_{min} (blue dots) shifts with the reduce bias current s. The continuous red curve is the approximate dependence $\varphi_{min} = \pi - \arcsin(s)$.

$\varphi_{min} \simeq \pi - \arcsin(s)$ (solid red line).

F.2.3 *The tilted washboard potential*

As already explained in Section E.2, to take into account the quantum fluctuations of the phase, one needs to consider the full potential U describing the dynamics

of the phase x of the SQUID. It is the sum of the work performed by the current source, the Josephson potential and the Andreev one:

$$U(x,\varphi) = -\varphi_0 I_b \varphi + E_J \cos(x - \tfrac{\varphi}{2}) - \Delta\sqrt{1 - \tau \sin^2(\tfrac{x}{2} + \tfrac{\varphi}{4})} \tag{F.16}$$

with $E_J = \varphi_0 I_1$. φ just appears as a phase between theses two potentials. The classical calculation of the plasma frequency described in the previous sub-section only considers the curvature $\varphi_0^2 L_{SQUID}^{-1}(\varphi, I_b)$ of the potential at his minimum $x_0(\varphi, I_b)$.

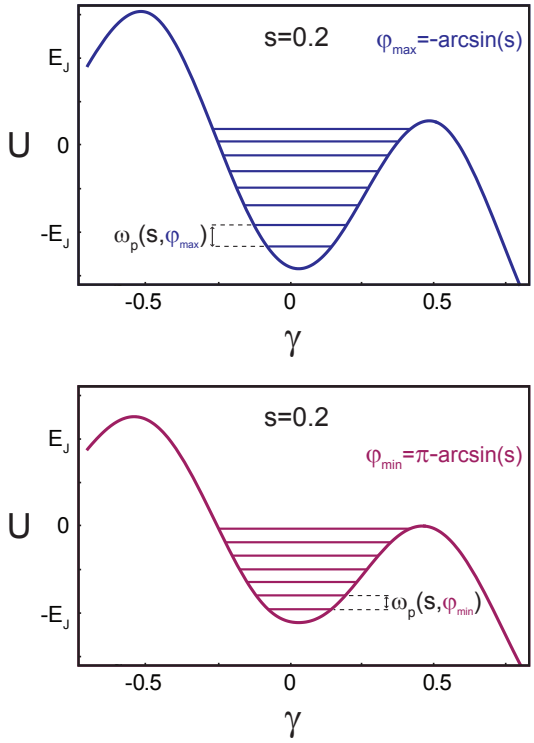

Figure F.8: Tilted washboard potential $U(\gamma)$ as a function of the phase γ on the JJ, for a tilt $s = 0.2$, a transmission $\tau = 0.95$, an asymmetry $\alpha = 0.4$, and for the two extremal values of the phase threading the loop $\varphi_{max} = -\arcsin(s)$ (**top**) and $\varphi_{min} \simeq \pi - \arcsin(s)$ (**bottom**), for which the plasma frequency is respectively maximum and minimum.

If one considers a JC of very big transmission (or an atomic contact made of several channels, whose critical current is comparable with the one of the JJ), the potential starts to be very anharmonic close to its minimum[1]. Then, the energy levels (as illustrated in Fig. F.8) can be obtained from a semi-classical calculation, by imposing the quantization of the action on one oscillation period.

Note that in this section, we have always considered the Andreev doublet as being in its ground state $|-\rangle$. To take into account the Andreev internal degree of freedom, one needs to consider a potential for each configuration (as done in Section E.2) or to derive a full quantum theory (as the one done in Chapter 7).

1 The potential can even have a two minima separated by a local maximum.

G

SUPPLEMENTARY MATERIALS ON SPECTROSCOPY EXPERIMENTS

G.1 Equivalent circuit for sample JT6

A schematic of the sample closer to the actual geometry than Fig. 6.1 is shown in Fig. G.1. Importantly, the capacitors are obtained with two capacitors in series, with the intermediate electrode capacitively coupled to the ground plane. Instead of 2 inductors in Fig. 6.1, there are in fact 3 of them in the actual circuit. Each bias source sees a filtering inductance of $2L'$ in Fig. G.1, L in Fig. 6.1. The inductance in parallel to the SQUID is, due to the shunting of the side arms by the capacitors to the ground plane, is L' in Fig. G.1, $L/2$ in Fig. 6.1. As a consequence, Fig. 6.1 is a good representation of the electrical circuit by choosing $L = 2L'$.

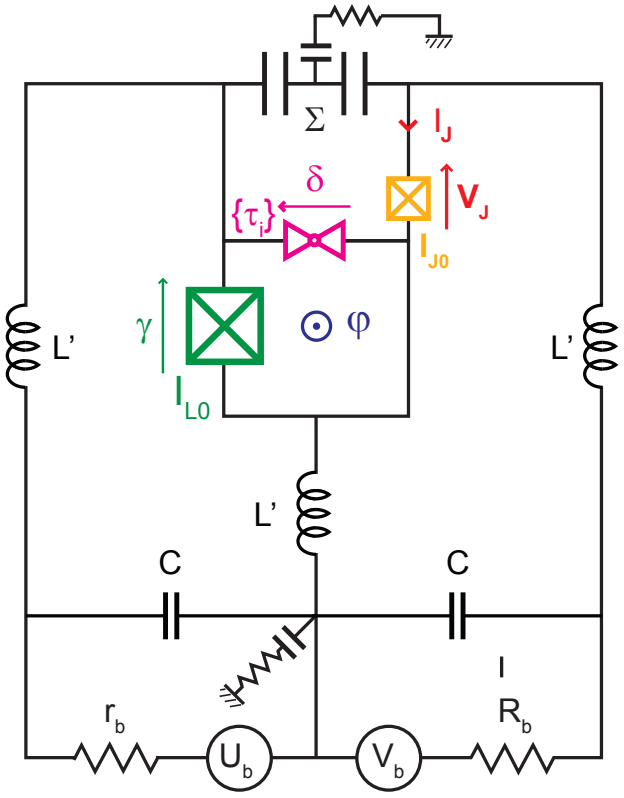

Figure G.1: Schematic of the sample JT6. The JJS [respectively the SQUID] is biased by a voltage source V_b [U_b] through an on-chip LC filter ($L' \simeq 450\,\text{pH}$, $C \simeq 20\,\text{pF}$) and a series resistance $R_b = 2\text{k}\Omega$ [$r_b = 200\Omega$] mounted at the same temperature as the sample.The current I_J (red) [I_S (magenta)] is measured from the voltage drop across R_b [r_b]. These two parts, which are independent from the dc point of view, are coupled through an on-chip capacitor $\Sigma \simeq 30$ pF. The extra capacitors ($\sim 1\,\text{pF}$) and resistances represent the capacitive coupling to the resistive (chrysocal) ground plane.

G.2 Determination of the transmissions of contacts U and V

The IV characteristics of contact U and V are shown in Fig. G.2. They are obtained by subtraction of the IV of the JJ alone from that of the SQUIDs. These measurements are performed while the JJS is at zero voltage.

The MAR theory (see Section 3.4.1) is used to obtain the transmissions of the conduction channels. However, because of the subtraction of a large current ($I_{L0} \simeq 1\ \mu A$), the accuracy on the determination of the transmissions of the channels is not as good as in experiments with atomic contacts alone [89].

The spectra give a more precise information on the transmissions of the two first channels. The precise set of transmissions therefore result from a simultaneous fit of the MAR current and of the spectrum, yielding for contact U :$\{0.942, 0.26, 0.08 \times 4\}$ and for V $\{0.987, 0.37, 0.12 \times 4\}$. The transmissions of the channels not visible in the spectra are adjusted to reproduce the current, but their values are not precise.

The corresponding fits are shown as solid lines in Fig. G.2 for contacts U and V.

G.3 Determination of the voltage V_J across the JJS

In the spectroscopy experiment, the voltage V_J across the JJS was not directly measured. It was determined from the external bias voltage V_b and the measured voltage V_I across the bias resistance using the relation

$$V_J = \alpha V_b - V_I \tag{G.1}$$

with $\alpha^{-1} = 1069$, the attenuation of the bias line[1].

1 It was measured using the lower wire of the twisted-pair measuring the current I_J through the JJS and the lower wire (connected to the ground) of the twisted-pair measuring the voltage V_S across the SQUID (see Fig. 10.5 for wiring). Since these two wires are not twisted together and therefore pick flux noise, this technique could not be used to measure the voltage V_J for each spectrum. It was only used once for a calibration of α.

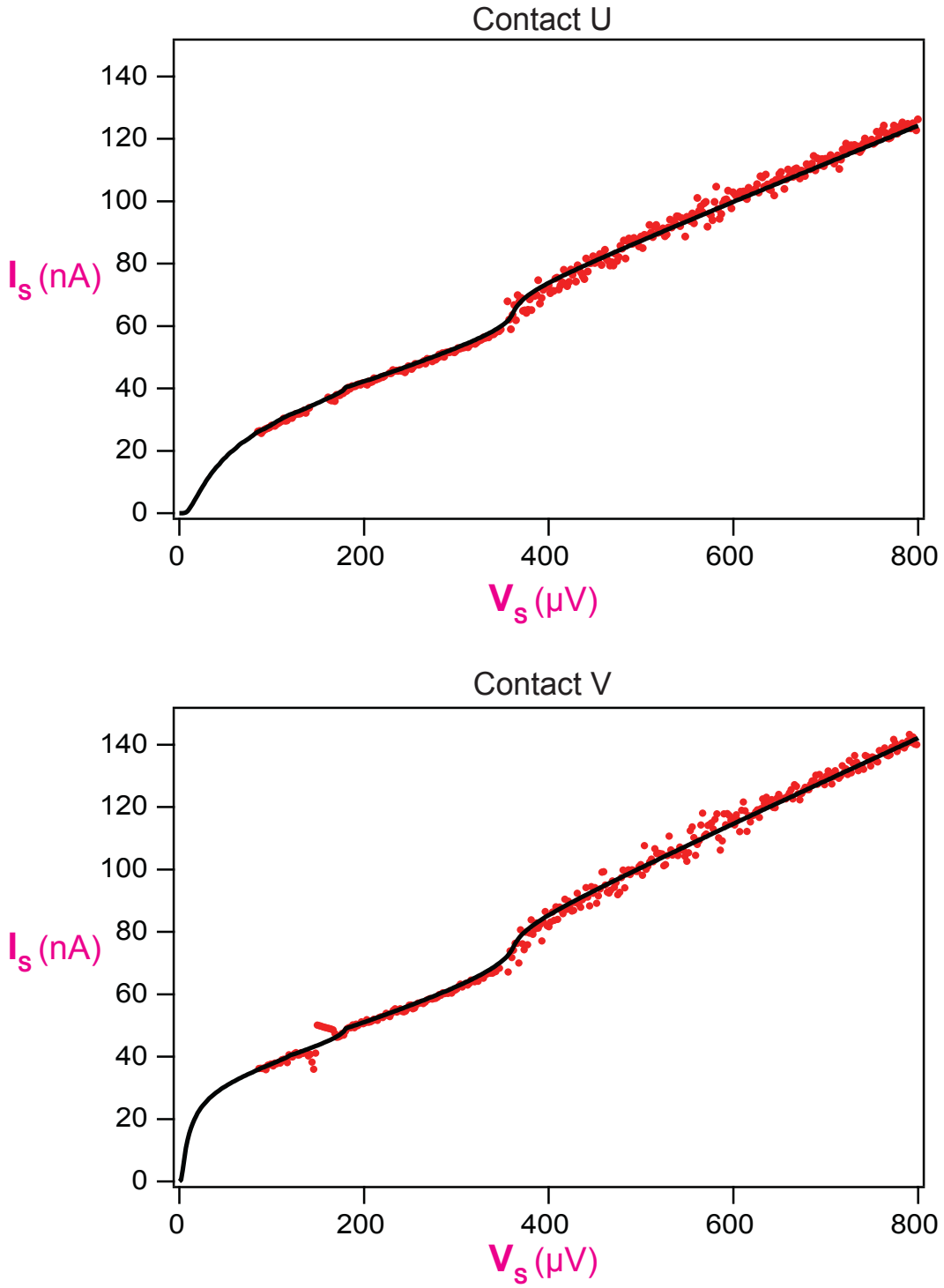

Figure G.2: IV characteristics of two different atomic contacts, while the JJS is at zero voltage. By fitting them with the MAR theory (green solid curve), one finds the transmissions $\{0.942, 0.26, 0.08 \times 4\}$ for contact U (**top**) and $\{0.985, 0.37, 0.12 \times 4\}$ for contact V (**bottom**).

G.4 Subtraction procedure for the absorption spectroscopy

IVs of the JJS display peaks which do not change with φ, as seen in Fig. 6.4. We have subtracted them from the spectra using the following procedure:

- One takes an averaged $I_J(V_J)$ over a small flux range $\pm\pi/4$, around flux $\varphi = 0$. In this flux region, the Andreev resonances are not visible and the plasma resonance does not change position significantly.
- A fit of this curve is performed using a set of Lorenzian peaks, and eventually a linear background. Two peaks at voltages $V_J \simeq 45\,\mu V$ and $90\,\mu V$ correspond to the plasma resonance and to its harmonic. The corresponding Lorentzians are subtracted from the averaged $I_J(V_J)$, and one obtains the background, shown in Fig. G.3.
- This background is subtracted to all the $I_J(V_J)$ curves at different φ.

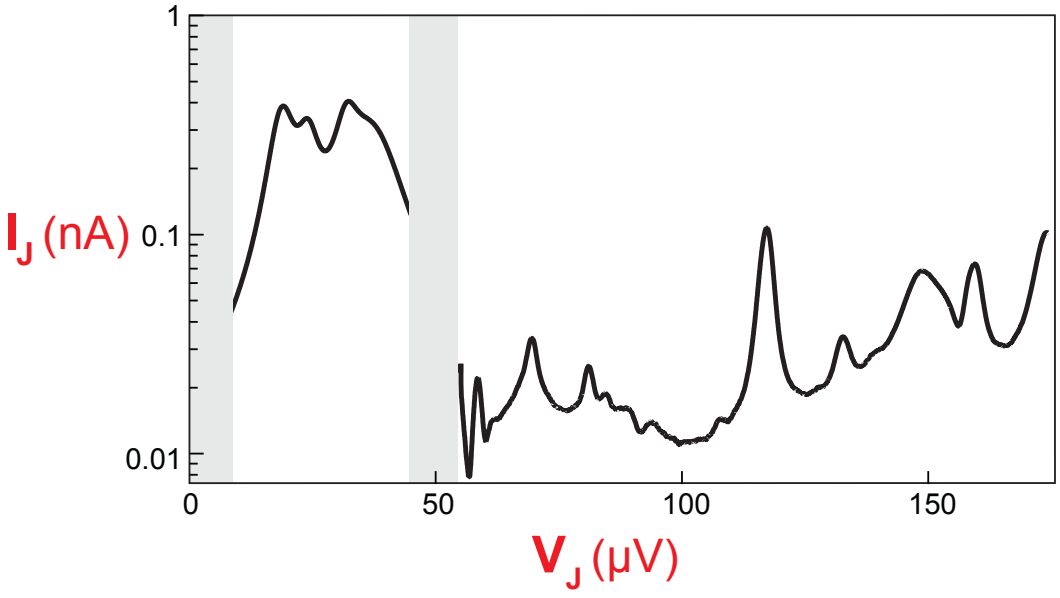

Figure G.3: Background subtracted from all IVs for contact V.

G.5 Additional theoretical spectra

The measured and theoretical spectra for contacts J and I are shown in Fig. G.4. An attempt of modeling the big contacts E and G is shown in Fig. G.5. Only the three most-transmitted channels have been taken into account, which explains the poor agreement.

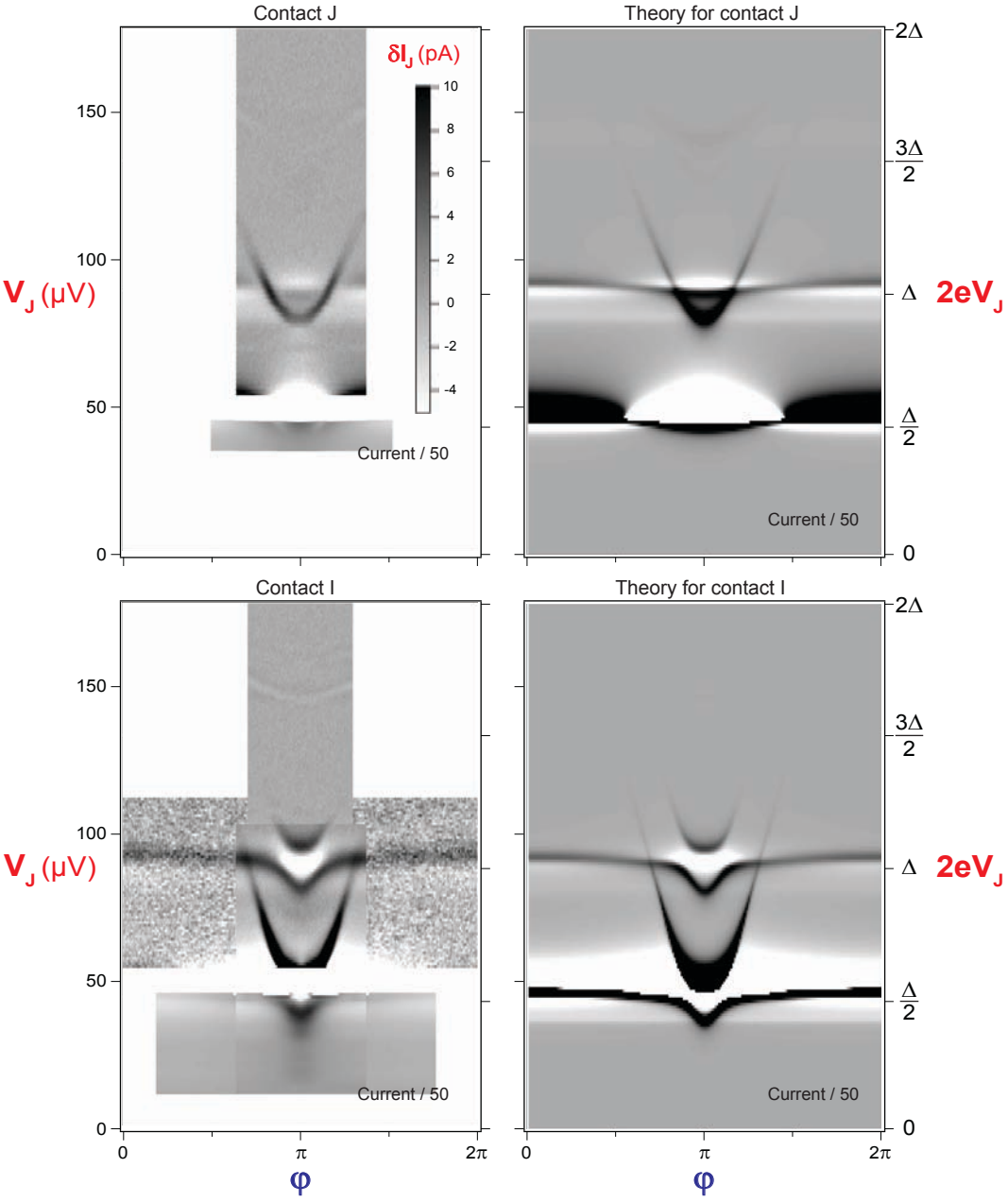

Figure G.4: Comparison between experimental (**left**) and calculated (**right**) spectra $\delta I_J(\varphi, V_J)$ for contact J (**top**) and I (**bottom**). The currents below the plasma resonance have been divided by 50 (in theory plots, currents for $2eV_J < \Delta/2$). The calculated spectra were obtained using the quantum model detailed in Chapter 7. The current gray scale is the same for the four spectra. The calculated currents have been multiplied by 0.56 to match the measured ones.

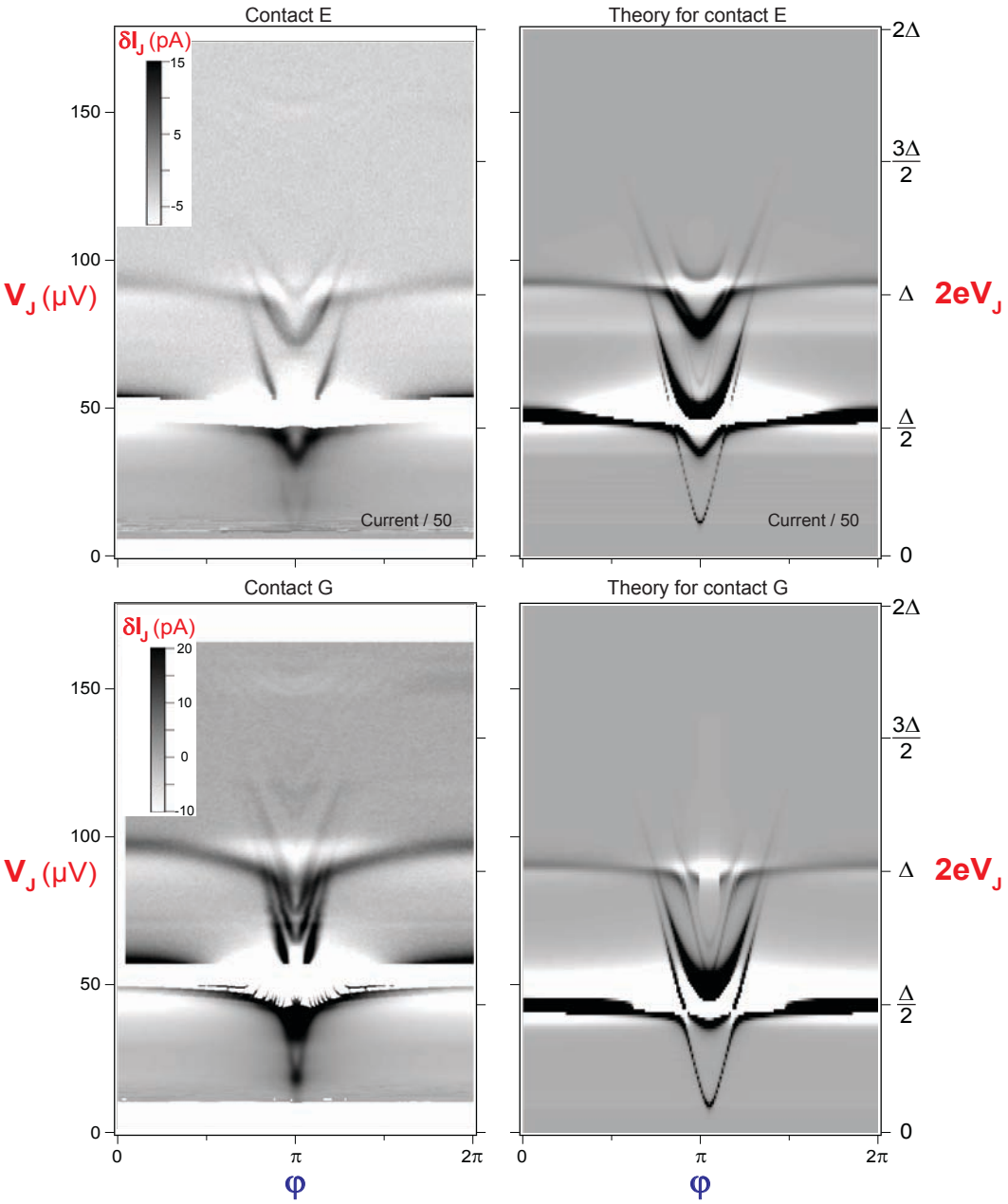

Figure G.5: Comparison between experimental (**left**) and calculated (**right**) spectra $\delta I_J(\varphi, V_J)$ for contact E (**top**) and G (**bottom**). (following of Fig. G.4) Only the three most-transmitted channels have been taken into account which gives a poor agreement.

G.6 Switching spectrum for contact U

The spectrum by switching for contact U was not obtained with the same method as for contact V. The switching probability was measured with a pulse height $s(\varphi)$ intermediate between that for which $P_{sw}(\varphi) = 0.5$ for the SQUID, $s_U(\varphi)$ and that for which $P_{sw} = 0.5$ for the SQUID JJ alone, s_0:

$$s^\star(\varphi) = (s_U(\varphi) + 2s_0)/3. \tag{G.2}$$

With such a procedure, in the absence of biasing of the JJS, $P_{sw}(s(\varphi)) = 1$ in the regions where the AC current is negative, and $P_{sw}(s(\varphi)) = 0$ in the regions where it is positive[2]. Biasing the JJS results in changes of P_{sw} from 0 or from 1, represented with a log gray scale. More precisely, what is plotted is

$$p = \begin{cases} P_{sw} & \text{if } P_{sw} < 0.5 \\ 1 - P_{sw} & \text{if } P_{sw} > 0.5 \end{cases}. \tag{G.3}$$

This technique is more sensitive than the one presented in Section 8.2.1. Fig. G.6 shows the corresponding switching spectrum.

In this spectrum, one measures as well:

- Andreev transitions: $2eV_J = 2E_A$ (dashed lines in the left panel of Fig. G.7). Note that one can detect them up to 2Δ.
- Higher order processes involving multi-Cooper pair tunneling (yellow dotted lines in the left panel of Fig. G.7): $4eV_J = 2E_A - 45\,\mu eV$, $4eV_J = 2E_A - 7\,\mu eV$ and $4eV_J = 2E_A + 228\,\mu eV$. There are also some constant energies to add or subtract that we do not understand.
- Transitions from the lower ABS to the continuum: $2eV_J = \Delta + E_A$ (blue solid line in the right panel of Fig. G.7).

One also detects here a new type of excitation. There is a broad pocket around $V_J \simeq 70\,\mu V$ centered at $\varphi = \pi$, whose upper border has the opposite concavity of an Andreev line. It is well accounted for by the energy $\Delta - E_A(\varphi, \tau_1)$ (pink solid line in the right panel of Fig. G.7), where $\tau_1 = 0.942$ is the transmission of the most transmitted channel. We interpret this pocket as a transition from the upper ABS of the most transmitted channel to the continuum (in the bottom right sketch of Fig. G.7). Such a mechanism implies to start from an out-of-equilibrium state.

At last, one can see another resonance around $\varphi = \pi$, between 100 and 120 μV that might correspond to the hybrid transition $h\nu_p + 2E_A$ for the most transmitted channel.

Fig. G.8 shows a comparison between spectra by absorption and by switching for contact V.

2 In the two regions ($\varphi \simeq$ Pi/4 and $\varphi \simeq$ 3Pi/4) where the difference between $s_U(\varphi)$ and s_0 is smaller than the width of the s-curves, $P_{sw}(s(\varphi))$ has intermediate values.

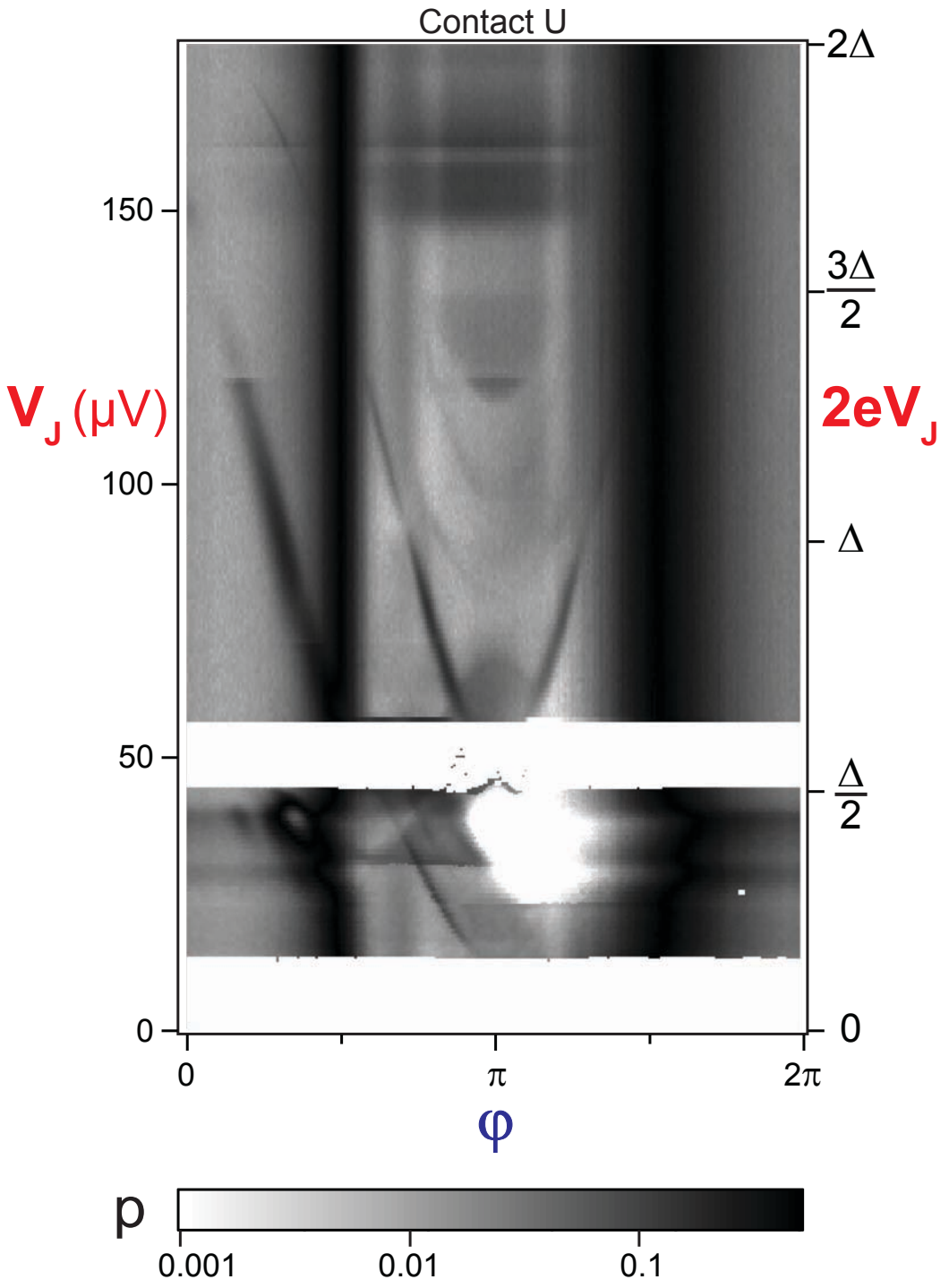

Figure G.6: Switching spectrum $p(\varphi, s)$ for contact U $\{0.942, 0.26, ...\}$. The reduced bias current is $s^* = (s_U + 2s_0)/3$, where $P_{sw}(s_U(\varphi), \varphi) = 0.5$ for the SQUID and $P_{sw}(s_0) = 0.5$ for the SQUID JJ alone, at $V_J = 0$. What is plotted is $p = P_{sw}$ if $P_{sw} < 0.5$ and $p = 1 - P_{sw}$ if $P_{sw} > 0.5$ (log gray scale).

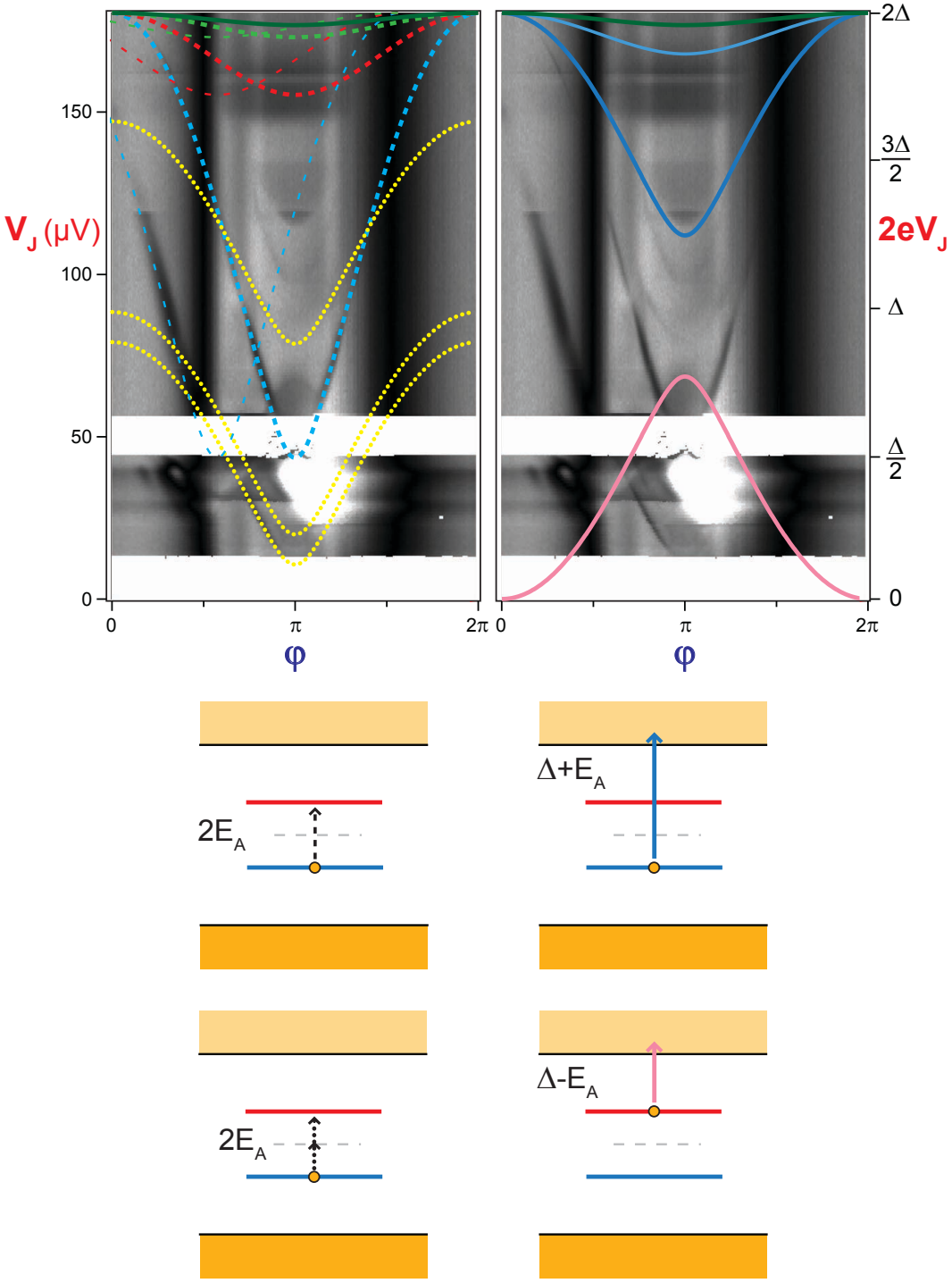

Figure G.7: Switching spectrum $p(\varphi, s)$ for contact U (same scale as Fig. G.6), with different theoretical transition energies as a function of the flux φ. **Left**: The thick dashed lines are the Andreev resonances $2eV_J = 2E_A(\varphi, \tau_i)$. The thin dashed lines are the Andreev resonances $2eV_J = 2E_A(\varphi + 0.3\pi, \tau_i)$ shifted in flux by $\arcsin(s_0) \simeq 0.3\pi$. These transitions occur during the measurement pulse. The dotted lines correspond to higher order transitions of energies $2eV_J = E_A(\varphi, \tau_1) - 4\,\mu eV$, $2eV_J = E_A(\varphi, \tau_1) - 23\,\mu eV$ and $2eV_J = E_A(\varphi, \tau_1) + 114\,\mu eV$. **Right**: The blue, cyan and green solid lines correspond to the energy thresholds of transitions from the lower ABS to the continuum $2eV_J = \Delta + E_A(\varphi, \tau_i)$. The pink solid line correspond to transition from the higher ABS to the continuum $2eV_J = \Delta - E_A(\varphi, \tau_1)$ for the most transmitted channel. **Bottom**: Sketch of the different transitions.

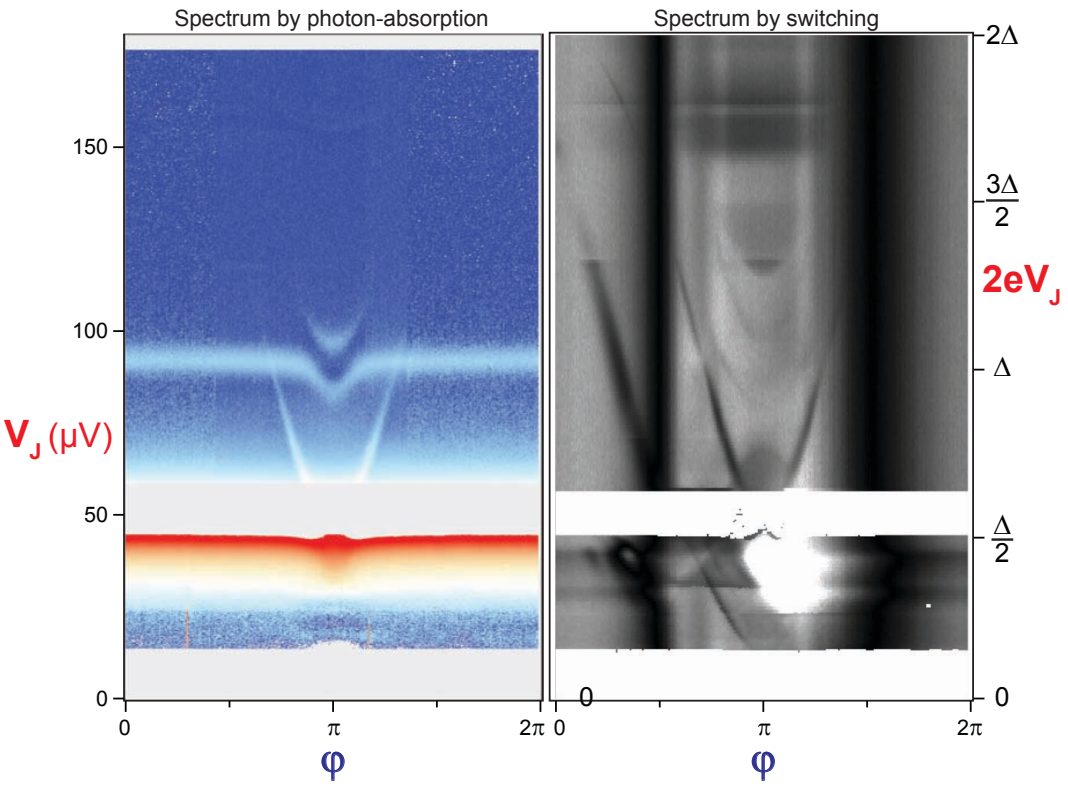

Figure G.8: Comparison between spectra by photon-absorption $I_J(\varphi, V_J)$ (**left**) and by switching (**right**) for contact U. The color and gray scales are the same as for Fig. 6.5 and Fig. G.6.

H

ALTERNATIVE METHOD FOR SPECTRUM CALCULATION: SOLVING H_{ENV} IN THE ANDREEV⊗CHARGE BASIS

In Section 7.5, we have solved the environment Hamiltonian by means of successive approximations. We have chosen to write it in second quantization, in a natural basis made of the Andreev spin and of the plasmon number. I will expose hereafter an alternative method, without the approximations made previously (Taylor expansion of the Josephson and the Andreev Hamiltonians). We will remain in first quantization and write the Hamiltonian in a basis made of the charge number and the Andreev spin. However, this method is simpler only if the Andreev Hamiltonian is periodic in phase. This is why we use here the Hamiltonian derived by Ivanov and Feigelman (see Ref. [108] and Appendix B).

H.1 Matrix representation of H_{env}

As shown in Eq. 7.29, the total environment Hamiltonian is

$$H_{env}(\varphi) = E_C N^2 - E_L \cos(\gamma) + H_A(\varphi+\gamma). \tag{H.1}$$

Instead of writing the Andreev Hamiltonian in the energy basis, we express it in a phase independent Pauli basis. Using the Hamiltonian derived by Ivanov and Feigelman (see Ref. [108] and Appendix B), it is

$$H_A(\gamma) = \Delta\left(\cos(\frac{\gamma}{2})\sigma_z + r\sin(\frac{\gamma}{2})\sigma_x\right). \tag{H.2}$$

Thus, the Andreev spin degree of freedom and the phase degree of freedom are naturally separated and one does not need to perform a Taylor expansion. Moreover, the phase operator γ appears only through two simple functions $\cos(\gamma/2)$ and $\sin(\gamma/2)$ that involve charge translation operators. We introduce the translation operator of half a Cooper pair

$$T = \exp(i\gamma/2). \tag{H.3}$$

Because $[N,\gamma] = -i$, it verifies $T|N\rangle = |N+1/2\rangle$, where $|N\rangle$ is a number state such that $\hat{N}|N\rangle = N|N\rangle$. Therefore

$$\begin{cases} \cos(\frac{\varphi+\gamma}{2}) = \frac{1}{2}\left(e^{i\frac{\varphi}{2}}T + h.c.\right) \\ \sin(\frac{\varphi+\gamma}{2}) = -\frac{i}{2}\left(e^{i\frac{\varphi}{2}}T - h.c.\right) \\ \cos(\gamma) = \frac{1}{2}\left(T^2 + T^{\dagger 2}\right) \end{cases} \tag{H.4}$$

couple number states differing by $1/2$ or by 1. It is then straightforward to write this Hamiltonian as a matrix in the basis $\{|\sigma,N\rangle, |\sigma,N+\frac{1}{2}\rangle\}$, where $\sigma = \rightarrow$ or $\leftarrow$ labels the Andreev degree of freedom in this phase-independent Pauli basis, and $N \in \mathbb{Z}$ is the Cooper pair number.

In the subspace $\{|\rightarrow, N-\frac{1}{2}\rangle, |\leftarrow, N-\frac{1}{2}\rangle, |\rightarrow, N\rangle, |\leftarrow, N\rangle, |\rightarrow, N+\frac{1}{2}\rangle, |\leftarrow, N+\frac{1}{2}\rangle\}$

$$H_{env} = \frac{1}{2}\begin{pmatrix} U(N-\frac{1}{2}) & 0 & \Delta^* & ir\Delta^* & -E_L & 0 \\ 0 & U(N-\frac{1}{2}) & ir\Delta^* & -\Delta^* & 0 & -E_L \\ \Delta & -ir\Delta & U(N) & 0 & \Delta^* & ir\Delta^* \\ -ir\Delta & -\Delta & 0 & U(N) & ir\Delta^* & -\Delta^* \\ -E_L & 0 & \Delta & -ir\Delta & U(N+\frac{1}{2}) & 0 \\ 0 & -E_L & -ir\Delta & -\Delta & 0 & U(N+\frac{1}{2}) \end{pmatrix} \tag{H.5}$$

where we have introduced $U(N) = 2E_C N^2$ and $\Delta = |\Delta| e^{i\frac{\varphi}{2}}$. This elementary block allows to build the full matrix, which is infinite, by an extension of each diagonal.

Contrary to the matrix representation of the Josephson junction alone, we had to introduce here the half integer Cooper pair states, because the Andreev Hamiltonian is 4π-periodic and couples integer and half-integer Cooper pair states. This doubling of the basis corresponds to looking for solutions for a phase varying between 0 and 4π (instead between 0 and 2π) and makes the whole matrix degenerate. All its eigenvectors are doubly-degenerate, which is justified in the next section.

H.2 Symmetry and reduction of degeneracy

Let us introduce the unitary operator

$$\boxed{R_{2\pi} = \exp(i2\pi N)\exp\left(-i\frac{\pi}{2}\sigma_y\right) = -\exp(i2\pi N).i\sigma_y}. \tag{H.6}$$

It corresponds to a phase translation of 2π accompanied by a rotation of angle π around the y-axis of the Andreev degree of freedom. By using the commutation rules , one can prove that $[H_{env}, R_{2\pi}] = 0$[1].

The fact that the Hamiltonian commutes with $R_{2\pi}$ indicates a symmetry of the system. In absence of the Andreev degree of freedom, this symmetry operator would simply be $\exp(i2\pi N)$ and reflect the invariance of the system when the phase is shifted by 2π. But here, when the phase is translated, the Andreev spin rotates in the xOz plane, around the y-axis. Because the Andreev Hamiltonian is 4π-periodic, if the phase is translated by $2\pi = \frac{4\pi}{2}$, this corresponds to a rotation

1 To do so, one has to use the standard Pauli commutation rules and also the fact that $[\exp(i\gamma), \exp(i2\pi N)] = [\exp(-i\gamma), \exp(i2\pi N)] = 0$, $\left[\exp(i\frac{\gamma}{2}), \exp(i2\pi N)\right] = 2\exp(i\frac{\gamma}{2})\exp(i2\pi N)$, $\left[\exp(-i\frac{\gamma}{2}), \exp(i2\pi N)\right] = 2\exp(-i\frac{\gamma}{2})\exp(i2\pi N)$. Then,

$$\begin{aligned}
[H_{env}, R_{2\pi}] &= -i\left[\left(E_C N^2 - E_L\cos(\gamma) + \Delta\left(\cos(\tfrac{\gamma}{2})\sigma_z + r\sin(\tfrac{\gamma}{2})\sigma_x\right)\right), \exp(i2\pi N)\,\sigma_y\right] \\
&= -iE_C\left[N^2, \exp(i2\pi N)\right]\sigma_y + iE_L\left[\cos(\gamma), \exp(i2\pi N)\right]\sigma_y \\
&\quad -i\Delta\cos(\tfrac{\gamma}{2})\exp(i2\pi N)\left[\sigma_z, \sigma_y\right] - i\Delta\left[\cos(\tfrac{\gamma}{2}), \exp(i2\pi N)\right]\sigma_y\sigma_z \\
&\quad -i\Delta r\sin(\tfrac{\gamma}{2})\exp(i2\pi N)\left[\sigma_x, \sigma_y\right] - i\Delta r\left[\sin(\tfrac{\gamma}{2}), \exp(i2\pi N)\right]\sigma_y\sigma_x \\
&= 0 - 0 - i\Delta\cos(\tfrac{\gamma}{2})\exp(i2\pi N)(-2i\sigma_x) - i\Delta\left(2\cos(\tfrac{\gamma}{2})\exp(i2\pi N)\right)\sigma_x \\
&\quad -i\Delta r\sin(\tfrac{\gamma}{2})\exp(i2\pi N)[2i\sigma_z] - i\Delta r\left(2\sin(\tfrac{\gamma}{2})\exp(i2\pi N)\right)(-\sigma_z) \\
&= 0
\end{aligned}$$

of the spin by an angle π, which explains the need for the additional operator $\exp\left(-i\frac{\pi}{2}\sigma_y\right)$.

$R_{2\pi}$ has two different eigenvalues, $\pm i$:

$$\forall N\in\tfrac{1}{2}\mathbb{Z},\quad R_{2\pi}\tfrac{1}{\sqrt{2}}(|\rightarrow,N\rangle\pm i|\leftarrow,N\rangle)=\mp i\exp(i2\pi N)\tfrac{1}{\sqrt{2}}(|\rightarrow,N\rangle\pm i|\leftarrow,N\rangle). \tag{H.7}$$

which defines two orthogonal subspaces, one for each eigenvalue:

$$\forall N\in\mathbb{Z},\quad \begin{cases} S_i=\left\{\frac{1}{\sqrt{2}}\left(|\rightarrow,N\rangle-i|\leftarrow,N\rangle\right),\frac{1}{\sqrt{2}}\left(\left|\rightarrow,N+\frac{1}{2}\right\rangle+i\left|\leftarrow,N+\frac{1}{2}\right\rangle\right)\right\} \\ S_{-i}=\left\{\frac{1}{\sqrt{2}}\left(|\rightarrow,N\rangle+i|\leftarrow,N\rangle\right),\frac{1}{\sqrt{2}}\left(\left|\rightarrow,N+\frac{1}{2}\right\rangle-i\left|\leftarrow,N+\frac{1}{2}\right\rangle\right)\right\} \end{cases}. \tag{H.8}$$

Now, one can write the Hamiltonian in this new basis and restrict just to one subspace to get rid of the degeneracy.

In the basis introduced above,

$$R_{2\pi}=\begin{pmatrix} 0 & 1 & 0 & 0 & 0 & 0 \\ -1 & 0 & 0 & 0 & 0 & 0 \\ 0 & 0 & 0 & -1 & 0 & 0 \\ 0 & 0 & 1 & 0 & 0 & 0 \\ 0 & 0 & 0 & 0 & 0 & 1 \\ 0 & 0 & 0 & 0 & -1 & 0 \end{pmatrix}. \tag{H.9}$$

Its corresponding transformation matrix is simply

$$P=\tfrac{1}{\sqrt{2}}\begin{pmatrix} 1 & 0 & 0 & 0 & 0 & 1 \\ -i & 0 & 0 & 0 & 0 & i \\ 0 & 1 & 0 & 0 & 1 & 0 \\ 0 & i & 0 & 0 & -i & 0 \\ 0 & 0 & 1 & 1 & 0 & 0 \\ 0 & 0 & -i & i & 0 & 0 \end{pmatrix} \text{ and } P^\dagger R_{2\pi}P=i\begin{pmatrix} -1 & 0 & 0 & 0 & 0 & 0 \\ 0 & -1 & 0 & 0 & 0 & 0 \\ 0 & 0 & -1 & 0 & 0 & 0 \\ 0 & 0 & 0 & 1 & 0 & 0 \\ 0 & 0 & 0 & 0 & 1 & 0 \\ 0 & 0 & 0 & 0 & 0 & 1 \end{pmatrix}. \tag{H.10}$$

Now, one writes H_{env} in the eigenstates basis of $R_{2\pi}$:

$$P^\dagger H_{env}P=\frac{1}{2}\begin{pmatrix} \tilde{H}_{env} & 0 \\ 0 & \tilde{H}_{env} \end{pmatrix} \tag{H.11}$$

with

$$\boxed{\tilde{H}_{env}=\frac{1}{2}\begin{pmatrix} 2E_C\left(N-\frac{1}{2}\right)^2 & -\Delta e^{-i\frac{\varphi}{2}}(1-r) & -E_L \\ -\Delta e^{i\frac{\varphi}{2}}(1-r) & 2E_CN^2 & -\Delta e^{-i\frac{\varphi}{2}}(1+r) \\ -E_L & -\Delta e^{i\frac{\varphi}{2}}(1+r) & 2E_C\left(N+\frac{1}{2}\right)^2 \end{pmatrix}}. \tag{H.12}$$

This matrix is composed of two identical blocks on the diagonal. To get rid of the degeneracy, one selects one block. $\tilde{H}_{env}$ is written (for instance) in the subspace

$\left\{\frac{1}{\sqrt{2}}(|\rightarrow,N-\frac{1}{2}\rangle-i|\leftarrow,N-\frac{1}{2}\rangle),\frac{1}{\sqrt{2}}(|\rightarrow,N\rangle+i|\leftarrow,N\rangle),\frac{1}{\sqrt{2}}(|\rightarrow,N+\frac{1}{2}\rangle-i|\leftarrow,N+\frac{1}{2}\rangle)\right\}$. This is the building block of the complete matrix and can be extended along each diagonal to increase the size of the subspace. In this new basis, T^2 is simply

$$\tilde{T}^2 = \begin{pmatrix} 0 & 0 & 0 \\ 0 & 0 & 0 \\ 1 & 0 & 0 \end{pmatrix}. \tag{H.13}$$

H.3 Numerical resolution

To diagonalize the Hamiltonian, one needs to truncate this infinite matrix and find numerically its eigenvectors and eigenvalues. Note that the eigenvectors are directly expressed in term of number states. Therefore the JJS Hamiltonian is proportional to T^2, and the computation of the overlap matrix element is totally straightforward. For the numerical computation, I have centered the matrix around $N = 0$. One needs a big enough matrix to have accurate enough results. I have typically taken 81×81 matrices.

Fig. H.1 shows the transition probabilities (top panel) and the excitation spectrum (bottom panel) for a channel of transmission $\tau = 0.98$.

The energy spectra obtained with both methods agree very well. The two methods are also in very good agreement for the transition probabilities. One can see some tiny differences at very small probabilities, certainly due to the finite Taylor expansions made in the first model. However, note that with this new method, there is no asymmetry around π.

This alternative method is therefore convenient since it does not require approximation besides the truncation, which is simply a low energy approximation valid as long as one deals with lower energy states localized in phase. The matrix representation of Ivanov and Feigelman's Hamiltonian is particularly simple because of its phase dependence which is 4π-periodic and harmonic. This would not be the case with the two-level Hamiltonian used in Section 7.5.

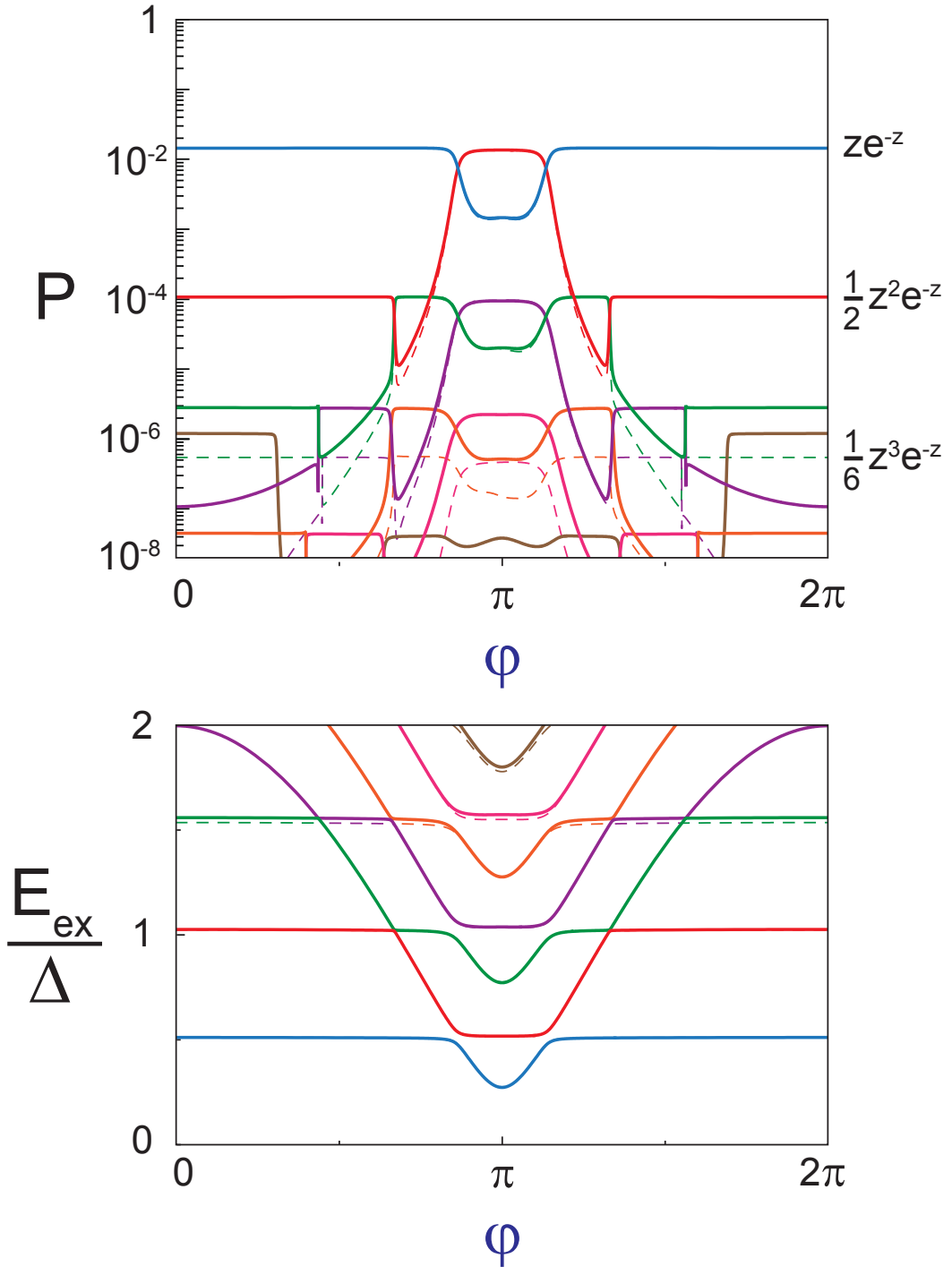

Figure H.1: Transition probabilities $P(\varphi)$ (**top**) and excitation energies $E_{ex}(\varphi)$ (in units of Δ) (**bottom**) of the first resonances, as a function of the reduced flux φ, for a channel of transmission $\tau = 0.98$. The solid lines are obtained by numerical diagonalization of a 81×81 matrix Hamiltonian in the charge basis. They are compared with the numerical diagonalization of a 14×14 matrix Hamiltonian in the plasmon basis (thin dashed lines).

I

SPECTROSCOPY OF THE PLASMA MODE OF A SYMMETRICAL SQUID

In this chapter, we present an experiment preliminary to the spectroscopy of ABS (see Chapter 6) which was intended to validate the spectroscopy scheme based on a voltage-biased Josephson junction.

I.1 Experimental setup

This experiment was performed on the sample JPS6, whose equivalent circuit is shown in Fig. I.1. It is similar to sample JT6 (see Fig. 6.1) but contains, in place of the atomic-SQUID, a SQUID with two identical Josephson junctions (critical current $I_{L0} \sim 1\,\mu A$ per junction). An external superconducting coil is used to apply a dc flux φ through the SQUID loop. The SQUID is capacitively coupled to a JJS (critical current $I_{J0} \sim 200\,nA$). Note that in this geometry, the same capacitors are used for the filtering of the bias line and for the coupling of the microwave radiated by the JJS towards the SQUID.

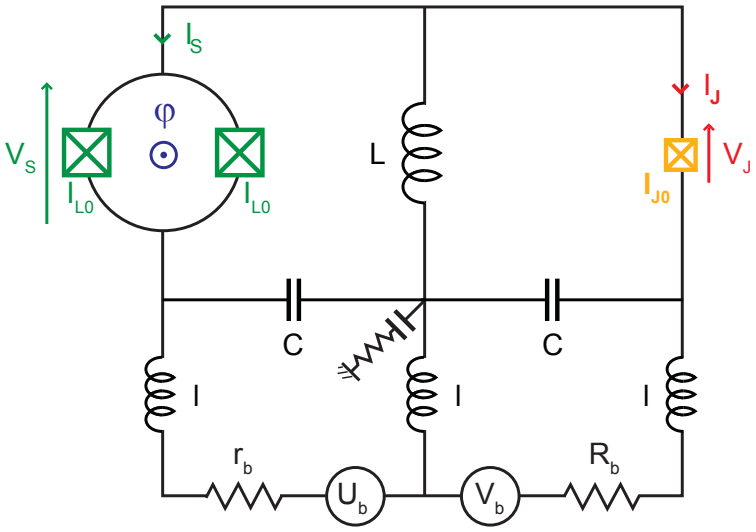

Figure I.1: Equivalent circuit of sample JPS6. Right part: a voltage-biased Josephson junction (yellow checked box) behaves as a microwave current source, emitting photons at Josephson frequency ν_J. Left part: two identical Josephson junctions (green checked boxes) form a SQUID. Reduced flux threading the loop φ is imposed by a superconducting coil. The JJS [respectively the SQUID] is biased by a voltage source V_b [U_b] through an on-chip lC filter and a series resistance R_b [r_b] placed at the same temperature as the sample.

The parameters of sample JPS6 are shown in Table I.1.

PARAMETER	SAMPLE JT6
JJS critical current I_{J0}	215 nA
SQUID JJ critical current I_{L0}	1.17 µA
Junctions total capacitance C_t	440 fF *
Plasma frequency $\nu_p(\varphi = 0) \simeq \frac{1}{2\pi}\sqrt{\left(\frac{1}{L} + \frac{2I_{L0}}{\varphi_0}\right)\frac{1}{C_t}}$	21.3 GHz
Inductor L	1.3 nH *

Table I.1: Parameters of Sample JPS6 presented in this chapter. Stars (*) indicate values inferred from fits of the spectrum.

I.2 Experimental results

The top panel of Fig. I.2 shows the current-voltage $I_J(V_J)$ characteristic of the JJS at flux $\varphi = 1.85\,\pi$, measured at ~ 280 mK. The fit of the IV curve at $eV > 2\Delta$ (not visible on this graph) and the Ambegaokar-Baratoff formula [68] yield the critical current of the JJS: $I_{J0} \simeq 215$ nA. In the sub-gap region, there are four peaks near ± 43 µV and ± 85 µV.

The bottom panel of Fig. I.2 shows the current I_J through the JJS as a function of both the flux φ and the voltage V_J across the JJS. When changing the flux, the position of these peaks changes with flux φ indicating that they correspond to modes associated with the SQUID.

We identify these resonances as excitations of the plasma mode of the SQUID, at frequency ν_p and $2\nu_p$. Neglecting the geometrical inductance of the loop, a SQUID behaves as a single JJ, whose critical current $I_c(\varphi)$ and plasma frequency $\nu_p(\varphi)$ are tunable with the reduced flux φ threading the SQUID loop (see Appendix F). The plasma frequency is renormalized by the environment inductance L and is given by

$$\nu_p(\varphi) = \frac{1}{2\pi}\sqrt{\left(\frac{1}{L} + \frac{2I_{L0}}{\varphi_0}\left|\cos\left(\frac{\varphi}{2}\right)\right|\right)\frac{1}{C_t}}. \tag{I.1}$$

The fit of the $I_S(V_S)$ of the SQUID (not shown) yields the critical current of the JJs of the SQUID $I_{L0} = 1.17$ µA. By fitting the experimental spectrum of Fig. I.2, we found the junctions total capacitance $C_t = 440$ fF and the environment parallel inductance $L = 1.3$ nH. The position of the theoretical transition energies are plotted as black lines in the negative-voltage region in Fig. I.2. The lower-energy resonance corresponds to the one-photon transition $|2eV_J| = h\nu_p$ (solid-line) and the higher-energy one to the two-photon transition $|2eV_J| = 2h\nu_p$ (dashed-line). They are in good agreement with the experimental data.

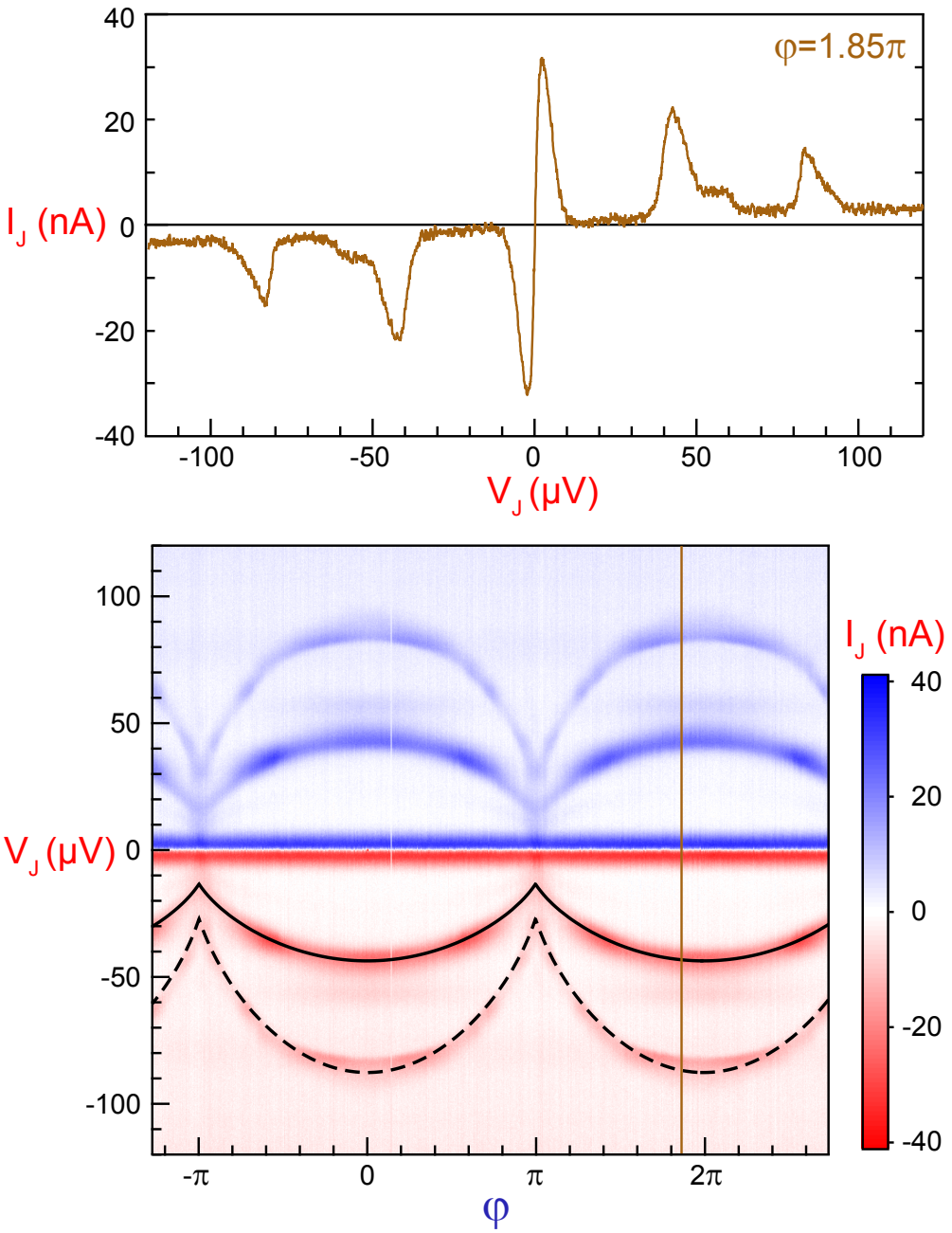

Figure I.2: **Top**: Current-voltage $I_J(V_J)$ characteristic of the JJS, for flux $\varphi = 1.85\,\pi$ (brown line). **Bottom**: Current I_J as a function of both the flux φ and the voltage V_J. Black lines: theoretical transition energies (in voltage units) of the plasma mode of the SQUID, as a function of the flux φ. The solid line is the one-photon process $|2eV_J| = \hbar\nu_p$, and the dashed line the two-photon process $|2eV_J| = 2\hbar\nu_p$.

J

AC JOSEPHSON EFFECT AND DYNAMICAL COULOMB BLOCKADE OF A JOSEPHSON JUNCTION: CLASSICAL CALCULATION

In Chapter 7, we have developed a quantum theory to describe the spectroscopy of an atomic-SQUID by a Josephson junction. It is necessary to derive such quantum treatment since the Andreev doublet is by essence quantum. This modeling is reminiscent from $P(E)$ theory, which was derived to describe dynamical Coulomb blockade in voltage-biased Josephson junctions, connected to a linear, classical environment of impedance $Z(\omega)$. However, this problem can also be treated classically, just starting from the Josephson relations. These two approaches (quantum and classical) yield different predictions. To understand this point, we will make explicit the classical derivation in this chapter.

The goal of this chapter is three-fold. First, we work out explicitly the case of a purely ohmic resistance environment, which is analytic. Then, we derive in perturbation the first harmonics (multi-Cooper pair processes) for an arbitrary impedance (this derivation was performed in collaboration with Benoît Douçot). At last, we discuss to which extent the sub-harmonics (multi-photons processes) are quantum. In the end, we solve numerically this problem in the case of a specific environment, an harmonic oscillator, and compare with the perturbation calculations.

J.1 Motivations

In presence of a constant bias voltage V, the current through a Josephson junction (of critical current I_0) oscillates at the Josephson pulsation $\omega_J = \frac{V_{dc}}{\varphi_0}$, where $V_{dc} = \langle V_J \rangle$ is the dc voltage across the JJ. In presence of a series environment (described by its impedance $Z(\omega)$), the voltage V_J across the JJ (and the corresponding phase α) can fluctuate and the energy $\hbar\omega_J$ irradiated by the JJ can be absorbed by the environment. This results in a dc current $I_{dc} = \langle I_J \rangle$ flowing through the JJ.

From the microscopic point of view, Cooper pairs tunnel through the barrier, while emitting photons which are absorbed by the environment. In full generality, n Cooper pairs can tunnel while emitting m photons, such as $n2eV = m\hbar\omega$ to satisfy energy conservation. One can distinguish two opposite regimes:

- In the charge regime, Cooper pairs tunnel independently and the multi-Cooper pairs processes are negligible. This phenomenon is called **Dynamical Coulomb Blockade** (DCB) and is well modeled through the quantum $P(E)$ theory (see Ref. [40] and Chapter 7).
- In the phase regime, the tunneling of Cooper pairs is coherent and the multi-Cooper pairs processes are possible. This phenomenon is simply called **ac Josephson effect** and is usually modeled through a classical theory (see Ref. [148]).

Strikingly, the first order terms (which correspond to the tunneling of 1 Cooper pair emitting 1 photon $2eV = \hbar\omega$) predicted by these two theories (quantum and classic) are the same:

$$I_{dc}(V_{dc}) = \frac{1}{2}\frac{\mathrm{Re}\left[Z\left(\frac{V_{dc}}{\varphi_0}\right)\right] I_0^2}{V_{dc}} \tag{J.1}$$

and do not depend explicitly on the Planck constant $\hbar$ except through I_0. To first order, the capability for the environment to absorb the energy at frequency ω depends on the real part of the impedance at this frequency $\mathrm{Re}\,[Z(\omega)]$.

In addition to first order terms, the $P(E)$ theory also predicts **sub-harmonics** (**multi-photons processes** in $2eV = m\hbar\omega$). However, since the $P(E)$ theory is a perturbation theory to first order, it neglects the **harmonics** (**multi-Cooper pairs processes** in $n2eV = \hbar\omega$). But an extension of this theory is possible to take them into account (this is formally done in Ref. [129], but it is not practically usable), and is necessary to deal with the intermediate regime.

However, the classical theory only predicts the harmonics (multi-Cooper pairs processes in $n2eV = \hbar\omega$), but no multi-photons processes are usually found. Moreover, the probability of the harmonics terms in the quantum $P(E)$ theory depend explicitly on the Planck constant $\hbar$. This indicates that the multi-photons processes are somehow quantum.

J.2 Notations

The schematic of the circuit is represented in Fig. J.1.

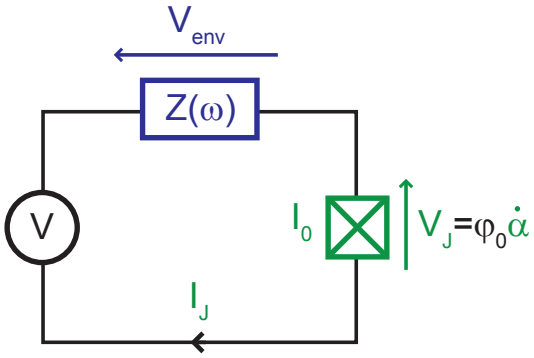

Figure J.1: Schematic of the circuit. A JJ is voltage biased through a series impedance $Z(\omega)$.

We consider the over-damped limit[1] in which the junction capacitance C_0 can be neglected. According to voltage conservation and Josephson laws:

$$\begin{cases} V = & V_{env}(t) + V_J(t) \\ V_J(t) = & \varphi_0 \frac{d\alpha}{dt}(t) \\ I_J(t) = & I_0 \sin(\alpha(t)) \end{cases}, \tag{J.2}$$

1 For an impedance $Z(\omega) = R$, this condition writes $R \ll \sqrt{\varphi_0/(I_0 C_0)}$.In the experiment JT6, this hypothesis is not fulfilled since $R = 200\,\Omega$ and $\sqrt{\varphi_0/(I_0 C_0)} \simeq 180\,\Omega$. However, this hypothesis simplifies a lot the calculations ...

with $V_{env}(\omega) = Z(\omega)I_J(\omega)$, where $V_{env}(\omega)$ and $I_J(\omega)$ are the Fourier transform of $V_{env}(t)$ and $I_J(t)$. We will take the convention

$$\begin{cases} FT(f)(\omega) = \frac{1}{\sqrt{2\pi}} \int_{-\infty}^{\infty} f(t) e^{-i\omega t}\, dt \\ f(t) = \frac{1}{\sqrt{2\pi}} \int_{-\infty}^{\infty} FT(f)(\omega) e^{i\omega t}\, d\omega \end{cases} \tag{J.3}$$

and we will write abusively: $FT(f)(\omega) = f(\omega)$.

Therefore, one gets for the phase α a non linear integrate-differential equation:

$$\boxed{\varphi_0 \frac{d\alpha}{dt}(t) + [Z * I_0 \sin(\alpha)](t) = V}, \tag{J.4}$$

where $*$ is the convolution product.

One wants to compute $I_{dc} = \langle I_J(t) \rangle$and $V_{dc} = \langle V_J(t) \rangle$. Unfortunately, the differential equation (J.4) is not analytically solvable for an arbitrary impedance. We fill first consider the analytical case of an ohmic resistance. Then, we will solve in perturbation the case of an arbitrary impedance. Note that all the calculations performed in the following are done assuming a zero temperature.

J.3 Ohmic resistance as an environment: analytical resolution

J.3.1 *Notations*

When the impedance is a resistance $\forall \omega,\ Z(\omega) = R$, the differential equation becomes much simpler:

$$V = \varphi_0 \frac{d\alpha}{dt}(t) + RI_0 \sin(\alpha(t)). \tag{J.5}$$

This problem has first been studied by Ivanchenko and Zilberman [148]. One defines:

$$\boxed{x = \frac{V}{\varphi_0} t\,,\ r = \frac{RI_0}{V}\,, f(x) = \alpha\left(\frac{\varphi_0}{V} x\right) \text{ and } i(x) = \sin(f(x))}. \tag{J.6}$$

Then, one gets a dimensionless non-linear differential equation:

$$\boxed{f'(x) + r \sin(f(x)) = 1}. \tag{J.7}$$

One wants to compute

$$\frac{I_{dc}}{I_0} = \langle i(x) \rangle \text{ and } \frac{V_{dc}}{V} = \left\langle f'(x) \right\rangle. \tag{J.8}$$

The solutions are different depending on the value of r.

J.3.2 $r \geqslant 1$

When $r \geqslant 1$, the stationary solution

$$f(x) = \arcsin\left(\frac{1}{r}\right) \tag{J.9}$$

is possible. Therefore, $f'(x) = 0$, *i.e.* there is no voltage across the Josephson junction

$$V_{dc} = 0, \tag{J.10}$$

and all the voltage drops on the resistance. It corresponds to the supercurrent branch regime. As a consequence, the phase is constant and adjusts itself to match $\arcsin\left(\frac{1}{r}\right)$. Then, the dc current is simply equal to the constant current

$$\frac{I_{dc}}{I_0} = \frac{1}{r} \Leftrightarrow I_{dc} = \frac{V}{R}. \tag{J.11}$$

J.3.3 $r < 1$

J.3.3.1 *Phase and current as a function of the time*

One introduces the inverse function $g = f^{-1}$. Since $f(g(\omega)) = \omega$, $f'(g(w)).g'(w) = 1$ and, using Eq. J.7

$$g'(w) = \frac{1}{1 - r\sin(w)} \tag{J.12}$$

which is now a linear differential equation. By integrating, choosing the integration constant such as $g(0) = 0$, one finds

$$g(w) = \frac{2}{\sqrt{1-r^2}}\left(\arctan\left(\frac{\tan\left(\frac{w}{2}\right) - r}{\sqrt{1-r^2}}\right) + \arctan\left(\frac{r}{\sqrt{1-r^2}}\right)\right). \tag{J.13}$$

Therefore

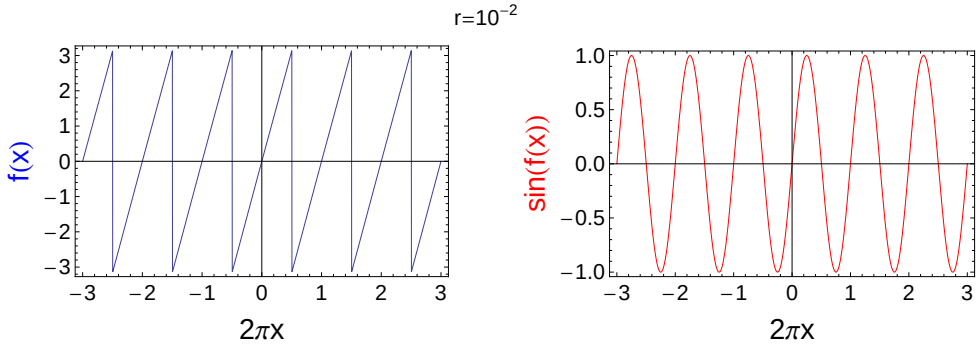

Figure J.2: Dimensionless phase f across the JJ and current i through the JJ, as a function of the reduced time x, for a reduced resistance $r = 0.01$. Because $r \ll 1$, the phase runs linearly in time and the current is essentially harmonic, oscillating at the bare Josephson pulsation $\frac{V}{\varphi_0}$.

$$\boxed{f(x) = 2\arctan\left(r + \sqrt{1-r^2}\tan\left(\frac{1}{2}\sqrt{1-r^2}x - \arctan\left(\frac{r}{\sqrt{1-r^2}}\right)\right)\right)} \tag{J.14}$$

which satisfies $f(0) = 0$. Consequently, one gets

$$\boxed{i(x) = \sin\left(2\arctan\left(r + \sqrt{1-r^2}\tan\left(\frac{1}{2}\sqrt{1-r^2}x - \arctan\left(\frac{r}{\sqrt{1-r^2}}\right)\right)\right)\right)}. \tag{J.15}$$

As long as $r < 1$, i is a X-periodic function, with period

$$X = \frac{2\pi}{\sqrt{1-r^2}}. \tag{J.16}$$

Therefore, the Josephson pulsation is

$$\boxed{\omega_J = \frac{V}{\varphi_0}\sqrt{1-r^2}}. \tag{J.17}$$

Note that $\omega_J \underset{r\to 1}{\longrightarrow} 0$, *i.e.* the current becomes constant, in agreement with previous sub-section.

For $r \ll 1$, $f(x) \simeq x$ and $X = 2\pi$: $i(x)$ is quasi-harmonic with pulsation $\frac{V}{\varphi_0}$ (see Fig. J.2).

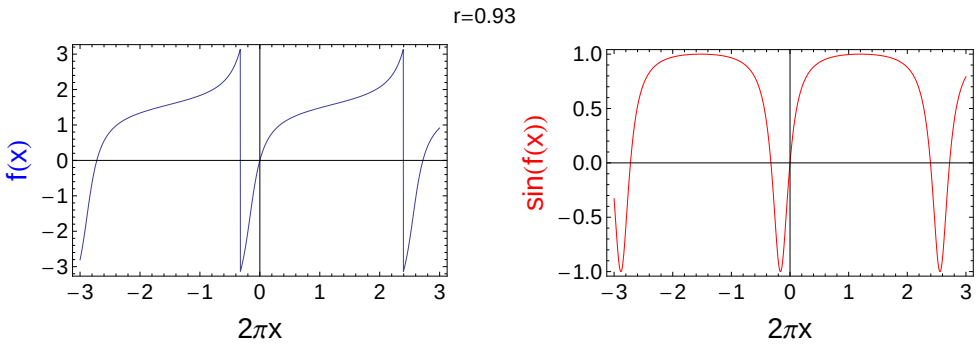

Figure J.3: Dimensionless phase f across and current i, as a function of the reduced time x, for a reduced resistance $r = 0.93$.

When r increases, the period X increases, *i.e.* the plasma frequency decreases to 0, and the current develops more and more higher harmonic terms (see Fig. J.3).The numerical Fourier transform of the current is plotted in Fig. J.4.One sees that the Josephson frequency goes to zero when r goes to 1. This is simply the fact that, at constant external bias voltage V, when r gets larger, a larger part of the voltage drops on the resistance, therefore a smaller part drops on the Josephson junction. One also sees that the larger r, the more harmonic frequencies contribute to the current. These modes are integer multiples of the Josephson pulsation $\omega_J = \frac{V}{\varphi_0}\sqrt{1-r^2}$. Because $\omega_J = \frac{V_{DC}}{\varphi_0}$, the order n harmonic term $\omega = n\omega_J$ verifies $\hbar\omega = n * 2eV_{DC}$. Therefore, in a microscopic point of view, it corresponds to the inelastic co-tunneling of n Cooper pair emitting only one photon. However, note that no lower harmonic terms $\frac{\omega_J}{n}$ are predicted.

J.3.3.2 *Dc current calculation*

The dc current is

$$\frac{I_{dc}}{I_0} = \langle \sin(f(x)) \rangle = \frac{1}{X}\int_0^X \sin(f(x))\, dx \tag{J.18}$$

where X is the period of $\sin(f(x))$. Because f verifies the differential equation (J.7), one gets the exact solution

$$\frac{I_{dc}}{I_0} = \frac{X - f(X) + f(0)}{rX} \tag{J.19}$$

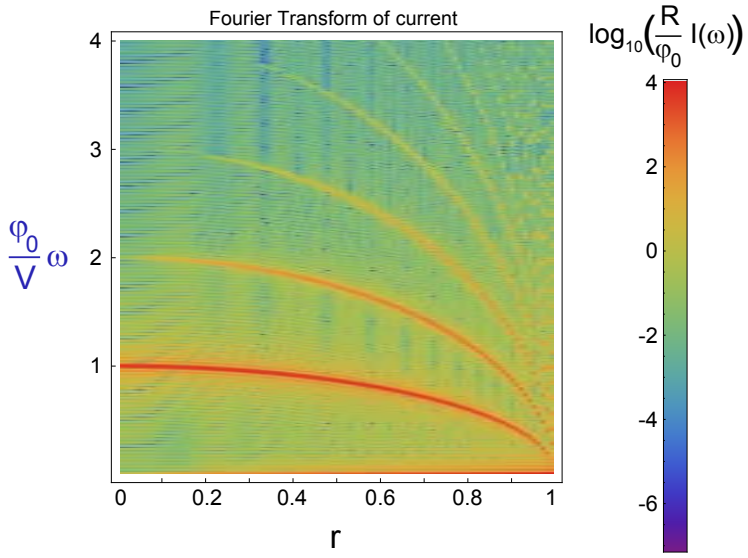

Figure J.4: Reduce Fourier transform of the current (log scale) as a function of both the reduced pulsation and the reduced resistance.

Because $f(X) - f(0) = 2\pi$ and $X = \frac{2\pi}{\sqrt{1-r^2}}$, one gets

$$\boxed{\frac{I_{dc}}{I_0} = \frac{1-\sqrt{1-r^2}}{r}}. \tag{J.20}$$

This is represented in Fig. J.5 (left, red). In absence of environment, $r = 0$, there are no longer phase fluctuations across the JJ and the dc current is zero $I_{dc} = 0$. When $r = 1$, the dc current is equal to the critical current $I_{dc} = I_0$, in agreement with the previous sub-section.

J.3.3.3 *Dc voltage calculation*

By definition,

$$\frac{V_{dc}}{V} = \left\langle f'(x) \right\rangle = \frac{f(X) - f(0)}{X} = \frac{2\pi}{X}. \tag{J.21}$$

As expected, one finds that

$$\boxed{\omega_J = \frac{V_{dc}}{\varphi_0}} \tag{J.22}$$

and[2]

$$\boxed{\frac{V_{dc}}{V} = \sqrt{1-r^2}}. \tag{J.23}$$

This is represented in Fig. J.5 (left, blue).

2 Note that this expression also reads $V^2 = V_{dc}^2 + R^2 I_0^2$. There may be a conservation law associated to this equation.

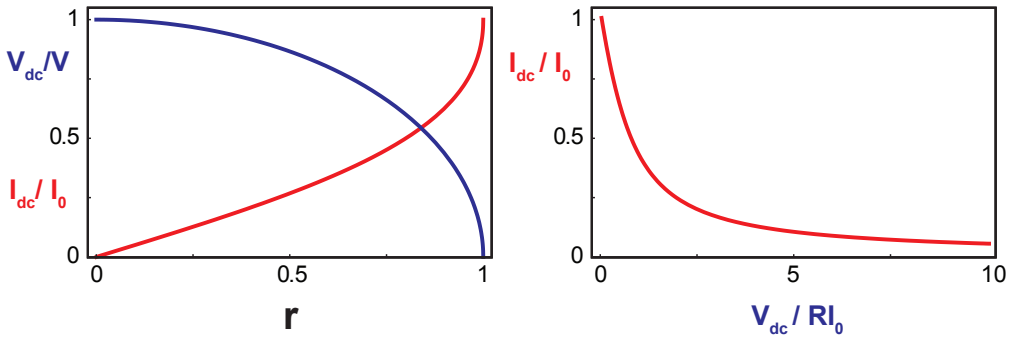

Figure J.5: **Left**: dc current (red) and voltage (blue) on the JJ as a function of the reduce resistance r. **Right**: $I_{dc}(V_{dc})$ characteristic.

J.3.3.4 *Current-voltage characteristic*

Using Eq. J.20 and Eq. J.23, one obtains the $I(V)$ characteristic (see Fig. J.5 (right)):

$$\boxed{\frac{I_{dc}}{I_0} = \sqrt{1 + \left(\frac{V_{dc}}{RI_0}\right)^2} - \frac{V_{dc}}{RI_0}}. \tag{J.24}$$

This result was first derived in Ref. [148] by Ivanchenko and Zilberman.

J.3.3.5 *Voltage and power conservation*

Using Eq. J.20 and Eq. J.23, one gets

$$V = V_{dc} + RI_{dc} \tag{J.25}$$

which is simply the voltage conservation.

By power conservation

$$VI_{dc} = R\left\langle I^2(t)\right\rangle + \left\langle V_J(t)I(t)\right\rangle. \tag{J.26}$$

The power dissipated by the junction is

$$\left\langle V_J(t)I(t)\right\rangle = VI_0\left\langle \sin(f(x))f'(x)\right\rangle = \frac{VI_0}{X}\left(\cos(f(0)) - \cos(f(X))\right) = 0 \tag{J.27}$$

One recovers that a Josephson junction is a non-dissipative dipole. The power is dissipated only by the resistance:

$$R\left\langle I^2(t)\right\rangle = VI_{dc}. \tag{J.28}$$

J.3.3.6 *Perturbative development of the exact solution*

For further developments, it is interesting to perform the Taylor expansions for small $r \ll 1$ of $f(x)$, X , I_{dc} and V_{dc} :

$$\begin{cases} f(x) = & x + r\left[\cos(x) - 1\right] - \frac{1}{4}r^2\left[2x - 4\sin(x) + \sin(2x)\right] \\ & -\frac{1}{12}r^3\left[-6x\sin(x) + 3\cos(x) - 6\cos(2x) + \cos(3x) + 2\right] \\ & +\frac{1}{32}r^4\left[-4x + 8\sin(x) + 12\sin(2x) - 8\sin(3x)\right. \\ & \left. + \sin(4x) + 8x\left(\cos(2x) - 2\cos(x)\right)\right] + O(r^5) \\ X = & 2\pi\left(1 + \frac{r^2}{2} + \frac{3r^4}{8} + + \frac{5r^6}{16} + O(r^8)\right) \\ \frac{I_{dc}}{I_0} = & \frac{r}{2} + \frac{r^3}{8} + \frac{r^5}{16} + O(r^7) \\ \frac{V_{dc}}{V} = & 1 - \frac{r^2}{2} - \frac{r^4}{8} - \frac{r^6}{16} + O(r^8) \end{cases} . \tag{J.29}$$

Using the two last last formulas to first order, one recovers

$$I_{DC} \simeq \frac{RI_0^2}{2V}. \tag{J.30}$$

J.4 Arbitrary impedance $Z(\omega)$: perturbative resolution

J.4.1 *Notations*

Contrary to the case of the resistance, there is no analytical solution of Eq. J.4 in the case of an arbitrary impedance. We will perform a perturbative development of this equation, perturbative in the sense that the voltage drop on the impedance is small compared to the one on the junction. To make the derivation easier, we introduce a small dimensionless parameter ϵ, and we replace the impedance Z by ϵZ. Thus, the starting equation reads

$$\varphi_0 \frac{d\alpha}{dt}(t) + \epsilon\left[Z * I_0 \sin(\alpha)\right](t) = V. \tag{J.31}$$

If $\epsilon = 0$, $\frac{d\alpha}{dt}(t) = \frac{V}{\varphi_0}$, and all physical observables oscillate at the pulsation $\omega_J(0) = \frac{V}{\varphi_0}$. For $\epsilon \neq 0$, one wants to find the solutions of this problem whose observables remain periodic functions with a pulsation $\omega_J(\epsilon)$. More precisely, it means that

$$\alpha(t) = \omega_J(\epsilon)t + \delta\alpha\left(\omega_J(\epsilon)t\right), \tag{J.32}$$

where $\delta\alpha$ is a 2π-periodic function.

While doing the perturbative resolution of this differential equation, one faces a major problem. Starting from order 2, solutions are no longer periodic; one does not know the perturbative development of the period and cannot compute the dc current and voltage. This problem can be circumvented by fixing the pulsation $\omega_J(\epsilon) = \omega_J$ and looking for an ϵ-dependent bias voltage $V(\epsilon)$. In a perturbative development, the bias voltage writes

$$V(\epsilon) = \sum_{n=0}^{\infty} \epsilon^n V_n. \tag{J.33}$$

Each of the V_n is unknown and will be found self-consistently to satisfy the periodic nature of the solutions. What is known is the full sum $V(\epsilon)$. Thus, the Josephson pulsation remains constant and is equal to

$$\boxed{\omega_J = \frac{V_0}{\varphi_0}}. \tag{J.34}$$

One defines the dimensionless parameters

$$\begin{aligned} &u = \omega_J t\,,\ z = \tfrac{ZI_0}{V_0}\,, \nu_n = \tfrac{V_n}{V_0}\,, \\ &f(u) = \alpha\left(\tfrac{u}{\omega_J}\right),\ i(u) = \sin\left(f(u)\right) \text{ and } \nu_J(u) = f'(u). \end{aligned} \tag{J.35}$$

One looks for a perturbative solution

$$f(u) = \sum_{n=0}^{\infty} \epsilon^n f_n(u) \tag{J.36}$$

of the differential equation

$$\boxed{f'(u) + \epsilon\left[z * \sin\left(f\right)\right](u) = \sum_{n=0}^{\infty} \epsilon^n \nu_n} \tag{J.37}$$

with f_n 2π-periodic $\forall n \geqslant 1$. At each integration, one has to choose an integration constant. We will choose them such as $f_n(0) = 0\ \forall n$.

Because $z(t) \in \mathbb{R}$, $\left[z * \sin\left(f\right)\right](u) = \mathrm{Im}\left(\left[z * e^{if}\right](u)\right)$. The Taylor expansion of e^{if} to order 3 in ϵ reads:

$$e^{if} = e^{if_0}\left[1 + i\epsilon f_1 + \epsilon^2\left(if_2 - \frac{1}{2}f_1^2\right) + \epsilon^3\left(if_3 - f_1 f_2 - \frac{i}{6}f_1^3\right)\right] + \mathcal{O}(\epsilon^4). \tag{J.38}$$

In the following, one will use the identity

$$\left(z * \exp\left(inu\right)\right)(u) = z(n\omega_J)\exp\left(inu\right). \tag{J.39}$$

At each order, one will derive the phase, current and voltage, and compute the dc current $\frac{I_{dc}}{I_0} = \langle i \rangle$. There is no need to compute the dc voltage since

$$\boxed{\frac{V_{dc}}{V_0} = \left\langle f' \right\rangle = 1} \tag{J.40}$$

by construction (because $\forall n \geqslant 1,\ f_n$ is 2π-periodic). However, at each step one has to express V_0 as a function of the total voltage $V = V(\epsilon)$. Thus, one will find out the Josephson pulsation. At each step one can apply the formula found to the purely resistive situation $Z(\omega) = R$ and compare them with the Taylor expansion of the exact solution (J.29) to check their validity.

For clarity, we define the parameters:

$$x_n = \mathrm{Re}\left[z(n\omega_J)\right]\,,\quad y_n = \mathrm{Im}\left[z(n\omega_J)\right]\,,\quad z_n = z(n\omega_J)\,. \tag{J.41}$$

J.4.2 *Order 0*

To order 0 in ϵ, Eq. J.37 writes

$$f_0'(u) = 1. \tag{J.42}$$

Therefore one finds

$$\begin{cases} f_0(u) = & u \\ i(u) = & \sin(u) \\ v(u) & = 1 \end{cases} \tag{J.43}$$

and the dc current is

$$\frac{I_{dc0}}{I_0} = 0. \tag{J.44}$$

To order 0 in ϵ, Eq. J.33 writes

$$V = V_0 = V_{dc0}. \tag{J.45}$$

Therefore, the Josephson pulsation and period are

$$\omega_{J0} = \frac{V}{\varphi_0} \text{ and } X_0 = \frac{V}{\varphi\omega_{J0}} = 2\pi. \tag{J.46}$$

J.4.3 *Order 1*

The terms of Eq. J.37 of order 1 in ϵ give

$$f_1'(u) + \operatorname{Im}\left(\left[z * e^{if_0}\right](u)\right) = v_1. \tag{J.47}$$

Using Eq. J.43 and Eq. J.39 one gets

$$f_1'(u) + \operatorname{Im}\left(z_1 \exp(iu)\right) = v_1. \tag{J.48}$$

By integrating over 2π, and using the fact that f_1 is 2π-periodic, one finds that

$$v_1 = 0. \tag{J.49}$$

Therefore, using Eq. J.33, the dc voltage to first order is still

$$V_{dc1} = V. \tag{J.50}$$

Thus, the Josephson pulsation and period are unchanged

$$\omega_{J1} = \frac{V}{\varphi_0} \text{ and } X_1 = 2\pi. \tag{J.51}$$

By integrating Eq. J.48, one gets

$$\begin{cases} f_1(u) & = \operatorname{Re}\left(z_1\left(\exp(iu) - 1\right)\right) \\ & = x_1\left(\cos(u) - 1\right) - y_1 \sin(u). \end{cases} \tag{J.52}$$

Therefore the current and the voltage read

$$\begin{cases} i(u) = & \sin\left(u + \epsilon\left(x_1\left(\cos(u) - 1\right) - y_1\sin(u)\right)\right) \\ v(u) = & 1 - \epsilon\left(x_1\sin(u) + y_1\cos(u)\right). \end{cases} \tag{J.53}$$

Using Eq. J.38, the dc current to first order is

$$\frac{I_{dc1}}{I_0} = \frac{\epsilon x_1}{2}. \tag{J.54}$$

Consequently, the current voltage relation to first order is (forgetting about the ϵ)

$$\boxed{I_{dc1} = \frac{1}{2}\frac{\mathrm{Re}\left[Z\left(\omega_{J1}\right)\right] I_0^2}{V_{dc1}}}. \tag{J.55}$$

This formula corresponds to the result of P(E) theory.

Let us consider a single-mode environment at frequency ω_0 with quality factor Q. Then, the impedance writes

$$Z(\omega_0\omega_r) = QZ_0 z_r(\omega_0\omega_r) \tag{J.56}$$

where ω_r is the reduced pulsation and z_r the reduced impedance, defined as (see Appendix C)

$$\begin{cases} \mathrm{Re}\left[z_r(\omega_0\omega_r)\right] = & \frac{1}{1+\left(Q\frac{1-\omega_r^2}{\omega_r}\right)^2} \\ \mathrm{Im}\left[z_r(\omega_0\omega_r)\right] = & \frac{1}{Q}\frac{x(1-\omega_r^2)}{(\omega_r/Q)^2+(1-\omega_r^2)^2} \end{cases}. \tag{J.57}$$

Introducing the reduced voltage and current

$$\begin{cases} v_{dc1} = & \frac{V_{dc1}}{\varphi_0\omega_0} \\ i_{dc1} = & \frac{I_{dc1}}{I_0} \end{cases}, \tag{J.58}$$

the current voltage characteristics reads

$$\boxed{i_{dc1}\left(v_{dc1}\right) = \frac{1}{2}\frac{\mathrm{Re}\left[z_r\left(\omega_0 v_{dc1}\right)\right] i_0}{v_{dc1}}} \tag{J.59}$$

with the reduced critical current

$$\boxed{i_0 = \frac{QZ_0 I_0}{\varphi_0\omega_0}}. \tag{J.60}$$

For an infinite quality factor, the formula (J.59) means that a dc current can flow through the JJ if and only if $v_{dc1} = 1 \Leftrightarrow 2eV_{dc1} = \hbar\omega_0 \Leftrightarrow \omega_{J1} = \omega_0$. This lower order process corresponds to the tunneling of 1 Cooper pair emitting 1 photon, and results in a current peak at the voltage $V_{dc1} = \hbar\omega_0/2e$ in the I(V) characteristic (see Fig. J.6).

In the case of this specific impedance, the parameter i_0 is actually the true perturbation parameter (instead of ϵ which was introduce artificially to make the

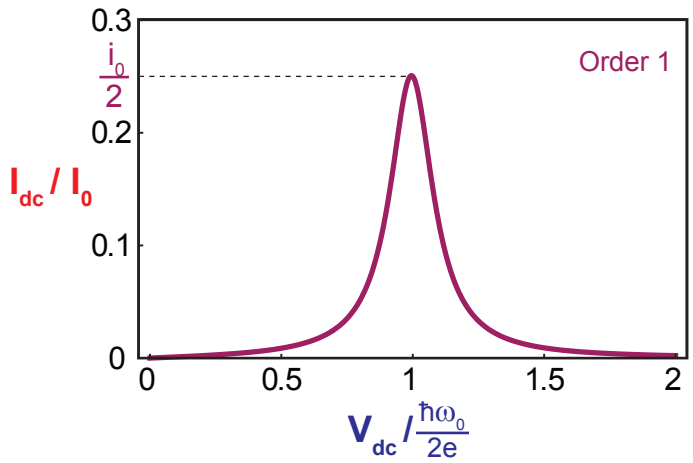

Figure J.6: I(V) characteristic of a single-mode environment of resonance pulsation ω_0, characteristic impedance Z_0 and quality factor $Q = 5$. This corresponds to the first order prediction (J.59). There is a current peak at the voltage $\hbar\omega_0/2e$. This calculation is done for $i_0 = 0.5$.

derivation easier). The perturbation calculation is valid for $i_0 \ll 1$. This parameter determines the tendency to have multi-Cooper pair processes. It is proportional to the critical current I_0, which determines the amplitude of the ac current, *i.e.* of the excitation. Note that it also depends on the environment through $\frac{QZ_0}{\varphi_0\omega_0}$: this determines the capability for the environment to absorb the energy at the Josephson frequency $\omega_J = \omega_0$.

J.4.4 *Order 2*

To order 2 in ϵ, Eq. J.37 writes

$$f_2'(u) + \mathrm{Im}\left(\left[z * ie^{if_0} f_1\right](u)\right) = v_2. \tag{J.61}$$

Using Eq. J.43, Eq. J.52 and Eq. J.39, one gets

$$f_2'(u) - v_2 = -\frac{1}{2}\mathrm{Re}\left[x_1 x_0 - 2x_1\left(z_1 \exp(iu)\right) + z_1 z_2 \exp(i2u)\right]. \tag{J.62}$$

By integrating over 2π and using the fact that f_2 is 2π-periodic, one finds that

$$v_2 = \frac{1}{2}x_0 x_1. \tag{J.63}$$

Therefore, using Eq. J.33, the dc voltage to second order is

$$\frac{V_{dc2}}{V} = 1 - \epsilon^2\frac{1}{2}x_0 x_1, \tag{J.64}$$

and the Josephson pulsation and period are

$$\omega_{J2} = \frac{V}{\varphi_0}\left(1 - \epsilon^2\frac{1}{2}x_0 x_1\right) \text{ and } X_2 = 2\pi\left(1 + \epsilon^2\frac{1}{2}x_0 x_1\right). \tag{J.65}$$

By integrating Eq. J.62, one gets

$$\begin{aligned} f_2(u) &= \tfrac{i}{4}\mathrm{Im}\left[-2x_1z_1\left(\exp(iu)-1\right)+\tfrac{1}{2}z_1z_2\left(\exp(i2u)-1\right)\right] \\ &= x_1\left(y_1\left(\cos(u)-1\right)+x_1\sin(u)\right) \\ &\quad -\tfrac{1}{4}\left(\left(y_1x_2+x_1y_2\right)\left(\cos(2u)-1\right)+\left(x_1x_2-y_1y_2\right)\sin(2u)\right). \end{aligned} \tag{J.66}$$

Therefore the current and the voltage read

$$\begin{cases} i(u) &= \sin\left[u+\epsilon\left(x_1\left(\cos(u)-1\right)-y_1\sin(u)\right)\right. \\ &\quad +\epsilon^2\left(x_1\left(y_1\left(\cos(u)-1\right)+x_1\sin(u)\right)\right. \\ &\quad \left.\left.-\tfrac{1}{4}\left(\left(y_1x_2+x_1y_2\right)\left(\cos(2u)-1\right)+\left(x_1x_2-y_1y_2\right)\sin(2u)\right)\right)\right] \\ v(u) &= 1-\epsilon\left(x_1\sin(u)+y_1\cos(u)\right) \\ &\quad +\epsilon^2\left(x_1\left(-y_1\sin(u)+x_1\cos(u)\right)\right. \\ &\quad \left.+\tfrac{1}{2}\left(\left(y_1x_2+x_1y_2\right)\sin(2u)-\left(x_1x_2-y_1y_2\right)\cos(2u)\right)\right) \end{cases}. \tag{J.67}$$

Using Eq. J.38, one computes the dc current to second order. One finds[3] that is is unchanged:

$$\frac{I_{dc2}}{I_0} = \frac{1}{2}\epsilon x_1. \tag{J.68}$$

Whereas there is no new correction of the current voltage relation to second order, the dc voltage and the Josephson pulsation are modified according to equations (J.64) and (J.65). Note that not only $\mathrm{Re}\left[Z\left(\omega_J\right)\right]$ matters but also $Z(0)$.

J.4.5 *Order 3*

To order 3 in ϵ, Eq. J.37 writes

$$f_3'(u) + \mathrm{Im}\left(\left[z * e^{if_0}\left(if_2-\frac{1}{2}f_1^2\right)\right](u)\right) = v_3. \tag{J.69}$$

Using Eq. J.43, Eq. J.52, Eq. J.66 and Eq. J.39, one gets

$$\begin{aligned} f_3'(u)-v_3 = &-\tfrac{i}{8}\mathrm{Im}\left[z_1\left(z_1z_2-2i\left[4x_1y_1-\left(y_1x_2+x_1y_2\right)\right]+4\left|z_1\right|^2+z_1^{*2}\right)\exp(iu)\right. \\ &\left.-8x_1z_1z_2\exp(i2u)+\left(z_1+z_2\right)z_1z_3\exp(i3u)\right]. \end{aligned} \tag{J.70}$$

By integrating over 2π and using the fact that f_3 is 2π-periodic, one finds that

$$v_3 = 0. \tag{J.71}$$

Therefore, the dc voltage, the Josephson pulsation and period are unchanged: $V_{dc3} = V_{dc2}$, $\omega_{J3} = \omega_{J2}$ and $X_3 = X_2$.

3 Because $\left\langle\cos\left(f_0(u)\right)f_2(u)\right\rangle - \frac{1}{2}\left\langle\sin\left(f_0(u)\right)f_1^2(u)\right\rangle = \frac{x_1y_1}{2} - \frac{x_1y_1}{2} = 0$.

By integrating Eq. J.70, one gets

$$\begin{aligned} f_3(u) &= -\tfrac{1}{8}\mathrm{Re}\left[z_1\left(z_1z_2-2i\left[4x_1y_1-(y_1x_2+x_1y_2)\right]+4|z_1|^2+z_1^{*2}\right)(\exp(iu)-1)\right. \\ &\quad \left.-4x_1z_1z_2(\exp(i2u)-1)+\tfrac{1}{3}(z_1+z_2)z_1z_3(\exp(i3u)-1)\right] \\ &= -\tfrac{1}{8}\left(5x_1^3+x_1^2x_2-3x_2y_1^2+x_1y_1(13y_1-4y_2)\right)(\cos(u)-1) \\ &\quad +\tfrac{1}{8}\left(4x_1x_2y_1+y_1^2(3y_1-y_2)-x_1^2(5y_1-3y_2)\right)\sin(u) \\ &\quad +\tfrac{1}{2}x_1\left((x_1x_2-y_1y_2)(\cos(2u)-1)-(y_1x_2+x_1y_2)\sin(2u)\right) \\ &\quad -\tfrac{1}{24}\left(x_3\left(x_1(x_1+x_2)-y_1(y_1+y_2)\right)-y_3\left(x_2y_1+x_1(2y_1+y_2)\right)\right)(\cos(3u)-1) \\ &\quad +\tfrac{1}{24}\left(x_3\left(x_2y_1+x_1(2y_1+y_2)\right)+y_3\left(x_1(x_1+x_2)-y_1(y_1+y_2)\right)\right)\sin(3u)\,. \end{aligned} \tag{J.72}$$

Using Eq. J.38, one computes the dc current to third order. One finds[4]:

$$\boxed{\frac{I_{dc3}}{I_0}=\frac{1}{2}\epsilon x_1-\frac{1}{8}\epsilon^3\left(x_1^3+y_1\left[11x_1y_1-3(x_1y_2+y_1x_2)\right]\right)}. \tag{J.73}$$

To order 3, the current voltage relation is changed. All of this is in agreement with the resistive case Eq. J.29.

J.4.6 *Interpretation*

The corresponding $I(V)$characteristic (for a single-mode environment) is represented in Fig. J.7 (red continuous line) and compared with the order 1 prediction (purple dashed line). In the formula (J.73):

- The term in $-\epsilon^3x_1^3 \sim (\mathrm{Re}[Z(\omega_{J3})])^3$ is just a negative correction to order 1 and does not bring new physics.
- $\epsilon^3y_1(11x_1y_1-3(x_1y_2+y_1x_2))$ contains terms in $\mathrm{Im}[Z]$. Therefore, the imaginary part of the impedance matters and can give a contribution to the dc current. However, it is always combined with some real part of the impedance sine no purely imaginary impedance can absorb energy.
- $\epsilon^3y_1(x_1y_2+y_1x_2)$ contains term in $Z(2\omega_{J3})$. Let us consider a single-mode environment at frequency ω_0. Then, a dc current can flow through the JJ not only when $\omega_{J3}=\omega_0$ but also when $2\omega_{J3}=\omega_0 \Leftrightarrow 4eV_{dc3}=\hbar\omega_0$. From a microscopic point of view, it corresponds to the **inelastic tunneling of two Cooper pairs emitting only one photon**. It results in a current peak at the voltage

$$V_{dc31}=\frac{1}{2}\frac{\hbar\omega_0}{2e}, \tag{J.74}$$

4 Because

$$\begin{cases} \langle\cos(f_0)f_1\rangle=\frac{x_1}{2} \\ \langle\cos(f_0)f_3\rangle=-\frac{1}{16}\left(5x_1^3+x_1^2x_2-3x_2y_1^2+x_1y_1(13y_1-4y_2)\right) \\ -\langle\sin(f_0)f_1f_2\rangle=\frac{1}{16}\left(8x_1^3+x_1^2x_2+3x_2y_1^2+2x_1y_1(-4y_1+y_2)\right) \\ -\frac{1}{6}\langle\cos(f_0)f_1^3\rangle=-\frac{1}{16}x_1(5x_1^2+y_1^2) \end{cases}.$$

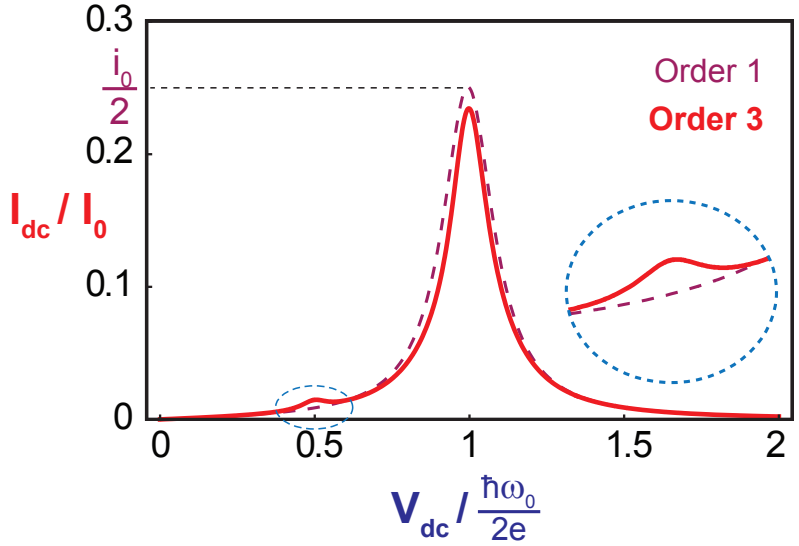

Figure J.7: I(V) characteristic of a single-mode environment of resonance pulsation ω_0 and quality factor $Q = 5$. The third order prediction (J.73) (red continuous line) is compared with the first order prediction (J.59) (purple dashed line). In addition to the peak at the voltage $\hbar\omega_0/2e$ (whose amplitude is slightly corrected), there is a current peak at the half voltage $\hbar\omega_0/4e$ (zoom). This calculation is done for a reduce critical current $i_0 = 0.5$.

in the I(V) characteristic, which is the half of the voltage of the order one peak (see Fig. J.7). However, these terms are in ϵ^3, and thus less probable. Moreover, terms $Z(2\omega_J)$ are always in product with terms $Z(\omega_J)$. Therefore, this process can happen only if the impedance has a non zero weight at ω_J and $2\omega_J$ at the same time. If the single-mode environment has a large enough quality factor, one can have $\epsilon x_1 \ll \epsilon^3 x_2 y_1^2$ at the voltage $\frac{1}{2}\frac{\hbar\omega_0}{2e}$ and the order-3 process can be dominant compared with the first order process.

J.5 Discussion

J.5.1 *What comes from this calculation ? Harmonics: multi-Cooper pairs processes*

Both the Fourier transform of the current in the purely restive case and the order 3 of the dc current for an arbitrary impedance, prove that, in presence of an environment, harmonic terms in $n\omega_J$ are generated. They correspond to higher order tunneling events like the inelastic co-tunneling of two Cooper pairs emitting one photon.

The perturbative resolution presented above gives the amplitude of the first order correction in the case of an arbitrary impedance. It also allows to realize that imaginary part of the impedance actually matters and can contribute, when combined with some real part of impedance, to the dc current.

J.5.2 *What is quantum ? Sub-harmonics: multi-photons processes*

However no sub-harmonic terms in $\frac{\omega_J}{n}$ are generated. It seems that they are somehow deeply quantum. To understand this point, it is useful to draw a parallel:

- When shining a monochromatic light ω_0 on a non-linear medium, one can generate harmonic terms at $n\omega_0$. The microscopic picture is that packet of photons bunch together to form photons of bigger energy. However, this phenomenon can be described by a fully classical treatment.
- One can also[5] generate sub-harmonic terms $\frac{\omega_0}{n}$. The phenomenon behind this is the **parametric down-conversion**: the light excites slightly the medium which modulates its resonance frequency ω_r. Like in a parametric oscillator, if the light frequency is n times the medium frequency $\omega_0 = n\omega_r$, sub-harmonic terms in $\frac{\omega_0}{n}$ are generated. This phenomenon is completely classical. However, if the initial amplitude of the mode $\frac{\omega_0}{n}$ is zero, it will remain so. To start, this process needs a seed like a non-zero noise at this frequency. In particular, in presence of a thermal noise, one can predict classically this parametric down-conversion. However, at zero temperature, there is no thermal noise and a fully classical theory does not predict this phenomenon. That is where one needs quantum physics and Heisenberg principle which provides **zero-point noise**. At zero temperature, this process can start thanks to spontaneous emission.

In the previous scenario, the emitter is linear whereas the medium is non linear. Here, the problem that we considered is dual: the medium, described by an impedance, is linear, and the emitter, the Josephson junction, is non linear. The results are the same and one can generate harmonics and sub-harmonics.

The previous classical treatment has been derived at zero temperature. That is why only harmonic terms were generated. At finite temperature, one has to add a stochastic noise in the previous equations. Then, one needs to solve a Fokker-Planck equation which describes the time evolution of the probability density function of the phase density. This has been already done in the purely resistive case, by Ivanchenko and Zilberman [148] . It would be interesting to do it for an arbitrary impedance, and solve the problem in perturbation. This treatment should allow to predict the sub-harmonics[6].

At zero temperature, like in the classical theory of laser, one could add, by hand, a noise accounting for spontaneous emission. Because $P(E)$ theory is quantum, the zero-point noise is built in: that is why it predicts multi-photons processes. They explicitly depend on the Planck constant, through Heisenberg principle which gives the amplitude of the zero-point noise.

5 In a quantum regime this process can create the famous intricated twin photons.

6 An easier way to convince oneself of the existence of sub-harmonic terms in the classical treatment is just to add to the constant voltage of the generator a small ac signal at any frequency $\frac{\omega_J}{n}$.

J.6 Numerical resolution

The former results are interesting because they are analytical but approximate and quite cumbersome. For a specific electromagnetic environment, the equation J.4 can be solved numerically.

J.6.1 *Harmonic oscillator*

The excitation scheme used in the experiments described in Part III is schematized in Fig. J.8. Instead of the atomic-SQUID (or the tunnel SQUID), we just consider an

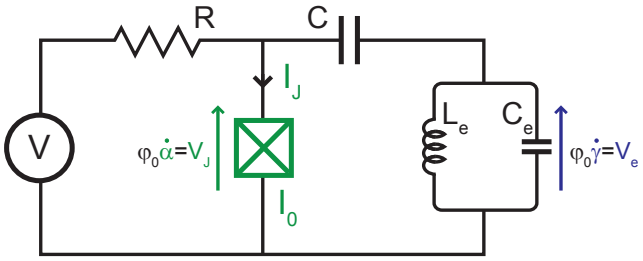

Figure J.8: Schematic of the typical excitation scheme used in experiments, with an LC oscillator as an environment.

harmonic LC oscillator as an environment. The phase α across the JJ and the phase γ across the oscillator verify a system of differential equations:

$$\begin{cases} \varphi_0\dot{\alpha} + R\left[I_0\sin(\alpha) + \frac{\varphi_0}{L_e}\gamma + \varphi_0 C_e\ddot{\gamma}\right] = V \\ \varphi_0\ddot{\gamma} + \frac{1}{C}\left[\frac{\varphi_0}{L_e}\gamma + \varphi_0 C_e\ddot{\gamma}\right] - \varphi_0\ddot{\alpha} = 0 \end{cases} . \tag{J.75}$$

One defines

$$\begin{array}{c} \omega_e = \frac{1}{\sqrt{L_e C_e}},\ y = \omega_e t,\ i_0 = \frac{RI_0}{\varphi_0\omega_e}, \\ c = \frac{C}{C_e},\ Q = R\sqrt{\frac{L_e}{C_e}} \text{ and } \nu = \frac{V}{\varphi_0\omega_e} \end{array} . \tag{J.76}$$

Then Eq. J.75 writes

$$\begin{cases} Q\gamma'' + \alpha' + Q\gamma + i_0\sin(\alpha) = \nu \\ (c+1)\gamma'' + \gamma - c\alpha'' = 0 \end{cases} . \tag{J.77}$$

I have solved these equations numerically[7] with *Mathematica*, and computed the reduced dc voltage $\nu_{dc} = \langle\alpha'\rangle$ and the reduced dc current $i_{dc} = \langle\sin(\alpha)\rangle$. They

7 Such a computation needs a fine tuning to find converging results. In particular, one needs to choose proper initial conditions. I have taken $\alpha(0) = \gamma(0) = \gamma'(0) = 0$ and $\alpha'(0) = \nu$. One also needs to impose a cutoff time. It has to be large enough to have stable results out of transient regime. I have taken $y_\infty = 4000$. Thus, one gets $\forall y \in [0, y_\infty]$, $\alpha(y)$ and $\gamma(y)$. Then, one solves $\alpha(y) = \alpha(y_\infty)$ and takes the last value $y_{\infty-1}$ before y_∞ verifying this equation (thus one only consider the last period) and computes

$$\nu_{dc} = \langle\alpha'\rangle = \frac{\alpha(y_\infty) - \alpha(y_{\infty-1})}{y_\infty - y_{\infty-1}}$$

and

$$i_{dc} = \langle\sin(\alpha)\rangle = \frac{1}{y_\infty - y_{\infty-1}}\int_{y_{\infty-1}}^{y_\infty}\sin(\alpha(y))\,dy.$$

are represented in Fig. J.9 as a function of the reduced voltage v for[8] a quality factor $Q = 5$, an oscillator frequency $\omega_e/2\pi = 20$ GHz, a reduced current $i_0 = 0.5$ and a capacitance ratio $c = 1000$. The dc voltage is essentially equal to the bias

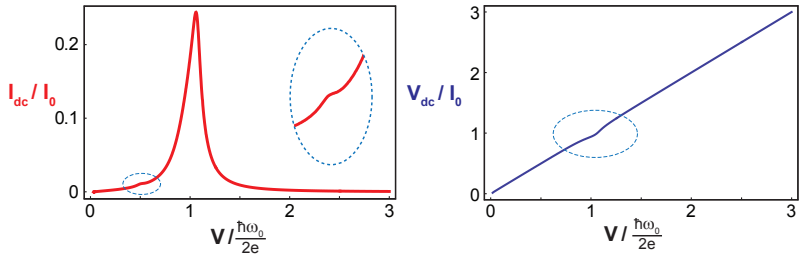

Figure J.9: Dc current (**left**) and dc voltage (**right**) as a function of the reduced bias voltage v. These calculation is performed for a quality factor $Q = 5$, an oscillator frequency $\omega_e/2\pi = 20$ GHz, a reduced current $i_0 = 0.5$ and a capacitance ratio $c = 1000$.

voltage, except on the current resonances (where there is a finite voltage across the resistor). The corresponding $I(V)$ characteristic is shown in Fig. J.10, and compared with the perturbation theory to order 3 (J.73). Because $i_0 = 0.5$, the harmonics

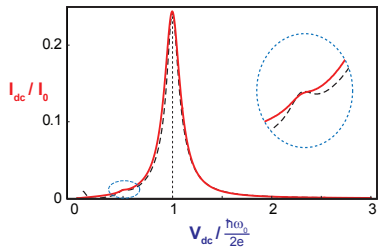

Figure J.10: $I(V)$ characteristic for the same parameters as Fig. J.9. The numerical calculation (continuous red curve) is in a good agreement with the perturbation theory to order 3 (J.73) (dashed black line). In addition to the peak at the voltage $\hbar\omega_0/2e$ (whose amplitude is slightly corrected), there is another one at the half voltage $\hbar\omega_0/4e$ (zoom).

processes are very small and one hardly sees the order 2 current peak (see zoom of Fig. J.10). Indeed, i_0 determines the probability of multi-Cooper pair processes and accounts both for the strength of the excitation by the JJ, and the capability of the environment to absorb energy.

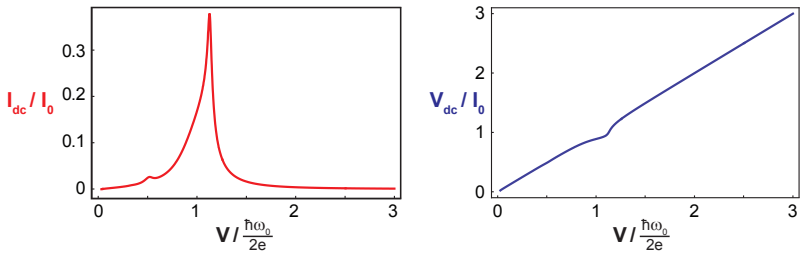

Figure J.11: Dc current (**left**) and dc voltage (**right**) as a function of the reduced bias voltage v. These calculation is performed for a quality factor $Q = 5$, an oscillator frequency $\omega_e/2\pi = 20$ GHz, a reduced current $i_0 = 0.9$ and a capacitance ratio $c = 1000$.

8 In real units, I have taken $I_0 = 240$ nA, $R = 85\Omega$, $L_e = 140$ pH, $C_e = 500$ fF and $C = 10$ pF.

Fig. J.11 shows the reduced dc current and voltage for the same parameters but with[9] $i_r = 0.9$. The current peaks are bigger and the reduction of dc voltage is also more pronounced. The corresponding $I(V)$ characteristic is shown in Fig. J.12, and compared with the perturbation theory to order 3 J.73. As expected, there is a big discrepancy and the perturbation calculation is no longer valid.

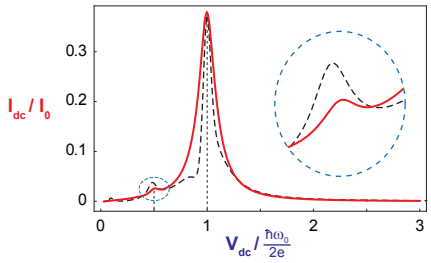

Figure J.12: $I(V)$ characteristic for the same parameters as Fig. J.11. The numerical calculation (continuous red curve) is compared with the perturbation theory to order 3 (J.73) (dashed black line). The current peak at the half voltage $\hbar\omega_0/4e$ (zoom) in now much more visible.

One can increase even more the reduced critical current. The $I(V)$ characteristic for the same parameters but with[10] $i_0 = 2.16$ is shown in Fig. J.13. The harmonics 3 and 4 are now visible. They correspond the the co-tunneling of respectively 3 and 4 Cooper pairs, while emitting 1 photon.

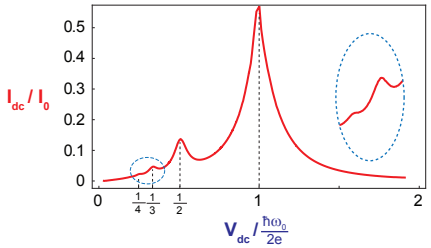

Figure J.13: $I(V)$ characteristic for a quality factor $Q = 5$, an oscillator frequency $\omega_e/2\pi = 20$ GHz, a reduced current $i_0 = 2.16$ and a capacitance ratio $c = 1000$. In addition to the peak at the half voltage $\hbar\omega_0/4e$, one can also distinguish (zoom) two other current peaks at the voltages $\hbar\omega_0/6e$ and $\hbar\omega_0/8e$.

9 With $I_0 = 415$ nA.
10 With $I_0 = 1$ µA.

K

AC JOSEPHSON EFFECT AND DYNAMICAL COULOMB BLOCKADE OF A JOSEPHSON CHANNEL: CLASSICAL CALCULATION

In Appendix J, we have performed a classical calculation of the irradiation of a JJ in an arbitrary environment. The goal of this chapter is to extend the previous results to the case of a JC of transmission τ, and more precisely to see if there is any qualitative change.

K.1 Hypothesis and notations

Let us consider a JC of transmission τ in series with an impedance $Z(\omega)$, under a constant bias voltage V (see Fig. K.1).

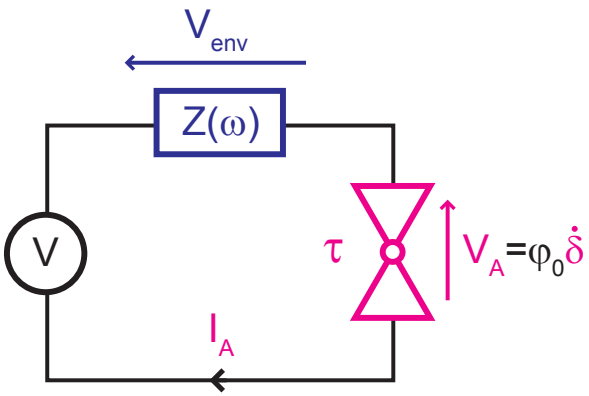

Figure K.1: Schematic of the circuit. A JJ is voltage biased through a series impedance $Z(\omega)$.

We assume that the system remain in its ground Andreev state. For a JJ, this hypothesis is legitimate because ABS are stuck to the gap, and the Andreev internal degrees of freedom are frozen. In a finite transmission system, this assumption consists in neglecting the Landau-Zener transitions between the two states, which lead to the dissipative MAR current. It is legitimate as long as the Landau-Zener transition probability 3.14 is small. This is valid when $eV \ll \Delta(1-\tau)$, *i.e.* for small voltage and small transmission.

The current-phase relation depends on the channel transmission τ:

$$I_A(\delta,\tau) = I_0(\tau)\frac{1+\sqrt{1-\tau}}{2}\frac{\sin(\delta)}{\sqrt{1-\tau\sin^2\left(\frac{\delta}{2}\right)}} \tag{K.1}$$

where

$$I_0(\tau) = \frac{e\Delta}{\hbar}\left(1-\sqrt{1-\tau}\right) \tag{K.2}$$

is the critical current. Then, equation J.4 has to be replaced by

$$\boxed{\varphi_0 \frac{d\delta}{dt}(t) + I_0(\tau)\frac{1+\sqrt{1-\tau}}{2}\left[Z * \frac{\sin(\delta)}{\sqrt{1-\tau\sin^2\left(\frac{\alpha}{2}\right)}}\right](t) = V}. \tag{K.3}$$

One wants to compute

$$I_{dc} = \langle I_A(t)\rangle \text{ and } V_{dc} = \langle V_A(t)\rangle . \tag{K.4}$$

K.2 Ohmic resistance as an environment: analytical resolution

K.2.1 *Notations*

When the impedance is a resistance $\forall\omega,\ Z(\omega) = R$, the dimensionless non-linear differential equation is:

$$f'(x) + r(\tau)\frac{1+\sqrt{1-\tau}}{2}\frac{\sin(f(x))}{\sqrt{1-\tau\sin^2\left(\frac{f(x)}{2}\right)}} = 1, \tag{K.5}$$

with

$$x = \frac{V}{\varphi_0}t,\ r(\tau) = \frac{RI_0(\tau)}{V},\ f(x) = \delta\left(\frac{\varphi_0}{V}x\right) \text{ and } i(x) = \frac{I_A(f(x),\tau)}{I_0(\tau)}. \tag{K.6}$$

One wants to compute

$$\frac{I_{dc}}{I_0} =< i(x) > \text{ and } \frac{V_{dc}}{V} =< f'(x) > . \tag{K.7}$$

K.2.2 $r \geqslant 1$

When $r(\tau) \geqslant 1$, the stationary solution $f'(x) = 0$ is possible. Therefore, there is no voltage across the Josephson junction

$$V_{dc} = 0 \tag{K.8}$$

all voltage being dropped on the resistance. It corresponds to the supercurrent branch regime. By consequence, the phase is constant and adjusts itself to satisfy

$$I_A(f(x),\tau) = \frac{R}{V}. \tag{K.9}$$

The dc current is simply equal to the constant current

$$\frac{I_{dc}}{I_0} = \frac{1}{r} \Leftrightarrow I_{dc} = \frac{V}{R}. \tag{K.10}$$

K.2.3 $r = 0$

When $r = 0$, the phase is linear in time

$$f(x) = x. \tag{K.11}$$

Then, the current is

$$i(x) = \frac{1+\sqrt{1-\tau}}{2} \frac{\sin(x)}{\sqrt{1-\tau\sin^2\left(\frac{x}{2}\right)}}. \tag{K.12}$$

This is an odd and 2π - periodic function. Therefore

$$I_{dc} = 0. \tag{K.13}$$

However, it is non-sinusoidal. One can decompose it in Fourier series:

$$i(x,\tau) = \sum_n i_n(\tau)\sin(nx). \tag{K.14}$$

The first three coefficients are

$$\begin{cases} i_1(\tau) = & \frac{8\left(\sqrt{1-\tau}+1\right)}{3\pi\tau^2}\left((2-\tau)E(\tau) - 2(1-\tau)K(\tau)\right) \\ i_2(\tau) = & -\frac{16\left(\sqrt{1-\tau}+1\right)}{15\pi\tau^3}\left((16(1-\tau)+\tau^2)E(\tau) - 8(2-\tau)(1-\tau)K(\tau)\right) \\ i_3(\tau) = & -\frac{8\left(\sqrt{1-\tau}+1\right)}{35\pi\tau^4}\left((2-\tau)(128(1-\tau)+3\tau^2)E(\tau) - 2(1-\tau)(128(1-\tau)+27\tau^2+)K(\tau)\right) \end{cases} \tag{K.15}$$

where $E(\tau) = \int_0^{\frac{\pi}{2}} \sqrt{1-\tau\sin^2(x)}dx$ and $K(\tau) = \int_0^{\frac{\pi}{2}} \frac{1}{\sqrt{1-\tau\sin^2(x)}}dx$ are elliptic integrals. The first four Fourier coefficients are shown in Fig. K.2 as a function of the transmission τ. Similarly, the numerical Fourier transform of the current is represented in Fig. K.3 for three different transmissions. Therefore, the bigger the transmission the bigger the harmonics are.

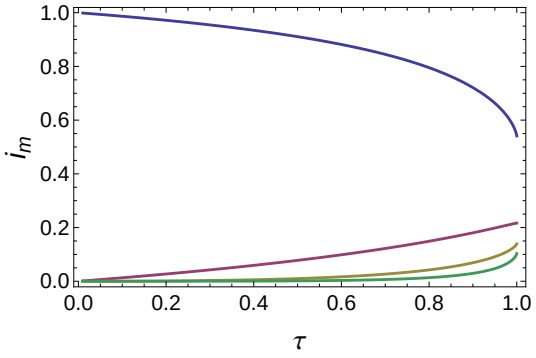

Figure K.2: Relative amplitude of the Fourier coefficients i_1 (blue), i_2 (purple), i_3 (yellow) and i_4 (green) as a function of the transmission τ.

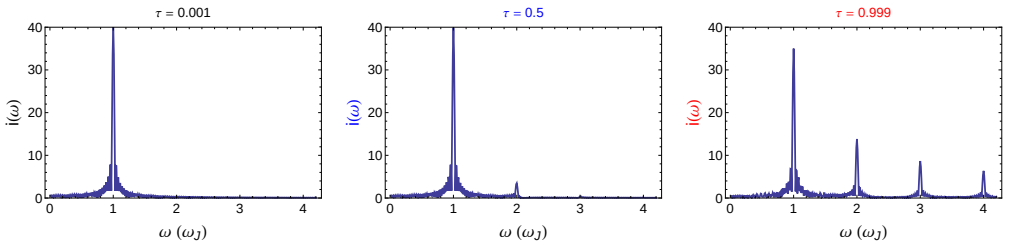

Figure K.3: Reduce Fourier transform of the current as a function of the pulsation, for three different transmissions.

K.2.4 $r < 1$

K.2.4.1 *Inverse phase as a function of the time:*

One introduces the inverse function $g = f^{-1}$. Then

$$g'(w) = \frac{1}{1 - r\frac{1+\sqrt{1-\tau}}{2}\frac{\sin(w)}{\sqrt{1-\tau\sin^2\left(\frac{w}{2}\right)}}} \tag{K.16}$$

which is now a linear differential equation. By integration, one finds[1]

$$\begin{aligned} g(w) = \; & \frac{1}{m}\left(c_1\left[\arctan\left(\frac{m+4k^2+\tau}{c_1}\tan\left(\frac{w}{2}\right)\right) - \arctan\left(\frac{4k}{c_1}\sqrt{1-\tau\sin^2\left(\frac{w}{2}\right)}\right)\right]\right. \\ & \left. +c_2\left[\arctan\left(\frac{m-4k^2-\tau}{c_2}\tan\left(\frac{w}{2}\right)\right) + \arctan\left(\frac{4k}{c_2}\sqrt{1-\tau\sin^2\left(\frac{w}{2}\right)}\right)\right]\right) \end{aligned} \tag{K.17}$$

with

$$\begin{cases} k(\tau) = & r(\tau)\frac{1+\sqrt{1-\tau}}{2} \\ m(\tau) = & \sqrt{[\tau+4k(k+1)][\tau+4k(k-1)]} \\ c_1(\tau) = & \sqrt{2}\sqrt{\tau(\tau+m)+4k^2(\tau-2)} \\ c_2(\tau) = & \sqrt{2}\sqrt{\tau(\tau-m)+4k^2(\tau-2)} \end{cases}. \tag{K.18}$$

The function g is represented in Fig. K.4.

K.2.4.2 *Josephson pulsation, dc current and dc voltage*

It is hard to invert g to derive the analytical expression of the phase as a function of the time. However, knowing g is enough to find the period X of the current $i(f(x))$. Indeed, the period X is defined as

$$\begin{aligned} & \forall x,\; f(x+X) = f(x) + 2\pi \\ & \Rightarrow\; x + X = g(f(x) + 2\pi) \end{aligned}. \tag{K.19}$$

Note that to define properly an inverse function, it has to be single-valued. Therefore, for both f and g functions, we have to consider continuous functions, by

1 When $r = 0$: $k = 0$, $c_1 = 2\tau$, $c_2 = 0$ and one recovers $g(w) = w \Leftrightarrow f(x) = x$.

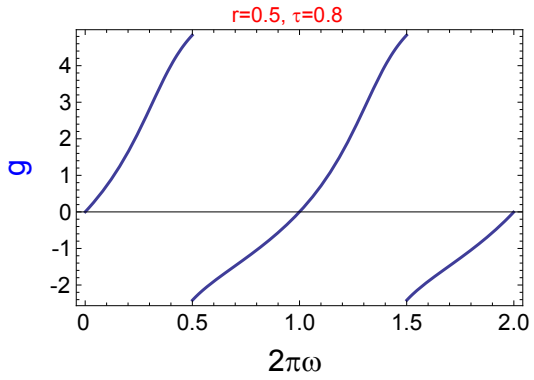

Figure K.4: Inverse phase g as a function of the reduced frequency $2\pi w$, for a reduce resistance $r = 0.01$. Because $r \ll 1$, the phase runs linearly in time and the current is essentially harmonic, oscillating at the bare Josephson pulsation $\frac{V}{\varphi_0}$.

unrolling them. Thus, because the g function defined in Eq. K.17 is not continuous at $w = \pi$, one gets $g(w + 2\pi) = g(w) + (g(\pi^-) - g(\pi^+))$. By consequence

$$X = g(\pi^-) - g(\pi^+). \tag{K.20}$$

One computes this using Eq. K.17:

$$X(\tau) = \frac{2\pi}{\sqrt{1 - r^2(\tau)}}. \tag{K.21}$$

Therefore, the Josephson pulsation is

$$\boxed{\omega_J(\tau) = \frac{V}{\varphi_0}\sqrt{1 - r^2(\tau)}}. \tag{K.22}$$

Knowing X is enough to derive the dc current and voltage, by using equations (J.19) and (J.21):

$$\boxed{\begin{cases} \frac{I_{dc}}{I_0}(\tau) = & \frac{1-\sqrt{1-r^2(\tau)}}{r(\tau)} \\ \frac{V_{dc}}{V}(\tau) = & \sqrt{1 - r^2(\tau)} \end{cases}}. \tag{K.23}$$

Strikingly, these are exactly the same results as the ones of the tunnel JJ (see Section J.3). Whereas the actual time dependence of the phase and the current directly depend explicitly on the transmission τ, all dc quantities depend on τ only through $I_0(\tau)$. Regarding the dc quantities, a JC of transmission τ, connected to a resistance R, is just like a JJ (*i.e.* with a sinusoidal current-phase relation) with a transmission-dependent critical current $I_0(\tau)$.

K.2.4.3 *Current-voltage characteristic:*

Consequently, the $I(V)$ characteristic is exactly the same:

$$\boxed{\frac{I_{dc}}{I_0(\tau)} = \sqrt{1 + \left(\frac{V_{dc}}{RI_0(\tau)}\right)^2} - \frac{V_{dc}}{RI_0(\tau)}}. \tag{K.24}$$

K.3 Arbitrary impedance $Z(\omega)$: perturbative resolution

K.3.1 *Notations*

We use the same protocol as the one used for the tunnel JJ (see *Section J.4*). The dimensionless differential equation writes

$$f'(u) + \epsilon \left[z(\tau) * \frac{\sin(f)}{\sqrt{1-\tau\sin^2\left(\frac{f}{2}\right)}} \right](u) = \sum_{n=0}^{\infty} \epsilon^n v_n \tag{K.25}$$

where the dimensionless parameters are defined as

$$\begin{gathered} u = \omega_J t\,,\ z(\tau) = \frac{Z I_0(\tau)}{V_0}, v_n = \frac{V_n}{V_0}\,, \\ f(u) = \delta\left(\frac{u}{\omega_J}\right),\ i(u) = \frac{\sin(f(u))}{\sqrt{1-\tau\sin^2\left(\frac{f(u)}{2}\right)}} \text{ and } v_A(u) = f'(u)\ . \end{gathered} \tag{K.26}$$

One looks for a perturbative solution

$$f(u) = \sum_{n=0}^{\infty} \epsilon^n f_n(u), \tag{K.27}$$

with $\forall n \geqslant 1$, f_n is 2π-periodic and $f_n(0) = 0$.

To do the perturbative development, one performs the Taylor expansion (up to order 1):

$$\frac{\sin(f)}{\sqrt{1-\tau\sin^2\left(\frac{f}{2}\right)}} = \frac{\sin(f_0)}{\sqrt{1-\tau\sin^2\left(\frac{f_0}{2}\right)}} + \epsilon f_1 \frac{4(2-\tau)\cos(f_0) + \tau(3+\cos(2f_0))}{2\sqrt{2}(2-\tau+\tau\cos(f_0))^{3/2}} + \mathcal{O}(\epsilon^2). \tag{K.28}$$

At each order, one derives the phase, current and voltage, and computes the dc current $\frac{I_{dc}}{I_0} = \langle i \rangle$. There is no need to compute the dc voltage since $V_{dc} = \langle f' \rangle = V_0$. For clarity, we define the parameters:

$$x_n = \mathrm{Re}z(n\omega_J)\ ,\quad y_n = \mathrm{Im}z(n\omega_J)\ ,\quad z_n = z(n\omega_J)\,. \tag{K.29}$$

K.3.2 *Order 0*

To order 0 in ϵ, Eq. K.25 writes

$$f_0'(u) = 1. \tag{K.30}$$

Therefore one finds

$$\begin{cases} f_0(u) = & u \\ i(u) = & \frac{\sin(f(u))}{\sqrt{1-\tau\sin^2\left(\frac{f(u)}{2}\right)}} \\ v(u) = & 1 \end{cases} \tag{K.31}$$

and the dc current is

$$\frac{I_{dc0}}{I_0} = 0. \tag{K.32}$$

The dc voltage is

$$V = V_{dc0}. \tag{K.33}$$

Therefore, the Josephson pulsation and period are

$$\omega_{J0} = \frac{V}{\varphi_0} \text{ and } X_0 = \frac{V}{\varphi\omega_{J0}} = 2\pi. \tag{K.34}$$

K.3.3 *Order 1*

To order 1 in ϵ, Eq. K.25 writes

$$f_1'(u) + \frac{1+\sqrt{1-\tau}}{2}\left(z(\tau) * \frac{\sin(f_0)}{\sqrt{1-\tau\sin^2\left(\frac{f_0}{2}\right)}}\right)(u) = v_1. \tag{K.35}$$

By integrating over 2π, and using the fact that f_1 is 2π-periodic and f_0 is is 2π-periodic and odd, one finds that

$$v_1 = 0. \tag{K.36}$$

Therefore, the dc voltage to first order is still

$$V_{dc1} = V. \tag{K.37}$$

Thus, the Josephson pulsation and period are unchanged

$$\omega_{J1} = \frac{V}{\varphi_0} \text{ and } X_1 = 2\pi. \tag{K.38}$$

However, contrary to the tunnel case, it is not easy to derive $z * \frac{\sin(u)}{\sqrt{1-\tau\sin^2\left(\frac{u}{2}\right)}}$. Indeed, there is no analytical Fourier transform or no full Fourier series expansion of $\frac{\sin(u)}{\sqrt{1-\tau\sin^2\left(\frac{u}{2}\right)}}$. Therefore, it is hard to find analytically f_1.

K.3.4 *Perturbation in* $\tau \ll 1$

One looks for a perturbative development of the solution f_1:

$$f_1(u) = \sum_{n=0}^{\infty} \tau^n f_{1n}(u). \tag{K.39}$$

Taylor expansions in τ give

$$\begin{aligned}\frac{\sin(u)}{\sqrt{1-\tau\sin^2\left(\frac{u}{2}\right)}} = \quad & \sin(u) - \tfrac{1}{8}\tau\sin(2u) + \tfrac{1}{128}\tau^2\left[-\sin(u)\right. \\ & \left.-8\sin(2u) + 3\sin(3u)\right] + \mathcal{O}(\tau^3)\end{aligned} \tag{K.40}$$

and

$$\begin{aligned}\frac{1+\sqrt{1-\tau}}{2}\left\langle\frac{\sin(f)}{\sqrt{1-\tau\sin^2\left(\frac{f}{2}\right)}}\right\rangle &= \frac{1+\sqrt{1-\tau}}{2}\left\langle\frac{\sin(u)}{\sqrt{1-\tau\sin^2\left(\frac{u}{2}\right)}}\right\rangle\\ &+\epsilon\frac{1+\sqrt{1-\tau}}{2}\left\langle f_1\frac{4(2-\tau)\cos(u)+\tau(3+\cos(2u))}{2\sqrt{2}(2-\tau+\tau\cos(u))^{3/2}}\right\rangle+\mathcal{O}(\epsilon^2)\\ &= 0+\epsilon\left\langle f_{10}\cos(u)\right\rangle+\epsilon\tau\left\langle f_{11}\cos(u)-\frac{1}{4}f_{10}\cos(2u)\right\rangle\\ &+\epsilon\tau^2\frac{1}{128}\left\langle-16(f_{10}+2f_{11})\cos(2u)+(128f_{12}-f_{10})\cos(u)\right.\\ &+\left.+9f_{10}\cos(3u)\right\rangle+\mathcal{O}\left(\tau^2\right)+\mathcal{O}(\epsilon^2).\end{aligned} \tag{K.41}$$

K.3.4.1 *Order 0 in* τ

To order 1 in ϵ, order 0 in τ, Eq. K.25 writes

$$f'_{10}(u)+[z*\sin(u)](u)=0. \tag{K.42}$$

Therefore

$$f_{10}(u)=x_1(\cos(u)-1)-y_1\sin(u) \tag{K.43}$$

and the dc current is

$$\frac{I_{dc10}}{I_0}=\frac{\epsilon x_1}{2}. \tag{K.44}$$

K.3.4.2 *Order 1 in* τ

To order 1 in ϵ, order 1 in τ, Eq. K.25 writes

$$f'_{11}(u)-\frac{1}{8}\tau[z*\sin(2u)](u)=0. \tag{K.45}$$

Therefore

$$f_{11}(u)=-\frac{1}{16}\left[x_2(\cos(2u)-1)-y_2\sin(2u)\right]. \tag{K.46}$$

Because $\left\langle f_{11}\cos(u)-\frac{1}{4}f_{10}\cos(2u)\right\rangle=0$, the dc current remains unchanged.

K.3.4.3 *Order 2 in* τ

To order 1 in ϵ, order 2 in τ, Eq. K.25 writes

$$f'_{12}(u)+\frac{1}{128}\tau^2[z*(-\sin(u)-8\sin(2u)+3\sin(3u))](u)=0. \tag{K.47}$$

Therefore

$$\begin{aligned}f_{12}(u)=\ &\tfrac{1}{128}\left[y_1\sin(u)-x_1(\cos(u)-1)+4y_2\sin(2u)\right.\\ &\left.-4x_2(\cos(2u)-1)-y_3\sin(3u)+x_3(\cos(3u)-1)\right].\end{aligned}$$

and the dc current is[2]

$$\boxed{\frac{I_{dc12}}{I_0}=\frac{\epsilon x_1}{2}+\epsilon\tau^2\frac{x_2-x_1}{128}}.$$

2 Because

$$\begin{aligned}&\tfrac{1}{128}\left(-16(f_{10}+2f_{11})\cos(2u)+(128f_{12}-f_{10})\cos(u)+9f_{10}\cos(3u)\right)\\ &=\tfrac{1}{64}\left(x_2\cos^2(2u)-x_1\cos^2(u)\right).\end{aligned}$$

One recovers the result of the resistive case, where $x_2 = x_1$ and $\frac{I_{dc12}}{I_0} = \frac{\epsilon x_1}{2}$: the dc current in a JC of transmission τ is the same as the one of a JJ with a transmission dependent critical current $I_0(\tau)$.

However, for an arbitrary impedance it is not true: there is an explicit dependence on τ. Moreover, already to order 1 in ϵ, harmonics of the impedance (x_2) contribute to dc current, in contrast with the case of a tunnel JJ. The corresponding $I(V)$ characteristic is shown in Fig. K.5 for a single-mode environment. Even if it is not valid, the calculation is done with $\tau = 1$ to emphasize the effect of the transmission.

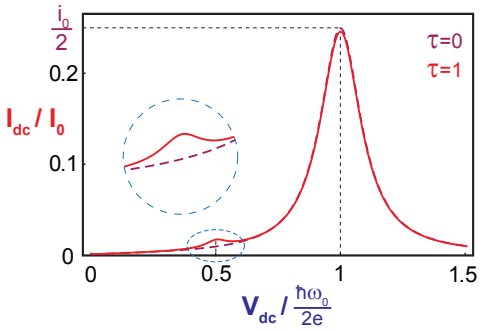

Figure K.5: $I(V)$ characteristic of a single-mode environment of resonance pulsation ω_0 and quality factor $Q = 5$. This calculation corresponds to the prediction to first order in ϵ, second order in τ. This is computed for $\tau = 0$ (purple dashed line) and $\tau = 1$ (red continuous line). Whereas we are treating the environment to first order, the current peak at the half voltage $\hbar\omega_0/4e$ is present.

K.4 Conclusion

Forgetting about dc MAR current, a JC of transmission τ and a JJ behave quite similarly. In the case of a purely resistive environment, their $I(V)$ characteristic should be exactly the same (in units reduced by their respective critical current). In the case of an arbitrary impedance, it is no longer true.

In absence of an environment (short circuit), a JJ oscillates at only one frequency, the Josephson frequency ω_J. In presence of a finite impedance, the current is anharmonic and oscillates at ω_J and its multiple $n\omega_J$. The "larger" the environment, the more and larger these harmonics are, *i.e.* the more probable the Cooper pair co-tunneling events are.

The main qualitative difference is that already in absence of an environment, the current through a JC is anharmonic. The higher the transmission τ, the larger the harmonics. Therefore, even at very "small" environment impedance, higher harmonics can appear. It means that harmonic peaks corresponding to multi-Cooper tunneling are bigger in the $I(V)$ characteristic of a JC of finite transmission than in the one of a tunnel JJ (for the same environment and critical current). However, for the experimentalist[3], it is only a quantitative change since it does not predict new types of peaks as it does for Shapiro steps.

3 Note that such an experiment has already been performed (see Ref. [44]).

L

REFLECTOMETRY MEASUREMENTS OF AN ATOMIC-SQUID IN A SUPERCONDUCTING CAVITY

In this chapter, we present an additional experiment accessing the Andreev transition by measuring the resonance frequency of a superconducting microwave resonator coupled to a superconducting atomic contact.

L.1 Experimental setup

The results presented in this chapter were obtained on sample RAC2. A simplified equivalent circuit of the setup is shown in Fig. L.1.

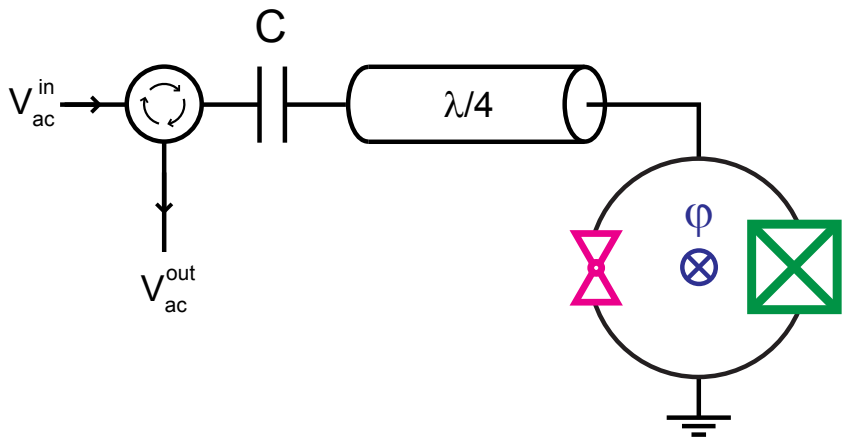

Figure L.1: Simplified equivalent circuit of sample RAC2. A λ/4 resonator is terminated by an atomic-SQUID. The cavity resonance frequency is determined by measuring the amplitude $|V_{ac}^{in}/V_{ac}^{out}|$ or phase $\arg(V_{ac}^{in}/V_{ac}^{out})$ of the reflected microwave. This frequency depends on the configuration of the atomic contact and on the flux φ threading the SQUID loop.

- On the right-hand side, an aluminum AC is placed in parallel with a tunnel JJ (critical current $I_0 \sim 610\,nA$) to form an atomic-SQUID. An external superconducting coil is used to apply a dc flux φ through the SQUID loop.
- It terminates an on-chip coplanar wave guide acting as a λ/4 resonator.
- Additionally the atomic SQUID is connected to a dc bias source (not represented, see Fig. 10.6) in order to measure its IV characteristics. To avoid loading the resonator, the connection is done through a cascade of two λ/4 transformers designed to step the 50 Ω impedance of the dc source up to$\sim$ 13 kΩ at the cavity resonance frequency.

We have used a nominally 50 Ω line to inject microwaves (V_{ac}^{in}) into the circuit and measured the reflected signal (V_{ac}^{out}) (see wiring in Fig. 10.6). The input and

output signals are separated with a circulator at 20 mK. Measuring the amplitude $\left|V_{ac}^{in}/V_{ac}^{out}\right|$ or phase $\arg\left(V_{ac}^{in}/V_{ac}^{out}\right)$ of the reflected coefficient gives direct access to the cavity resonance frequency.

The bare resonance frequency of the $\lambda/4$ resonator is about 8.93 GHz. It was measured before breaking the contact, when the suspended bridge behaves as a short-circuit. In presence of the atomic-SQUID, the frequency is shifted to lower value ($\sim$ 8.47 GHz for the JJ alone, when the contact is open). From a naive electrokinetic point of view, the atomic-SQUID behaves as a lumped inductor that can be tuned by the flux φ threading the SQUID loop[1]. The resonance frequency then depends on the configuration of the atomic contact, and on the flux φ. For a one-atom contact, the SQUID is very asymmetric and one expects a small frequency modulation.

L.2 Experimental results

The top panel of Fig. L.2 shows the phase of the reflected signal as a function of the microwave frequency ν for two different fluxes. It was taken for a one-atom contact whose transmissions $\{0.97, 0.43, 0.11\}$ were independently measured from the IVs of the SQUID. The bottom panel of Fig. L.2 displays the phase of the reflected signal as a function of both the reduced flux φ and the microwave frequency ν. The cavity frequency appears as a dark green line and modulates with flux by 300 MHz range.

Fig. L.3 shows similar curves, taken for a different contact $\{0.983, 0.438\}$ with a more transmitting channel. This results in a larger modulation of the cavity frequency. Note that the resonance disappears in a narrow flux region around π (see red curve in the top panel of Fig. L.3).

For an even bigger transmission (contact $\{0.997, 0.19\}$), the resonance disappears on two very small flux intervals, but reappears in the central region (see Fig. L.4).

1 This is valid as long as one considers frequency much smaller than the Andreev and plasma frequency.

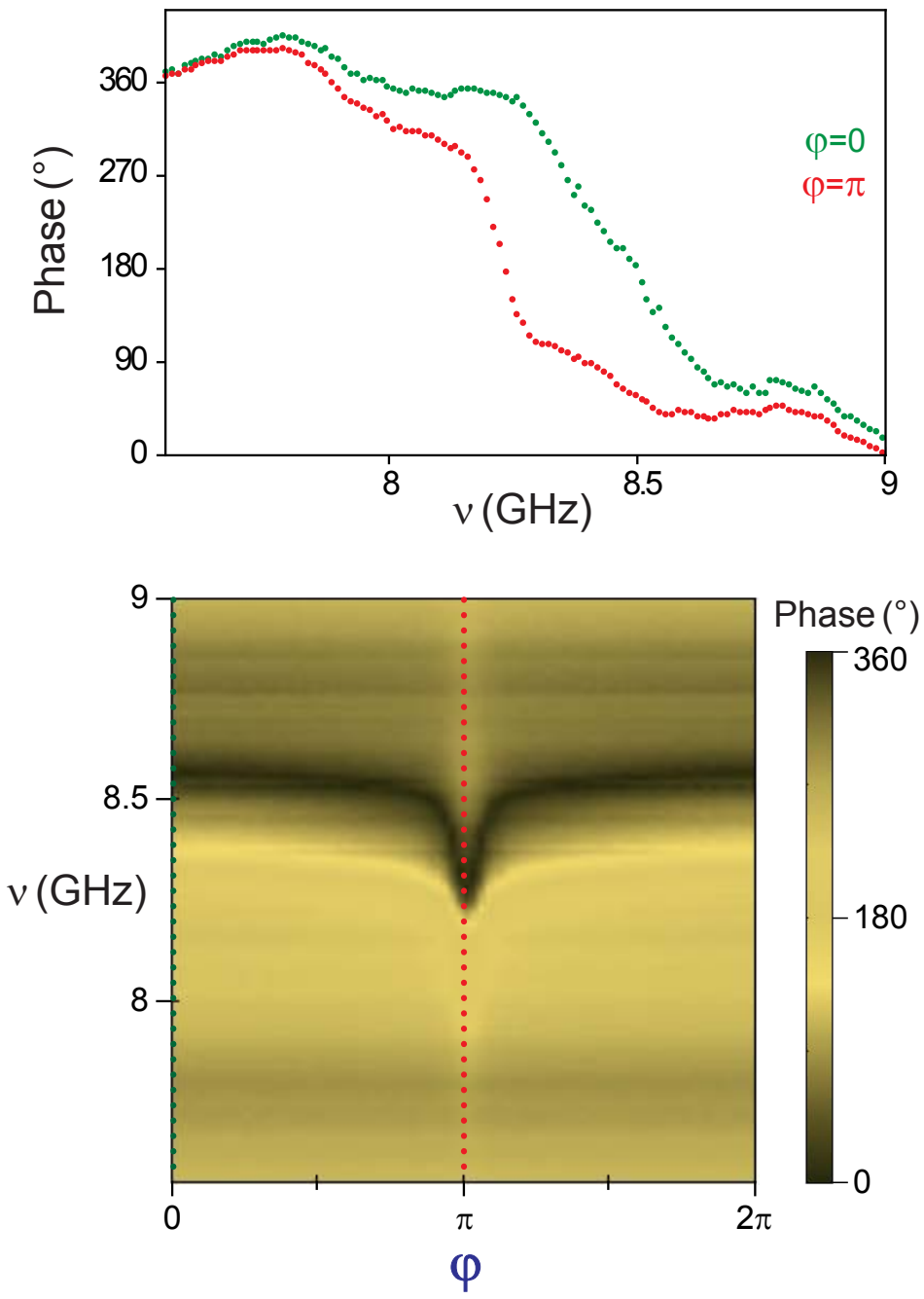

Figure L.2: **Top**: Phase of the reflected signal as a function of the microwave frequency ν, for contact $\{0.97, 0.43, 0.11\}$, for fluxes $\varphi = 0$ (green dots) and $\varphi = \pi$ (red dots). **Bottom**: Phase of the reflected signal as a function of both the reduced flux φ and the frequency ν.

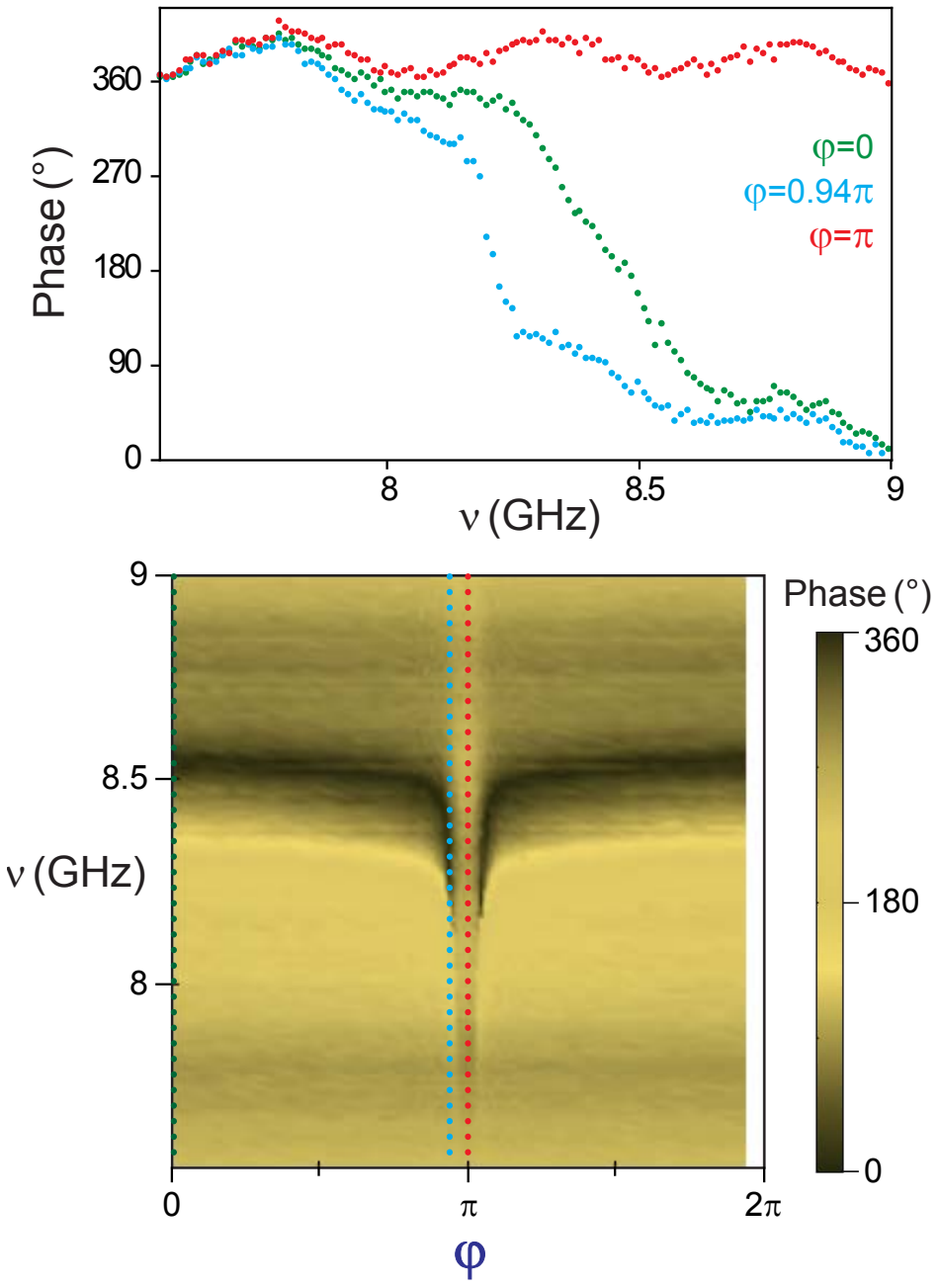

Figure L.3: **Top**: Phase of the reflected signal as a function of the microwave frequency ν, for contact $\{0.983, 0.438\}$, for fluxes $\varphi = 0$ (green dots), $\varphi = 0.94\pi$ (blue dots) and $\varphi = \pi$ (red dots). **Bottom**: Phase of the reflected signal as a function of both the reduced flux φ and the frequency ν.

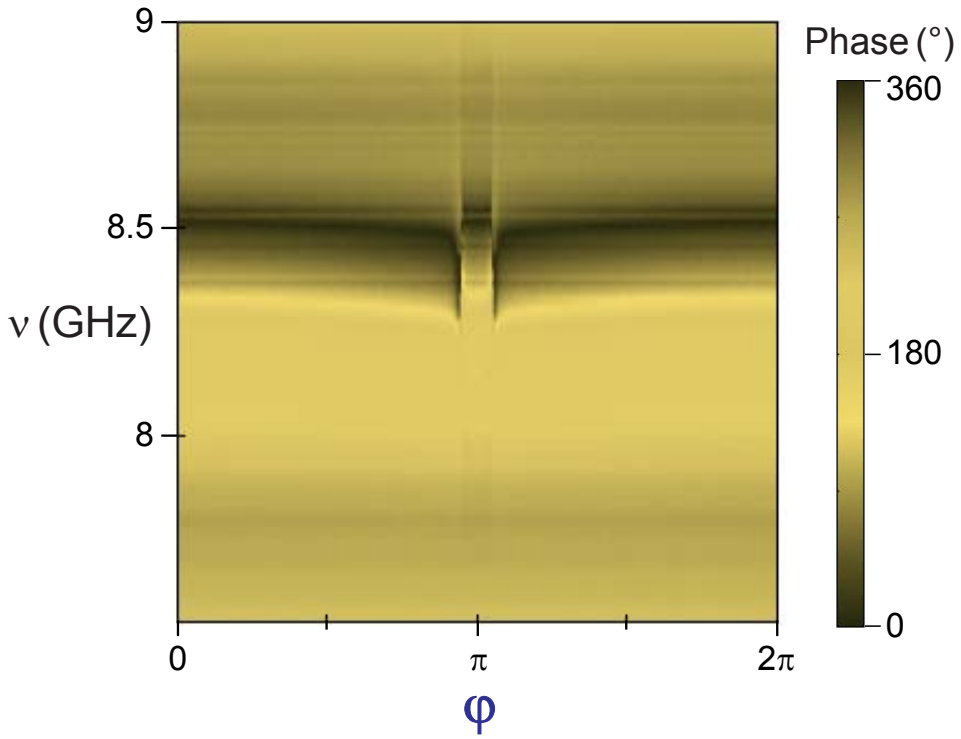

Figure L.4: **Bottom**: Phase of the reflected signal as a function of both the reduced flux φ and the frequency ν, for contact $\{0.997, 0.19\}$.

L.3 Interpretation

L.3.1 *Level repulsion and avoided crossing*

A blow-up of the reflectometry signal around $\varphi = \pi$ is shown in Fig. L.5 for the three contacts.

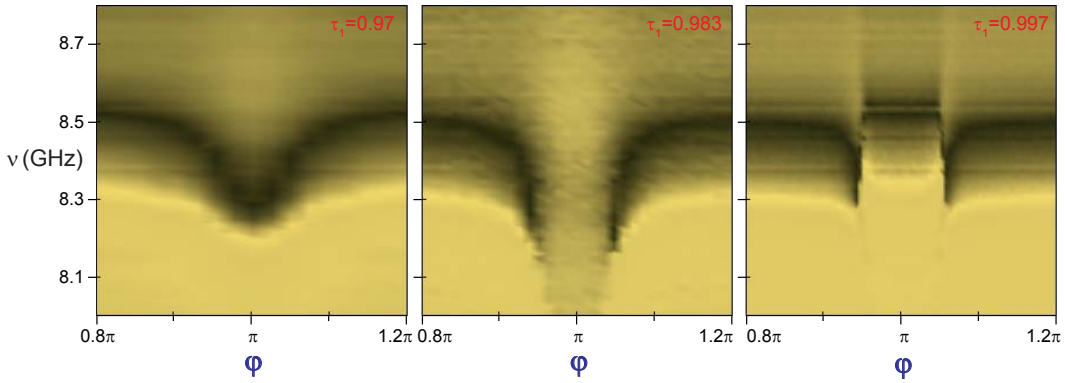

Figure L.5: Blow-up of the spectra of the three atomic contacts: $\{0.97, 0.43, 0.11\}$ (**left**), $\{0.983, 0.438\}$ (**middle**) and $\{0.997, 0.19\}$ (**right**). The color scale is the same as for Fig. L.4.

We interpret the observed features as the manifestation of the coupling between the cavity and the Andreev mode [127]. Close to degeneracy, the cavity and Andreev mode hybridize. This leads to a **level repulsion** (left and central panels of Fig. L.5) or an **avoided crossing** (right panel of Fig. L.5) depending on the relative position of the undressed states[2]. In Fig. L.3, the level repulsion is so large that the cavity resonance frequency gets out of the accessible measurement window. This suggests that the coupling between the two modes is very strong.

In the right panels of Fig. L.6, we superimpose the expected Andreev transition frequency $\nu = 2E_A(\varphi, 0.997)/h$ of the most transmitting channel for contact $\{0.997, 0.19\}$. Because of the small frequency range accessed in the experiment, the position of the Andreev transition frequency, which varies from 4.65 GHz at $\varphi = \pi$ to 85 GHz at $\varphi = 0$ (see Fig. L.8),y appears as almost vertical lines in the figure. Their intersection with the bare resonator frequency coincides precisely with the observed anticrossings.

2 This is similar to what we observed in the absorption spectroscopy experiment of Chapter 6: level repulsion for contact U and avoided crossing for contact V (see Fig. 6.6).

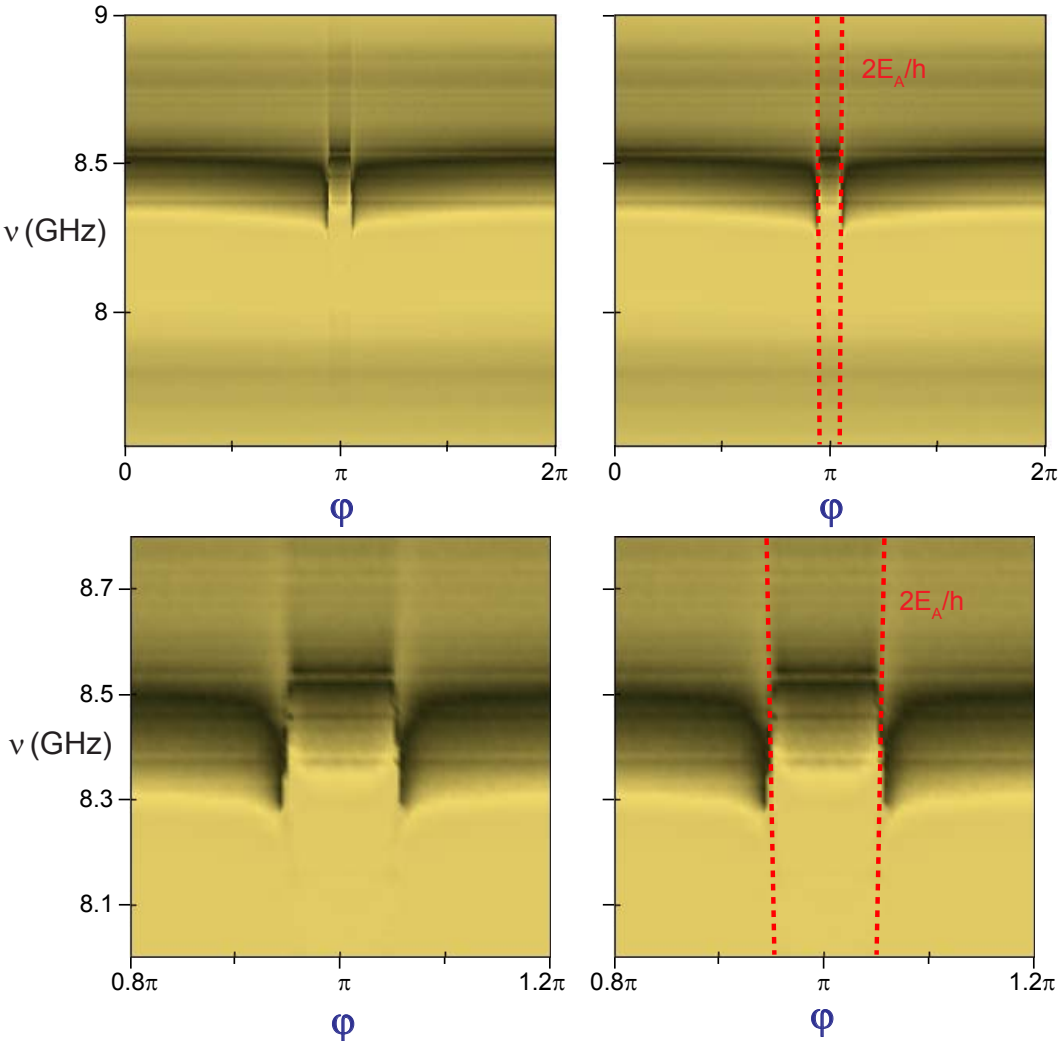

Figure L.6: Spectrum for contact $\{0.997, 0.19\}$ at two different magnifications. The red dashed lines are the theoretical positions of the bare Andreev transition $\nu = 2E_A(\varphi, 0.997)/h$ of the most transmitting channel. The color scale is the same as for Fig. L.4.

L.3.2 *Additional experiment on sample RAC3*

This experiment was also performed on a similar but different sample, named RAC3. The essential difference was that the cavity was designed to resonate at a higher frequency, about ~ 12 GHz. In this experiment, we could measure similar features. In particular, Fig. L.7 shows the spectrum for a contact with transmissions $\{0.996, 0.65, 0.32\}$, as well as the expected Andreev transition frequency $\nu = 2E_A(\varphi, 0.996)/h$ of the most transmitting channel. There, one also observes a clear anticrossing.

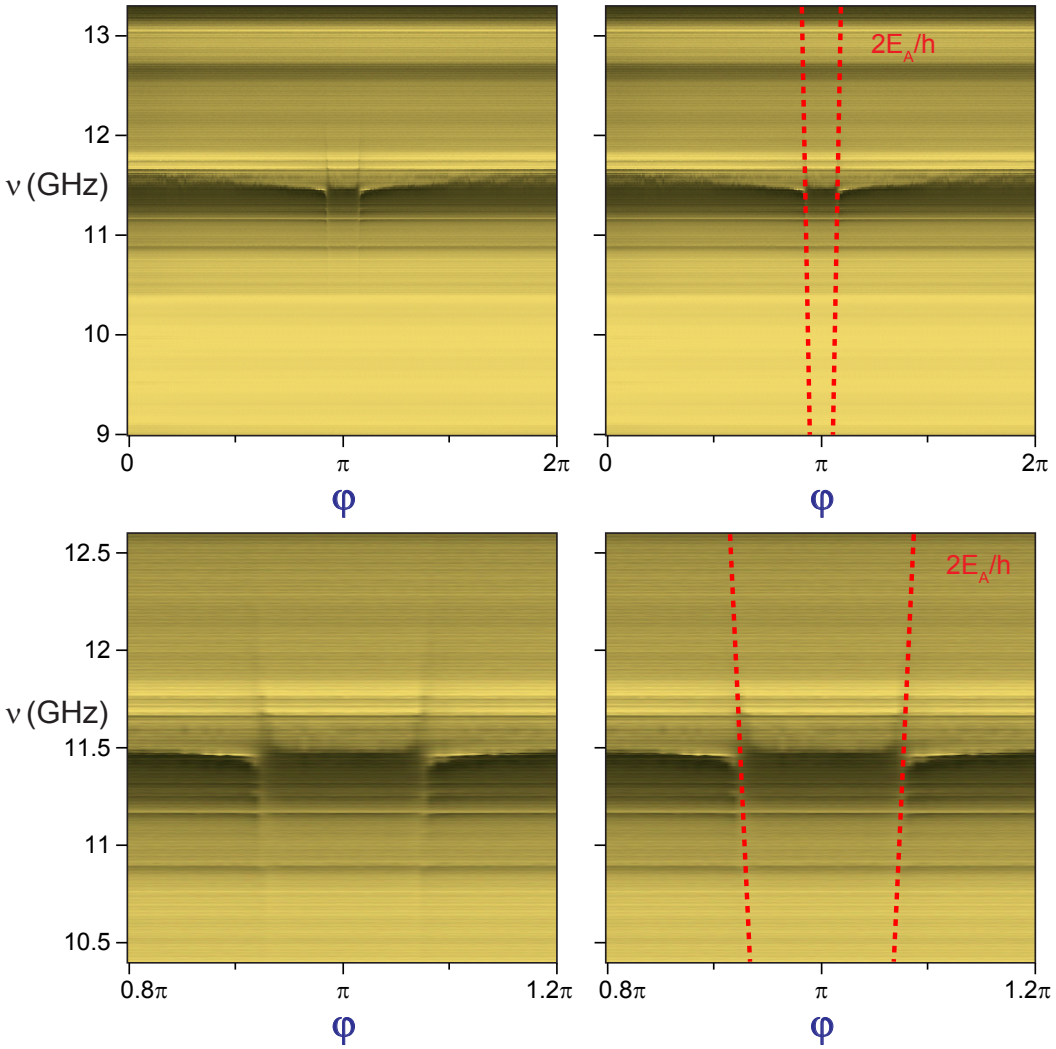

Figure L.7: Spectrum for contact $\{0.996, 0.65, 0.32\}$ at two different magnifications. This measurement was taken on a different sample, named RAC3. The red dashed lines are the theoretical positions of the bare Andreev transition $\nu = 2E_A(\varphi, 0.996)/h$ of the most transmitting channel.The color scale is the same as for Fig. L.4.

Although we have not done it yet, the theories developed in Chapter 7 and Ref. [127] could in principle quantitatively account for these experimental results.

L.3.3 *Towards coherent manipulation of the ABS ?*

Although this reflectometry experiment probes the Andreev transition, from the ground state $|-\rangle$ to the excited even state $|+\rangle$, it does so only in a small range around the cavity frequency. Therefore, contrary to the absorption spectroscopy with a JJ presented in Chapter 6, this technique is not really appropriate to detect the full Andreev spectrum (see Fig. L.8) .

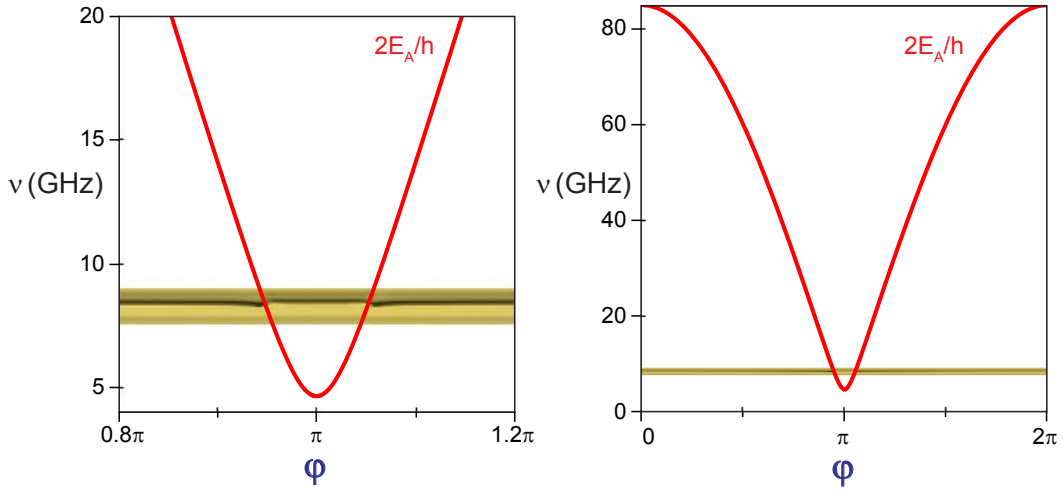

Figure L.8: Full theoretical (solid red line) Andreev spectrum $2E_A(\varphi, 0.\tau)/h$, for $\tau = 0.997$. The experimental spectrum for contact $\{0.997, 0.19\}$ is superimposed at the same scale.

However, this narrow band detection should be less invasive in term of injected noise, and one could expect larger lifetimes for state $|+\rangle$. This technique could allow the coherent manipulation of the ABS using the protocols developed for superconducting qubits.

BIBLIOGRAPHY

[1] B. Josephson. Possible new effects in superconductive tunnelling. *Phys. Lett.* **1**, 251–253 (1962). *(Cited on page 1.)*

[2] J. Nicol, S. Shapiro and P. H. Smith. Direct measurement of the superconducting energy gap. *Phys. Rev. Lett.* **5**, 461–464 (1960). *(Cited on page 1.)*

[3] I. Giaever. Electron tunneling between two superconductors. *Phys. Rev. Lett.* **5**, 464–466 (1960). *(Cited on page 1.)*

[4] P. W. Anderson and J. M. Rowell. Probable observation of the Josephson superconducting tunneling effect. *Phys. Rev. Lett.* **10**, 230–232 (1963). *(Cited on page 1.)*

[5] S. Shapiro. Josephson currents in superconducting tunneling: the effect of microwaves and other observations. *Phys. Rev. Lett.* **11**, 80–82 (1963). *(Cited on pages 1 and 42.)*

[6] G. Wendin and V. S. Shumeiko. Quantum bits with Josephson junctions (review article). *Low Temp. Phys.* **33**, 724–744 (2007). *(Cited on page 1.)*

[7] M. Hofheinz, H. Wang, M. Ansmann, R. C. Bialczak, E. Lucero, M. Neeley, A. D. O'Connell, D. Sank, J. Wenner, J. M. Martinis and A. N. Cleland. Synthesizing arbitrary quantum states in a superconducting resonator. *Nature* **459**, 546–549 (2009). *(Cited on page 1.)*

[8] A. A. Golubov, M. Y. Kupriyanov and E. Il'ichev. The current-phase relation in Josephson junctions. *Rev. Mod. Phys.* **76**, 411–469 (2004). *(Cited on page 1.)*

[9] P. G. de Gennes and D. Saint-James. Elementary excitations in the vicinity of a normal metal-superconducting metal contact. *Phys. Lett.* **4**, 151–152 (1963). *(Cited on pages 1 and 25.)*

[10] D. Saint-James. Excitations ï¿œlïï¿œmentaires au voisinage de la surface de sï¿œparation d'un mï¿œtal normal et d'un mï¿œtal supraconducteur. *J. Phys. France* **25**, 7 (1964). *(Cited on pages 1, 25, 27, and 190.)*

[11] A. F. Andreev. Thermal conductivity of the intermediate state of superconductors. *Sov. Phys. JETP* **19**, 1228 (1964). *(Cited on pages 1, 25, 27, and 190.)*

[12] I. Kulik. Macroscopic quantization and proximity effect in S-N-S junctions. *Sov. Phys. JETP* **30**, 944 (1970). *(Cited on pages 1 and 27.)*

[13] A. Furusaki and M. Tsukada. Dc Josephson effect and Andreev reflection. *Solid State Commun.* **78**, 299–302 (1991). *(Cited on pages 1, 2, and 27.)*

[14] C. W. J. Beenakker and H. van Houten. Josephson current through a superconducting quantum point contact shorter than the coherence length. *Phys. Rev. Lett.* **66**, 3056–3059 (1991). *(Cited on pages 1, 2, 3, 27, and 30.)*

[15] P. F. Bagwell. Suppression of the Josephson current through a narrow, mesoscopic, semiconductor channel by a single impurity. *Phys. Rev. B* **46**, 12573–12586 (1992). *(Cited on pages 1, 2, 27, and 37.)*

[16] E. Scheer, P. Joyez, D. Esteve, C. Urbina and M. H. Devoret. Conduction channel transmissions of atomic-size aluminum contacts. *Phys. Rev. Lett.* **78**, 3535 (1997). *(Cited on pages 1, 4, and 48.)*

[17] E. Scheer, N. Agraït, J. C. Cuevas, A. Levy Yeyati, B. Ludoph, A. Martín-Rodero, G. R. Bollinger, J. M. van Ruitenbeek and C. Urbina. The signature of chemical valence in the electrical conduction through a single-atom contact. *Nature* **394**, 154–157 (1998). *(Cited on pages 1 and 183.)*

[18] J. M. van Ruitenbeek, A. Alvarez, I. Piñeyro, C. Grahmann, P. Joyez, M. H. Devoret, D. Esteve and C. Urbina. Adjustable nanofabricated atomic size contacts. *Rev. Sci. Instrum.* **67**, 108 (1996). *(Cited on pages 1 and 55.)*

[19] S. Datta and P. F. Bagwell. Can the Bogoliubov-de Gennes equation be interpreted as a "one-particle" wave equation? *Superlatt. Microstruct.* **25**, 1233–1250 (1999). *(Cited on pages 2, 15, 17, 19, and 184.)*

[20] N. M. Chtchelkatchev and Y. V. Nazarov. Andreev quantum dots for spin manipulation. *Phys. Rev. Lett.* **90**, 226806 (2003). *(Cited on pages 3, 4, 11, 83, and 195.)*

[21] M. L. Della Rocca, M. Chauvin, B. Huard, H. Pothier, D. Esteve and C. Urbina. Measurement of the current-phase relation of superconducting atomic contacts. *Phys. Rev. Lett.* **99**, 127005 (2007). *(Cited on pages 3, 5, 38, 57, 59, and 80.)*

[22] M. Chauvin, P. vom Stein, H. Pothier, P. Joyez, M. E. Huber, D. Esteve and C. Urbina. Superconducting atomic contacts under microwave irradiation. *Phys. Rev. Lett.* **97**, 067006 (2006). *(Cited on pages 3, 4, 42, and 50.)*

[23] R. Cron, M. F. Goffman, D. Esteve and C. Urbina. Multiple-charge-quanta shot noise in superconducting atomic contacts. *Phys. Rev. Lett.* **86**, 4104–4107 (2001). *(Cited on pages 4 and 50.)*

[24] A. F. Morpurgo, T. M. Klapwijk and B. J. van Wees. Hot electron tunable supercurrent. *App. Phys. Lett.* **72**, 966–968 (1998). *(Cited on pages 4, 39, and 43.)*

[25] J. J. A. Baselmans, A. F. Morpurgo, B. J. van Wees and T. M. Klapwijk. Reversing the direction of the supercurrent in a controllable Josephson junction. *Nature* **397**, 43–45 (1999). *(Cited on pages 4, 39, and 43.)*

[26] M. Fuechsle, J. Bentner, D. A. Ryndyk, M. Reinwald, W. Wegscheider and C. Strunk. Effect of microwaves on the current-phase relation of SNS Josephson junctions. *Phys. Rev. Lett.* **102**, 127001 (2009). *(Cited on pages 4 and 39.)*

[27] F. Chiodi, M. Ferrier, K. Tikhonov, P. Virtanen, T. T. Heikkilä, M. Feigelman, S. Guéron and H. Bouchiat. Probing the dynamics of Andreev states in a coherent normal-superconducting ring. *Sci. Rep.* **1** (2011). *(Cited on pages 4 and 41.)*

[28] J.-D. Pillet, C. H. L. Quay, P. Morfin, C. Bena, A. Levy Yeyati and P. Joyez. Andreev bound states in supercurrent-carrying carbon nanotubes revealed. *Nat. Phys.* **6**, 965–969 (2010). *(Cited on pages 4, 51, and 52.)*

[29] S. B. Kaplan, C. C. Chi, D. N. Langenberg, J. J. Chang, S. Jafarey and D. J. Scalapino. Quasiparticle and phonon lifetimes in superconductors. *Phys. Rev. B* **14**, 4854–4873 (1976). *(Cited on pages 4 and 89.)*

[30] C. M. Wilson, L. Frunzio and D. E. Prober. Time-resolved measurements of thermodynamic fluctuations of the particle number in a nondegenerate Fermi gas. *Phys. Rev. Lett.* **87**, 067004 (2001). *(Cited on page 4.)*

[31] J. M. Martinis, M. Ansmann and J. Aumentado. Energy decay in superconducting Josephson-junction qubits from nonequilibrium quasiparticle excitations. *Phys. Rev. Lett.* **103**, 097002 (2009). *(Cited on pages 4 and 86.)*

[32] P. J. de Visser, J. J. A. Baselmans, P. Diener, S. J. C. Yates, A. Endo and T. M. Klapwijk. Number fluctuations of sparse quasiparticles in a superconductor. *Phys. Rev. Lett.* **106**, 167004 (2011). *(Cited on pages 4 and 86.)*

[33] M. D. Shaw, R. M. Lutchyn, P. Delsing and P. M. Echternach. Kinetics of nonequilibrium quasiparticle tunneling in superconducting charge qubits. *Phys. Rev. B* **78**, 024503 (2008). *(Cited on pages 4 and 86.)*

[34] M. Lenander, H. Wang, R. C. Bialczak, E. Lucero, M. Mariantoni, M. Neeley, A. D. O'Connell, D. Sank, M. Weides, J. Wenner, T. Yamamoto, Y. Yin, J. Zhao, A. N. Cleland and J. M. Martinis. Measurement of energy decay in superconducting qubits from nonequilibrium quasiparticles. *Phys. Rev. B* **84**, 024501 (2011). *(Cited on pages 4 and 86.)*

[35] P. Joyez, P. Lafarge, A. Filipe, D. Esteve and M. H. Devoret. Observation of parity-induced suppression of Josephson tunneling in the superconducting single-electron transistor. *Phys. Rev. Lett.* **72**, 2458–2461 (1994). *(Cited on pages 4 and 69.)*

[36] A. J. Ferguson, N. A. Court, F. E. Hudson and R. G. Clark. Microsecond resolution of quasiparticle tunneling in the single-Cooper-pair transistor. *Phys. Rev. Lett.* **97**, 106603 (2006). *(Cited on pages 4 and 69.)*

[37] J. Aumentado, M. W. Keller, J. M. Martinis and M. H. Devoret. Nonequilibrium quasiparticles and 2e periodicity in single-Cooper-pair transistors. *Phys. Rev. Lett.* **92**, 066802 (2004). *(Cited on pages 4 and 69.)*

[38] M. Zgirski, L. Bretheau, Q. Le Masne, H. Pothier, D. Esteve and C. Urbina. Evidence for long-lived quasiparticles trapped in superconducting point contacts. *Phys. Rev. Lett.* **106**, 257003 (2011). *(Cited on pages 4, 5, 86, and 217.)*

[39] M. H. Devoret, D. Esteve, H. Grabert, G. Ingold, H. Pothier and C. Urbina. Effect of the electromagnetic environment on the Coulomb blockade in ultrasmall tunnel junctions. *Phys. Rev. Lett.* **64**, 1824–1827 (1990). *(Cited on pages 7, 9, 119, 121, and 122.)*

[40] G. L. Ingold and Y. Nazarov. Single charge tunneling. chap. 2, 21–91 (Plenum, New York, 1992). *(Cited on pages 7, 9, 119, 121, 122, 138, and 249.)*

[41] T. Holst, D. Esteve, C. Urbina and M. H. Devoret. Effect of a transmission line resonator on a small capacitance tunnel junction. *Phys. Rev. Lett.* **73**, 3455–3458 (1994). *(Cited on pages 7 and 119.)*

[42] J. Basset, H. Bouchiat and R. Deblock. Emission and absorption quantum noise measurement with an on-chip resonant circuit. *Phys. Rev. Lett.* **105**, 166801 (2010). *(Cited on pages 7 and 119.)*

[43] M. Hofheinz, F. Portier, Q. Baudouin, P. Joyez, D. Vion, P. Bertet, P. Roche and D. Esteve. Bright side of the Coulomb blockade. *Phys. Rev. Lett.* **106**, 217005 (2011). *(Cited on pages 7 and 119.)*

[44] A. H. Dayem and C. C. Grimes. Microwave emission from superconducting point-contacts. *App. Phys. Lett.* **9**, 47–49 (1966). *(Cited on pages 7, 96, 116, and 277.)*

[45] J. Edstam and H. K. Olsson. Josephson broadband spectroscopy to 1 THz. *App. Phys. Lett.* **64**, 2733–2735 (1994). *(Cited on pages 7, 96, and 116.)*

[46] R. Lindell, J. Penttilä, M. Sillanpää and P. Hakonen. Quantum states of a mesoscopic SQUID measured using a small Josephson junction. *Phys. Rev. B* **68**, 052506 (2003). *(Cited on pages 7 and 119.)*

[47] J. Leppäkangas, E. Thuneberg, R. Lindell and P. Hakonen. Tunneling of Cooper pairs across voltage-biased asymmetric single-Cooper-pair transistors. *Phys. Rev. B* **74**, 054504 (2006). *(Cited on pages 7 and 119.)*

[48] P.-M. Billangeon, F. Pierre, H. Bouchiat and R. Deblock. Very high frequency spectroscopy and tuning of a single-Cooper-pair transistor with an on-chip generator. *Phys. Rev. Lett.* **98**, 126802 (2007). *(Cited on pages 7, 96, and 119.)*

[49] P.-M. Billangeon, F. Pierre, H. Bouchiat and R. Deblock. ac Josephson effect and resonant Cooper pair tunneling emission of a single-Cooper-pair transistor. *Phys. Rev. Lett.* **98**, 216802 (2007). *(Cited on pages 7 and 119.)*

[50] A. Zazunov, V. S. Shumeiko, E. N. Bratus', J. Lantz and G. Wendin. Andreev level qubit. *Phys. Rev. Lett.* **90**, 087003 (2003). *(Cited on pages 9, 81, 198, 201, and 203.)*

[51] A. J. Leggett, S. Chakravarty, A. T. Dorsey, M. P. A. Fisher, A. Garg and W. Zwerger. Dynamics of the dissipative two-state system. *Rev. Mod. Phys.* **59**, 1–85 (1987). *(Cited on pages 11, 34, 123, and 215.)*

[52] U. Weiss. *Quantum dissipative systems* (World Scientific, 1999). *(Cited on pages 11, 34, 123, and 215.)*

[53] C. Padurariu and Y. V. Nazarov. Spin blockade qubit in a superconducting junction. *Europhys. Lett.* **100**, 57006 (2012). *(Cited on pages 11 and 89.)*

[54] L. Fu and C. L. Kane. Superconducting proximity effect and Majorana fermions at the surface of a topological insulator. *Phys. Rev. Lett.* **100**, 096407 (2008). *(Cited on page 11.)*

[55] D. Rainis and D. Loss. Majorana qubit decoherence by quasiparticle poisoning. *Phys. Rev. B* **85**, 174533 (2012). *(Cited on page 12.)*

[56] P. G. de Gennes. *Superconductivity of metals and alloys* (Addison-Wesley, New York, 1989). *(Cited on pages 15, 20, and 184.)*

[57] M. Tinkham. *Introduction to superconductivity* (Courier Dover Publications, 2004). *(Cited on pages 15 and 184.)*

[58] D. Chevallier, D. Sticlet, P. Simon and C. Bena. Mutation of Andreev into Majorana bound states in long superconductor-normal and superconductor-normal-superconductor junctions. *Phys. Rev. B* **85**, 235307 (2012). *(Cited on page 21.)*

[59] V. Mourik, K. Zuo, S. M. Frolov, S. R. Plissard, E. P. a. M. Bakkers and L. P. Kouwenhoven. Signatures of Majorana fermions in hybrid superconductor-semiconductor nanowire devices. *Science* **336**, 1003–1007 (2012). *(Cited on page 21.)*

[60] L. P. Rokhinson, X. Liu and J. K. Furdyna. The fractional a.c. Josephson effect in a semiconductor-superconductor nanowire as a signature of Majorana particles. *Nat. Phys.* **8**, 795–799 (2012). *(Cited on page 21.)*

[61] C. Kittel. *Quantum theory of solids* (John Wiley & Sons Inc, 1987), 2nd revised edition edn. *(Cited on page 23.)*

[62] A. F. Andreev. Electron spectrum of the intermediate state of superconductors. *Sov. Phys. JETP* **22**, 455 (1966). *(Cited on page 27.)*

[63] P. G. de Gennes, J. Bok, J. Prost and F. Brochard-Wyart. *P. G. De Gennes' impact on science: solid state and liquid crystals* (World Scientific, 2009). *(Cited on page 27.)*

[64] R. Landauer. Electrical resistance of disordered one-dimensional lattices. *Phil. Mag.* **21**, 863–867 (1970). *(Cited on pages 27 and 190.)*

[65] J. Lantz, V. S. Shumeiko, E. Bratus and G. Wendin. Phase-dependent multiple Andreev reflections in SNS interferometers. *Phys. Rev. B* **65**, 134523 (2002). *(Cited on page 29.)*

[66] A. Zazunov, V. S. Shumeiko, G. Wendin and E. N. Bratus'. Dynamics and phonon-induced decoherence of Andreev level qubit. *Phys. Rev. B* **71**, 214505 (2005). *(Cited on pages 33, 81, 89, 179, 198, 199, and 201.)*

[67] M. A. Despósito and A. Levy Yeyati. Controlled dephasing of Andreev states in superconducting quantum point contacts. *Phys. Rev. B* **64**, 140511 (2001). *(Cited on pages 34, 81, 88, 213, 214, and 216.)*

[68] V. Ambegaokar and A. Baratoff. Tunneling between superconductors. *Phys. Rev. Lett.* **10**, 486 (1963). *(Cited on pages 38, 100, and 246.)*

[69] Q. Le Masne, H. Pothier, N. O. Birge, C. Urbina and D. Esteve. Asymmetric noise probed with a Josephson junction. *Phys. Rev. Lett.* **102**, 067002 (2009). *(Cited on pages 38, 55, and 153.)*

[70] B. Huard. Interactions between electrons, mesoscopic Josephson effect and asymmetric current fluctuations. Ph.D. thesis. *Ann. Phys. (Paris)* **31**, No. 4–5 (2006). *(Cited on pages 39, 40, 41, 57, and 80.)*

[71] M. C. Koops, G. V. van Duyneveldt and R. de Bruyn Ouboter. Direct observation of the current-phase relation of an adjustable superconducting point contact. *Phys. Rev. Lett.* **77**, 2542–2545 (1996). *(Cited on page 39.)*

[72] Q. Le Masne. Asymmetric current fluctuations and Andreev states probed with a Josephson junction. Ph.D. thesis, Universitï¿œ Paris 6. *Available on-line at* `http://tel.archives-ouvertes.fr` (2009). *(Cited on pages 39, 43, 57, 59, 62, 63, 80, 154, 169, 217, and 220.)*

[73] P. Virtanen, F. S. Bergeret, J. C. Cuevas and T. T. Heikkilä. Linear ac response of diffusive SNS junctions. *Phys. Rev. B* **83**, 144514 (2011). *(Cited on page 39.)*

[74] J.-P. Cleuziou, W. Wernsdorfer, V. Bouchiat, T. Ondarçuhu and M. Monthioux. Carbon nanotube superconducting quantum interference device. *Nat. Nano.* **1**, 53–59 (2006). *(Cited on page 39.)*

[75] R. Maurand, T. Meng, E. Bonet, S. Florens, L. Marty and W. Wernsdorfer. First-order 0-Pi quantum phase transition in the Kondo regime of a superconducting carbon-nanotube quantum dot. *Phys. Rev. X* **2**, 011009 (2012). *(Cited on page 39.)*

[76] J. C. Cuevas, J. Heurich, A. Martín-Rodero, A. Levy Yeyati and G. Schön. Subharmonic shapiro steps and assisted tunneling in superconducting point contacts. *Phys. Rev. Lett.* **88**, 157001 (2002). *(Cited on pages 42 and 50.)*

[77] R. Duprat and A. Levy Yeyati. Phase diffusion and fractional Shapiro steps in superconducting quantum point contacts. *Phys. Rev. B* **71**, 054510 (2005). *(Cited on page 42.)*

[78] M. Chauvin. The Josephson effect in atomic contacts. Ph.D. thesis, Universitï¿œ Paris 6. *Available on-line at* `http://tel.archives-ouvertes.fr` (2005). *(Cited on pages 42, 43, 50, 51, 57, 80, and 169.)*

[79] C. Zener. Non-adiabatic crossing of energy levels. *Proc. R. Soc. A* **137**, 696–702 (1932). *(Cited on pages 44 and 210.)*

[80] D. Averin and A. Bardas. ac Josephson effect in a single quantum channel. *Phys. Rev. Lett.* **75**, 1831–1834 (1995). *(Cited on pages 44 and 46.)*

[81] Y. Naveh and D. V. Averin. Nonequilibrium current noise in mesoscopic disordered SNS junctions. *Phys. Rev. Lett.* **82**, 4090–4093 (1999). *(Cited on pages 45 and 50.)*

[82] G. E. Blonder, M. Tinkham and T. M. Klapwijk. Transition from metallic to tunneling regimes in superconducting microconstrictions: excess current, charge imbalance, and supercurrent conversion. *Phys. Rev. B* **25**, 4515 – 4532 (1982). *(Cited on page 46.)*

[83] E. N. Bratus', V. S. Shumeiko and G. Wendin. Theory of subharmonic gap structure in superconducting mesoscopic tunnel contacts. *Phys. Rev. Lett.* **74**, 2110 (1995). *(Cited on page 46.)*

[84] J. C. Cuevas, A. Martín-Rodero and A. Levy Yeyati. Hamiltonian approach to the transport properties of superconducting quantum point contacts. *Phys. Rev. B* **54**, 7366 (1996). *(Cited on page 46.)*

[85] R. Cron. Atomic contacts: a test-Bed for mesoscopic physics. Ph.D. thesis, Universitï¿œ Paris 6. *Available on-line at* `http://tel.archives-ouvertes.fr` (2001). *(Cited on pages 48, 49, 50, and 169.)*

[86] J. J. Riquelme, L. de la Vega, A. Levy Yeyati, N. Agraït, A. Martin-Rodero and G. Rubio-Bollinger. Distribution of conduction channels in nanoscale contacts: evolution towards the diffusive limit. *Europhys. Lett.* **70**, 663–669 (2005). *(Cited on page 48.)*

[87] J. C. Cuevas, A. Martín-Rodero and A. Levy Yeyati. Shot noise and coherent multiple charge transfer in superconducting quantum point contacts. *Phys. Rev. Lett.* **82**, 4086–4089 (1999). *(Cited on page 50.)*

[88] T. Hoss, C. Strunk, T. Nussbaumer, R. Huber, U. Staufer and C. Schönenberger. Multiple Andreev reflection and giant excess noise in diffusive SNS junctions. *Phys. Rev. B* **62**, 4079–4085 (2000). *(Cited on page 50.)*

[89] N. Agraït, A. Levy Yeyati and J. M. van Ruitenbeek. Quantum properties of atomic-sized conductors. *Phys. Rep.* **377**, 81 (2003). *(Cited on pages 50, 59, and 230.)*

[90] L. Bretheau, c. Ğirit, L. Tosi, M. Goffman, P. Joyez, H. Pothier, D. Esteve and C. Urbina. Superconducting quantum point contacts. *C. R. Physique* **13**, 89–100 (2012). *(Cited on page 50.)*

[91] R. S. Deacon, Y. Tanaka, A. Oiwa, R. Sakano, K. Yoshida, K. Shibata, K. Hirakawa and S. Tarucha. Tunneling spectroscopy of Andreev energy levels in a quantum dot coupled to a superconductor. *Phys. Rev. Lett.* **104**, 076805 (2010). *(Cited on page 51.)*

[92] T. Dirks, T. L. Hughes, S. Lal, B. Uchoa, Y.-F. Chen, C. Chialvo, P. M. Goldbart and N. Mason. Transport through Andreev bound states in a graphene quantum dot. *Nat. Phys.* **7**, 386–390 (2011). *(Cited on page 51.)*

[93] J. Moreland and J. W. Ekin. Electron tunneling experiments using Nb-Sn ''break'' junctions. *J. App. Phys.* **58**, 3888 (1985). *(Cited on page 55.)*

[94] C. Muller, J. van Ruitenbeek and L. de Jongh. Experimental observation of the transition from weak link to tunnel junction. *Physica C* **191**, 485–504 (1992). *(Cited on page 55.)*

[95] N. E. Booth. Quasiparticle trapping and the quasiparticle multiplier. *App. Phys. Lett.* **50**, 293 (1987). *(Cited on page 56.)*

[96] T. Greibe, T. Bauch, C. Wilson and P. Delsing. Improvement of chip design to reduce resonances in subgap regime of Josephson junctions. *J. Physics: Conf. Ser.* **150**, 052063 (2009). *(Cited on page 59.)*

[97] W. C. Stewart. Current-voltage characteristics of Josephson junctions. *App. Phys. Lett.* **12**, 277–280 (1968). *(Cited on pages 61 and 219.)*

[98] D. E. McCumber. Effect of ac impedance on dc voltage-current characteristics of superconductor weak-link junctions. *J. App. Phys.* **39**, 3113–3118 (1968). *(Cited on pages 61 and 219.)*

[99] V. Ambegaokar and B. I. Halperin. Voltage due to thermal noise in the dc Josephson effect. *Phys. Rev. Lett.* **22**, 1364–1366 (1969). *(Cited on pages 61 and 219.)*

[100] R. M. Dickson, A. B. Cubitt, R. Y. Tsien and W. E. Moerner. On/off blinking and switching behaviour of single molecules of green fluorescent protein. *Nature* **388**, 355–358 (1997). *(Cited on page 64.)*

[101] S. Volkan-Kacso, P. A. Frantsuzov and B. Janko. Correlations between subsequent blinking events in single quantum dots. *Nano Lett.* **10**, 2761–2765 (2010). *(Cited on page 64.)*

[102] M. Sillanpää, T. Lehtinen, A. Paila, Y. Makhlin and P. Hakonen. Continuous-time monitoring of Landau-Zener interference in a Cooper-pair box. *Phys. Rev. Lett.* **96**, 187002 (2006). *(Cited on page 77.)*

[103] S. Shevchenko, S. Ashhab and F. Nori. Landau–Zener–Stückelberg interferometry. *Phys. Rep.* **492**, 1–30 (2010). *(Cited on page 78.)*

[104] J. Lantz, V. Shumeiko, E. Bratus and G. Wendin. Flux qubit with a quantum point contact. *Physica C* **368**, 315–319 (2002). *(Cited on page 81.)*

[105] P. G. de Gennes. Boundary effects in superconductors. *Rev. Mod. Phys.* **36**, 225–237 (1964). *(Cited on page 81.)*

[106] J. P. Morten, A. Brataas and W. Belzig. Spin transport in diffusive superconductors. *Phys. Rev. B* **70**, 212508 (2004). *(Cited on page 86.)*

[107] D. González Olivares and A. Levy Yeyati. A simple model for the relaxation rates of quasiparticles trapped in SQPCs. *Private communication* (2012). *(Cited on page 87.)*

[108] D. A. Ivanov and M. V. Feigel'man. Two-level Hamiltonian of a superconducting quantum point contact. *Phys. Rev. B* **59**, 8444–8446 (1999). *(Cited on pages 89, 198, 201, 202, 203, 213, 214, 216, and 239.)*

[109] P. Santhanam and D. E. Prober. Inelastic electron scattering mechanisms in clean aluminum films. *Phys. Rev. B* **29**, 3733–3736 (1984). *(Cited on page 89.)*

[110] F. Pierre. Electron-electron interaction in mesoscopic wires. Ph.D. thesis. *Ann. Phys. (Paris)* **26**, No. 4 (2001). *(Cited on page 89.)*

[111] A. Anthore. Decoherence mechanisms in mesoscopic conductors. Ph.D. thesis, Universitï¿œ Paris 6. *Available on-line at* `http://tel.archives-ouvertes.fr` (2003). *(Cited on page 89.)*

[112] P. Joyez, D. Vion, M. Götz, M. H. Devoret and D. Esteve. The Josephson effect in nanoscale tunnel junctions. *J. Sup.* **12**, 757–766 (1999). *(Cited on page 100.)*

[113] C. Ciuti and I. Carusotto. Input-output theory of cavities in the ultrastrong coupling regime: the case of time-independent cavity parameters. *Phys. Rev. A* **74**, 033811 (2006). *(Cited on page 104.)*

[114] M. Devoret, S. Girvin and R. Schoelkopf. Circuit-QED: how strong can the coupling between a Josephson junction atom and a transmission line resonator be? *Ann. Phys. (Leipzig)* **16**, 767–779 (2007). *(Cited on page 104.)*

[115] T. Niemczyk, F. Deppe, H. Huebl, E. P. Menzel, F. Hocke, M. J. Schwarz, J. J. Garcia-Ripoll, D. Zueco, T. Hümmer, E. Solano, A. Marx and R. Gross. Circuit quantum electrodynamics in the ultrastrong-coupling regime. *Nat. Phys.* **6**, 772–776 (2010). *(Cited on page 104.)*

[116] S. M. Girvin, L. I. Glazman, M. Jonson, D. R. Penn and M. D. Stiles. Quantum fluctuations and the single-junction Coulomb blockade. *Phys. Rev. Lett.* **64**, 3183–3186 (1990). *(Cited on page 119.)*

[117] D. Averin, Y. Nazarov and A. Odintsov. Incoherent tunneling of the Cooper pairs and magnetic flux quanta in ultrasmall Josephson junctions. *Physica B* **165–166, Part 2**, 945–946 (1990). *(Cited on page 119.)*

[118] P. Delsing, K. K. Likharev, L. S. Kuzmin and T. Claeson. Effect of high-frequency electrodynamic environment on the single-electron tunneling in ultrasmall junctions. *Phys. Rev. Lett.* **63**, 1180–1183 (1989). *(Cited on page 119.)*

[119] L. J. Geerligs, V. F. Anderegg, C. A. van der Jeugd, J. Romijn and J. E. Mooij. Influence of dissipation on the Coulomb blockade in small tunnel junctions. *Europhys. Lett.* **10**, 79 (1989). *(Cited on page 119.)*

[120] A. N. Cleland, J. M. Schmidt and J. Clarke. Charge fluctuations in small-capacitance junctions. *Phys. Rev. Lett.* **64**, 1565–1568 (1990). *(Cited on page 119.)*

[121] F. D. Parmentier, A. Anthore, S. Jezouin, H. le Sueur, U. Gennser, A. Cavanna, D. Mailly and F. Pierre. Strong back-action of a linear circuit on a single electronic quantum channel. *Nat. Phys.* **7**, 935–938 (2011). *(Cited on page 119.)*

[122] G. Ponchak and A. Downey. Characterization of thin film microstrip lines on polyimide. *IEEE Trans. Comp. Pack. Manuf. Tech. Part B* **21**, 171 –176 (1998). *(Cited on pages 120 and 162.)*

[123] A. O. Caldeira and A. J. Leggett. Influence of dissipation on quantum tunneling in macroscopic systems. *Phys. Rev. Lett.* **46**, 211–214 (1981). *(Cited on pages 122, 123, 207, and 220.)*

[124] C. Cohen-Tannoudji, J. Dupont-Roc and G. Grynberg. *Atom-photon interactions: basic processes and applications* (Wiley, 1998). *(Cited on page 123.)*

[125] J. I. Cirac, A. S. Parkins, R. Blatt and P. Zoller. ''Dark'' squeezed states of the motion of a trapped ion. *Phys. Rev. Lett.* **70**, 556–559 (1993). *(Cited on page 123.)*

[126] C. A. Blockley, D. F. Walls and H. Risken. Quantum collapses and revivals in a quantized trap. *Europhys. Lett.* **17**, 509–514 (1992). *(Cited on page 123.)*

[127] G. Romero, I. Lizuain, V. S. Shumeiko, E. Solano and F. S. Bergeret. Circuit quantum electrodynamics with a superconducting quantum point contact. *Phys. Rev. B* **85**, 180506 (2012). *(Cited on pages 125, 284, and 286.)*

[128] E. Jaynes and F. Cummings. Comparison of quantum and semiclassical radiation theories with application to the beam maser. *Proc. IEEE* **51**, 89 – 109 (1963). *(Cited on page 129.)*

[129] H. Grabert, G. Ingold and B. Paul. Phase diffusion and charging effects in Josephson junctions. *Europhys. Lett.* **44**, 360–366 (1998). *(Cited on pages 138 and 250.)*

[130] A. C. Doherty. A note on a master equation approach to P(E) theory for the dynamical Coulomb blockade. *Private communication* (2011). *(Cited on page 140.)*

[131] M. H. Devoret, J. M. Martinis, D. Esteve and J. Clarke. Resonant activation from the zero-voltage state of a current-biased Josephson junction. *Phys. Rev. Lett.* **53**, 1260–1263 (1984). *(Cited on page 149.)*

[132] D. Vion, P. F. Orfila, P. Joyez, D. Esteve and M. H. Devoret. Miniature electrical filters for single electron devices. *J. App. Phys.* **77**, 2519–2524 (1995). *(Cited on page 171.)*

[133] K. Bladh, D. Gunnarsson, E. Hürfeld, S. Devi, C. Kristoffersson, B. Smålander, S. Pehrson, T. Claeson, P. Delsing and M. Taslakov. Comparison of cryogenic filters for use in single electronics experiments. *Rev. Sci. Instrum.* **74**, 1323–1327 (2003). *(Cited on page 171.)*

[134] H. le Sueur and P. Joyez. Microfabricated electromagnetic filters for millikelvin experiments. *Rev. Sci. Instrum.* **77**, 115102 (2006). *(Cited on page 171.)*

[135] J. Cuevas. Microscopic origin of conducting channels in metallic atomic-size contacts. *Phys. Rev. Lett.* **80**, 1066–1069 (1998). *(Cited on page 183.)*

[136] J. Michelsen, V. S. Shumeiko and G. Wendin. Manipulation with Andreev states in spin active mesoscopic Josephson junctions. *Phys. Rev. B* **77**, 184506 (2008). *(Cited on page 195.)*

[137] M. Buttiker. Coherent and sequential tunneling in series barriers. *IBM J. Res. Develop.* **32**, 63–75 (1988). *(Cited on page 197.)*

[138] A. Martín-Rodero, A. Levy Yeyati and F. J. García-Vidal. Thermal noise in superconducting quantum point contacts. *Phys. Rev. B* **53**, R8891–R8894 (1996). *(Cited on pages 198 and 203.)*

[139] C. W. J. Beenakker and H. van Houten. The superconducting quantum point contact. *arXiv:cond-mat/0512610* (2005). *(Cited on page 199.)*

[140] F. S. Bergeret, P. Virtanen, T. T. Heikkilä and J. C. Cuevas. Theory of microwave-assisted supercurrent in quantum point contacts. *Phys. Rev. Lett.* **105**, 117001 (2010). *(Cited on page 210.)*

[141] L. D. Landau. A theory of energy transfer II. *Phys. Z. Sowjetunion* **2**, 46–51 (1932). *(Cited on page 210.)*

[142] J. M. B. Kellogg, I. I. Rabi, N. F. Ramsey and J. R. Zacharias. The magnetic moments of the proton and the deuteron. The radiofrequency spectrum of H2 in various magnetic fields. *Phys. Rev.* **56**, 728–743 (1939). *(Cited on page 212.)*

[143] M. V. Berry. Quantal phase factors accompanying adiabatic changes. *Proc. R. Soc. A* **392**, 45–57 (1984). *(Cited on page 212.)*

[144] D. Xiao, M.-C. Chang and Q. Niu. Berry phase effects on electronic properties. *Rev. Mod. Phys.* **82**, 1959–2007 (2010). *(Cited on page 212.)*

[145] P. Hänggi, P. Talkner and M. Borkovec. Reaction-rate theory: fifty years after Kramers. *Rev. Mod. Phys.* **62**, 251 (1990). *(Cited on page 220.)*

[146] M. H. Devoret, D. Esteve, C. Urbina, J. M. Martinis, A. N. Cleland and J. Clarke. Quantum tunneling in condensed media. chap. Macroscopic quantum effects in the current-biased Josephson junction, 313 (Elsevier Science Publishers, 1992). *(Cited on page 220.)*

[147] H. Fritz and J. Ankerhold. Nonadiabatic transitions between adiabatic surfaces: phase diffusion in superconducting atomic point contacts. *Phys. Rev. B* **80**, 064502 (2009). *(Cited on page 220.)*

[148] Ivanchenko and Zilberman. Josephson effect in small tunnel contacts. *Sov. Phys. JETP* **28**, 1272 (1969). *(Cited on pages 249, 251, 255, and 264.)*

INDEX